# 19TH INTERNATIONAL COSMIC RAY CONFERENCE

LA JOLLA, USA AUGUST 11-23, 1985

NASA-CP-2376-VOL-2
19850025693



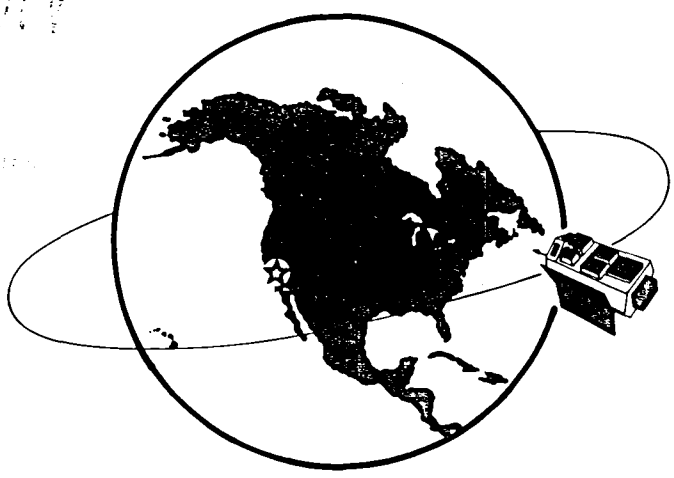

# CONFERENCE PROGRAM SESSIONS VOL. 2

# 19TH INTERNATIONAL COSMIC RAY CONFERENCE

LA JOLLA, USA AUGUST 11-23, 1985

## CONFERENCE PAPERS

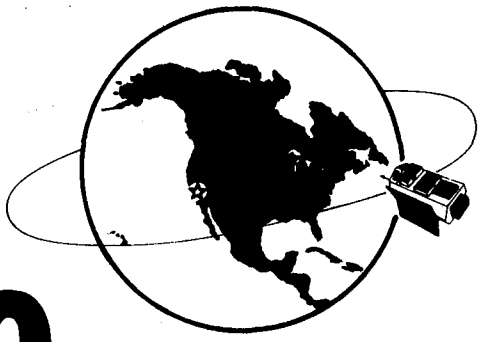

# OG

## SESSIONS
## VOL. 2

PUBLICATION COMMITTEE

F.C. Jones, Chm.
J. Adams
G.M. Mason

NASA Conference Publication 2376

Published by
Scientific and Technical Information Branch
National Aeronautics and Space Administration
Washington, D.C. 20546

August 1985

For sale by the National Technical Information Service, Springfield, VA 22151

# PREFACE

The 19th International Cosmic Ray Conference, under the auspices of the Cosmic Ray Commission of the International Union of Pure and Applied Physics, is being held on the campus of the University of California, San Diego, on 11 through 23 August 1985. In keeping with the tradition begun in 1971 by the Australian organizers of the 12th ICRC, the Proceedings of this conference are appearing in two sets of volumes. The first set, consisting of volumes 1 through 8, is being distributed to all participants at the beginning of the conference. This set contains the contributed papers. The second set, distributed after the conference, contains invited, rapporteur, and highlight papers. The papers are reproduced here exactly as they were received from the authors, without refereeing.

For the 19th ICRC, the scientific program was organized according to three major divisions— OG (cosmic rays and gamma rays of Galactic Origin), SH (Solar and Heliosphere), and HE (High Energy). Technical papers are included in each of the three divisions.

This conference depended on funds from several agencies of the United States government, including major financial support from the National Aeronautics and Space Administration and support from the National Science Foundation, the Department of Energy, and the Air Force Geophysics Laboratory. Important financial support also came from the Center for Astrophysics and Space Sciences of the University of California, San Diego, from the California Space Institute of the University of California, from the Department of Physics and Astronomy of the University of Maryland, College park, from the International Union for Pure and Applied Physics, and from several corporate sponsors who will be acknowledged by name in the post-conference volumes.

We appreciate the confidence placed in the conference organizers by the Cosmic Ray Commission, and acknowledge with thanks the role of the Commission members in setting up the rules for the conference and in advising the organizers during its planning.

We are grateful to all of the members of the various organising committees listed at the front of this volume. The three Program Committees went to great effort to organize a coherent scientific program and to schedule four parallel sessions with a minimum of conflicts. The Local Organising Committee has worked long and hard to ensure efficient and hospitable accommodations for all the participants, both in the scientific sessions and outside them. The Publications Committee not only took great pains to assemble these volumes but also maintained an orderly data base of papers and authors which was extremely helpful to the program committees. The General Organising Committee made important contributions of ideas and efforts to make the conference possible; this committee included international representation from all of North America, thus the departure from the traditional name of National Organising Committee. And the entire effort was coordinated by the dedicated members of the Steering Committee.

Martin H. Israel, Chairman
General Organising Committee

August, 1985

# LETTER FROM THE EDITORS

This conference marks a departure from previous conferences in this series in that the publication of the Conference Papers was carried out an entire continent away from the activities of Local Organizing Committee. This posed some problems but, to the considerable surprise of the Publications Committee members, the one that was expected to be the most trouble turned out not to be significant. The overwhelming majority of those submitting papers and abstracts sent them to the correct address, not to La Jolla as was feared. We wish to thank our many authors for their alertness and commend them for handling a complicated situation so well.

There are eight volumes to be distributed to the conference participants in addition to the Conference Program and Author Index: three volumes for OG, two for SH and three for HE. the detailed makeup of these volumes is described in the prefaces written by the Scientific Program chairmen for their respective volumes. Out of some 1100 abstracts that were accepted by the Scientific Program Committees for inclusion in the conference some 929 papers were finally received in time for inclusion in the Conference Papers. This represents a response of approximately 84 percent, a modest improvement. Even if one excludes the 42 one page papers that should be considered as "confirming abstracts", even though there was no such formal category, the response was somewhat higher than that of recent years. We attribute this to the carrot of a later deadline than before coupled with the stick of there being no printing of post deadline contributed papers. We believe that this decision of the General Organizing Committee was a wise one. Of course invited, rapporteur, and highlight talks will be printed in volumes to be distributed to the participants after the conference as usual.

The Publications Committee had much generous help in performing its duties: from Goddard Space Flight Center we had the help of B. Glasser, L. Harris, E. Schronce, N. Smith, J. Esposito and T. Smith. From the Naval Research Laboratory we were helped by T. Mazzotta, and at the University of Maryland M. L. Snidow and J. Mucha gave much needed assistance. Special thanks are due to Caryl Short, the lone staff member of the Publications Committee. She maintained the computer data base, organized the abstracts as they arrived, and kept track of the papers themselves to see that the finally arrived in the right place at the right time. Without her help the job would have been far more difficult than it was.

PUBLICATIONS COMMITTEE — August, 1985

Frank C. Jones, Chm.
Jim Adams
Glen M. Mason

# OG SESSIONS
# VOLUME II

# 19th INTERNATIONAL COSMIC RAY CONFERENCE
LA JOLLA, USA
AUGUST 11-23, 1985

## INTERNATIONAL UNION OF PURE AND APPLIED PHYSICS
## MEMBERS OF THE COMMISSION ON COSMIC RAYS OF IUPAP

A.E. Chudakov, Chm.
F.B. McDonald
G.C. Castagnoli
P.H. Fowler
D. Hovestadt
J. Kota
T.O. Montmerle
H. Moraal
J.R. Prescot
B.V. Sreekantan
K. Suga
J. Wdowczyk

## STEERING COMMITTEE

F. McDonald, Chm.
G. Burbage
M. Forman
T. Gaisser
M. Israel
F. Jones
R. Lingenfelter
R. Mewaldt
L. Peterson

## GENERAL ORGANIZING COMMITTEE

M. Israel, Chm.
M. Bercovitch
P. Freier
R. Gall
R. Jokipii
L. Jones
V. Jones
S. Krimigis
J. Kurfess
J. Lockwood
P. Meyer
B. Price
R. Ramaty
F. Reines
M. Shapiro
M. Shea
J. Simpson
E. Stone
D. Venkatesan
J. Waddington
S. White

## PROGRAM COMMITTEES

**OG SESSIONS**
R. Mewaldt, Chm.
G. Cassiday
C. Fichtel
A. Harding
J. Matteson
D. Muller
W. Webber

**SH SESSIONS**
M. Forman, Chm.
H. Hudson
G. Mason
B. McKibben
M. Pomerantz

**HE SESSIONS**
T. Gaisser, Chm.
K. Lande
J. Linsley
E. Loh
G. Yodh

**PUBLICATIONS**
F. Jones, Chm.
J. Adams
G. Mason

## LOCAL ORGANIZING COMMITTEE

L. Peterson,Chm.
G. Burbidge
R. Lingenfelter
R. Rothschild
J. Arnold
W. Baity
A. Buffington
M. Burbidge
W. Fillius
R. Gall
R. Gould
H. Hudson
J. Linsley
K. Marti
G. Masek
J. Matteson
C. McIlwain
R. Mewaldt
O. Piccioni
M. Thiemens
W. Thompson
H. Ticho
R. White

**Sponsored by**
National Aeronautics and Space Administration
National Science Foundation
Department of Energy
Center for Astrophysics and Space Science, University of California, San Diego
California Space Institute, University of California
Department of Physics and Astronomy, University of Maryland, College Park

## Preface to the OG Volumes

The contributed papers presented at the 19th International Cosmic Ray Conference were arranged into three major divisions: OG (for cosmic ray and $\gamma$-ray Origin and Galactic phenomena); SH (for Solar and Heliospheric phenomena); and HE (for High Energy phenomena). The OG division encompasses topics related to the origin of galactic cosmic rays and $\gamma$-rays, the nature and distribution of their sources, and their interactions with galactic fields and matter. Contributed papers for OG sessions were organized under the following headings:

OG1 $\gamma$-ray Bursts
OG2 $\gamma$-rays from Point Sources
OG3 Diffuse $\gamma$-ray Emission
OG4 Cosmic Ray Nuclei with <1 TeV (Composition, Spectra, and Anisotropy)
OG5 Cosmic Ray Nuclei with >1 TeV (Composition, Spectra, and Anisotropy)
OG6 Electrons, Positrons, and Antiprotons
OG7 Interstellar Propagation and Nuclear Interactions
OG8 Cosmic Ray Sources and Acceleration
OG9 Techniques and Instrumentation

Note that the present OG division is broader than in the past; it includes papers from both the OG and XG divisions at previous International Cosmic Ray Conferences, as well as many papers previously in the T division.

Approximately 400 preliminary abstracts were received under the OG headings listed above. These were organized into 32 contributed paper sessions for purposes of oral presentation. Papers and confirming abstracts for OG papers are contained in Volumes 1, 2, and 3 of these Proceedings. Volume 1 contains papers under headings OG1, OG2, and OG3; Volume 2 contains OG4, OG5, and OG6; while OG7, OG8, and OG9 are contained in Volume 3. Papers on topics of related interest appear in the SH proceedings (Volumes 4 and 5) and the HE proceedings (Volumes 6, 7, and 8).

Four rapporteur speakers were invited to review the OG contributed paper sessions and report on new results and developments, areas of controversy, and future research directions. The written versions of these papers will appear in a later volume of these proceedings, along with other invited papers.

I wish to thank the other members of the OG Program Committee for their help in defining the OG topics, in reading the abstracts and organizing the sessions, and for their advice on the selection of rapporteur, highlight, and invited speakers. Members of the committee include: G. L. Cassiday, Jr. (University of Utah); C. E. Fichtel and A. K. Harding (Goddard Space Flight Center); R. E. Lingenfelter and J. L. Matteson (University of California at San Diego); D. Muller (University of Chicago); and W. R. Webber (University of New Hampshire).

Richard A. Mewaldt
Chairman, OG Program Committee

This conference is the 19th in a series. Previous conferences in this series were held at:

| | | |
|---|---|---|
| Cracow, Poland | – | 1947 |
| Como, Italy | – | 1949 |
| Bagneres-de-Bigorre, France | – | 1953 |
| Guanjuato, Mexico | – | 1955 |
| Varenna, Italy | – | 1957 |
| Moscow, USSR | – | 1959 |
| Kyoto, Japan | – | 1961 |
| Jaipur, India | – | 1963 |
| London, UK | – | 1965 |
| Calgary, Canada | – | 1967 |
| Budapest, Hungary | – | 1969 |
| Hobart, Australia | – | 1971 |
| Denver, USA | – | 1973 |
| Munchen, FRG | – | 1975 |
| Plovdiv, Bulgaria | – | 1977 |
| Kyoto, Japan | – | 1979 |
| Paris, France | – | 1981 |
| Bangalore, India | – | 1983 |

## OG 4.1
## ELEMENTAL COMPOSITION AND ENERGY SPECTRA

VOLUME 2

VOLUME 2

OG 4.2
H AND He ISOTOPES

## OG 4.3
## COSMIC-RAY ISOTOPES

## OG 4.4
## OBSERVATIONS OF ULTRA HEAVY COSMIC-RAY NUCLEI

OG 5.1
COSMIC RAYS ABOVE 1 TEV: SPECTRA AND COMPOSITION

VOLUME 2

OG 5.2
COSMIC RAYS ABOVE 1 TEV: COMPOSITION

## OG 5.3
## COSMIC-RAY ANISOTROPY

VOLUME 2

OG 5.4
ORIGIN OF ULTRA-HIGH-ENERGY COSMIC RAYS

OG 6.1
ANTI-PROTONS AND RELATED SUBJECTS

OG 6.2
ELECTRONS, POSITRONS, AND RADIO MEASUREMENTS OF SYNCHROTRON RADIATION

# Absolute Rigidity Spectrum of Protons and Helium Nuclei Above 10 GV/c

R. L. Golden, S. Horan, B. Kimbell
Department of Electrical and Computer Engineering
New Mexico State University
Las Cruces, NM 88003
USA

G. D. Badhwar, J. L. Lacy, J. E. Zipse
NASA, Johnson Space Center
Houston, TX 77058
USA

R. R. Daniel, S. A. Stephens
Tata Institute of Fundamental Research
Homi Bhabha Road
Bombay, India 400 005

Abstract

Proton and helium nuclei differential spectra were gathered with a balloon borne magnet spectrometer. The data were fitted to the assumption that the differential flux can be represented by a power law in rigidity. In the rigidity range 10-25 GV/c the spectral indices were found to be $-(2.74 \pm 0.04)$ for protons and $-(2.71 \pm 0.05)$ for helium nuclei.

1. Introduction. The absolute rigiditiy spectra of protons and Helium nuclei have become particularly important due to the recent measurements of secondaries of these particles. The recent publication of the absolute e- spectrum necessitated a very careful analysis of the detection efficiencies and sensitivities of the New Mexico State University magnetic spectrometer. The maximum detectable momentum for the 1976 flight (reported here) was 80 GV/c. During the analysis, it was found that magnet spectrometer measurements in general are subject to systematic errors that affect the spectral index but not the absolute flux at low energies. In this paper we present a brief discussion of the systematic errors, and spectral indices for protons and helium nuclei in the rigidity range 10-25 GV/c. Absolute fluxes will be presented at the conference.

2. Data Analysis. The apparatus is described in detail in references (1) and (2). It was comprised of (top to bottom): a gas Cherenkov counter (G) with a proton Cherenkov threshold of 40 GV/c (rigidity); two plastic scintillators (S1 and S2); 8 multiwire proportional counters (MWPC); and a lead-scintillator shower counter consisting of 7 layers each containing 1 radiation length of lead (P1-P7). The MWPC provide 8 readouts on the x axis (axis of bending) and 4 readouts on the (orthogonal) y axis. All phototubes were pulse-height analyzed. Data readout was initiated for all occurences of an S1*P1*P7 and/or an S1*P1*P7*G coincidence. The geometric factor of the instrument was $324 \pm 5$ cm^2-str and the live-time fraction was 0.80. The data were

gathered on a balloon flight from Palestine, Texas on May 20, 1976. The data gathering period lasted 6.4 x 10^4 seconds at an average altitude of 5.8 gm*cm^-2. Data for the spectral analysis were selected from the flight tapes by requiring the following:

(1) The charge of the particle (as determined from S1 and S2) correspond to 0.0-1.8 charge units for protons or 1.8-2.7 charge units for helium.

(2) All MWPC readouts be valid and that the measured trajectory fit to a continuous track with a chi-square of 30 in the x axis, and 8 in the y axis.

Failure of particles to pass the above criteria was dominated by criterion 2. Each MWPC is only about 90% efficient. The measured efficiency for passing criterion 2 was 33% for protons and 24% for helium nuclei.

3. Results. Figures 1a and 1b show the proton and helium data gathered during the flight. The plots show number of events vs magnetic deflection (1/magnetic rigidity), measured in c/GV. The central part (deflection = 0) of each plot represents the highest rigidities. Moving toward the right corresponds to lower rigidities. The decline in number of particles to the right of 0.12 c/GV is due to the combined effects of solar modulation and the geomagnetic cutoff.

The data in Figure 1 have been analyzed by fitting them to the assumption that the differential flux is a power law in rigidity. Other factors which enter the fit are: the resolution function of the instrument, solar modulation, and the exact location of the zero-deflection point. The zero-deflection point in Figure 1 was determined by operating the instrument with the magnet off just prior to the flight. The center of the deflection distribution gathered with the magnet off is taken as the zero-deflection point, and the distribution of deflections is taken as the resolution function for the instrument. Figure 2 shows the resolution function.

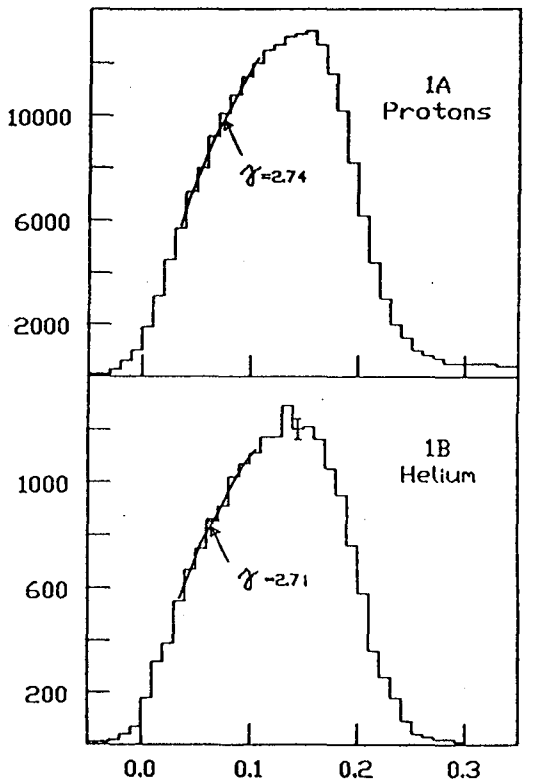


Figure 1. Deflection spectra

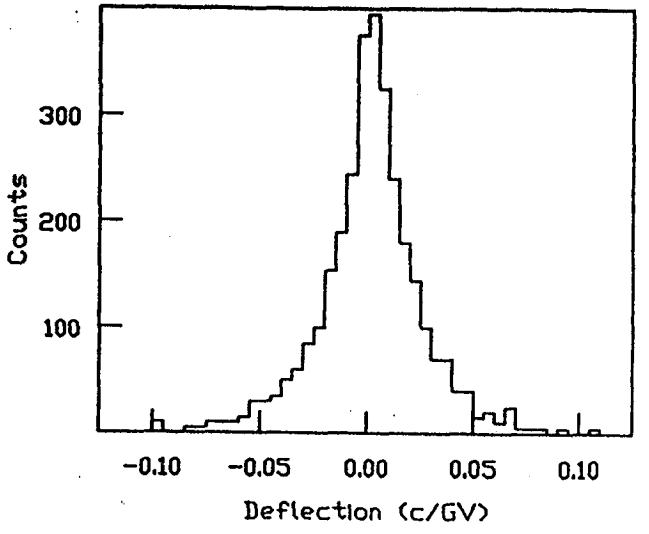


Figure 2
Resolution
Function

One of the most serious sources of possible systematic error for spectral indices is a change in the zero-deflection point between the calibration and the flight. It was hoped to turn the magnet off at the end of the flight for another calibration, but the instrument operation ended abruptly due to battery failure and the calibration was not performed. A cross-check was made however, by using the G-on protons and helium gathered during the flight. These two samples were fit assuming the proton Cherenkov threshold of 40 GV/c (helium threshold of 80 GV/c). Since the Cherenkov thresholds are near the upper limit of the instrument to resolve the deflection, the dominant factor in the fits was the offset of the zero-deflection point. The offset was determined to be $-(0.002\pm0.002)$ c/GV. In order to minimize the effects of the offset error, solar modulation and possible changes in the resolution function, we limit our analyses to the deflection range 0.1-0.04 c/GV (10-25 GV/c rigidity). Further, we have used a solar modulation of 600 MeV, which was determined using the data below 10 GV/c. Under these circumstances we find $\gamma = -(2.74\pm0.04)$ for protons and $-(2.71\pm0.05)$ for helium nuclei. The uncertainty in the proton spectral index is dominated by the offset uncertainty, and statistics dominates the uncertainty for helium nuclei.

References

(1) Golden, R. L. et al. (1978), Nuc. Instr. and Meth. 148, 179.

(2) Golden, R. L. et al. (1984), Ap. J. 287, 622.

# SOURCE SPECTRAL INDEX OF HEAVY COSMIC RAY NUCLEI

J.J. Engelmann, P. Ferrando, L. Koch-Miramond, P. Masse, A. Soutoul
Service d'Astrophysique, CEN Saclay, F-91191 Gif sur Yvette Cedex
FRANCE
W.R. Webber
Space Science Center, University of New Hampshire, Durham, NH 03824
USA

1. Introduction. From the energy spectra of the heavy nuclei observed by the French-Danish experiment on HEAO-3, we have derived the source spectra of the mostly primary nuclei (C, O, Ne, Mg, Si, Ca and Fe) in the framework of an energy dependent leaky box model (Engelmann et al. 1985). The energy dependence of the escape length was derived from the observed B/C and sub-iron/iron ratios and the presently available cross sections for C and Fe on H nuclei (Koch-Miramond et al., 1983). A good fit to the source energy spectra of all these nuclei was obtained by a power law in momentum with an exponent $\gamma = -2.4 \pm 0.05$ for the energy range 1-25GeV/n (Engelmann et al. 85). Comparison with data obtained at higher energy suggested a progressive flattening of these spectra.
In the present paper we want to derive more accurate spectral indices by using better values of the escape length based on the latest cross section measurements (Webber 1984, Soutoul et al. this conference). Our aim is also to extend the analysis to lower energies down to 0.4GeV/n (kinetic energy observed near earth), using data obtained by other groups. The only nuclei for which we have a good data base in a broad range of energies are O and Fe , so the present study is restricted to these two elements.

2. Derivation of the source spectra. We work along the same lines as in Engelmann et al. 1985. We first derive the interstellar spectrum by "demodulating" the observed spectrum, using the "force field approximation" (Gleeson and Axford, 1968) ; then we correct the demodulated flux values for the nuclei of secondary origin produced the interstellar medium and for the energy loss suffered by the particles during their propagation. We get the interstellar flux of the "surviving" primaries J(E), which is related to the source strength dQ/dE by the relationship :

$$\frac{dQ}{dE} \propto J(E)\left(\frac{1}{\lambda_{di}} + \frac{1}{\lambda_e(E)}\right) - \frac{\partial}{\partial E}\left[J(E)\frac{dE}{dx}\right] \qquad (1)$$

where $\lambda_{di}$ is the pathlength for nuclear destruction of the element i in the interstellar medium and $\lambda_e$ is the escape length, the value of which is derived in a companion paper (Soutoul et al., 1985). $\partial / \partial E$ is the ionization energy loss term and dE/dx is the stopping power of the particle in pure H.
When applying this step by step procedure, we are faced with two difficulties : i) if the modulation correction is too large, the uncertainty on its value will lead to a large uncertainty in the interstellar flux value. To keep this kind of error at a relatively low level, we select among the published data those registered in such conditions (energy range, modulation level) that the modulation

correction on the flux values does not exceed 35%. When this condition is fulfilled an error of 0.10 GV on the modulation parameter around a mean value of 0.40GV leads to a maximum error of 10% on the flux value corrected for modulation. ii) For the flux value registered by a particular experiment at a given energy, there are two major causes of errors : the statistical error and a systematic error due to the uncertainties on the exposure factor of the instrument and on the atmospheric corrections for balloon experiments. If we renormalize the data in order to put certain flux values from different experimenters in agreement we introduce a subjective feeling in the choice of these flux values. To avoid this problem we do not try to derive from the data the absolute flux values but merely the spectral indices measured by each experimenter in given energy ranges.

3. Data base used in this study. Our data base is listed in Table I

| Reference | Date of measurement | Mont Washington neutron monitor count rate | Modulation parameter $\Phi$ GV | Type of particle | Selected energy range |
|---|---|---|---|---|---|
| Webber 85[1] | 1974, July | 2290 | 0.50 | O,Fe | 0.95-6 |
| Webber 85[1] | 1977, Sept. | 2360 | 0.35 | O,Fe | 0.65-6 |
| Webber 85[1] | 1974,77,78 | 2300 | 0.50 | O,Fe | 10.5-112 |
| HEAO-3[2] | 1979 Oct. to 1980 June | 2190 | 0.60 | O,Fe | 1.3-25 |
| Juliusson 74 | 1971-72 Sept | 2350 | 0.40 | O | 23-76 |
| Orth & al.78 | 1972 Sept | 2350 | 0.40 | O,Fe | 2.4-11 |
| Maehl & al77 | 1973 Aug. | 2350 | 0.40 | O,Fe | 0.85-2.25 |
| Caldwell 77 | 1974 Sept | 2310 | 0.50 | O | 5.5-95 |
| Minagawa 81 | 1975 Sept | 2404 | 0.30 | Fe | 1.5-8.0 |
| Simon & al80 | 1976 Oct. | 2420 | 0.30 | O,Fe | 2.5-630 |

(1) These data consist of revisited flux values obtained in several balloon flights and published in Lezniak and Webber 1978 and Webber 1983. More accurate atmospheric corrections have been applied.
(2) Juliusson et al., 1983 ; Engelmann et al., 1985.

The modulation parameter $\Phi$ characterising the conditions prevailing at the time of each experiment can be correlated to the counting rate of the Washington neutron monitor (Lockwood and Webber 1979, 1981).
The interstellar energy spectra dJ/dE of O and Fe derived from these selected data after demodulation have been plotted in Fig. 1 as a function of the momentum of the particle.

4. Results. As can be seen in Fig. 1, the differences between the experimental points obtained at the same energy are much larger than the errors quoted by the authors. As mentioned above this is probably due to errors on the geometry and efficiency of the experiments and on the atmospheric corrections. So we consider separately each experiment, and for some of them we devide the energy range they cover into several energy intervals. For each experiment and energy domain we derive the spectral index $\gamma$ of the source strength assumed to follow the law :

$$dQ/dE = KP^{-\gamma} \qquad (2)$$

where P is the momentum of the particle in GeV/c/n. The values of the $\gamma$ index for O and Fe have been plotted as a function of momentum in

Fig.2 and 3 respectively.
For O the data seem to be consistent with a constant $\gamma$ index above 4GeV/c/n with a weighted mean value $\gamma_o$=2.29+0.03 (Note that the HEAO results are significantly above the average ; excluding these data would lead to a weighted mean $\gamma_o$=2.22+0.04). Below 4GeV/c/n, the index seems to increase when the momentum decreases, up to $\gamma_o \simeq 2.9$ at 1.5GeV/c/n. For Fe we find for the weighted mean a value of $\gamma_{Fe}$=2.36+0.05 which is nearly the same as that found for O at high energy. But the increase observed for O at low energy does not seem present for Fe, although the large error bars and the scarcity of the points at low energy prevent us from drawing any definite conclusion.
The quoted errors on $\gamma$ are due to the errors on the flux values and to the spread of the corresponding points. If we include in addition the error on $\lambda_e$ due to cross section errors on the production of B by spallation of heavier nuclei and of Fe secondaries by spallation of Fe, we get the final values $\lambda_o$ (H.E.)=2.29+0.06 and $\lambda_{Fe}$=2.36+0.07. Therefore a unique power law in momentum does not hold for the O source spectrum. What about a power law in total energy, which we have used earlier (Perron et al., 1981)?:

$$dQ/dE = K' E_{Tot}^{-\gamma'} \qquad (3)$$

The $\gamma'$ index values from the experimental data have been plotted as a function of the kinetic energy for O nuclei in Fig. 4. The weighted mean $\gamma$ value above 3 GeV/n is again 2.29+0.03 and the same type of increase is observed when going towards lower energies.
It is worthwhile to stress that this type of increase cannot be due to an error in the modulation correction (unless the modulation theory is grossly in error). An error of +0.1GV around an average value of 0.4GV for the modulation parameter would lead to an error of +0.07 on the spectral index around 1GeV/n, i.e. about 10 times less than the index variation observed between 1 and 3GeV/n (interstellar kinetic energy).

4. Conclusion. We find, at least for O nuclei an apparent increase of the $\gamma$ index of the source spectrum below 3GeV/n. Is this low energy steepening of the spectrum real ? As discussed above, the careful selection of the data used in this study should prevent the demodulation to be responsible for this result. As concerns the partial cross sections from which the escape length is derived, the uncertainty in their values may introduce an error on the source abundances. If some energy dependences were left on the cross section errors, these would propagate into an error on the source spectral index. It is precisely in the energy region where the $\gamma$ index is changing (0.8 to 3GeV/n) that the cross sections were measured with the best accuracy (Webber,1984). From the quoted errors, we calculate that a possible energy dependence on $\sigma$ could be responsible at maximum for an apparent slope of 0.05, far smaller than the observed $\gamma$ variation.
This apparent increase of the source spectrum at low energy can be brought together with the flattening of the CNO source spectrum observed in the TeV energy region (Engelmann et al. 1985). It is in agreement with our suggestion that a soft component with a source spectral index around 2.7 may be superposed on a common source spectrum, including H and He, with a spectral index $\gamma \simeq 2.1$. In the few GeV/range, both components would contribute to the observed flux of heavies, leading to a spectral index around 2.3 .

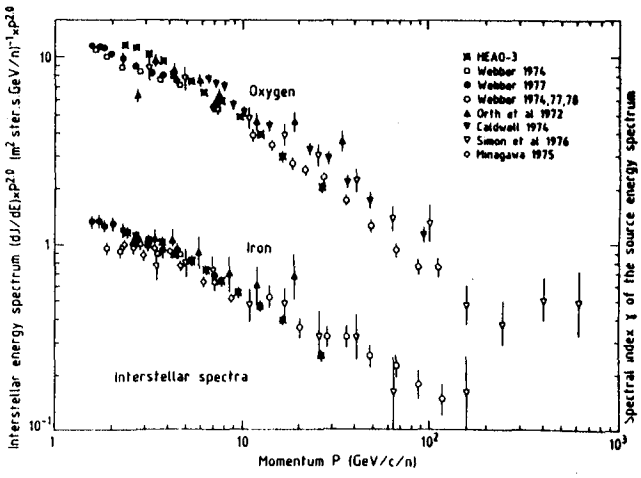


Fig. 1 : Near-earth interstellar spectra of O and Fe nuclei, derived from experimental data corrected for the effect of solar modulation. The differential energy flux values have been plotted as a function of the momentum P. The spectra have been "flattened" by multiplication by $P^{2.0}$.

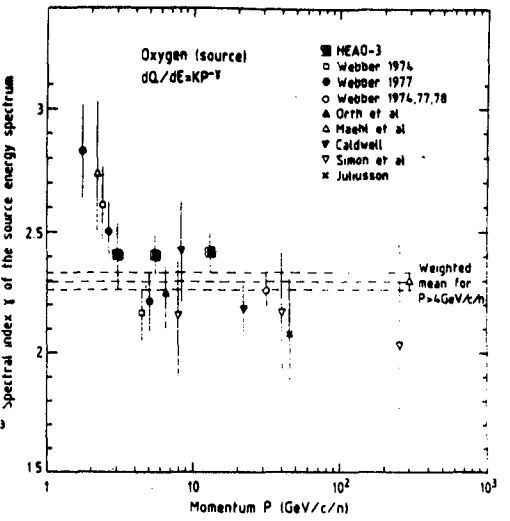


Fig. 2 : Oxygen source spectral index $\gamma$ plotted as a function of momentum P, assuming for the spectral shape a power law in momentum.

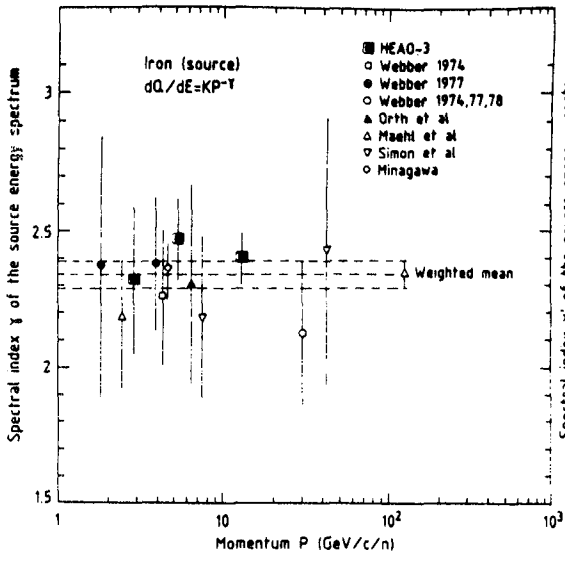


Fig. 3 : Iron source spectral index plotted as a function of momentum, assuming for the spectral shape a power law in momentum.

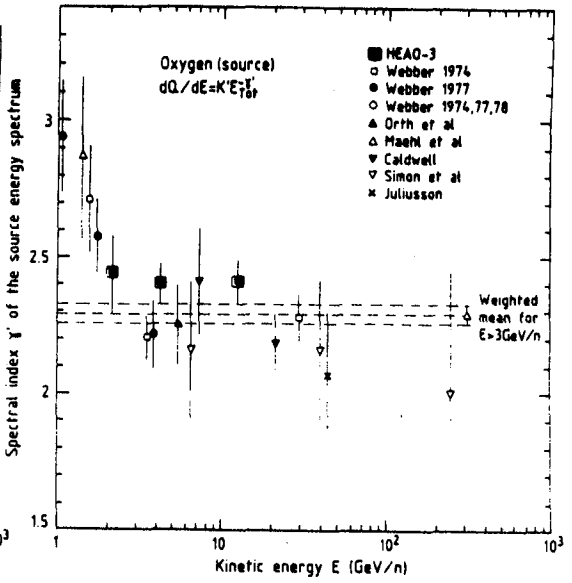


Fig. 4 : Oxygen source spectral index $\gamma$ plotted as a function of kinetic energy, assuming for the spectral shape a power law in total energy.

References

Caldwell, J.H., 1977, Astrophys. J. 218, 269
Engelmann, J.J. et al. 1985, to be published in Astron. Astrophys.
Garcia Munoz, M. et al., 1977, 15th ICRC, Plovdiv, 1, 230
Gleeson, L.J., Axford, W.I., 1968, Astrophys. J., 154, 1011
Juliusson, E., 1974, Astrophys. J. 191, 331
Koch-Miramond L. et al., 1983, 18th ICRC, Bangalore, 9, 275
Lezniak, J.A. , Webber, W.R., 1978, Astrophys. J., 223, 676
Lockwood, J.A., Webber W.R., 1981, 17th ICRC, Paris, 3, 259
Maehl, R.C. et al., 1977, Astrophys. and Space Science 47, 163
Minagawa, G., 1981, Astrophys. J. 248, 847
Orth, C.D. et al., 1978, Astrophys. J., 226, 1147
Perron C. et al., 1981, 17th ICRC, Paris, 9, 118
Simon, M. et al., 1980, Astrophys. J., 239, 712
Soutoul, A. et al., 1985, this conf., paper OG.4.1-3.
Webber, W.R., 1983, in Composition and origin of Cosmic Rays, ed. M.M. Shapiro, Reidel, Dordrecht.
Webber, W.R., 1984, Cosmic Ray Workshop, Baton-Rouge.

# CHARGE AND ENERGY DEPENDENCE OF THE RESIDENCE TIME OF COSMIC RAY NUCLEI BELOW 15 GEV/NUCLEON

A. Soutoul, J.J. Engelmann, Ph. Ferrando, L. Koch-Miramond, P. Masse
Service d'Astrophysique, CENSaclay, F-91191 Gif sur Yvette CEDEX FRANCE

W.R. Webber
Space Science Center, University of New Hamsphire, Durham,NH03824 USA

## 1 INTRODUCTION.

The relative abundance of nuclear species measured in cosmic rays at earth has often been interpreted with the simple leaky box model. For this model to be consistent an essential requirement is that the escape length does not depend on the nuclear species. The discrepancy between escape length values derived from iron secondaries and from the B/C ratio was identified by Garcia-Munoz and his co-workers using a large amount of experimental data [7-10]. Ormes and Protheroe found a similar trend in the HEAO data although they questioned its significance against uncertainties [9]. They also showed that the change in the B/C ratio values implies a decrease of the residence time of cosmic rays at low energies in conflict with the diffusive convective picture [11-12]. These conclusions crucially depend on the partial cross section values and their uncertainties. Recently new accurate cross sections of key importance for propagation calculations have been measured [6] Their statistical uncertainties are often better than 4% and their values significantly different from those previously accepted [6]. In this paper we use these new cross sections to compare the observed B/C+O and (Sc to Cr)/Fe ratio to those predicted with the simple leaky box model.

## 2 PROPAGATION CALCULATIONS.

We have used the Comstock computer code previously used by Koch et al,Perron et al.[1-2-3]. The calculation is performed for the simple leaky box model, with an exponential distribution of path lengths in pure hydrogen and takes into account $\beta$-decay for long lived species,ionisation energy losses and solar modulation using the force field approximation [4].
The neglect of interstellar helium in propagation calculations is questionable (see OG 7.2-11 this conference).
The input source spectra are identical for all species with a power law in momentum [5].
Nuclear cross sections are based on experimental data wherever possible and are listed in Perron et al. [2]. The cross sections for boron and iron secondaries are those measured by Webber [6]. We otherwise use Silberberg and Tsao's formulae [19].
The computer code uses a stepwise procedure to solve the set of first order differential equations. In the energy and charge range of this paper the energy loss term cannot be neglected and we have checked that it is accurately calculated.

## 3 RESULTS.

Above 1 GeV/n and at low energies we analyse satellite data which are free from atmospheric effects and have high statistical accuracy [7-8]. At intermediate energies we analyse balloon data as well [13-14-15-16-17-18]. The experimental data for the B/C+O ratio are shown in figure 1. This ratio was

chosen because it is relatively insensitive to possible small differences between observed and computed C/O ratio throughout the whole energy range [5]. Also we adjust the source abundances especially those of the main progenitors of boron so that their calculated abundances are close enough to their observed values.

We first compare the calculation to the HEAO B/C+O data. The deceleration parameter appropriate for these data is taken equal to 600MV [5]. We try values of the mean escape length varying with energy according to:

$$(1)\quad \lambda esc=\lambda b*\beta*R^{-\delta} \qquad R > 5.5GV$$
$$\lambda esc=\lambda b*\beta*5.5^{-\delta} \qquad R < 5.5GV$$

where R and $\beta$ are the interstellar values of the rigidity and the velocity relative to that of light.

We find that $\lambda b=24.0$ g/cm² and $\delta=.65$ provide a reasonably good agreement in the HEAO energy range (see figure1).

Then we perform a set of propagation calculations with a grid of slightly different values of $\lambda b$ around its nominal value. From this we can derive the values of $\lambda esc$ which precisely yield all the observed B/C+O values and their statistical uncertainties as well (figure 3).

This procedure is repeated for the (Sc to Cr)/Fe ratio with trial functions:

$$(2)\quad \lambda esc=\lambda f*\beta*(1+.4/Ekin)*R^{-\delta} \qquad R > 5.5GV$$
$$\lambda esc=\lambda f*\beta*(1+.4/Ekin)*5.5^{-\delta} \qquad R < 5.5GV$$

where Ekin is the interstellar kinetic energy in GeV/n. The term in parenthesis takes conveniently care of a steepening that is not present in the B/C+O data. Good agreement with the data is found for $\lambda f=26.8$ g/cm² and $\delta=.65$ (see figure2). From a set of propagation calculations with different $\lambda f$ we derive the $\lambda esc$ values yielding each experimental point (figure 3).

We then compare the B/C+O ratio calculated with (1) to the low energy data. For this ratio the calculation is dependent on the adopted solar modulation level. Figure 1 shows the calculated curves for 490MV and 350MV [7] (See also OG 4.1-2 this conference). We also wish to check the sensitivity of these results to the adopted $\beta$ dependence in (1) (constant residence time below 5.5GV). The ratio calculated with a mean escape length independent of energy and equal to 7 g/cm² is plotted on figure 1 for the same levels of modulation as above.

For the (Sc to Cr)/Fe the low energy results of calculations with constant escape length are shown on figure 2. Three distinct values are considered: 7g/cm², which is appropriate for comparison to the low energy B/C+O data; 11g/cm² consistent with that found around 2GeV/n and finally an infinite escape length correspondind to complete confinement.

## 4 DISCUSSION.

The abundance ratio calculated with (1) and (2) and a deceleration parameter of 600MV agree reasonably well with the HEAO data (figure 1 and 2).

Perron et al. have suggested that these data are consistent with larger values of $\delta$ than previously calculated from balloon data [2]. Further calculations showed that even larger values of $\delta$ would provide a better fit [3-9]. Our adopted value of $\delta$ is in agrement with these results. The flattening in $\lambda esc$ for boron is not observed for iron secondaries, in the HEAO data (see figure 3).This difference could be even more marked below 1GeV/n although large statistical uncertainties of the (Sc to Cr)/Fe ratio in balloon data do not allow to draw firm conclusions. Interestingly enough the low energy satellite

data and the HEAO data around 1 GeV/n are consistent with the same value of λesc within uncertainties for iron secondaries (see figure 2).
At low energies the dependence of the escape length with energy from the B/C+O ratio is less than previously reported [7-9-10]. Indeed if a modulation level as low as 350MV is adopted a constant grammage(7 g/cm$^2$) would keep agreement with the B/C+O data,whereas for a larger modulation level a constant residence time would agree better.
The values of λesc yielding the experimental HEAO ratio are shown in figure 3 together with those calculated from (1) and (2). The differences between the escape length values derived from iron secondaries and from boron are statistically significant especially below 4 GeV/n. They are larger than those reported by Koch et al. and similar to those from Ormes and Protheroe [3-9]. At low energies, calculations with the escape length from B/C+O ratio underestimate iron secondaries by a large factor (see figure 2). Above 1GeV the (Sc to Cr)/Fe ratio predicted from (1) is also plotted on figure2. The underestimate of this ratio resulting from the use of (1) could be accounted for by a 5% overestimate of partial cross sections for boron and an underestimate of similar amount for those of subiron secondaries. Systematic errors can be generated by the calculation of cross sections. Partial cross sections from iron have been accurately measured at several energies below 2GeV/n and show a rather steep and quite consistent energy dependence [6]. Starting from this grid the program calculates the cross sections at all other energies.We estimate that for reasonably smooth interpolation , possible systematic errors on the calculated ratio below 2 GeV/n are less than 4% for iron secondaries and even smaller for boron where partial cross sections are nearly independent of energy.

## 5 CONCLUSION.

We have compared the observed B/C+O and (Sc to Cr)/Fe ratio between 100 MeV/n and 15 GeV/n to those calculated with the simple leaky box model. This calculation incorporates several important cross sections recently measured with high accuracy [6]. The large energy range considered here allows a detailed study of their energy dependence. At high energies our adopted rigidity dependence agrees well with previous studies [3-9].
For the B/C+O ratio the data from 2 GeV/n down to 100 MeV/n can be accounted for with a constant escape length if the modulation is moderately strong(350MV). If the modulation is as strong as 500MV a turn over may be present around 2.GeV/n and a constant residence time consistent with diffusion convection theory would agree better with the data [12].
The (Sc to Cr)/Fe ratio is less sensitive than the B/C+O ratio to the precise shape of the escape length energy dependence below 2Gev/n. The IMP data at low energy and the HEAO data below 2Gev/n can be accounted for with similar values of the escape length within uncertainties,whereas at intermediate energies larger values would provide a better agreement with the ballon data.
However, our calculations fails to reproduce the observed ratios with the same escape length for boron and iron secondaries. This effect is quite marked at low energies and it is still present in the HEAO data at least up to 4GeV/n. Part of this discrepancy may be due to our interpolation of partial cross sections. Some truncation of pathlength may be indicated by the low and high energy data as well [7-10].

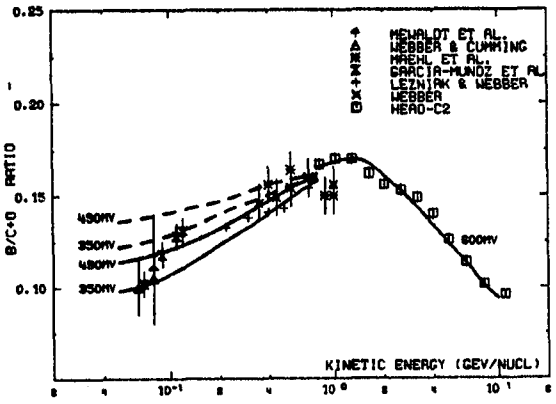


FIG 1- B/C+O RATIO
Full lines: calculated with formula (1). See text.
Dashed lines:calculated with escape length 7 g/cm2. Modulation level as indicated.

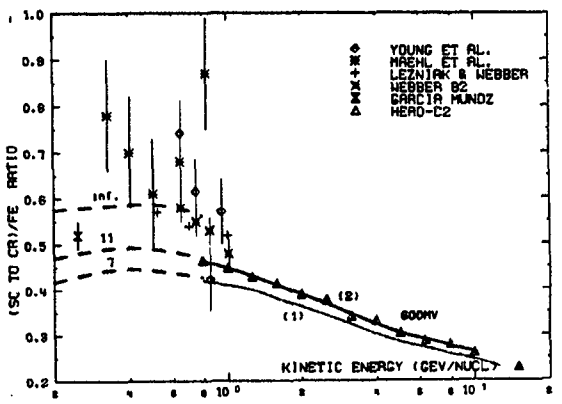


FIG 2- (Sc to Cr)/Fe RATIO
Full lines: calculated with formula (1) or (2). See text.
Dashed lines:calculated with constant escape length. From top to bottom: infinite (complete confinement), λesc=11 g/cm2 , λesc=7 g/cm2

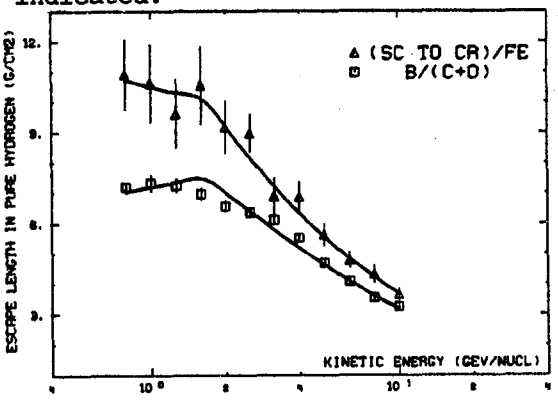


FIG 3- ESCAPE LENGTH IN PURE HYDROGEN FROM THE HEAO DATA.
Data points:escape length values from observed ratio of fig 1 and fig 2. Uncertainties: statistical only. Full lines:calculated from formula(1) (bottom) and formula(2) (top).

REFERENCES

1.Koch L. et al., 1981, 17th ICRC, Paris, 2, 18.
2.Perron C. et al.,1981, 17th ICRC, Paris, 9,118.
3.Koch L. et al., 1983, 18th ICRC, Bangalore, 9,275.
4.Gleeson L.J. and Axford W.I., 1968, Ap.j. 154,1011.
5.Engelmann JJ. et al., 1985,to be published in Astron. Astrophys.
6.Webber W.R.,Oct 1984, Workshop on Cosmic Rays, Baton-Rouge.
7.Garcia-Munoz et al., 1984, Ap. J. 280, L13 and references therein.
8.Engelmann JJ. et al.,1983, 19th ICRC, Bangalore, 9,97.
9.Ormes J.F. and Protheroe R.J, 1983, Ap. J., 272,756.
10.Gusik T.G. and Wefel J.P. 1984, Adv. Space Res. Vol.4, No.2-3, 93.
11.Jokipii J.R. 1976, Ap. J. 208, 900.
12.Jones F.C. 1979, Ap. J. 229, 747.
13.Young J.S. et al., 1981, Ap. J. 246,1014.
14.Webber W.R., Cumming A.C, 1983, Proceeding of Solar Wind V.
15.Maehl R.C et al., 1977, Ast. Sp. Science 47, 163.
16.Lezniak J.A. and Webber W.R.,1978, Ap. J. 223, 676. in Webber 1983.
Lezniak J.A and Webber W.R., 1979, Ap. Space Science, 63, 35. in Webber 1983.
17.Webber W.R., 1983, In composition and origin of CR, ed.MM. Shapiro Reidel, Dordrecht.
18.Mewalt R.A. et al., 1981, Ap. J. 251 127.
19.Silberberg R. and Tsao C.H., 1973, Ap. J. suppl. 25, 315.
Silberberg R. and Tsao C.H., 1977, 15th ICRC, Plodiv, 2, 84.
Tsao C.H. and Silberberg R., 1979, 16th ICRC, Kyoto, 2, 202.

# RELATIVE ABUNDANCES OF SUB-IRON TO IRON NUCLEI IN LOW ENERGY (50-250 MeV/N) COSMIC RAYS AS OBSERVED IN THE SKYLAB EXPERIMENT

N.Durgaprasad, J.S.Yadav and S. Biswas
Tata Institute of Fundamental Research, Bombay 400005 India.

## ABSTRACT

A Lexan polycarbonate detector exposed on the exterior of Skylab-3 for 73 days during a solar quiet period was used to study the relative abundances of calcium to nickel ions in low energy cosmic rays of 50-250 MeV/N. The method of charge identification is based on the measurement of conelength (L) and residual range (R) of these particles in various Lexan sheets. Since more than one cone (sometimes as many as five) is observed and is measured, the charge accuracy becomes precise and accurate. The ratio of (calcium to manganese) to (iron and cobalt) obtained at three energy intervals of 50-80, 80-150, 150-250 and 50-250 MeV/N are 7.6 $\pm$ 3.8, 2.7 $\pm$ 0.8, 1.4 $\pm$ 0.6 and 3.3 $\pm$ 0.7 respectively. These data thus indicate a large increase of this ratio with decreasing energy. The origin of this strong energy dependence is not understood at present.

1. Introduction. The origin and propagation of low energy (<200 MeV/N) cosmic ray nuclei in source regions, interstellar space and interplanetary space could be inferred from a study of the composition and energy spectra of calcium to nickel nuclei of the same energy. For this purpose, it is assumed that iron is the most abundant element in this group in the source region. It is further assumed that most of the other elements (calcium to manganese) result from the spallation of iron nuclei in the interstellar medium. The balloon studies relate to particles of energy above 200 MeV/N. The intensity of calcium to iron ions in the vicinity of the earth are quite low, so that fairly large detector areas with long exposure times outside the earth's atmosphere are necessary to study the nuclei in the cosmic radiation. In the present work, we report the results of fluences and relative abundances of calcium to nickel ions in the energy range 50-250 MeV/N. The detector used is a plastic Lexan polycarbonate detector of collecting power $1.1 \times 10^9$ $cm^2$ sec exposed for 73 days during a solar quiet time, from 22nd Nov.1973 1800 UT to 2nd Feb.1974 1800 UT.

No prominent solar activity was recorded during this period. Thus low energy galactic cosmic ray nuclei could be easily observed at the Skylab orbit. The method and accuracy of charge identification used, the estimation of energy, fluences and relative abundances were described earlier (Biswas and Durgaprasad 1980). A discussion of the results will be made in the third section. Earlier results of the work were reported before (Biswas et al.,1975, Durgaprasad et al.,1979 and Ramadurai et al.,1984).

2. Experimental Procedure. A stack of 32 sheets of Lexan polycarbonate sheets, each of dimensions 20 x 8.8 x 0.025 cm, covered with aluminium foil of various thicknesses ranging from 27 mg $cm^{-2}$ to 108 mg $cm^{-2}$ was used to record nuclei from calcium to iron. Actual dimensions of sheets used in this analysis, is one-fourth sheet, each of dimensions 10 x4.4 x 0.025 cm. The top ten and bottom ten sheets of 32 plates were scanned for double cones and followed further till they were either brought to rest or left the stack. An area of about 25.0 $cm^2$ was scanned in each of the top ten sheets. The trajectories of the tracks were followed through the stack, until the end of their ranges. Tracks due to heavy nuclei entering through the top surface and stopping in the first ten sheets were used for analysis of particles of energy around 60 MeV/N, while those stopping in the bottom ten sheets were used for analysis of particles around 150 MeV/N. The measurement and analysis of track parameters were done according to standard procedures (see for details Biswas and Durgaprasad, 1980).

The charge calibration of nuclei was done as follows: For each nucleus, track conelength (L) vs residual range(R) plots were made. In such a plot, well defined groups of tracks occurring for tracks of $R < 100\mu$ were assigned to oxygen. The highest range points were ascribed to iron nuclei. Calcium to iron nuclei in passing through the stack give rise to various cones before coming to rest. Charge assignment for each cone has been made to the nearest charge $\triangle Z = 0.1$. A nucleus may produce more than one cone. In such a case, the most probable value is estimated to the nearest value of 0.1 charge accuracy ($\triangle Z/\sqrt{n}$ where n is the number of cones).

Charge values have been assigned to all the cones and later to the incident nuclei. From the residual range and charge value, the energies have been assigned using the range-energy relationship of Henke and Benton (1967).

3. Results and Discussion. In Table 1, we show the fluences of particles of charges ranging from 20 to 27 for energy intervals of 50-80, 80-150, 150-250 and 50-250 MeV/N.

Table 1 - Relative Abundances(R, A) of Ca-Co Nuclei in Skylab Experiment

| Z / E | 50-80 MeV/N | | 80-150 MeV/N | | 150-250 MeV/N | | 50-250 MeV/N | |
|---|---|---|---|---|---|---|---|---|
| | N | R.A. | N | R.A. | N | R.A. | N | R.A. |
| 20 | 6 | 1.52 | 3 | 0.37 | 2 | 0.81 | 11 | 0.67 |
| 21 | 1 | 0.25 | 3 | 0.39 | 0 | 0.00 | 4 | 0.26 |
| 22 | 7 | 1.76 | 8 | 0.97 | 0 | 0.00 | 15 | 0.91 |
| 23 | 5 | 1.27 | 3 | 0.36 | 1 | 0.33 | 9 | 0.54 |
| 24 | 9 | 2.30 | 7 | 0.77 | 0 | 0.00 | 16 | 0.90 |
| 20-24 | 28 | 7.11 | 24 | 2.86 | 3 | 1.15 | 55 | 3.29 |
| 25 | 2 | 0.48 | 3 | 0.34 | 1 | 0.21 | 6 | 0.33 |
| 20-25 | 30 | 7.59 | 27 | 3.20 | 4 | 1.35 | 61 | 3.61 |
| 26 | 4 | 1.00 | 10 | 1.00 | 5 | 1.00 | 19 | 1.00 |
| 27 | 0 | 0.00 | 2 | 0.19 | 0 | 0.00 | 2 | 0.10 |
| 26-27 | 4 | 1.00 | 12 | 1.19 | 5 | 1.00 | 21 | 1.10 |
| 25-27 | 6 | 1.48 | 15 | 1.53 | 6 | 1.21 | 27 | 1.43 |
| Ratio | | | | | | | | |
| $\frac{20-24}{25-27}$ | 4.8 ± 2.2 | | 1.9 ± 0.6 | | 1.0 ± 0.7 | | 2.30± 0.5 | |
| $\frac{20-25}{26-27}$ | 7.6 ± 3.8 | | 2.7 ± 0.8 | | 1.4 ± 0.6 | | 3.3 ± 0.7 | |

The relative abundances of the particles of charges of Z = 20-24 and Z = 20-25 as well as of Z = 25-27 are shown in this table. It can be seen from this table that nuclei of even charge Z = 20, 22, 24 are as abundant, if not more than, as iron nuclei in the low energy 50-80 MeV/N range. Their abundances decrease with increasing energy. The ratios of Z = 20-25/26-27 in the energy intervals of 50-80, 80-150, 150-250 and 50-250 MeV/N are 7.6 ± 3.8, 2.7 ± 0.8, 1.4 ± 0.6 and 3.3 ± 0.7.

In Fig. 1, we plot the ratio Ca-Mn/Fe obtained in balloon and other experiments. This ratio also shows a decreasing trend towards increasing energy. This is interpreted as that the matter traversed by the Fe group nuclei is much larger, may be as nearly as five times (Ramadurai, et al.,1984) than the ones by the high energy particles.

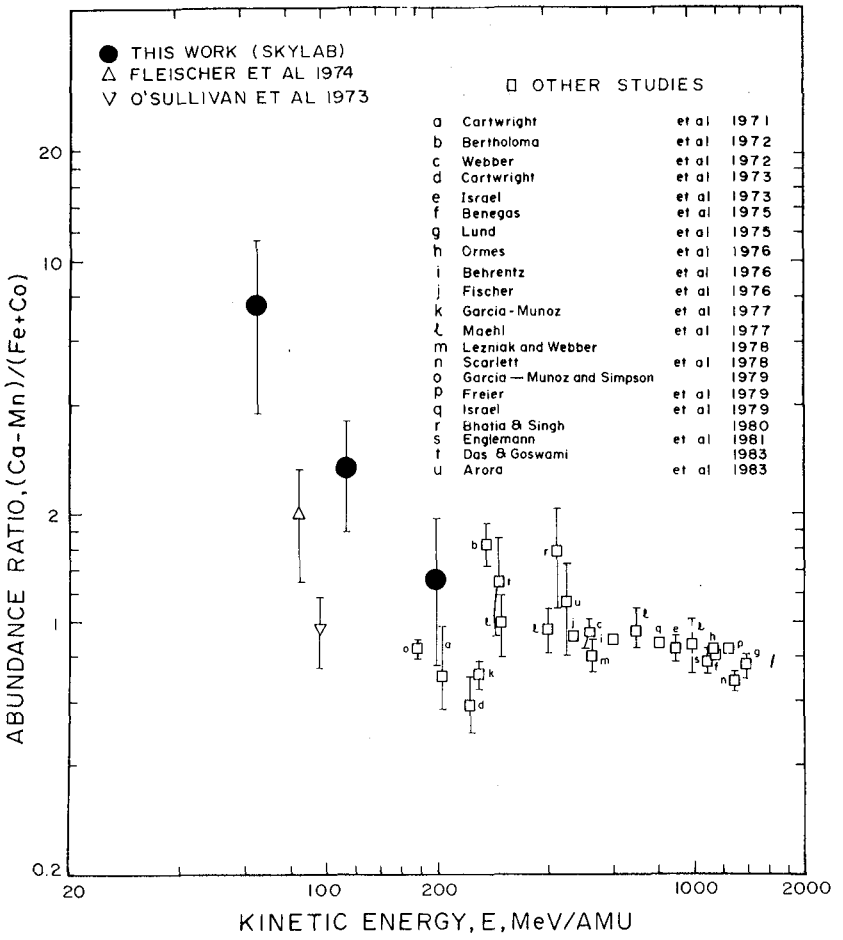


Fig. 1 Ratio of abundances of (Ca-Mn) to (Fe+Co) group as a function of energy.

## References

1. Biswas, S. and Durgaprasad, N., Space Sci. Rev., 25, 285, 1980.
2. Biswas, S., Nevatia, J., Durgaprasad, N., and Venkatavaradan, V.S., Nature, 258, 409, 1975.
3. Durgaprasad, N., Venkatavaradan, V.S., Sarkar, S. and Biswas, S., Proc. 16th ICRC, Kyoto, 1, 296, 1979.
4. Ramadurai, S., Vahia, M.N., Yadav, J.S., Biswas, S. and Durgaprasad, N., Proc. of COSPAR meeting, 1984, Advances in Space Research, 4, 97, 1984.
5. Henke, R.P. and Benton, E.V., US Naval Rad. Defence Lab., TR-67-122, 1967.

# COSMIC RAY CHARGE AND ENERGY SPECTRUM MEASUREMENTS USING A NEW LARGE AREA CERENKOV x dE/dx TELESCOPE

*W. R. Webber, J. C. Kish & D. A. Schrier*
*Space Science Center*
*University of New Hampshire*
*Durham, NH 03824*

1. Introduction. A detailed study of the energy spectra and relative abundance of Z = 4 - 14 nuclei contains valuable information relating to the acceleration and propagation of cosmic rays in the galaxy. Nuclei such as C, O, Ne, Mg and Si are mainly source nuclei and possible differences in their spectra at both high and low energies are sensitive measures of cosmic ray source spectra and propagation effects. Nuclei such as Be, B and N are mainly produced by interstellar fragmentation and their relative abundances provide a direct measure of the interstellar path length as a function of energy.

The most precise and complete study of the relative abundances of these nuclei is from the French-Danish experiment on board HEAO-3. This experiment, which flew in 1979-80, measured nuclei with Z = 4 - 30, over the energy range ~ 1 - 15 GeV/nuc. Engelmann et al., 1983. Absolute intensities were not reported in this experiment and a possible energy dependent bias in the flash tube efficiency for lower Z nuclei could affect the B/C ratio.

We have flown in September, 1981, a new 0.5$m^2$ ster cosmic ray telescope to study the charge composition and energy spectrum of cosmic ray nuclei between 0.3 and 4 GeV/nuc. A high resolution Cerenkov counter, and three dE/dx measuring scintillation counters, including two position scintillators were contained in the telescope used for the charge and energy spectrum measurements. The analysis procedures did not require any large charge or energy dependent corrections, and absolute fluxes could be obtained to an accuracy ~ 5%. The spectral measurements made in 1981, at a time of extreme solar modulation, could be compared with measurements with a similar telescope made by our group in 1977, at a time of minimum modulation and can be used to derive absolute intensity values for the HEAO measurements made in 1979-80. Using both data sets precise energy spectra and abundance ratios can be derived over the entire energy range from 0.3 to greater than 15 GeV/nuc.

1. Instrumentation & Data Analysis. The telescope used in these studies is shown in Figure 1a. The registration of an event is accomplished by a coincidence between PS1 & PS2, defining a geometry factor of 0.46 ± 0.01 $m^2$-ster. The total live time is 95,800 sec. including a measured data analysis and transmission efficiency of 0.93 ± 0.01, giving an A Ω t of 44,050$m^2$-ster-sec. To obtain absolute intensities at the instrument the observed events need only be divided by A Ω t. All events are initially accepted for analysis, however consistency criteria are placed on the relative outputs of the three separate dE/dx counters to remove nuclear interactions etc. in the telescope. Matrices of C1 vs. the avg. of the three S counters, subject to these criteria, exhibit clearly defined charge lines as shown in Figure 1b and these matrices are directly used to obtain the various charge abundances. The major source of charge dependent uncertainity in the absolute abundances, and in the ratios we derive, comes from the

above consistency criterion correction which varies from 1.217 for B to 1.086 for S. Finally to correct the intensities to the top of the atmosphere one must consider the 7.1 g/cm$^2$ of material in the telescope and gondola and the 3.6 g/cm$^2$ of residual atmosphere. This correction amounts to a factor of 1.596 for Oxygen nuclei with an uncertainty of ± 5%. This correction ranges from 1.332 for B to 1.887 for S, and the relative uncertainty in the ratios of this correction is less than 3%.

For each charge we have constructed a histogram of events in the C dimension from the matrices as illustrated in Figure 1b. Histograms for Be through O nuclei are shown in Figure 2. This distribution of events vs. $C/C_{max}$ may be transformed into an energy spectrum using deconvolution procedures similar to those discussed by Lezniak, 1975. In this approach there are several key steps. First the $\beta = 1$ point must be determined for each charge to an accureacy of < 1%. Second the resolution function for $\beta = 1$ particles for each charge must be determined and finally an appropriate Cerenkov relation modified for residual scintillation and knock-on electrons must be used to transform from Cerenkov output to energy. Space does not permit these procedures to be discussed in detail, however there are many tests that can be used to verify their accuracy. When one is comparing ratios of adjacent charges, for example, it is useful to form ratios of events vs. $C/C_{max}$ such as shown in Figure 3 for B/C. The instrumental effects that could change this ratio are easily identified (e.g. the increase above $C/C_{max} = 1.0$ is caused by the different resolution for B and C nuclei) and most of the change that is observed is believed to be due to a real change in the B/C ratio with energy.

3. Data and Discussion. In Figure 4 we show the B/C ratio derived from this measurement and that observed by Engelmann et al., 1983. In general, there is quite good agreement, but below ~ 3 GeV/nuc our values of this ratio are lower by ~ 5-10%. Some of this difference may be due to the larger solar modulation at the time of our measurement but we believe there is also a significant difference in the two results in this energy range. Since this ratio is used by most workers to derive the amount of interstellar material traversed as well as its energy dependence, this result will lead to modifications of these conclusions. In Figure 5 we show that N/O ratio derived from this measurement and that reported by Engelmann et al., 1983. Here the agreement is excellent. We are not aware of any charge or energy dependent effects in our analysis that could produce differences of > 1-2% in our relative B/C and N/O ratios and this N/O measurement therefore seems to support the suggestion of a systematic effect in the B/C ratio.

In Figure 6 we show the Oxygen spectrum derived from this work as well as the spectrum previously reported from a 1977 balloon flight with a similar type of instrument (Webber et al., 1979). The earlier reported spectra have been modified slightly as a result of using improved data analysis procedures compatible with the analysis of the 1981 balloon flight data. It is seen that the intensity in 1981 is a factor ~ 2 lower at 1 GeV/nuc than in 1977. This is compatible with the Mt. Washington neutron monitor rates on the dates of the two measurements, which were 2365 in 1977 and 2118 in 1981 for a decrease of 10.5%. At the time of the HEAO measurement in 1979-80 we obtain an average neutron monitor rate = 2190, and the HEAO spectrum, normalized accordingly, is shown in Figure 6. This spectrum is ~ 30% lower than that utilized by Engelmann et al., 1984 where they normalized to intensity measurements made at 10 GeV/nuc. However with this new normalization, which essentially fits data between ~ 0.7 and 4.0 GeV/nuc, the HEAO intensities above ~ 10 GeV/nuc are now ~ 30% lower than the average reported intensities from several observers. This suggests possible systematic differences between the high and low energy spectra ~ 30%, which could distort the spectral shape of the derived interstellar energy spectrum in this energy range.

In Table I we present integral intensities of various nuclei > 400 MeV/nuc and 4 GeV/nuc obtained in 1981, that may be used to compare with earlier values reported in the literature.

4. Acknowledgements. This work was supported by a NASA Grant #NGR-30-002-052.

5. References.

Engelmann, J. J., et al., Proc. 18th ICRC, 2, 17, 1983.
Engelmann, J. J. et al., Astron. Astrophys., in press, 1985.
Lezniak, J. A., Nuc. Inst. & Methods, 126, 129, 1975.
Webber, W. R., & Yushak, S. M. Proc. 16th ICRC, 1, 383, 1979.

6. Figure Captions.

Figure 1a, b. Outline drawing of telescope and matrix of C, N, O events.
Figure 2. Cerenkov distributions for Be-O nuclei. Estimated resolution for $\beta = 1$ particles is shown.
Figure 3. Ratio of B/C events as a function of $C/C_{max}$.
Figure 4. Observed B/C ratio at top of atmosphere in 1981. HEAO data from Engelmann et al., 1983 also shown.
Figure 5. Observed N/O ratio + HEAO data.
Figure 6. Observed Oxygen spectra in 1977 and 1981 ( $xE^{2.5}$ ) along with normalized HEAO spectrum.

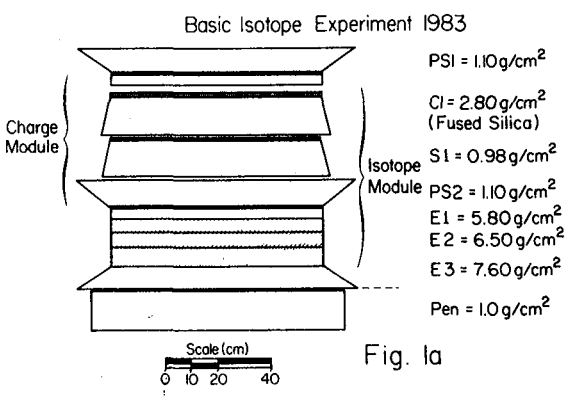


Fig. 1a

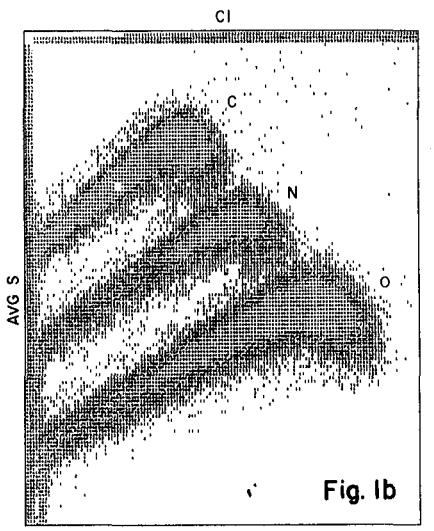


Fig. 1b

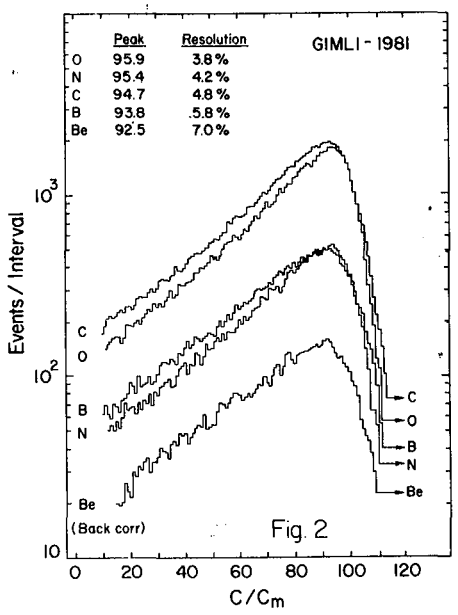


Fig. 2

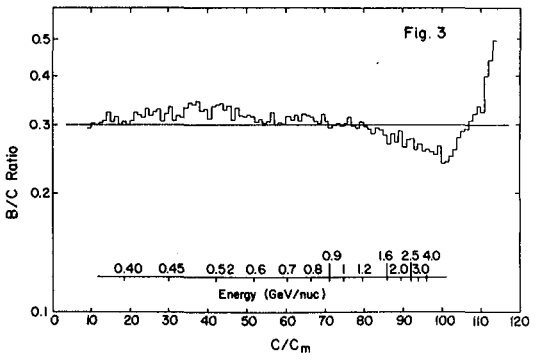

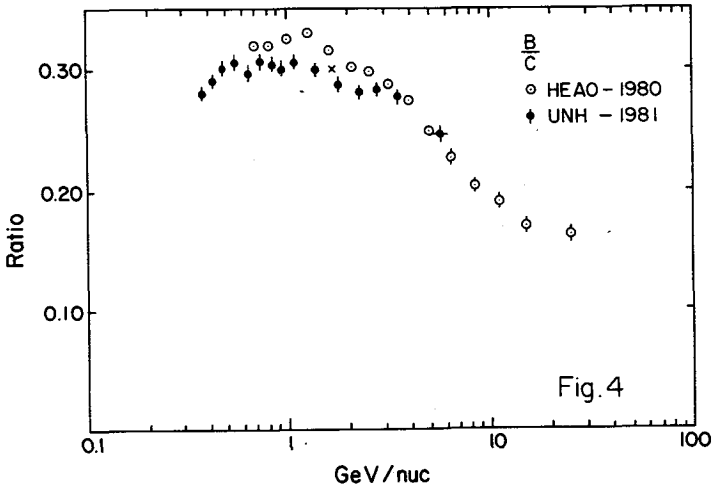


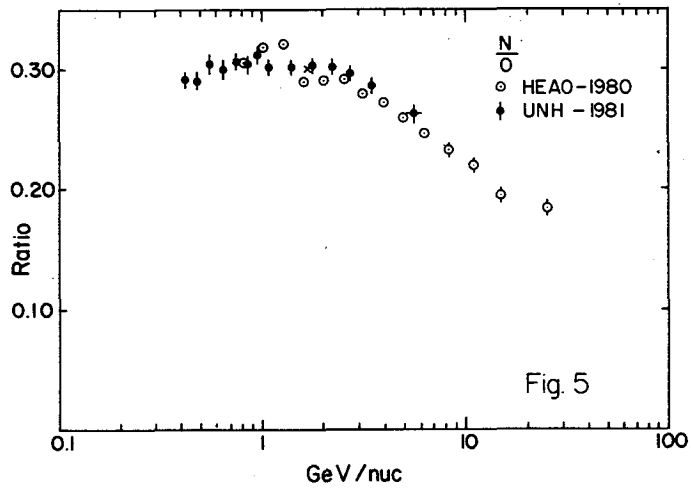


Table I

Absolute Intensities
At Top of Atmosphere
Aug. 27-28, 1981
Balloon Flight

| | > 400 MeV/nuc | > 4.0 GeV/nuc |
|---|---|---|
| Be | 9258c[a] → 0.314p[b] | 2,328c → 0.0764p |
| B | 28,824c → 0.937p | 7,140c → 0.215p |
| C | 100,860c → 3.28p | 28,020c → 0.876p |
| N | 26,526c → 0.898p | 6,960c → 0.224p |
| O | 89,184c → 3.03p | 26,105c → 0.845p |
| Ne | 14,436c → 0.498p | 4,241c → 0.143p |
| Mg | 17,604c → 0.632p | 5,304c → 0.186p |
| Si | 13,056c → 0.487p | 3,876c → 0.144p |
| S | 2,832c → 0.109p | 862c → 0.0327p |

a Number of events observed after selection criteria

b Intensity at top of atmosphere in particles/$m^2$ ster-sec. ≡ peters

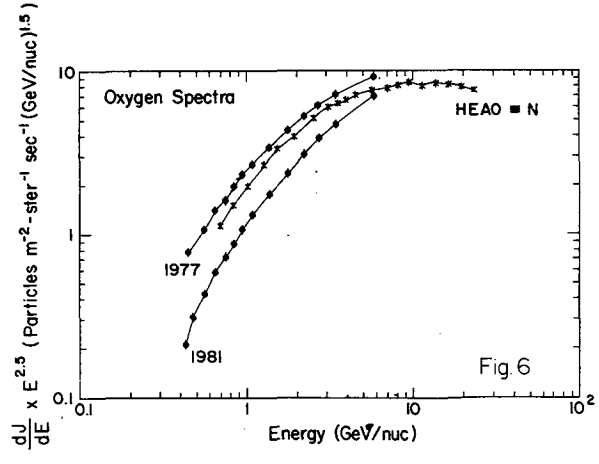

# A MEASUREMENT OF THE COSMIC RAY ELEMENTS C TO Fe IN THE TWO ENERGY INTERVALS 0.5-2.0 GeV/n AND 20-60 GeV/n

J.H. Derrickson, T.A. Parnell, and J.W. Watts
Space Science Laboratory, NASA, Marshall Space Flight Center, USA

J.C. Gregory
Department of Chemistry, University of Alabama Huntsville, Huntsville, Alabama

Introduction. The study of the cosmic ray abundances beyond 20 GeV/n provides additional information on the propagation and containment of the cosmic rays in the galaxy. Since the average amount of interstellar material traversed by cosmic rays decreases as its energy increases, the source composition undergoes less distortion in this higher energy region. However, data over a wide energy range is necessary to study propagation parameters. We present some measurements of some of the primary cosmic ray abundance ratios at both low (near 2 GeV/n) and high (above 20 GeV/n) energy and compare them to the predictions of the leaky box model. In particular, the integrated values (above 23.7 GeV/n) for the more abundant cosmic ray elements in the interval C through Fe and the differential flux for carbon, oxygen, and the Ne,Mg,Si group will be presented. Limited statistics have prevented the inclusion of the odd Z elements.

Instrument and the Exposure. The instrument has been previously described [1] and will be briefly reviewed here with the exposure parameters. The apparatus consists of a freon -12 gas Cerenkov detector (index of refraction = 1.001) for differential energy measurements between 20 and 60 GeV/n. Two banks of six 5-inch photomultiplier tubes viewed the freon gas which was contained in a thin fiberglass tank lined with millipore paper. The pulse height information from each set of tubes allowed correction for those cosmic ray events where a particle passage or delta rays obviously affected one bank of tubes. Two solid Cerenkov radiators (teflon and lucite) were included for charge identification. The teflon (effective index = 1.36) and pilot 425 (effective index = 1.52) radiators were placed in individual white boxes coated with $BaSO_4$ paint and each was observed by eight 5-inch photomultiplier tubes.

To further aid in event selection, two dual gap ion chambers filled with Xenon and a plastic scintillator (NE 102) were included. The scintillator was also housed in a light collecting box viewed by four tubes. An eight plane multi-wire hodoscope was used to determine the particle trajectory through the instrument. The track information was used in correcting the pulse height information for path length variations and for nonuniform response in the detectors, and it was an effective tool in removing background events such as showers, fragmentation events, and events outside the defined geometry of the experiment. For the detector arrangement, refer to Figure 2 in reference [1]. This instrument was flown from Pierre, South Dakota in September of 1978 at an average depth in the atmosphere of 3.6 g/cm$^2$. The collection factor for the flight was 2.8 M$^2$ ster.hrs.

Corrections to the Data. The track fitting routines screened the majority of atmospheric showers, some interacting events, and events that missed one or more of the detectors. The detector signals were corrected for the path length difference and the nonuniformity in detector response. Pulse height consistency criteria were then applied to eliminate remaining background events, mainly those interacting in the instrument. The energy calibration of the freon-12 Cerenkov counter was accomplished by isolating the elements and finding saturation values ($\beta = 1$). For oxygen, close to 150 photoelectrons were collected. Eight percent of this saturation signal was a scintillation component due to various effects including energetic delta rays. With this information, the energy measurement was unfolded following the method found in the appendix of reference [2]. The charge of the events above 20 GeV/n was determined by summing the saturated signals of the lucite and teflon Cerenkov detectors. The charge resolution ($\sigma$) obtained for events with kinetic energy >25 GeV/n was slightly better than 0.25. The separation into charge groups was done as suggested in both references [2] and [3]. The even integer charge is defined as $Z_{even} \pm 0.625$, and the odd integer charge is $Z_{odd} \pm 0.375$. The charge deconvolution or overlap corrections for C, N, and O are respectively 0.98, 1.09, 0.99 for energies greater than 25 GeV/n.

Finally nuclear fragmentation corrections for both the instrument and overlying atmosphere were performed according to the method outlined in reference [4] with the fragmentation cross-sections taken from reference [5]. The cross-sections were evaluated in the asymtotic region (E = 2 GeV/n) and applied to the 25 to 60 GeV/n energy interval with the assumption that the scaling correction is minor.

Results and Conclusions The results of the 1978 flight are listed in Tables I and II. The errors quoted are based on counting statistics only.

Table I

($E_K$ > 23.7 GeV Per nucleon)

| | Integrated Flux in particles/($M^2$·Ster·Secs) | Ratios* |
|---|---|---|
| C | $(5.2 \pm 0.3) \times 10^{-2}$ | 0.98 ± 0.08 |
| N | $(1.2 \pm 0.1) \times 10^{-2}$ | 0.23 ± 0.02 |
| O | $(5.3 \pm 0.3) \times 10^{-2}$ | 1.00 ± 0.08 |
| Ne | $(1.1 \pm 0.1) \times 10^{-2}$ | 0.21 ± 0.02 |
| Mg | $(1.2 \pm 0.1) \times 10^{-2}$ | 0.23 ± 0.02 |
| Si | $(8.8 \pm 1.3) \times 10^{-3}$ | 0.17 ± 0.03 |
| MnFeCo | $(5.9 \pm 1.1) \times 10^{-3}$ | 0.11 ± 0.02 |

* Normalized to Oxygen

Table II

Differential Flux

in particles/($M^2$·Ster·Secs·GeV per nucleon)

$(N \pm \Delta N)^{-m} \equiv (N \pm \Delta N) \times 10^{-m}$

| Kinetic Energy (GeV/n) | Carbon | Oxygen | NeMgSi |
|---|---|---|---|
| 25.8 | $(3.6 \pm 0.3)^{-3}$ | $(3.6 \pm 0.4)^{-3}$ | $(2.3 \pm 0.3)^{-3}$ |
| 30.0 | $(2.7 \pm 0.3)^{-3}$ | $(2.3 \pm 0.3)^{-3}$ | $(1.4 \pm 0.2)^{-3}$ |
| 33.9 | $(1.6 \pm 0.2)^{-3}$ | $(1.7 \pm 0.3)^{-3}$ | $(8.3 \pm 1.9)^{-4}$ |
| 39.8 | $(7.2 \pm 1.1)^{-4}$ | $(9.3 \pm 1.3)^{-4}$ | $(4.4 \pm 1.0)^{-4}$ |
| 50.6 | $(1.9 \pm 0.4)^{-4}$ | $(2.3 \pm 0.5)^{-4}$ | $(1.6 \pm 0.5)^{-4}$ |
| 61.8 | $(4.6 \pm 0.8)^{-4}$ | $(3.7 \pm 0.8)^{-4}$ | $(2.5 \pm 0.7)^{-4}$ |

The data is in general agreement with previous balloon results. A comparison of the ratios in Table I with the French-Danish experiment on HEAO-3 [6] is within one to two sigma of their values at 25 GeV/n except for the ratio Ne/O.

In Table III, we have selected some key primary to primary cosmic-ray abundance ratios at two widely separated energies. The lower energy values were taken from a 1976 balloon flight experiment that is fully described in reference [7].

Table III

| | '76' Experiment $E_k$ = 1.2 GeV per nucleon | This Experiment $E_k$ > 23.7 GeV per nucleon |
|---|---|---|
| O/C | 0.91 ± 0.02* | 1.02 ± 0.08 |
| Fe/O | 0.086 ± 0.006 | 0.111 ± 0.022 |
| Si/Fe | 2.08 ± 0.16 | 1.49 ± 0.35 |

* Statistical error only

These ratios seem consistent with the phenomenological leaky box model for cosmic-ray propagation described in reference [8]. Specifically we compared our O/C data to the theoretical prediction plotted on figure 15 of reference [8]. Taking note of the uncertainty in our data, we find good agreement with this propagation model that uses the source abundances of Shapiro, Silberberg, and Tsao [9].

References

1. Gregory, J.C. and Parnell, T.A., Proc. 16th Intl. Cosmic-Ray Conf., Kyoto, 12, 355, (1979).

2. Juliusson, E., Ap.J., 191 331, (1974).

3. Caldwell, J.H., Ap.J., 218, 269, (1977).

4. Hagen, F.A., Ph.D. Dissertation, University of Maryland (1975).

5. Silberberg, R. and Tsao, C.H., Astrophysical J. Supplement Series, 25, 315 and 335, (1973).

6. Engelmann, J.J., Goret, P., Juliusson, E., Koch-Miramond, L. Masse, P., Soutoul, A., Byrnak, B., Lund, N., Peters, B., Rasmussen, I.L., Rotenberg, M., Westergaard, N.J., Proc. 18th Intl. Cosmic-Ray Conf., Bangalore, 2, 17, (1983)

7. Derrickson, J.H., Ph.D. Dissertation, University of Alabama in Huntsville (1983)

8. Simon, M., Spiegelhauer, H., Schmidt, W.K.H., Siohan, F., Ormes, J.F., Balasubrahmanyan, V.K., and Arens, J.F., Ap. J. 239, 712, (1980)

9. Shapiro, M.M., Silberberg, R., and Tsao, C.H. Proc. 14th Intl. Cosmic-Ray Conf., Munich, 2, 532, (1975)

# Relative Abundances of Elements ($20 \leq Z \leq 28$) at Energies up to 70GeV/amu Using Relativistic Rise in Ion Chambers

*S.D. Barthelmy* [1], *M.H. Israel, J. Klarmann*

Physics Department and McDonnell Center for the Space Sciences
Washington University, St. Louis, Missouri 63130, USA

**1. Introduction** This paper reports on the results of a new balloon borne cosmic ray detector flown from Palestine, TX in Sept 1982. The exposure of 62 $m^2$-ster-hr is sufficient to prove the concept of using gas ionization chambers as energy measuring devices in the relativistic rise region. We have measured the abundances, relative to $_{26}$Fe, of the pure secondaries $_{22}$Cr and $_{24}$Ti, the pure primary $_{28}$Ni, and the mixed primary and secondary $_{20}$Ca between 6 and 70GeV/amu.

**2. Instrument** The instrument, shown in figure 1, is composed of 1.0cm NE114 plastic scintillator(**S**), and 0.6cm Pilot 425 plastic Cherenkov(**P**), detectors in light diffusion boxes. These two detectors determine the charge of the cosmic rays. Interspaced around the **S** and **P** detectors are pairs of 10cm dual gap P-10 gas ionization chambers(**I**). In addition to being the energy measuring devices they are also used for identification of nuclear interactions in **S** and **P** detectors. At the bottom of the stack is a one atmosphere $CO_2$ gas Cherenkov(**G**), whose nominal threshold energy is 34.8GeV/amu. This detector provides the energy calibration of the relativistic rise region of the ion chambers. The two layers of x-y multiwire ionization hodoscopes(**H**) provide the trajectory information which allows for the path length correction and for correction to the areal variations of the various detectors. The stack, 160cm x 160cm x 190cm, with the electronics is flown inside a one atmosphere pressure vessel.

Figure 1

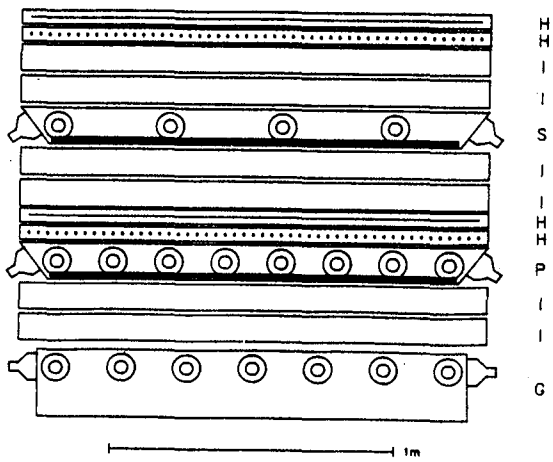


**3. Data Reduction** Figure 2 is a plot of the mean ionization signal(**I**) versus the plastic Cherenkov signal(**P**). The dashed lines are the charge tracks for the even Z elements 20 to 28. The vertical pairs of lines mark the $\beta$=1 saturation of **P**, the events of interest in this experiment. With **I** and **P** alone it is impossible to separate, say, relativistically risen charge 24 from low energy charge 26. To remove this ambiguity a third dimension, scintillation(**S**), is added.

[1] Presently at Goddard Space Flight Center, Greenbelt, Maryland 20771, USA

Figure 3 is a plot of the same events for **S** versus **P**. The energy dependence is almost entirely in the **P** dimension. The relativistic events pile up at the right side of the cluster and lower energy events trail off towards the left. The superposed boxes are the **S** and **P** cuts used to select events that will be used to form abundance spectra. We observe that **S** has negligible (less than 0.5%) relativistic rise at 100GeV/amu, so the **S** cuts do not introduce a significant energy dependence.

Figure 2

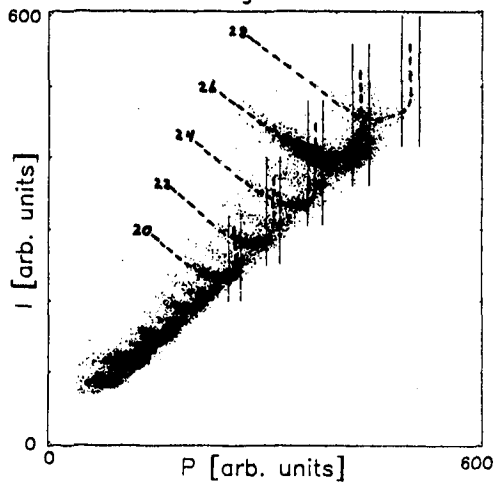


Figure 3

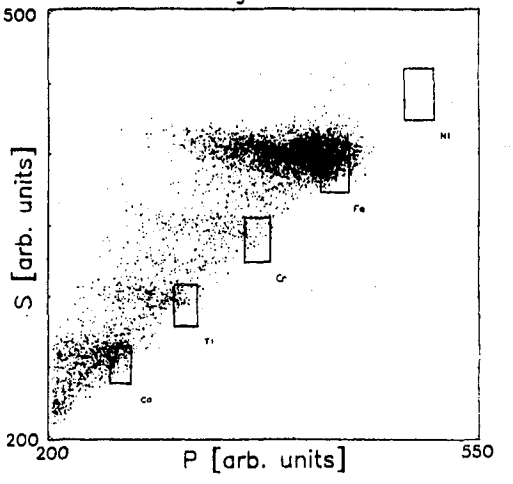


The **S** cuts are asymmetric about the charge tracks. This is because almost all the contamination from adjacent charges into a given charge selection box is from the lower energy next higher charge. The **P** cuts are symmetric about the $\beta$=1 track of the given charge. Both the **S** and **P** cuts are made in constant sigma units for each charge. This insures a constant fraction of the desired charge to be included within the **S-P** box cuts. Taking the events within these cuts, histograms were formed in $\mathbf{I}/\mathbf{I}_{min}$. Ratios of these histograms to that for iron are the abundance ratio spectra that are discussed in section 5.

**4. Energy Calibration** Figure 4 is a plot of **I** vs **G** for the events satisfying the **S** and **P** cuts in figure 3 for iron. The line through the data is a result of a least-squares fitting with the semi-empirical model described by equations 1.

$$I = I_m \ln(E) + B \qquad (1a)$$

$$G = K(1 - E_{thresh}^2/E^2) + D \qquad (1b)$$

I is the ratio of the **I** signal over the minimum value (at 2.4GeV/amu). The D term represents the scintillation emission from the reflective paint coating on the inside of the **G** light diffusion box.

The fitting was done in two steps. The first attempt only fit the events between the **G** values of 450 and 1100. Using this fit a swath through **I** and **G**

Figure 4

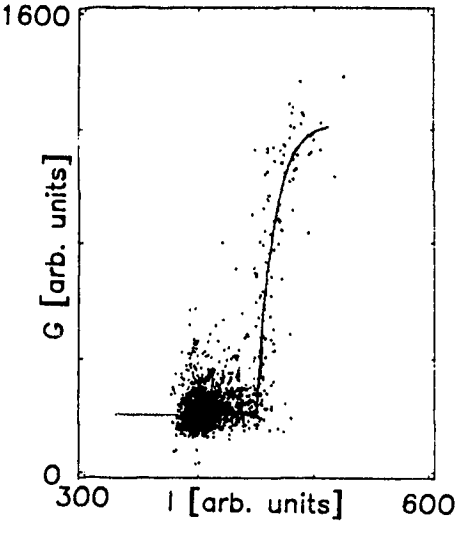

space was made to allow for the inclusion of events down beside the paint emission clump and to extend the high end to include the $\beta$=1 events in the **G** detector. The sharp threshold in **G** can be seen and it is the **I** value at this $E_{thresh}$ that provides one well defined calibration point. Given the limited number of events the slope (Im) was very poorly determined from this **I** vs **G** comparison, and so we instead determined the slope by comparison between our iron data and the iron spectrum from previous experiments (summarized by Webber[1]).

For various values of Im, with B selected to give the previously determined $\mathbf{I}(E_{thresh})$, we convolved the Webber spectrum with equation 1 and with the resolution function of the detector. We then determined the value of Im which gave the best least-squares fit to our observed **I**-spectrum for iron. The final values of the parameters in equation 1 are $I_m$ = 0.0738 ± 0.0023, B = 0.8889 ± 0.0019, K = 1220.0 ± 15, and D = 207.0 ± 4.0. The numerical values of the parameters for equation 1a apply to an **I** scale in which minimum-ionizing iron gives **I**=1.000, and this equation is taken as applicable for energies greater than 5.0 GeV/amu.

**5. Results** Even with the tight **S** cuts near the Z+1 charge track, there is still some contamination. While these contamination events are of low intrinsic energy, their **I** mimics relativisticly risen events because they have a greater charge. The upper **S** cut was fixed by requiring that the contamination to any of the five charges never be more than 20% of the charge of interest at the appropriate $\mathbf{I}/\mathbf{I}_{min}$ value. Subtractions were made for these contaminations. After producing the number versus $\mathbf{I}/\mathbf{I}_{min}$ spectra, they are binned into three differential points, one integral point, and using similar **S** and **P** cuts, a point at $\mathbf{I}_{min}$ (2.4GeV/amu).

Our results are listed in table 1 and plotted (points with error bars) in figure 5. In the energy interval 6 to 25 GeV/amu our results are consistent with those of Englemann[2] (their data has been propagated through 4.1 g/cm$^2$ of air). Above 25 GeV/amu our results indicate an energy dependence of relative abundances which continues the trend observed by Englemann, et al.

TABLE 1 - Abundance Ratios to Iron for Ti, Cr, Ca, and Ni

| Energy Range | | Element | | | |
|---|---|---|---|---|---|
| Lower | Upper | Ti | Cr | Ca | Ni |
| ~1.45 | ~3.35 | 0.158 ± 0.007 | 0.161 ± 0.007 | 0.217 ± 0.009 | 0.055 ± 0.004 |
| 5.90 | 11.62 | 0.129 ± 0.013 | 0.124 ± 0.013 | 0.225 ± 0.018 | 0.052 ± 0.008 |
| 11.62 | 22.87 | 0.101 ± 0.023 | 0.086 ± 0.021 | 0.178 ± 0.032 | 0.037 ± 0.014 |
| 22.87 | 45.02 | 0.059 ± 0.023 | 0.074 ± 0.026 | 0.092 ± 0.029 | 0.034 ± 0.017 |
| 45.02 | ∞ | 0.070 ± 0.023 | 0.075 ± 0.024 | 0.126 ± 0.032 | 0.043 ± 0.018 |

**6. Acknowledgements** We are grateful to W. R. Webber for valuable suggestions regarding the design of this experiment, and to John Epstein and John Vogel for essential contributions to the construction of the instrument. This work was supported in part by NASA grant NGR-26-008-001.

**References:**

[1] Webber, W.R, 1982 Erice NATO Conference, 1983, Reidel, pp 25-45
[2] Englemann J.J., et al, 1983, ICRC, Bangalore, India, OG1-9, pp 17

Figure 5

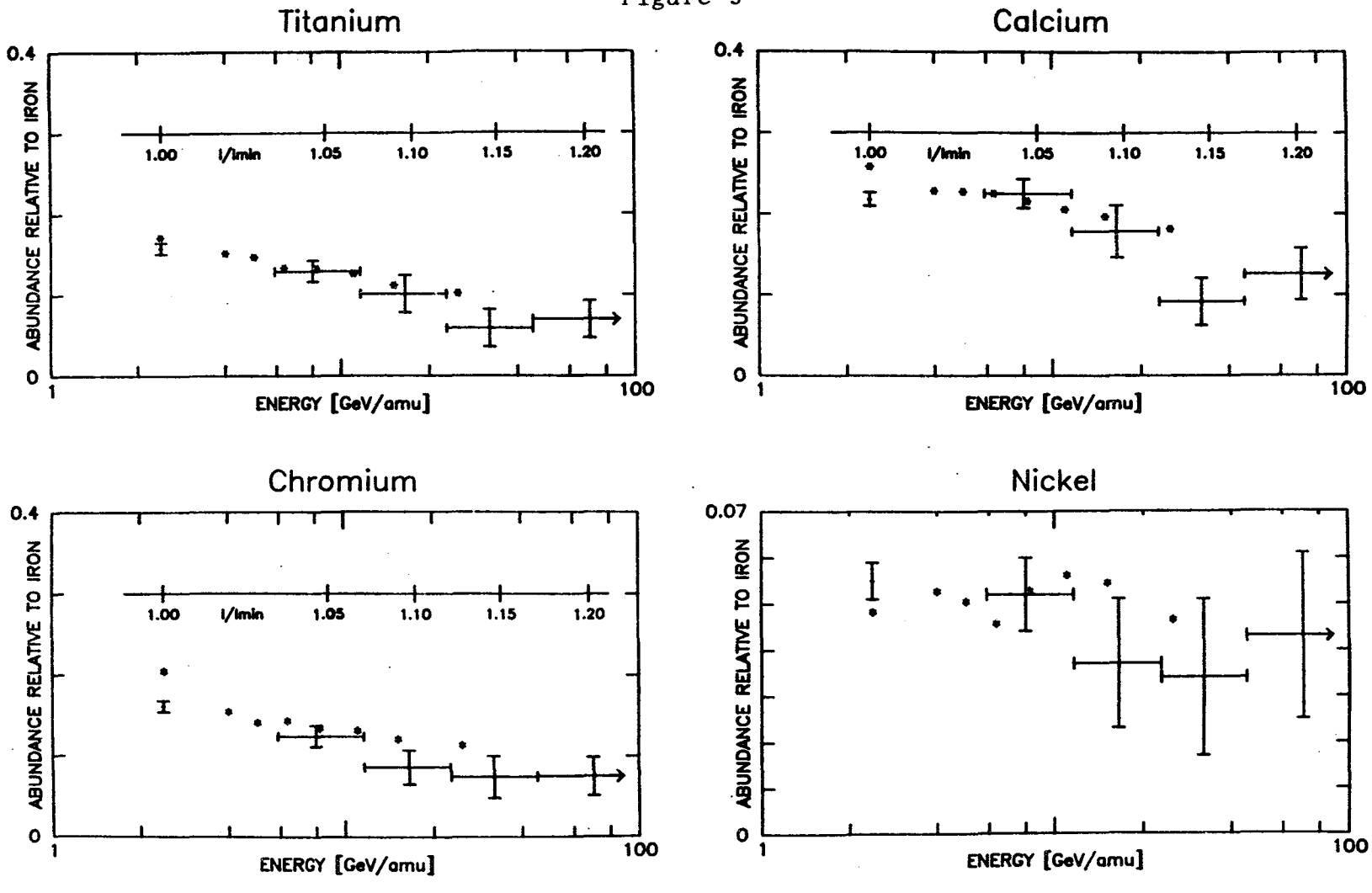
Titanium
Calcium
Chromium
Nickel
ABUNDANCE RELATIVE TO IRON
ENERGY [GeV/amu]
1.00
1/Imin
1.05
1.10
1.15
1.20
0.4
0.07
0
1
100

# ENERGY SPECTRA OF ELEMENTS WITH $18 \leq Z \leq 28$ BETWEEN 10 AND 300 GeV/amu

Michael D. Jones[a], J. Klarmann[a], E. C. Stone[b], C. J. Waddington[c], W. R. Binns[a], T. L. Garrard[b], M. H. Israel[a]

a) Washington University, St. Louis, MO 63130, USA

b) California Institute of Technology, Pasadena, CA 91125 USA

c) University of Minnesota, Minneapolis, MN 55455, USA

1. Introduction. The HEAO-3 Heavy Nuclei Experiment (Binns, *et al.*, 1981) is composed of ionization chambers above and below a plastic Cherenkov counter. We have measured the energy dependence of the abundances of elements with atomic number, Z, between 18 and 28 at very high energies where they are rare and thus need the large area x time of this experiment. We extend the measurements of the Danish-French HEAO-3 experiment (Englemann, *et al.*, 1983) to higher energies, using the relativistic rise of ionization signal as a measure of energy, and determine source abundances for Ar and Ca.

2. Data Analysis. We confine this analysis to events in the 1.1 $m^2sr$ in which the cosmic rays penetrate all six ionization chambers, and to the first 370 days of the flight, when all six ionization chambers were functioning properly. These selections give the highest possible ionization resolution. We select only events incident with geomagnetic cutoff greater than 8 GV, so Z is determined by the Cherenkov signal. We further require agreement between the means of the three ionization chamber signals above the Cherenkov and those below, to eliminate most nuclear interactions inside the instrument.

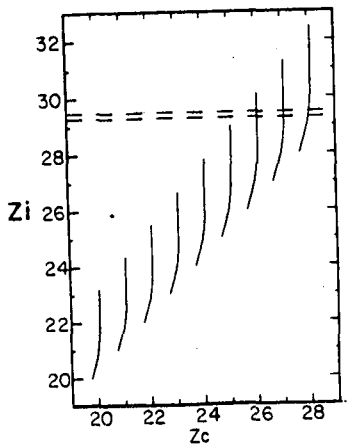


Figure 1

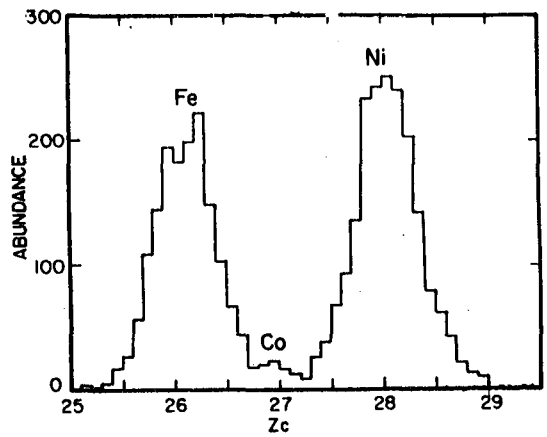


Figure 2

Figure 1 is a schematic plot showing the locus of events for each element, $20 \leq Z \leq 28$. Zc is the square-root of the Cherenkov signal normalized so $Zc \simeq Z$ at high energy. Zi is the square-root of the ionization normalized so $Zi = Z$ at minimum-ionizing. Figure 2 is a histogram of Zc for events with $29.3 < Zi < 29.5$, the region between the dashed lines in figure 1. This histogram includes Fe, Co, and Ni at about 130, 34, and 12 GeV/amu respectively. The abundance of each element in each of eighty such histograms is determined by maximum-likelihood fitting.

Corrections to these raw abundances were calculated to account for interactions both in the lid in front of the first ionization chamber and in the Cherenkov counter and other material between the ionization chambers. The latter calculation included only charge changes of one or two charge units, other interactions having been eliminated by the requirement for agreement between upper and lower ionization chambers. The calculation assumed that at all energies the total cross-sections were given by the formula of Westfall *et al.* (1979) and the partial cross-sections for changing by n charge units were the same fraction of the total cross-section for any projectile as was measured by Webber and Brautigam (1982) at 980 MeV/amu for Fe on C. These calculated corrections lowered the raw abundance ratios by typically 10 to 30 percent.

3. Energy Scale. We used Zi/Z as a measure of energy, and derived an empirical energy calibration by comparing our Fe observations with an Fe energy spectrum derived from a compilation of previously published measurements (Webber, 1982). This Fe spectrum was multiplied by an empirical geomagnetic transmission function which represented the fraction of time when the geomagnetic cutoff permitted Fe of that energy to reach the instrument; the product was the effective Fe spectrum at the instrument, averaged over many orbits. This energy spectrum was then converted to a Zi/Z spectrum using a trial form of the energy dependence of Zi/Z. Finally this calculated spectrum was folded with the instrument's ionization resolution, and the resulting Zi/Z spectrum was compared with the data. The process was iterated, by changing the assumed form of the energy dependence of Zi/Z, until the calculated and observed spectra of Fe agreed.

The resulting energy dependence is consistent, between about 10 and 100 GeV/amu, with one derived independently for a different detector system by Barthelmy *et al.* (1985, OG 4.1-7). Above about 200 GeV/amu, the shape of our calibration curve depends upon the assumption we made that the Fe energy spectrum falls as a power-law with exponent -2.7 at energies above those where it has been measured.

Abundance ratios derived from data in a particular Zi/Z histogram were plotted at the mean energy from which those particles came, assuming the Fe energy spectrum and the calibration curve described above. The energy resolution implied by our ionization resolution of 0.40 charge units is comparable to the spacing of the points in figure 3.

4. Results. Figure 3 gives the resulting abundances of several elements relative to Fe as a function of energy. The X symbols are the results of the DF experiment (Englemann, 1983), while the O symbols are the results of this experiment. In every case our results are consistent with those of the DF experiment in the interval where both experiments apply, 10 to 25 GeV/amu. At higher energies our data generally continue the DF trend.

Our data above 10 GeV/amu suggest a Ni/Fe ratio slightly dependent upon energy, with a best fit power law of exponent $-0.050 \pm 0.016$. If we ignore this slight variation with energy, then the mean value of the Ni/Fe ratio over our data is $0.054 \pm 0.001$.

For the secondary ratios, K/Fe, Sc/Fe, Ti/Fe, and V/Fe, our data indicate an extension to about 100 GeV/amu of the same power law dependence as was indicated by the DF data. Figure 4 shows the best fit exponent for each of these ratios combining the DF and our data. The steepening of the slope with decreasing Z is expected as lower Z elements have greater contributions from tertiary nuclei.

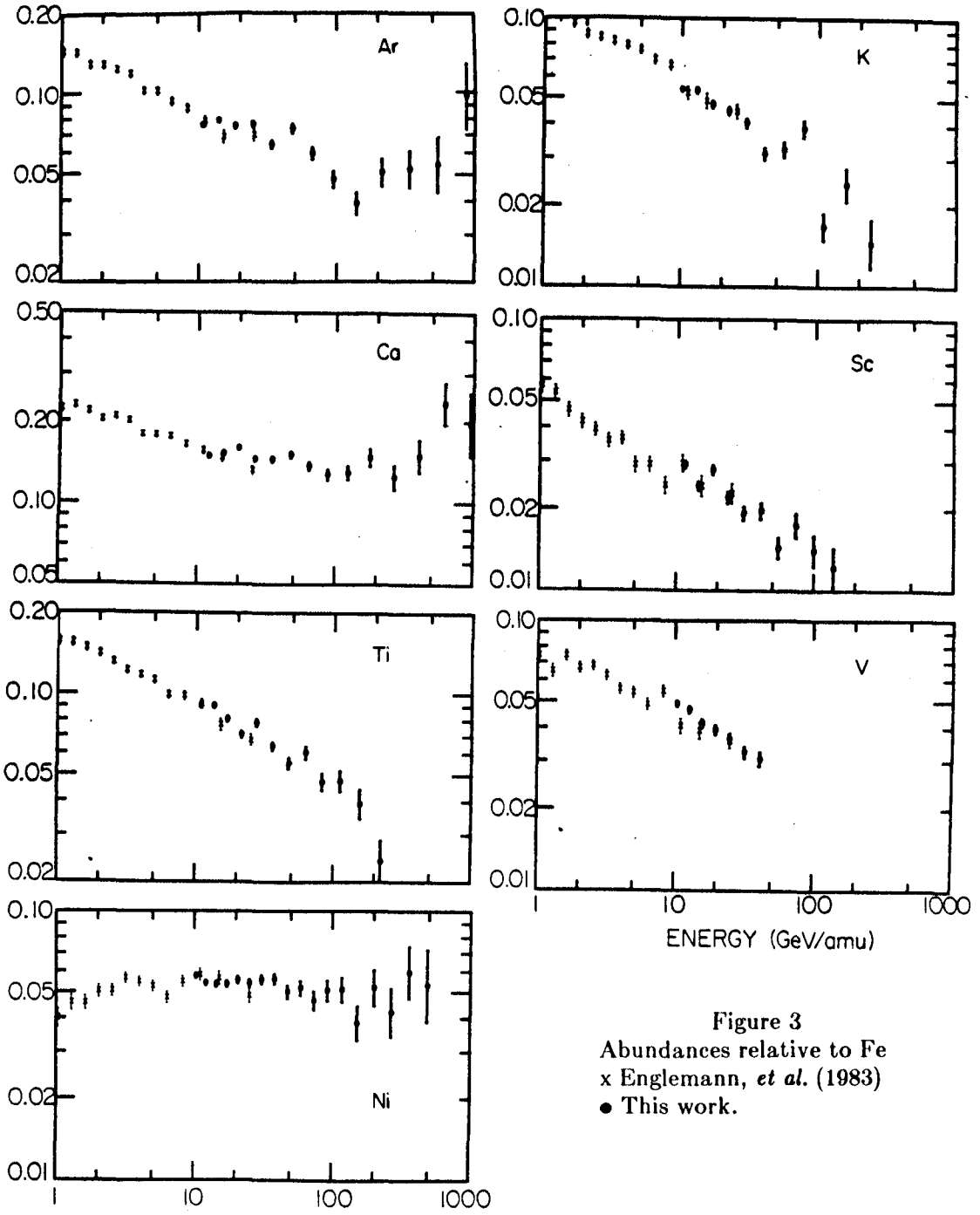


Figure 3
Abundances relative to Fe
x Englemann, *et al.* (1983)
• This work.

Our data indicate a leveling of the Ca/Fe ratio above the energies of the DF experiment, as would be expected from an energy-independent primary component becoming increasingly significant at higher energies as the secondary component becomes less abundant. We fitted the combination of the DF and our ratios to a function $aE^p+b$. With $p = -0.295 \pm 0.010$, interpolated from figure 4, the result is primary Ca/Fe = $0.094 \pm 0.004$. A galactic propagation calculation on the DF data (Lund, 1984) gives a source abundance of Ca/Fe = $0.065 \pm 0.019$.

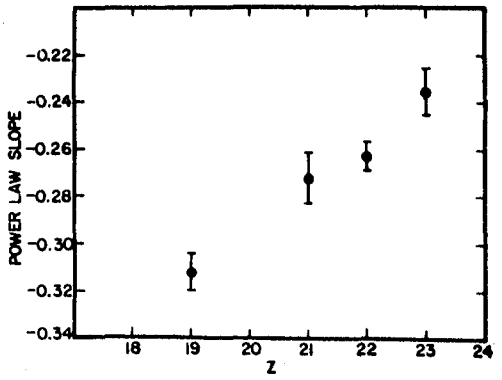


Figure 4
Exponent of power law fit to abundance of element Z relative to Fe.

A similar fit to the energy dependence of Ar/Fe, but with $p = -0.33 \pm 0.01$, gives primary Ar/Fe = $0.026 \pm 0.003$. Propagation of the DF data (Lund, 1984) gives Ar/Fe = $0.032 \pm 0.008$. Source abundances inferred from such galactic propagations on observed abundances 2.5 to 5 times higher must depend critically upon the adopted fragmentation cross-sections, while our extension of observations above 100 GeV/amu permits inference of source abundances without galactic propagation calculations.

5. Acknowledgement. This work was supported in part by NASA grants NAG 8-498, 500, 502, and NGR 05-002-160, 24-005-050, and 26-008-001.

6. References

Barthelmy, S.D., M.H. Israel, J. Klarmann, 1985, this conference OG4.1-7.
Binns, W.R., *et al.*, 1981, *Nucl. Instr. Meth., 185*, 415.
Englemann, J.J., *et al.*, 1983, *18th ICRC (Bangalore) 2*, 17.
Lund, N., 1984, *Adv. Space Res., 4*, (No.2-3), 5.
Webber, W.R., 1982, *Comp. Origin of Cos. Rays*, ed. M.M.Shapiro, 25.
Webber, W.R. and D.A. Brautigam, 1982, *Ap. J., 260*, 894.
Westfall, G.D., *et al.*, 1979, *Phys. Rev. C, 19*, 1309.

# PRIMARY COSMIC RAY SPECTRA IN THE RANGE 20-60 GeV/n

The JACEE Collaboration+

T. H. Burnett[h], S. Dake[b], J. Derrickson[f], M. Fuki[d], W. Fountain[f], J. C. Gregory[g], T. Hayashi[b], T. Hayashi[g], R. Holynski[i], J. Iwai[h], W. V. Jones[e], A. Jurak[i], J. J. Lord[f], C. A. Meegan[f], O. Miyamura[c], T. Ogata[c], T. A. Parnell[f], T. Saito[a], S. Strausz[h], T. Tabuki[a], Y. Takahashi[f], T. Tominaga[c], J. Watts[g], B. Wilczynska[i], R. J. Wilkes[h], W. Wolter[i], and B. Wosiek[i]

[a]Institute for Cosmic Ray Research, University of Tokyo;
[b]Department of Physics, Kobe University;
[c]Department of Applied Mathematics, Osaka University;
[d]Okayama University of Science;
[e]Department of Physics and Astronomy, Louisiana State University;
[f]Space Science Laboratory, NASA Marshall Space Flight Center;
[g]Department of Chemistry, University of Alabama, Huntsville;
[h]Visual Techniques Laboratory, University of Washington;
[i]Institute for Nuclear Physics, Krakow.
+Japanese-American Cooperative Emulsion Experiment

## ABSTRACT

Energy spectra for primary cosmic rays C-Fe above 20 GeV/n were measured on a balloon flight from Greenville S.C. in June 1982 with a hybrid electronic counter-emulsion chamber experiment. Fluxes above the atmosphere appear in general agreement with previously published values. The heavy events included in this data will be used along with the JACEE passive chamber data to provide a heavy composition direct measurement from $10^{12}$ to $\sim 10^{15}$ eV total energy.

## INTRODUCTION

The JACEE collaboration has been using emulsion chambers since 1979 in a series of balloon flights to measure the composition, energy spectra, and interactions of energetic (>1 TeV/n) cosmic rays. The apparatus used in JACEE's 0,1,2,4,5 have been largely passive, events being detected by the development of dense electromagnetic showers which produced visible dark spots in x-ray films. In 1982 a different kind of experiment was flown by the collaboration. This incorporated electronic detectors mounted above an emulsion chamber. The counters were used to define the charge and energy of incident primaries and provide trajectory information so the primaries could be traced through the emulsion chamber from the top down. For heavy ions this has proven to be an efficient process, and the results of measurements on ~130 heavy interactions ($Z \geq 22$) at primary energies >20GeV/n are described at this conference.

The primary objective of this experiment was to obtain a statistically significant sample of heavy ion interactions in the energy range 20-60 GeV/n, below the energy range of detection for totally passive chambers. Other objectives were to allow direct calibration of some techniques used in JACEE, albeit in a lower energy range than the other experiments. The electronic counters also allowed the direct measurement of heavy primary cosmic ray fluxes in the range 20-100 GeV/n (1-5 TeV total energy for Fe) for comparison with the other JACEE direct composition measurements above $10^{13}$ eV total energy, (see paper OG4.1-13 this conference). In this paper we describe the measurement of the abundances and spectra of elements from C to Fe above 20 GeV/n.

## Experimental

The apparatus was previously described (Ref.1) and is only briefly reviewed here. It consisted of two solid Cerenkov counters (Teflon and lead-glass) which were in saturation at the energies reported here and provided primary charge definition; a gas Cerenkov counter (1 atmosphere Freon-12, 81 cm most probable depth) which provided differential energy measurement in the range Eo = 20 - 65 GeV/n; and an eight-plane multiwire proportional counter hodoscope which enabled particle trajectory intersection points in the top layers of the emulsion chamber to be found with rms position error 3.5 mm. A scintillation counter was placed below the emulsion chamber to provide a measure of shower-size from individual energetic interactions within the chamber. (paper HEI.4-1 this conference)

A cross-plot of the outputs of the Teflon (CT) and lead-glass (ClG) Cerenkov counters allowed separation of individual charge identification. The ratio CT/CLG at Eo>20GeV/n gives a narrow distribution for all particles passing through both counters without interacting. This effect was used, together with the hodoscope track information to reject most events interacting in the electronic instrument. All detector signals were corrected for path-length in the detector, PM tube temperature, detector non uniformities, and ADC offsets. Charge resolution was limited by back-scatter from the emulsion chamber, an effect which was assessed by correlation of CT and CLG signals with the burst scintillator. Charge resolution was = 0.25 charge units FWHM at oxygen and 0.5 at Fe. Figure 1 shows a charge histogram of a portion of the data. For the gas Cerenkov detector, in which the PM tube outputs were analyzed in four sets of tubes, assessment and correction for δ-ray effects in tube windows was possible. Energy assignment for individual events was made using a Monte Carlo method which incorporated the instrument response function and an assumed cosmic ray spectrum. The response function was based on normal statistics of photoelectrons from Cerenkov light plus a scintillation and $BaSO_4$ paint Cerenkov contribution. The flight oxygen gas-Cerekov data is shown in Figure 3. It should be noted that energy assignments based on this method are insensitive to changes in $\gamma$ of 0.3 or so.

The balloon and instrument were launched on June 2nd from Greenville, S.C. and cut down near Roswell, N.M., after 39 hours at a mean float depth of 4.9 g $cm^{-2}$. Effective live time was 35.6 hrs. yielding an exposure of 5.7 $m^2$ sr hrs of the best quality data. The geometric aperture 0.16 $m^2$ sr in this case included all the electronic detectors except the burst-counter.

RESULTS

The derived differential energy spectra for the principal elements and groups are shown in Figures 3 to 6, using data at the instrument. Note that the amplitudes given in these figures are per 5 GeV bin and for the whole flight. Calculation of the differential and integral intensities at the top of the atmosphere using average values of atmosphere and instrument fragmentation show essential agreement with the HEAO C-2 data. Maximum likelihood fits have been made to the raw spectra above 25 GeV/n and derived values of $\gamma$ are given in the table ($dN/dE = AE^{-\gamma}$). Although primary/secondary element ratios await the full interaction correction, an estimate of the Fe/C+O ratio above 25 GeV/n is $5.4 \times 10^{-2}$, if the ratio of the interaction corrections for Fe and (C+O) is taken as 1.12. This primary ratio has been reported as $6 \times 10^{-2}$ (Refs. 2,3).

References:

1. Austin, R.W., et.al., Papers of 18th ICRC T2-15, (1983)
2. French-Danish HEAO-3 Collaboration, Papers of 18th ICRC Vol 2, p 17 et. seq. (1983)
3. Simon, M. et.al., ApJ, 239, 712-724 (1980)

TABLE 1

MAXIMUM LIKELIHOOD FITS TO ELEMENTAL SPECTRA ABOVE 25 GeV/n
ASSUMING SIMPLE POWER LAW, $dN/dE = AE^{-\gamma}$

| | A | $\gamma$ |
|---|---|---|
| | Particles $(m^2 sr\ s\ GeV/n)^{-1}$ | |
| Oxygen | 21.7 | 2.77 + 0.07 (-0.04) |
| Neon | 4.2 | 2.72 + 0.13 (-0.12) |
| Magnesium | 1.5 | 2.44 + 0.12 (-0.10) |
| Silicon | 5.8 | 2.85 + 0.15 (-0.10) |
| 16 z 25 | 1.4 | 2.89 + 0.18 (-0.10) |
| Iron | 0.51 | 2.79 + 0.25 (-0.19) |
| Sum of Z=8,10,12,14 | 5.8 | 2.72 + 0.05 (-0.06) |

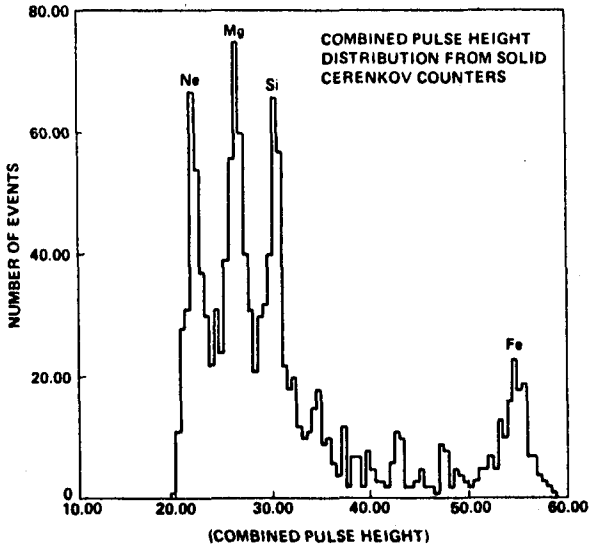


Fig. 1. Charge Histogram of Flight Data; $E_o \geq 20$ GeV/n

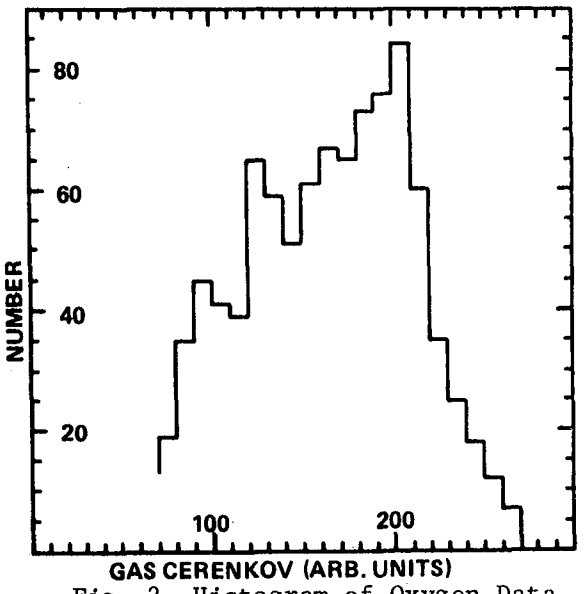


Fig. 2. Histogram of Oxygen Data in the Gas Cerenkov

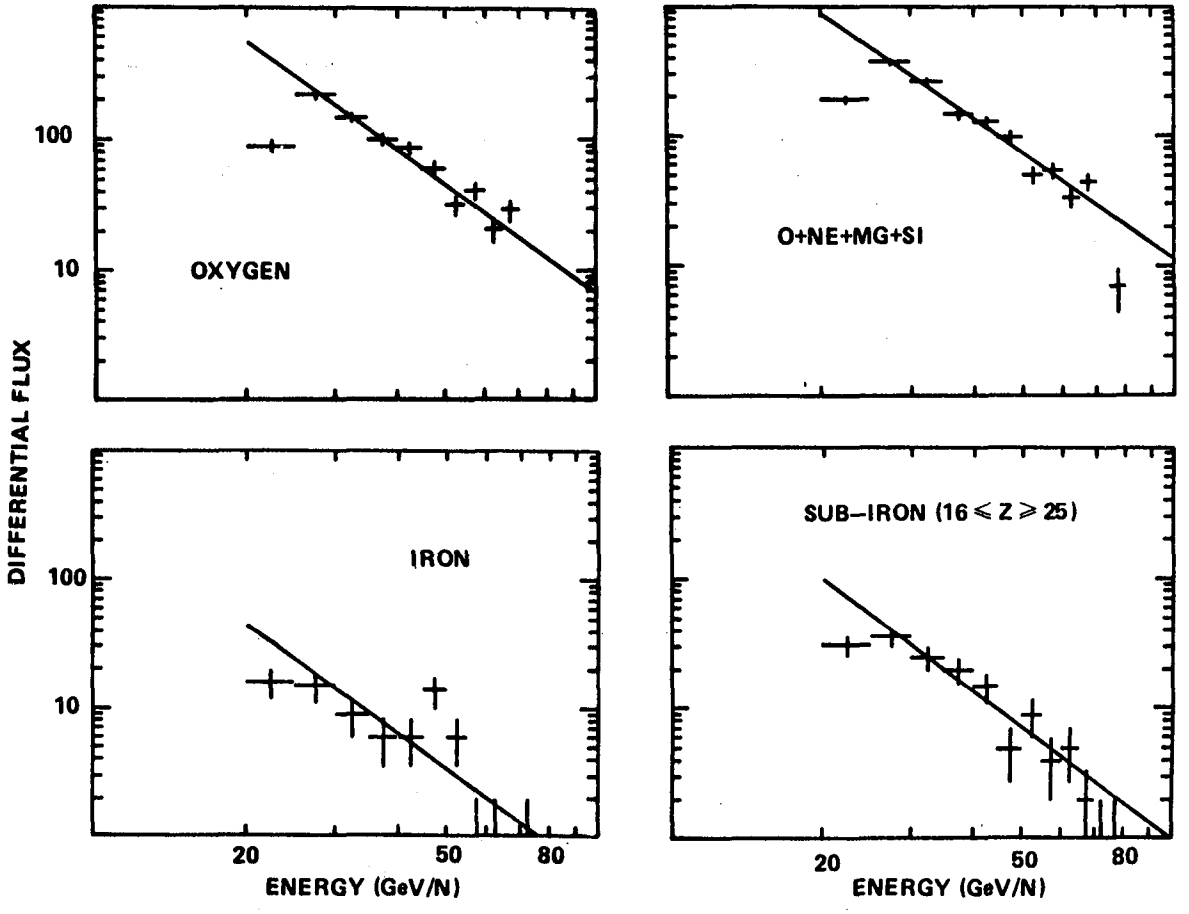


Figures 3-6. Differential Spectra of Individual Elements and Groups of Elements Measured at the Instrument. Note that Amplitudes are per 5 GeV bin and per Entire Flight, and Interaction Corrections have not yet been applied. Straight Lines are M-L fits to the Data.

OG 4.1-10

# ENERGY SPECTRUM OF COSMIC-RAY IRON NUCLEUS OBSERVED WITH EMULSION CHAMBER

Yoshihiro Sato, Etuo Shimada, Itaru Ohta
Faculty of Education, Utsunomiya University, Utsunomiya 321
Shigeki Tasaka, Shinichiro Tanaka
Faculty of Education, Gifu University, Gifu 502
Hisahiko Sugimoto, Kunio Taira
Sagami Institute of Technology, Kanagawa 251
Nobuto Tateyama
Faculty of Engineering, Kanagawa University, Kanagawa 221

## ABSTRACT

Energy spectrum of cosmic-ray Fe-nucleus has been measured from 4 GeV per nucleon to beyond 100 GeV per nucleon. The data were obtained using emulsion chambers on a balloon from Sanriku, Japan. The energies were estimated by the opening angle method after calibrated using 1.88 GeV per nucleon Fe collisions. The spectrum of Fe is approximately $E^{-2.5}$ in the range from 10 to 200 GeV per nucleon. This result is in good agreement with those of other experiments.

## 1. Introduction.

The current experimental data on the primary spectrum above 1 GeV/n are recently reviewed[1]. Concerning iron nucleus spectrum, it is interesting to establish the spectrum above 100 GeV/n, because the propagation and escape of cosmic rays from galactic confinement would make a effect on the primary spectrum above 100 GeV/n on basis of energy dependent L/M and sub-iron/iron ratio. But, the statistics of high energy data around 100 GeV/n is not sufficient for the discussion. The recent spectrum results have been obtained using instruments such as ionization spectrometers[2], gas Cerenkov counters[1,3,4], magnetic spectrometers[5], and emulsion chambers[6,7]. There were some differences between different techniques. In this experiment, we used an emulsion chamber and applied the opening angle method for estimating the primary energy. In an emulsion chamber experiment, there were three problems to be solved: (1) The shortening of the scanning time for nucleus-nucleus collisions. (2) Charge determination of heavy nuclei. (3) Energy determination of primary nucleus, whose problem was pointed out by Kullberg et al.[8]. By developing a new detection method with plastic detector CR-39, the scanning time was shortened[9]. To reach the reliable results on 2) and 3) problem, the calibration experiments were carried out by exposing the same type of chambers as the balloon-borne one to 1.0 GeV/n and 1.88 GeV/n Fe beams at LBL heavy iron accelerator.

## 2. Experimental procedure

A schematic diagram of the instruments is shown in Fig.1. The emulsion chamber consists of 9 plastic track detector CR-39 plates, 27 nuclear emulsion plates and 20 polyethylen target

plates. which are piled alternately. The CR-39 plates are about 1.7 mm thick. The emulsion plate is coated with 50 $\mu$m thick nuclear emulsion gel on both sides of a 1.0 mm thick lucite plate. The target plates are 1.0 mm thick polyethylen. The overall size of 6 chambers is 1.5 m x 0.8 m x 8.9 cm and the total depth is 8.3 g/cm$^2$ . These chambers have been exposed by balloon flight at Sanriku Balloon Center, Japan, for about 15.5 hours at an altitude of 7.6 g/cm$^2$ .

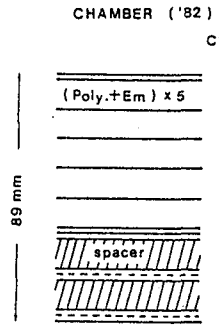

Fig.1 Chamber design.

A CR-39 sheet at the top of chamber was generally scanned with a microscope of 40 magnification and the radius of located cones was measured on an adjacent downstream CR-39 plate. The charge resolution is about $\Delta Z=+/-1$ . Selected cones of charge Z=26+/-1 were followed downstream using CR-39(No.3,5,7). Collisions were found by checking whether or not the cone became smaller or disappeared downstream. The angles of secondary particles and fragments were measured in nuclear emulsion plates.

For iron nucleus of Z=26+/-1, the integral flux is obtained using collision mean free path of $\lambda$ = 15.6 g/cm$^2$ for Fe-air collision as follows;

$$I(>= 4.0\ \mathrm{GeV/n}) = (1.2 +/- 0.1)\times 10^{-1}\ \ (\mathrm{m^2 \cdot str \cdot sec})^{-1}$$

where 4.0 GeV/n is vertical-cut-off kinetic energy at Sanriku.

## 3. Energy determination and correction.

We carried out an experiment using 1.88 GeV/n Fe beam at LBL to calibrate the primary energy estimated by the opening angle method. There are two methods to estimate the incident energy from the emission angle of alpha particles and heavy fragments. One is by the mean angle and the other is by root-mean-square angle. The incident kinetic energy can be calculated by the following relations;

$$P_o = \langle P_t \rangle / \langle \theta \rangle \quad , \quad P_o = \sqrt{\frac{M \langle E^*_k \rangle}{3}} \Big/ \sqrt{\langle \theta^2 \rangle}$$

where $P_o$ is incident momentum, and $\langle P_t \rangle$ and $\langle E^*_K \rangle$ are parameters. As it is very difficult to measure the incident axis of interaction in the cosmic ray, emulsion chamber experiment, we must take the center of geometrical weight of heavy and alpha fragments in the forward cone as the axis of interaction. The parameters were calculated for the events of $Nh+N_\alpha >= 3$, where Nh means number of heavy fragments with charge greater than 3 and $N_\alpha$ is number of alpha particles. They are shown in Table 1 for each charge range of fragment.

| Zf | < Pt > (MeV/c) | < E*k > (MeV) |
|---|---|---|
| 2 | 86.7 +/- 6.5 | 33.5 +/- 5.1 |
| 3 - 8 | 64.6 +/-11.4 | 18.7 +/- 7.5 |
| 9 - 12 | 61.4 +/- 4.4 | 17.4 +/- 2.8 |
| 13 - 15 | 54.0 +/- 5.5 | 14.2 +/- 3.1 |
| 16 - 21 | 37.3 +/- 4.1 | 5.9 +/- 1.2 |

Table 1. Parameters for primary energy estimation.
Zf means a charge of fragment.

Using these parameters, we can conversely estimate the incident energy from experimental values of $\langle\theta\rangle$ and $\langle\theta^2\rangle$, and can obtain the error distribution of estimated energy when the incident energies are known. Figure 2 shows $E/E_0$ distribution for 114 events with $Nh + N_\alpha \geq 3$ obtained by the above two methods, where E means the estimated primary energy and $E_0$ means the beam kinetic energy of 1.88 GeV/n. The mean values of estimated energy are larger than beam energy. It is mainly due to the tail of angular distribution of alpha particles and fragments at large angles. So, if we apply the opening angle method to observe the primary energy spectrum of heavy nuclei, we must be careful of the overestimation of primary energy.

To check the effect of the estimated energy error on the primary spectrum, a Monte Carlo simulation has been made assuming the integral spectrum is a $E^{-1.5}$ spectrum at high energy, which is modulated by cut-off rigidity at Sanriku, and using the $E/E_0$ distribution in Fig.2, which has an approximate form of gamma function, i.e. $f(x)= x^a \cdot \exp(-bx)$ with a=3.1 and b=0.42 . It is also assumed that a form of $E/E_0$ distribution does not vary with primary energy $E_0$ . The results is shown in Fig.3 . The spectra are multiplied by $E^{2.5}$ to emphasize spectral features. It can be seen that the observed spectrum by the opening angle method is higher than the true one. Then we must correct the observed spectrum. We can also obtain a correction factor from this simulation if spectral index is known.

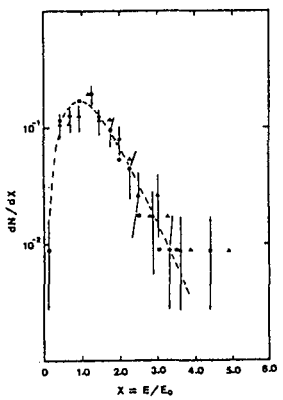


Fig.2 Estimated energy error distribution. E means the estimated primary energy and $E_0$ means the beam kinetic energy 1.88 GeV/n. ● and ▲ denotes the $E/E_0$ data obtained by mean angle and root-mean-square angle method, respectively.

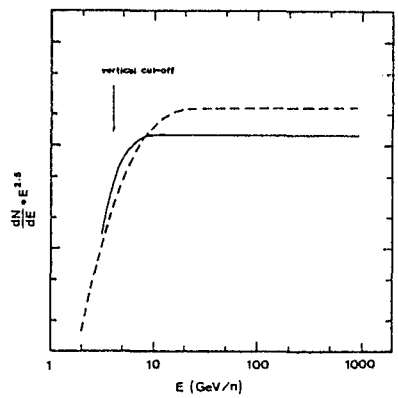


Fig.3 Results of a simulation. A differential spectrum is assumed to be $E^{-2.5}$. The broken curve is a estimated spectrum using the error distribution in Fig.2.

## 4. Results and discussion.

We observed 294 events of primary charge, Z=26+/-1, which make a collision in a chamber and have secondary fragments of $Nh+N_\alpha \geq 3$ . The primary energies of these events were calculated from mean emission angle and root-mean-square angle, respectively, using parameters shown in Table 1. The spectral index is consistent to -2.5 within an experimental error by comparing the experimental with a Monte Carlo simulation of spectral index of -2.3,-2.5 and -2.7 . Using this index, the

simulation makes it possible to correct the observed spectrum. The corrected energy spectrum is shown in Fig.4 along with some data from other groups. The agreement between different measurements is quite good within the quoted errors. This experiment shows that an iron spectrum has a spectral index -2.5 in the range from 10 GeV/n to 100 GeV/n. The present data do not suggest that iron spectrum gradually becomes steep to an index -2.7 above 100 GeV/n, which is expected from a conventional leaky box model, although the statistics is not yet sufficient.

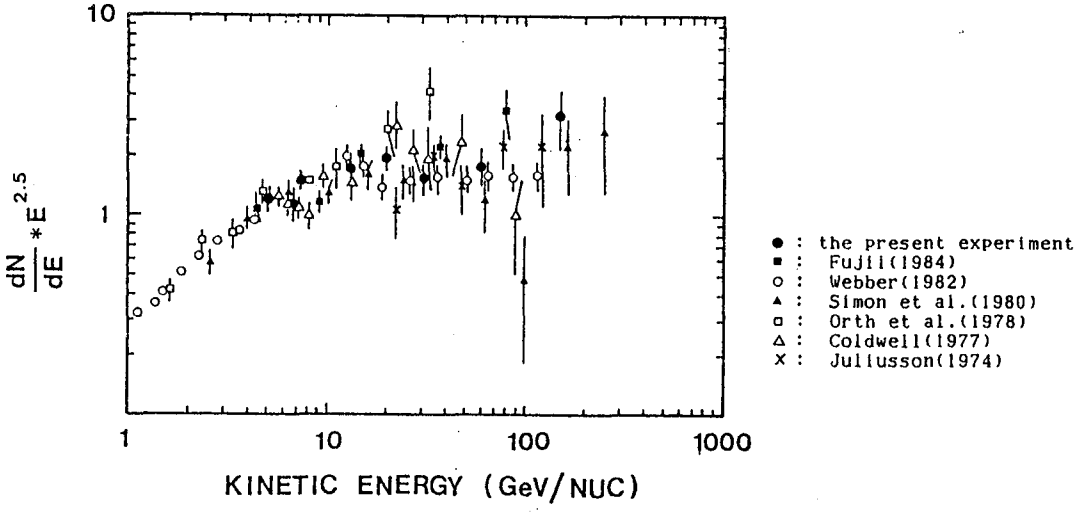


Fig.4 The iron spectra as compared with measurements of other values. The spectra have been multiplied by $E^{2.5}$ (kinetic energy) to emphasize differences. The intensities are in particles/$m^2$·str·sec·GeV per nucleon and kinetic energy is in GeV per nucleon.

**Acknowledgements.**

Authors acknowledge the staff of Sanriku Balloon Center, Institute of Space and Astronautical Science, for the successful flight and also the staff of Emulsion division, Institute for Cosmic Ray Research, University of Tokyo, for giving us the facilities of processing the nuclear emulsion and etching CR-39. We thank Dr. M.Ohashi of Nagoya University who exposed our chamber to the BEVALAC Fe beam and Dr. O.Hashimoto of Institute for Nuclear Study for the successful beam exposure.

**References**

Ref.1 W.R.Webber: Composition and Origin of Cosmic Rays, edited by M.M.Shapiro (Reidel Publishing Company, 1983) p.25
Ref.2 M.Simon et al. : Ap.J. 237(1980) 712
Ref.3 J.H.Caldwell: Ap.J. 218(1977) 269
Ref.4 C.Juliusson: Ap.J. 191(1974) 321
Ref.5 C.D.Orth et al.: Ap.J. 226(1978) 1147
Ref.6 T.Saito et al.: J.Phys.Soc.Japan. 37(1974) 1462
Ref.7 M.Fujii : Bull.Inst.Space and Astronaut.Sci. 22(1984)
Ref.8 R.Kullberg and I.Otterlund: Z.Physik 259(1973) 245
Ref.9 S.Tasaka et al.: ICR-Report-105-82-8(1982), to be published in N.I.M..
Ref.10 A.Inoue et al.: Bull. Inst.Space and Astronaut.Sci. Specialized Series, 1(1981) 79

**40**

# MEASUREMENT OF THE IRON SPECTRUM FROM 60 TO 200 GeV PER NUCLEON

R. E. Streitmatter, V. K. Balasubrahmanyan, J. F. Ormes,
and B. S. Acharya*

1. Introduction. The high energy gas Cherenkov Spectrometer (HEGCS) was flown by balloon from Palestine, Texas on September 30, 1983. The instrument maintained an altitude of 118,000 ft. (4.7 g/cm$^2$) for 6 hours. Here we report details of the ongoing data analysis and preliminary results on the Fe spectrum up to $10^{13}$ eV/nucleus.

2. Charge Measurement. A description of the HEGCS instrument is given in the proceedings of the Paris ICRC (Streitmatter, et al., 1981)(1). Incident charge is determined by measurement of the scintillation light which escapes from the 6 m$^2$ hodoscopes of scintillator triangles located in the top and bottom optical chambers. The escaped scintillation light is collected by 12 RCA 4525 PMT's externally located around the circumference of each chamber, giving two independent measurements of the charge.

Four corrections are made to these signals. (1) A cosine correction is made. Position of the incident cosmic ray as it passes through each of the two hodoscopes is determined from the relative size of signal from the three photomultipliers optically coupled to the struck scintillator triangle. The uncertainty in position is about ± 10 cm at present. (2) A correction for variations in scintillator thickness is made. As the cost of machining flat and polishing 12 m$^2$ of scintillator was prohibitive, the thickness of the hodoscope triangles was mapped. During assembly, an acoustic thickness gage was used to measure (± 0.001 inch) the thickness at 120 points on each of the 48 array triangles. Typically, thickness varies by ± 5 percent over a triangle. (3) The geometrically trapped scintillation light in a triangle has a small probability of escape at each internal surface reflection. The amount of such light escaping over the total triangle surface is a weak function of the position at which the cosmic ray is incident. A systematic correction of up to 12 percent is made for this effect. (4) The top and bottom diffusion chambers are not ideal white boxes. There are position dependent effects upon the relative amount of light collected by each of the twelve external photomultipliers. We are currently working on improvements in the correction of these effects. For charges above 16, the present $\sigma/\mu$ (resolution/mean) of the corrected PMT signals from each chamber is 0.069, corresponding to a charge resolution of 0.8 for Fe. The resolution is dominated by nonphotostatistical systematics.

3. Cherenkov Signal. Cherenkov light from the central gas volume was collected by 24 RCA 4522 photomultipliers located at the upper circumference of the drum. The signal from each PMT was separately digitized. The Freon-12 was kept at a pressure of 2.47 psi, corresponding to a Cherenkov threshold energy of 49 GeV/nucleon. In addition to the above-threshold gas Cherenkov light, incident nuclei at

* NAS/NRC

all energies above the Palestine cutoff made Cherenkov light in the $BaSO_4$ white paint covering the inner surfaces of the upper and lower pressure bulkheads. The Cherenkov light generated in the two painted surfaces is about 14 percent of the saturated gas signal, displays a cosine effect, and is statistically broadened in a manner indicating that over the painted surfaces there is 20 percent variation in effective emitting thickness of the $BaSO_4$. Figure 1, taken from flight data, is a histogram of the "paint-light" signals to one 4522 PMT from incident iron. The first and second photoelectron peaks are clearly visible. Thus, the Cherenkov signals can be directly expressed in terms of the number of photoelectrons collected. For an iron nucleus passing vertically through the detector, the paint-generated Cherenkov light results in an average of 51 photoelectrons, total, being collected. The saturated ($\beta = 1$) gas signal from a vertical iron is best fit (see below) as 370 total collected photoelectrons.

Because the 4522 PMT's are separately digitized, it is possible to note individual PMT's struck by delta-rays. Typically, one PMT saturates, while the average signal to the other PMT's is increased by less than one photoelectron. The probability of events with a delta-ray tube hit is a strong function of position, being greatest at the periphery of the detector (radius 150 cm) near the PMT's. At the largest radii, multiple delta-ray events can be seen. Although these events can be recovered, we are presently making a conservative geometric cut, restricting accepted events to be within 115 cm of the center of the top hodoscope.

4. High Energy Data. In addition to the geometric cut, we require that the top and bottom charge determination agree within two standard deviations, and that the hodoscope signals be consistent with the passage of a single particle through the detector. These restrictions effectively eliminate fragmentations and nascent air showers. Figure 2 is a cross plot of Cherenkov signal versus charge. For plotting, a cut has been made surpressing events with only "paint-light". The upward fluctuating "paint-light" events appear as a band across the bottom of the plot. For the purpose of analysis, iron is defined as those events with determined charge between 24.7 and 27.7, corresponding to standard deviations in signal of two and three, respectively. The larger acceptance on the high side was made because of the tendency, seen in Figure 2, of high Cherenkov events to deviate toward higher determined charge. We attribute this trend to relativistic rise, but have deferred a quantitative investigation pending improvement in the charge resolution.

The maximum likelihood technique has been used to determine the iron spectral index. The total Cherenkov signal in photoelectrons has been modeled, including the statistical fluctuations from the paint-generated and gas-generated photons. The number of photoelectrons corresponding to the gas $\beta = 1$ point is a free parameter of the model. The assumed spectra used as input to the model have been normalized to the HEAO-3 (Lund, 1984)[2] iron data. That is, the modeled spectra are assumed to attach to the HEAO iron flux at 25 GeV/nucleon and to be a single-index power law above this energy. The index of the power law is the second free parameter of the model. Making a low energy cut of

60 GeV/nucleon and calculating likelihoods from the data in Figure 2, we find that the best fit spectral index is 2.77 ± 0.12. The best fit value for the total number of photoelectrons from gas-generated photons from a vertical, β = 1 iron is 370. This indicates that the Cherenkov signal retains statistical power in energy discrimination up to about 215 GeV/nucleon.

Future improvement of the charge resolution and inclusion of the full geometric factor should allow improvement of the error in determination of the iron spectral index and sufficient statistics to determine the index of the iron secondaries.

References

1. Streitmatter, R. E., Balasubrahmanyan, V. K., and Ormes, J. F., 1981, 17th ICRC 8, 54.
2. Lund, N., 1984, Adv. Space Res., 4, 5.

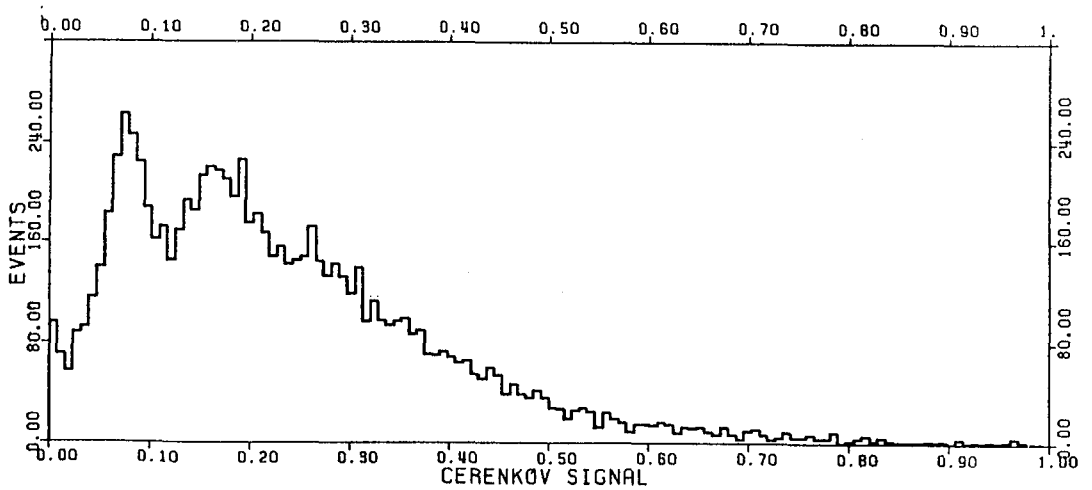


Figure 1

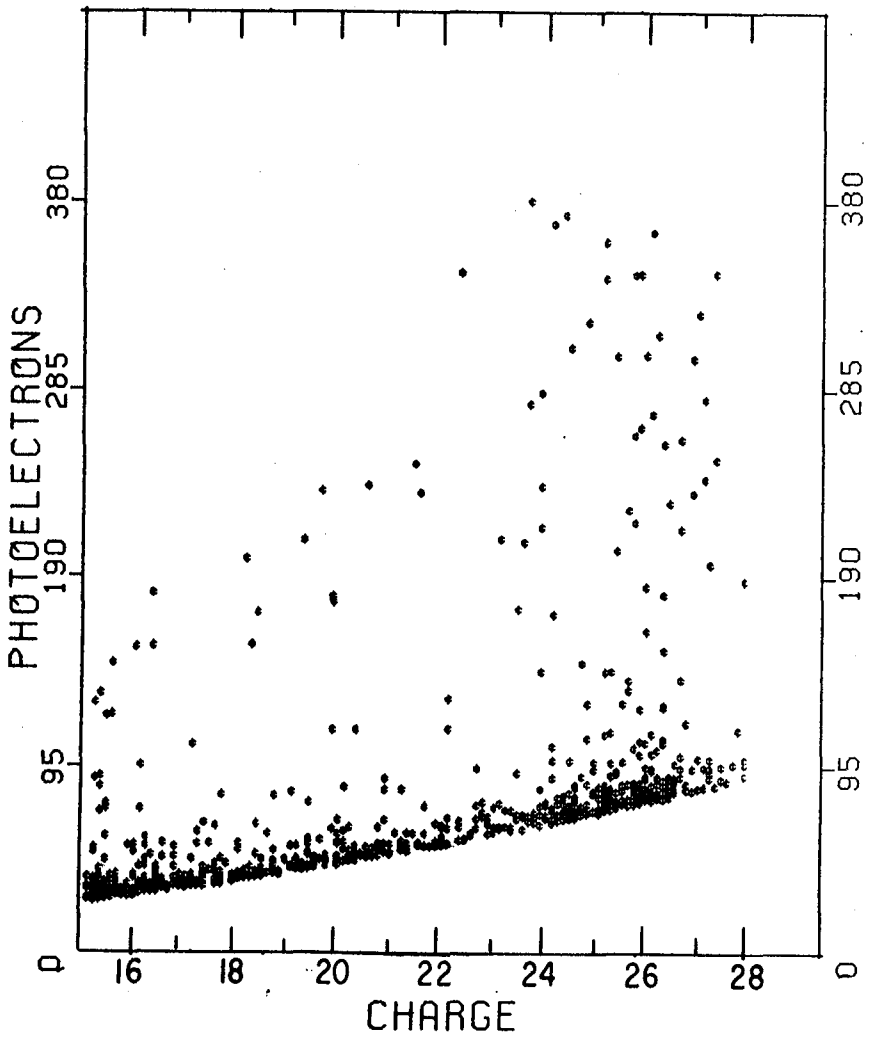


Figure 2

# COSMIC RAY NUCLEI OF ENERGY > 50 GeV/NUC

V. K. Balasubrahmanyan, R. E. Streitmatter, and J. F. Ormes
NASA/Goddard Space Flight Center, Greenbelt, MD 20771

## ABSTRACT

Preliminary results from the High Energy Gas Cherenkov Spectrometer indicate that the sub-iron to iron ratio increases beyond 100 GeV/nucleon. This surprising finding is examined in light of various models for the origin and propagation of galactic cosmic rays.

1. Introduction. The study of the composition of cosmic radiation and its energy distribution has resulted in the development of several models of cosmic ray propagation and information about sources and acceleration phenomena (Cesarsky, 1980) [1]. The results from several balloon experiments and the good statistics data from the HEAO-C measurement (Englemann et al., 1985) [2] indicate that the matter traversed by cosmic rays decreases with energy. In the energy range 1-25 GeV/nuc, this dependence of matter traversed by cosmic rays is expressed as $(\text{rigidity})^{-0.6}$. This trend, if continued beyond 50 GeV/nuc, would result in matter traversed decreasing below 1 g/cm$^2$. As the amount of matter becomes small, the effects of nuclear interaction in the Interstellar Medium (ISM) become difficult to detect if the nuclear mean free path ($\lambda$) in the ISM is much larger than 1 g/cm$^2$. For Fe nuclei $\lambda$ = 2.8 g/cm$^2$ and so relatively Fe becomes a more suitable nucleus to study compared to C, O. The widely differing consequences predicted by the leaky box, nested leaky box, and the closed galaxy models could be tested by studying the relative amounts of primary Fe nuclei and the secondaries from the breakup process.

In addition to these theoretical models, the results from the experiments on the detection of antiprotons (Golden et al., 1979, [3] Bogomolov et al., 1979, [4] Buffington et al., 1981) [5] suggest that the matter traversed by cosmic ray protons may not be consistent with cosmic ray propagation models derived from the study of heavy nuclei. In this, we discuss some of the suggestive trends seen in the preliminary data of the High Energy Gas Cherenkov Spectrometer (HEGCS) and see what we can learn about the conflicting requirement of these phenomena. Details regarding the HEGCS experiment and data analysis are reported in the proceedings of the Conference (paper OG 4.1-11, Streitmatter et al., 1985) [6].

2. Data in Fe and Sub-Fe Region. In the lower energy region up to 25 GeV/nuc, the HEAO-C (Englemann et al., 1985) [2] with its excellent charge resolution and statistics gives a reliable data base. Beyond 25 GeV/nuc, several balloon experiments (Simon et al., 1980, [7] and references therein, and Streitmatter et al., 1985) [6] provide data. The very low flux of the particles to be detected is the most serious problem for statistical reliability. Beyond a few hundred GeV/nuc, the situation is even more murky. JACEE's (Burnett et al., 1983) [8] finding that the highest energy particle was not an Fe but a Ca and the absence of Fe nuclei up to a total energy of $10^{14}$ eV is in contrast with

the delayed particle EAS experiment of the Maryland group (Goodman et al., 1982) [9]. The Maryland group concludes that their results are consistent with a Fe spectrum with a power law exponent -2.39 ± .09. It is to be remembered, however, that EAS experiments have no charge resolution to discriminate between Fe primaries and secondaries of Fe.

In Figure (1) we show the preliminary results from HEGCS in the Fe and sub Fe group. The secondaries of Fe seem to cluster at either the low or high Cherenkov signal, with a paucity of points in between. Fe, however, seems to be distributed more uniformly throughout, with the number of points tapering off at the high signal limit.

Maximum likelihood estimates of the power law exponent for iron give -2.77 ± 0.12, in good agreement with the energy spectrum of protons and He nuclei, as obtained by Ryan et al., 1972 [10] and the JACEE group [9].

3. Double Diffusive Galaxy Model. We have considered a model which has characteristics of both the two component models previously discussed, the nested leaky box model (Cowsik and Wilson, 1973) [11] and the closed galaxy model (Peters and Westergaard, 1977) [12]. The model is characterized by two leaky boxes one inside the other as in the nested leaky box model. The observer is inside the inner box as in the closed galaxy model. Particles are held in both boxes by diffusive scattering and so both boxes would act like leaky boxes. The inner box represents the local interstellar region and the local sources. The lifetime of particles within this source region would be given by the $^{10}$Be observations and the mean matter traversed would be that given by the HEAO-3 observations of B and C, N, O elements. The nuclei observed from a local source region would be relatively young. The composition consists of heavy nuclei.

The outer box would be the galaxy and its halo. This outer box would contain "old" particles, including protons and their secondary antiprotons. Particles would propagate therein under the control of a diffusion coefficient which has the same rigidity dependence as in the inner box, namely, scattering controlled by magnetic inhomogenieties. This would be required by the observation that the proton spectrum is assymptotically the same as those of the heavier nuclei, i.e., $\gamma \approx 2.75$. The matter traversed by particles in this outer box would have to be about three times that of the inner box. Since the mean density is much lower, the lifetime in the outer box would have to be 50-200 time longer than in the inner box.

The source spectra would be given by shock acceleration and the equilibrium spectra observed would be steepened by the energy dependent diffusion in both boxes. This model would remove any conflict between the low energy composition data and the high energy isotropy, which is determined by the conditions in the outer box. The 1 GeV/amu particles observed at Earth contain "young" heavy nuclei from nearby sources ($\lesssim$ 0.5 kpc) and "old" protons and helium nuclei from the galaxy as a whole.

We may be effectively outside the source of the very lowest energy particles (~ 100 MeV/amu) because, at this low energy, the diffusion

coefficient will be very small. This could explain the increasing truncation of the path length distribution below 1 GeV/amu (Wefel et al.).

4. Discussion. Remembering that these results are preliminary, one can note that if iron secondaries do increase at high energies, the conventional leaky box with a monotonic decrease of matter with energy will need modification to account for the ratio of Fe secondaries/Fe at high energies. The antiprotons detected (Golden et al., 1979) [3] do need more matter traversal than the leaky box model would allow. Cowsik and Gaisser 1982, [13] postulate separate sources for antiprotons and heavy nuclei. The normalization of the strengths of these sources would depend on the relative amounts of antiprotons, secondary, and primary heavy nuclei. Various considerations of the nature suggest a two component model for the propagation of cosmic rays.

A leaky box like the outer box with a mean matter traversed would produce an iron secondary to iron ratio approximately twice that of a $7 g/cm^2$ inner box, but both boxes produce a ratio which falls with increasing energy due to the energy dependence of the diffusion coefficient. It, therefore, seems to be difficult to find an admixture of the relative abundances of iron from the two components that could produce a sub-iron to iron ratio which would increase with energy unless the outer box contributes only at higher energy. This could be the case probably only if the relative size of the diffusion coefficient were contrived in the same manner.

In conclusion, it seems difficult to match the increase in the sub-iron to iron ratio with a shock acceleration model including a local source on a general galactic background without introducing a new parameter, namely, the variation of diffusion coefficient with position in the galaxy. Of course, the closed galaxy model itself requires source spectra which are as steep as proton spectrum. One variant of this model might be that high energy particles can penetrate into regions of dense matter. This is the functional equivalent of having a diffusion coefficient which is contrived in a manner which allows higher energy particles to pass through more matter.

References

1. Cesarsky, C. J., 1980, Ann. Revs. Astron. Astrophys., 18, 289.
2. Engelmann, J. et al., 1985, to be published in Astron. and Astrophys.
3. Golden, R. et al., 1979, Phys. Rev. Letters, 43, 1179.
4. Bogomolov, E. A. et al., 1979, Proc. 16th Intl. Cosmic Ray Conf. (Kyoto), 1, 330.
5. Buffington, A. et al., 1981, Ap. J., 248, 1179.
6. Streitmatter, R. et al., 1985, paper OG 4.1-11, this Conference.
7. Simon, M. et al., 1980, Ap. J., 239, 712.
8. Burnett, T. H. et al., 1983, Proc. 18th Intl. Cosmic Ray Conf. (Bangalore), 2, 105.
9. Goodman, J. et al., 1982, Phys. Rev. D26, 1043.
10. Ryan, M. J., et al., 1982, Phys. Rev. Letters, 28, 985.

11. Cowsik, R. and Wilson, L. W., 1973, Proc. 13th Intl. Cosmic Ray Conf. (Denver), 5, 500.
12. Peters, B. and Westergaard, N. J., 1977, Astrophys. and Space Sci., 48, 21.
13. Cowsik, R. and Gaisser, T. K., 1981, Proc. 17th Intl. Cosmic Ray Conf. (Paris), 2, 218.

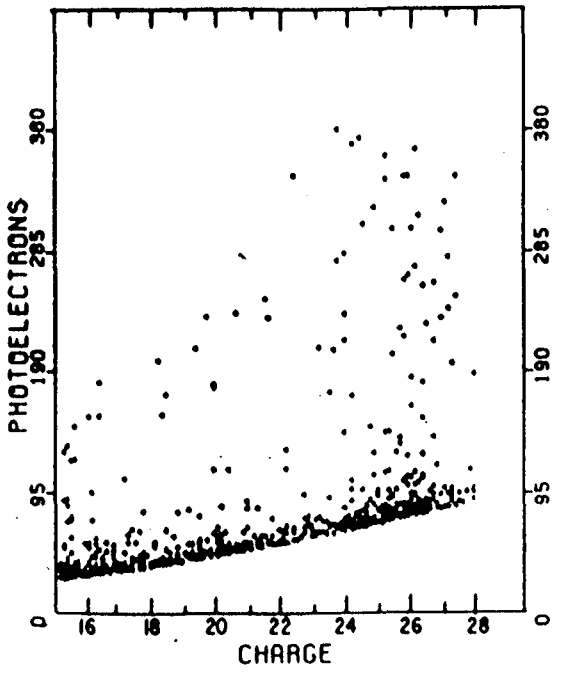


Figure 1

# COMPOSITION AND ENERGY SPECTRA OF COSMIC RAY NUCLEI ABOVE 500 GeV/NUCLEON FROM THE JACEE EMULSION CHAMBERS+

THE JACEE COLLABORATION*

T.H.Burnett(i), S.Dake(b), J.H.Derrickson(g), W.F.Fountain(g), M.Fuki(c), J.C.Gregory(h), T.Hayashi(e,h), R.Holynski(j), J.Iwai(i), W.V.Jones(f), A.Jurak(j), J.J.Lord(i), O.Miyamura(d), H.Oda(b), T.Ogata(a), A.Olszewski (f,j), T.A.Parnell(g), E.Roberts(g), T.Saito(a), S.Strausz(i), M.Szarska (j), T.Tabuki(a), Y.Takahashi(g), T.Tominaga(d), J.W.Watts(g), J.P.Wefel (f), B.Wilczynska(j), R.J.Wilkes(i), W.Wolter(j), and B.Wosiek(j)

(a) Institute for Cosmic Ray Research, University of Tokyo, Tokyo, Japan
(b) Department of Physics, Kobe University, Kobe, Japan
(c) Department of Physics, Okayama University of Science, Okayama, Japan
(d) Department of Applied Mathematics, Osaka University, Osaka, Japan
(e) Science and Engineering Research Laboratory, Waseda University, Tokyo, Japan
(f) Department of Physics and Astronomy, Louisiana State University, Baton Rouge, USA
(g) Space Science Laboratory, NASA Marshall Space Flight Center, Huntsville, USA
(h) Department of Chemistry, University of Alabama in Huntsville, Huntsville, USA
(i) Department of Physics, University of Washington, Seattle, USA
(j) Institute of Nuclear Physics, Krakow, Poland

ABSTRACT

The composition and energy spectra of charge groups(C - O), (Ne - S), and ($Z \geq 17$) above 500 GeV/nucleon from the experiments of JACEE series balloon borne emulsion chambers are reported.

## 1. Introduction.

Studies of cosmic ray elemental composition at higher energies provide information on propagation through interstellar space, acceleration mechanisms, and their sources. One of the present interests is the elemental composition at energies above 100 GeV/nucleon. Statistically sufficient data in this energy region can be decisive in judgement of propagation models from the ratios of SECONDARY/PRIMARY and source spectra (acceleration mechanism), as well as speculative contributions of different sources from the ratios of PRIMARY/PRIMARY. At much higher energies, i.e., around $10^{15}$ eV, data from direct observation will give hints on the "knee" problem, as to whether they favor an escape effect possibly governed by magnetic rigidity above $10^{16}$ eV.

The JACEE balloon flight experiments continue to measure composition and energy spectra of cosmic rays (Z = 1 to 26) directly at energies $10^{12}$ to $10^{15}$ eV using large area thin emulsion chambers [1 - 5]. The previous JACEE results indicated no significant change of spectral indices up to 500 TeV and 50 TeV/nucleon for proton and helium spectra, respectively [4]. Flux values of each group (C - O), (Ne - S), and (Fe) at least up to $10^{14}$ eV also indicated no significant evidence for heavy nuclei dominance within the limited statistics [5]. In this paper, the results for the

energy spectra of charge groups (C - O), (Ne - S), and ($Z \geq 17$) above 500 GeV/nucleon are updated.

## 2. Apparatus and Experimental Procedure.

Details of the apparatus and techniques of JACEE emulsion chambers have been reported in refs. [1 - 5]. Each detector, comprised more than 350 layers of materials, is functionally divided into three sections: (1) the primary charge determination module at the top, (2) the target module where nuclear interactions occur preferentialy (3) the calorimeter at the bottom to measure the energies of released gamma rays from interactions.

Events were detected by visual scanning of X-ray films for dark spots produced by electromagnetic cascades in the calorimeter under the same criterion of darkness (D) in an area of 200 x 200 $\mu m^2$. For these events, primary charge Z ($\Delta Z < 1$) above the interaction and the total energy of released gamma rays $\Sigma E_\gamma$ ($\Delta \Sigma E_\gamma < 25$ %) were measured [1 - 5].

The maximum value of darkness ($D_m$) in the cascade development is a function of not only $\Sigma E_\gamma$ but also the vertex height (H) from the top of the calorimeter, incident angle ($\theta$), and interaction characterstics (transverse momentum and multiplicity). Among these parameters, the main factors are $\Sigma E_\gamma$ and H. For a fixed $\Sigma E_\gamma$ value, $D_m$ distributes around some mean value. The width of this distribution $g(D_m)dD_m$ depends on the primary charge (mass) and the chamber design. $g(D_m)$ has been calculated by a Monte Carlo method using the chamber design adopted here, interaction characteristics (CKP and superposition models), and characteristic curves of the response of X-ray films. Then, the detection efficiency $P(Z, \Sigma E_\gamma)$ under the threshold $D_m^{th}$ is calculated by,

$$P(Z, \Sigma E_\gamma) = \int_{>D_m^{th}} g(D_m)dD_m \; / \; \int_{D_m} g(D_m)dD_m \; .$$

In case of calorimeter jets, i.e., H = 0, $P(\Sigma E_\gamma)$ rapidly reaches 100 % at $\Sigma E_\gamma$ = 1 TeV for all elements under the threshold level $D_m^{th} = 0.1$ which is a practical threshold, because of no fluctuation of H. On the other hand, in the case of target jets, the practical threshold $D_m^{th}$ becomes about 0.15 and the width of $g(D_m)$ becomes larger due to a fluctuation of H values. This gives higher values of $\Sigma E_\gamma$ to obtain $P(\Sigma E_\gamma) = 100$ %. The critical $\Sigma E_\gamma$ values have been estimated by the above method for different nuclear species. For light elements such as proton and helium, the critical $\Sigma E_\gamma$ was about 1.5 TeV which has been achieved in an analysis of selected JACEE chambers. Under the present standard event selection ($D_m^{th} = 0.3$) the detection efficiency $P(\Sigma E_\gamma \geq 10$ TeV) is confirmed to be 100 % for all elements and for all existing JACEE chambers.

## 3. Deconvolution of Primary Spectrum.

The observed $\Sigma E_\gamma$ spectrum is a convolution of the primary spectrum and the distribution function $f(k_\gamma)$ where $k_\gamma$ ($= \Sigma E_\gamma / E_0$) is a partial inelasticity into gamma rays; $E_0$ is primary energy. $f(k_\gamma)$ has been also calculated by the above Monte Carlo method [6], including succesive interactions, assuming its energy independence. The $\Sigma E_\gamma$ spectrum $F(\Sigma E_\gamma)d\Sigma E_\gamma$ is given by,

$$F(\Sigma E_\gamma)d\Sigma E_\gamma = \int_{k_\gamma} f(k_\gamma)dk_\gamma \int_{E_0} G(E_0)dE_0 \; \delta(\Sigma E_\gamma - k_\gamma E_0) \; ,$$

where $G(E_0)dE_0$ is primary spectrum. This formula directly shows that the $\Sigma E_\gamma$ spectrum is uniquely a power law with the same index as the primary

spectrum when $G(E_0)dE_0 \propto E_0^{-\beta}\, dE_0$. The energy conversion factor $Ck_\gamma$ from the $\Sigma E_\gamma$ spectrum to primary spectrum is then given by,

$$Ck_\gamma = [\int_{k_\gamma} k_\gamma^{\beta-1} f(k_\gamma)\, dk_\gamma]^{1/(\beta-1)}$$

$Ck_\gamma$ is applied to obtain the same flux between the $\Sigma E_\gamma$ spectrum and the primary spectrum at $E_0 = \Sigma E_\gamma / Ck_\gamma$. Values of $Ck_\gamma$ for each element in case of calorimeter and target jets were calculated as follows,

| | P | He | N | Mg | Ca | Fe |
|---|---|---|---|---|---|---|
| calorimeter | 0.240 | 0.174 | 0.100 | 0.082 | 0.064 | 0.058 |
| target | 0.222 | 0.159 | 0.120 | 0.117 | 0.115 | 0.115 |

for chambers mainly used in this work [7].

The collecting power of the detectors was calculated by a Monte Carlo method using both the geometric aperture and the probability of interactions for each element. Absolute fluxes above chambers were estimated considering the resolution function of $\Sigma E_\gamma$ measurements which is an almost constant Gaussian type with a 25 % width in our case. After atmospheric correction at the depth of 3 - 5 g/cm$^2$, the flux values at the top of atmosphere were obtained.

4. Results and Discussion.

Figs. 1, 2, and 3 show the results of the integral energy spectra for groups (C - O), (Ne - S), and ($Z \geq 17$) above 500 GeV/nucleon under the present event selection criterion of $D_m^{th}$ based upon a simulation. In Fig. 3, Fe spectrum at energies 20 to 80 GeV/n from the JACEE-3 hybrid detector experiment [8] is also shown. In these figures, the low energy results from two experiments [9, 10], recently reported, are included for comparison. Solid lines are the extrapolation from the flux value at 25 GeV/n of ref. [9] with the spectral indices 1.7 and 1.5. Data around 4 TeV/n for (C - O) and (Ne - S), and those around 1 TeV/n for ($Z \geq 17$) are corrected, by empolying the Monte Carlo calculations for data analysis below the sub-threshold $\Sigma E_\gamma$ = 10 TeV. In these figures, at energies higher than sub-threshold, data of each group indicate slightly higher flux values (to about one s.d. from the extrapolated spectra with an index 1.7) with the statistics of only 4, 2, and 1 of 3 (Ca at 78 TeV/n) events for respective groups, while (C - O) data around 1.5 TeV/n with the statistics of 10 events are in agreement with the low energy data for index 1.7. Statistical improvements are obviously desired for our continueing efforts at the highest energies above $10^{14}$ eV.

Can emulsion chamber technique identfy a bending of the primary spectrum by using of the $\Sigma E_\gamma$ method under the convolution of $k_\gamma$ distribution? Monte Carlo studies have shown a positive answer for this question, at least for heavy nuclei component. If materials of more than about 3 interaction length are available, then the distribution function $f(k_\gamma)$ approaches the Gaussian type with about 35 % width, by virtue of succesive interactions. Hence, it is sufficient to detect any narrow peaks or bends in the energy spectrum, provided sufficient statistics are gathered. For observations above $10^{15}$ eV, however, the energy resolution becomes poorer than our current observations, because the shower maximum of electromagnetic cascades in the calorimeter becomes too deep for thin chambers currently adopted. Even in this case, emulsion chamber techniques still

provide measurements of cosmic ray energy above $10^{15}$ eV without increasing the thickness of calorimeter if the $e^{\pm}$ pair method is used to augment the $\Sigma E_{\gamma}$ energy determination [11].

References.

[1] Huggett, R.W. et al., Proc. 17th ICRC(Paris), 8, 20 (1981).
[2] Gregory, J.C. et al., Proc. 17th ICRC(Paris), 9, 154 (1981).
[3] Burnett, T.H. et al., Proc. Workshop on Very High Energy Interactions (Philadelphia), 221 (1982).
[4] Burnett, T.H. et al., Phys. Rev. Lett., 51, 1010 (1983).
[5] Burnett, T.H. et al., Proc. Intern. Symposium on Cosmic Ray and Particle Physics (Tokyo), 468 (1984).
[6] Recent results for Fe-nucleus interactions at energies 20 to 60 GeV/n from JACEE-3 experiment indicated that the inclusive data of multiplicities support the use of superposition model of proton-nucleus interactions for this calculation. See Burnett, T.H. et al., HE 1.4-2 of this conference.
[7] Possible systematic error about 10 % of these values is insensitive to the present status of our high energy composition.
[8] Burnett, T.H. et al., OG 4.1-9 of this conference.
[9] Simon, M. et al., Astrophys. J., 239, 712 (1980).
[10] Juliusson, E. et al., Proc. 18th ICRC (Bangalore), 2, 21 (1983).
[11] Takahashi, Y. et al., Proc. Workshop on Cosmic Ray and High Energy Gamma Ray Experiments for the Space Station Era (Baton Rouge), (1984).

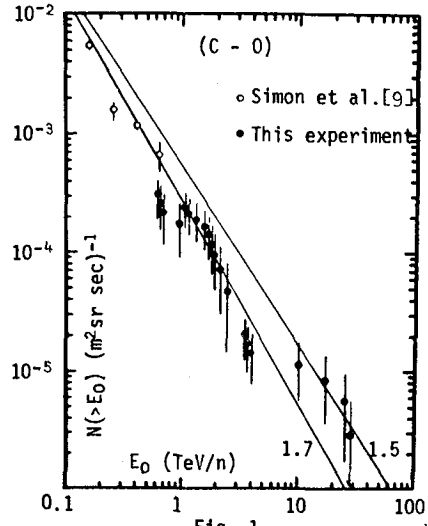


Fig. 1

+ This work was supported in part by the ICR, the JSPS, and Kashima Foundation in Japan; in part by the DOE, the NASA, and the NSF in the USA.

* Mailing Address Dept. Chemistry, Univ. of Alabama in Huntsville, Huntsville, AL 35899, and ICR, Univ. Tokyo, Tanashi, Tokyo 188, Japan.

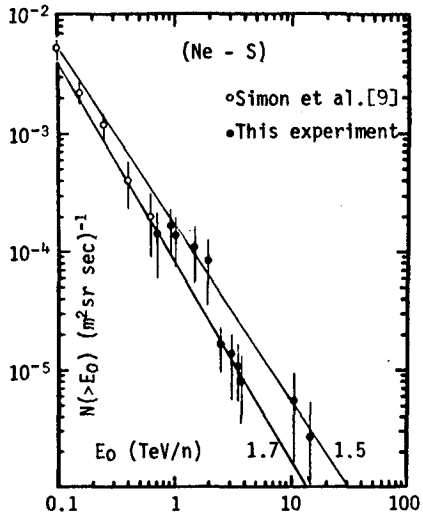


Fig. 2

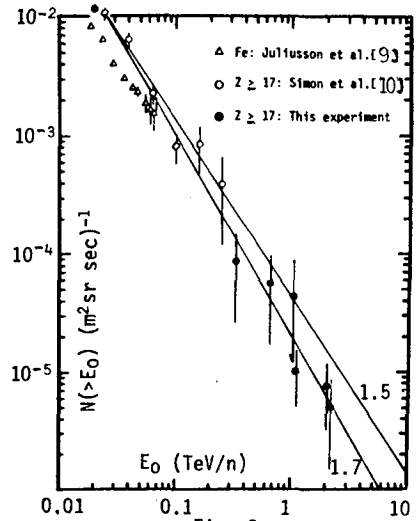


Fig. 3

# CHARGE COMPOSITION AND ENERGY SPECTRUM OF COSMIC RAY PRIMARY PARTICIES FOR ENERGIES HIGHER THAN I TEV

Vernov S.N., Ivanenko I.P., Grigorov N.L., Basina Yu.V., Vakulov P.V., Vasilyev Yu.Ya., Golinskaya R.M., Grigoryeva L.B., Zhuravlev D.A., Zatsepin V.I., Ilyichev D.I., Kasakova A.E., Kozlov V.D., Kumpan I.P., Laputin Yu.A., Mishchenko L.G., Nikanorov B.M., Papina L.P., Platonov V.V., Podorozhny D.M., Rapoport I.D., Samsonov G.A., Smolensky L.G., Sobinyakov V.A., Sokolov V.K., Tambovtsev G.E., Tretyakova Ch.A., Trigubov Yu.V., Fateyeva I.M., Khein L.A., Chikova L.O., Shestoperov V.Ya., Shiryaeva V.Ya., Yakovlev B.M., Yashin I.V..

Institute of Nuclear Physics, Moscow State University, Moscow II9899, USSR

ABSTRACT

Onboard the "Cosmos-I543" satellite an experiment was performed to investigate the charge composition and primary cosmic ray energy spectrum for energies higher than I TeV. Preliminary experimental data are reported.

I. Introduction. Investigation of the energy spectrum of various groups of primary cosmic ray nuclei in the high and superhigh energy regions is one of the most important problems of cosmic ray physics and astrophysics. In the energy range I-I0 GeV per nucleon the situation is rather clear [I], while in the range of $E > I00$ GeV per nucleon the problem is not solved yet [2] . To perform investigations in this energy region we have elaborated a special apparatus [3] and carried out in I984 the experiment beyond the atmosphere.

2. Methods. We used as energy detector the ionization calorimeter with the total thickness of absorber 5.5 paths for proton interaction. It consisted of 8 steel plates each I0 cm thick and located above 8 scintillators. Each scintillator was attached to a lightguide and viewed by a PMT-84. The calorimeter is situated below the aluminium target about 8 cm thick, two lead absorbers 3 cm and 2 cm

thick, and two rows of scintillators employed to estimate the energy of electromagnetic cascades generated in the target.

Above the installation two types of Cerenkov charge detectors are located. The first-type detector consists of II directed action counters. Each counter comprises a radiator in optical contact with a PMT-49 and measures charges in the range of $I \leq Z \leq 5 \div 7$. Above this detector the second one is located, which composed of four counters to measure charges in the range of $3 \leq Z \leq 60$. Every counter consists of a radiator enclosed in a light-proof box and is viewed by a PMT--49. An accuracy of determination of Z under onground conditions is about 4%.

The device comprised the total of I99 amplitude analysers serving 95 detectors. The device's construction, characteristics, stability, and energy consumption are described in detail in [3].

3. Results. The device was exposed in an almost circular orbit with a mean removal from the Earth of 330 km and an inclination angle of $62.8^{\circ}$. It was oriented along three axes with the longitudinal axis being vertical.

The main mode for the device to put into operation required a signal in the directed action Cerenkov detector excited by a particle of $Z \geq I$, the total energy release in the calorimeter being $\gtrsim$ I.5 TeV at energy release $\gtrsim$ 35 GeV at least in eight absorbers. The rate of event registration remained constant during the whole experiment. The performed analysis showed that all the experimental apparatus work had been stable.

Up to date a small fraction of the data obtained has been processed, and the material presented below is mainly qualitative.

Figs. I and 2 show the examples of registered events. Two projections of the device and the avalanche position in the calorimeter are shown. The height of rectangles is proportional to the particle number in the corresponding scintillator. In the topr part of the position of the operated charge detectors is shown. The first event was initiated by a proton with energy I5 TeV and the second one by a neon nucleus of energy 20 TeV.

Fig. 3 characterises the separation of both proton and helium

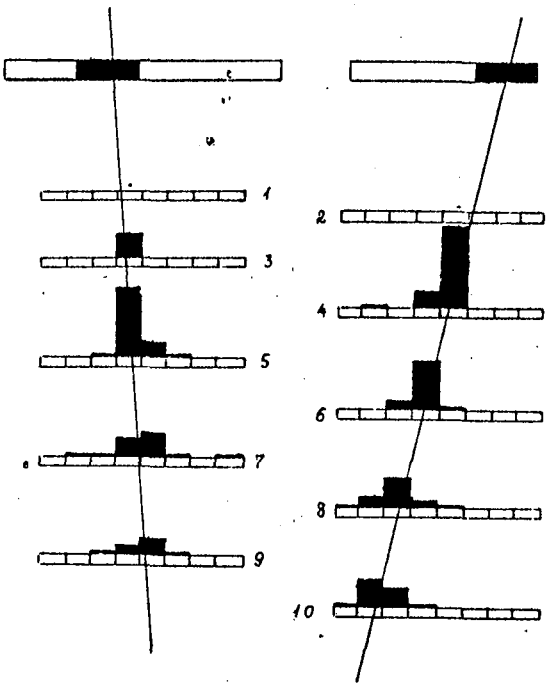


Fig. I

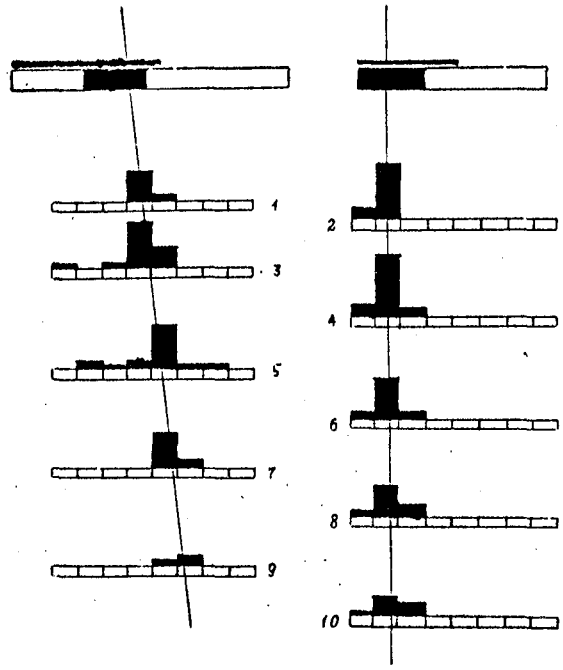


Fig. 2

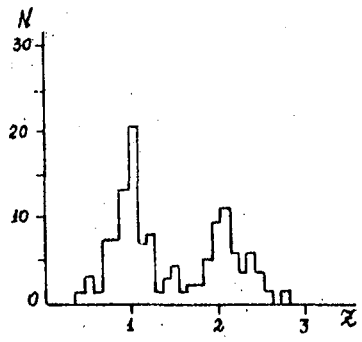


Fig. 3

of both proton and helium nuclei by the d directed action charge detectors. The ratio of particles with Z = 2 and Z = I (0.6-0.7) is close to that of at low energies.

The charge distribution at $Z \geq 5$ obtained with the aid of the upper detector is shown in Fig.4, alongside with the expected distribution, provided that the distribution on Z is the same as that of the lower energies, and the amplitude distribution at fixed Z is characterized by the rms spread $\sigma \approx 4\%$. An examination of Fig. 4 shows that at $Z \geq 5$ the nucleus charge composition is, within error limits, the same as that of at low energies.

Fig. 5 presents the differential spectrum of nuclei with $Z \geq 2$. At low energies the spectrum is limited by $E_{thr} \approx$ I.0 + + I.5 TeV, and at higher energies $\gamma = 2.50 \pm 0.25$.

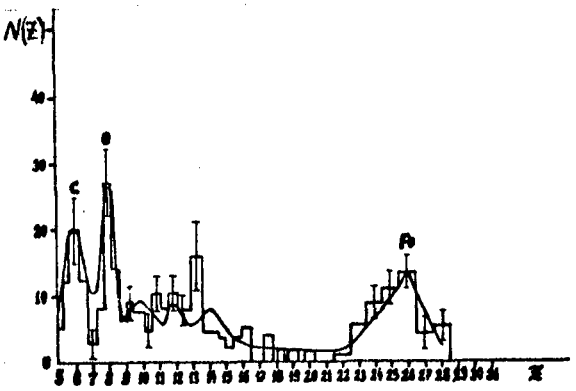


Fig. 4

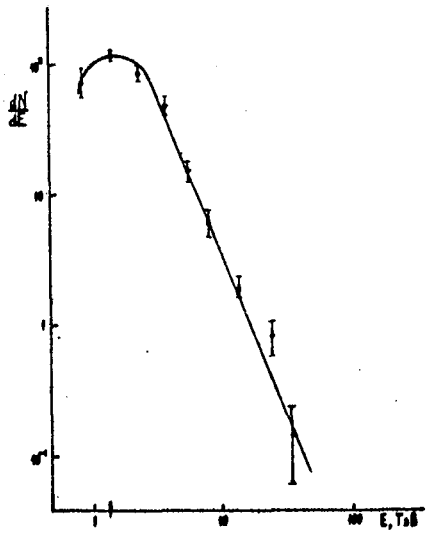

Fig. 5

Conclusions. It shoud be noted that the above presented experimental data do not indicate any abrupt variations of the spectrum and charge composition, however, they require further clarification. The presented distributions were plotted for all the events processed, while the threshold energies and the possibilities of particle registration may be a function of Z.

References

I. Juliusson, E., (I983), Proc. I8 ICRC, v.I2, II7
2. Linsley, J., (I983), Proc. I8 ICRC , v.I2, I35
3. Vernov, S.N. et al., (I98I), Proc. I7 ICRC, v.8, 49.

# INTERSTELLAR PROPAGATION AND THE ISOTOPIC COMPOSITION OF HYDROGEN IN THE GALACTIC COSMIC RAYS

James J. Beatty
Enrico Fermi Institute and Department of Physics
University of Chicago, Chicago, Illinois, USA

Abstract Preliminary results of a study of the propagation of the quartet of stable isotopes of hydrogen and helium are reported. A mean pathlength of $7.5\pm0.5$ g/cm$^2$ at $\sim$300 MeV/nucleon is required to explain the low-energy deuterium spectrum. This pathlength is consistent with pathlengths derived from the elements with Z>2, but is a factor $\sim$2 lower than the value required to explain the ($^3$He/$^4$He) measurement of Jordan and P. Meyer (1984). The propagation calculations reported here incorporate the preliminary results of an updated nuclear-interaction cross section survey covering the period since the review by J.P. Meyer (1972).

Introduction. The quartet of isotopes of hydrogen and helium constitute a closely-coupled set of nuclides which provide strong constraints on the cosmic ray source spectra and on the escape pathlength of cosmic rays from the galaxy. (See Simpson (1971) for a review.) The recent measurements of ($^3$He/$^4$He) in the energy range 5-10 GeV/nucleon by Jordan and P. Meyer (1984) and Jordan (1985) require a pathlength of $\sim$15 g/cm$^2$ to account for the experimental data, which is inconsistent with the value $\sim$6 g/cm$^2$ inferred from CNO and their secondaries. (e.g. Garcia-Munoz et. al. (1981)) In this paper, the pathlength traversed by low-energy H and He during interstellar propagation is studied using the high-resolution, low energy spectra of $^1$H, $^2$H and $^4$He determined using the University of Chicago IMP-8 telescope under solar minimum (1976-1977) conditions (Beatty et. al. 1985 and references therein). It is found that the observed fluxes of these nuclei at low-energy are consistent with the pathlength deduced from the elements with Z>2, but not with the much longer pathlengths required by the high energy He isotopic ratio.

Measurements. The $^2$H measurements used in this work were obtained using the University of Chicago IMP-8 telescope during the period June 1976 to April 1977, at solar minimum modulation. $^2$H is identified by the (dE/dx) vs. residual E method. The measurement of $^2$H is most reliable near the end-of-range, where the $^2$H energy deposit in the CsI(Tl) residual E detector (D4) is $\sim$30% greater than the largest energy deposited by the more abundant $^1$H (Figure 1,insert).

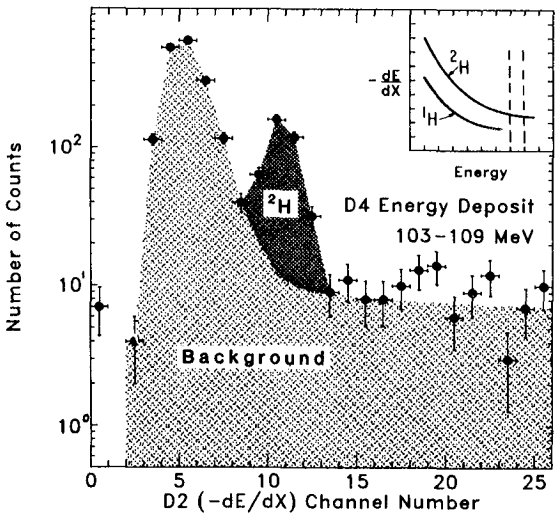


Figure 1

Plotting the number of counts per (-dE/dx) channel (D2), the $^2H$ appears as a peak superposed on a high energy interaction background. At solar minimum, subtraction of this background leads to a correction of only 25%. The r.m.s. width of the $^2H$ peak is 0.13 amu, corresponding to a FWHM of 0.31 amu. A more detailed discussion of the data analysis has been presented in Beatty et. al. (1985).

Modeling of Cosmic Ray Propagation. The effects of interstellar propagation on an assumed cosmic ray source spectrum are computed using a weighted-slab model (WSM), in which solutions of the equation describing the passage of nuclei through interstellar matter

$$\frac{\partial J}{\partial x} = \frac{\partial}{\partial E}\left(\frac{dE}{dx} J_i\right) + \sum_k \int \frac{J_k}{\Lambda_{ki}} dE' - \frac{J_i}{\Lambda_i}$$

are weighted by a pathlength weighting function (PLWF) to obtain the local interstellar cosmic ray flux:

$$J_{c.r.}(E) = \int dx\, P(E,x) J_{slab}(E,x)$$

For a leaky-box model (LBM) with energy-independent escape pathlength , it can be shown that the PLWF is an exponential: $P(x)=\exp(-x/\lambda)$. (Lezniak,1979)

The calculation procedure used in this work includes the effect of ionization energy loss at all energies, and includes kinematic energy-changing effects in the reactions H(p,d $\pi$+ ) and He(p,d) He. Kinematic effects in other reactions and energy losses due to elastic scattering are small and have been neglected. Results of calculations including the small effects neglected here will be published elsewhere (Beatty, 1985).

The nuclear interaction cross sections used here are the preliminary result of a survey in this laboratory of the experimental cross section measurements performed since the compilation by J.P. Meyer (1972). The remaining uncertainties in the cross sections are largest for the production of deuterium by the spallation of cosmic ray helium on the interstellar medium at energies above $\sim$500 MeV per nucleon.

Solar modulation has been taken into account using the model of Evenson et. al. (1983). For the solar minimum data discussed here, the adiabatic deceleration parameter is 440 MV.

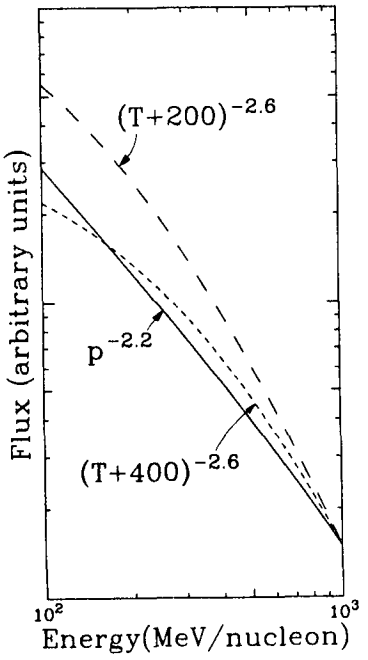


Figure 2

The Primary Energy Spectra. In the leaky box propagation model, the local interstellar spectra of $^1H$ and $^4He$ are simply related to the source spectrum and to the functional form of $\lambda(E)$. The pathlength for nuclear inelastic interaction with the interstellar medium is long compared with the expected escape pathlength. Secondary production of these species can be neglected because of their large source abundances. Energy loss effects are less important than for heavier elements: the lowest energy local interstellar particles

which are seen at Earth (i.e., which have local interstellar energies greater than the energy lost during solar modulation) have lost <20% of their initial energy during interstellar propagation. Under these conditions, the leaky box model solution can be approximated by the simple algebraic result $J(E) = \lambda(E)\, Q(E)$. In this paper, momentum power law source spectra of the form $\frac{dN}{dP} = \frac{dJ}{dT} \propto p^{-\gamma}$ have been used. Figure 2 compares the chosen source spectrum $p^{-2.2}$ with the spectra $(T+200MeV)^{-2.6}$ used by J.P. Meyer (1974), and $(T+400MeV)^{-2.6}$ used by Garcia-Munoz et. al. (1981). The latter two spectra lead to a spectrum which is too steep when the energy dependence of $\lambda(E)$ at high energies is taken into account, but are similar to the momentum power-law spectrum above at energies below several GeV/nucleon.

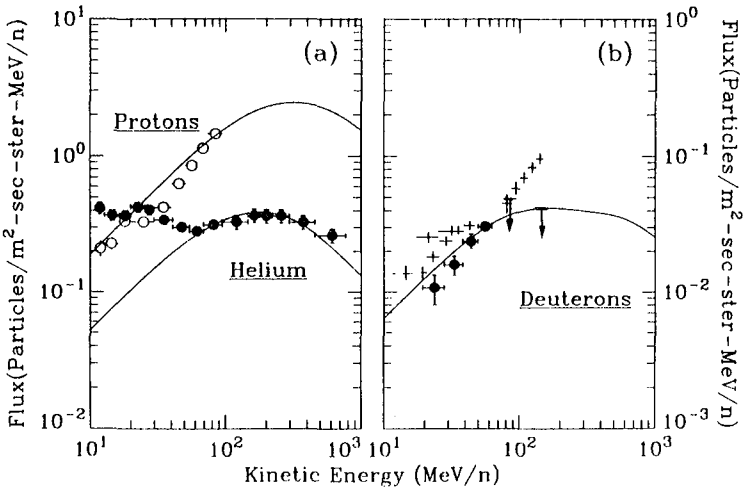


Figure 3 Computed 1 A.U. H, H, and He spectra for a 7.5 g/cm pathlength under 1976-1977 solar minimum conditions. Panel (a): open circles, protons; filled circles, helium; Garcia-Munoz et. al. (1977). Panel (b), deuterium: filled circles, Beatty et. al. (1985); crosses, Webber and Yushak (1983); upper limits, Leech and O'Gallagher (1978).

The source abundances used in this work are those of J.P. Meyer (1985), except that the ratio $^1H/^4He$ at constant energy/nucleon is determined to be $\sim$12.2 at low energy.

Deuterium Production. The pathlength is determined by the requirement that the modulated deuterium flux at 1 A.U. match the value measured under solar minimum conditions by the University of Chicago telescope on IMP-8. Figure 3 shows the computed $^1H$, $^2H$, and $^4He$ spectra together with experimental data from this period. (See caption) The pathlength required is 7.5 g/cm$^2$, using the model of Evenson et. al. (1983) to describe the effects of modulation during the 1976-1977 solar minimum. The error in this pathlength due to the experimental uncertainties in the measured fluxes is 0.5 g/cm$^2$.

Figure 4 illustrates the relative importance of contributions from cosmic ray $^1H$, $^4He$, and CNO. The local interstellar spectrum has been divided by the momentum power law source spectrum used in the calculations. Because the contribution from cosmic ray $^1H$ is entirely due to energy-changing kinematic processes, the importance of these reactions is strongly dependent on the source spectral form and on the low-energy behavior of $\lambda(E)$.

Difficulties in the interpretation of weighted-slab models arise when energy-changing processes become important. Lezniak (1979) has compared the LBM to the WSM, and has noted cases in which the mean of the WSM exponential PLWF and the value of the LBM escape pathlength are not equivalent. We have investigated the importance of these effects on the quartet. For the case where $\lambda(E)$ increases with increasing energy as $E^{0.5}$ (Garcia-Munoz et. al. 1981; Ormes and Protheroe 1983), the effect of ionization energy loss will increase $^2H$ production by $\sim$5%, and the effect of energy-changing processes involving cosmic ray $^1H$ will increase $^2H$ by $\sim$10-20%. It should be noted that in both cases the WSM underestimates the production of $^2H$ relative to the corresponding LBM, and therefore overestimates the pathlength traversed in the case where $\lambda(E)$ increases with increasing energy. The quantitative analysis of the case of energy-dependent PLWFs will be published elsewhere (Beatty, 1985).

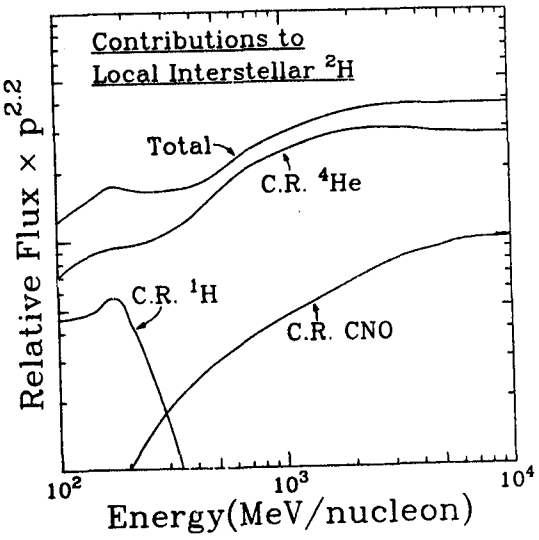


Figure 4

Acknowledgements. Discussions with M. Garcia-Munoz, T.G. Guzik, R.A. Kroeger, K.R. Pyle, and J.A. Simpson are greatly appreciated. This research was supported in part by NASA Grant NGL 14-001-006 and NASA Contract NAS 5-28442.

References.

Beatty, J.J., 1985, Thesis, University of Chicago, in preparation.
Beatty, J.J., Garcia-Munoz,M., and Simpson, J.A., 1985, Ap.J. 294, 455.
Evenson, P., Garcia-Munoz, M., Meyer, P., Pyle, K.R., and Simpson, J.A., 1983, Ap. J., 275, L15.
Jordan, S.P., 1985, Ap. J. 291, 207.
Jordan, S.P., and Meyer, P., 1984, Phys. Rev. Lett. 53, 505.
Leech,H.W., and O'Gallagher, J.J., 1978, Ap.J. 221, 1110.
Lezniak, J.A., 1979, Ap. Space Sci. 63, 279.
Garcia-Munoz, M., Guzik, T.G., Simpson, J.A., and Wefel, J.P., 1981, Proc. 17th Internatl. Cosmic Ray Conf.(Paris) 9, 195.
Garcia-Munoz, M., Mason, G.M., and Simpson, J.A., 1977, Proc. 15th Internatl. Cosmic Ray Conf.(Plovdiv) 3, 209.
Meyer, J.P., 1972, Astron. Astrophys. Suppl., 7, 417.
------, 1974, Thesis, University of Paris.
------, 1985, Ap. J. Suppl. 57, 173.
Ormes, J.F., and Protheroe, R.J., 1983, Ap. J. 272, 756.
Simpson, J.A., 1971, Proc. 12th Int. Conf. on Cosmic Rays (Hobart), Invited and Rapporteur Papers, 324-356.
Webber, W.R., and Yushak, S.M., 1983, Ap. J. 275, 391.

# MEASUREMENTS OF GALACTIC HYDROGEN AND HELIUM ISOTOPES FROM 1978 THROUGH 1983*

Paul Evenson[+], Richard Kroeger[x], Peter Meyer[x], and Dietrich Müller[x]

[+]Bartol Research Foundation, University of Delaware
Newark, Delaware 19716 USA

[x]Enrico Fermi Institute and Department of Physics
University of Chicago, Chicago, Illinois 60637 USA

ABSTRACT. We have measured the differential flux of the hydrogen and helium isotopes using our instrument on the ISEE-3 spacecraft during solar quiet time periods from August 1978 through December 1983. These measurements cover the energy range from 26 MeV/nucleon through 138 MeV/nucleon for both $^{1}H$ and $^{4}He$, from 24 to 89 MeV/nucleon for $^{2}H$, and from 43 to 146 MeV/nucleon for $^{3}He$. During the observations, the level of solar activity varied from near minimum to maximum conditions causing the observed flux of galactic cosmic rays to modulate by an order of magnitude. To describe the propagation in the galaxy, we find that the standard leaky box approximation with an escape path length of 6.7 g/cm$^2$ forms a self-consistent model for the light cosmic ray nuclei at the observed energies.

1. INTRODUCTION. Both cosmic ray $^{2}H$ and $^{3}He$ are secondary particles resulting from spallation of primary cosmic rays on interstellar matter. Measurements of the local flux of these particles are particularly interesting because the light cosmic rays have a path length for nuclear destruction which is greater than the mean confinement path length in the galaxy. Therefore, they are sensitive to the average amount of matter penetrated by the cosmic rays but not to details of the path length distribution.

We present here new measurements of the hydrogen and helium isotopes $^{1}H$, $^{2}H$, $^{3}He$, and $^{4}He$ (the "quartet") made with the University of Chicago experiment on the ISEE-3 spacecraft. Although this instrument was primarily designed to observe the electron component, it achieves excellent isotopic resolution of the light nuclei, and permits reliable background determination over the energy range of nuclei stopping in the detector. A complete description of this instrument is given by Meyer and Evenson [1]. Isotopic resolution is achieved using the standard $\Delta E$ vs. E method. Details of the analysis procedure will be given by Kroeger [2]. We achieved a mass resolution of approximately $\pm 0.34$ amu FWHM (see figure 1).

2. RESULTS. The abundance ratios of secondary to primary particles are presented in figure 2. The average ratios are $^{2}H/^{4}He=0.127\pm0.006$ (65-87 MeV/n), $^{3}He/^{4}He=0.075\pm0.008$ (65-87 MeV/n), and $^{3}He/^{4}He=0.074\pm0.005$ (87-120 MeV/n). These ratios are not affected by anomalous helium fluxes

*Supported, in part, by NASA contract NAS 5-26680 and NASA grants NGL 14-001-005 and NSG 7464.

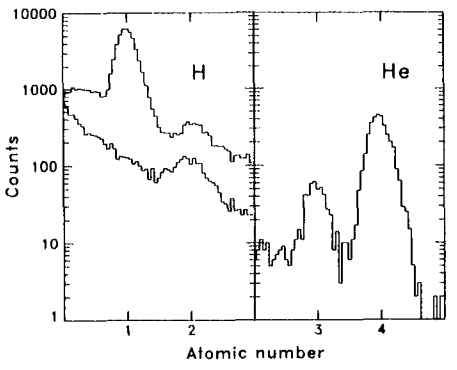


*Figure 1*

*Mass histograms showing the isotopic resolution of the ISEE-3 instrument. The data were collected in 1979 in an energy range of 65-87 MeV/n for both $^{2}H$ and $^{3}He$. The two hydrogen histograms are from using different detectors for the ΔE measurement. The bottom curve is composed of events classified as $^{2}H$ by the upper curve. Note the effective elimination of the structured background due to protons.*

since these are significant only below 60 MeV/n. Calculations of solar modulation indicate that these ratios should vary by a factor of 1.26 for $^{2}H/^{4}He$ (top panel) with the lowest ratio occurring in 1978 and the highest in 1981. The $^{3}He/^{4}He$ ratio should vary by 1.15 in the same manner (bottom two panels). The modulation effects are within the statistical errors of our measurements.

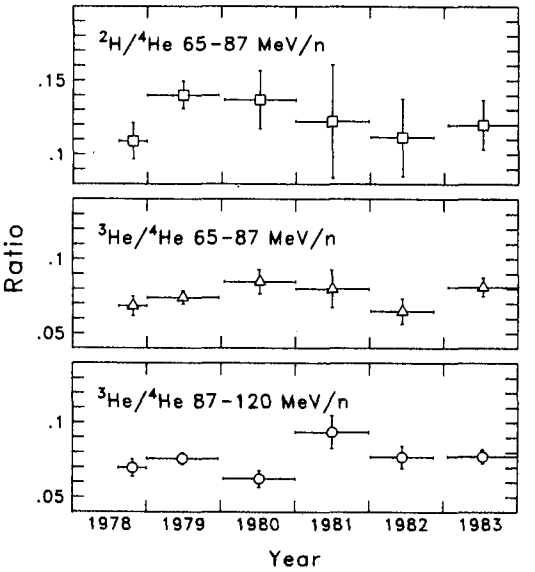


*Figure 2*

3. DISCUSSION. The abundance ratios are interpreted using a leaky box approximation for the confinement of cosmic rays in the galaxy. In this model effects due to interactions with the interstellar medium are included (i.e. energy loss due to ionization, nuclear destruction and production). It is assumed that the source spectrum of cosmic rays is a power law in rigidity with a spectral index of -2.2, and that the mean escape path length is given by,

$$\Lambda_e = \begin{cases} X & \text{for } R < 5.5 \text{ GV} \\ X\,(R / 5.5)^{-0.6} & \text{for } R > 5.5 \text{ GV}, \end{cases}$$

where R is rigidity and X is the mean escape path length. We determine the path length X which best fits our data.

During our measurements, solar activity changed from near minimum conditions to solar maximum. Consequently, the flux of galactic particles changed by an order of magnitude as measured at 1 AU. We account for modulation using a spherically symmetric convection diffusion model [3]. This model requires a suitable choice of the diffusion coefficient for particles in the heliosphere in order to simulate particular levels of modulation. The selection we make enables us to match the local interstellar $^{4}He$ spectrum calculated from the leaky box model to our

measured data. The diffusion coefficient we use is derived by interpolating between the solar maximum and solar minimum diffusion coefficients obtained from Garcia-Munoz [4]. His choice of diffusion coefficients were gained originally from a comparison of the interstellar electron spectra with local measurements. In figure 3 we display the local interstellar $^4$He spectrum and the modulated spectra that fit our 1978 and 1981 data. Figure 4 compares our calculation of the modulated proton spectra with the measurements using the same diffusion coefficients that were determined from the $^4$He fit. The fit to the proton data is excellent for the years 1978-1980. However, the calculation predicts too many protons for the years when modulation is strongest (a factor of 1.3). This apparent discrepancy can easily be resolved by small changes in the assumptions used in the leaky box model which effect the shape of the calculated interstellar spectra. However, rather than introduce additional free parameters we prefer to use the simplest model possible and neglect this discrepancy. Both $^2$H or $^3$He are expected to follow the modulation of $^4$He more closely than protons since their rigidities are closer to that of $^4$He for a given energy/nucleon.

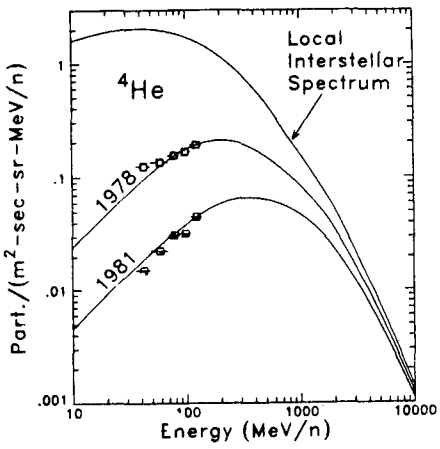


*Figure 3*

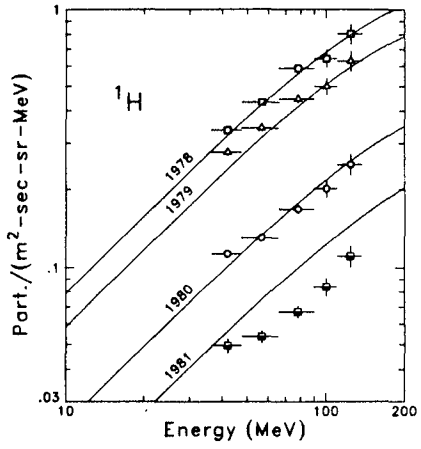


*Figure 4*

All of the parameters in the propagation and modulation models have been either specified or determined except for the mean escape path length, X. Figure 5 shows our calculation of the $^2$H/$^4$He ratio as a function of energy for various path lengths X. The shaded region in this figure represents the range of variability caused by changing solar modulation. The upper side of the shaded region results from modulation for 1981. We compare our measurements (closed circles) with other recent measurements (open symbols, references 6-10) in this figure. Figure 6 is a similar display, but for the ratio $^3$He/$^4$He.

The mean path length X that best fits our measured abundance ratios is 7.6±0.4 g/cm$^2$ for the $^2$H/$^4$He ratio (65-87 MeV), 6.0±0.3 g/cm$^2$ for the $^3$He/$^4$He ratio (65-87 MeV), and 5.6±0.2 g/cm$^2$ for the $^3$He/$^4$He ratio (87-120 MeV). These ratios are weighted averages of the results from all six years. The difference between the best fit path length for H and He may be due to uncertainties in the production cross sections [5] used in this calculation. The mean between the two determinations is approximately X=6.7 g/cm$^2$.

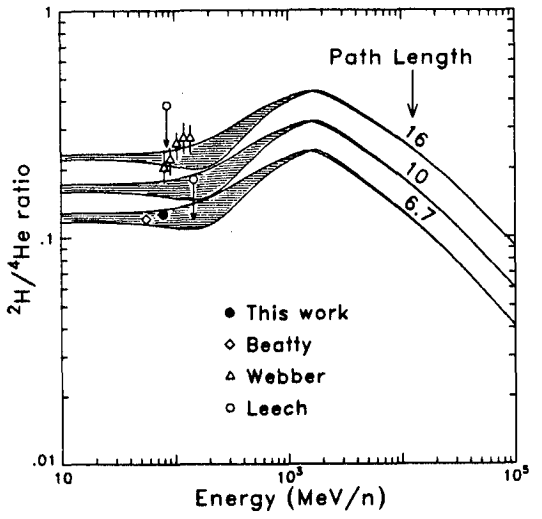


*Figure 5*

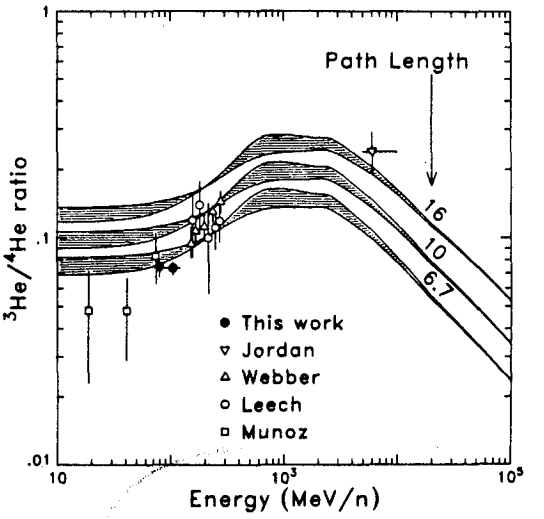


*Figure 6*

4. CONCLUSION. Our measurements of the spectra and fluxes of $^1H$, $^2H$, $^3He$, and $^4He$ can be fit using a standard leaky box model for galactic cosmic ray confinement. This model is essentially the same as that used by other authors to fit the B/C ratio with a similar leakage path length [11,12]. This model has also been successful in explaining the abundances of iron secondaries at higher energies [13].

5. ACKNOWLEDGEMENTS. We would like to thank L. Krawczyk and C. Sethuraman for their valuable assistance in data processing and reduction.

6. REFERENCES.

1. P. Meyer and P. Evenson, IEEE trans GeoSci Electr, GE-16, 180, (1978)
2. R. Kroeger, thesis, to be submitted to Ap. J.
3. P. Evenson, M. Garcia-Munoz, P. Meyer, K. R. Pyle, and J. A. Simpson, Ap. J. 275, L15 (1983)
4. M. Garcia-Munoz, private communication (1985)
5. J. P. Meyer, Astron. Astrophys Suppl., 7, 417 (1972)
6. S. Jordan, Ap. J., 291, 207 (1985)
7. M. Garcia-Munoz, G. M. Mason, and J. A. Simpson, Ap. J., 202, 265 (1975)
8. J. J. Beatty, M. Garcia-Munoz, J. A. Simpson, Ap. J., 294, 455 (1985)
9. W. R. Webber and S. M. Yushak, Ap. J., 275, 391 (1983)
10. H. W. Leech and J. J. O'Gallagher, Ap. J., 221, 1110 (1978)
11. J. F. Ormes and R. J. Protheroe, Ap. J., 272, 756 (1983)
12. J. J. Engelmann, P. Goret, E. Juliusson, L. Koch-Miramond, M. Masse, A. Soutoul, N. Lund, and IL. Rasmussen, to be published in Astronomy and Astrophysics
13. R. Dwyer and P. Meyer, Ap. J., 294 (1985)

# Cosmic Ray $^3$He Measurements

R. A. Mewaldt
California Institute of Technology
Pasadena, California 91125 USA

Cosmic ray $^3$He/$^4$He observations, including a new measurement at ~65 MeV/nucleon from ISEE-3, are compared with interstellar propagation and solar modulation models in an effort to understand the origin of cosmic ray He nuclei.

**1. Introduction** - The rare isotopes $^2$H and $^3$He in cosmic rays are believed to be of secondary origin produced by nuclear interactions of primary $^1$H and $^4$He with the interstellar medium. There has recently been renewed interest in these isotopes as a result of indications from high-energy antiproton, positron, and $^3$He observations that the origin of some primary H and He nuclei may differ from that of heavier cosmic rays. In this paper we report a new observation of low-energy $^3$He, examine previously reported $^3$He/$^4$He measurements at both low and high energies, and compare these with calculations of the expected $^3$He/$^4$He ratio at 1 AU. We find no evidence for an excess of low-energy $^3$He such as that reported at high energies.

**2. Observations** - The new observation reported here was made with the Caltech Heavy Isotope Spectrometer Telescope (HIST) on ISEE-3 (now renamed ICE) during quiet-time periods from 8/13/78 to 12/1/78. Figure 1 shows the He isotope distribution from the two highest energy intervals covered by HIST. This data results in a $^3$He/$^4$He ratio of 0.066±0.016 from 58 to 77 MeV/nucleon. Some of the $^4$He in this energy interval is "anomalous" cosmic ray (ACR) $^4$He, which has been corrected for using a decomposition of the ACR and galactic cosmic ray (GCR) fluxes [1], and their time history. The derived correction factor of 1.12±0.06 results in an "observed" GCR $^3$He/$^4$He ratio of 0.074±0.018.

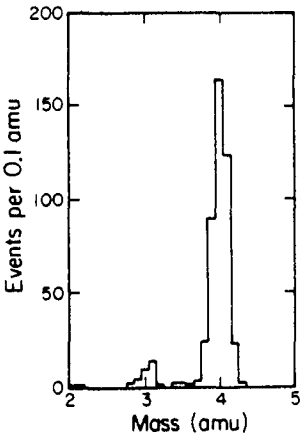


Figure 1: The distribution of quiet-time $^3$He (48 to 77 MeV/nucleon) and $^4$He (41 to 67 MeV/nucleon) observed by the Caltech experiment on ISEE-3 during late 1978.

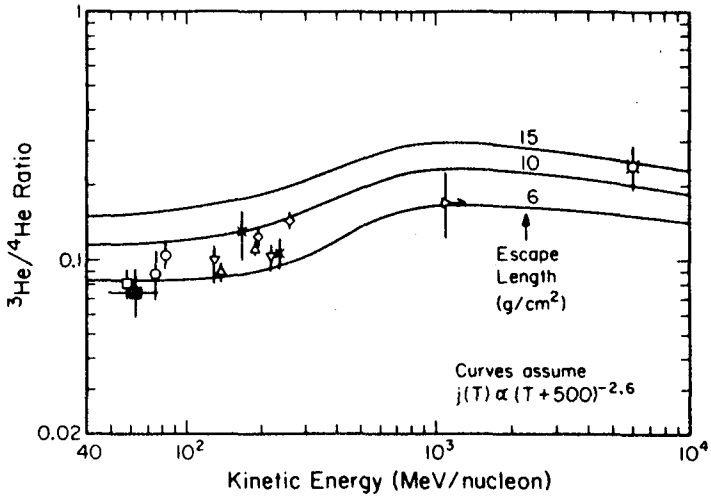


Figure 2: Measured and calculated $^3$He/$^4$He ratios. Spacecraft observations: ■ This work, 1978; □ Goddard-UNH, 1972 [2]; ○ Chicago, 1973-1974. Balloon data: ▽ Rochester, 1966 [5]; △ UNH, 1972 [6]; × UMd., 1972 [7]; ◇ UNH, 1977 [8]. Geomagnetic method: ▷ Ioffe, 1976 [11]; ⋈ Chicago, 1981 [9,10].

Figure 2 shows our new measurement along with selected other $^3He/^4He$ observations. The spacecraft observations [2,3,4] are from the 1972-1978 solar minimum period and are limited to the 50 to 100 MeV/nucleon interval where contamination by ACR $^4He$ is minimized. Since the reported observations include ACR $^4He$, each has been corrected as described above. Figure 2 also includes observations from ~100 to 300 MeV/nucleon by balloon-borne instruments [5,6,7,8] (here referred to as "the balloon observations"). As discussed in the Appendix, we believe that the observations as reported (and as plotted in Figure 2) have not adequately corrected for $^3He$ produced in the atmosphere, and a proposed correction (typically ~16%) is therefore applied in subsequent Figures. At >300 MeV/nucleon the only observations use the geomagnetic method, including the recent Jordan and Meyer (J&M) measurement at ~6 GeV/nucleon [9,10], and an earlier result [11]. These experiments also fly on balloons, but are not subject to the same atmospheric corrections.

**3. Interpretation of $^3He/^4He$ Observations** - To interpret the available $^3He/^4He$ data we use propagation calculations by J. P. Meyer [12], who calculated *interstellar* spectra for $^1H$, $^2H$, $^3He$, and $^4He$ for a variety of source spectra and mean pathlengths, using the standard "leaky-box" propagation model. The source spectra were of the form $dJ/dT \propto (T+U)^{-2.6}$, where T is kinetic energy per nucleon and $0 \leqslant U \leqslant 938$ MeV/nucleon. We calculated the effects of solar modulation on these spectra using the solar-minimum form of the interplanetary diffusion coefficient from Cummings et al. [13] and numerical solutions of the Fokker-Planck equation including the effects of diffusion, convection, and adiabatic deceleration. Results of these calculations are shown in Figure 2 for source spectra with U=500.

By comparison with the calculations (e.g., Figure 2) each observation determines a "leaky-box" escape-length ($\lambda_e$), as shown for U=500 spectra in Figure 3. Note that the spacecraft and (corrected) balloon observations all favor $\lambda_e \simeq 6$ to 7 g/cm$^2$; only the J&M measurement at ~6 GeV/nucleon indicates $\lambda_e \geqslant 10$ g/cm$^2$. Table 1 summarizes the mean escape-lengths obtained. Note that the proposed atmospheric correction (see Appendix) lowers the mean escape-length for the balloon observations by ~1.6 to 1.9 g/cm$^2$ (depending on the spectrum), and generally improves agreement with the spacecraft observations. Table 1 indicates that softer source spectra (e.g., U=200) lead to a somewhat greater $\lambda_e$ at low energies. This is both a propagation effect (see [12]), and a result of the increased solar modulation required for soft spectra.

**4. Discussion** - We wish to determine whether the $^3He$ observations are consistent with the propagation/modulation models derived for heavier nuclei, or whether there is evidence for He nuclei with a separate origin and/or history. For the J&M measurement at ~6 GeV/nucleon we find a pathlength of ~15±6 g/cm$^2$ (in agreement with their value), independent of the assumed source spectrum. This value is significantly greater than derived from the B/C or other $Z \geqslant 3$ secondary/primary ratios, which imply $\lambda_e \simeq 5.5$ g/cm$^2$ at ~6 GeV/nucleon [14]. Thus, if the J&M measurement (and its interpretation) is correct, it does imply a high-energy $^3He$ excess, and a different origin for at least some high-energy He nuclei.

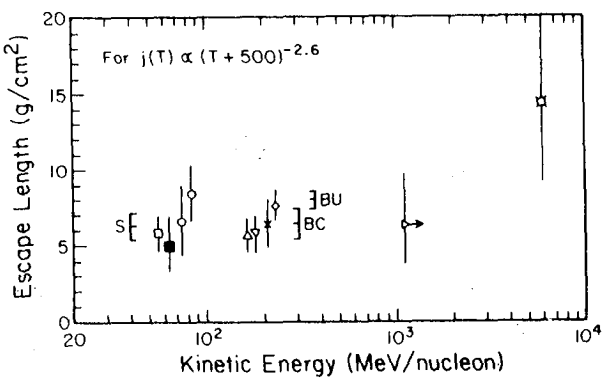


Figure 3: Plot of the escape length determined by the observations in Figure 2. The mean and uncertainty of the spacecraft (S), corrected (BC), and uncorrected (BU) balloon observations are indicated.

Table 1 - Mean Escape-Lengths (in g/cm²)

| Source Spectrum | Spacecraft Observations (~ 70 MeV/nuc) | Balloon Observations (~ 200 MeV/nuc) w/o atm. corr. | atm. corr.(1) |
|---|---|---|---|
| $(T+500)^{-2.6}$ | 6.3±0.9 | 8.0±0.6 | 6.4±1.1 |
| $(T+200)^{-2.6}$ | 8.9±1.0 | 9.7±0.7 | 7.8±1.3 |

(1) Uncertainty includes systematic uncertainty in the magnitude of the atmospheric correction.

At low energies, the required $\lambda_e$ ranges from ~6 to ~9 g/cm$^2$ (see Table 1), with the lower value appropriate to U≃500, a spectral form consistent with most studies of the propagation and solar modulation of Z≥3 nuclei (e.g., [15,14]). An escape length of 6 g/cm$^2$ agrees well with that derived from the B/C ratio at similar energies (see, e.g., [16,14]). We conclude that low-energy observations of $^3$He/$^4$He are in excellent agreement with the propagation and modulation parameters derived for heavier nuclei.

The above conclusion agrees with most earlier studies of low-energy H and He isotopes that have included both propagation and solar modulation effects (e.g., [17,4,8]), but it is in marked *disagreement* with the recent interpretation of low-energy observations by J&M [9,10]. They suggested that balloon observations at ~100 to 300 MeV/nucleon were consistent with the $\lambda_e \simeq 15$ g/cm$^2$ escape-length required by their own measurement. After repeating their analysis in detail we conclude that J&M have significantly overestimated the pathlength required by the balloon data, as a result of a combination of factors, and that self-consistent interpretations of the low-energy data imply $\lambda_e(^4\text{He}) \leqslant 10$ g/cm$^2$. This conclusion is independent of the magnitude of the proposed atmospheric correction for the balloon data, but it is strengthened by the apparent need for this correction, and also by the spacecraft observations.

Measurements of Z≥3 nuclei imply a energy-dependent escape-length that decreases with energy above several GeV/nucleon. Figure 4 shows the expected $^3$He/$^4$He ratio for the energy-dependent escape-length ($\lambda_{OP}(E)$) of Ormes and Protheroe [14], for two spectral forms. Both spectra can be seen to be consistent with the low-energy $^3$He/$^4$He observations and inconsistent with the J&M measurement. Although the U=500 curve falls somewhat above the data, it should be pointed out that $\lambda_{OP}(E) \simeq 9$ g/cm$^2$ at several hundred MeV/nucleon, which is also greater than required by the B/C ratio. Thus the marginal agreement for U=500 is most likely the result of an inadequacy of the energy dependence of $\lambda_{OP}$ at low energies.

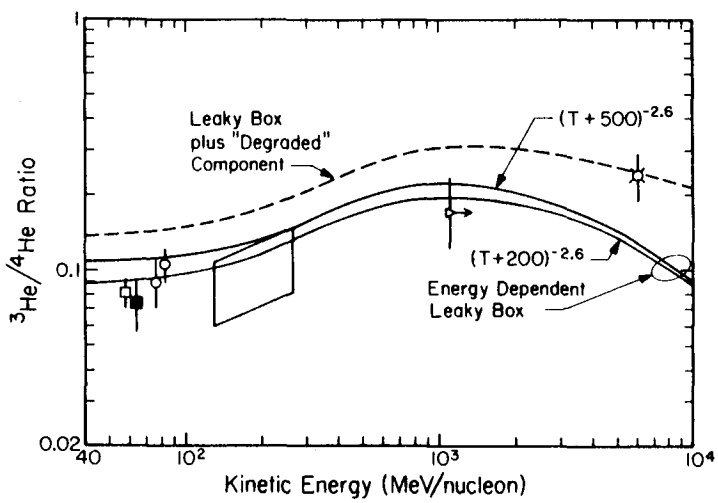


Figure 4: Comparison of the observations with various energy-dependent propagation models (see text). The box indicates the envelope of the corrected balloon observations.

Recent observations of an excess of antiprotons and positrons at high energies have led to several new cosmic ray origin and propagation models in which some nuclei have traversed a great deal of material. Such models also produce an excess of $^2$H and $^3$He. As an example, Figure 4 shows the predicted $^3$He/$^4$He ratio for the model of Cowsik and Gaisser [18], in which a "degraded" component of cosmic rays originates in "thick" sources surrounded by $\sim$50 g/cm$^2$ of material. While this model is consistent with the J&M observation, it exceeds the observed $^3$He/$^4$He ratio at low energies. By relaxing the assumption that the "normal" and "thick" sources have the same energy spectra and composition, it might be possible to fit both the high energy data (including the antiproton data) and the low-energy $^2$H and $^3$He observations.

**Acknowledgements:** I thank Dr. J. D. Spalding for performing most of the HIST $^3$He data analysis, Drs. M. Garcia-Munoz, C. J. Waddington, W. R. Webber, and M. E. Wiedenbeck for discussions of $^3$He measurements, and Dr. E. C. Stone for helpful comments. This work was supported by NASA under grant NGR 05-002-160 and contracts NAS5-28441 and NAS5-28449.

**Appendix** - Atmospheric secondaries are an important source of background for balloon-borne $^2$H and $^3$He observations. One such contribution, which arises from the breakup of atmospheric N and O nuclei, leads to steeply falling spectra of $^2$H and $^3$He that are most significant below $\sim$100 MeV/nucleon (see, e.g., [19,20]). While this source *has* been taken into account in most previous studies, an additional source, due to the breakup of *primary* $^4$He and heavier nuclei, has generally been ignored. Although we are not aware of appropriate cross section measurements for $^4$He breaking up into $^3$He in collisions with CNO, with $^4$He + p cross sections [12] at $\sim$100 to 300 MeV/nucleon $\sim$0.5 $^3$He and $\sim$0.4 $^2$H are produced per inelastic $^4$He interaction. We might expect $^4$He + CNO interactions to produce somewhat fewer $^3$He and more $^2$H than $^4$He + p interactions [12], since CNO targets tend to fragment $^4$He to a greater degree. As an estimate of the "fragmentation parameter" for producing $^3$He from $^4$He in interactions with CNO we take $P_{43}=0.25\pm0.15$, in which case a typical $^3$He/$^4$He ratio of 0.1 at 0 g/cm$^2$ will increase by $\sim$17% at 3 g/cm$^2$ due to this process. Using this estimate (see also [21]) we have re-corrected the balloon observations in Figure 2 to the top of the atmosphere. This presently uncertain correction might be measured with observations of $^3$He/$^4$He vs. atmospheric depth.

## References

1. A.C. Cummings, W.R. Webber and E.C. Stone, *Ap. J., 287,* L99, 1984.
2. B.J. Teegarden et al., *Ap. J. 202,* 815, 1975.
3. M. Garcia-Munoz, G.M. Mason and J.A. Simpson, *Ap. J. 202,* 265, 1975.
4. -----, *Proc. 14th Int. Cosmic Ray Conf. 1,* 319, 1975.
5. G.D. Badhwar, C.L. Deney, B.R. Dennis and M.F. Kaplon, *Phys. Rev. 196,* 1327, 1967.
6. W.R. Webber and N.J. Schofield, *Proc. 14th Int. Cosmic Ray Conf. 1,* 312, 1975.
7. H.W. Leech and J.J. O'Gallagher, *Ap. J. 221,* 1110, 1978.
8. W.R. Webber and S.M. Yushak, *Ap.J. 275,* 391, 1983.
9. Steven P. Jordan and Peter Meyer, *Phys. Rev. Lett. 53,* 505, 1984.
10. Steven P. Jordan, to be published in *Ap.J.,* 1985.
11. M.G. Jodko, V.K. Karakadko and V.A. Romanov, *Proc. 15th Int. Cosmic Ray Conf. 1,* 292, 1977.
12. J.P. Meyer, thesis, L'Universite Paris, 1974.
13. A.C. Cummings, E.C. Stone and R.E. Vogt, *Proc. 13th Int. Cosmic Ray Conf. 1,* 335, 1973.
14. J.F. Ormes and R.J. Protheroe, *Ap.J. 272,* 756, 1983.
15. M. Garcia-Munoz, G.M. Mason and J.A. Simpson, *Proc. 15th Int. Cosmic Ray Conf. 1,* 301, 1977.
16. M. Garcia-Munoz et al., *Proc. 17th Int. Cosmic Ray Conf. 9,* 195, 1981.
17. R.A. Mewaldt, E.C. Stone and R.E. Vogt *Ap.J. 206,* 616, 1976.
18. R. Cowsik and T.K. Gaisser *Proc. 17th Int. Cosmic Ray Conf. 2,* 218, 1981.
19. P.S. Freier and C.J. Waddington *J. Gepophys. Res. 73,* 4261, 1968.
20. D.J. Hofmann and J.R. Winkler *Planet. Sp. Sci. 15,* 715, 1967.
21. We also assume inelastic mean free paths of 45 and 50 g/cm$^2$ for $^4$He and $^3$He, respectively [8], and that the energy/nucleon and angle of the incident $^4$He and outgoing $^3$He are the same.

# Results of a Search for Deuterium at 25-50 GV/c Using a Magnetic Spectrometer

R. L. Golden
Department of Electrical and Computer Engineering
New Mexico State Univertsity
Las Cruces, NM 88003

S. A. Stephens
Tata Institute for Fundamental Research
Homi Bhabha Road
Bombay, India

W. R. Webber
Department of Physics
University of New Hampshire
Durham, NH 03824

## Abstract

A method is presented for separately identifying isotopes using a Cherenkov detector and a magnet spectrometer. Simulations of the method are given for separating deuterium from protons. The simulations are compared with data gathered from the 1979 flight of the New Mexico State University balloon-borne magnet spectrometer. The simulation and the data show the same general characteristics lending credence to the technique. The data show an apparent deuteron signal which is (11 ± 3)% of the total sample in the rigidity region 38.5-50 GV/c. Until further background analysis and subtraction is performed this should be regarded as an upper limit to the deuteron/(deuteron+proton) ratio.

1. Introduction. Measurement of particle mass by combining information about a particle's velocity and its momentum is a concept usually introduced in lower division physics courses. We employ a variation on the technique wherein the quantities measured are the light level in a Cherenkov detector and the magnetic deflection (1/magnetic rigidity). Cosmic ray Cherenkov detectors and magnet spectrometers have limited capabilities at present. In this paper these limitations are explored using monte-carlo simulations based on the characteristics of the NMSU spectrometer. We then compare the expected performance with data gathered in the most recent flight of the spectrometer.

2. Simulations. The basic approach used here to separate isotopes is to plot the two measured quantities, light level (in the Cherenkov detector) vs magnetic deflection. For a given particle the light level should be consistent with zero at deflections larger than the Cherenkov threshold (ie at rigidities below the Cherenkov threshold). At deflections less than the Cherenkov threshold a small amount of light would be registered and at progressively smaller deflections, the light level should rise to a maximum which is determined by the characteristics of the particular detector (and the charge of the particle). The relationship between deflection and light level can be derived from the more classical representations ( see eg (1) ) by

defining $d_T$ as the deflection threshold and Nmax as the light level for a $\beta = 1$ (ie deflection = 0) particle. In this case we have:

$$\bar{N} = N_{max}(1 - (d_T/d)^2) \qquad (1)$$

where $\bar{N}$ is the average number of photoelectrons and **d** is the magnetic deflection.

The deflection thresholds for particles of different masses are related by:

$$(d_T)_1 / (d_T)_2 = m_2 / m_1 \qquad (2)$$

For the flight in question, the Cherenkov detector had a proton Cherenkov threshold corresponding to a deflection of 0.43 c/GV (23 GV/c rigidity). Figure 1a shows light level vs deflection curves derived from equations 1 and 2 using a proton threshold of 0.23 GV. These curves neglect uncertainties in the light level and the deflection. Note that two types of particles (protons and deuterium) are shown. The two types have different Cherenkov rigidity thresholds and different light-level vs deflection curves owing to their different masses.

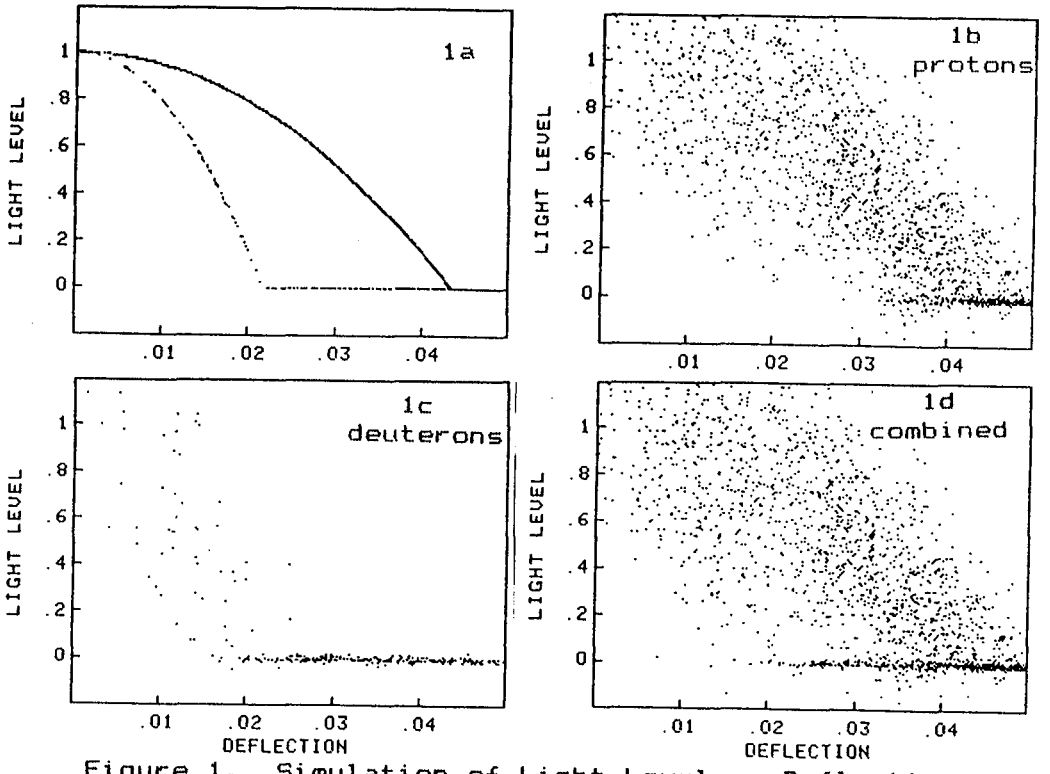


Figure 1. Simulation of Light Level vs Deflection

In order to assess the effects of finite deflection resolution and statistical fluctuations in the photoelectron count, we have repeated the calculation for Figure 1a with the addition of gaussian errors in the deflection and light level for each event. The deflection error distribution had a sigma of 0.029 c/GV (corresponding to an MDM of 350 GV/c), and the light level was varied by a gaussian whose sigma was sqrt(N). The maximum light level was taken to be 10 photoelectrons. A poisson distribution in light level would have been more correct but the difference is only noticeable at low light levels. Figure 1b shows the distribution for 3000 protons; Figure 1c shows the expected distribution for 300 deuterons, and Figure 1d shows the distribution for 3000 protons and 300 deuterons, combined. Note that the deuteron signal is still visible in Figure 1d. By comparing Figs. 1b, 1c and 1d we see that the best place to test for deuterons is at low light levels at deflections just to the right of the deuteron threshold. Note also that as one moves progressivly left of the deuteron threshold, the counts should diminish to zero.

3. Observations. Initial selection of events to be used in the deuterium hunt was similar to the selection of protons in the antiproton hunt reported elsewhere (2),(3). The quoted deflection resolution for this sample 0.08 c/GV corresponding to a maximum detectable rigidity of 125 GV/c. Studies of e- encountered during the flight showed that the maximum light level for the experiment (averaged over all trajectories) was about 7 photoelectrons. In order to obtain a data sample with a deflection resolution of 0.029 c/GV, only trajectories that traversed more than 5 KG-m of magnetic field were selected. Studies of the e- indicated that by eliminating trajectories that went near the mirror edges, and by using only events whose photons should have been centered within 14 cm of a phototube face, the average maximum light level could be raised to about 10 photoelectrons. About 15% of the protons reported in the antiproton papers (2),(3) survived these additional criteria. Figure 2 shows the light-level vs deflection points from the events selected. The similarity between Figure 2 and Figure 1d indicates that at least qualitatively the instrument response is as expected. The region where deuterons should be detectable does indeed have a few counts in it, and the region from zero deflection to the deuteron Cherenkov threshold appears to contain relatively few counts. The reader is cautioned however that a detailed background subtraction has not yet been performed. It is possible that the events at low light-level near the deuteron threshold are due to spillover from the protons near their Cherenkov threshold.

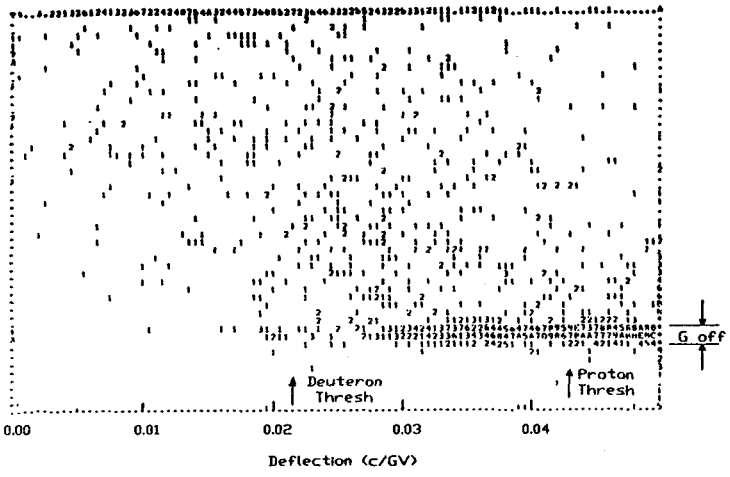


Figure 2. Light Level vs Deflection (3115 events)

In order to estimate the deuteron content (upper limit for now) indicated by Figure 2, we have computed the ratio of G-off events to all events as a function of deflection. G-off events are defined as those whose light-level is within the limits shown on Figure 2. This ratio is shown in Figure 3. Note the apparent "shelf" in the deflection region 0.02-0.03 c/GV. The average value of the leftmost three intervals is (11± 3)%. This could be regarded as a measurement of the deuteron/(deuteron + proton) ratio except that a background subtraction has not been made. Thus the result must for now be regarded as an upper limit.

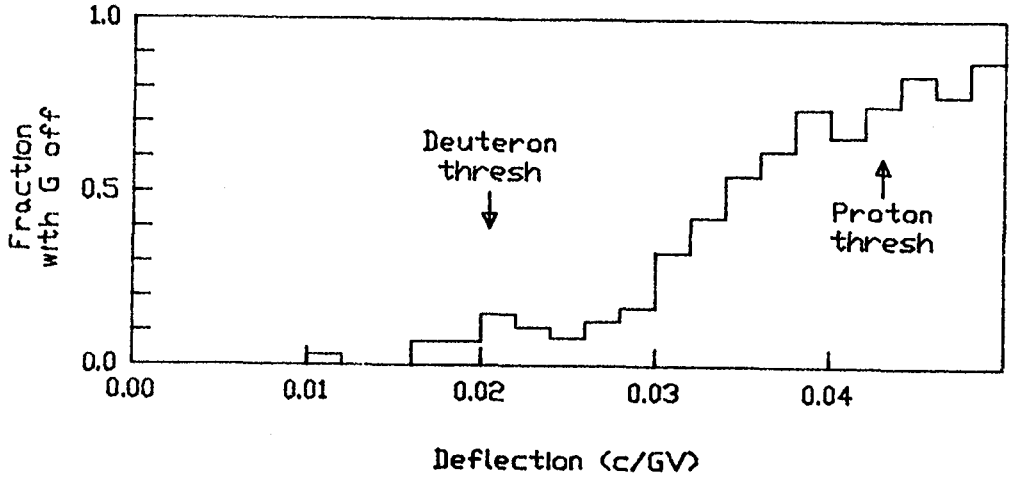


Figure 3. Fraction of G-off Events vs Deflection

References

(1) Jelly, J. V., (1958) Cerenkov Light and its Applications, Pergamon Press.
(2) Golden, R. L. et al. (1979), Phys. Rev. Let., 43, 1196.
(3) Golden, R. L. et al. (1984), Ap. J. Let., 24, 75.

# PARAMETRIZED ENERGY SPECTRUM OF COSMIC-RAY PROTONS WITH KINETIC ENERGIES DOWN TO 1 GeV

L.C.Tan
Department of physics and Astronomy
University of Maryland
College Park, MD 20742
USA

A new estimation of the interstellar proton spectrum is made in which the source term of primary protons is taken from shock acceleration theory and the cosmic-ray propagation calculation is based on our proposed nonuniform galactic disk model.

It appers that above 10 GeV the interstellar proton spectrum can be determined with an absolute accuracy of ±20%. However, at lower energies the divergence among various spectral estimations is much more serious; this is due to the existence of solar modulation. Thus one needs to deduce the interstellar proton spectrum through his own demodulation calculation. The deduced proton spectrum is obviously dependent upon the model of solar modulation used.

Recently, an interesting attempt for deducing the interstellar proton spectrum is reported(1), in which a source term of primary protons suggested by shock acceleration theory is adopted and the cosmic-ray propagation calculation is based on the leaky box model. Since from our recent analysis of the high-energy electron spectrum(2) we are aware that the dominant part of observed protons comes from the dence $H_2$ cloud region, it is argued that the corresponding propagation calculation should be based on the nonuniform galactic disk (NUGD) model(3).

Here we will present a brief introduction to the NUGD model. According to it the observed cosmic rays contain two components: the distant component and the local component. As shown in Fig. 1 by the double-line arrows, the distant (left) component of cosmic rays, starting from the cosmic-ray confinement volume above the $H_2$ cloud region (Box 2) can reach the solar neighbourhood by escaping into the $H_2$ cloud region (Box II), then by propagating along the magnetic tube (Box I) inside which the solar system is located. On the other hand, the local (right) component of cosmic rays originates from their confinement volume in the solar vicinity (Box 1). The fraction, $\mathcal{E}$, of locally produced protons in the observed proton flux is found to be only 5±1 %(2).

The main problem in extending the application range of the NUGD model to the low energy range is caused by a lack of knowledge of the convection velocity (V) of cosmic rays. Thus at low energies one is unable to determine a precise shape of the cosmic-ray escape pathlength ($\lambda_e$) in Box II or to estimate the cosmic-ray intensity variation along the magnetic tube (Box I). Nevertheless, it is noted that if we limit ourselves to interstellar protons with kinetic energy, $T_p \geq 1$ GeV, to a great extent we can avoid the difficulties shown above. Actually, the proton intensity in the $H_2$ cloud region (Box II) should be the same as in

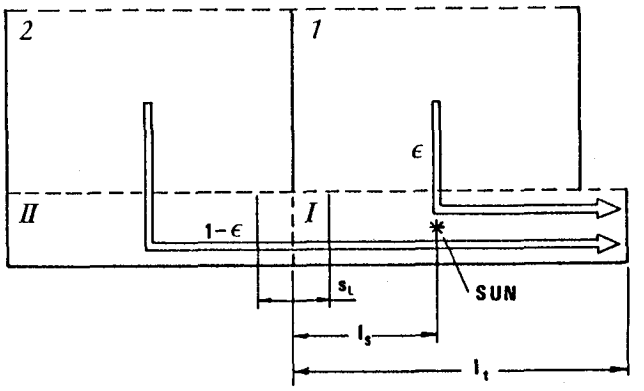


Fig. 1

Box 1 or Box 2, because it is found experimentally that there is a lack of any cosmic-ray gradient, at least in the inner Galaxy (see Ref. 4). Note that at any given rigidity (R) protons are the dominant component of cosmic rays. Hence we do not need to use the unknown parameter $\lambda_{eII}$ to estimate the proton intensity in Box II (hereafter the subscripts 1, 2, I and II represent the quantities referred to Boxes 1, 2, I and II respectively).

Regarding the $\lambda_e$ value in Box 1 or Box 2 we will use the empirical relationship(1) deduced from measured data on heavy nuclei. Furthermore, in Box I the pathlength ($x_I$) of cosmic rays to reach the solar neighbourhood has been estimated(2). It is noticeable that even if cosmic-ray particles lack any convection motion in Box I, protons with $T_p \geq 1$ GeV should have a value of $x_I$ less than $0.3\,\lambda_p^i$, where $\lambda_p^i$ is the mean inelastic interaction length of interstellar protons, to reach the solar neighbourhood. As a result, the proton intensity variation along the magnetic tube should be insignificant, and we will only consider two extreme cases (V= 0 and V= 300 km/s) to estimate the range of variation of the proton spectrum.

In order to deduce the proton intensity $N_{p12}$ in Box 1 or Box 2 we need to solve the continuity equation of primary protons,

$$N_{p12}\left(\frac{1}{\lambda_{e12}}+\frac{1}{\lambda_p^i}\right) = q_{p12} + \int_{T_p}^{\infty} \frac{1}{\lambda_p^i}\,\frac{dN_p(T'_p,T'_p)}{dT_p}\,N_{p12}(T'_p)\,dT'_p \,, \qquad (1)$$

where $q_p$ is the source term of primary protons and $dN_p/dT_p = 1/T'_p$ is the energy distribution of protons after their inelastic interactions. From shock acceleration theory we have

$$q_{p12} = k_{0p}\, p^{-(2+\eta)}/\beta_p c \,, \qquad (2)$$

where p is the proton momentum, $k_{0p}$ is a constant, $\eta = 0.05$ and $\beta_p c$ is the proton velocity. Since at low energies the power law approximation of $N_{p12}$ and the constant approximation of $\lambda_p^i$ cannot be used, an iteration procedure is used to obtain the numerical solution of $N_{p12}$.

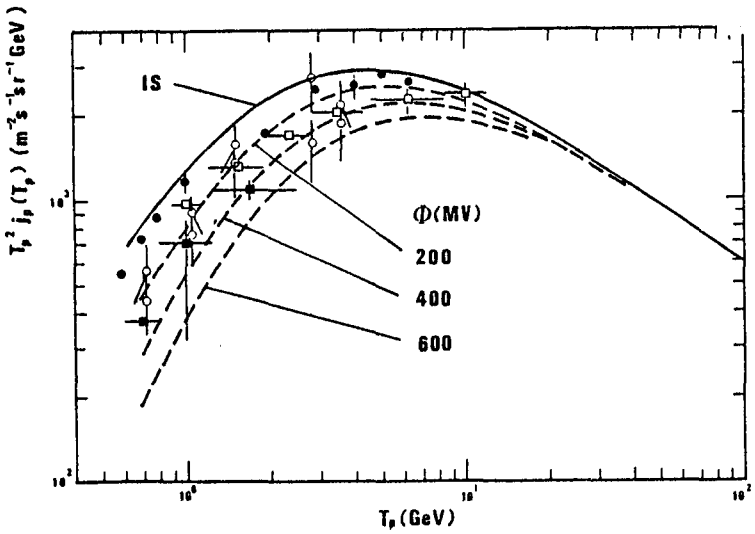


Fig. 2

Further, the propagation of interstellar protons along the magnetic tube (Box I) can be described by using a slab model,

$$\frac{dN_{pI}(T_p,x_I)}{dx_I} = -\frac{N_{pI}(T_p,x_I)}{\lambda_p^i} + \int_{T_p}^{\infty} \frac{1}{\lambda_p^i} \frac{dN_p(T_p,T_p')}{dT_p} N_{pI}(T_p',x_I)\,dT_p' \,, \qquad (3)$$

where the initial value of $N_{pI}$ should be $N_{pII}$ after any possibly adiabatic deceleration in the assumed boundary layer $s_1$ (see Fig. 1)(3). At lower energies we also have

$$x_I = 4x_{I0}\, R^{-0.7}\, (1+(1+2q_s)^{1/2})^{-2} \,, \qquad (4)$$

where $x_{I0}$ is a constant, $q_s = Vl_s/K_I$ and $K_I$ is the diffusion coefficient of cosmic rays. Similarly, a numerical method is developed to obtain the solution of Eq. (3) in the solar neighbourhood, $N_{ps}$. Thus the proton intensity predicted for the NUGD model should be

$$N_{pp} = (1-\varepsilon)\, N_{ps} + \varepsilon N_{p12} \,, \qquad (5)$$

where $\varepsilon = 5\pm1$ % as deduced from Ref. (2).

It is found that the effect of taking various values of V is negligible, and the resultant cosmic-ray proton spectrum in the solar neighbourhood can be parametrized as

$$j_{pp}(T_p(\mathrm{GeV})) = \frac{2\times10^4\, T_p^{-2.75}}{1+C_1\, T_p^{-1.58}} \,, \qquad (m^{-2}s^{-1}sr^{-1}GeV^{-1}) \qquad (6)$$

where $$C_1 = 15.0 - 6.051nT_p + 2.841n^2T_p + 0.1691n^3T_p \,. \qquad (7)$$

The predicted $j_{pp}$ spectrum is not only in accordance with the existing proton data at $T_p \geq 10$ GeV, but also is consistent with the low-energy proton data measured in the period of solar minimum(5) (see Fig.2).

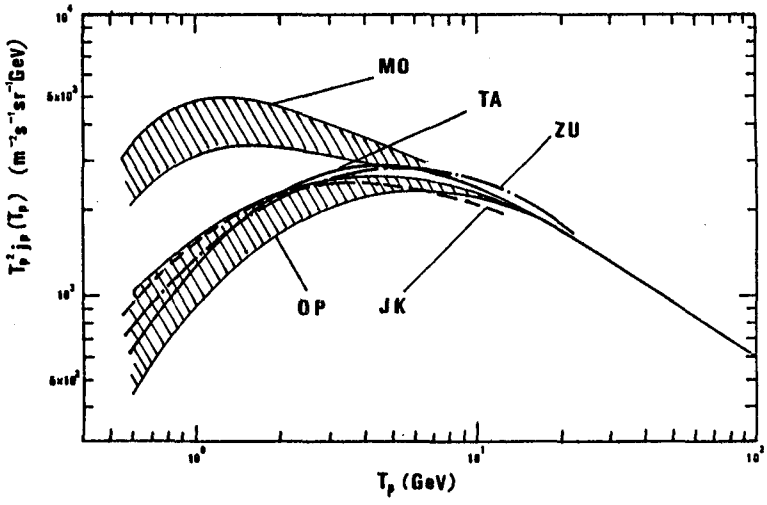


Fig. 3

The modulated spectra in Fig. 2 are obtained from our predicted $j^{PP}$ spectrum by using the force field approximation. It appears that the measured data are consistent with our modulated spectrum with $\phi = 200 \pm 200$ MV, where $\phi$ is the mean energy loss per nucleon in the heliosphere for cosmic-ray nuclei(6).

Finally, in Fig.3 our deduced interstellar proton spectrum (TA) is compared with the results of other authors (OP(1),MO(7),ZU(8) and JK(9)). It is noticeable that our proton specrum is close to the demodulated spectra recently suggested in Refs. (8) and (9), indicating the general reasonableness of the demodulation processes used in these works. In conclusion, the parametrized expression of our deduced interstellar proton specrum should be useful in various cosmic-ray calculations, in particular in the estimation of the production rates of cosmic-ray secondary particles in interstellar spase.

References:

1. Ormes,J.F. and Protheroe,R.J. 1983, Ap. J., 272, 756.
2. Tan,L.C. 1985, Ap. J., in press.
3. Tan,L.C. and Ng,L.K. 1983,Ap. J., 269, 751.
4. Kniffen,D.A. et al., 1983, Proc. 18th Intenat. Cosmic Ray Conf. (Bangalore) 1, 165.
5. e.g., Ormes,J.F. and Webber, W.R. 1965, Proc. 9th Internat. Cosmic Ray Conf. (London), 1, 349.
6. Glesson,L.J. and Axford,W.I. 1968, Ap. J., 154, 1011.
7. Morfill,G.E. et al., J. Geophys. Res., 81, 5841.
8. Zusmanovich,A.G. et al.,1983, Proc. 18th Internat. Cosmic Ray Conf. (Bangalore), 3, 102.
9. Jokipii,J.R. and Kopriva,D.A. 1979, Ap. J., 234, 384.

# GALACTIC PROPAGATION MODELS CONSISTENT WITH THE COSMIC RAY LIFETIME DERIVED FROM $^{10}$Be MEASUREMENTS

T. Gregory Guzik and John P. Wefel
Dept. of Physics and Astronomy, Louisiana State University
Baton Rouge, LA 70803-4001 USA

Moises Garcia-Munoz and John A. Simpson
Enrico Fermi Institute, University of Chicago
Chicago, IL 60637 USA

## ABSTRACT

Using a propagation calculation with energy dependent parameters, including the depletion of short pathlengths, and incorporating experimental nuclear excitation functions, the variation of the $^{10}$Be/$^{9}$Be ratio with the matter densities in two nested confinement regions is investigated. It is shown that there is no unique correspondence between a $^{10}$Be/$^{9}$Be measurement at low energy and the density of matter in the galaxy. $^{10}$Be/$^{9}$Be measurements at both low and high energy are needed to fully specify the matter densities.

1. Introduction In recent years considerable progress has been made in determining the energy dependence of the pathlength distribution (PLD) for cosmic ray propagation at low energies in the interstellar medium (Garcia-Munoz et al., 1985). However, previous analyses of radioactive cosmic ray isotopes have been done in the context of the simple "leaky box" model, which does not explain, simultaneously, the energy dependence of the measurements of both light and heavy secondary to primary elements (such as B/C and V/Fe or Sc/Fe). In this report, we present results of propagation calculations for $^{10}$Be/$^{9}$Be using experimental nuclear excitation functions and energy dependent parameters in the PLD which give results in agreement with both B/C and sub-Fe/Fe ratios from 100 MeV/n to 30 GeV/n.

2. The Propagation Calculations The propagation code employs the weighted slab technique to calculate the abundances of 96 stable, long-lived or electron capture isotopes from $^{4}$He to $^{64}$Ni. Radioactive decay ($\beta^+$, $\beta^-$, electron capture) is treated explicitly; the effects of ionization energy loss are included; and energy dependent total inelastic cross sections, based upon compiled experimental data, are employed. The partial fragmentation cross sections are based upon semi-empirical formulae of Silberberg and Tsao (1973), modified using available experimental data. Cosmic ray source abundances are from Garcia-Munoz and Simpson (1979), and the ratio of H to He in the interstellar medium is from Cameron (1981). The majority of the cosmic ray data used here were collected during the last period of minimum solar modulation (1974-1979), and the calculations include modulation with an adiabatic deceleration parameter $\phi$ = 490 MV (Evenson et al., 1984).

The propagation code was run in two modes: single and double runs. In a single run, the abundances of all species were calculated for a series of slabs and then weighted by a single, energy dependent pathlength probability distribution. Such a PLD is illustrated in Fig. 1 where the inset (B) shows the overall shape of the Double Exponential (DE) form, composed of two exponentials with means $X_1$ and $X_2$, where $X_2$ represents the depeletion of short pathlengths (Garcia-Munoz et al., 1984). The energy dependences of $X_1$ and $X_2$, shown on part A along with the mean pathlength <X>, are determined by fitting the B/C and sub-Fe/Fe data over the energy range 0.1 - 30 GeV/nucleon (Guzik and Wefel, 1984). The DE PLD is qualitatively similar to earlier models (Garcia-Munoz and Simpson, 1970), e.g. the PLD in the "nested leaky-box" model (Cowsik and Wilson, 1975), but is quantitatively different since our DE PLD includes energy dependent parameters.

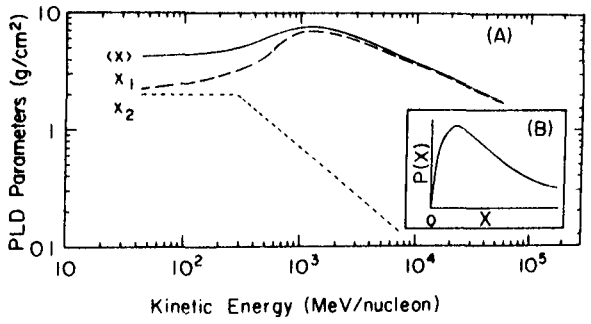


Fig. 1: The energy dependent DE PLD.

Fig. 2 shows a comparison of the calculated $^{10}Be/^{9}Be$ ratio for different PLD's, for a constant density of 0.5 atoms/cm$^3$. The dashed line is for a simple energy independent exponential which is characteristic of the "leaky box" model. Note that when energy dependence of the mean of the PLD is included (lower solid line) the shape of the predicted $^{10}Be/^{9}Be$ is modified. However, neither of these PLD's fit both the B/C and sub-Fe/Fe ratios. Such a fit requires an energy dependent depletion of short pathlengths (a truncated PLD, see Garcia-Munoz et al., 1984) and results for two types of truncation (yielding essentially identical results) are shown on Fig. 2 (upper solid and dot-dashed curves). Note that above several GeV/nucleon the curves converge, as expected, since at higher energies the truncation becomes negligable (c.f. $X_2$ on Fig. 1).

In analogy with the "nested leaky box" model, the two components of the energy dependent DE PLD can be associated with confinement in an inner region of density $\rho_{IN}$ (i.e. around the sources) nested within an outer region of density $\rho_{OUT}$ (i.e. the Galaxy) (Guzik and Wefel, 1984).

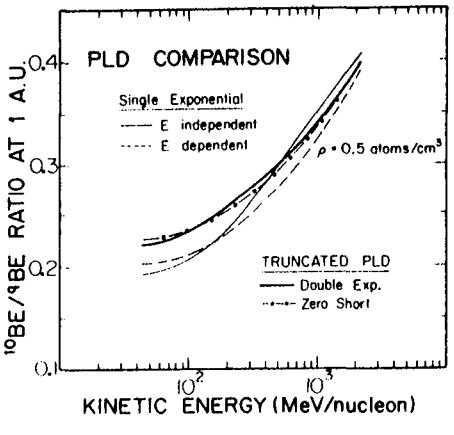


Fig. 2: $^{10}Be/^{9}Be$ results for different PLD's.

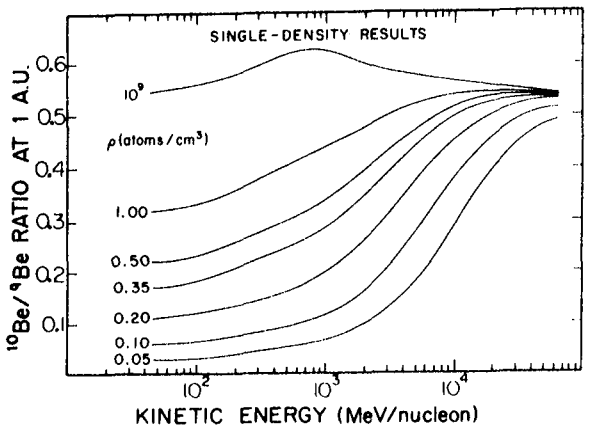


Fig. 3: $^{10}Be/^{9}Be$ ratio as a function of density.

Double runs were used to study this configuration of confinement regions. In the first step, the propagation code is run with an exponential PLD whose mean follows the curve given by $X_2$ on Fig. 1. For this step the matter density has the value $\rho_{IN}$. Next, the results of step 1 are used as the source for a second calcualtion (with matter density $\rho_{OUT}$) whose PLD mean follows the $X_1$ curve on Fig. 1. This two step method allows us to treat separately the densities in the inner and outer regions, which, physically, could be quite different.

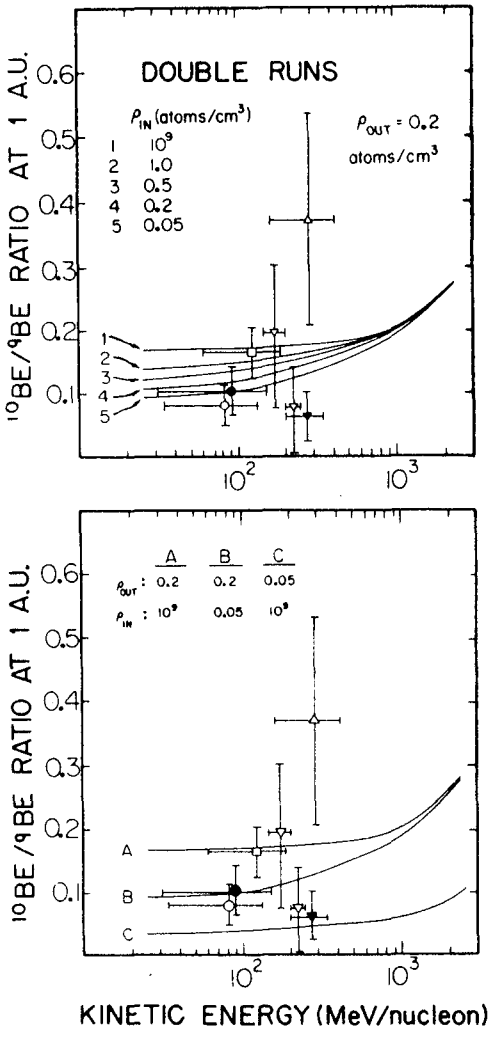


Fig. 4: Results of the two-step analysis compared to experimental data.

3. Results Figure 3 shows results for different matter densities from single runs using the DE PLD with $\rho_{IN} = \rho_{OUT}$. The curves converge at high energy due to relativistic effects, and for low energy, the survival of $^{10}Be$ is directly dependent upon the matter density. The low energy satellite experiments give a mean value $^{10}Be/^{9}Be = 0.13 \pm 0.03$ at ~100 MeV/n which implies from Fig. 3, a matter density of $0.23 \pm 0.06$ atoms/cm$^3$, consistent with previous results which employed single density analysis.

Fig. 4 shows the result of the two-step calculations compared to experimental data (o, ● - Garcia-Munoz et al., 1977, 1981; □ - Wiedenbeck and Greiner, 1980; ▽ - Webber et al., 1977; ▼ - Webber and Kish, 1979; △ - Hagen et al., 1977). The top panel shows the calculated $^{10}Be/^{9}Be$ ratio for fixed $\rho_{OUT}$ with $\rho_{IN}$ allowed to vary from 0.05 to $10^9$ atom/cm$^3$. Different values for $\rho_{IN}$ spread the predicted $^{10}Be/^{9}Be$ ratio at low energy by about a factor of two. The curves converge above 1 GeV/n since the effect of the inner region decreases with increasing energy. In this model a measurement of the $^{10}Be/^{9}Be$

ratio does not uniquely determine the density in the confinement region.

The measured $^{10}Be/^{9}Be$ ratio at low energy can provide bounds on the density in the outer region. This is illustrated in the lower panel of Fig. 4 where curves A and B show the total spread in the predicted ratio for $\rho_{OUT} = 0.2$ atoms/cm$^3$. Assuming a large value for $\rho_{IN}$ allows a smaller value of $\rho_{OUT}$ to be used to reproduce a given value of the $^{10}Be/^{9}Be$ ratio, as shown by curve C which forms a lower bound to the experimental data. Conversely, assuming a minimum value for $\rho_{IN}$, a value of $\rho_{OUT} = 0.5$ atom/cm$^3$ give an upper limit to the low energy data. Thus, the available measurements constrain $\rho_{OUT}$ to the range 0.05 - 0.50 atoms/cm$^3$, below the average density of ~1 atom/cm$^3$ for the galactic disk and above the density of 0.01 atoms/cm$^3$ of a galactic halo.

4. Conclusions The cosmic ray PLD, including an energy dependent depletion of short pathlengths, can be represented as two "nested" confinement regions having different matter densities. The available $^{10}Be/^{9}Be$ measurements do not uniquely determine the density in the outer region, but they do limit the allowed values to a range of 0.05 and 0.50 atoms/cm$^3$. $^{10}Be/^{9}Be$ data at high energy (currently unavailable) combined with existing measurements at low energy can determine the matter density in both volumes.

5. Acknowledgements This work was supported by NASA, at LSU under grant NAGW-550 and at the U. of Chicago under grant NGL-14-001-006 and contract NAS 5-25731. The propagation code was initially developed under NSF grants at the University of Chicago.

REFERENCES

Cameron, A. G. W., 1981, in Essays in Nuclear Astrophysic (Cambridge University Press) p. 23.

Cowsik, R. and Wilson, L. W., 1975, 14th I.C.R.C. (Munich), 2, 659.

Evenson, P., Garcia-Munoz, M., Meyer, P., Pyle, K. R. and Simpson, J. A., 1983, Ap. J. Lett., 275, L15.

Garcia-Munoz, M. and Simpson, J. A., 1970, Acta Physica Academiae Scientiarum Hungaricae, 29, Suppl. 1, 317.

Garcia-Munoz, M. and Simpson, J. A., 1979, 16th I.C.R.C. (Kyoto) 1, 270.

Garcia-Munoz, M., Mason, G. M. and Simpson, J. A., 1977, Ap. J., 217, 859.

Garcia-Munoz, M., Simpson, J. A. and Wefel, J. P., 1981, 17th I.C.R.C. (Paris), 2, 72.

Garcia-Munoz, M., Guzik, T. G., Simpson, J. A. and Wefel, J. P., 1984, Ap. J. Letters, 280, L13.

Garcia-Munoz, M., Guzik, T. G., Simpson, J. A., Wefel, J. P. and Margolis, S. H., 1985, (in preparation).

Guzik, T. G., and Wefel, J. P., 1984, Adv. Space Res., 4, 215.

Hagan, F. A., Fisher, A. J. and Ormes, J. F., 1977, Ap. J., 212, 262.

Silberberg, R. and Tsao, C. H., 1973, Ap. J. Supplement 25, 315.

Webber, W. R., Lezniak, J. A., Kish, J. C. and Simpson, G. A., 1977, Astro. Letters, 18, 125.

Webber, W. R. and Kish, J. C., 1979, 16th I.C.R.C. (Kyoto), 1, 389.

Wiedenbeck, M. E. and Greiner, D. E., 1980, Ap. J. Letters, 239, L139.

# IMPLICATIONS OF NEW MEASUREMENTS OF $^{16}O + p \rightarrow {}^{12,13}C, {}^{14,15}N$ FOR THE ABUNDANCES OF C, N ISOTOPES AT THE COSMIC RAY SOURCE

T. G. Guzik and J. P. Wefel
Dept. of Physics and Astronomy, Louisiana State University
Baton Rouge, LA 70803-4001

H. J. Crawford,* D. E. Greiner, P. J. Lindstrom,
W. Schimmerling and T. J. M. Symons
Lawrence Berkeley Laboratory
Berkeley, CA 94720 USA

ABSTRACT

The fragmentation of a 225 MeV/n $^{16}O$ beam has been investigated at the Bevalac. Preliminary cross sections for mass = 13,14,15 fragments are used to constrain the nuclear excitation functions employed in galactic propagation calculations. Comparison to cosmic ray isotopic data at low energies shows that in the cosmic ray source $^{13}C/C \leq 2\%$ and $^{14}N/O = 3 - 6\%$. No source abundance of $^{15}N$ is required with the current experimental results.

1. Introduction: The interpretation of cosmic ray measurements in terms of the source abundances and the propagation conditions requires accurate nuclear physics parameters. The current cosmic ray data is, in many cases, better than our ability to interpret it. In particular, the interpretation of the isotopic abundances of carbon and nitrogen, as a function of energy, requires nuclear excitation functions for masses 13, 14 and 15, and we report here preliminary results from an experiment designed to study the fragmentation of $^{16}O$ at intermediate energy.

2. The Bevalac Experiment: Figure 1 shows the experimental arrangement at the LBL Bevalac. The $^{16}O$ beam, incident from the right, passed through monitors S1 and S2, focussing and bending magnets, and steering scintillators upstream of the target, located in a vacuum tank. Fragments from interactions in the targets (~ 1 g/cm$^2$ C and $CH_2$) were measured ~7 meters downstream in the cave with a solid state detector telescope (Scope) which was moveable in order to study the angular distributions of the fragments. The Scope consisted of three x-y

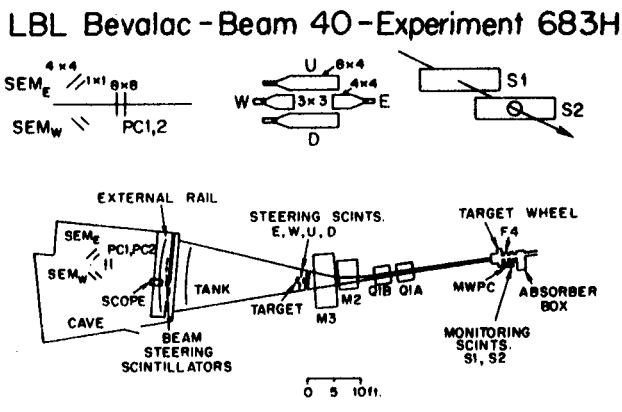


Fig. 1: Experimental Configuration

*U. of California, Berkeley, Space Science Laboratory

planes of position-sensitive detectors and a stack of 30 Li-drifted detectors. The $\Delta E$-E technique was employed to measure the mass of each particle stopping in the scope.

Six angular positions from 0° to 2.75° were studied and the cross sections were obtained by integrating under the normalized angular distributions after correction for background, beam effects, and interactions in the detector stack. Hydrogen target cross sections were obtained by $CH_2$-C subtraction. The isotopes of B, C, N and O have been analyzed to date, and here we focus on the A= 13, 14, 15 isobars for which the cross sections in hydrogen are:

| | This Work | Predicted |
|---|---|---|
| A = 13: | 24 ± 2 mb | (23.9 mb) |
| A = 14: | 40 ± 4 mb | (50.4 mb) |
| $^{15}$N: | 27 ± 2 mb | (24.6 mb) |
| $^{15}$O: | 50 ± 20 mb | (34.2 mb) |

compared to the predictions of the semiempirical equations (Silberberg and Tsao, 1973). For $^{14,15}$O, significant measurements were obtained only at large angles due to a beam veto circuit used at small angles to reduce the number of $^{16}$O nuclei analyzed. The $^{14,15}$O measurements were extrapolated to 0° thereby accounting for the large uncertainty. For the astrophysical interpretation, we prefer to rely on the semiempirical values for $^{14,15}$O, until additional experimental data can be analyzed.

Figure 2 shows the results of this experiment compared to previous data and to various excitation functions: solid curves -- semiempirical formulae; dashed curves -- scaled from $^{12}$C measurements; dot-dash curves -- "limiting" cases (Guzik, 1981; Guzik and Wefel, 1984a). For A = 15, the predicted excitation functions are similar, and the present results are in agreement with semiempirical or scaled predictions. For A = 14, however, the present results are closest to the scaled curve, while for mass 13 the semiempirical curve is indicated. In all cases the

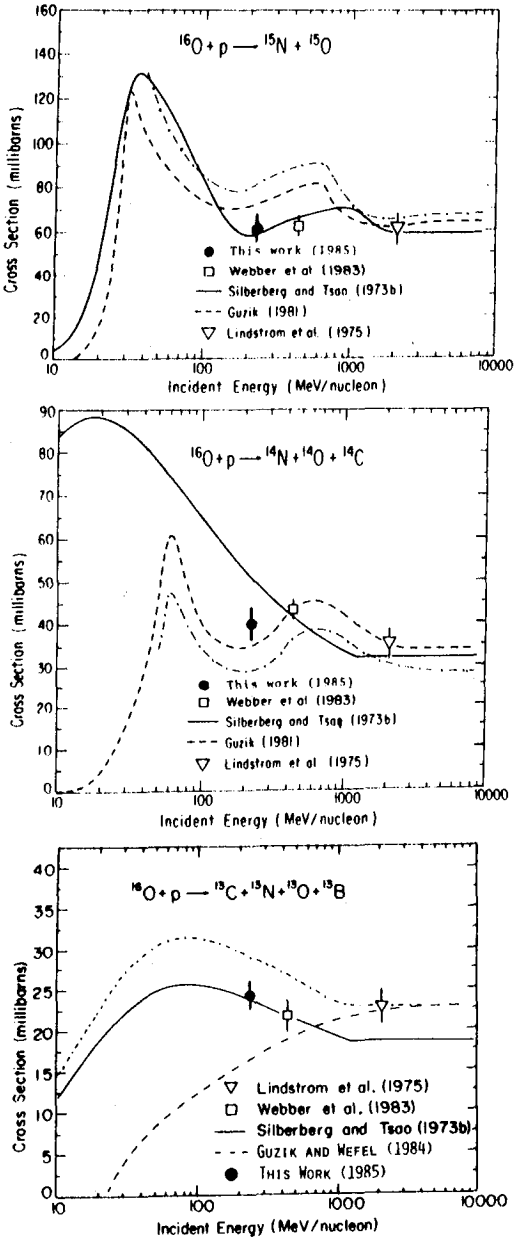


Fig. 2: Excitation Functions for A = 13,14,15 Isobars

measurements do not support the "limiting" curves. It should be noted here that the present results are still preliminary and that measurements at additional energies will be necessary to fully determine the energy dependence of these excitation functions.

3. The Astrophysical Interpretation: Isotopic measurements of nitrogen are presently available at both low and high energy. In the latter case, the results at the cosmic ray source give $(^{14}N/O)_S$ = 5 - 10% with no $^{15}N$ required (Goret et al., 1983; see also review in Guzik, 1981). At low energy (~ 150 MeV/n), there are several reported isotopic measurements (Guzik, 1981; Wiedenbeck et al., 1979; Mewaldt et al., 1981) whose interpretation depends upon the adopted nuclear excitation functions. Isotopic measurements of $^{13}C/C$ (Mewaldt et al., 1981; Wiedenbeck et al., 1981) provide a $(^{13}C/C)_S$ ratio which can be compared to $^{13}C/C$ measured in different regions of the galaxy (Wannier, 1980).

The three excitation functions shown on Fig. 2 have been incorporated into cosmic ray propagation calculations using a pathlength distribution with energy dependent parameters, including the depletion of short pathlengths which reproduces the measured B/C and sub-Fe/Fe ratios over the full energy range 0.1 - 50 GeV/n (for details see Garcia-Munoz et al., 1984; Guzik et al., 1985; Guzik and Wefel, 1984a;b). The results are shown on Figures 3 and 4 where the curves correspond to the excitation functions shown on Fig. 2.

The weighted mean of the low energy nitrogen data points (shown individually for comparison) is indicated as the solid box in the center of Fig. 3, and the dashed lines labeled $(^{14}N/O)_S$ give the locus of points for different source abundances (no $^{15}N$ at the source). For the calculations to reproduce both the elemental and isotopic ratios, at the 1$\sigma$ level, excitation functions between the scaled and

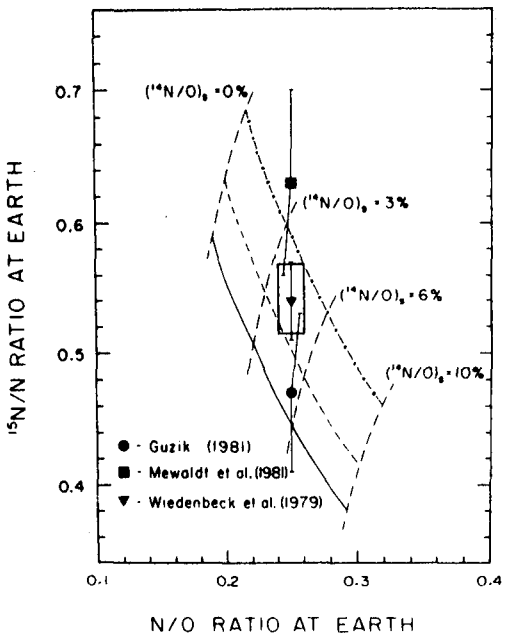


Fig. 3: Results for Nitrogen

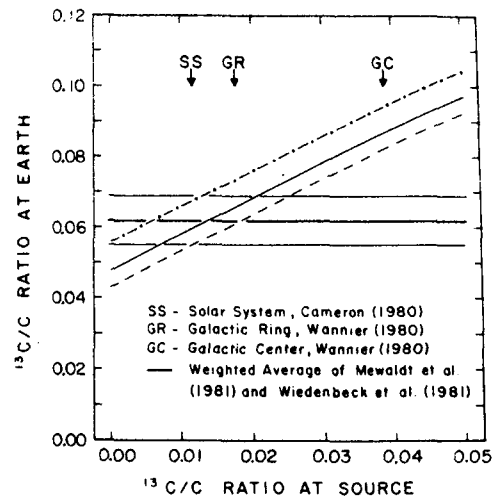


Fig. 4: Results for Carbon

limiting cases are required. Our preliminary cross section measurements, however, indicate a more complicated excitation function falling between the solid and the dashed curves. The results of a propagation calculation using such an excitation function is inconsistent with the 1σ data box on Fig. 3, but in agreement at the 2σ level for $(^{14}N/O)_S$ = 3 - 6%.

Fig. 4 shows the results for $^{13}C/C$. The center horizontal line is the measured ratio with the uncertainty indicated by the lighter horizontal lines. The solid excitation function is favored on Fig. 2 which implies $(^{13}C/C)_S$ = 1.4 ± 0.6%, in agreement with material found in the solar system but below the ratio observed for matter at the galactic center.

4. Conclusions: Using new cross section data, measured at the Bevalac, for the fragmentation of $^{16}O$ at intermediate energies, galactic propagation calculations can reproduce the measured $^{13}C/C$ data with a source component $(^{13}C/C)_S$ = 1.4 ± 0.6%, a value below that observed in the galactic center. The calculated results for nitrogen fall below the average $^{15}N/N$ and N/O ratios but are consistent with the data at the 2σ level for $(^{14}N/O)_S$ = 3 - 6% and no $^{15}N$ in the cosmic ray source. Additional nuclear physics measurements are needed to fully specify the excitation functions and to explain, completely, the existing cosmic ray data.

5. Acknowledgements: This work was supported by DOE, under grant DE-FG05-84ER40147 at LSU, and by NASA grant NGR-05-003-513 at Berkeley.

References

Garcia-Munoz, M., Guzik, T. G., Simpson, J. A. and Wefel, J. P., 1984, Ap. J. Letters, 280, L13.

Goret, P., et al., The Saclay-Copenhagen Collaboration, 1983, 18th I.C.R.C (Bangalore), 2, 29.

Guzik, T. G., Wefel, J. P., Garcia-Munoz, M. and Simpson, J. A., 1985, paper OG 4.3-1, this volume.

Guzik, T. G. and Wefel, J. P., 1984a, Adv. Space Res., 4, 93.

Guzik, T. G. and Wefel, J. P., 1984b, Adv. Space Res., 4, 215.

Guzik, T. G., 1981, Ap. J., 244, 695.

Lindstrom, P. J., Greiner, D. E., Heckman, H. H., Cork, B. and Bieser, F. S., 1975, LBL Report 3650, (unpublished).

Mewaldt, R. A., Spalding, J. D., Stone, E. C. and Vogt, R. E., 1981, Ap. J. Letters, 251, L27.

Silberberg, R. and Tsao, C. H., 1973, Ap. J. Supplement, 25, 315.

Wannier, P. G., 1980, Ann. Rev. Astr. and Astrophys., 18, 399.

Webber, W. R., Brautigam, D. A., Kish, J. C. and Schrier, D., 1983, 18th I.C.R.C. (Bangalore), 2, 198.

Wiedenbeck, M. E. and Greiner, D. E., 1981, Ap. J. Letters, 247, L119.

Wiedenbeck, M. E., Greiner, D. E., Bieser, F. S., Crawford, H. J., Heckman, H. H. and Lindstrom, P. J., 1979, 16th I.C.R.C. (Kyoto), 1, 412.

# THE ISOTOPIC COMPOSITION OF COSMIC RAY CHLORINE

M. E. Wiedenbeck

Enrico Fermi Institute and Department of Physics
University of Chicago, Chicago, IL 60637 USA

ABSTRACT

The isotopic composition of galactic cosmic ray chlorine (E≃225 MeV/amu) has been studied using the high energy cosmic ray experiment on the ISEE-3 spacecraft. The abundances of $^{35}$Cl and $^{37}$Cl are found to be consistent with the secondary production expected from a propagation model developed to account for both light and sub-iron secondaries. An upper limit on the abundance of the radioactive isotope $^{36}$Cl (halflife ≃ 0.3 Myr) is used to set a lower limit on the confinement time of cosmic rays of ∿1 Myr.

1. Introduction. Studies of the abundances of secondary cosmic ray nuclides at low energies (<500 MeV/amu) have shown that no single exponential distribution of pathlengths is adequate for the simultaneous interpretation of both the light secondaries, Li, Be, and B, and the sub-iron secondaries, Sc through Mn (see [1], and references therein.) As a consequence, more elaborate models involving pathlength distributions which are exponential for long pathlenghts, but which are deficient in short pathlengths (<1-2 g/cm$^2$), have been developed [1]. The necessity of introducing a second parameter (the amount of truncation) in order to explain the abundances of two groups of secondary nuclides raises the question of whether the propagation model is generally applicable or simply an empirical fit with enough free parameters to permit agreement with a relatively small body of data. This question is of considerable practical importance since such propagation models are used to calculate the secondary corrections needed to derive cosmic ray source abundances from the observed abundances of nuclides of intermediate mass, including the isotopes of neon, magnesium, and silicon, which are found to differ significantly from solar system composition. If the propagation model used did not accurately predict the secondary production of species of mass intermediate between the light elements and the sub-iron elements, sizeable errors in the derived source composition would result.

It is important to directly check the adequacy of accepted propagation models by testing their predictions of abundances of intermediate mass secondary nuclides. However, few elements between Z=10 and Z=20 are clearly dominated by secondaries. Observations of the elemental abundance of cosmic ray chlorine (Z=17) suggest that the isotopes $^{35}$Cl and $^{37}$Cl may both be dominantly secondary, but direct measurements of the isotopic composition of chlorine are needed to check whether this is indeed the case.

In addition, the radioactive isotope $^{36}$Cl (halflife ≃ 0.3 Myr) is one of the relatively small number of nuclides with $Z \lesssim 28$ which beta decay on a time scale suitable for studying the confinement time distribution of cosmic rays. Since its halflife is shorter than that of the other beta-active nuclides which have previously been investigated ($^{10}$Be

1.6 Myr; $^{26}$Al, 0.87 Myr), it is useful for investigating the density of the matter encountered by cosmic rays during the final few percent of the time required for transport to the vicinity of the Earth.

2. Observations. We have investigated the isotopic composition of galactic cosmic ray chlorine using data from the high energy cosmic ray experiment on the ISEE-3 spacecraft. These data, collected between August 1978 and April 1981, cover an energy interval from 140 to 360 MeV/amu. The instrument consisted of a silicon solid state detector telescope used to measure energy losses and total energy and a gas proportional drift chamber used to measure cosmic ray particle trajectories. The mass uncertainty is dominated by trajectory errors, and therefore increases rapidly with the angle of the particle's incidence, measured from the normal to the detector surfaces. In previous studies of the isotopic composition of elements with Z<16 it was possible to restrict the analysis to events with incidence angles less than some maximum chosen to permit nearly complete separation of the individual mass peaks while retaining reasonable statistical accuracy. For 16<Z<26 however, the combination of poorer mass resolution (which is approximately proportional to mass) and small natural abundances does not permit the selection of a fully resolved data set. Figure 1 shows the chlorine mass histogram obtained by utilizing data with incidence angles of 20° or less. Peaks corresponding to masses of 35 and 37 are evident, while $^{36}$Cl is significantly less abundant and is not resolved from the other isotopes.

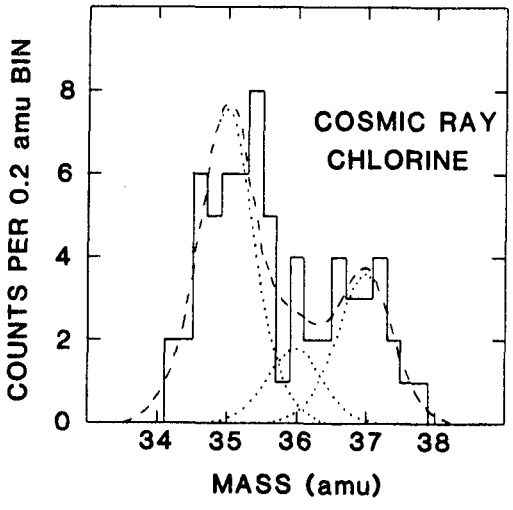


*Figure 1. Observed chlorine mass histogram is shown together with the fitted mass distribution (dashed curve) and the three isotope peaks of which it is composed (dotted curves.)*

Quantitative evaluation of the isotopic abundances (especially of $^{36}$Cl) requires a detailed understanding of the instrument's response to a mono-isotopic particle population. In order to obtain such an understanding, we have studied the dependence of mass resolution on incidence angle ($\theta<20°$) for a number of abundant nuclides which are resonably well resolved from adjacent isotopes. The angular dependence is well fit by

$$\sigma_M = \sqrt{(a^2 + b^2 \cdot \sin^2 2\theta)}.$$

This form, with $b \propto M$, is expected as a result of the fact that the mass resolution is dominated by trajectory uncertainties. The dependence of the coefficients a and b on the mass (or, equivalently, the charge) of the nuclide was studied by fitting this form for stable nuclides with mass numbers between 6 and 34, and for $^{45}$Sc and $^{56}$Fe. These coefficients were found to depend smoothly on mass over the entire range studied, and the b coefficient was proportional to mass, as expected.

The abundances of the three chlorine isotopes were obtained using a

maximum likelihood fit to the observed distribution of calculated masses, assuming the above functional dependence of mass resolution on incidence angle. The values of a and b obtained for chlorine agree, within errors, with the trend found for the other nuclides studied. The fitted mass distribution, together with the three isotope peaks of which it is composed, is shown superimposed on the observations in Figure 1. The derived isotope fractions, when combined with our observation of the element ratio Cl/S = 0.20 ± 0.02, yields the following near-Earth abundance ratios: $^{35}$Cl/S = 0.116 ± 0.024, $^{36}$Cl/S < 0.048, and $^{37}$Cl/S = 0.058 ± 0.016. The errors shown are one standard deviation, and the $^{36}$Cl upper limit is at the 84% confidence level. The element sulfur was chosen for the normalization since it is the nearest dominantly primary element to chlorine.

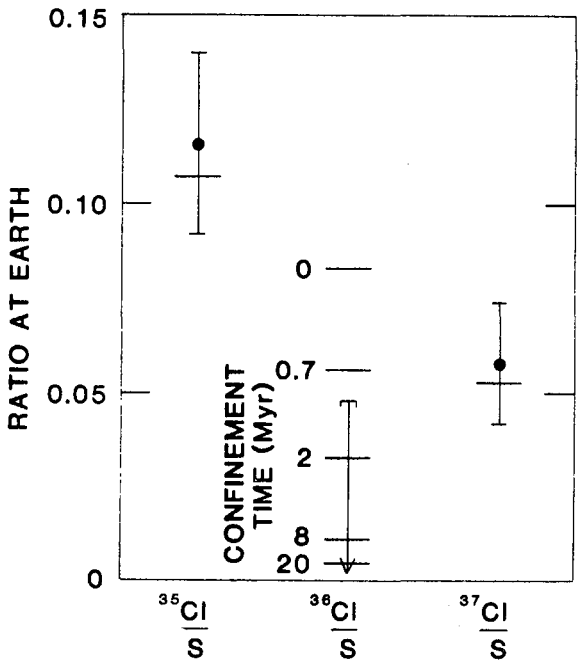


*Figure 2. Observed chlorine isotope abundances (relative to the elemental sulfur abundance) are compared with the results of a propagation calculation (horizontal lines.) For $^{36}$Cl the calculation depends on the cosmic ray confinement time.*

3. Discussion. Figure 2 compares the observed abundance ratios with the predictions of a propagation model which is consistent with both light and sub-iron secondary element abundances (specifically, the ratios B/C and Sc+V/Fe) in low energy (∿100-300 MeV/amu) cosmic rays. This model employs a nested leaky box with mean pathlengths of 1.5 and 3.0 g/cm$^2$ (with H:He=10:1) and standard cross section formulae. Solar modulation effects were taken into account using a force field approximation with mean energy loss Φ=325 MeV/amu (for A=2Z nuclides.) We have assumed that chlorine is entirely absent at the source, although the calculated abundances near Earth are not changed significantly if one assumes that the source abundance of chlorine is comparable to its solar system value (Cl/S=0.01). As seen in the figure, the $^{35}$Cl and $^{37}$Cl abundances are well fit by this model.

The calculation of the $^{36}$Cl abundance at Earth depends on the assumed cosmic ray confinement time (or, equivalently, the assumed density of interstellar gas) since this parameter determines the fraction of the $^{36}$Cl which decays between the time it is produced by spallation and the time it is observed at Earth. As previously pointed out [3], the $^{36}$Cl abundance in the absence of beta decay is a sizeable fraction of the chlorine element abundance, so this isotope is useful for studying the cosmic ray confinement time in spite of the fact that its halflife is significantly shorter than that time (as determined from $^{10}$Be), $T_{1/2}/\tau_{esc} \simeq 0.04$.

Figure 2 includes calculated values of the $^{36}$Cl/S ratio for various

values of the cosmic ray confinement time. Our lower limit on the near-Earth abundance of $^{36}$Cl implies a cosmic ray confinement time greater than $\sim$1 Myr. This limit is consistent with the confinement time values we previously reported based on the abundances of $^{10}$Be [4] (8.4 [+4.0, -2.4] Myr), and $^{26}$Al [5] (9 [+20, -6.5] Myr.)

The limited statistics and resolution in the present observations of $^{36}$Cl do not allow a very stringent test of the homogeneity of the matter in the cosmic ray confinement volume. However, the consistency of both the interstellar pathlength distribution and the confinement time deduced from the observed chlorine isotopic abundances with those previously obtained from other stable and unstable secondary nuclide abundances indicate that no major differences exist in the confinement of different elements, at least in the range $3 \lesssim Z \lesssim 26$.

4. Acknowledgments. This work was supported, in part, by NASA under Contract NAS5-20995 and Grant NAG5-308. The instrument used for this study was developed by the Heckman/Greiner group at the Lawrence Berkeley Laboratory.

References

1. Garcia-Munoz, M. *et al.*, Ap. J. (Letters), 280, L13 (1984).
2. Greiner, D.E. *et al.*, IEEE Trans. Geosci. Elect., GE16, 163 (1978).
3. Meyer, J.P. *et al.*, Proc. 15th ICRC (Plovdiv), 2, 213 (1975).
4. Wiedenbeck, M.E. *et al.*, Ap. J. (Letters), 239, L139 (1980).
5. Wiedenbeck, M.E., Proc. 18th ICRC (Bangalore), 9, 147 (1983).

# COSMIC RAY ISOTOPE MEASUREMENTS WITH A NEW CERENKOV X TOTAL ENERGY TELESCOPE

*W. R. Webber, J. C. Kish & D. A. Schrier*
*Space Science Center*
*University of New Hampshire*
*Durham, NH 03824*

1. Introduction and Experimental Data. In this paper we report measurements of the isotopic composition of cosmic ray nuclei with Z = 7-20. These measurements were made with a new version of a Cerenkov x total E telescope. This telescope and the details of the balloon flight are described in paper OG 4.1-5. Path length and uniformity corrections are made to all counters to a RMS level < 1%. Since the Cerenkov counter is crucial to mass measurements using the C x E technique - special care was taken to optimize the resolution of the 2.4 cm thick Pilot 425 Cerenkov counter. This counter exhibited a $\beta$ = 1 muon equivalent LED resolution of 24%, corresponding to a total of 90 p.e. collected at the 1st dynodes of the photomultiplier tubes.

Events to be analyzed using the C x E mass analysis technique are first selected according to charge by a two dimensional method using both dE/dx xE and dE/dx xC matrices. Three separate dE/dx measurements are utilized. Charge overlap is neglible. Mass histograms are constructed from C x E matrices for each charge as illustrated in Figure 1 for Oxygen nuclei. Mass histograms for N, O, Ne and Mg nuclei are shown in Figure 2, and for Al, Si, S, Ar and Ca nuclei in Figure 3. The mass resolution is $\sigma \sim 0.23$ AMU for $^{16}$O and 0.27 AMU for $^{28}$Si.

The data from the 30 hour balloon flight is summarized in Table I. Column 1 gives the energy interval for mass analysis. The upper limit is taken to be $C/C_{max} = 0.45$ for Mg and heavier nuclei. Column 2 gives the number of events observed. Errors are shown only for isotopes where significant mass overlap occurs - all other errors are taken to be statistical. Column 3 shows the charge fraction for each isotope corrected to equal energy/nucleon intervals. And finally Column 4 shows this charge fraction corrected to the top of the atmosphere.

2. Interpretation of the Data. The basic goal of this experiment is to compare the observed isotopic ratios with those expected after interstellar propagation in order to derive the cosmic ray source abundance ratios. The secondary abundances produced during propagation are calculated using new cross sections measured by our group at the BEVALAC (Webber et al., paper OG 7.2-2). The propagation program utilizes a simple exponential path length distribution in hydrogen with a mean path length $\lambda_e = 23.0\ \beta\ P^{-0.6}\ g/cm^2$ above 5.5GV and $\lambda_e = 8.33\ \beta$ below 5.5GV. The solar modulation parameter $\Phi$ = 600 MV. At an interstellar energy ~ 800 MeV/nuc appropriate to these measurements, $\lambda_e \sim 6.8 g/cm^2$.

The extrapolation to the source for selected isotope ratios is shown in Table II. Also shown for comparison are previously measured isotope ratios (at a slightly lower energy) from a summary by Wiedenbeck, 1984. These differ slightly from the original values quoted by Wiedenbeck and co-workers from the ISEE experiment.

Below is a charge by charge summary of our results.
Nitrogen. Nitrogen above the Cerenkov threshold stops near the end of the 2nd and

last total E counter in our telescope. The resulting energy range of analysis is narrow, thus limiting the statistical accuracy of the data. The results obtained here are consistent with earlier results showing a significantly greater abundance of $^{15}N$ than $^{14}N$ at earth.

Oxygen. The $^{17}O$ and $^{18}O$ abundances that we observe are slightly larger than, but consistent with those originally reported by Wiedenbeck and Greiner, 1981a. It is seen that the secondary production of $^{18}O$ is ~ 10 x the solar system abundance ratio making it very difficult to achieve a meaningful source abundance determination of this isotope.

Neon. The relative abundances for $^{21}Ne$ and $^{22}Ne$ we measure are in good agreement with those reported by Wiedenbeck and Greiner, 1981a. $^{21}Ne$ is consistent with being all secondary and the source abundance ratio $^{22}Ne/^{20}Ne$ that we derive is ~ 4 x the solar system value in agreement with earlier measurements.

Magnesium. The relative abundances of $^{25}Mg$ and $^{24}Mg$ we measure are again consistent with, but slightly smaller than those originally reported by Wiedenbeck and Greiner, 1981a. (They agree even better with the average abundance ratios summarized by Wiedenbeck, 1984 - see Table II) These slightly lower abundance fractions - coupled with a secondary production which appears to be 20 - 40% larger than that used by the above authors leads to cosmic ray source abundances of these nuclei that are 1.43 ± 0.50 x the solar system ratio for $^{25}Mg/^{24}Mg$, and 1.24 ± 0.28 x the solar system ratio for $^{26}Mg/^{24}Mg$. These values are lower than those originally reported by the above authors, but are in agreement within the quoted ± 1 $\sigma$ experimental errors. They are also consistent with cosmic ray source to solar system ratios of one.

Aluminum. The fraction $^{26}Al/^{27}Al$ of 2.2 ± 1.8% that we measure compares with the fraction of 3.6 ± 2.9% reported by Wiedenbeck, 1983.

Silicon. The fractions we measure for $^{29}Si$ and $^{30}Si$ are about 1 $\sigma$ lower than those originally reported by Wiedenbeck and Greiner, 1981b. For the secondary production of these isotopes we obtain ~ 30-40% more than appears to have been obtained by the above authors. This leads to cosmic ray source fractions of these isotopes which are 0.79 ± 0.42 and 0.82 ± 0.58 x the solar system values respectively. These values are ~ 2 $\sigma$ below the original values quoted by the above authors. About 1 $\sigma$ of this difference is due to the larger secondary production we use.

Sulpher. For $^{34}S$ our source abundance fraction is ~ 1 $\sigma$ lower than that reported by Wiedenbeck, 1984. In arriving at a source abundance we use a secondary production ~ 33% larger than that which appears to have been used by Wiedenbeck. The actual cosmic ray source abundance ratios we find for both $^{33}S$ and $^{34}S$ are consistent with zero. This is not a realistic value, however, since the interstellar secondary production is ~ 5 x the source abundance ratio for $^{34}S$ and the experimental errors in all measurements to date are greater than the source abundance fraction itself.

Argon & Calcium. Both of these charges are somewhat different than the previous charges discussed. Individually they are dominated by one rather rare isotope in the source, $^{36}Ar$ or $^{40}Ca$ and the possible source abundances of the other isotopes are expected to be completely dominated by interstellar secondary production if we consider solar system abundance fractions. The isotopic abundance fractions that we measure as shown in Table I are indeed consistent with purely secondary production with the exception of $^{36}Ar$ and $^{40}Ca$. The fractions of these isotopes we measure are ~ 1.5 x larger than expected for pure solar system abundances however. This could be suggestive of a somewhat larger abundance of these isotopes relative to Fe in the cosmic ray source. Unfortunately we are unable to derive absolute ratios of these isotopes to Fe from this analysis to confirm this suggestion.

3. Summary. In this analysis we find one decisive example of an isotopic abundance difference in the cosmic ray source, $^{22}Ne$ as has been observed several times before. We also find a suggestion that $^{25}Mg$ & $^{26}Mg$ are enhanced but only at the 1 $\sigma$ level. For

all of the other isotopes we measure, including $^{29}Si$ & $^{30}Si$, our results are consistent with a solar system isotopic composition. About 30% of the difference in the source abundance ratio derived in this paper and those previously reported appears to be due to differences in the cross sections used, the remaining differences are in the experimental results themselves.

4. Acknowledgements. This work was supported by NASA grant NGR - 30-002-052.

5. References.

Wiedenbeck, M. E., & Greiner, D. E., Phys. Rev., 48, 682, 1981a
Wiedenbeck, M. E., & Greiner, D. E., Ap. J., 247, L122, 1981b
Wiedenbeck, M. E., Proc. 18th ICRC, 9, 147, 1983
Wiedenbeck, M. E., paper presented at COSPAR symposium, Graz., August, 1984

6. Figure Captions.

Figure 1. C x E matrix of events for Oxygen nuclei. Calculated mass lines for $^{15}O$, $^{16}O$, $^{17}O$ and $^{18}O$ are shown.
Figure 2. Mass histograms for N, O, Ne and Mg nuclei.
Figure 3. Mass histograms for Al, Si, S, Ar and Ca nuclei

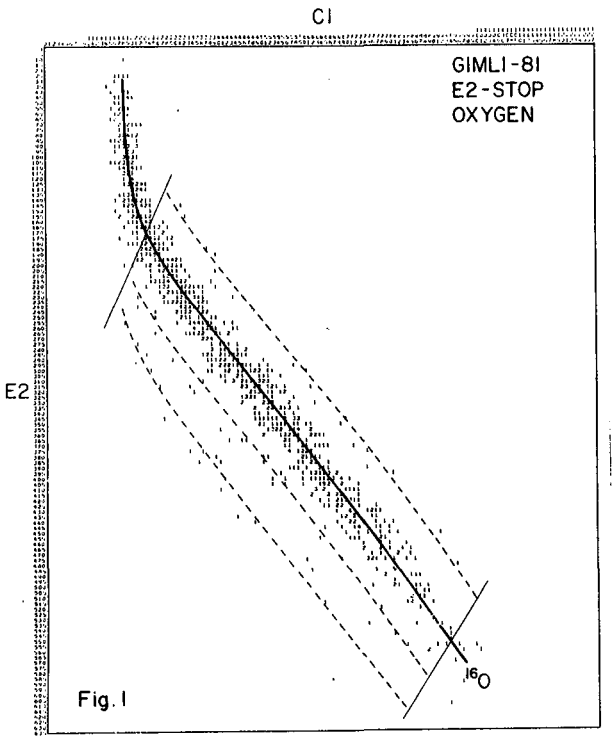


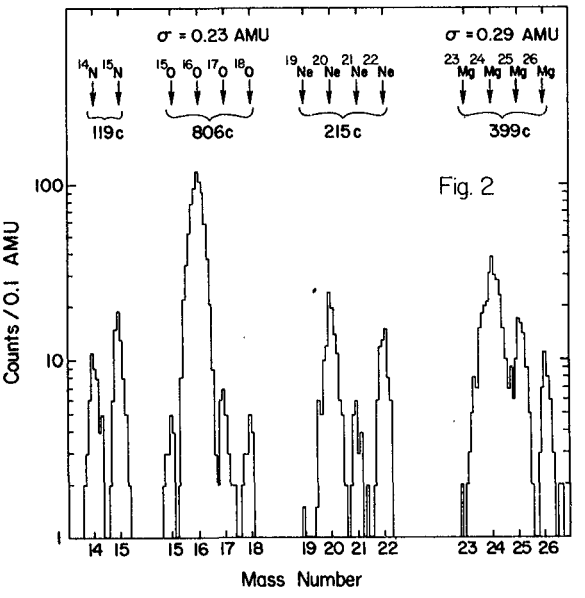

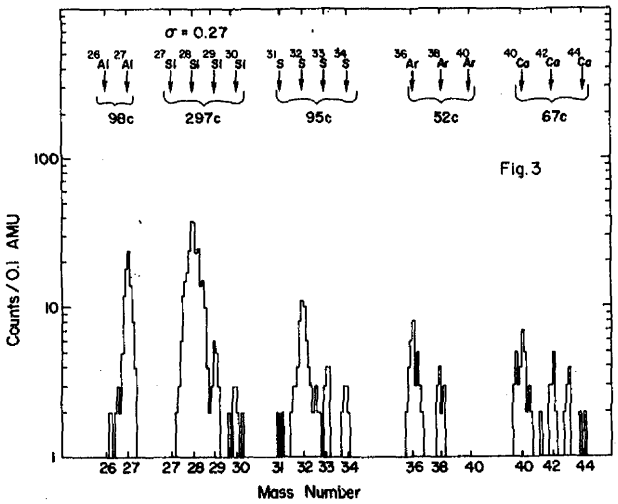


Table I

Isotopic Abundances

| Isotope | Energy Interval (MeV/nuc) | Events Observed | % of Charge equal E int. | % of Charge at Top of Atm | Predicted* |
|---|---|---|---|---|---|
| $^{14}N$ | 383 - 450 | 49 | 39.7 | 38.2±5.6 | |
| $^{15}N$ | 375 - 438 | 70 | 60.3 | 61.8±5.1 | |
| $^{16}O$ | 390 - 485 | 752 | 94.1 | 94.4 | |
| $^{17}O$ | 386 - 472 | 22 | 3.0 | 2.8±0.6 | |
| $^{18}O$ | 381 - 460 | 19 | 2.8 | 2.7±0.6 | |
| $^{20}Ne$ | 410 - 554 | 121 | 55.0 | 54.7 | |
| $^{21}Ne$ | 406 - 542 | 23 | 11.0 | 10.6±2.1 | |
| $^{22}Ne$ | 401 - 530 | 67 | 34.0 | 34.7±4.0 | |
| $^{24}Mg$ | 429 - 610 | 270 | 66.5 | 64.8 | |
| $^{25}Mg$ | 425 - 601 | 66±8 | 17.0 | 17.5±2.6 | |
| $^{26}Mg$ | 420 - 592 | 61 | 16.5 | 17.7±2.4 | |
| $^{26}Al$ | 435 - 635 | 5±3 | 5.0 | 2.2±1.8 | |
| $^{27}Al$ | 430 - 627 | 94 | 95.0 | 97.8 | |
| $^{28}Si$ | 446 - 642 | 251 | 88.1 | 88.7 | |
| $^{29}Si$ | 441 - 637 | 18±3 | 6.3 | 5.9±1.8 | |
| $^{30}Si$ | 436 - 632 | 16 | 5.6 | 5.4±1.5 | |
| $^{32}S$ | 462 - 660 | 64 | 68.7 | 69.9 | |
| $^{33}S$ | 457 - 656 | 14 | 15.2 | 14.5±3.9 | |
| $^{34}S$ | 453 - 651 | 15 | 16.1 | 15.6±4.1 | |
| $^{36}Ar$ | 478 - 678 | 33 | 63.5 | 63.7 | 42.6 |
| $^{37}Ar$ | 474 - 674 | 2 | 3.8 | 2.6±2.0 | 12.8 |
| $^{38}Ar$ | 470 - 669 | 16 | 30.8 | 31.4±8.7 | 38.9 |
| $^{39}Ar$ | 466 - 665 | 0 | 0.0 | 0.0 | 0.0 |
| $^{40}Ar$ | 462 - 660 | 1 | 1.9 | 2.2±2.2 | 5.7 |
| $^{40}Ca$ | 494 - 697 | 31 | 46.1 | 46.9 | 30.8 |
| $^{41}Ca$ | 490 - 692 | ~3 | 4.5 | 4.1±2.7 | 6.2 |
| $^{42}Ca$ | 486 - 688 | 16 | 24.0 | 23.8±6.6 | 22.0 |
| $^{43}Ca$ | 482 - 684 | 10 | 15.0 | 14.3±5.1 | 19.8 |
| $^{44}Ca$ | 478 - 680 | 7 | 10.4 | 10.9±4.4 | 21.2 |

* Assuming $\left(\frac{^{36}Ar}{Fe}\right)_S = 3.0\%$, $\left(\frac{^{40}Ca}{Fe}\right)_S = 6.8\%$

TABLE II

Isotope Fractions

| Ratio | This Measurement (%) | Wiedenbeck, 1984 (%) | Secondary Production (%) | Cosmic Ray Source (%) | Solar System (%) |
|---|---|---|---|---|---|
| $^{17}O/^{16}O$ | 2.9±0.7 | 1.7±0.4 | 2.1 | 0.8±0.6 | - |
| $^{18}O/^{16}O$ | 2.8±0.7 | 1.9±0.2 | 2.1 | 0.7±0.6 | 0.2 |
| $^{21}Ne/^{20}Ne$ | 19.4±4.1 | 21±5 | 20.5 | -1.1±4.5 | 0.3 |
| $^{22}Ne/^{20}Ne$ | 63.4±8.6 | 58±6 | 16.5 | 46.9±9.0 | 12.2 |
| $^{25}Mg/^{24}Mg$ | 27.1±4.4 | 27±4 | 8.6 | 18.5±4.6 | 12.9 |
| $^{26}Mg/^{24}Mg$ | 27.4±2.6 | 27±3 | 10.1 | 17.3±4.0 | 14.2 |
| $^{29}Si/^{28}Si$ | 6.9±2.0 | 13±2 | 3.3 | 3.6±2.7 | 5.1 |
| $^{30}Si/^{28}Si$ | 6.4±1.8 | 7.2±1.7 | 3.8 | 2.6±2.3 | 3.4 |
| $^{33}S/^{32}S$ | 20.7±5.8 | - | 20.5 | 0.2±6.4 | 0.8 |
| $^{34}S/^{32}S$ | 22.5±6.1 | 28±8 | 23.2 | -0.7±6.7 | 4.4 |

# THE ISOTOPIC COMPOSITION OF COSMIC RAY CALCIUM

K.E. Krombel and M.E. Wiedenbeck*
Enrico Fermi Institute, University of Chicago
Chicago, Illinois 60637 USA

## ABSTRACT

Data from the high energy cosmic ray experiment on the ISEE-3 spacecraft have been used to study the isotopic composition of cosmic ray calcium at an energy of ~260 MeV/amu. The arriving calcium is found to consist of (32 ± 6)% $^{40}$Ca. A propagation model consistent with both the light and the sub-iron secondary element abundances was used for the interpretation of the observed calcium composition. The measured $^{42}$Ca+$^{43}$Ca+$^{44}$Ca abundance is consistent with the calculated secondary production, while the $^{40}$Ca abundance implies a source ratio of $^{40}$Ca/Fe = (7.0 ± 1.7)%.

1. Introduction. In the cosmic radiation, most of the elements in the sub-iron region ($17 \lesssim Z < 26$) are predominantly secondary in origin, resulting from the fragmentation of heavier cosmic ray nuclei during propagation from the source to the Earth. Calcium is one exception to this pattern, having a significant contribution from primary cosmic rays, particularly for the isotope $^{40}$Ca, the dominant isotope (~97%) of solar system calcium [1]. In this paper, we present new measurements of the galactic cosmic ray calcium isotopic composition and compare them with measurements made by other experimenters and the values found for solar system material.

2. Data. The observations reported here were taken with the high energy isotope experiment on the ISEE-3 spacecraft during the time period from August 1978 to April 1981. The energy range for calcium is approximately 170 to 380 MeV/amu with an average of approximately 260 MeV/amu. Cuts were made on the data to eliminate nuclear interactions in the instrument and to choose only those events which have well determined trajectories. In addition, only those particles having incident angles of less than 15 degrees with respect to the detector normal were used in the data set presented here in order to obtain the best mass resolution compatible with the desired statistical accuracy.

For calcium, a direct measure of the instrument resolution can be obtained from a comparison with the adjacent element, scandium, which has a single stable isotope, $^{45}$Sc. The scandium mass distribution can be used as a measure of both the absolute mass scale and the resolution expected at calcium.

Figure 1(a) shows the scandium mass distribution in 0.25 amu bins, along with a best fit Gaussian curve. The Gaussian has a standard deviation of 0.49 amu and the histogram has been adjusted to be centered at mass 45. The difference between the calculated mean mass and the true mass was 1.1 amu, and is simply an artifact of systematic errors in the mass calculation. This value is consistent with the smoothly varying trend seen for lighter elements and for iron. Figure 1(b) shows the cal-

*and Department of Physics

cium distribution in 0.25 amu bins, again with a best fit distribution superimposed. This fitted distribution is a superposition of five Gaussian peaks (corresponding to isotopes of mass 40 through 44) with center-to-center spacings of 1 amu and equal widths. The common width and the position of the mass 40 peak were allowed to vary in the fit along with the individual abundances. The deduced resolution was 0.53 amu and an offset of 1.07 amu was needed to center the mass 40 peak.

Although the mass resolution achieved is insufficient to cleanly resolve $^{42}Ca$, $^{43}Ca$, and $^{44}Ca$, the relative lack of $^{41}Ca$ permits separation of the dominantly primary $^{40}Ca$ from the dominantly secondary $^{42}Ca$, $^{43}Ca$ and $^{44}Ca$. Comparison with the scandium mass distribution cleary demonstrates that the structure seen in the calcium histogram is due to actual abundance variations and not just statistical fluctuations since the width of the $^{45}Sc$ peak, 0.49 amu, is significantly less than the overall width of the calcium distribution and is consistent with the resolution determined from the calcium data. In addition, the scandium permits an unambiguous determination of the absolute mass scale verifying that $^{40}Ca$ is assigned the correct mass.

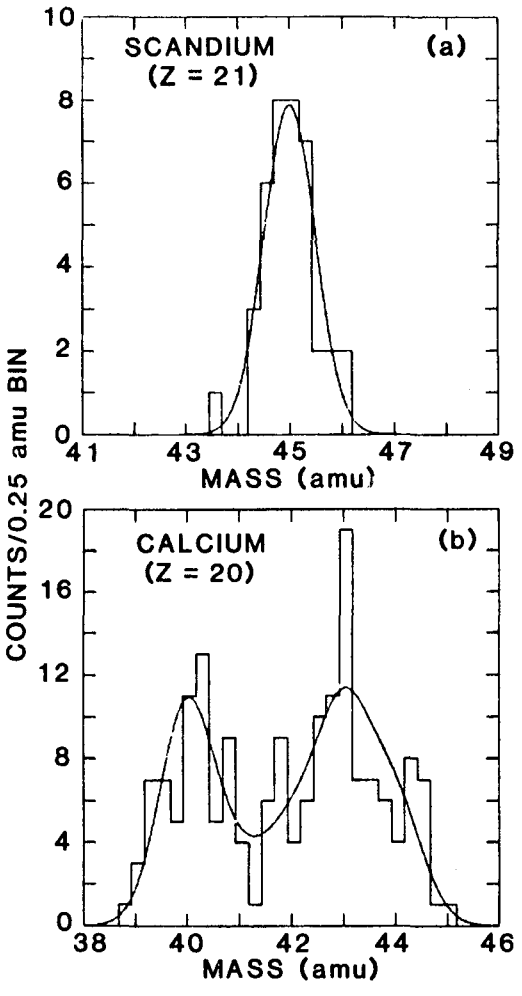


Figure 1

3. Discussion. Because $^{42}Ca$, $^{43}Ca$, and $^{44}Ca$ are not clearly separated in this data set, determination of their individual abundance values requires a more detailed analysis of the resolution systematics. However, a way of viewing these data which is less dependent on the details of the peak shapes is to divide the calcium into primary species ($^{40}Ca$) and secondaries ($^{42}Ca$, $^{43}Ca$ and $^{44}Ca$) since the low abundance of $^{41}Ca$ permits resolution at this scale. Our data imply an arriving cosmic ray calcium composition of (32 $\pm$ 6)% $^{40}Ca$ and (60 $\pm$ 6)% 'secondary group', as defined above. Since the $^{41}Ca$ could be expected to be sensitive to the exact peak shape used, no value is reported here.

These isotope fractions are plotted in Figure 2, along with the results reported by other experimenters [2, 3, and 4]. Since the New Hampshire [3] and Minnesota [2] groups presented individual isotopic abundances, the uncertainties shown for their $^{42}Ca+^{43}Ca+^{44}Ca$ measurements are estimated from the individual errors that they reported. Additionally, Tarlé et al. [4] did not present an explicit $^{40}Ca/Ca$ ratio. The value used here is the result of counting events on their calcium mass histogram. As can be seen from Figure 2, there is reasonable agree-

ment between experiments when the data are presented in this way.

Also shown in Figure 2 (dashed line) are the results of a cosmic ray propagation calculation employing a nested leaky box model with mean escape lengths of 1.5 g/cm² for the inner leaky box and 3.0 g/cm² for the outer box (H:He = 10:1). Solar modulation is taken into account using a numerical integration based on the method of Fisk [5]. Solar system isotopic composition [1] was assumed for elements with $Z \geq 19$ in the cosmic ray source, and source elemental abundances were chosen to reproduce the elemental abundances observed near Earth at 70-280 MeV/nucleon [6]. The pathlength values used were those needed to simultaneously reproduce the observed B/C and the (Sc+V)/Fe ratios at these energies.

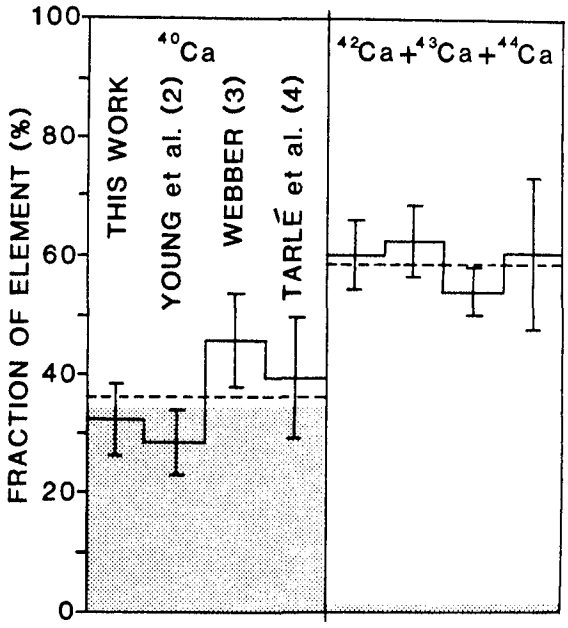


Figure 2

The shaded areas on the figure indicate the fraction of each group which is primary. As can be seen, the division into $^{40}$Ca and $^{42}$Ca+$^{43}$Ca+$^{44}$Ca provides a very clean separation between primary and secondary calcium.

This propagation model, based on light and sub-iron secondary elements, is also compatible with the observed abundance of calcium secondaries (Figure 2). The present observations imply that the ratio $^{42}$Ca+$^{43}$Ca+$^{44}$Ca/$^{40}$Ca in the cosmic ray source does not exceed its solar system value (0.03) by more than a factor of ~30. Although our measured abundance of this secondary group does not require a finite source abundance of any calcium isotope other than $^{40}$Ca, separation of this group into its constituent isotopes is required to firmly establish this conclusion.

Because the calcium elemental abundance observed at Earth is 60% secondary while the isotope $^{40}$Ca is only 4% secondary, the use of the calcium isotope information can significantly reduce the uncertainties involved in deriving the source abundance of calcium. If we ignore the isotope information and employ only the elemental abundances of [6], we find that the source Ca/Fe ratio is $(8.2 \pm 7.8)$%, where the uncertainty includes the effects both of observation errors and of propagation errors [7]. The latter source of uncertainty, due mostly to assumed 35% correlated errors in fragmentation cross sections, is found to dominate. If the $^{40}$Ca isotope fraction is used in conjunction with the elemental abundances, we obtain, at the source, $^{40}$Ca/Fe = $(7.0 \pm 1.7)$%. The relative uncertainty in this source ratio is only 24%, as compared with the 95% uncertainty in the ratio obtained using elemental abundances alone. Furthermore, the uncertainty in our deduced $^{40}$Ca/Fe source ratio is dominated by the observation errors (rather than by uncertainties in the propagation calculation), so future improvements in the resolution and statistical accuracy of calcium isotope measurements will further improve the accuracy of the deduced $^{40}$Ca source abundance. In Table 1 we compare our value of the $^{40}$Ca/Fe source abundance ratio with values reported by

other investigators. While these values are all in reasonable agreement, one must exercise caution in comparing them because the specifics of the propagation models and error calculations used by the various authors differ.

The ratios of cosmic ray source elemental abundances (GCRS) to the corresponding solar system values (SS) have been found to be reasonably well organized by the first ionization potential of the element (e.g. [8], and references therein), although other possible ordering parameters (such as volatility [9]) have been proposed. By combining our $^{40}$Ca/Fe source ratio with the value of this ratio in the solar system (6.73% [1]), we find $(^{40}Ca/Fe)_{GCRS}/(^{40}Ca/Fe)_{SS} = 1.04 \pm 0.25$. Two general functional forms have been suggested for representing the dependence of such ratios on first ionization potential. The first is an exponential dependence of the form $GCRS/SS \propto \exp(-I/I_o)$, while the second is a step function where all elements with low first ionization potential ($I \lesssim 9$ eV) have one value and all those with high first ionization potential have a single, lower value. Calcium has a first ionization potential of 6.1 eV and for iron the value is 7.9 eV. Our present results are thus consistent with the step-function dependence. They are consistent with an exponential dependence only if a relatively low value of the parameter $I_o$ is used. Brewster et al. [10] have reported the results of two different exponential fits. One, excluding the light noble gas elements, has $I_o = 3.47$ eV, and implies that the GCRS $^{40}$Ca/Fe ratio should be 1.66 times the solar system value. The other has $I_o = 5.6$ eV and implies that the $^{40}$Ca/Fe enhancement should be 1.37. These two predictions exceed our deduced value by 2.5 and 1.3 standard deviations, respectively. While discrepancies at this level for a single element are not sufficient to rule out such exponential dependence on first ionization potential, they do suggest that extreme exponential dependencies are unsatisfactory in this case or that some other ordering parameter may be more appropriate.

TABLE 1
Derived Values of $^{40}$Ca/Fe in the Cosmic Ray Source

| Value | Reference |
|---|---|
| 7.0 ± 1.7 % | this work |
| 6.2 ± 1.1 % | 2 |
| 8.8 ± 1.6 % | 3 |
| 5.9 ± 1.9 % | 4 |

4. Acknowledgements. This work was supported in part by NASA Contract NAS 5-20995 and NASA Grant NAG 5-308. The instrument was developed by the Heckman/Greiner group at the Lawrence Berkeley Laboratory. Christopher Smith provided valuable program development aid.

References

1. Cameron, A.G.W. (1982), in Essays in Nuclear Astrophysics, p. 23.
2. Young, J.S., et al. (1981), Ap. J., 246, 1014.
3. Webber, W.R. (1981), Proc. 17th ICRC (Paris), 2, 80.
4. Tarlé, G., et al. (1979), Ap.J. (Letters), 232, L161.
5. Fisk, L.A. (1971), JGR, 76, 221.
6. Garcia-Munoz and Simpson (1979), Proc. 16th ICRC (Kyoto), 1, 270.
7. Hinshaw and Wiedenbeck (1983), Proc. 18th ICRC (Bangalore), 9, 263.
8. Meyer, J.P. (1985), Ap. J. Supp., 57, 173.
9. Meyer, J.P. (1981), Proc. 17th ICRC (Paris), 2, 281.
10. Brewster, N.R., et al. (1983), Ap. J., 264, 324.

# A NEW ANALYSIS OF COSMIC RAY ISOTOPES AT 3 GeV/n FROM HEA03-C2 DATA

Ferrando P., Goret P., Koch-Miramond L.,
Petrou N., Soutoul A.

Service d'Astrophysique, Centre d'Etudes Nucleaires de Saclay
France

ABSTRACT

We present results on mean masses of cosmic rays at energy about 3 GeV/n, for Ne, Al, Mg, Si, S, Ca, and Fe, derived from the data collected by the Danish-French experiment C2 on board HEA03. We used a method based upon comparison between observed transmission function and a predicted one computed from a geomagnatic field model. We find enhancement factors of 2.9 +-.7 for 22Ne/20Ne, 2.1 +-.4 for (25Mg+26Mg)/24Mg, and 1.6 +-.8 for (29Si+30Si)/28Si at GCRS when compared to LG.

## Introduction

Cosmic ray isotopic rather than elemental composition is a major clue to the understanding of cosmic rays history because while the elemental source composition can a priori be interpreted in terms of any kind of scenario involving either atomic or nuclear processes, isotopic anomalies almost certainly imply specific nucleosynthetic processes (at least for Z > 4). If elemental abundances and spectra are now well established /1,2/ and show remarkable similarities with Solar System abundances and Solar Energetic Particles /3/ , isotopic composition measurements available at low energy (<1 GeV/n) show significant differences when compared to Local Galactic material (see /4/ for a review). Measurements at higher energy present the advantage to be less dependent upon solar modulation; however they are more difficult to perform . Peters /5/ has developed a method allowing determination of mean masses with the help of the geomagnetic field; analysis of HEA03-C2 data were already performed using the transmission function method /6,7/ but dealed with part of the data because of geomagnetic selections. In this study a different approach is used: we also start from the observed transmission function (OTF) which reflects the filtering effect of the geomagnetic field upon relativistic particles; this effect depends upon rigidity so that isotopes with different A/Z ratios show different OTF. The point of our method is that we compute the theoretical filtering effect in the frame of a geomagnetic field model (MAGSAT 4/81); we are then able to predict the various transmission functions corresponding to all possible isotopic fractions. Isotopic composition is derived by adjusting the predictions to the actually observed transmission function.

## Method

Building an OTF requires the knowledge for each detected particle of the momentum by nucleon P and the main cut-off Rc corresponding to the position and direction of arrival in the instrument /6,7/. P is measured by the instrument and Rc is computed with a trajectory tracing method /8/. The number of particles observed with momentum by nucleon p° at a main cut-off Rc is given by :

$$d^2N/dp^\circ dRc = Tex(Rc).\ \sum_i \int_p F(Rc,Ri).\beta i.f(p).P(p,p^\circ)dp \qquad (1)$$

with Ri= Ai.p/Z . Tex(Rc) is the exposure time at main cut-off Rc, f(p) the differential momentum spectrum of the element, ßi the isotopic fraction of isotope Ai , and P(p,p°) the momentum resolution function of the instrument. Tex(Rc) and f(p) are derived from the data. F(Rc,R) is the mean geomagnetic filter function at main cut-off Rc. Let us recall that a particle can reach a given point of observation in a given direction only if it passes the geomagnetic field barrier, which may be described as a filter function ff(R) which only depends upon rigidity. For each point and direction there exists a main cut-off Rc so that ff(R)= 1 if R>Rc. For R<Rc one may have either ff(R)= 1, if the associated trajectory is allowed, or 0 if it is forbidden (penumbra region). The mean filter function F(Rc,R) represents the average of all filters ff(R) at a given Rc. Practically, for each particle, we compute Rc as the highest forbidden rigidity; then we randomly select 30 rigidities in the penumbra region for which we compute if they are allowed or forbidden. The mean filter function F(Rc,R) is obtained by averaging all these statistical penumbra at given Rc. Preliminary calculations have shown that the penumbra vanishes below .75 Rc for the region of interest here. To avoid biases in the computation of mean filters only particles with p/Rc>.6 were selected. Predicted transmission functions corresponding to given isotopic fractions are computed by summation of (1) at constant p/Rc.

Determination of experimental parameters

We analysed data with rigidity between 7 and 9 GV and momentum between 3.2 and 6.1 GeV/cn; the fit region (p/Rc= .4 to .52) corresponds to a mean energy of 3 GeV/n. 21 mean filters were computed by step of 0.1 GV from 7 to 9 GV. The instrumental function P(p,p°) is taken as a gaussian function with a standard deviation S. To account for a possible drift in momentum we introduce another parameter, D, so that p observed = D times p true. To determine S and D oxygen is used as a reference element assuming 96% of 160, 2% of 170, and 2% of 180. However these two parameters alone do not allow us to account for the OTF of oxygen which is systematically higher than prediction in the penumbra. The discrepancy is removed by assuming a scaling factor SF by which we multiply all computed F(Rc,R) in the region R/Rc < 1.0. The three parameters are simultaneously optimized by minimising the chi² between observed and predicted transmissions. Values of .990, 4.3%, and 1.18 are respectively found for S,D and SF. Fig 1 shows the agreement between predicted and observed transmission functions for oxygen. The shift of 1% between actual and observed momentum, which is compatible with the error on the measurement of the refractive index of the Cerenkov detector, indica-

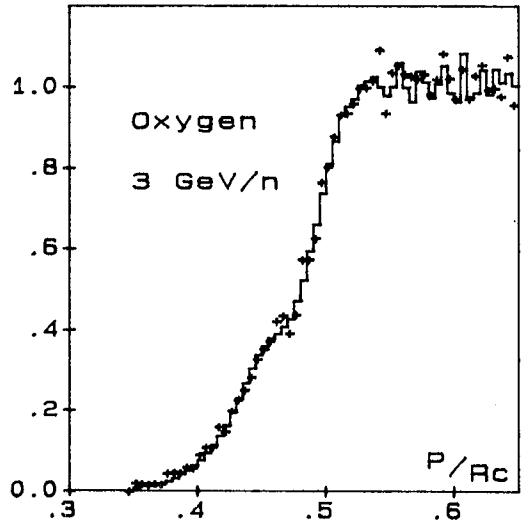


Fig 1: Observed transmission function (+), and best fit prediction (full line).

tes that the geomagnetic field model gives an accurate estimate of the main cut-off. The value of SF shows that more than 80% of the penumbra is well accounted for by the model; the missing 20% may come either from complex trajectories not handled properly by the tracing program, or from possible instrumental background. S is twice higher than the value expected from the statistics of Cerenkov photoelectrons alone. It reflects other effects like delta rays, and a possible slight distorsion in the shape of the estimated mean filters.

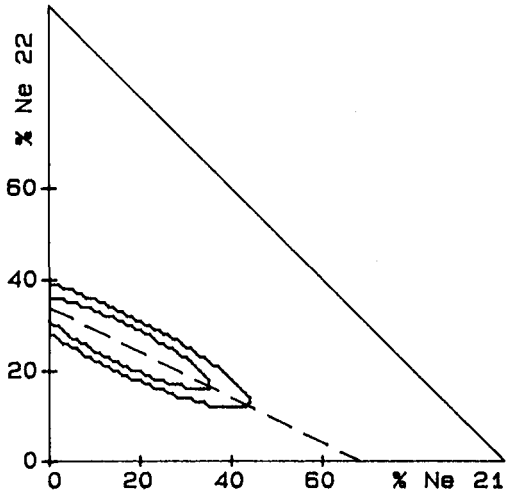


Fig 2: 68 and 90% confidence level regions for observed fractions of 21Ne and 22Ne. Broken line is the line of mean mass 20.68 .

Results

The same parameters D and SF derived from O were used to analyse higher elements. A 1/Z dependence of S was found suitable; it's value has only a little influence on mean masses. We computed all chi² between OTF and prediction for all possible isotopic composition; the minimum chi² gives the measurement. Contours of 68 and 90% confidence level from chi² analysis are plotted in fig 2 for Ne isotopes. The strongly elliptical form of the contours is the sign of highly correlated parameters; the major axis of ellipses are aligned with the equal mean mass lines, showing that the fundamental parameter of the method is the mean mass. Results are therefore given as mean masses with quoted errors corresponding to a chi² increase of 1.0 from minimum chi². A check is provided by Na (which has a single isotope), 311 Na are predicted, in agreement with the 324 observed in the fit region. In table 1 we report our results together with the mean masses obtained from a propagated solar source (SS) composition. S,Ca, and Fe have an observed mean mass quite compatible with a propagated SS composition, while Ne ( confirmed by /9/, also from HEA03-C2 data, but with a different method), Mg, and possibly Si are found to be neutron enriched.

Discussion

Results were propagated back to Galactic Cosmic Ray Sources (GCRS) in a leaky-box model, including energy losses, radioactive decay, in a pure H (density 0.3 $cm^{-3}$) I.S.M. . An escape length equal to 22.R-0.6 (6.2 $g/cm^{-2}$ at 3 GeV/n), and a modulation parameter $\phi$ = 600 MV were assumed according to /2/. We also assume 0 % of 21 Ne, an equal fraction of 25 and 26Mg, an equal fraction of 29 and 30Si in GCRS. Errors only include statistical measurement uncertainties. In table 2 the ratios of GCRS abundances to Local Galactic (LG, from /10/) are given for Ne, Mg and Si. It is seen that Ne and Mg are definetely neutron enriched in GCRS, with enhancement factors comparable to the low energy results of 4.1 (+.8,-.6) for Ne, and 1.6 (+.3,-.2) for Mg, at # 200 MeV/n, /4/. There is therefore no evidence for an energy dependence of these isotopic source anomalies. The poorer resolution for Si isotopes does not allow us to distinguish between a LG composition or a neutron rich one. These results are compatible

with the suggestion that the bulk of Cosmic Rays is injected in the acceleration process from solar like stellar coronae with normal abundances, while a minor part of it (2-3 %) would come from sites having experienced more evolved nucleosynthesis. Wolf-Rayet stars could explain the neutron rich component for Ne and Mg, as well as the overabundance of C but predicts a normal isotopic composition for Si, /11/. If the enhancement factor for Si, found at low energy, is confirmed, metal rich supernovae could also contribute to GCRS isotopic anomalies, /12/. Isotopic ratios such as 36S/32S, 57Fe/56Fe, 58Fe/56Fe ,still to be measured, could help distinguishing between various models.

Table 1: Observed mean masses at 3 GeV/n

| Element | Number in the fit region | Observed mean mass | Propagated SS composition |
|---|---|---|---|
| Ne | 1681 | 20.68 (+-.06) | 20.48 +-.08 |
| Mg | 1910 | 24.59 (+-.06) | 24.42 +-.04 |
| Al | 323 | 26.91 (+.09,-.16) | 26.90 +-.03 |
| Si | 1373 | 28.25 (+-.07) | 28.19 +-.035 |
| S | 275 | 32.70 (+.22,-.20) | 32.56 +-.16 |
| Ca | 210 | 41.80 (+.35,-.30) | 41.65 +-.22 |
| Fe | 1114 | 55.75 (+-.20) | 55.82 +-.03 |

Table 2:

| | | |
|---|---|---|
| Enhancement factors GCRS ratios/LG ratios | 22Ne/20Ne : | 2.88 (+.77, -.65) |
| | (25Mg + 26Mg)/24Mg : | 2.03 (+.49, -.42) |
| | (29Si + 30Si)/28Si : | 1.55 (+.84, -.74) |

References

/1/: Lund N., 1984, Adv. Space Res. Vol4, n°2-3, p. 5.
/2/: Engelmann J.J., & al, to be published in Astron. Astrophys.
/3/: Meyer J.P., 1985, Ap.J. Suppl. 57, 173.
/4/: Wiedenbeck M.E., 1984, Adv. Space Res. Vol4, n°2-3, p. 15.
/5/: Peters B., 1974, Nucl.Instr.Meth; 121, 205.
/6/: Soutoul A., & al, 1981, 17th ICRC, Paris, 9, p.105.
/7/: Koch-Miramond L., 1981, 17th ICRC, Paris, 12, 21.
/8/: Mac Cracken K.G., & al, 1962, MIT Techn. Rep. 77 NYO 2670
/9/: Lund N., Herrstroem N.Y., this conference.
/10/: Cameron A.W.C., 1982, in "Essays in Nuclear Astrophysics" eds C. Barnes, D. Clayton and D. Schramm, Cambridge University Press, p.23.
/11/: Prantzos, 1984, Adv. Space Res. Vol4, n°2-3, p. 109.
/12/: Woosley S.E., Weaver T.A., 1983, Ap. J. 243, 651.

# THE ENERGY DEPENDENCE OF THE NEON-22 EXCESS IN THE COSMIC RADIATION

**Nils-Yngve Herrström and Niels Lund**
**The Copenhagen-Saclay HEAO collaboration**
**Danish Space Research Institute, Lundtoftevej 7, DK-2800.**

## Introduction

It has been recognized now for some time that the heavy neon isotope, neon-22, is overabundant by a factor of 3 to 4 with respect to neon-22 in the cosmic ray source compared to the ratio of these isotopes in the Solar System (1-8).

In view of the otherwise remarkable similarity of the chemical composition of the cosmic ray source and the composition of the Solar Energetic Particles (9), the anomaly regarding the neon isotopes is so much more striking.

The observed excess of neon-22 is too large to be explained as a result of the chemical evolution of the Galaxy since the formation of the Solar System (10).

Further information on the origin of the neon-22 excess may come from a comparison of the energy spectra of the two neon isotopes. If the cosmic radiation in the solar neighborhood is a mixture of material from several sources, one of which has an excess of neon-22, then the source energy spectra of neon-20 and neon-22 may differ significantly.

## Data

We have compiled the available data on the neon-22 to neon-20 ratio as function of energy. The data are shown in figure 1a. The observed ratio is sensitive to the level of solar modulation at the time of observation; therefore we show in figure 1b the same data extrapolated to zero solar modulation (the interstellar flux). We have used the force field approximation for the solar modulation and have applied a correction for each data point corresponding to the relevant period of observation.

Finally figure 1c shows the calculated source ratio corresponding to each data point. For this calculation we have used the propagation model described in (11).

The error bars in figure 1 are everywhere those of the experimenters. We have not attempted to assign errors to the correction for solar modulation or for the propagation calculation. The uncertainties in these corrections are appreciable despite the fact that we are only concerned with a flux ratio, not with absolute fluxes.

We note however, that the best fit straight line to the source fluxes has a slope of $-0.031 \pm 0.040$, i.e. it is consistent with an energy

independent source ratio, even considering only the original statistical errors on the data points.

## Discussion

The best fit, energy independent, source ratio of neon-22 to neon-20 is $0.35 \pm 0.05$. This is nearly three times the solar value of 0.12.

The apparent similarity of the source energy spectra for the two neon isotopes speaks in favor of a common acceleration mechanism for both, i.e. for the neon-22 excess already existing in the source material before the acceleration.

Since, as mentioned above, a neon-22 excess of the observed magnitude is unlikely to be a general feature of the present day interstellar medium, we are led to conclude that either there is a direct connection between the nucleosynthesis chain leading to excess neon-22 and the cosmic events leading to particle acceleration, or the local cosmic ray flux is dominated by a single source with an accidental excess of neon-22.

A dominance of a single source is incompatible with the observed high degree of isotropy of the cosmic radiation. The local source picture is therefore only tenable if restricted to the heavy nuclei; the bulk of the cosmic ray nucleons, in the hydrogen/helium component, must in any case arise in a multitude of sources distributed in the Galaxy (12).

## Acknowledgements

The authors would like to thank all their collaborators in the Copenhagen-Saclay Collaboration for their efforts in providing the data for this work. In particular we want to thank J. J. Engelmann and P. Masse for propagation calculations and useful discussions.

## References

1) Fisher, A. J. et al: 1976, Ap J 205, 938.
2) Dwyer, R,. Meyer, P.: 1979, 16th ICRC, Kyoto 12, 97.
3) Garcia-Munoz, M. et al: 1979, Ap J (Letters) 232, L95.
4) Freier, P. S. et al: 1980, Ap J (Letters) 240, L53.
5) Mewaldt, R. A. et al: 1980, Ap J (Letters) 235, L95.
6) Wiedenbeck, M. E, Greiner, D. E.: 1981b, Ap J (Letters) 247, L119.
7) Webber, W. R.: 1982, Ap J 252, 386.
8) Herrström, N-Y. et al, To be submitted to Astronomy and Astrophys.
9) Meyer, J. P., Ap J Suppl. 57, 173, (1985).
10) Adonze et al, 17th ICRC, 2, 296, 1981.
11) Engelmann, J. J. et al, Astronomy and Astrophysics in press.
12) Lund, N., Adv. Sp. Res. 4, no. 2-3, p 5, (1984).

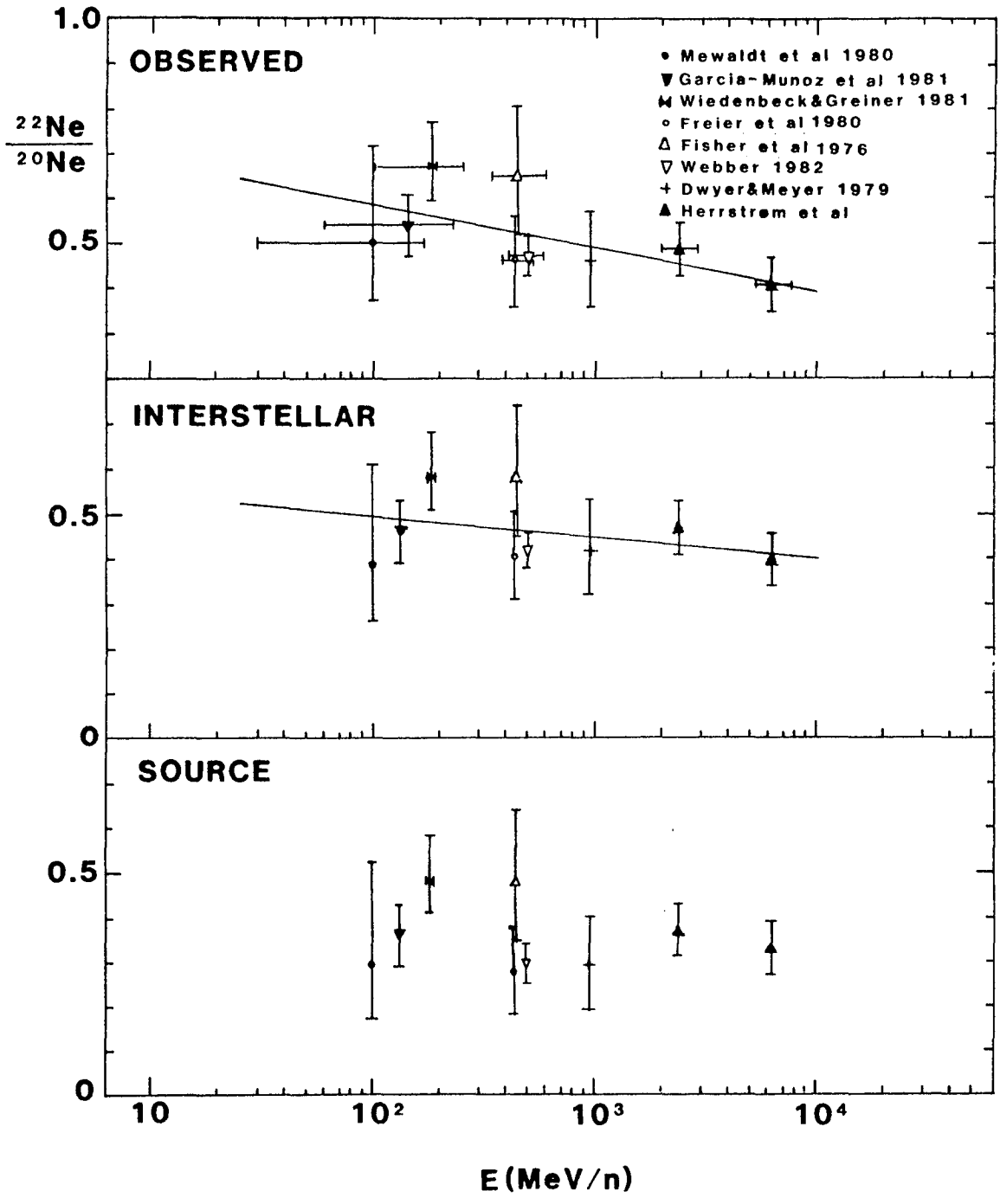


Fig. 1. The neon-22 to neon-20 ratio as function of energy.

# INITIAL RESULTS FROM THE CALTECH/DSRI BALLOON-BORNE ISOTOPE EXPERIMENT

*S. M. Schindler, A. Buffington†, E. C. Christian, J. E. Grove, K. H. Lau & E. C. Stone*

California Institute of Technology
Pasadena, California 91125

*I. L. Rasmussen & S. Laursen*

Danish Space Research Institute, Denmark

*ABSTRACT*

The Caltech/DSRI balloon-borne High Energy Isotope Spectrometer Telescope (HEIST) was flown successfully from Palestine, Texas on 14 May, 1984. The experiment was designed to measure cosmic ray isotopic abundances from neon through iron, with incident particle energies from ~ 1.5 to 2.2 GeV/nucleon, depending on the element. During ~ 38 hours at float altitude, > $10^5$ events were recorded with $Z \geq 6$ and incident energies $\gtrsim$ 1.5 GeV/nucleon. We present results from the ongoing data analysis associated with both the pre-flight Bevalac calibration and the flight data.

1. Introduction. The experiment described here is a joint undertaking by Caltech and the Danish Space Research Institute. A large-area (geometric factor ~ 0.25 $m^2$ sr) balloon-borne instrument has been developed to measure cosmic-ray isotopic abundances from neon through iron, with incident particle energies from ~ 1.5 to 2.2 GeV/nucleon, depending on the element (1). The experiment was first flown on 14 May, 1984, from Palestine, Texas. Prior to flight, the detector was exposed to beams of carbon, neon, argon, and manganese at the Berkeley Bevalac, with the latter exposure providing the principal calibration for the instrument. Preliminary results associated with the development of mapping techniques and position-determining algorithms are discussed, with application to flight data.

2. Instrument Description. The experiment employs either Cerenkov-ΔE-Cerenkov or Cerenkov-total energy techniques for isotope resolution (see reference 1), depending on whether the incident particle traverses the entire detector, or stops at an intermediate position in the instrument. Figure 1 shows a schematic diagram of the detector. A stack of twelve NaI(Tl) disks (each nominally 2 cm thick, 52 cm diameter; 87.2 gm/$cm^2$ total thickness) directly measures the energy change ΔE for an incident particle. Two Cerenkov counters (C1 and C2), measure the change in Lorentz factor, $\Delta\gamma = \gamma_1 - \gamma_2$, for the event. For a stopping particle $\gamma_2 = 1.0$. Mass M is obtained from:

$$M = \Delta E / \Delta\gamma$$

Each disk making up the stack is viewed by six individually digitized photomultiplier tubes (PMT). This permits not only a measurement of the energy deposition per layer, but through intercomparison of the six PMT responses, yields the particle's position in that layer (2,4). Because of the large amount of material

† Present address: Univ. of California, San Diego; CASS C-011, La Jolla, CA 92093

necessary to slow down the high-energy nuclei, typically 85% of the incident particles meeting the trigger requirements will undergo charge-changing fragmentation reactions in the detector. For the NaI stack, these events are removed through a comparison of the individual layer responses. Plastic scintillators (S1 and S2), define the geometry factor, and provide additional rejection against events fragmenting within the Cerenkov counters.

The top Cerenkov counter consists of a mosaic of 48 aerogel radiators of refractive index n ~ 1.1, while the bottom counter employs a combination of teflon (n = 1.34) and Pilot 425 (n = 1.49). Results associated with the $^{55}$Mn Bevalac calibration of the aerogel counter have been presented previously (3).

In its flight configuration, the detector and associated electronics are mounted in an insulated pressure vessel. An on-board evaporative cooling system is employed to maintain constant detector temperature, minimizing the need for thermal corrections in the data. Along with housekeeping information, the 108 digitized PMT outputs are recorded on-board using two video recorders, and are also transmitted to the ground through a telemetry link for real-time analysis.

3. Flight Details. The experiment was flown from Palestine, Texas on 14 May, 1984, using a 17.2 x $10^6$ ft$^3$ Winzen balloon. The instrument maintained float altitude for ~ 38 hours, at a typical atmospheric depth of ~ 5.5 gm/cm$^2$. During the flight, the geomagnetic cutoff ranged from ~ 4.5 to 5.5 GV. The experiment was recovered with minimal damage to the instrument.

For the flight, ~ 4.25 x $10^5$ events were recorded, which included > $10^5$ events with $Z \geq 6$ and kinetic energy > 1.5 GeV/nucleon. While only a fraction of the events will be usable for isotope analysis, the remainder are being employed for in-flight mapping of the detector, gain balancing, and stability checks.

Analysis of the flight data has shown that with minor exceptions, all systems performed as designed. The evaporative cooler maintained a constant detector temperature of 25.0 ± 0.5°C for the majority of the flight, with a gradient across the NaI stack of ≤ 0.2°C. Examination of threshold settings and detector gains and offsets, have indicated an overall average stability for the flight of better than 1%.

4. Data Analysis. One innovation in this experiment is that the NaI stack provides both trajectory and energy loss information for an incident particle. However, this requires that the response of the individual disks making up the stack be accurately mapped. Previous analysis results have been presented based on the November, 1982 Bevalac calibration, which employed a beam of $^{55}$Mn ions, at 1.75 GeV/nucleon (4). Those results were based on analysis of data from two central regions of the instrument. Our primary analysis objective has been to use the $^{55}$Mn calibration data to generate full-disk response maps of each PMT viewing each stack layer, and to obtain full-disk maps of the response ratios with various PMT combinations, for position determination.

The response maps for each PMT are generated using an overlay of 1 cm bins on each NaI disk. Typically, the response of a single PMT varies by a factor of 5 to 7 across the disk. The current mapping technique uses calibration data to assign an average response to the center of each bin. For each event, a multi-point interpolation process is employed to obtain correction factors from the maps, with the final response generated from a weighted average over all six PMT's viewing the disk.

Figure 2 shows a histogram of the normalized energy loss (response) for layer 1, averaged over the entire disk. The resolution achieved of ~ 2.8% FWHM is only slightly worse than the 2.4% previously reported for central regions of the stack (4). We estimate that Landau fluctuations account for approximately one-half the distribution width. Results for layers 2 and 3 exhibit similar distributions, with a FWHM of ~ 3.0%. Additional refinements in the mapping technique are expected to improve the energy

resolution further.

In addition to generating full-disk response maps, work is progressing on developing position determining algorithms for the disks. Position resolution is obtained from the calibration data, by comparing the measured event position obtained from Bevalac wire-chamber data, and that inferred from algorithms employing ratios of disk PMT responses. The use of PMT response *ratios* effectively removes the energy dependence from the position determination. Currently, six ratio maps are generated for each NaI disk, using a 1 cm spatial grid. The maps employ ratios of opposite sums of two and three adjacent PMT's viewing each disk. Intermediate positions are obtained using an interpolation process. For a given event, the best estimate of particle position is determined from an algorithm which minimizes the difference between the mapped ratios and the measured event ratios.

Figure 3 shows the difference distribution for a single position coordinate ($\Delta X$), as determined from $^{55}Mn$ calibration data averaged over approximately the central two-thirds area of layer 1. The central portion of the distribution has a FWHM of 4mm, in good agreement with the results previously presented, that were limited to data near the stack axis (4). Similar results are obtained for the orthogonal coordinate $\Delta Y$. Combining both position coordinates for layer 1 produces the difference distribution shown in Figure 4, where:

$$\Delta R = (\Delta X^2 + \Delta Y^2)^{1/2}$$

From these results, the rms position resolution for layer 1 is found to be of order 3mm. In extending the analysis to deeper stack layers, the distribution broadens to $\sim$ 4.4mm by layer 5. We consider these results as upper limits to the intrinsic stack resolution, in that contributions from wire-chamber uncertainties and multiple Coulomb scattering have not yet been unfolded from the data.

5. Discussion. While we anticipate further improvement in the analysis results described here, our results for energy resolution are already consistent with the design goals for isotope resolution in the instrument. In particular, if we extrapolate these results to the full 12 layers of the stack for stopping $^{55}Mn$, the expected contribution to mass error from uncertainty in $\Delta E$ is of order 0.3%. This uncertainty results in an associated mass error for the instrument of $\sim$ 0.19 amu for Mn at the Bevalac energies, with a correspondingly smaller uncertainty for the lighter elements.

Prior to the detailed analysis of the flight data, the maps and position-determining algorithms developed from the $^{56}Mn$ Bevalac exposure must be extended to the remaining stack layers. Concurrent with this effort, we are optimizing techniques for trajectory determination, and extending the position-determining algorithms to the outer edges of the disks.

6. Acknowledgements. This work was partially supported by NASA, under grant NGR 05-006-160.

References.

1. Buffington, A., Lau, K., Laursen, S., Rasmussen, I. L., Schindler, S. M., and Stone, E. C., "Proc. 18th International Conference, Bangalore, 2, 49-52, 1983

2. Buffington, A., Lau, K., and Schindler, S. M., "Proc. 17th International Cosmic Ray Conference", Paris, 8, 117-120, 1981.

3. Rasmussen, I. L., Laursen, S., Buffington, A., and Schindler, S. M., "Proc. 18th International Cosmic Ray Conference, Bangalore", 8, 77-80, 1983.

4. Schindler, S. M., Buffington, A., Lau, K., and Rasmussen, I. L., "Proc. 18th International Cosmic Ray Conference, Bangalore", 8, 73-76, 1983.

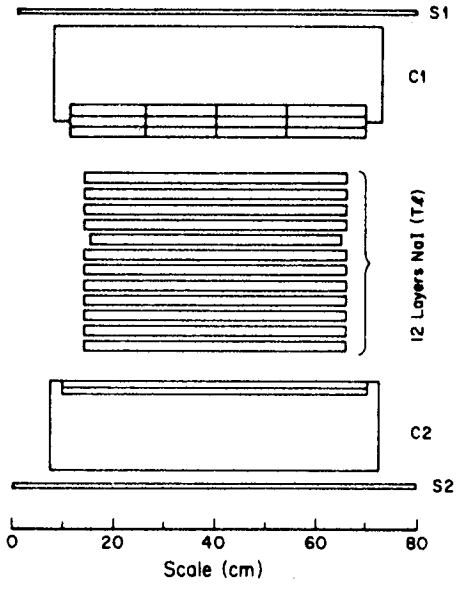


Fig. 1. Schematic diagram of the detector.

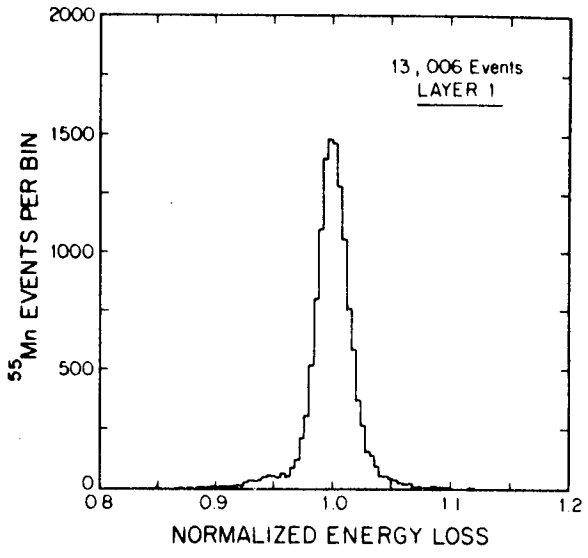


Fig. 2. Layer 1 response distribution for $^{55}$Mn, averaged over the full NaI disk.

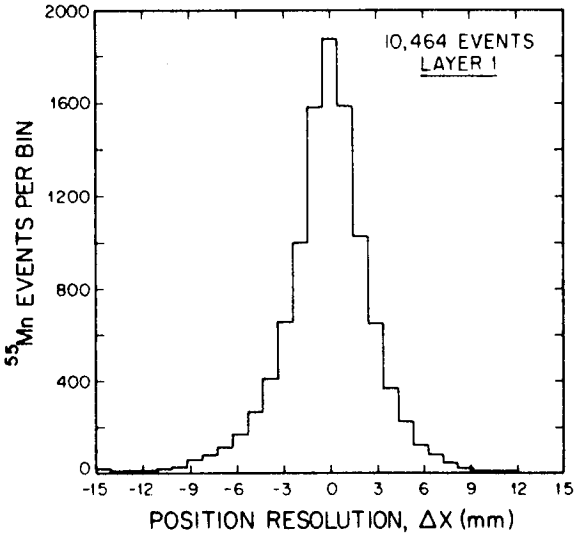


Fig. 3. Difference distribution between a single Bevalac wire-chamber coordinate, and that obtained from layer 1 NaI response ratios, averaged over the central two-thirds area of the disk, for $^{55}$Mn ions.

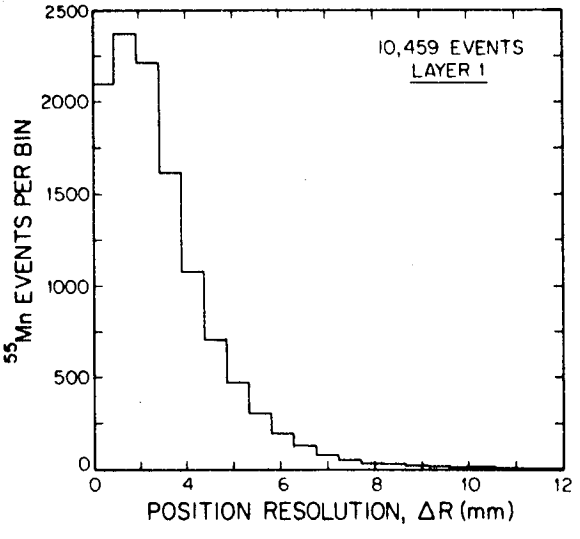


Fig. 4. Difference distribution between Bevalac wire-chamber positions, and those obtained from layer 1 NaI response ratios, averaged over the central two-thirds area of the disk, for $^{55}$Mn ions.

# THE INNER GRANULOMETRIC DENSITY OF THE TRACKS IN NUCLEAR EMULSIONS AND ITS APPLICATION TO DETERMINE THE CHEMICAL SPECTRUM OF PRIMARY COSMIC RAY NUCLIDI.

G. ALVIAL

Laboratorio de Rayos Cósmicos. Departamento de Física. Facultad de Ciencias Físicas y Matemáticas. Universidad de Chile. Casilla 1314. Santiago.

1.- Introduction. The classical formula of Lattes, Fowler and Cüer (1),

$$(1) \quad E = b\, Z^{2a}\, A^{1-a}\, R^{a}$$

which gives the energy E of a non-relativistic nuclide as function of the atomic number Z, the relative atomic mass A and the linear residual range R (b and a = constants) is valid for residual ranges of the order of 2,000 μm under the assumption that the nuclide itself does not capture electrons before its stopping point inside the nuclear emulsions. For a given interval $\Delta R = L$ (referred as a cell in this paper), with an effective ionizing atomic number $Z_{eff}$ (due to a given number of captured electrons) formula (1) becomes,

$$(2) \quad \Delta E = b\, Z_{eff}^{2a}\, A^{1-a} \left\{ R_{eff}^{a} - (R_{eff} - L)^{a} \right\}$$

Actually, the linear residual ranges which are determined with the microscope (here denoted as $R_r$) neither are represented by R of (1) nor by $R_{eff}$ of (2) because of the effect of the successive electron captures along the linear residual range. However, at a given value of $R_r$ - or of $Z_{eff}$ - the expression $R_r^a - (R_r - L)^a$ differs from the corresponding one of (2) as an infinitesimal of second order.

Therefore, if we measure $R_r$ and determine $\Delta E$ in a cell $\Delta R = L$, we can obtain the particular value of the expression $(Z_{eff})^{2a} A^{1-a}$ at $R_r$.

2.- The Method. A direct counting of the number of developed grains inside a cell $\Delta R = L$ at a given residual range $R_r$ was carried out on tracks of stopping monocharged nuclidi as those of protons and deuterons. By applying formula (2) with $R_r$ instead of $R_{eff}$ (taking a = 0.568 and b = 0.281 for our G-5 Ilford emulsions), $\Delta E$ was determined and consequently, also the value w of the energy transferred to each microcrystal of $Ag^{+} Br^{-}$ - involved in the formation of a single silver developed grain - was obtained.

For $Z \geq 2$, the inner granulometric density is defined by the ratio between the volume of the track segment of length $\Delta R = L$ and that one of the single proton developed grain.

The corresponding measurements of diameters of grains and thicknesses of tracks were carried out by strictly applying the Occhialini's Track Profile Method (2).

As it has already shown for protons and deuterons in Table I, the experimental measurements resulted coherent and compatible with the assumption that at a given value of the function $\chi$ (Partition Function) given by,

$$(3)\quad \chi = E/(Z^{2a} A^{1-a}) = b R^{a}$$

the energy loss of a nuclide involved in the formation of a simgle silver developed grain which, in turn, is located inside a small part of the track (e.g. L = 20 μm ) is the same for any nuclide stopping inside a given plate, independently of the value of Z . This fact together with the value of the inner granulometric density permit us to determine $\Delta E$ corresponding to this track segment at the residual range $R_r$ and consequently , to know the magnitude $Z^{2a} A^{1-a}$.

TABLE I

| $R_r$ (μm) | $w_p$ (MeV/grain) | $w_D$ (MeV/grain) |
|---|---|---|
| 0-20 | 0.0423 ± 0.0040 | 0.0400 ± 0.0041 |
| 20-40 | 0.0204 ± 0.0019 | 0.0195 ± 0.0038 |
| 40-60 | 0.0163 ± 0.0015 | 0.0154 ± 0.0016 |
| 60-80 | 0.0140 ± 0.0013 | 0.0140 ± 0.0014 |
| 80-100 | 0.0117 ± 0.0012 | 0.0110 ± 0.0011 |
| ..... | ..... | ..... |
| 260-280 | 0.0078 ± 0.0008 | 0.0078 ± 0.0009 |
| ..... | ..... | ..... |
| 540-560 | 0.0055 ± 0.0005 | 0.0054 ± 0.0009 |

The extrapolated curve of $w_p$ or $w_D$ as function of $R_r$ leads to the relativistic limit of $w = 3.0$ KeV/grain.

Besides, for the electron tracks with $R_r \leq 20.0$ μm it was determined that $w_e = (0.0433 \pm 0.0042)$ MeV/grain. Actually this result was directly obtained with a radioactive standard source of $^{210}Bi_{83}$ .

Table II shows the results of the measurements which were carried out on the last 20 μm of residual range. These short linear residual ranges were chosen to test the reliability of the method. The tracks were selected by a non systematic scanning. For any of these nuclidi, $\chi = 1.540605$ MeV.

The experimental value of $\Delta E$ was determined by the number of

TABLE II

| Atomic Nuclide | E(experimental) (MeV) | E(theor.) (MeV) | $\bar{d}$ (um) | $\bar{Z}_{eff}$ | Isotopic mass ratio. |
|---|---|---|---|---|---|
| $^{1}H_1$ | (calibration nuclide) | 1.540605 | 0.700 ± 0.023 | 1.0 | $^{2}H_1/^{1}H_1$ = 2.00082 ±0.50701 |
| $^{2}H_1$ | 2.07880 ± 0.22757 | 2.078434 | 1.000 ± 0.080 | 1.0 | |
| $^{4}He_2$ | 5.4400 ± 0.6100 | 5.467274 | 1.217 ± 0.023 | 1.8 | $^{4}He_2/^{3}He_2$ = 1.34253 ± 0.50812 |
| $^{3}He_2$ | 4.7900 ± 0.5700 | 4.822833 | 1.142 ± 0.026 | 1.8 | |
| $^{7}Li_3$ | 6.67546 ± 0.52357 | 6.962469 | 1.343 ± 0.021 | 1.8 | $^{8}Li_3/^{7}Li_3$ = 1.12271 ± 0.14071 |
| $^{8}Li_3$ | 7.01512 ± 0.52336 | 7.375913 | 1.377 ± 0.020 | 1.8 | |
| $^{12}C_6$ | 9.6377 ± 1.9482 | 9.905302 | 1.614 ± 0.030 | 2.0 | $^{13}C_6/^{12}C_6$ = 1.18083 ± 0.1100 |
| $^{13}C_6$ | 10.3589 ± 2.2643 | 10.253803 | 1.6733 ± 0.048 | 2.0 | |

The following number of nuclidi are shown in this Table ; 11, $^{1}H$; 6, $^{2}H$; 5, $^{4}He$; 3, $^{3}He$; 7, $^{7}Li$; 5, $^{8}Li$; 7, $^{12}C$ and 7, $^{13}C$.

the inner silver developed grains times the value of $w_p$ corresponding to $R_r$ = 20.0 μm (Table I). The theoretical one, by formula (2). All the tracks were also identified by the classical method. Once knowing the experimental value of E, $Z_{eff}$ ( average value in 20 μm ) and the ratio between isotopic masses were deduced.

Table III indicates the results corresponding to a part of the 29 nuclidi which were inside of 37 central plates of a package of emulsions which flew at an average altitude of 4.5 g/cm$^2$ during 16 hours, in 19 to 20 of July of 1958 over Minneapolis, Minn.; the 200 plates of Ilford G-5 emulsions of 15x15 cm x 600 μm each, were kindly afforded to the author of the present paper by the late Professor of The University of Chicago, Dr. Marcel Schein.

The above mentioned 29 nuclear tracks, which had $Z \geq 3$ and stopped inside the emulsions, entered at 7 mm from the superior edge of each sheet and were distributed as it follows:

| $^{6}Li$ - | $^{7}Be$ - | $^{10}Be$ - | $^{10}B$ - | $^{11}B$ - | $^{11}C$ - | $^{12}C$ - | $^{13}C$ - | $^{13}N$ - | $^{14}N$ - |
|---|---|---|---|---|---|---|---|---|---|
| 1 | 3 | 1 | 1 | 1 | 3 | 6 | 1 | 2 | 5 |

$^{18}O - ^{21}Ne - ^{24}Mg - ^{27}Al - ^{35}Cl$

TABLE III

| $Z^{1.136}A^{0.432}$ (exp.) | $Z^{1,136}A^{0.432}$ (theo.) | Assigned Nuclide | w (MeV/grain) | $R_r$ |
|---|---|---|---|---|
| 7.361951±0.730232 | 7.553897 | $^{9}Li_3$ | 0.0081 | 205.28 |
| 11.640685±1.316993 | 11.194959 | $^{7}Be$ | 0.0066 | 348.51 |
| 13.619709±1.540894 | 13.0599089 | $^{10}Be$ | 0.0077 | 230.02 |
| 16.687503±1.887975 | 16.827900 | $^{10}B$ | 0.0071 | 283.19 |
| 26.877412±2.994446 | 27.621999 | $^{13}N$ | 0.0062 | 422.50 |
| 27.933732±3.160341 | 28.520602 | $^{14}N$ | 0.0063 | 374.98 |
| 20.847880±2.358668 | 21.570562 | $^{11}C$ | 0.0063 | 372.12 |
| 22.305500±1.596050 | 22.396808 | $^{12}C$ | 0.0056 | 497.80 |
| 22.953260±2.596865 | 23.184799 | $^{13}C$ | 0.0054 | 550.20 |
| 50.933117±5.762424 | 50.956400 | $^{21}Ne$ | 0.0056 | 554.87 |
| 67.491854±7.635832 | 66.405056 | $^{24}Mg$ | 0.0055 | 540.74 |
| 117.16624±13.25585 | 116.098704 | $^{35}Cl$ | 0.0055 | 546.63 |

3.- Conclusions. Taking into account that the identification of the above measured nuclidi was done by determining the inner granulometric density in only two successive cells of 23.44 μm each and which were located at a residual range $R_r$ ( see Table III), to improve the precision of the determination of Z and A it is suggested that the measurements of each track have at least to observe the following steps:

(a)Start the determination of the inner granulometric density, in 2 or 3 consecutive cells, from the stopping point of the track. This zone has a very small number of standard $\delta$-rays.

(b) Measurements of that granulometric density have to be carried out in several consecutive cells which should permit to determine the transition from $Z_{eff}$ to Z .

(c) Measurements of several cells have to be done in the track segment in which the value of $Z^{1.136}\,A^{0.432}$ should remain as a constant one inside its experimental errors.

In (b) and (c) it is necessary to add the energy of the standard $\delta$ -rays ( of 2 or more grains) which in our case resulted at a rate of 0.0423 MeV/grain.

To obtain the above given 29 nuclidi, the author of this paper has observed only point (c). Complementary measurements on this group of particles by taking into account points (a) and (b) shall improve the spectral distribution of A and Z . Besides, with this criterion measurements will be carried out on another group of 60 stopping nuclidi belonging to the same package of nuclear emulsions.

References:

(1) C.M.Lattes et al.: Proc.Phys.Soc.,59,883(1947(

(2) G.P.S.Occhialini et al.:Suppl.Nuovo Cimento , 4, 244 (1956).

OG 4.4-2

# OBSERVATIONS OF ULTRAHEAVY COSMIC RAY PARTICLES AT 10 GV CUTOFF RIGIDITY

T. Yanagimachi, K. Hisano, K. Ito, S. Kobayashi
Department of Physics, Rikkyo University, Nishi-Ikebukuro, Toshima-ku, Tokyo 171, Japan

T. Doke, R. Hamasaki, T. Hayashi, T. Takenaka
Science and Engineering Research Laboratory, Waseda University, Kikuicho, Shinjuku-ku, Tokyo 162, Japan

K. Nagata
Faculty of Engineering, Tamagawa University, Machida, Tokyo 194, Japan

ABSTRACT

Ultraheavy cosmic ray particles with Z>45 and Fe were observed in two balloon flights at a mean geomagnetic cutoff rigidity of 10 GV. Fluxes of these particles at the top of the atmosphere are presented. A ratio of (Z>45)/(Fe) is compared with other experimental results. The ratio decreases with increasing energy in the energy range from 1 to 10 GeV/amu. A possibility is presented to explain the variation of the ratio with energy.

1. Introduction. Early observations of ultraheavy cosmic ray particles (UH) were mainly made by balloon-borne track detectors at high geomagnetic latitude regions (1, 2, 3). In the observations, UH were collected enough to obtain approximate chemical compositions. Recently, more precise measurements on the abundances of UH were achieved by using electronic detector systems on board the Ariel 6 (4) and the HEAO-3 (5) satellites and a picture of the origin of the cosmic rays based on the early results was suffered significant alteration. However, to determine energy spectra of UH, more data are required.

Plastic detectors are useful instruments for measurements on the fluxes of charge groups of UH, since a large area array can be easily constructed. For observations of relativistic particles, in particular we can realize an extremely large area array, because nuclear charges of such particles can be determined with singly layered plastic sheets.

In our observations at a mean cutoff rigidity of 10 GV, no cosmic ray particles of $E \leqq 2$ GeV/amu can enter from any direction.

2. Experimental Configuration. Two arrays $A_1$ and $A_2$ were launched from Sanriku Balloon Center at a mean cutoff rigidity of 10 GV in 1976 and in 1982, respectively. A total collecting power of $A_1$ expanded vertically with an area of 50.4 $m^2$ was 846.2 $m^2 \cdot$ hr at a mean residual atmosphere of 11.2 $g/cm^2$ and that of $A_2$ expanded horizontally with an area of 28.8 $m^2$ was 238.5 $m^2 \cdot$ hr at a mean residual atmosphere of 7.7 $g/cm^2$. Each array was composed of plastic detector stacks of 40 cm × 50 cm in area consisting of three CN, two CTA and two or one PC sheets. To measure the flux of Fe, several small size stacks of emulsion and of CR-39 were also included in $A_1$ and $A_2$, respectively. In both observations, two CN sheets in each stack were used to detect tracks by ammonia vapour method and the others to determine the charges.

In the CN sheets, 9 tracks produced by UH with $Z \gtrsim 40$ were found; 5 in $A_1$ and 4 in $A_2$.

For calibrations, CN and CTA stacks were exposed to $^{40}Ar$ beams of 400 MeV/amu at the Bevalac. The charge resolutions were characterized by standard deviations of about 3 and 5 charge units at $Z \sim 50$ for the CN and the CTA, respectively.

3. Data Analysis. For the emulsion, $\delta$-ray counting method were applied. On the other hand for the CR-39, using growth rate ($V_t$) data of etch pits, we first prepared scatter plots of normalized etch rates ($V_t/V_g - 1$) vs. $\sin\delta$, where $V_g$ and $\delta$ are a bulk etch rate of the CR-39 and a dip angle of a track, respectively. From these analyses, frequency distributions of $\delta$-ray densities along tracks in the emulsion and of the normalized etch rates projected on the line of $\sin\delta = 1$ were obtained. Compared with well-known chemical composition of

cosmic rays with $Z \leqq 26$, the frequency distributions were converted into charge distributions. One of the results obtained from the CR-39's data is shown in Fig. 1. No correction was made for geometric factor which varies with atomic number. The observed charge resolutions were characterized by standard deviations of 0.55 and 0.34 charge units at Fe for the emulsion and the CR-39, respectively.

The data of track etch rates in the CN and the CTA were used to determine nuclear charges of UH. No track was recorded in the PC sheets which are insensitive to relativistic particles with $Z \lesssim 70$. The track etch rate data and the charges assigned to all events are shown in table 1. In CTA, there is an apparent difference in sensitivity between front and back surfaces.

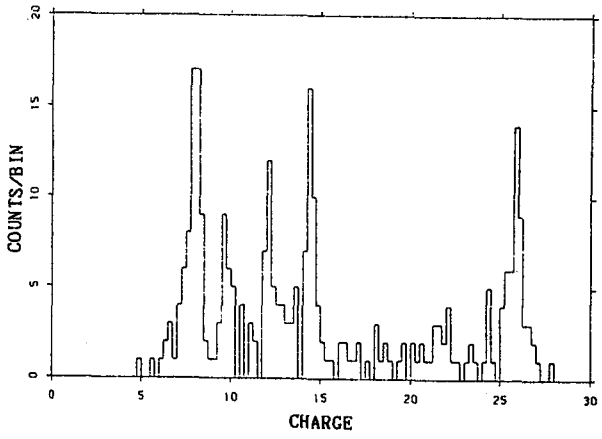


Fig. 1 Chemical composition of the particles found in the CR-39 of 100 cm².

Taking account of nuclear spallations in the overlaying atmosphere, we obtained the fluxes of Fe and UH at the top of the atmosphere. For the calculations of the nuclear spallations, we used Hagen's formula(6) for the total cross sections and extrapolations of Silberberg and Tsao formulae(7) for the partial ones. Scanning efficiency for lighter particles being insufficient, we restricted our attention to the particles with $Z>45$.

TABLE 1
The Track Etch Rates and The Charges Assigned to All Events

| | Event No. | CN Etch Rate ($\mu$m/hr) | Z | CTA (Front) Etch Rate ($\mu$m/hr) | Z | CTA (Back) Etch Rate ($\mu$m/hr) | Z |
|---|---|---|---|---|---|---|---|
| $A_1$ | 23 | 27.4 | 46 | ---- | -- | ---- | -- |
| | 36 | 27.9 | 47 | 2.35 | 53 | 1.38 | 52 |
| | 62 | 29.5 | 47 | 2.87 | 52 | 1.83 | 54 |
| | 208 | 16.9 | 42 | ---- | -- | ---- | -- |
| | 235 | 12.0 | 40 | ---- | -- | ---- | -- |
| $A_2$ | 1-19 | 46.1 | 55 | 2.46 | 54 | 1.43 | 52 |
| | 3-23 | 69.3 | 67 | ---- | -- | 26.0 | 75 |
| | 3-27 | 53.1 | 58 | 2.00 | 52 | 2.57 | 54 |
| | 3-34 | 69.1 | 67 | 4.58 | 60 | 8.92 | 60 |

4. Results and Discussion. The fluxes of both Fe and UH obtained from two observations were consistent with each other. The combined values of the fluxes were as follows;

$0.11 \pm 0.01$ particles/m² · sr · sec for Fe and

$(3.9 \pm 1.5) \times 10^{-6}$ particles/m² · sr · sec for $Z>45$.

As a flux ratio of (Z>45)/(Fe), the following value was obtained;

$(3.5 \pm 1.6) \times 10^{-5}$ for R>10 GV.

This value is shown in Fig. 2 with other experimental results. The datum of the

HEAO-3 was infered from a charge composition summarized by Mewaldt(8). The result of Blanford et al. (3) was that obtained from a balloon observation by using plastic detectors at a cutoff energy of 1 GeV/amu. Assuming a power law spectrum with a index of 2.6, we plotted the ratios deduced from integral fluxes at mean energies in the figure.

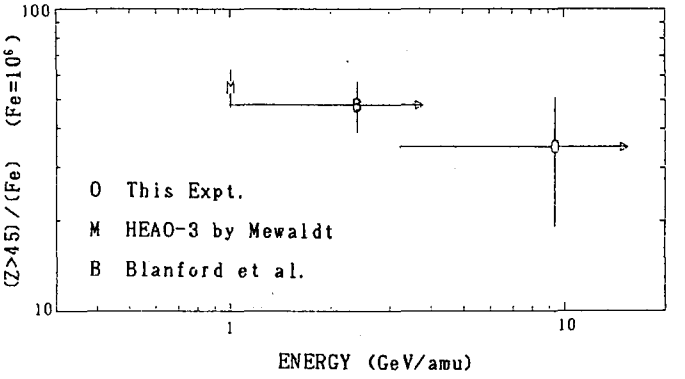


Fig. 2 Observed abundances of the particles with Z>45 relative to Fe (Fe=$10^6$).

It is clear in the figure that the ratio decreases with increasing energy in the energy range from 1 to 10 GeV/amu. The decrease means that the energy spectrum of UH with Z>45 is steeper than that of Fe. The difference in the energy spectra is to be ascribed to the effects of cosmic ray propagation in the Galaxy, if indices of injection energy spectra of all particles are assumed to be the same.

To examine the effects, propagation calculations based on a exponential path length distribution were made(9). In the calculations, we used

(1) Cameron's(10) solar system abundances for source composition,
(2) Silberberg and Tsao(11,12) semiempirical formulae with the modifications of 1977(13), 1979(14) and 1983(15), for the spallation cross-sections and
(3) the semiempirical formulae by Silberberg et al. (16) for the total inelastic cross-sectios,

and included the effects of

(1) first ionization potential enhancement and
(2) solar modulation with a deceleration parameter of 500 MV.

The effects of the ionization losses were neglected, since they are not so important in the energy range of interest.

All injection spectra were taken to be proportional to $W^{-2.2}$, where W is total energy per nucleon.

We considered collisions up to nine times and treated individually 323 isotopes from Nb to Bi, which are either stable, long lived or decayable exclusively by electron capture, and about 800 short lived isotopes produced by collisions and subsequent radio active decays.

The following energy dependent escape mean free path $\lambda_e$ was determined to explain the experimental results for the ratio of (sub-Fe)/(Fe) in the energy range from 0.6 to 30 GeV/amu;

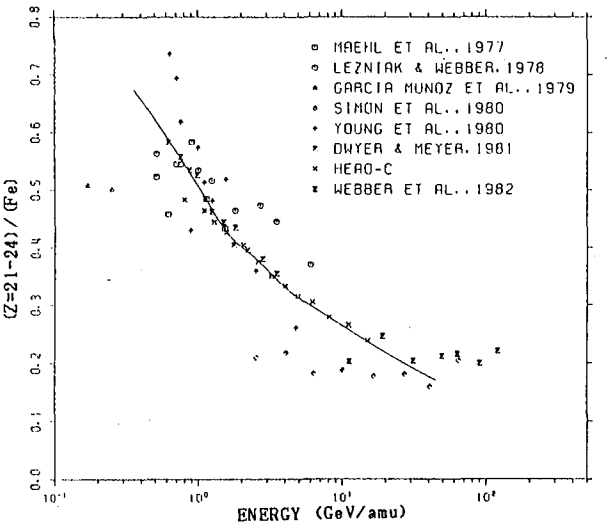


Fig. 3 The variation with energy of the (sub-Fe)/(Fe) ratio.

$$\lambda_e = \begin{cases} 8.0 & g/cm^2 \quad \text{for } E \leq 2 \text{ GeV/amu}, \\ 8.0(E/2) & g/cm^2 \quad \text{for } E > 2 \text{ GeV/amu}. \end{cases}$$

Figure 3 shows the variation with energy of the (sub-Fe)/(Fe) ratios. The predicted curve is consistent with the experimental results over the above range of energy.

The result of the calculation is presented for the (Z>45)/(Fe) ratio on

Fig. 4 and compared with the experimental data. The curve reproduces well the variation of the observed ratios. An increase around 800 MeV/amu is due mainly to similar increases in the spallation cross-sections of heavy nuclei around 1 GeV/amu. An increase in the partial cross-sections in the mass range of $10<\Delta Z<40$ at 1 GeV was shown in the measurements of Kaufman and Steinberg (17) on the spallation of $^{197}$Au. The data obtained from the measurements were incorporated into the semiempilical formulae by Tsao et al. (15).

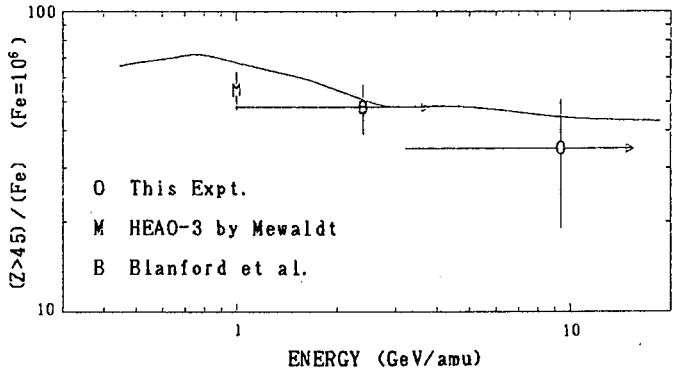


Fig. 4 The variation of the predicted ratio of (Z>45)/(Fe) compared with the observed data.

A possible interpretation of the variation with energy of the (Z>45)/(Fe) ratio shown by the propagation calculation is as follows.

The ratio of (secondaries with Z>45)/(Fe) increases significantly around 1 GeV/amu because it depends strongly on the spallation cross-sections. The alternative ratio of (primaries with Z>45)/(Fe) depends on the attenuation and the escape mean free paths and varies with a simple manner with energy. And the calculations showed that the secondaries are dominant in UH at 1 GeV/amu. Therefore, the (Z>45)/(Fe) ratio in the interstellar space increases at 1 GeV/amu. The effects of the solar modulation shift the increase to lower energy side.

Above 3 GeV/amu, where the spallation cross-sections change little with energy, the (primaries)/(Fe) ratio increases with increasing energy, while the (secondaries)/(Fe) ratio continues decreasing, because the interstellar matter traversed by cosmic rays decreases with increasing energy. As a result, the (Z>45)/(Fe) ratio decreases gradually with increasing energy at least up to ~10 GeV/amu.

The increase around 800 MeV/amu dominates the variation of the ratio of (Z>45)/(Fe). It results mainly from the increases in the spallation cross-sections at 1 GeV/amu. This emphasizes the importance of another measurements of the spallation cross-sections.

References

1. Fowler, P.H. et al., 1967, Proc. Roy. Soc. London, A301, 39.
2. Shirk, E.K. et al., 1973, Phys. Rev., D7, 3220.
3. Blanford, G.E. et at., 1973, Phys. Rev., D8, 1707.
4. Fowler, P.H. et al., 1981, Nature, 291, 45.
5. Binns, W.R. et al., 1982, Astrophys. J., 261, L117.
6. Hagen, F.A., 1976, Ph.D. thesis, University of Marryland.
7. Silberberg, R., and Tsao, C.H., 1977, Proc. 15th Int. Cosmic Ray Conf., (Plovdiv), 2, 89.
8. Mewaldt, R.A., 1981, Proc. 17th Int. Cosmic Ray Conf., (Paris), 13, 49.
9. Yanagimachi, T., Ph.D. Thesis, 1985, Rikkyo University, in Japanese.
10. Cameron, A.G.W., 1980, Center for Astrophysics Preprint Series No. 1357.
11. Silberberg, R., and Tsao, C.H., 1973, Ap. J. Suppl., 25, 315.
12. Silberberg, R., and Tsao, C.H., 1973, Ap. J. Suppl., 25, 335.
13. Silberberg, R., and Tsao, C.H., 1977, Proc. 15th Int. Cosmic Ray Conf., (Plovdiv), 2, 84.
14. Silberberg, R., and Tsao, C.H., 1979, Proc. 16th Int. Cosmic Ray Conf., (Kyoto), 2, 202.
15. Tsao, C.H., et al., 1983, Proc. 18th Int. Cosmic Ray Conf., (Bangalore), 2, 194.
16. Silberberg, R., et al., 1983, in Composition and Origin of Cosmic Rays, ed. Shapiro, M.M., (Dordrecht; Reidel), p. 321.
17. Kaufman, S.B., and Steinberg, E.P., 1980, Phys. Rev., C22, 167.

# ARIEL VI MEASUREMENTS OF ULTRA-HEAVY COSMIC RAY FLUXES IN THE REGION $34 \leq Z \leq 48$

P.H. Fowler, M.R.W. Masheder, R.T. Moses,
R.N.F. Walker, A. Worley and A.M. Gay
H.H. Wills Physics Laboratory, University of Bristol,
Tyndall Avenue, Bristol BS8 1TL, England.

1. Introduction. The Ariel VI satellite was launched by NASA on a Scout rocket on 3rd June 1979 from Wallops Island, Virginia, USA, into a near-circular 625 km orbit inclined at 55°. It carried a spherical cosmic ray detector designed by a group from Bristol University. The salient features of this detector are shown in Fig. 1.

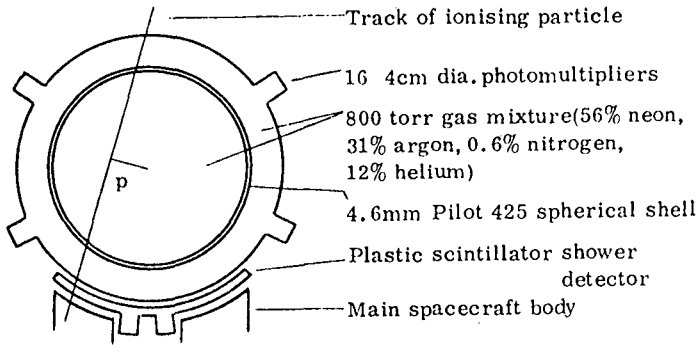


Fig. 1 Schematic cross-section of Ariel VI Cosmic ray detector

A spherical aluminium vessel of diameter 75 cm contains a gas scintillation mixture and a thin spherical shell of Pilot 425 plastic, and forms a single optical cavity viewed by 16 photomultipliers. Particle tracks through the detector may be characterised by their impact parameter p and by whether or not they pass through the cup of plastic scintillator placed between the sphere and the spacecraft body (referred to below as the Anti-Coincidence Detector or ACD). Individual particle charges are determined by separately measuring the gas scintillation and the Cerenkov emission from the plastic shell. This is possible because of the quite different distribution in time of these emissions. See also (1).

The last data from Ariel VI was received in February 1982, but spacecraft power supply problems had restricted data collection to only 427 of the days in orbit, with actual experiment live-time equivalent to 352 complete days at 100% efficiency.

2. Data Selection. Results from a first analysis of part of the Ariel VI data set have already been reported (2). The present analysis covers all available high charge data collected by Ariel VI. It includes improvements to the cut-off map used to apply cut-off labels to individual events and new event timings which allow for imperfections in the spacecraft clock by using measured cosmic ray fluxes as clock calibrations. Event timing, and the subsequent allocation of an inferred local vertical cut-off to an individual event, is important for the Ariel VI data analysis because a small number of low energy iron nuclei, which can stop in the detector at

high impact parameters, can simulate higher charges up to a limit of apparent charge 47. Hence, for abundance measurements in the charge region $34 \leq Z \leq 48$, data can only be accepted from those regions where the earth's magnetic field excludes such low energy iron nuclei. This is empirically determined to be for vertical cut-offs greater than 3.4 GV.

Finally, with the improved statistics from the complete mission, it is seen that events which produce a signal in the ACD (hits) have a cut-off distribution indicative of pollution from electron showers to the highest charges, though hardly statistically significant for $Z \geq 70$. The hit spectrum also shows evidence of additional fragmentation due to passage through the body of the spacecraft. Consequently these ACD hits require separate analysis and are not included in the results quoted in this paper or in the companion paper OG4.4-4.

3. Results. Fig. 2 shows the distribution of accepted data for this charge region. Numbers given are actual numbers of detected events, with two provisos: i) a correction has been made for the exponential tail associated with the relativistic rise in energy loss for charges 30,31,32 using measured abundances from HEAO3-C2 (3); this affects the first five bins: ii) some events in the lower part of this charge region have been collected as events of second highest priority (1), at lower efficiency, and in this case scaling has been made event by event to an equivalent 100% efficiency; this effect has become small by bin 8 onwards.

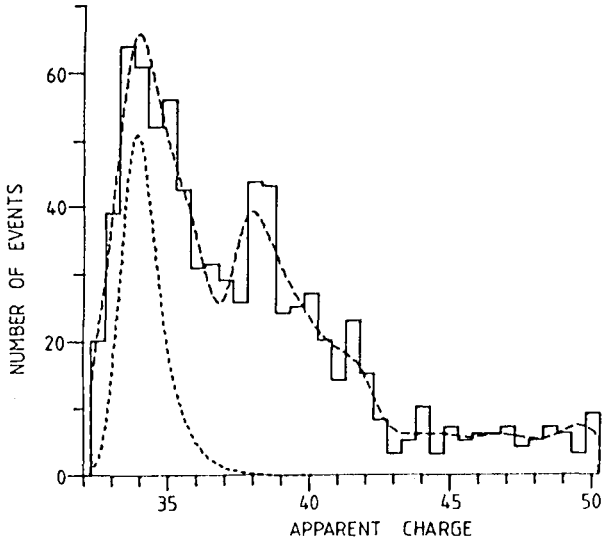


Fig. 2 Distribution of accepted data for determination of $33 \leq Z \leq 48$ abundances. Dotted insert shows distribution of $_{34}Se$ content from Table 1.

During data re-analysis small improvements have been made to charge allocation as a function of gain setting and an energy dependent non-$Z^2$ correction has been applied to all data. This is discussed further in OG4.4-4. Its effects are in any case small for $Z \leq 48$.

In order to allot events to individual charge species the effects of the resolution function of the experiment must be removed from the data in a deconvolution procedure. The resolution function is well determined

Table 1 Elemental Abundances for $33 \leq Z \leq 48$

| Z | Ariel VI: Deconvolved Numbers | Ariel VI: Corrected to outside expt | Ariel VI: Charge pairs | Comparison Data: HEAO3-C3 | Comparison Data: SS + FIPD propagations: Brewster et al. | Comparison Data: SS + FIPD propagations: Letaw et al. |
|---|---|---|---|---|---|---|
| | $3.46 \times 10^6$ | $10^6$ | $10^6$ | | $10^6$ | $10^6$ |
| 33 | (81 ± 21) | (21 ± 6) | 72 ± 5 | [9]<19 | 11 | 68 |
| 34 | 180 ± 29 | 51 ± 8 | | $43^{+10}_{-6}$ | 55 | |
| 35 | 84 ± 25 | 24 ± 7 | 43 ± 4 | [7]<14 | 10 | 31 |
| 36 | 71 ± 23 | 19 ± 6 | | $23^{+8}_{-5}$ | 24 | |
| 37 | 22 ± 20 | 6 ± 5 | 38 ± 4 | [9]<16 | 20 | 47 |
| 38 | 110 ± 24 | 32 ± 7 | | $35^{+10}_{-6}$ | 46 | |
| 39 | 54 ± 25 | 14 ± 7 | 26 ± 4 | [5]<12 | 8 | 24 |
| 40 | 42 ± 20 | 12 ± 6 | | $13^{+5}_{-4}$ | 16 | |
| 41 | 33 ± 22 | 9 ± 6 | 19 ± 4 | [3]< 6 | 2.5 | 10 |
| 42 | 35 ± 13 | 10 ± 4 | | 8 ± 2 | 6.5 | |
| 43 | 0 | | 3 ± 2 | | | 7.0 |
| 44 | 12 ± 8 | | | | | |
| 45 | 13 ± 14 | | 6 ± 2 | | | 6.0 |
| 46 | 9 ± 12 | | | | | |
| 47 | 14 ± 13 | | 6 ± 2 | | | 4.9 |
| 48 | 9 ± 13 | | | | | |

for $_{26}Fe$ and is found to fit well to a Gaussian part and an exponential tail to high charge (2). In addition the shapes of the abundance peaks at $_{12}Mg$, $_{14}Si$ and $_{20}Ca$ allow the variance of the Gaussian to be separated into a Poisson part and a part varying as $Z^2$. A resolution function may then be constructed for any higher charge by extrapolation. The resolution function for $_{34}Se$ is shown as a dotted insert in Fig. 2. Using these functions the observed data may be deconvolved into a best-fit set of abundances, giving the numbers shown in column 2 of Table 1. These numbers yield the curve shown in Fig. 2 when operated on by the appropriate resolution functions. The fit is seen to be reasonably good, though the $Z = 38$ peak appears offset. The decrease in numbers of detected events around $Z = 43$ is too steep for the measured resolution function of the experiment. This fluctuation results in a best-fit abundance for $Z = 43$ which is approximately 1½ s.d. below zero. This value was set at zero and not varied in subsequent fitting procedures.

4. Discussion. The limited charge resolution achieved by the Ariel VI detector reveals only one clear charge peak in this region, at $Z = 38$, and only one odd charge, $Z = 35$, is strictly necessary to obtain a good fit to the data. Nevertheless the best-fit abundances in column 3, which have been corrected for fragmentation in the experiment, form the most convenient comparison with other work. The errors shown are the excur-

sions needed in a given abundance to produce a change of one unit of $\chi^2$, the two neighbouring abundances being adjusted to keep the total area constant. They may be regarded as approximations to 1 s.d. errors for individual charges. With this procedure, fluctuations are strongly anti-correlated between neighbouring abundances and a significant decrease in the errors results when abundances for charge pairs are constructed as in column 4.

The best-fit values and upper limits presented by the HEAO3-C3 group at Bangalore (4) are shown in column 5, and agreement between the two experiments for individual charges is seen to be uniformly good, though the integrated total is rather higher for the Ariel VI data. Columns 6 and 7 of the table quote results from two propagations of Cameron (1982) solar system abundances (5) through about 6 $gmcm^{-2}$ of ISM with slightly different assumed First Ionisation Potential Dependence (Brewster et al. (6) and Letaw et al. (7)). Agreement between observed cosmic ray abundances and propagated SS is seen to be reasonably good in this area, with the FIPD of ref. (7), which saturates at potentials less than 7 eV, producing better agreement around charge 38.

5. Acknowledgements. The Ariel VI project has been supported throughout its lifetime by the UK Science and Engineering Research Council. A team from the Appleton Laboratory was responsible for project management and raw data handling when in orbit. Main spacecraft contractor was MSDS, Portsmouth. The Bristol experiment was built partially by support personnel within the Bristol Physics Department and partially by British Aerospace, Filton. The electronics for the Bristol experiment was built by Pye Telecommunications Ltd., Cambridge. We are indebted to all of the above for a successful mission.

6. References.

1. P.H. Fowler et al., 1979, Proc. 16th ICRC, Kyoto, 12, 338
2. P.H. Fowler et al., 1981, Nature, 291, 45
3. B. Byrnak et al., 1983, Proc. 18th ICRC, Bangalore, 2, 29
4. W.R. Binns et al., 1983, Proc. 18th ICRC, Bangalore, OG1-16
5. A.G.W. Cameron, 1982, in "Essays in Nuclear Astrophysics" ed. C.A. Barnes et al.
6. N.R. Brewster et al., 1983, Ap. J. 264, 324
7. J.R. Letaw et al., 1984, Ap. J. 279, 144

# ARIEL VI MEASUREMENTS OF ULTRA-HEAVY COSMIC RAY FLUXES IN THE REGION Z $\geq$ 48

P.H. Fowler, M.R.W. Masheder, R.T. Moses,
R.N.F. Walker, A. Worley and A.M. Gay
H.H. Wills Physics Laboratory, University of Bristol,
Tyndall Avenue, Bristol BS8 1TL, England.

1. Introduction. The Bristol cosmic ray detector on the Ariel VI satellite is described briefly in OG4.4-3 and more fully in Ref.(1). The data for charges Z $\geq$ 48 discussed in this paper were obtained with the same data selection and analysis criteria set out in OG4.4-3, except that, for this high charge region, pollution from slowing iron nuclei is not possible and data collected at all vertical cut-offs may be used.

For this re-analysis of the Ariel VI data, the contribution of non-$Z^2$ effects to the restricted energy loss and to Cerenkov radiation in the Bristol sphere has been evaluated using the Mott cross section ratios tabulated in (2) and the non-relativistic Bloch correction given clearly in (3). Results obtained were similar in form to those derived for HEAO3 by Derrickson et al. (4) but with maximum deviations $\sim$10% rather than 15% for the Mott term, corresponding to a thinner detector. Because of the large uncertainties in the parameters involved, no relativistic Bloch term was included; in any case Waddington et al.(5) found no significant deviation from Mott plus non-relativistic Bloch in their experimental work. In addition the experiments of Garrard et al. (6) on the HEAO detector make the application of a correction to the Cerenkov response of doubtful justification and none has been applied in this analysis. An energy dependent correction was made using an effective energy calculated from the vertical cut-off for a given event. The maximum value of this correction was about 0.6% in Z for low cut-offs, declining to $\sim$ zero by 10 GV.

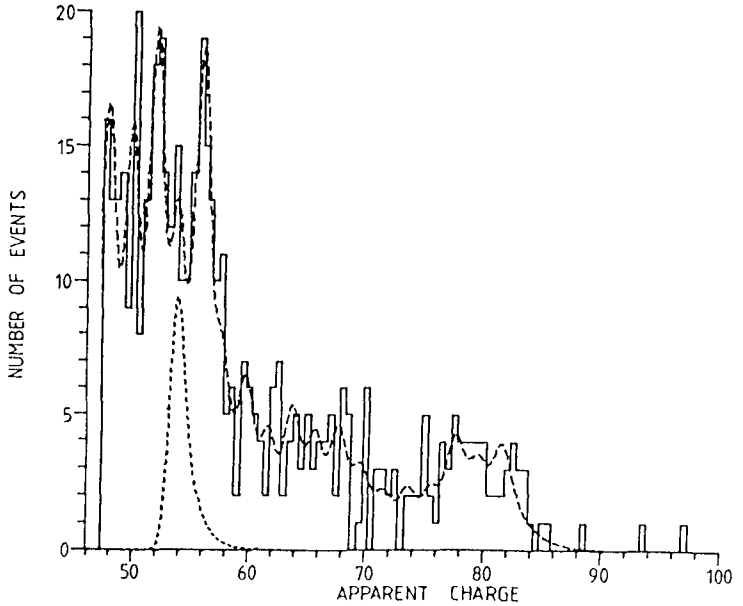


Fig. 1 Distribution of accepted data for determination of Z $\geq$ 48 abundances. Dotted insert shows distribution of $_{54}$Xe content (Table 1)

2. Results. Fig.1 shows the distribution of data for all charges $Z \geq 48$. These events were accompanied by $8.68 \times 10^6$ $_{26}Fe$ nuclei. In this distribution all events were collected at the highest priority and numbers given are actual numbers of detected events. The resolution function for $_{54}Xe$ is shown as a dotted insert and clearly resolved peaks are seen for $_{52}Te$ and $_{56}Ba$. A similar procedure of deconvolution was followed for this data to that described in OG4.4-3, but with a resolution function supplied only for each even charge, odd abundances being set to zero. The derived numbers are shown in column 2 of Table 1. The peaks at $_{52}Te$ and $_{56}Ba$ in Fig.1 are seen to be consistent with the predicted resolution, as is the precipitate fall from Z = 56 to Z = 60.

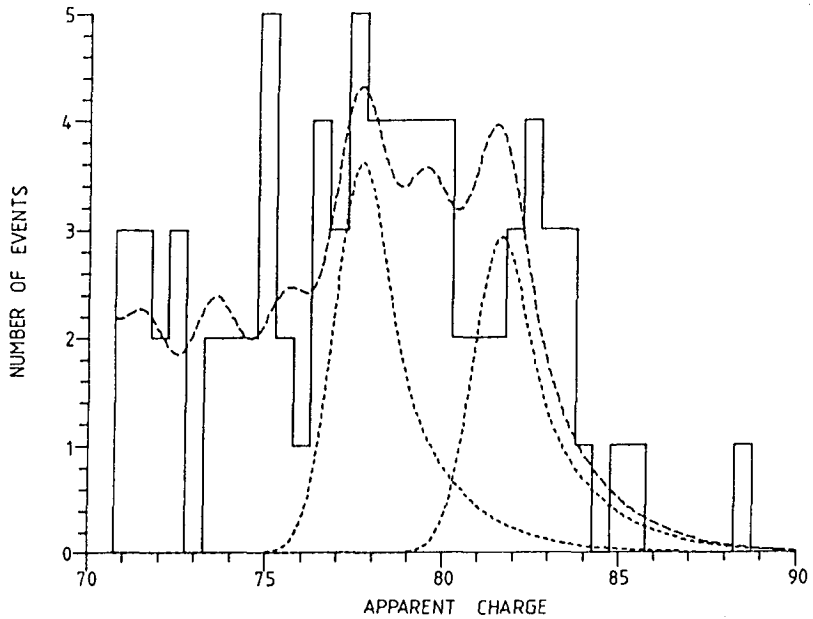


Fig. 2 Detail of the highest charges from Fig. 1. Dotted inserts show distributions for $_{78}Pt$ and $_{82}Pb$ content from Table 1.

Fig. 2 shows an expanded version of Fig. 1 for the $_{78}Pt$ - $_{82}Pb$ region alone. The inserted dotted lines show the predicted distribution in apparent charge of the $_{78}Pt$ and $_{82}Pb$ abundances obtained from the deconvolution. The tail of the $_{82}Pb$ distribution is seen to extend out to $Z_{app} \sim 88$ but only 0.1 event with $Z_{app} \gtrsim 90$ is predicted. Thus events with $84 \leq Z_{app} \leq 86$ are mainly the high energy $_{82}Pb$ nuclei which produce the exponential tail. Three events with $Z \geq 88$ were actually seen in this exposure, with $Z_{app}$ 88.5, 93.5 and 97.0 following the non-$Z^2$ correction discussed in section 1.

3. Discussion. Data collection on Ariel VI allowed $_{26}Fe$ events to be recorded whenever the experiment was operational, with a continuously-measured efficiency. Consequently the normalisation of the data to abundances relative to $_{26}Fe = 10^6$ is straightforward. Column 3 of Table 1 shows normalised abundances, with a small correction added to allow for fragmentation in the material of the experiment, and these values are plotted as data points in Fig. 3 (together with the numbers from $34 < Z < 46$ for completeness). The numbers are compared with a recent propagation of Letaw et al. (7) which used solar system abundances modified by a first ionisation potential dependence, an exponential pathlength

distribution with characteristic length 6 $gcm^{-2}$ of ISM and a propagation energy of 5 GeV/nucleon (histogram in Fig.3 and column 5 of Table 1). It is seen that the deconvolved Ariel VI abundances retain the over-abundance throughout the region $60 \leq Z \leq 80$ which has already been discussed (e.g. 7,8). The Ariel VI to Letaw et al. propagation ratio for $60 \leq Z \leq 82$ is $1.87 \pm 0.14$ based on 170 detected events. Letaw et al. attempted to go some way towards explaining this over-abundance by suggesting that propagation may take place mainly at a lower energy ($\sim$ 1 GeV/nucleon), where spallation into the $60 \leq Z \leq 74$ region is more favourable, but much of the discrepancy remains, the ratio being reduced only to $1.51 \pm 0.12$, suggesting an enhanced primary component in this region. The Letaw et al. propagations also produce consistently more $_{50}Sn$ than was seen in the Ariel VI data, and in that from HEAO3-C3 (9), which is shown for the charge region $50 \leq Z \leq 58$ in column 4 of Table 1 for comparison. Agreement between the two experiments is quite good in this region, but with a divergence of $\sim$ 3 s.d. at $_{52}Te$ where a separated peak is seen in the Ariel VI data.

For the highest charges, Binns et al. (10) quote a value for the abundance ratio $\frac{Z \geq 81}{74 \leq Z \leq 80}$ of $0.26 \pm 0.08$. Ignoring the three actinides our value for this ratio is $0.35 \pm 0.12$, higher, but not inconsistent with the HEAO value, and consistent with either the SS with no FIP fractionation or pure r-process with FIP fractionation values quoted in (10). Although the $_{82}Pb$ abundance seen in the Ariel VI data may not share the $60 \leq Z \leq 80$ over-abundance compared to propagated solar-system, it is not found to be depleted, being very close to the predicted abundance from the propagation.

Finally, three actinide candidates were seen in the Ariel VI exposure, compared to an expectation of 0.5 from the Brewster et al. propagation (11), a possible enhancement.

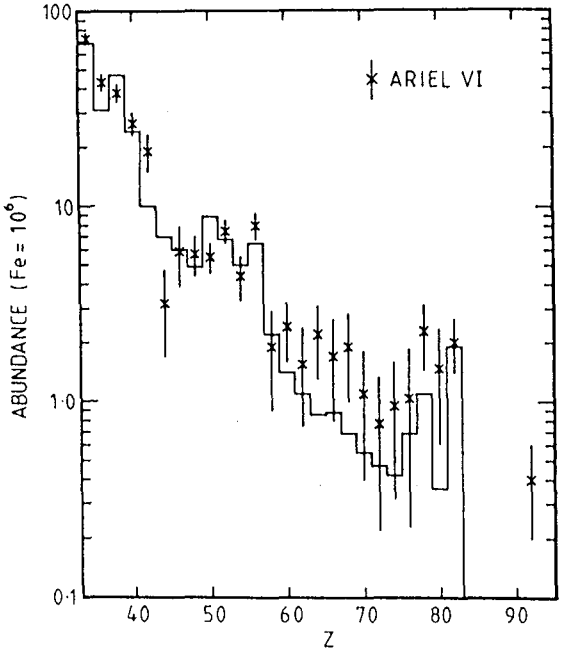


Fig. 3 Cosmic ray abundances normalised to $_{26}Fe = 10^6$. Data points are deconvolved abundances from Ariel VI corrected for fragmentation within the experiment. The histogram shows the Letaw et al. propagation of solar system material (7) referred to in the text.

Table 1 Elemental Abundances for $Z \geq 48$

| Z | Ariel VI Deconvolved Numbers | Ariel VI Corrected to outside expt. | HEAO3-C3 | SS + FIPD Propagation, Letaw et al. |
|---|---|---|---|---|
| 26 | $8.68 \times 10^6$ | $10^6$ | $10^6$ | $10^6$ |
| 48 | 54 ± 12 | 5.7 ± 1.3 | | 4.9 |
| 50 | 52 ± 9 | 5.5 ± 1.0 | 5.7 ± 1.3 | 8.9 |
| 52 | 68 ± 9 | 7.5 ± 1.0 | 3.4 ± 1.0 | 6.8 |
| 54 | 39 ± 10 | 4.4 ± 1.1 | 3.5 ± 0.9 | 5.0 |
| 56 | 69 ± 10 | 8.0 ± 1.2 | 6.2 ± 1.0 | 6.5 |
| 58 | 17 ± 9 | 1.9 ± 1.0 | 2.8 ± 0.9 | 2.2 |
| 60 | 22 ± 7 | 2.4 ± 0.8 | | 1.4 |
| 62 | 14 ± 7 | 1.6 ± 0.8 | | 1.1 |
| 64 | 20 ± 8 | 2.2 ± 0.9 | | 0.86 |
| 66 | 15 ± 8 | 1.7 ± 0.9 | | 0.88 |
| 68 | 17 ± 8 | 1.9 ± 0.9 | | 0.69 |
| 70 | 10 ± 6 | 1.1 ± 0.7 | | 0.55 |
| 72 | 7 ± 5 | 0.8 ± 0.6 | | 0.47 |
| 74 | 9 ± 6 | 0.9 ± 0.6 | | 0.42 |
| 76 | 9 ± 7 | 1.0 ± 0.8 | | 0.69 |
| 78 | 19 ± 7 | 2.3 ± 0.8 | | 1.1 |
| 80 | 12 ± 7 | 1.5 ± 0.9 | | 0.36 |
| 82 | 16 ± 5 | 2.0 ± 0.6 | | 1.9 |
| 84 | 0 | | | |
| $\geq 88$ | 3 | 0.4 ± 0.2 | | |

4. Acknowledgements. These are given in full in paper OG4.4-3.

5. References.

1. P.H. Fowler et al., 1979, Proc. 16th ICRC, Kyoto, 12, 338
2. J.A. Doggett et al., 1956, Phys. Rev. 103, 1597
3. S.P. Ahlen, 1978, Phys. Rev. (A), 17, 1236
4. J.H. Derrickson et al., 1981, Proc. 17th ICRC, Paris, 8, 88
5. C.J. Waddington et al., 1983, Phys. Rev. (A), 28, 464
6. T.L. Garrard et al., 1983, Proc. 18th ICRC, Bangalore, T2-10
7. J.R. Letaw et al., 1984, Ap. J. 279, 144
8. P.H. Fowler et al., 1981, Nature, 291, 45
9. E.C. Stone et al., 1983, Proc. 18th ICRC, Bangalore OG1-21
10. W.R. Binns et al., 1984, Adv. Space Res. 4, 25
11. N.R. Brewster et al., 1983, Ap. J. 264, 324

123

# Elemental Abundances of Cosmic Rays with Z > 33 as Measured on HEAO-3

*B.J. Newport[a], E.C. Stone[a], C.J. Waddington[b], W.R. Binns[c], T.L. Garrard[a], M.H. Israel[c], and J. Klarmann[c].*

[a]California Institute of Technology, Pasadena, California 91125, USA
[b]University of Minnesota, Minneapolis, Minnesota 55455, USA
[c]Washington University, St Louis, Missouri 63130, USA

## 1. Introduction

The Heavy Nuclei Experiment on HEAO-3 (Binns et al., 1981) uses a combination of ion chambers and a Čerenkov counter. During analysis, each particle is assigned two parameters, $Z_C$ and $Z_I$, proportional to the square roots of the Čerenkov and mean ionization signals respectively. Because the ionization signal is double valued, a unique assignment of particle charge, Z, is not possible in general. Our previous work (Binns et al., 1983, 1985, and Stone et al., 1983) has been limited to particles of either high rigidity or low energy, for which a unique charge assignment was possible, although those subsets contain less than 50% of the total number of particles observed. In this paper we discuss the use of the maximum likelihood technique to determine abundances for the complete data set from ~1.5 to ~80 GeV/amu.

Figure 1 shows the possible values of $Z_C$ and $Z_I$ for elements near iron, and indicates the substantial overlap between adjacent elements, even before smearing by the resolution function. In Figure 2, the curves of Figure 1 have been transformed using the variable $Z_C/Z_I$ instead of $Z_I$. This transformation simplifies the following data analysis.

## 2. Analysis

Particles were selected from the full exposure, 580 days, and were required to have a good Čerenkov signal, at least one good ion chamber and a reliable trajectory. These particles were assigned an initial charge estimate, $Z_{est}$, and 1/40 of those with $Z_{est} > 19.5$ were saved, together with all the remaining particles with $Z_{est} > 30$. The selected particles were binned in a two dimensional histogram, with one axis being the logarithm of $Z_C$ and the other being $Z_C/Z_I$. Figure 3 shows a contour plot of the region of this histogram near iron.

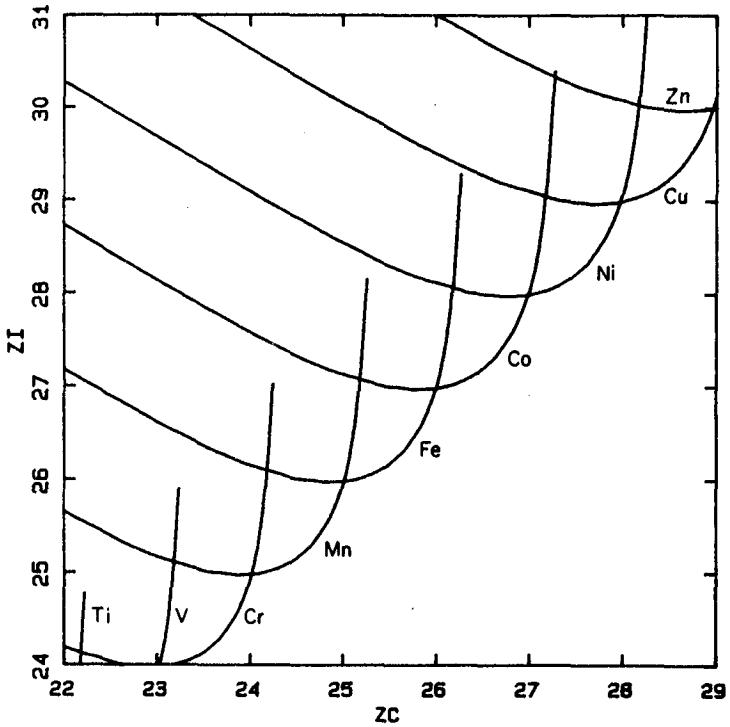


*Figure 1. Curves of $Z_I$ versus $Z_C$ for the elements near iron.*

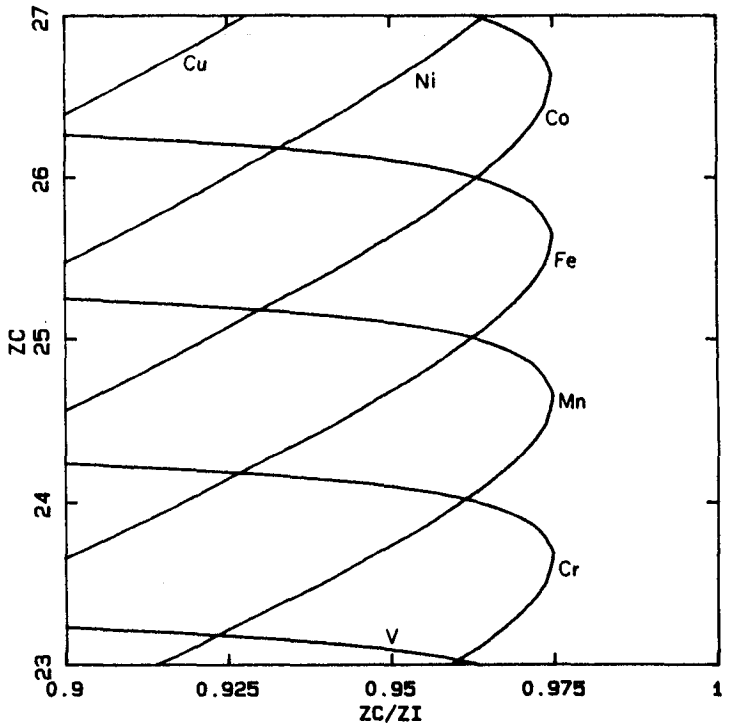


*Figure 2. The curves of Figure 1, displayed in $(Z_I/Z_C, Z_C)$ space.*

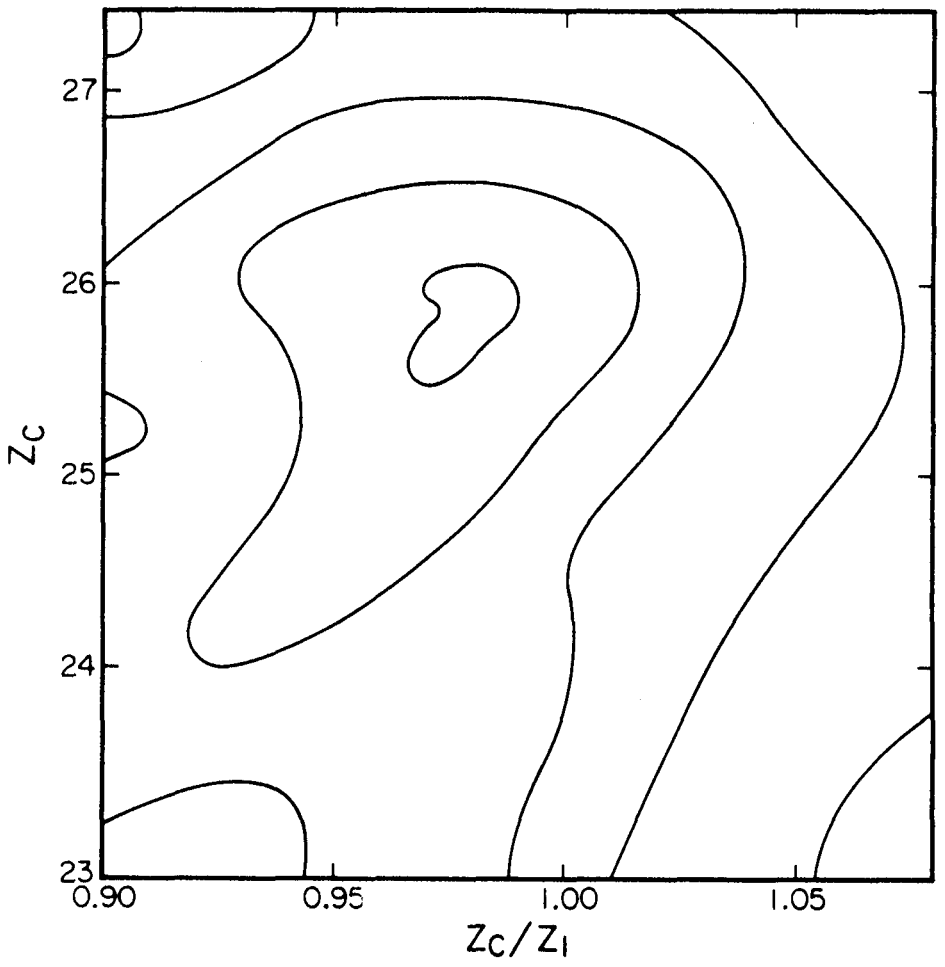


*Figure 3. A contour plot of particle density in* ($Z_1/Z_C$, $Z_C$) *space.*

We have used the iron distribution as a reference distribution for the other elements, by scaling it according to the following criteria:

1) All elements are assumed to have the same energy spectrum, although it is known that the sub-iron secondary elements have steeper spectra (e.g. Jones et al., 1985, OG 4.1-8).
2) Energy independent scaling factors have been used.
3) The resolution of the instrument is a constant fraction of the signal.
4) Non-$Z^2$ corrections to the scaling laws for $Z_C$ and $Z_C/Z_I$ have been determined directly from the data.

Those elements contaminating the iron distribution have been approximately removed by scaling the contaminated distribution and subtracting according to an assumed set of abundances. The resulting "clean" iron distribution was smoothed and then scaled to the high Z elements, using cubic interpolation techniques.

The likelihood of a given set of abundances may be calculated using Poisson statistics, and maximized by iterating until all the first derivatives are zero, yielding the best fit. Results from the application of this method will be reported.

## 3. Acknowledgements

We thank B.W. Gauld for assistance in programming for data analysis. This work was supported in part by NASA grants NAG 8-498, 500, 502 and NGR 05-002-160, 24-005-050, 26-008-001.

## 4. References

Binns, W.R., *et al.*, 1981, *Nucl. Inst. Meth.* **185,** 415
Binns, W.R., *et al.*, 1983, *Proc. 18th I.C.R.C. (Bangalore),* **9,** 106
Binns, W.R., *et al.*, 1985, *Ap. J.* (to be published Oct. 1)
Jones, M.D., *et al.*, 1985, *Proc. 19th I.C.R.C. (San Diego),* OG 4.4-5
Stone, E.C., *et al.*, 1983, *Proc. 18th I.C.R.C. (Bangalore),* **9,** 115

# ABUNDANCES OF 'SECONDARY' ELEMENTS AMONG THE ULTRA HEAVY COSMIC RAYS - RESULTS FROM HEAO-3

J. Klarmann[a], S. H. Margolis[a], E. C. Stone[b], C. J .Waddington[c],
W. R. Binns[a], T. L. Garrard[b], M. H. Israel[a] and M. P. Kertzman[c]

[a]Department of Physics and the McDonnell Center for the Space Sciences, Washington University, St. Louis MO 63130, USA.
[b]George W. Downs Laboratory, California Institute of Technology, Pasadena CA 91125, USA.
[c]School of Physics and Astronomy, University of Minnesota, Minneapolis MN 55455, USA.

**1.Introduction.** This paper discusses observations of the abundances of elements of charge $62 \leq Z \leq 73$ in the cosmic radiation from the HEAO-3 Heavy Nuclei Experiment (HNE). These elements, having solar, and presumably source, abundances much less than the heavier Pt and Pb groups, are expected to be largely products of spallation. Thus they are indicators of the conditions prevailing during the propagation of cosmic rays. The abundances have changed from those reported previously (Klarmann et al., 1983) due to a different data selection (Binns et al., 1985). This resulted in better charge resolution and in a higher mean energy for the particles. All the particles we have included in this paper were required to have had a cutoff rigidity $R_c > 5$ GV. This allowed the charge determination to be based solely on the Cherenkov measurement. For a description of the detector see Binns et al., (1981).

**2. Analysis.** The data selection in this paper is identical to that of Waddington et al., (1985, OG4.4-7). We have considered only the following physically significant groups of charges:

| Name | Abbreviation | Range | Number observed |
|---|---|---|---|
| Lead and Platinum | PbPt | $74 \leq Z \leq 86$ | 52 |
| Heavy secondary | HS | $70 \leq Z \leq 73$ | 10 |
| Light secondary | LS | $62 \leq Z \leq 69$ | 34 |

Our discussion will be in terms of the ratios: HS/PbPt and LS/PbPt. In the table, column a) shows the results observed in the detector. The correction factor to outside the detector was derived by propagating eight different plausible theoretical abundances outside the detector through slabs of hydrogen approximating the distribution of aluminum traversed by the particles going into and through the detector. The change of the abundance ratios from outside the detector to inside was nearly independent of the original ratios and is given as a multiplicative correction factor in column b). The abundance outside the detector, column c) is the product of columns a) and b).

| Ratio | HEAO Results | | | Ariel | HEAO/Ariel |
|---|---|---|---|---|---|
| | Inside Detector a) | Correction Factor b) | Outside Detector c) | Outside Detector d) | Outside Detector e) |
| HS/PbPt | 0.19±0.07 | 0.85±0.02 | 0.16±0.06 | 0.27±0.07 | 0.59±0.27 |
| LS/PbPt | 0.65±0.14 | 0.87±0.02 | 0.57±0.12 | 0.88±0.15 | 0.65±0.18 |

Results from the Ariel-6 UH-nuclei detector which was exposed in a 55° inclination orbit (Fowler et al., 1984) are given in column d), while column e) gives the ratio of our HEAO results to those of Ariel. It is seen that for both ratios our result is about 60%

to 65% that of Ariel's. While these differences are only significant at a level of 1.5 to 2.0 standard deviations, it is unlikely that they are just statistical fluctuations. The data of Ariel extend to significantly lower energy than ours. At lower energies the abundance of secondaries is expected to be greater since both the interaction cross sections and the escape length are larger. We cannot tell yet whether this energy dependence is sufficient to explain the difference.

**3. Comparison with Models.** The abundance ratios can be compared with predictions of various models. The source abundance used was either the solar system abundances of Anders and Ebihara (1982) (No FIP) or the same adjusted for an exponential dependence (Brewster et al., 1983a) on the first ionization potential (FIP). These were then propagated through the interstellar medium, assuming a leaky-box model, and using the revised code of Brewster et al., (1983a, 1985) with a rigidity dependent escape length (Ormes and Protheroe, 1983) that is 6.21 g/cm of hydrogen at 7 GV. The calculated values are for approximately the same mix of rigidities as the HEAO data. A different model of FIP fractionation (Cook et al., 1979; J. P. Meyer, 1981), in which the cosmic ray source is suppressed by a constant factor relative to solar abundances for elements with ionization potential above 9 eV, yields propagated abundance ratios which in, this charge range, are indistinguishable from those of the unfractionated source. Similarly, propagation of an r-process source abundance yielded ratios which in this charge region were close to those from a solar system source. Neither of the last two results is plotted in figure 1.

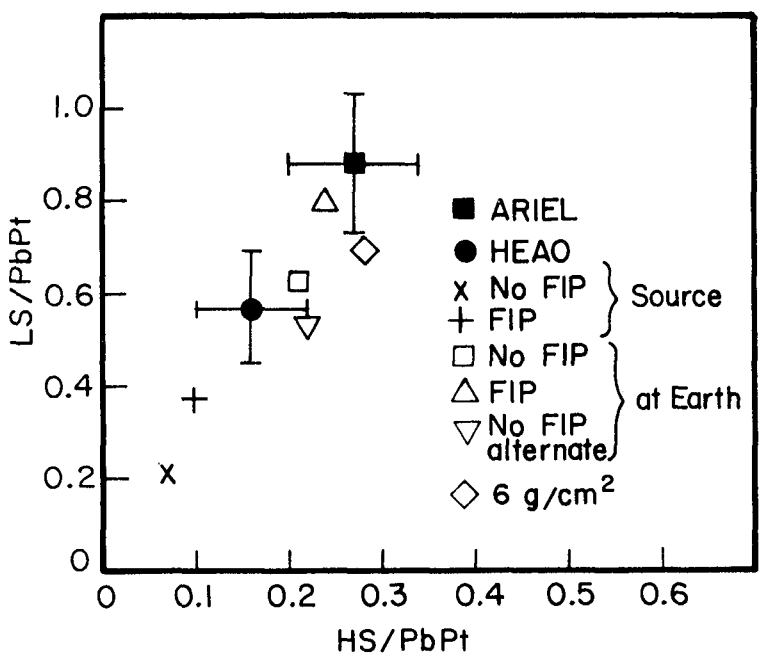


**Figure 1: Comparison of the observed and predicted abundance ratios.**

In the 'No FIP alternate' propagation an independent code was used (Margolis, 1983) to predict the abundance ratios after propagation through leaky boxes of various escape lengths. The results were then combined using the same rigidity dependent escape length distribution as above to yield the inverted triangle point in figure 1. With this rigidity dependent distribution the mean escape length encountered by the observed particles is $\sim 3 g/cm^2$. This point, when compared to the other No FIP point, is an

indication of the variation possible in the propagation calculation. The point labeled '6 g/cm$^2$' in figure 1 is the result of the same propagation through a leaky box with a single escape length of 6 g/cm$^2$ of hydrogen. The difference between this point and the 'alternate' point shows the dependence of the results on the escape-length distribution. In figure 1 experimental values are solid with error bars.

The dependence of the abundance ratio on propagation can also be demonstrated in a different way. Every point in figures 2 and 3 (Margolis and Blake, 1985) corresponds to the calculated ratio after propagation of a solar system source without FIP through hydrogen with a mean free path distribution rising linearly from zero to the desired 'truncation' then falling exponentially with the given 'escape length'(Margolis, 1983).

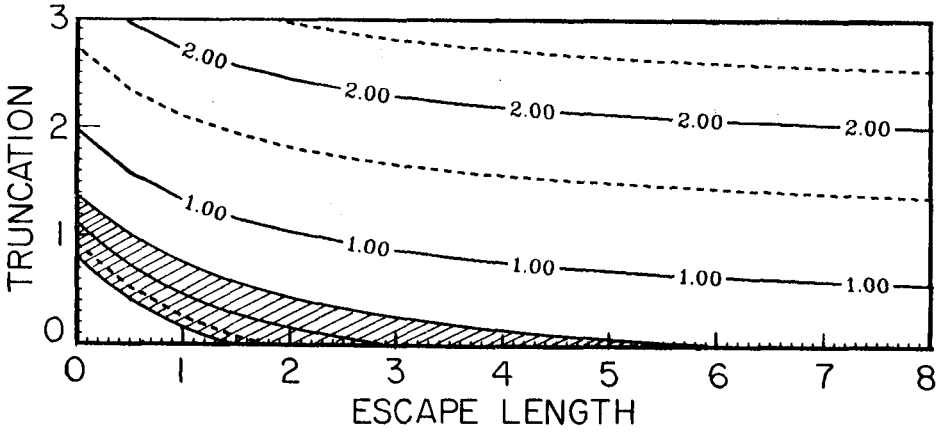


**Figure 2: LS/PbPt**

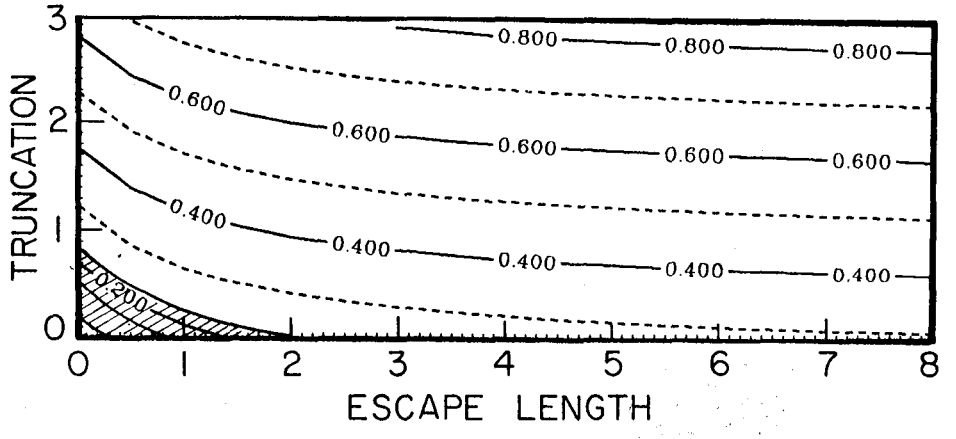


**Figure 3: HS/PbPt**

In contrast to the data in figure 1, these figures assume that all particles traverse the same path length distribution. Our results are represented by the cross-hatched region yielding possible combinations of escape length and truncation.

As expected the predictions in this charge region are nearly independent of escape-length since the interaction mean free path is so short. However the results do not agree with more than a minute amount of truncation of short path lengths. The fact that at zero truncation an escape length of $\sim 2 g/cm^2$ is indicated seems to support the rigidity dependent escape length proposed by Ormes and Protheroe, (1983).

**4. Discussion.** Our observed values of the secondary ratios are in reasonable agreement with the prediction based on a model without FIP fractionation or with a step function FIP fractionation at the source; however, our observations are in distinct disagreement with the models that include exponential FIP fractionation. This is contrary to the conclusions found at lower charges (Binns et al., 1982, 1983) where observed abundances agreed better with those expected from a solar system source with FIP fractionation than without. Thus other representations of source fractionation may be involved.

Our results do fit the predictions obtained using the standard leaky box model in this energy range. The applicability of this model to lower energies requires further investigation.

**5. Acknowledgements:** This work was supported in part by NASA grants NAG 8-448, NAG 8-498, 500, 502 and NGR 05-002-160, 24-005-050, 26-008-001.

**6. References:**

Anders, E., and Ebihara, M., 1982, Geochimica et Cosmochimica Acta, **46**, 2363.
Binns, W. R. et al., 1981, Nucl. Inst. Meth., **185**, 415.
_____., 1982, Ap.J. (Letters), **247**, L115.
_____., 1983, Ap.J. (Letters), **267**, L93.
_____., 1985, Ap.J. **297**, in press.
Brewster, N. R., Freier, P.S. and Waddington, C.J., 1983a, Ap.J., **264**, 324
Brewster, et al., 1983b, 18th ICRC, Vol. 9, p. 259.
Brewster, N.R., Freier, P. S. and Waddington, C. J., 1985, Ap.J. **294** in press.
Cook, W. R., et al., 1979, 16th ICRC, Vol. 12, p. 265.
Fowler, P. H. et al., 1984, 9th European Cosmic Ray Symposium.
Klarmann, J. et al., 1983, 18th ICRC Vol. 9, p.279.
Margolis S. H., 1983, 18th ICRC, Vol. 9, p. 267.
Margolis, S. H. and Blake, J. B., 1985, Ap. J. (in press).
Meyer, J. P., 1981, 17th ICRC, Vol. 2, p. 281.
Ormes, J. F., and Protheroe, R. J., 1983, Ap.J. **272**, 756.
Silberberg, R., and Tsao, C. H. 1983, Ap.J. Supp. **25**, 315 and 335.
Waddington, C. J. et al., 1985, this conference, paper OG 4.4-7.

# CAPABILITIES OF THE LDEF-II HEAVY NUCLEI COLLECTOR

J. Drach, P.B. Price and M.H. Salamon
Physics Department, University of California, Berkeley, CA

G. Tarle'
Physics Department, University of Michigan, Ann Arbor, MI

S.P. Ahlen
Physics Department, Indiana University, Bloomington, IN

1. Introduction. Less than about half a dozen relativistic actinide ($Z \geq 90$) nuclei have been detected in space experiments--one on HEAO-3 [1], three on Ariel-6 [2] and possibly two on Skylab [3]. Our studies of long-term track fading suggest that partial fading of tracks produced early in the Skylab mission relative to those produced later may have smeared the charge scale and resulted in misidentification of some of the seven events originally reported as actinides. Events attributed to actinide nuclei using plastic track detectors and nuclear emulsions on balloon flights some years ago are now believed to be due mostly to spillover from the platinum and lead peaks, due to a shift in detector response with temperature during the day-night cycle of the balloon payload [4]. The HEAO-3 experiment, which had the best charge resolution to date for ultraheavy cosmic rays, resolved even-Z charge peaks up to $Z \sim 56$ and reported ~60 events with $Z \geq 70$. Although their statistics and resolution were inadequate to resolve charges in this region, they were able to estimate the ratio of Pb-group to Pt-group nuclei to be ~1% based on one actinide event. Their data for all nuclei with $Z \geq 30$ are consistent with a solar system source for the heavy cosmic rays, with the exception of a few elements such as Pb, which may be depleted in the cosmic rays. To take the next big step beyond HEAO-3, the Heavy Nuclei Collector (HNC), to be carried on an LDEF reflight, has the goals of greatly increased collecting power (>30 actinides) and charge resolution ($\sigma_Z \leq 0.25e$ for Z up to ~100), which will provide abundances of all the charges $40 \leq Z \leq 96$ and permit sensitive searches for hypothetical particles such as monopoles, superheavy elements, and quark nuggets.

2. Mission. After the currently orbiting LDEF is retrieved, it will carry 45 trays of plastic track detectors ($A\Omega \approx 100$ m$^2$ sr) into a 28.5 degree orbit for a 6-year exposure at $T < -10°$ C, after which it will be retrieved for analysis of the tracks. (At this writing, a 2.7-yr exposure in a 57° orbit, which would yield ~10% more actinides, has not been ruled out.)

3. Design. To meet our goal of achieving a charge resolution $\sigma_Z < 0.25e$ at $Z = 92$, we used a number of novel features. Figure 1 is a cutaway sketch of the contents of one of the 45 trays, 41 of which are optimized for identification of nuclei with $Z \geq 70$ and 4 of which are optimized for nuclei with $30 \leq Z \leq 70$. Detector response depends on temperature and oxygen pressure, and stability of the latent track against fading demands a low

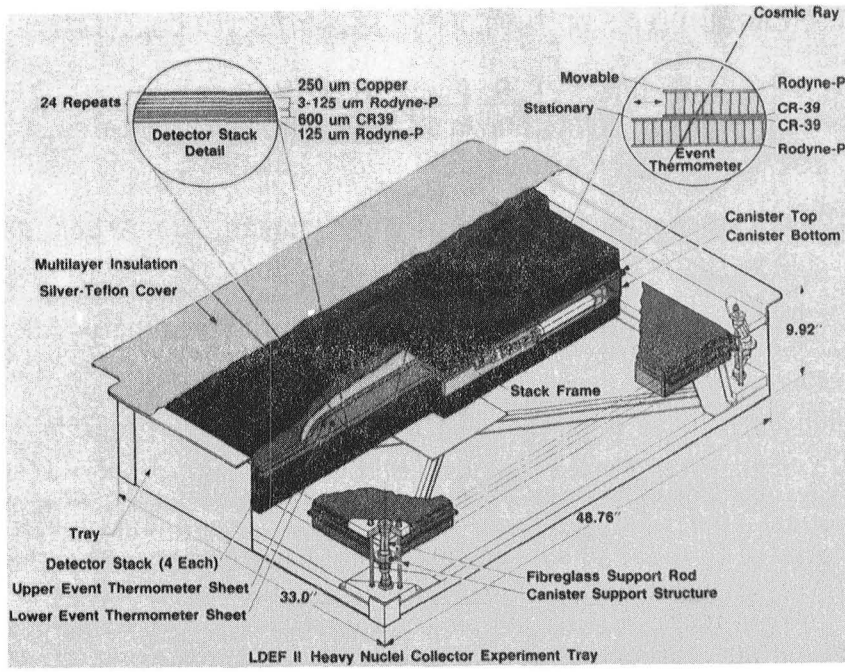


Fig. 1. HNC tray. Composition of stack and design of event thermometer are somewhat different than shown in drawing.

average detector temperature. Thus, each stack is sealed in 0.3 bar of air in a thermally isolated canister shielded from space with multilayer insulation and passive thermal coating, and each stack contains an event thermometer that enables the temperature of the stack at the time of passage of each heavy nucleus to be determined by measuring the displacement of a sliding plastic track-recording sheet with respect to the stack. The sliding sheet is driven by a plunger actuated by a silicone liquid whose volume depends on temperature.

Calibrations at the LBL Bevalac with relativistic beams of U, La, Kr, and Fe ions [5] enabled us to develop improved detectors of two classes: a polycarbonate plastic, Rodyne-P, with outstanding resolution in the region $50 < Z < 120$, and a poly- (allyl diglycol carbonate) plastic, CR-39(DOP), containing 1% dioctyl phthalate and 0.01% of an antioxidant, with outstanding resolution in the region $10 < Z < 70$. (See Fig. 2.) For fully stripped nuclei with $Z < 80$ passing through many sheets, we have verified that the resolution improves as $1/\sqrt{n}$, where n is the number of etchpits measured along the trajectory. For relativistic uranium, an electron is often retained in passage through more than one sheet, with the result that the resolution improves much less rapidly than $1/\sqrt{n}$. We showed that periodic insertion of copper foils in the stack eliminates the correlation in effective charge from sheet to sheet and restores the $1/\sqrt{n}$ dependence [6]. Use of copper, with its high Z, in place of plastic of equivalent mass thickness reduces the fraction of events that fragment within the stack.

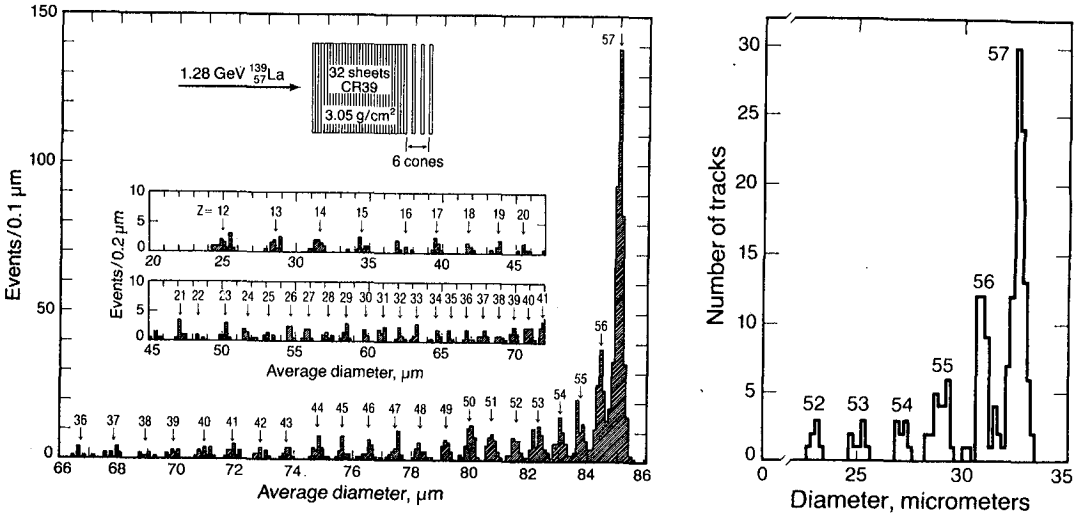


Fig. 2. Bevalac tests showing abililty of CR-39 (on left) and Rodyne-P (on right) to resolve individual charges using only a few successive etch pits.

Monte Carlo simulations of detector response enabled us to optimize the sequence of Rodyne-P, CR-39, and copper sheets so as to maximize charge resolution and minimize fragmentation loss within a weight constraint of ~8.7 g/cm$^2$ per tray. The 41 actinide stacks contain 59 Rodyne-P, 18 CR-39, and 28 copper sheets (not in that order) each 250 microns thick. The four mid-Z stacks contain more CR-39 than Rodyne-P sheets. The weight ratio Cu/plastic = 2.57 corresponds to 0.83 of an interaction length for uranium at normal incidence. For an assumed fractional standard deviation in measured cone length of 1% (2%), the charge resolution at uranium ranges from 0.19e (0.21e) at 1 GeV/amu to 0.21e (0.48e) at 4 GeV/amu. For calibration purposes, two sheets in each stack will be irradiated with a low density of uranium ions over their entire surface before the mission.

Figure 3 shows two Monte Carlo simulations. On the left is the charge spectrum of events with $Z \geq 70$ expected if the source of cosmic rays is entirely material with solar system composition. On the right is the charge spectrum expected if the cosmic rays consist of an equal mixture of material with solar system composition and of 10 million year-old r-process material. In a six year mission, as little as 20% admixture of r-process material would lead to a detectable number of plutonium and curium events. Such an admixture cannot be ruled out by HEAO-3 and Ariel-6 data.

4. Data Analysis. In a 28.5 degree orbit the earth's field will eliminate background tracks of slow, highly ionizing galactic iron nuclei and of solar flare particles. Recoil nuclei produced in interactions of trapped protons in the detector will have no significant effect on the insensitive Rodyne-P sheets and will give rise to a background of short etch pits in CR-39 which, on the basis of accelerator simulations, will not seriously degrade detector performance. The dependence of detector response on temperature

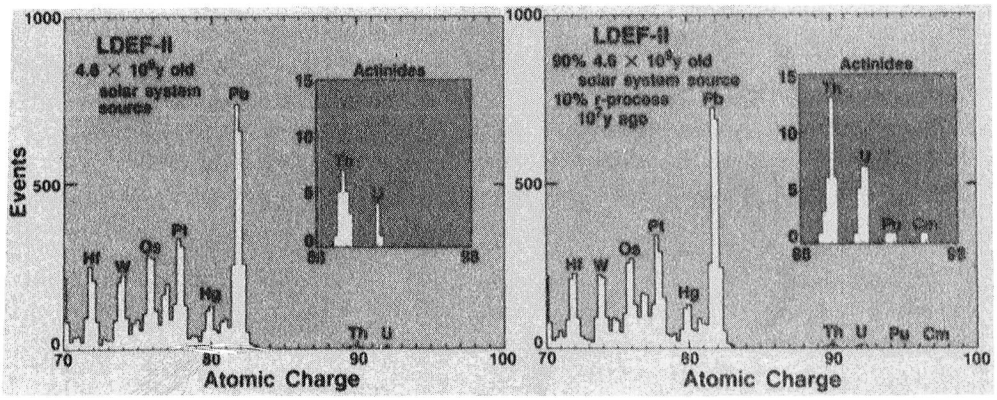


Fig. 3. Simulations of charge spectra.

increases with ionization rate [4]. In a 28.5 degree orbit the worst case is for a ~1 GeV/amu uranium ion, for which the apparent charge shifts by ~0.1e per deg C for Rodyne-P. Passive thermal coatings limit the temperature excursions to ±19 degrees C at the worst locations and ±5 degrees C at the best locations. These temperatures will be measured with adequate sensitivity by the event thermometer. Because all nuclei reaching the detector will be minimum-ionizing, the etching rate for a given plastic type will depend only on Z. For elements up to bismuth, measurements of etch pit elliptical mouths will suffice; for thorium and uranium both the mouth and the entire profile will be measured, using a three-dimensional image-analysis technique [7] illustrated in Fig. 4. We expect roughly 5000 events with Z > 60. About $5 \times 10^5$ etch pits will have to be measured. Commercial image processors can be used both to locate events and to perform measurements.

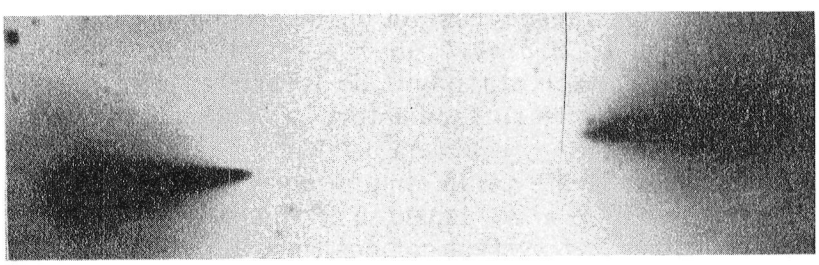

Fig. 4. Digitized, projected image of an inclined etched uranium track.

References

1. W.R. Binns et al., Ap. J. 261, L117 (1982).
2. P.H. Fowler et al., 9th European Cosmic Ray Sumposium, 1984.
3. E.K. Shirk and P.B. Price, Ap. J. 220, 719 (1978).
4. A. Thompson and D. O'Sullivan, Nucl. Tracks & Rad. Meas. 8, 567 (1984).
5. M.H. Salamon et al., Nucl. Instr. Meth. B6, 504 (1985).
6. M.H. Salamon et al., Nucl. Instr. Meth. 224, 217 (1984).
7. P.B. Price and W. Krischer, Nucl. Instr. Meth. A234, 158 (1985).

# ULTRAHEAVY COSMIC RAY TRACKS IN METEORITES: A REAPPRAISAL, BASED ON CALIBRATIONS WITH RELATIVISTIC IONS

Claude Perron
CNRS and Museum d'Histoire Naturelle
75005 Paris France

Experiments have been carried out on tracks of high energy U ions in olivine, a common meteoritic mineral. The results offer an explanation for the lack of success of previous attempts to derive the Ultraheavy Cosmic Ray composition from the study of tracks in meteorites. They also suggest how such experiments should be performed. The methods we are testing are described and illustrated.

## 1. Introduction

Prompted by the observation that the Cosmic Ray actinide abundance is extremely low (1,2), and difficult to measure with a satellite born experiment, a study of heavy ion tracks in a meteoritic mineral (olivine), has been started in our laboratory (3), to reevaluate the feasibility of a measurement of this abundance by means of tracks in meteorites. To this end, experiments have been carried out, which made use of high energy U ions, first to try to better understand the processes involved in very heavy ion track registration and etching in a mineral, then possibly, to achieve a real calibration of the meteoritic detectors.

The last results obtained allow us to fully confirm our statement (3) that the main difficulties of an Ultraheavy Cosmic Ray abundance measurement by means of tracks in meteorites would lie in the etching process itself. They demonstrate that, with classical techniques, and for very heavy ions, one should not expect any relationship between ion atomic number Z and etched track length. However, techniques can be devised to restore this relationship. Here we summarize what we have learnt about heavy ion tracks, without going into technical detail, before briefly describing the methods we are presently testing and the first results obtained with them, which make us reasonably optimistic about the chance of succeeding.

Fig. 1. see caption on last page of paper.

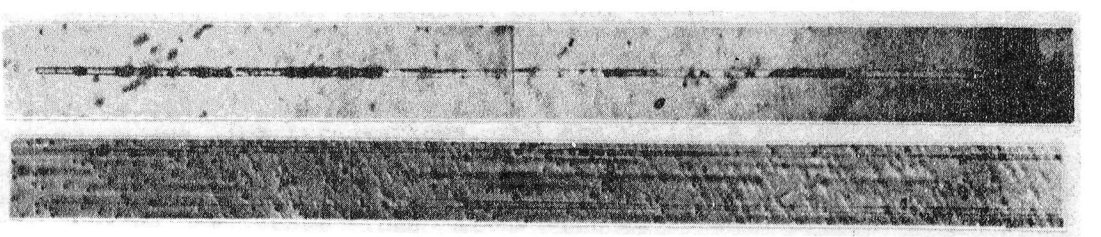

## 2. Heavy ion tracks: results and implications

Most important is the observation that the track etch rate in olivine (and probably in other mineral track detectors as well) is not only governed by the radiation damage intensity, but also by the etching chemistry (4). The etch rate may be limited, by the etching process, to a much lower value than would be allowed by the radiation damage intensity alone. In addition, the etch rate allowed by the etching process decreases as etching proceeds (i.e. as the etched track length gets longer). For relatively short tracks (i.e. "light" ions) this is generally not of much importance. But for very long tracks, it turns out that after some time, the etch rate becomes so low, that etching finally stops, although the remaining part of the latent track is still potentially etchable (5). Thus, with the usual techniques, in which a track is revealed from one point, generally by means of a crystal fracture - natural or artificial - which intersects it, and through which the etchant can penetrate, the long tracks can only be partially revealed. Since the length of the etched portions are only determined by the etching chemistry, they do not reflect the atomic numbers of the ions which induced the tracks. This may explain the lack of success of previous experiments.

In order to maintain the relationship between track length and Z, one has to reveal the whole etchable track length. For that, a method must be used, which allows the etchant to reach every track at many points along the ion path, so that the revelation of a long track comes to that of many short portions of it.

## 3. Methods for proper revelation of long tracks

We are presently testing 2 closely related methods allowing the complete revelation of any track. Both make use of medium energy (10-20 MeV/u) heavy ion irradiations, and are variants of the TINT and TINCLE techniques (6). In the first one, olivine crystals are bombarded by a low intensity heavy ion beam (about $10^6$ ions per $cm^2$). Upon etching, the tracks of these ions allow the etchant to penetrate inside the crystals, and reveal the long tracks which they happen to intersect. Each long track intersects many of these "feeding" tracks. In the second one, the crystals are bombarded by a much higher flux ($\sim 10^9$ $cm^{-2}$), through a mask, sufficiently thick to stop the ions, leaving them pass only through regularly spaced, narrow, parallel slits. Upon etching, the tracks of these ions in turn make sort of parallel grooves in the olivine, through which the long tracks, which cut many of them, can be entirely revealed. These techniques have been applied to the revelation of tracks of 190 MeV/u U ions from the Bevalac, and gave

Fig. 1. cont'd.

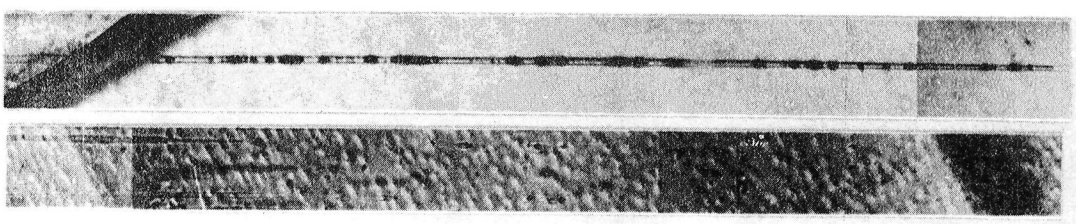

satisfactory results.

As an illustration, a photomicrograph of a U ion track in olivine, revealed by the TINT technique, is shown in Fig.1 (top), which has been cut into 4 parts, one on each page of the paper.The path of the 190 MeV/u U ion is parallel to the plane of the figure. The ion entered the crystal on the right hand side (this page) and came to rest on the left hand side (first page). The crystal has also been irradiated by 14 MeV/u Pb ions from the GSI accelerator (Darmstadt, FRG), perpendicularly to the plane of the figure. The tracks of these ions (seen as black dots on the photo) allowed the revelation of the track of the high energy U ion. It is seen that this track is etchable over the whole ion range ($\sim$2.8 mm) contrary to what we announced earlier (3), misled by an etch induction time effect (4,5). With usual techniques, less than one half of this length can be revealed (5). The high energy part of the track appears discontinuous. This is because the radiation damage intensity, linked to dE/dx, is getting lower in this region, so that in turn the etch rate is very low, and the different portions of the track have not been etched enough to meet.

This part is also the most thermally fragile, and may be responsible for a large broadening of the track length distribution corresponding to a given Z, for Cosmic Ray tracks in meteorites, because of differential annealing in space. The solution to maintain the charge resolution, may be to make length measurements after a stronger annealing in the laboratory (3,7). In Fig.1 (bottom) two 190 MeV/u U ion tracks can be seen (with some difficulty) after partial annealing by heating at 425°C during 5 hours. The length of the tracks have been reduced to 1.1 mm (so that they are seen only on the first 2 parts of the figure). After such a thermal treatment, the tracks of Kr and lighter ions are completely erased, and those of Xe ions reduced to 80 µm. The best conditions for an ion identification experiment in the U region are still to be determined. This will be done by comparing the results obtained for high energy U ion tracks with those for Au ions of a similar energy, which we should get at the Bevalac in the near future.

## 4. Conclusion

We feel that the results we have obtained, thanks to modern heavy ion accelerators, are extremely encouraging, and suggest that tracks in minerals might serve for ion identification purposes. Of course, tracks are tricky, and success is far from being certain. However, we may soon switch over, with some confidence, to real Cosmic Ray tracks.

The author is much indebted to H.J Crawford and D.E. Greiner

Fig. 1. cont'd.

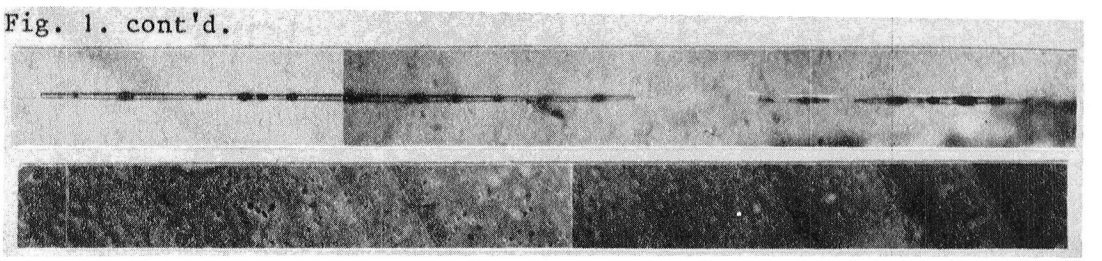

(Berkeley) and to R. Spohr (Darmstadt) for assistance with the heavy ion irradiations.

(1) Fowler P.H. et al. Nature 291, 45 (1981)
(2) Binns W.R. et al. Ap. J. 261, L117 (1982)
(3) Perron C. & Pellas P. 18th ICRC, 9, 127 (1983)
(4) Perron C. & Maury M. subm. to Nucl. Tracks (Feb. 1985)
(5) Perron C. Nature 310, 397 (1984)
(6) Lal D., Rajan R.S. & Tamhane A.S. Nature 221, 33 (1969)
(7) Lhagvasuren D. et al. in Solid State Nuclear Track Detectors, ed. H. Francois et al., Pergamon Press (1980) p.997

Fig.1. Top: photomicrograph of the track in olivine of a 190 MeV/u U ion from the Bevalac, revealed by the TINT technique. The photo has been cut into 4 parts. The ion entered the crystal on the right hand side (this page) and came to rest on the left hand side (first page of the paper). The feeding tracks (14 MeV/u Pb ions) perpendicular to the plane of the figure, are seen as black dots. For the discontinuous appearance of the U ion track at the high energy end, see text.
Bottom: same as top, but here, the tracks have been partially annealed (5 h at 425° C). Their etchable length has thus been reduced, and they are seen only on the first two pages of the paper.

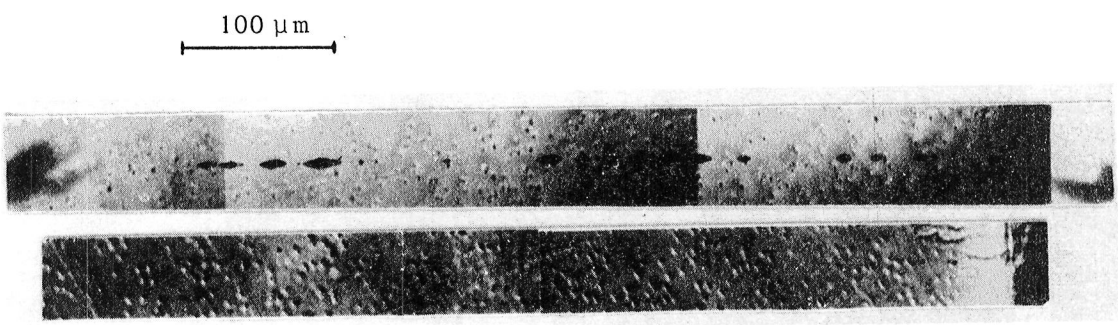

OG 4.4-11.

# EXPERIMENTAL TEST FOR INTERPRETING THE INCREASE IN SENSIBILITY OF DOPED CR-39.

A. Lavillë
INAOE, Tonantzintla, A.P. 51, 72000-Puebla, MEXICO.
J. Pérez-Peraza* M. Alvarez*
Instituto de Geofísica, UNAM, 04510-C.U., México 20, D.F.
M.R. Estrada
Instituto de Investigación en Materiales, UNAM, 04510-CU, México 20, D.F.

1. Introduction. In recent years the sensibility of CR-39 to nuclear tracks has been increased by doping the corresponding monomer with dioctyl phtalate. At this regard, two theoretical approaches are currently managed to explain this phenomenon: either the doping react with the active radicals in the chain blocking them, stopping crosslinking between chains, or alternatively that the doping gets between them giving wider space between the crosslinked chains.

We delimitate the contribution of each one of these effects in increasing sensibility by applying experimental techniques that will only block the active radicals of the chain.

Since the discovery that dioctyl phtalate (DOP) as a dopant, increases the sensibility of the plastic CR-39 [4], other dopants had been tested. This dopants were generally heavy phtalic esters, as was originally suggested in [4].

We believe that phtalic esters may have twoo possible ways of reacting. Either they can react completely with the active radicals in the monomer bloking and by this stopping crosslinking, or, as they have two reactive sites, they can react with two monomers belonging to two different chains, and by this not to stop crosslinking, but widening the space between crosslinked chains.

Terephtalic esters are suitable dopant openers of crosslinked chains and had also been used showing no great difference in sensibility as compared to the use of phtalic esters.

Here we use benzoic esters, which would be considered as blockers having just only one reactive site, as dopants, to see if they can increase the sensibility of CR-39.

An increase in sensibility with benzoic esters compared to the phtalic or terephtalic esters, would prove that the sensibility in CR-39 is increased by the dopant to stop crosslinking and not by widening the space between crosslinked chains.

2. Theory. When the monomer- dietilen glycol bis allyl carbonate- is catalyzed by the initiator, the monomer forms what is called free radicals. This free radicals are able to combine themselves within each other to form the polymer chain. However the free radicals of this monomer have two free electrons at both ends of the monomer molecule, which can become two covalent bonds at the ends of the molecule. This makes it possible for different chains which have only use one of the free electrons

to make the chain and leave the other electron for possible interaction between chains to form a covalent bond between them. This is what is call crosslinking.

If a phtalic ester (heavy) is added when polimerization starts, then the free radicals of monomer induce an inestability between the carboxilic group in the ester and the heavy chain attached to it; causing the ester to break also in free radicals precisely in this bond. The carboxilic group free radical has two oxigens with one free electron each, capable to react and form a covalent bond. So it can react with one monomer in one chain and at the same time, with another monomer in another chain, therefore widening the space between these two crosslinked chains. However, it can happen that only one oxygen has lost his heavy chain and just one electron is now available for reaction. If this happens then the ester will react with only one monomer in one chain, thus blocking that possibility for crosslinking and by this reduce and eventually stop the possibility for crosslinking. On the other side the heavy chain free radical can only interact as blocker.

The purpose of using benzoic esters instead of phtalic or terephtalic esters is that when breaking in free radicals, they can only have one electron for forming a covalent bond. Therefore they will only work stopping the crosslinking between chains. If the sensibility is the same as with the other esters, then phtalic esters work as blockers. If the sensibility decreases, then the phtalic esters work as openers.However if the sensibility increases, then we can not say anything about the work of the phtalic esters but a better dopant has been found.

3.Experimental. Five different preparations were made using the french monomer C.A.D. from the Société Française D'organo-synthèse. Each preparation was polymerized using as initiator 3% by weight of asoisobutironitryl (AIBN) from Dupont (peroxidicarbonates were not available in our country), and four of them were dopped with different esters according to TABLE I. All five polymers were polymerized at the same time, in the same oven with a thirtytwo hour curing cycle [1],[2].

TABLE 1.- INITIATOR AND DOPANT USE IN EACH POLYMER.

| PREPARATION N° | NAME | INITIATOR | INITIATOR CONC. | DOPANT | DOPANT CONC. |
|---|---|---|---|---|---|
| 1 | CR-39 | AIBN | 3% | — | — |
| 2 | CR-39(DOP) | AIBN | 3% | DOP | 3% |
| 3 | CR-39(MB) | AIBN | 3% | MB | 3% |
| 4 | CR-39(BB) | AIBN | 3% | BB | 3% |
| 5 | CR-39(SB) | AIBN | 3% | SB | 3% |

AIBN= asoisobutironitryl; DOP= dioctyl phtalate; MB= methyl benzoate; BB= benzyl benzoate; SB= sodium benzoate.

After the curing cycle was completed, the plastics thus obtained where soft and flexible. We irradiated them, together with some samples of CR-39 (DOP) from Pershore Mouldings Ltd., with $\alpha$-particles at different energies. We then etched them in a solution 25% NaOH at 70°C in three steps. A first step of two hours, a second one of two hours nineteen minutes and a third one of three hours .

4. Preliminary inference. At the time this confirming abstract was done, analysis of the irradiated plastics was in progress. The analysis will end with calibration curves describing the track velocity of attack as a function of the residual range, which would show the sensibility of each polymer compared to CR-39 (DOP) by Pershore.

Though analysis is not yet complete, some preliminary inferences can be made: From the size of the tracks in our five plastics compared to the size of the tracks in the CR-39 (DOP) from Pershore,we can infer that the sensibility of our plastics should be about the same as the CR-39 (DOP) from Pershore. Though, this should not be conclusive since calibration curves have not been obtained yet.If this inference results in becoming true, we would have proved then, that DOP works as a blocker and not as an opener that widens the space between crosslinked chains.

At the moment being, we have a conclusive result. This is that the tracks in the polymer doped with sodium benzoate are very hard to analyze since the polymer is quite turbid.

5. Acknowledgements.We are indebted to Dr. Miguel Balcázar for the facilities in the use of his nuclear track laboratory during the phase of irradiation, etching and observation of the tracks.

References.

1. Adams,Jr. J.H., (1981), Proc. 11th Int. Conf. on SSNTD, Bristol,145-148.
2. Société Française D'Organo-synthèse, (1984), Report JE/NC 27/2/84.
3. Somogyi, G., (1981), Proc. 11th Int. Conf. on SSNTD,Bristol, 101-113.
4. Tarlé, G., (1981), Proc. 17th Int. Cosmic Ray Conf.,Paris, T2-13,74-77.

-0-

* On leave for INAOE, Tonantzintla, A.P. 51, 72000-Puebla, Pue. México.

# Energy Spectrum and Arrival Direction of Primary Cosmic Rays of Energy above $10^{18}$eV

M.Teshima*, M.Nagano, N.Hayashida, C.X.He**, M.Honda, F.Ishikawa, K.Kamata, Y.Matsubara*, M.Mori* and H.Ohoka

Institute for Cosmic Ray Research, University of Tokyo, Tokyo, 188 Japan
*Department of Physics, Kyoto University, Kyoto, 606 Japan
**Institute of High Energy Physics, Academia Sinica, Beijing, China

Abstract

The observation of ultra high energy cosmic rays with 20km$^2$ array has started at Akeno. The preliminary results on energy spectrum and arrival direction of energies above $10^{18}$eV are presented with data accumulated for four years with the 1km$^2$ array, for two years with the 4km$^2$ array and for a half year with the new array. The energy spectrum is consistent with the previous experiments showing the flattening above $10^{18.5}$ eV.

## 1. Introduction

The detailed study on the energy spectrum and the arrival direction distribution of ultra high energy cosmic rays gives us the information about their origin, acceleration and propagation. There are still discrepancies among experimental results reported, especially in arrival direction distribution at highest energies. In order to clear up these problems, it is essential to increase the statistics. At Akeno the operation of the 20km$^2$ array has started. In this paper, the preliminary results about energy spectrum and arrival direction of EAS above $10^{18}$ eV are reported.

## 2. Experiment

The experiments have been carried out with 3 different arrays, 1km$^2$, 4km$^2$ and 20km$^2$. The arrangement of 1km$^2$ array is described in Hara et al[1]. For 1km$^2$ array, the data of 4 years are accumulated. The observation with 4km$^2$ array started at 23rd Dec. 1982[2] and continued until 26th Dec. 1984. The 20km$^2$ array has been in partial operation from 8th Sep. 1984 and full operation including the 4km$^2$ array from 27th Dec. 1984. The detector arrangement of 20km$^2$ array is described in Teshima et al[3].

The trigger requirements of 20km$^2$ array are 6-fold coincidence of neighbouring detectors of 23 deployed in about 1 km separation with each other. The discrimination level of the signal is 0.5 particle equivalence per detector of 2.25m$^2$ area.

In this experiment about 250 EAS's of energy above $10^{18}$eV and 5 EAS's of above $10^{19}$eV are observed.

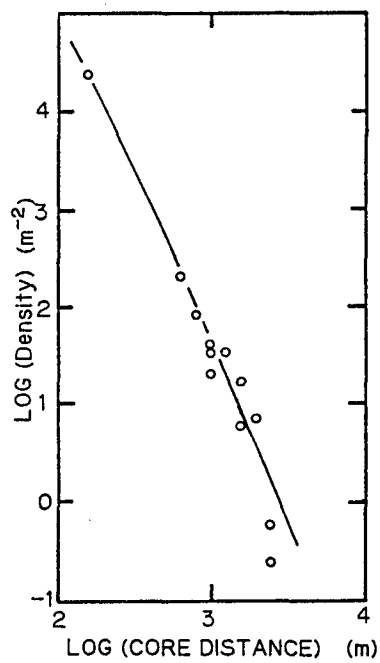


Fig.1(a) The lateral distribution of the largest event.

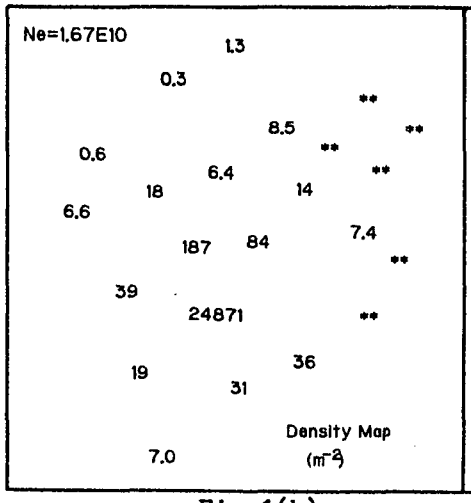


Fig.1(b)

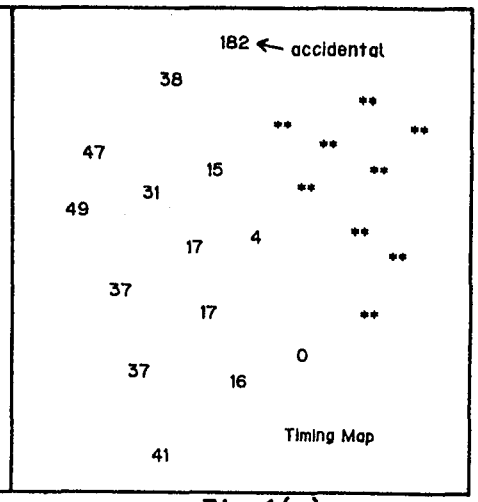


Fig.1(c)

## 3. The largest event at Akeno

In fig.1 are shown (a) the lateral distribution of electrons, (b) the density map and (c) the arrival time sequence of each detector of the largest event observed so far at Akeno. Numbers of particles per 1 $m^2$ are typed on the detector position. In (c) the arrival time differences between each detector and that of the fastest incident particle(indicated by 0) in a unit of 100 ns. This event was recorded in a period under construction of the 20$km^2$ array. The size of total electrons is $1.67 \times 10^{10}$ and the zenith angle is 30.3 degree. The core hits inside the array. The estimated primary energy is about $3 \times 10^{19}$eV.

## 4. The electron size spectrum

The electron size spectrum is derived only from the data of EAS's whose cores hit inside the array, because the error in size determination for those outside the array is so large that the spectrum is possibly deviated as described in Teshima et al[3]. Since the collection efficiency of the new array is not 100% for the showers smaller than $10^9$, the effective area is estimated by analyzing 100,000 artificial showers simulated by the Monte Carlo method, which distribute uniformly over the wide area following the size spectrum with exponent of -3. The collection factor due to the triggering inefficiency and the error of size determination can be estimated by reconstructing the size spectrum of these artificial showers. The size spectrum thus corrected is shown by open circles in fig.2. The new spectrum obtained by the 1 $km^2$

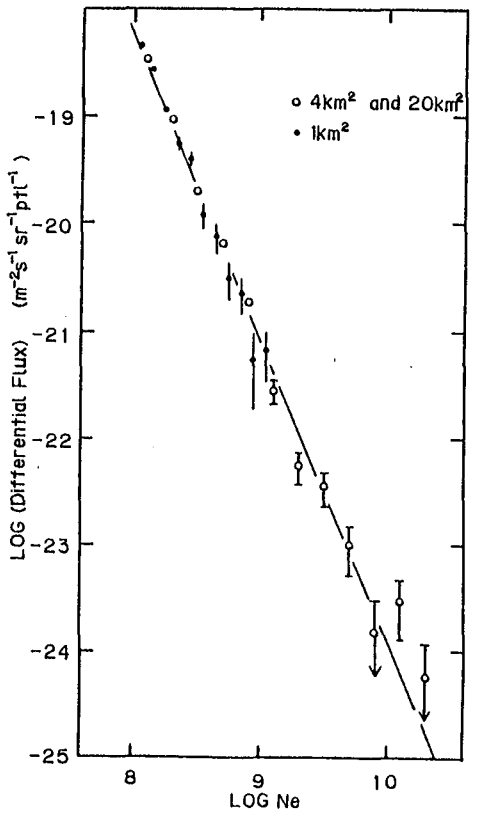


Fig.2 The electron size spectrum.

array with accumulated data are also plotted by solid circles. The effective area times observation time are $2.77 \times 10^8$ km$^2$s and $6.08 \times 10^7$ km$^2$s, respectively. The agreement is satisfactory showing the present correction to be reasonable. The differential size spectrum is expressed by

$$J(N_e)dN_e = (5.65 \sim 6.47) \times 10^{-19} \times (N_e/10^8)^{(-2.72 \sim -2.87)} dN_e m^{-2} s^{-1} sr^{-1},$$

up to $10^{10}$, which is consistent with the extrapolation of our previous results[4].

## 5. The arrival direction

The arrival direction of EAS above $10^{18}$ eV on the galactic coordinate is shown in fig.3. The area of the open circles are proportional to the primary energies. The smallest circle corresponds to $10^{18}$eV and the largest one to $3 \times 10^{19}$. These data are the compilation of 1km$^2$ ,4km$^2$ and 20km$^2$ array. The center of the figure is ($l^{II}$ ,$b^{II}$)=(120, 0). The dashed lines indicate the longitude and latitude of equatorial coordinate. The exposure is almost uniform along the longitude lines expressed by the dashed circles, but not along the latitude lines.

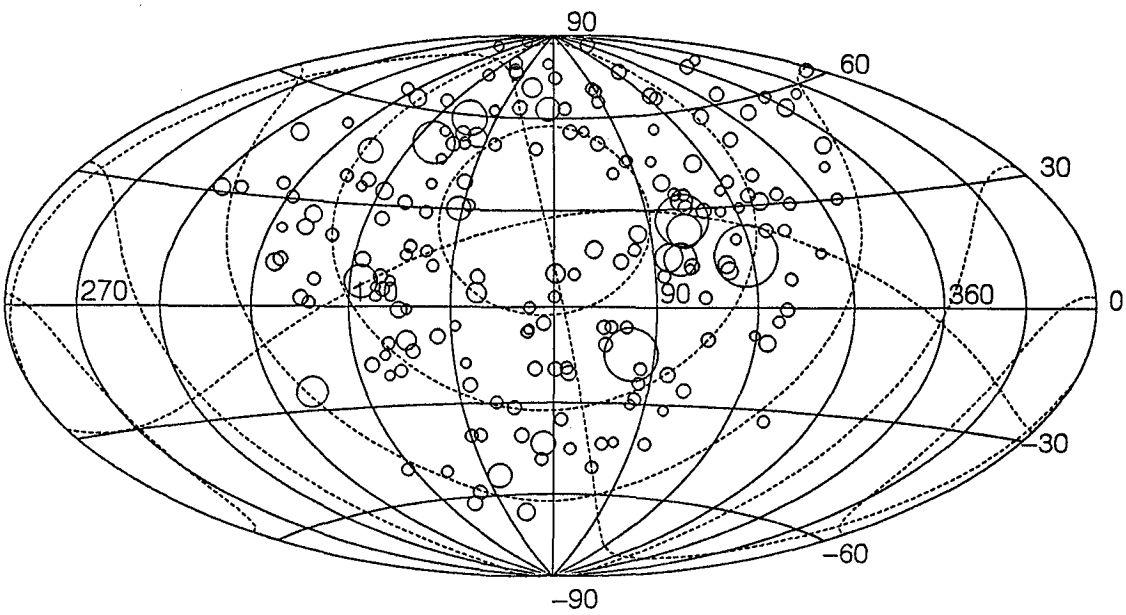


Fig.3 The arrival direction distribution of EAS's above $10^{18}$eV on the galactic coordinate.

## 6. Discussions

The primary energy spectrum is derived from the present size spectrum by multiplying the conversion factor which was derived at smaller size regions as $w \times R = 3.9 \times (Ne/10^6)^{-0.105}$ GeV[4]. Where w is the conversion factor from electron size at the maximum development, 1.4 GeV[5] and R is the ratio of the shower size at maximum to the size at 920gcm$^{-2}$.

In fig.4 the primary energy spectrum derived from the data of 4km$^2$ array and 20km$^2$ is shown by the open circles and compared with the previous experiments. The total exposure is about 10 km$^2$*year for the

showers of $10^{19}$ eV. This result shows the good agreement with our previous result with the Akeno 1km$^2$ array[4] at energy region between $10^{17}$ eV and $10^{18}$eV. Above $10^{18}$eV the present spectrum is consistent with the results of Haverah Park[4], Yakutsk[5] and Sydney[6] showing the flattening. Here the Sydney results are plotted by applying the conversion factor used in ref[4].

Though the statistics is not enough, some interesting features can be seen around $10^{18}$-$10^{19}$eV. That is, the largest showers are clustered around the Cygnus direction and the spectrum shape does not follow the simple power law.

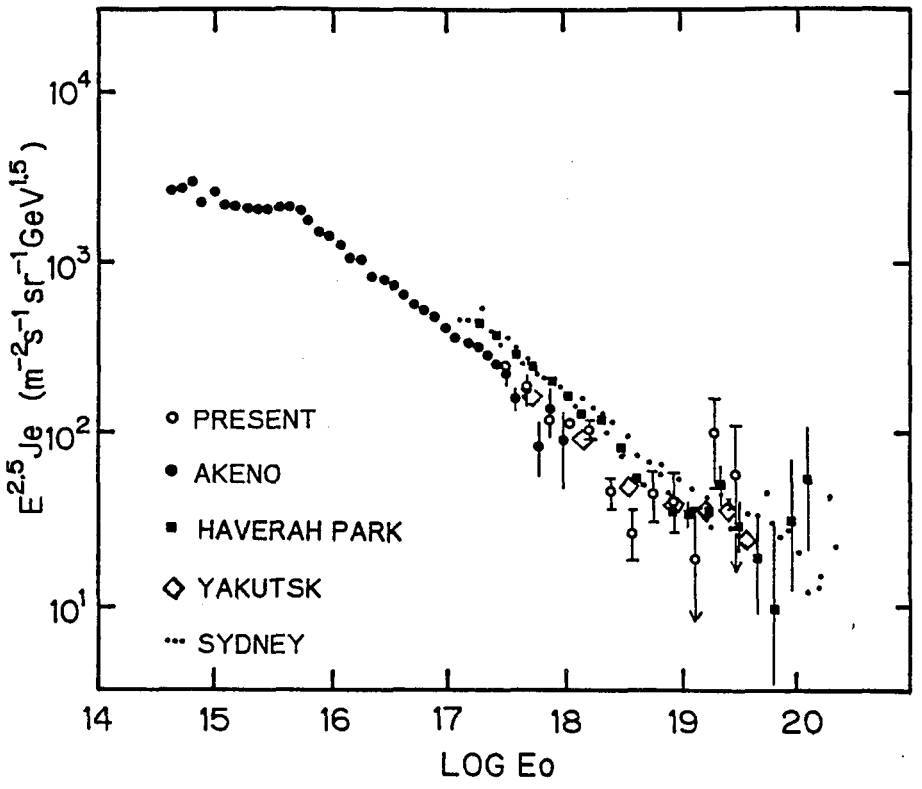


Fig.4 The primary energy spectrum.

**Acknowledgements**

The authors wish to thank the other members of Akeno A.S. Group for their help and fruitful discussions. The analysis and simulations were carried out with FACOM M380 at the Computer Room of Institute for Nuclear Study, University of Tokyo.

Reference

[1] T.Hara et al., Proc. 16th ICRC, Kyoto 8 (1979) 135.
[2] T.Hara et al., Proc. 18th ICRC, Bangalore 11 (1983) 276.
[3] M.Teshima et al., This conf. OG 9.4-8.
[4] M.Nagano et al., J. Phys. G: Nucl. Phys. 10 (1984) 1295-1310.
[5] A.M.Hillas, Proc. Cosmic Ray Workshop, University of Utah (1983) 16.
[6] L.Horton et al., Proc. 18th ICRC, Bangalore 6 (1983) 128.

# ULTRA HIGH ENERGY COSMIC RAY SPECTRUM

Baltrusaitis, R.M., Cady[7], R., Cassiday, G.L., Cooper, R., Elbert, J.W., Gerhardy, P.R., Ko, S., Loh, E.C., Mizumoto, Y., Salamon[8], M.H, Sokolsky, P., Steck, D.

Department of Physics, University of Utah, Salt Lake City, UT 84112

ABSTRACT

Ultra-high energy cosmic rays have been observed by means of atmospheric fluorescence with the Fly's Eye since 1981. The differential energy spectrum above 0.1 EeV is well fitted by a power law with slope 2.94 ± 0.02. Some evidence of flattening of the spectrum is observed for energies greater than 10 EeV, however only one event is observed with energy greater than 50 EeV and a spectral cutoff is indicated above 70 EeV.

1. Introduction. The Fly's Eye experiment has been described in detail elsewhere[1]. Since November 1981, it has been in operation with 67 mirrors and 880 photomultiplier tubes. Results of the analysis of the data collected up to September 1984 are presented here. During this period, 2408 well measured events with energies greater than 0.1 EeV were detected in 1278 hours of live time.

2. Energy and Spectral Calculation. The energy of an event is estimated by fitting the measured longitudinal development profile of the shower to both Gaussian and unconstrained (3 free parameters) Gaisser-Hillas[2] curves. These curves are integrated to obtain the total track length of the shower particles, and then converted to total 'electromagnetic' energy by the relation

$$E_{em} = \varepsilon_0/X_0 \int N_e(x)dx$$

where $\varepsilon_0/X_0$ is the ratio of critical energy of an electron to its radiation length in air, giving the total rate of energy loss by ionization and excitation. The loss rate used here is 2.18 MeV g cm$^{-2}$. Total energy of the primary particle is then calculated by correcting the 'electromagnetic' energy for undetected energy using estimates of this lost energy derived by Linsley[3]. These range from 13% at 0.1 EeV to 5% at 100 EeV. This method of energy estimation relies only on low energy interactions and is essentially model independent. Shown in Fig. 1 is the raw energy distribution of observed events.

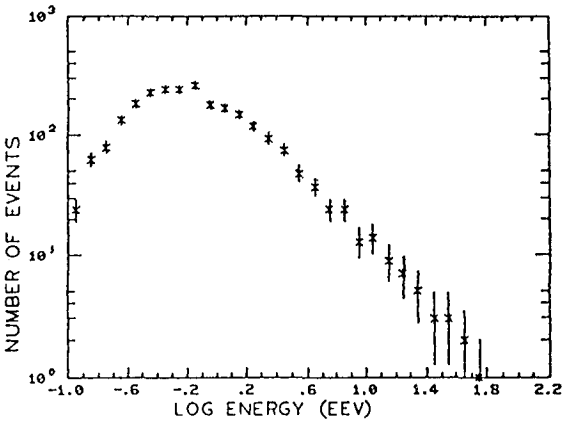


Figure 1. Raw Energy Distribution of Fly's Eye Data.

To obtain the energy spectrum from these data, the energy dependent Fly's Eye aperture must be calculated. This has been done using a Monte Carlo simulation of the system. In this simulation quasi-random trajectories and first interaction depths for the events are chosen from an isotropic distribution, and the showers are developed using the constrained Gaisser-Hillas[2] parameterization and shapes obtained from the real data sample, thereby ensuring consistency between the simulation and the data base. Triggering Monte Carlo events are stored and analyzed using the analysis programs which are used on the real data. The sensitive aperture of the Fly's Eye is then calculated from the ratio of accepted to tried Monte Carlo events. Scatterplots of the distribution of events in impact parameter and energy for both (a) Monte Carlo and (b) real events are shown in Fig. 2. There is excellent agreement between these distributions, indicating that the simulation is a good representation of the Fly's Eye. Figure 3 shows the effective Fly's Eye aperture calculated from the simulation.

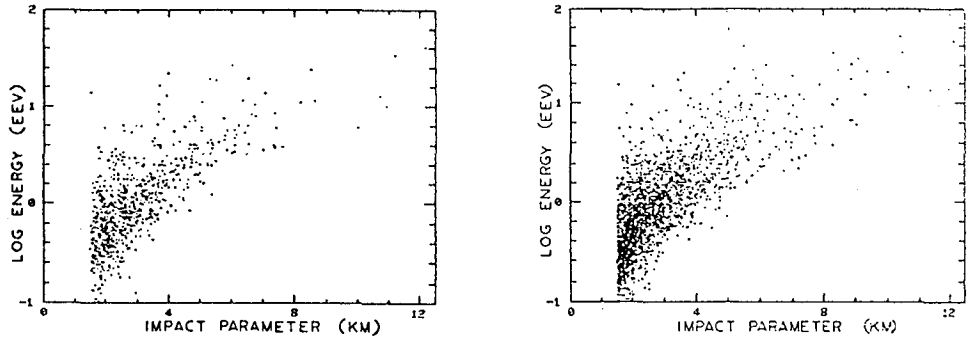


(a) (b)

Figure 2. Energy vs Impact Parameter Scatterplots for (a) Monte Carlo and (b) Fly's Eye Data.

The self-consistency of the analysis programs is also checked by the processing of the Monte Carlo events with the analysis routines and comparing the results with the original Monte Carlo event parameters. Response functions for (a) zenith angle, (b) impact parameter and (c) energy are shown in Figure 4.

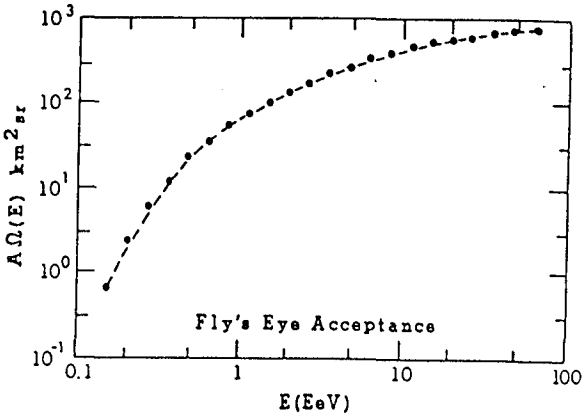


Figure 3. Fly's Eye Sensitive Aperture.

3. Results. Using the above techniques, the differential energy spectrum of the observed data has been calculated. It is shown in Figure 5 plotted as $E^3j(E)$. The spectrum is essentially flat between 0.1 and 10 EeV with a slope of $2.94 \pm 0.02$. Between 10 and 50 EeV, there is the appearance of a bump,

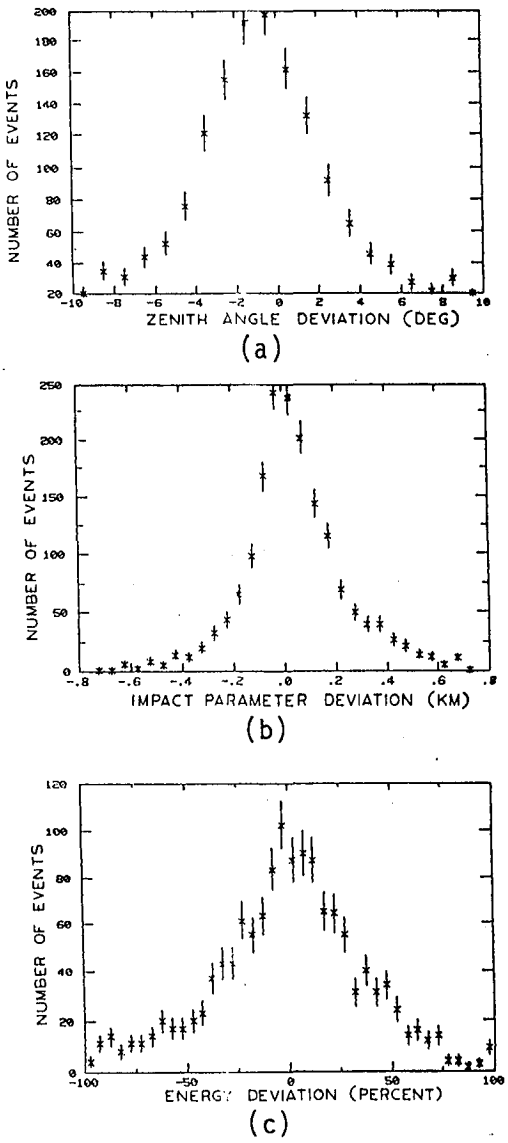


Figure 4. Analysis Response Functions for (a) Zenith Angle, (b) Impact Parameter, and (c) Energy.

with 62 events in this interval compared with 46 that would be expected if the spectrum continued with the same slope as at lower energies. Since the uncertainty in this predicted value is small, the significance of the bump is roughly $16/\sqrt{46} = 2.4\sigma$. If the spectrum between 10 and 50 EeV is fitted by a power law, the slope is found to be $2.42 \pm 0.27$, about $2\sigma$ flatter than the value at the lower energies. Only one event is observed with energy greater than 50 EeV. This should be compared with $11 \pm 5$ events which would be observed if the spectrum continued above 50 EeV with the same slope as between 10 and 50 EeV.

4. Discussion and Conclusions. It should be noted that between 1 and 50 EeV, the Fly's Eye energy spectrum is in good agreement with that of the Haverah Park[4] experiment, although differences exist above and below these energies. This agreement provides a useful check on the operation of the system, since in this energy regime, the Fly's Eye aperture is well simulated and data collection statistics are good. Below 1 EeV, the acceptance is rapidly changing and threshold simulations and errors in the estimates of analysis efficiency could acocunt for any differences. This possiblity is being investigated. However, above 50 EeV, the discrepancy appears to be real. Here the Fly's Eye aperture is increasing (albeit slowly) and most of the extra events expected would have fallen within the 50 EeV acceptance where the agreement is good. The efficiency for detection and analysis of these events should be higher due to the increased brightness of the resultant air shower.

The spectral shape derived is consistent with that predicted by Hill and Schramm[5] for source distances between 70 and 150 Mpc, with a Greisen[6] cutoff above a recoil pileup of the primaries.

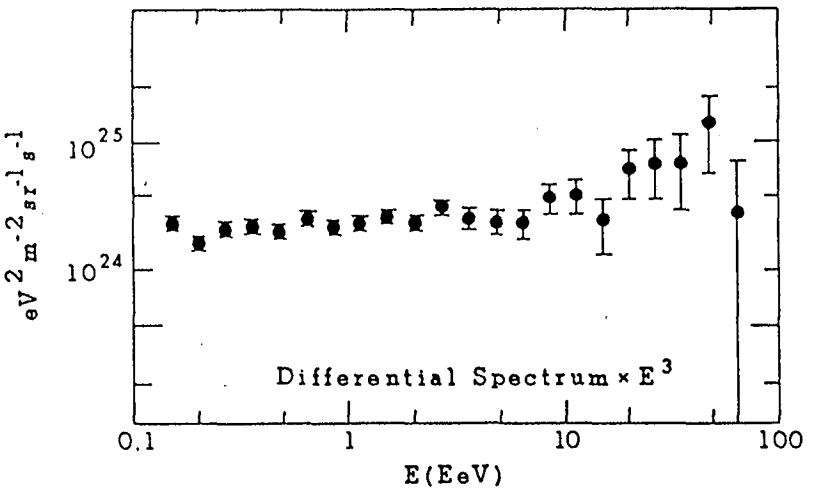


Figure 5. Fly's Eye Differential Energy Spectrum.

5. Acknowledgements. The support of the United States National Science Foundation is gratefully acknowledged.

References.

1. Baltrusaitis, R.M., et al submitted Nucl. Inst. Meth. (1985).
2. Gaisser, T.K., and Hillas, A.M. 15th PICCR (Plovdiv) 8, 353, (1977).
2. Linsley, J. 18th PICCR (Bangalore) 12, 135, (1983).
4. Cunningham, G. Ap. J. Lett. 236, L171, (1980).
5. Hill, C.T. and Schramm, D.N., Phys. Rev. D 31, 564, (1985).
6. Greisen, K., Phys. Rev. Lett. 16, 748, (1966).
7. Present address: Department of Physics, University of Hawaii, Manoa, HI 96822.
8. Present address: Space Sciences Laboratory, University of California, Berkeley, CA 94720.

# THE PRIMARY COSMIC RAY SPECTRUM ABOVE $10^{19}$ eV

G. Brooke, G. Cunningham†, P.J.V. Eames, M.A. Lawrence,
J.C. Perrett, R.J.O. Reid and A.A. Watson.

Department of Physics, University of Leeds, LEEDS 2.

† now at Institute of Transport Studies, University of Leeds.

ABSTRACT

We describe progress on a re-evaluation of the spectrum of cosmic rays determined with the Haverah Park shower array. Particular attention is paid to the reality of some giant showers.

1. Introduction. We are engaged in a re-appraisal of the energy spectrum of cosmic rays above $10^{18}$ eV as determined with the Haverah Park shower array. Here we offer a progress report on work which is motivated by the continuing controversy over the shape of the spectrum above $10^{19}$ eV - in particular the Yakutsk group have questioned the reality of events of $10^{20}$ eV - and by the recent re-investigation of the predicted shape of the spectrum above $10^{19}$ eV if the sources of these particles are at cosmological distances (Hill and Schramm 1985).

2. Cosmic Ray Energy Spectrum. The differential energy spectrum derived from our work above $10^{18}$ eV is shown in Figure 1. Above $3.5 \times 10^{18}$ eV the spectrum has been updated by the addition of events recorded to December 1983. A detailed analysis of possible sources of systematic error has been made taking into account the effects of uncertainties in zenith angle, lateral distribution fluctuations, core location and attenuation length, (Cunningham 1982). For energies between $8 \times 10^{17}$ and $3.5 \times 10^{18}$ eV systematic selection effects and analysis errors dominate over statistical uncertainties and detailed simulations have allowed a deconvoluted spectrum to be derived. Above $3.5 \times 10^{18}$ eV the error analysis has been conducted on a shower-by-shower basis and the statistical errors have been shown to be at least twice as great as the instrumental errors. We do not yet regard the spectrum of Figure 1 as our 'final' spectrum as further refinements will be possible as our detailed knowledge of showers increases but we wish to emphasise that we have considerable confidence in the durability of the intensities and energies assigned above $10^{19}$ eV. The major differences between this spectrum and those published at Kyoto are (a) the exclusion of events with $\theta > 45^{\circ}$ (as we now regard our knowledge of the structure function to be incomplete above this angle) and (b) use of an energy dependent structure function measured in showers of $10^{17} - 5 \times 10^{18}$ eV (Coy et al 1981) and in a small number of large showers which fell during the period of that experiment. The main features of the spectrum are the flattening above $10^{19}$ eV and its continuity to just beyond $10^{20}$ eV. At the Paris conference we pointed out that the flattening may also be interpreted as a dip in the spectrum (Bower et al 1981) and suggested that if particles above a few times $10^{18}$ eV were of extragalactic origin then the dip might well be due to electron-pair production. This interpretation has been confirmed by the detailed analysis of Hill and Schramm (1985).

The Haverah Park and Yakutsk spectra (Vaselev et al 1983) are compared

in the lower part of Figure 1. The spectra are found to agree reasonably well until about $3 \times 10^{19}$ eV when the absence of large showers in the Yakutsk spectrum becomes apparent.

In recent years a number of 1 $m^2$ blocks of scintillator have been incorporated in the Haverah Park array making possible a comparison between the model calculation conversion used by the Haverah Park group and the calorimetric approach of the Yakutsk group. We have shown elsewhere that the calibration is good (to within better than 20%) up to at least $5 \times 10^{19}$ eV and similarly that the Volcano Ranch energy estimates are in accord (Bower et al 1983a, b). Also the Sydney experiment offers evidence of a flattened spectrum above $\sim 4 \times 10^{19}$ eV (Horton et al 1983); that spectrum may extend to $4 \times 10^{20}$ eV (Linsley 1983). We do not plot the Sydney spectrum here because of uncertainties about the energy calibration.†

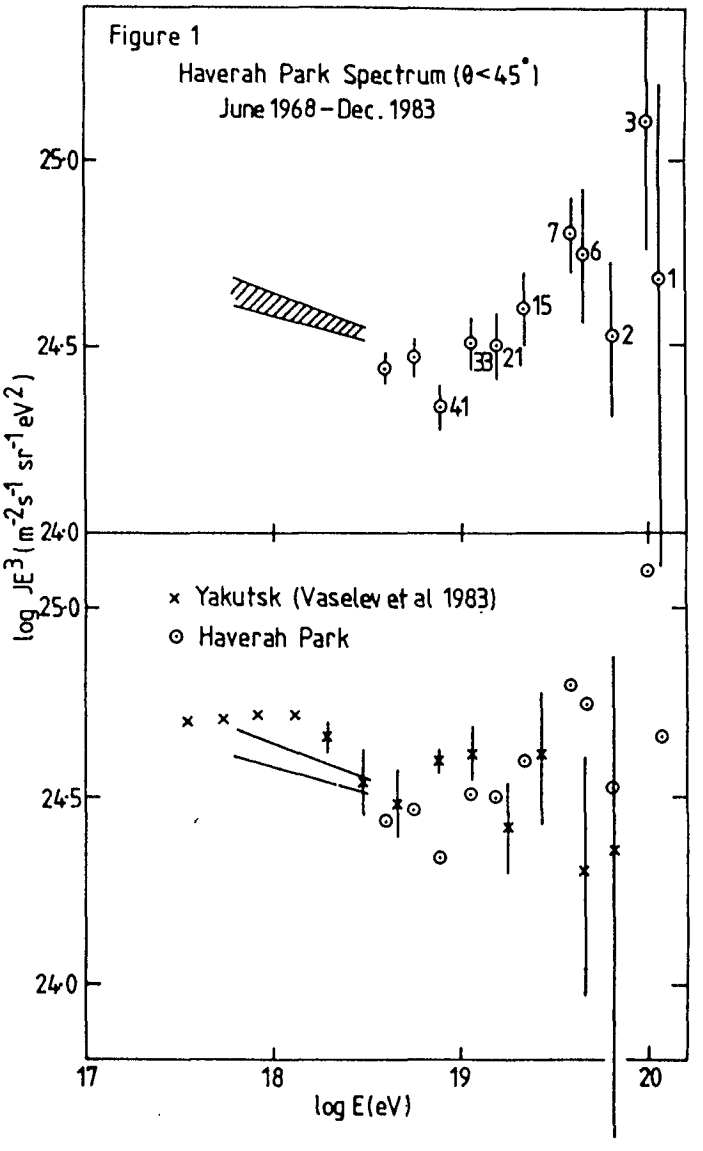


3. Events of $10^{20}$ eV. The 4 most energetic events included in the spectrum have been assigned energies $> 10^{20}$ eV. Brief details of these are given in Table 1; maps of the density pattern observed in each event were published in the World Data Catalogue although the sizes have been slightly altered as a result of the revised lateral distribution function now adopted. Three of the events have risetime information available at one or more of the 34 $m^2$ detectors and are discussed in that context in HE 4.7-6 (Lawrence et al).

Of the events in Table 1 by far the most outstanding in terms of number of densities and precision of core position is 17684312. Unfortunately this event was recorded in the epoch before scintillator densities were

being recorded. One of the most energetic events with scintillator density information is 21220296, a map for which has been published elsewhere (Bower et al 1983c) and these two events are contrasted in Table 2.

Table 1

| Reference number | angle $\theta$ | $\alpha$ | $\delta$ | b | $r_1$(m) | Energy (eV) | World Data Catalogue | Rise-times |
|---|---|---|---|---|---|---|---|---|
| 8185175 | 35 | $353^o$ | $19^o$ | $-40^o$ | 443 | $1.02 \times 10^{20}$ | p78 | None |
| 17684312 | 35 | $201^o$ | $71^o$ | $46^o$ | 376 | $1.05 \times 10^{20}$ | p86,87 | 1 |
| 9160073 | 30 | $199^o$ | $44^o$ | $73^o$ | 1384 | $1.05 \times 10^{20}$ | p79 | 2 |
| 12701723 | 29 | $179^o$ | $27^o$ | $78^o$ | 1093 | $1.21 \times 10^{20}$ | p83 | 4 |

Table 2 : Comparison of two giant air showers

| | 21220296 (J Phys G 9, 1569 1983) | 17683412 (World Data Catalogue pp86-7) |
|---|---|---|
| Zenith angle | $13^o$ | $35^o$ |
| Number of water-Cerenkov detectors and distance range | 24<br>$150 < r < 2170$ m | 50<br>$90 < r < 2500$ m |
| Number of 1 $m^2$ scintillators and distance range | 8<br>$420 < r < 680$ m | - |
| $S(600)$ $m^{-2}$ | 157 | |
| $\rho(600)$ $m^{-2}$ | 64 | 105 |
| $\rho_V(600)$ $m^{-2}$ | 66 | 136 |
| Primary energy: | | |
| Yakutsk calibration | $5.3 \times 10^{19}$ eV | - |
| Hillas relation | $5.0 \times 10^{19}$ eV | $1.1 \times 10^{20}$ eV |

The estimated error in the assigned size ($\rho(600)$) for each of these events is $\sim 10\%$; this error includes core location uncertainty, stationary error and allowance for lateral distribution uncertainty and is so small because of the exceptional symmetry in the detector density patterns. The risetime measurements in each event are also in agreement with these analyses. Event 17683412 is unquestionably twice as large as 21220296 which in turn, through the scintillator and water-Cerenkov densities, has two independent energy estimates of $\sim 5 \times 10^{19}$ eV.

In addition to the 4 events discussed above we have recorded a further 4 events which we believe are $\gtrsim 10^{20}$ eV. These are not included in our energy spectrum because they arrived from zenith angles $> 45^o$ and/or the

cores fell outside of the array boundary. The flux derived from all 8 events in this total exposure of 657 $km^2$ sr y is $\left(4\ ^{+2}_{-1}\right) \times 10^{-16}\ m^{-2}\ s^{-1}\ sr^{-1}$ and is consistent with that deduced for the 4 events of Table 1, namely $I(> 10^{20}\ eV) = \left(3\ ^{+2}_{-1}\right) \times 10^{-16}\ m^{-2}\ s^{-1}\ sr^{-1}$.

4. Discussion and Conclusions. The proven existence of cosmic ray events with $E > 10^{20}$ eV demands explanation. Presumably the source of these events must be relatively close to the earth but it can hardly be galactic as $|b| > 40^{o}$ for all 4 events of Table 1. The inferences drawn about the ability of the Cygnus X-3 system to accelerate large fluxes of cosmic ray nuclei to $10^{17}$ eV/nucleon (Hillas 1984) leads naturally to speculation that a suitably scaled up system, perhaps in the nucleus of an active galaxy, can accelerate particles to $10^{20}$ eV and beyond.

Our current best estimates of the integral intensities above $10^{18}$, $10^{19}$ and $10^{20}$ eV are

$$I(> 10^{18}\ eV) = (1.9 \pm 0.2) \times 10^{-12}\ m^{-2}\ s^{-1}\ sr^{-1}$$
$$I(> 10^{19}\ eV) = (2.1 \pm 0.2) \times 10^{-14}\ m^{-2}\ s^{-1}\ sr^{-1}$$
$$I(> 10^{20}\ eV) = (3 \pm 2) \times 10^{-16}\ m^{-2}\ s^{-1}\ sr^{-1}$$

Further details of our analysis will be published elsewhere.

Acknowledgements. The continuing assistance of Paul Ogden, Mansukh Patel, Sue Hopper and Julie Ingle in obtaining and reducing these data is gratefully acknowledged as is the financial support from the Science and Engineering Research Council (UK). AAW would like to thank the Yakutsk group for their hospitality during April 1984.

References

A.J. Bower et al 1981 Proc. 17th ICRC (Paris) 9, 166.
A.J. Bower et al 1983a J Phys G 9, L53.
A.J. Bower et al 1983b Proc. 18th ICRC (Bangalore) 9, 207.
A.J. Bower et al 1983c J Phys G 9, 1569.
R.N. Coy et al 1981 Proc. 17th ICRC (Paris) 6, 43.
G. Cunningham 1982 PhD Thesis, University of Leeds.
C.T. Hill and D.N. Schramm 1985 Phys Rev 31, 564.
A.M. Hillas 1984 Nature 312, 50.
L. Horton et al 1983 Proc. 18th ICRC (Bangalore) 2, 128.
J. Linsley 1983 Proc. 18th ICRC (Bangalore) 12, 135.
World Data Catalogue: Catalogue of Highest Energy Cosmic Ray Showers N° 1 (World Data Center C2 for Cosmic Rays) pp61-99.

† After preparation of this paper was completed (22 May 1985) the issue of Physical Review Letters (22 April 1985), which contains the new spectrum deduced from Fly's Eye, reached us. We do not agree with the Fly's Eye group's conclusion that an end to the cosmic ray spectrum has been observed. A comment on their letter is being prepared for submission to Physical Review Letters.

# NEW CALORIMETRIC ALL-PARTICLE ENERGY SPECTRUM

John Linsley
Department of Physics and Astronomy
University of New Mexico, Albuquerque, NM 87131
USA

ABSTRACT

Both the maximum size $N_m$ and the sea level muon size $N_\mu$ have been used separately to find the all-particle energy spectrum in the air shower domain. However the conversion required, whether from $N_m$ to E or from $N_\mu$ to E, has customarily been carried out by means of calculations based on an assumed cascade model. It is shown here that by combining present data on $N_m$ and $N_\mu$ spectra with data on 1) the energy spectrum of air shower muons and 2) the average width of the electron profile, one can obtain empirical values of the $N_m$ to E and $N_\mu$ to E conversion factors, and an empirical calorimetric all-particle spectrum, in the energy range $2 \cdot 10^6 < E < 2 \cdot 10^9$ GeV.

1. Introduction. The great majority of shower particles are electrons, so it is natural that in the earliest air shower experiments the energy estimates were based on the number of electrons at the observation level. The first estimates (Auger 1939) were too low by about a factor of 4, because 1) the correction for longitudinal development was too conservative, and 2) the energy given to muons, neutrinos and low energy hadrons ($E_{\mu\nu h}$) was ignored. (At the energies in question $E_{\mu\nu h}$ amounts to some 35% of the whole.) The first difficulty stems from the average electron energy being comparatively low ($\sim E_c$, so that electrons are continually absorbed and regenerated. In order to estimate the energy deposited in the atmosphere one must use an integral signal such as the yield of atmospheric Cerenkov or fluorescent light, or else face the problem of accurately evaluating a correction factor that may be as large as a factor 20. By observing showers near maximum development (which generally means at a very high altitude) one can reduce the uncertainty in $E_{EM}$ by minimizing the correction factor. Following this approach, one finds the all-particle energy spectrum by combining measurements of the $N_m$ spectrum with estimates of the conversion factor $E/N_m$.

The alternative is to use shielded counters, which respond only to muons, and measure the $N_\mu$ spectrum, where $N_\mu(>E_\mu)$ is the 'muon size', the number of muons with enough energy to penetrate the shielding. This was done on a very large scale in the SUGAR experiment (Horton *et al.* 1983) and more recently in experiments at Chacaltaya, Tien Shan and Akeno (Kakimoto *et al.* 1981, Kirov *et al.* 1981, Hara *et al.* 1983). The difficulty with this method is that calculations relating $N_\mu$ to primary energy are relatively complex and model-dependent (see for example McComb *et al.* 1977 and Hillas 1981). Calculations of $E/N_m$ are less affected by these difficulties, but they also require estimating the energy given to muons.

My purpose here is to show that by treating the experimental $N_m$ and $N_\mu$ spectra *simultaneously*, using also experimental data on 1) the energy spectrum of air shower muons and 2) the width of the electron profile, one can obtain conversion factors which are almost entirely empirically

based, and a new result on the all-particle energy spectrum which is almost entirely model independent.

2. Relation between maximum size and electronic energy. The energy dissipated by electrons is given by the track length integral

$$E_{EM} = (E_c/x_o) \int N(x) dx \ , \qquad (1)$$

where $N(x)$ is the number of electrons at depth $x$ g/cm$^2$, $E_c$ is the critical energy (=81 MeV in air according to Dovzhenko and Pomanskii 1964), and $x_o$ is the radiation length (= 37.1 g/cm$^2$ in air according to conference paper HE4.4-4). Writing $E_{EM} = K(E_c/x_o)\sigma N_m$, where $N_m$ is the height and $\sigma$ is the width (standard deviation) of the average shower profile, what can be said about the value of K? Using a Gaussian distribution for N (surely quite a crude approximation), $K = \sqrt{2\pi} = 2.51$. Using a gamma distribution, $N = N_o \xi^q \exp(-q\xi)$ where $\xi = x/x_m$, which can be adjusted to fit very well (see conference paper HE4.4-5), the value of K ranges from 2.35 for q=6 (small showers) to 2.42 for q=12 (large showers). Thus it hardly varies at all, so adopting an average value for K, and substituting for $(E_c/x_o)$, I obtain

$$E_{EM} = (\sigma/192)\ N_m \ , \qquad (2)$$

where $\sigma$ is in g/cm$^2$ and $E_{EM}$ is in GeV, accurate to 1-2%.* The profile width has been measured in the Yakutsk and Utah experiments (Grigoriev *et al.* 1983, Baltrusaitis *et al.* 1985), but only for $E \sim 10^9$ GeV. The energy dependence is expected on theoretical grounds to take the form $\sigma^2 = A + BD_{10}\log E$, where $D_{10}$ is the elongation rate per decade, $\cong$ 65 g/cm$^2$ (Linsley and Watson 1981) and B is a characteristic length of order 60-70 g/cm$^2$ (conference paper HE4.4-5). Using the Yakutsk-Utah data to fix the value of A, one obtains $\sigma^2 = 1.1 \cdot 10^4 + 4.2 \cdot 10^3 \log E$ (Linsley 1983),† and finally, by substitution in (2),

$$E_{EM} \cong 0.71\ N_m^{1.025} \ . \qquad (3)$$

3. Relation between muon size and $E_{\mu\nu h}$. There is good agreement among independent measurements of the energy spectrum of air shower muons (Atrashkevich *et al.* 1983 and references therein). This spectrum is quite hard; almost half of the observed energy is given to particles with individual energies above 30 GeV. Over the range of shower energies where it has been studied ($3 \cdot 10^5$-$10^8$ GeV), the shape of this spectrum is invariant; hence the total energy of the observed muons is proportional to $N_\mu$(>1GeV), the number of muons (at sea level) with energy > 1 GeV, where the proportionality constant equals 10.0±.5 GeV. To obtain the energy given to neutrinos the observed muons are propagated backward to a production spectrum. In the air shower region it is found that $E_\nu \sim 0.4\ E_{\mu,obs}$, where $E_\nu$ includes both $\nu_\mu$ and $\nu_e$. This result checks with a forward propagation calculation by Hillas (1981). Experiment based estimates of $E_h$, the energy deposited by low energy hadrons, range from $0.8\ E_{\mu,obs}$ (Greisen 1956) to $0.3\ E_{\mu,obs}$. Adopting $E_h \sim 0.4\ E_{\mu,obs}$ as a conservative estimate, the total non-electronic contribution is obtained:

$$E_{\mu\nu h} = (18\ ^{+3.5}_{-1.5}\ \text{GeV}) \cdot N_\mu(>1\text{GeV})_{\text{sea level}} \ . \qquad (4)$$

---

* An alternative form which may sometimes be more convenient is $E_{EM} = (x_{hm}/428)\ N_m$, where $x_{hm}$ is the full width at half maximum (Linsley 1981).

† In the energy range of interest here, the simpler formula $\sigma = 130 + 10.2 \log E$ is equivalent.

*Table 1. Muon size for a given intensity from various experiments.*

| integral intensity $(m^2 sr\ s)^{-1}$ | $N_\mu$ (>1GeV) | muon threshold (GeV) | Ref. |
|---|---|---|---|
| $10^{-6}$ | $2.3 \times 10^4$ | 10.0 | VK* |
| $10^{-7}$ | 6.5 " | " | " |
| $10^{-8}$ | $1.6 \times 10^5$ | " | " |
| " | 1.6 " | 1.0 | Ha@ |
| $10^{-9}$ | 3.8 " | 10.0 | VK* |
| " | 4.0 " | 1.0 | Ha@ |
| $10^{-10}$ | $1.0 \times 10^6$ | " | " |
| $10^{-11}$ | 2.5 " | 0.22 | L*@ |
| " | 2.0 " | 0.70 | Dm* |
| " | 3.5 " | 0.75 | Ho* |
| " | 2.4 " | 1.0 | Dx |
| " | 2.6 " | " | Ha@ |
| $10^{-12}$ | 5.7 " | 0.70 | Dm* |
| " | 9.1 " | 0.75 | Ho* |
| $10^{-13}$ | $1.6 \times 10^7$ | 0.70 | Dm* |
| " | 2.4 " | 0.75 | Ho* |
| $10^{-14}$ | 6.4 " | " | " |
| $10^{-15}$ | $1.7 \times 10^8$ | " | " |
| $10^{-16}$ | 4.5 " | " | " |
| $10^{-17}$ | $1.2 \times 10^9$ | " | " |

* adjusted to 1 GeV threshold
@ adjusted to sea level

Neither this result nor the one expressed by (3) depends on any assumption about the primary composition; they are properties of cosmic rays *as they occur*, in this energy range, at the solar system. As an experimental result, (4) applies to the energy range given above, $3 \cdot 10^5$-$10^8$ GeV. Extrapolation up to $10^{11}$ GeV is justified unless there occurs some radical change affecting the production of *very high energy* muons and neutrinos.

4. Calorimetric all-particle energy spectrum. Data on the $N_\mu$ and $N_m$ spectra are summarized in Tables 1 and 2, in inverse form ($N_\mu$ and $N_m$ as functions of integral intensity). The (inverse) all-particle energy spectrum is obtained by adding together $E_{EM}$ from (3) and $E_{\mu\nu h}$ from (4), using tabulated values of $N_\mu$ and $N_m$ for the same intensity, in the range $10^{-6}$-$10^{-12}/m^2 sr\ s$ where there are reliable data for both $N_\mu$ and $N_m$. The result, changed to differential form, is shown in Fig. 1. In case of Table 1 the various $N_\mu$ values for a given intensity were averaged; in case of Table 2, the later results at Chacaltaya were used. There is good agreement with the Yakutsk energy spectrum in this range (Efimov and Sokurov 1983), and with Haverah Park results (Cunningham *et al.* 1980). The present result supports a rather high location, nearly $10^7$ GeV, for the transition region where the change of slope (knee) occurs.

5. Other results: conversion factors. As I showed previously, this derivation of the energy spectrum yields as by-products factors for converting $N_m$ and $N_\mu$ separately to primary energy, and also yields the fraction of primary energy given to electrons, vs energy (Linsley 1983). These results are shown in Fig. 2. The low value found for $E/N_m$, 1.3±.2, confirms an important prediction by Hillas (1983). An apparent conflict between results from Chacaltaya and from lower elevations is resolved. The earlier values of $N_m$ (La Pointe *et al.* 1968) were somewhat too low, but energies were about correct because the conversion factor was somewhat too high. The later values of $N_m$ are more nearly correct, but the energies were too high because the conversion factor was much too high. Although here the conversions, $N_m$ to E and $N_\mu$ to E, have been treated symmetrically, the energy dependence of the $N_\mu$-E 'conversion factor' makes this inconvenient in practice. Convenient formulae for representing the

$N_\mu$ data in Fig. 2 and Table 1 are:

$$N_\mu(>1\text{GeV})_{s.l.} = E(\text{GeV})^{0.835}/6.8, \quad (5)$$

$$J[>N_\mu(>1\text{GeV})]_{s.l.} = 3\cdot10^4 N_\mu^{-2.4}, \quad (6)$$

where J is in $m^{-2}sr^{-1}s^{-1}$.

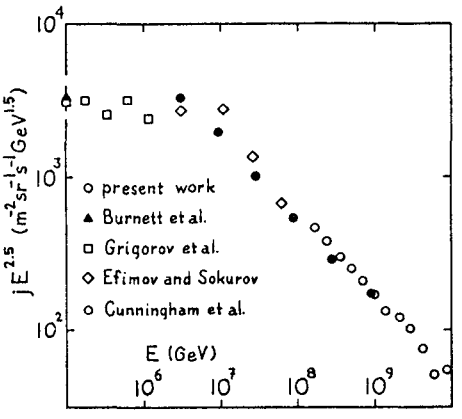


*Fig. 1. All-particle Energy Spectrum.*

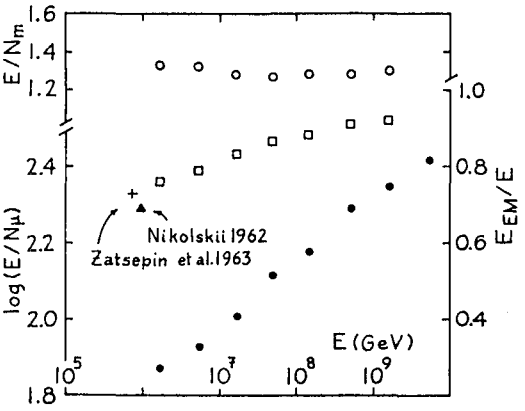


*Fig. 2. Other Results. Open circles $E/N_m$, squares $E_{EM}/E$ (r. h. scale), filled circles $\log(E/N_\mu)$.*

*Table 2. Maximum size for a given intensity from various experiments*

| integral intensity $(m^2 sr\ s)^{-1}$ | $N_m$ | obs. depth $g/cm^2$ | Ref. |
|---|---|---|---|
| $10^{-5}$ | $3.5 \times 10^5$ | 210 | AI |
| $10^{-6}$ | $1.3 \times 10^6$ | " | A |
| " | 1.3 " | 540 | LP |
| $10^{-7}$ | 4.2 " | " | " |
| $10^{-8}$ | $1.15 \times 10^7$ | " | " |
| " | 1.30 " | " | K |
| $10^{-9}$ | 3.6 " | " | LP |
| " | 4.0 " | " | K |
| $10^{-10}$ | $1.05 \times 10^8$ | " | LP |
| " | 1.20 " | " | K |
| $10^{-11}$ | 3.2 " | " | LP |
| | 4.0 " | " | K |
| $10^{-12}$ | $1.26 \times 10^9$ | " | " |
| " | $5. \times 10^8$ | 835 | L |
| $10^{-13}$ | $1.6 \times 10^9$ | " | " |
| $10^{-14}$ | $1. \times 10^{10}$ | " | " |

References. ANTONOV and IVANENKO 1975, Proc. 14th ICRC 8, 2708 (AI); ANTONOV *et al.* 1983, Proc. 18th ICRC 6, 19 (A); ATRASHKEVICH *et al.* 1983, Proc. 18th ICRC 11, 229; AUGER 1939, Rev. Mod. Phys. 11, 288; BALTRUSAITIS *et al.* 1985, Phys. Rev. Lett. 54, 1875; CUNNINGHAM *et al.* 1980, Ap. J. 236, L71; DIMINSTEIN *et al.* 1979, Proc. 16th ICRC 8, 122 (Dm); DIXON *et al.* 1974, J. Phys. A 7, 1010 (Dx); DOVZHENKO and POMANSKII 1964, Sov. Phys. JETP 18, 187; EFIMOV and SOKUROV 1983, Proc. 18th ICRC 2, 123; GREISEN 1956, *Progress in Cosmic Ray Physics* (North-Holland: Amsterdam); GRIGORIEV *et al.* 1983, Proc. 18th ICRC 6, 204; HARA *et al.* 1983, Proc. 18th ICRC 9, 198 (Ha); HILLAS 1981, *Proc. Paris Workshop on Cascade Simulations* (TCAST: Albuquerque) pp. 3, 13; 1983, *Proc. Cosmic Ray Workshop, Univ. Utah* (Bartol Res. Foundation: Newark) p. 1; HORTON *et al.* 1983, Proc. 18th ICRC 6, 124 (Ho); KAKIMOTO *et al.* 1981, Proc. 17th ICRC 11, 254 (K); KIROV *et al.* 1981, Proc. 17th ICRC 2, 109; LA POINTE *et al.* 1968, Can. J. Phys. 46, S68 (LP); LINSLEY and WATSON 1981, Phys. Rev. Lett. 46, 459; LINSLEY 1973, Proc. 13th ICRC 5, 3202 and 3205 (L); 1981, *Proc. Paris Workshop on Cascade Simulations* (TCAST, Albuquerque) p. 23; 1983, Proc. 18th ICRC 12, 135; McCOMB *et al.* 1977, J. Phys. G: Nucl. Phys. 5, 1613; VERNOV and KHRISTIANSEN 1968, Can. J. Phys. 46, S197 (VK).

# PRIMARY COSMIC RAY SPECTRUM IN THE $10^{13}$-$10^{16}$ eV ENERGY RANGE FROM THE NUSEX EXPERIMENT

G. Battistoni[1], E. Bellotti[2], C. Bloise[1], G. Bologna[3], P. Campana[1], C. Castagnoli[3], A. Castellina[3], V. Chiarella[1], A. Ciocio[1], D. Cundy[4], B. D'Ettorre Piazzoli[3], E. Fiorini[2], P. Galeotti[3], E. Iarocci[1], C. Liguori[2], G. Mannocchi[3], G. Murtas[1], P. Negri[2], G. Nicoletti[1], P. Picchi[3], M. Price[4], A. Pullia[2], S. Ragazzi[2], M. Rollier[2], O. Saavedra[3], L. Satta[1], S. Vernetto[3] and L. Zanotti[2].

[1] Laboratori Nazionali dell'INFN, Frascati, Italy.
[2] Dipartimento di Fisica dell'Università and INFN, Milano, Italy.
[3] Istituto di Cosmogeofisica del CNR, Torino, Italy.
[4] CERN, European Organization for Nuclear Research; Geneva, Switzerland.

## INTRODUCTION

The single muon intensity has been measured in the NUSEX experiment at various depth up to 10,000 hg/cm$^2$ s.r..

These intensities have been converted to a sea-level muon energy spectrum which is used to derive the primary all-nucleon flux.

From these data we are able to determine the slopes of the primary proton and helium spectra, which are thus used in a model for the primary composition producing the observed multiple muon rates.

## DATA REDUCTION AND PRIMARY SPECTRUM

The NUSEX detector is located in the Mt. Blanc tunnel at a vertical depth of about 5000 hg cm$^{-2}$ s.r. It consists of a cube of 150 t mass and 3.5 side, made of 136 horizontal planes 1 cm thick, interleaved with planes of tubes of 1 cm x 1 cm cross section, operating in the limited streamer mode. More details are reported elsewhere [1].

20429 muon events crossing at least 10 layers were recorded in a zenith angle range 0° - 75° during an effective working time of 18,946 hours from June 1982 to December 1984. The number of events for different multiplicities are reported in table 1.

The single muon intensity at different depths has been found using the procedure of Ref. 2. The general relation

$$I(h,\theta) = I_{\mu}^{\pi,K}(h) \cdot G^{\pi,K}(h,\theta) + I_{\mu}^{p}(h) \cdot G^{p}(h,\theta) \qquad (1)$$

has been fitted to the data. Here the $\pi$ and K superscripts refer to conventional muons from $\pi$ and K decay, the p superscript to prompt muons from charmed particle decays.

The angular enhancement functions have been calculated in Ref. 3 . The intensity of prompt muons is found < 4% on the considered range of depths, so that the second term in (1) has been neglected. The muon intensity is reported in Fig. 1. together with the intensity points measured with the spark chamber apparatus located in the Mt. Blanc tunnel, garage 27. The agreement is excellent, so giving a unique intensity-depth set of measurements from 3900 to 10000 hg/cm² s.r. very well represented by the relation

$$I_{\mu}^{\pi,K}(h) = (7.63\pm.48)\cdot 10^{-7}\exp[-h/(810.44\pm.84)]\,cm^{-2}s^{-1}sr^{-1}$$

Following the procedure of Ref. 2 we derive the primary all-nucleon spectrum in the relevant energy range $10^{13} \div 2\cdot 10^{14}$ eV :

$$\frac{dN}{dE_0} = (4.8\pm.2)E_0^{-2.79\pm.03}\ cm^{-2}s^{-1}sr^{-1}GeV^{-1}$$

The rates of events with exacty n muons have been calculated following the procedure described in Ref. 4.

$$\phi_n = \sum_i K_i(A) \int E_0^{-\gamma_i(A)} P_n(E_0,A)dE_0$$

where $P_n(E_0,A)$ is the probability to sample n muons of a shower resulting from the interaction of a primary with energy $E_0$, and mass A, and the primary spectrum is described as a superposition of single power spectra

$$\frac{dN}{dE_0} = \sum_i k_i(A)\ E_0^{-\gamma_i(A)} \qquad (i=p,\alpha,CNO,Mg,Fe)$$

Inputs to $P_n(E_0,A)$ come from the energy and radial muon distributions calculated by Gaisser and Stanev (Ref. 5) for our experimental site. We assume a value of -2.79 for the spectral index of proton and helium nuclei as determined from our data and normalize the flux at 10 TeV to the JACEE data. The spectral index for CNO and Mg groups is chosen slighty flatter as suggested by direct measurements to which we refer for relative normalization. The iron spectrum is normalized to a flux of $2.42\ 10^{-5}$ nuclei/(m²·sr·s·GeV/nucleon) at 100 GeV/nucleon, while its spectral index is considered as a free parameter.

Beyond a rigidity $R_c = 2\ 10^6$ GeV/c, all spectra steepen to $\gamma = 3.0$. The breaks for nuclei different from protons are at a total energy $(A/2)R_c$.

Fig. 2 shows that the measured rates are well described by an iron spectral index in the range 2.6 - 2.7.

This model describes very well both the all-nucleon flux in the range $10^{13}$ - $10^{14}$ eV and the all-particle flux between $10^{13}$ - $10^{16}$ eV (see for exemple the compilation of Hillas in Ref. 6). Normalization coefficients, slopes and breaking points or all components are summarized in table 2.

## CONCLUSION

We have determined a primary cosmic ray spectrum fitting both our experimental multiple muon rates and the all-nucleon flux derived from the single muon intensities underground.

In the frame of the interaction model developped by Gaisser, Elbert and Stanev, we are able to reproduce NUSEX muon data with a primary composition in which the iron spectrum is only slightly flatter than the proton one.

This result rules out the popular idea that the primary composition varies drastically with increasing energy, leading to the dominance of heavier nuclei at energies $10^{15}$ - $10^{16}$ eV.

## References

[1] G. Battistoni et al., Phys. Lett. 133B (1983) 454 and paper to be submitted to Nucl. Instr. and Meth.
[2] L. Bergamasco et al., Nuovo Cimento C6 (1983) 569.
[3] H. Bilokon et al., Nuovo Cimento C8 (1985) 93.
[4] G. Bologna et al., Nuovo Cimento C8 (1985) 76.
[5] T.K. Gaisser and T. Stanev : private communication.
[6] A.M. Hillas : Proceedings of the Cosmic Ray Workshop, edited by T.K. Gaisser (University of Utah, 1983), p.16.

## Figure Captions

Fig. 1 - Muon intensity underground at Mt. Blanc.
Fig. 2 - Comparison between experimental rates and the predictions of our model of primary composition for different values of the iron group spectral index.

Table 1

Rate of multiple muons

| Multiplicity | # events | Time |
|---|---|---|
| 1 | 20429 | |
| 2 | 211 | |
| 3 | 29 | 18946 hours |
| 4 | 4 | |
| 5 | 2 | |
| 6 | 1 | |

Table 2

| Group | K$_i$ ($m^{-2}s^{-1}sr^{-1}GeV^{-1}$) | $\gamma_i$ | Points of change of slope, E(GeV) |
|---|---|---|---|
| p | $3.28\ 10^4$ | 2.79 | $2\ 10^6$ |
| He | $1.75\ 10^4$ | 2.79 | $4\ 10^6$ |
| CNO | $6.20\ 10^3$ | 2.71 | $1.4\ 10^7$ |
| Mg | $9.20\ 10^3$ | 2.71 | $2.6\ 10^7$ |
| Fe | | 2.6÷2.7 | $5.2\ 10^7$ |

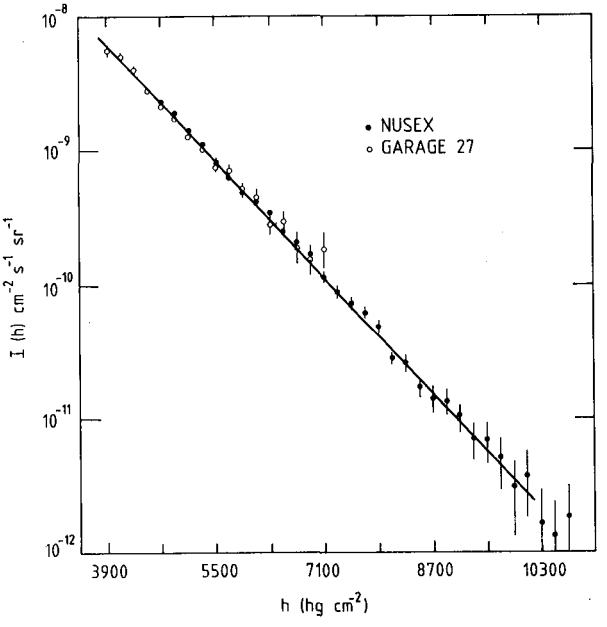


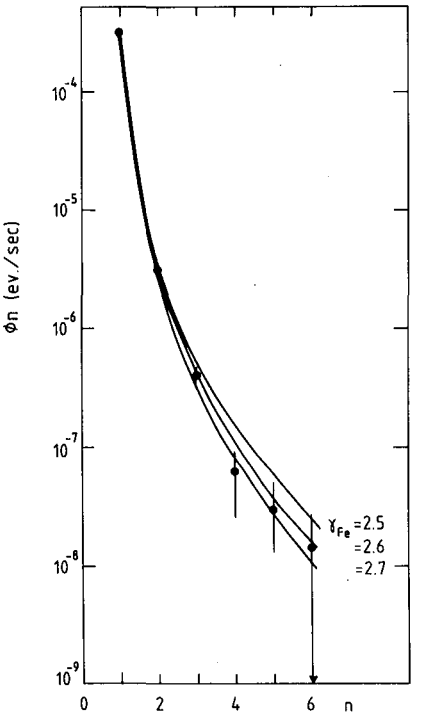

# A NEW MEASUREMENT OF THE COSMIC RAY ENERGY SPECTRUM BETWEEN $3x10^{15}$ eV AND $3x10^{16}$ eV

A.G. Gregory, J.R. Patterson and R.J. Protheroe
Department of Physics, University of Adelaide
Adelaide, South Australia, 5001.

ABSTRACT

We give the results of a new Cerenkov photon density spectrum measurement and present our derivation of the primary cosmic ray energy spectrum for energies from $3x10^{15}$eV to $3x10^{16}$eV.

1. Introduction. In a previous paper, Protheroe and Patterson[1] examined the information available from various types of Cerenkov light photon density spectrum measurements and proposed a conceptually simple but powerful experiment. From simulations, it was found that the photon density spectrum of nearly vertical air showers observed by a system of two detectors separated by 350 m was independent of nuclear mass composition and depended only on the primary energy spectrum. On the other hand, a system of two detectors close together (or a single detector) would be sensitive to the composition. By making these two measurements then, it is possible to determine the energy spectrum and obtain information about composition.

In practice, the experiment is complicated by the necessity to observe only near-vertical showers and to know the acceptance solid angle of the system. Either one severely collimates the detectors (or uses mirrors) or one allows the detectors an unrestricted field of view and selects the shower arrival directions by another technique, e.g. the use of a third detector and timing coincidence. Since the simulations in ref. 1 were made for unshielded detectors we have used the latter approach in order to avoid cutting out Cerenkov light produced in the later stages of development.

2. Techniques. Our system consisted of three 175 mm diameter 9623B photomultipliers (PMT), each with a collimator to cut out background light beyond 45° from the PMT axis. Full details of the experiment will be published elsewhere. In the energy spectrum measurement, two of these detectors were used to record photon densities and were separated by 350 m. The third detector was offset by 100 m to enable a coincidence timing system with pre-determined pulse widths and delays from each detector to restrict air shower arrival directions to a well defined solid angle (0.32 sr) centred about the zenith. For the composition measurement the density detectors were moved to 100 m separation, and the third detector to 31 m. The pulse widths and delays were adjusted to give an acceptance solid angle of 0.29 sr.

Calibrations were made throughout the night with a temperature stabilised green LED pulser mounted near the rim of the mechanical collimator to compensate for gain drifts. An absolute calibration of a blue LED system was made in the laboratory by comparing the PMT output with that due to a known flux of Cerenkov light photons produced by single muons passing through BK7 glass and has been described by Gregory et al[2]. This was used to calibrate the green pulsers in situ.

3. Observations. Initially, the fast PMT outputs were shaped by Ortec 485 main amplifiers, and the pulse heights were sampled and digitized. The system was tested at the Buckland Park field station and moved to a better observing site at Alice Springs for observations in May/June 1984. Alice Springs is at an elevation of 540 m and, for comparison with the simulations which were made for sea level, the detectors were tilted at 20° to the vertical in order to see showers at the same stages of development as in sea level observations. The pulse from the offset detector was appropriately delayed to tilt the acceptance solid angle for air showers by the same amount.

The results of this run for the May/June 1984 new moon period are shown in Fig. 1 by the open circles (details of the analysis are given below). With the rather slow electronics we were using, and the large field of view of the mechanical collimators, the results were subject to a fluctuating night sky noise component which became important below $\sim 3\times10^5$ photons $m^{-2}$. Estimates of the effect on the expected power law photon density spectra enabled approximate corrections to be made to these data and are indicated by the solid circles.

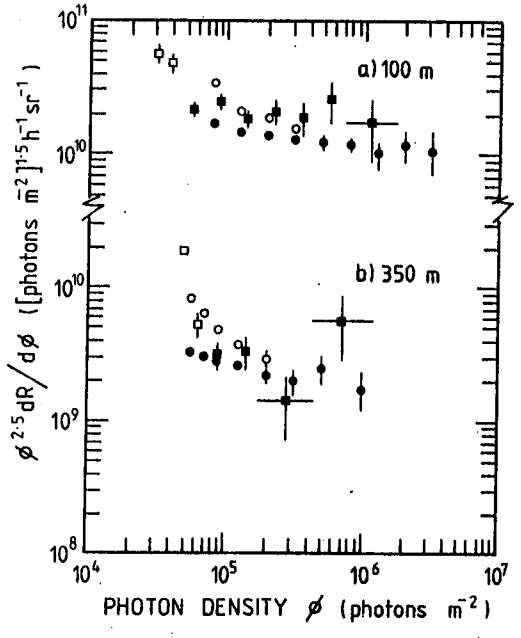


Fig. 1. Differential photon density spectra observed with (a) the 100 m system and (b) the 350 m system. Observations made at Alice Springs are indicated by open circles and are subject to biasses due to night sky noise below $\sim 3\times10^5$ photons $m^{-2}$. An approximate correction based on the characteristics of the system and an assummed night sky brightness of $6.4\times10^{11}$ photons $m^{-2}$ $s^{-1}$ $sr^{-1}$ has been made and these corrected data replotted as filled circles. Observations made subsequently at Woomera are indicated by filled squares and are subject to biasses due to night sky noise below $\sim 5\times10^4$ photons $m^{-2}$ (open squares).

Following the analysis of these observations, the electronics were redesigned around a LeCroy 2249SG Integrating ADC and the mechanical collimators were extended to reduce the sky background. The acceptance solid angle of the system for air showers was also reduced (to 0.082 sr and 0.11 sr for the 350 m and 100 m systems respectively) so that the mechanical collimators did not obstruct any Cerenkov light from those air showers accepted. The net result of this was to reduce the night sky noise, thus allowing reliable measurements to be made to lower photon densities. The modified system was operated at Woomera (altitude 166 m, tilted at 10° to the zenith) during the March 1985 new moon period. The results from this run are shown by the solid squares in Fig. 1 and are in excellent agreement with earlier runs at high photon densities. At low photon densities, the results are consistent with the corrected Alice Springs data except for the lowest two points (plotted as open squares) which are affected by night sky noise.

4. Data Analysis. For each event, the digitizer outputs from the two density measuring detectors were read by the computer and converted to photon densities using the calibration results. The lower of the photon densities was binned in photon density on a logarithmic scale. During the readout and analysis, the system was automatically inhibited and was de-inhibited by the computer on completion of its analysis. This resulted in a dead-time of ~0.3 s per event. An internal clock recorded the live time. Although each event is accurately calibrated, the discriminator threshold varied during the run due to gain drifts and changing night sky brightness within the field of view. For each run, only events with photon densities well above the discriminator threshold were included in the final analysis. The acceptance solid angle was calculated from the pre-set discriminator output pulse widths and delays. Thus, for each run the exposure (live time x solid angle) and minimum acceptable photon density were determined. The data from separate runs were then combined to obtain the results shown in Fig. 1. Our final result based on those data of Fig. 1 which were unaffected by night sky noise are replotted in Fig. 2.

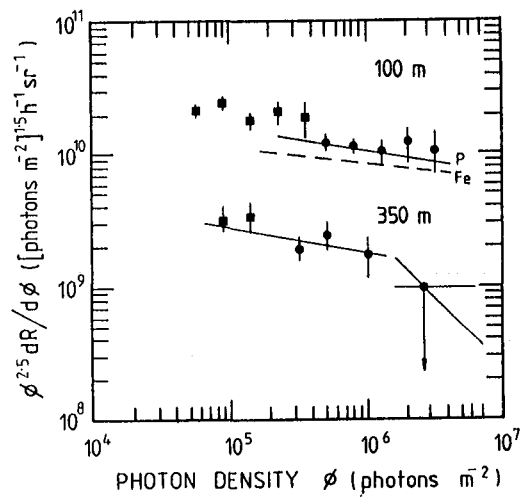


Fig. 2. Photon density spectrum data from Fig. 1 which are not subject to biasses due to night sky noise. Points with large error bars are also omitted for clarity. A power-law fit to the 350 m data is plotted. Upper limits to power law spectra above $1.6\times10^6$ photons $m^{-2}$ are also plotted. Expected 100 m photon density spectra based on the cosmic ray energy spectrum obtained from the 350 m data are plotted for two extreme assumptions about the nuclear mass composition.

5. Discussion. We can derive the primary cosmic ray energy spectrum from the 350 m data independently of the nuclear mass composition. The 350 m photon density spectrum data of Fig. 2 up to $10^6$ photons $m^{-2}$ are well fitted by a power law in photon density. The best fit is indicated in the figure and has a differential index of $\gamma_\phi = 2.7\pm0.2$. Above $1.6\times10^6$ photons $m^{-2}$, no events were recorded, indicating a steepening in the cosmic ray spectrum, and 1σ upper limits to power law spectra above this photon density have been plotted in Fig. 2 for $\gamma_\phi$ ranging from 2.5 to 3.5. Using Fig. 9(a) of ref. 1, which relates $\gamma_\phi$ to $\gamma_E$ for different spacings, this corresponds to a spectral index $\gamma_E = 2.72 \pm 0.2$ for the cosmic rays. The cosmic ray energy spectrum in the energy range $3\times10^{15}$ - $3\times10^{16}$ eV (corresponding to $10^5$-$10^6$ photons $m^{-2}$ for the 350 m system) may then be obtained directly with the aid of Figs. 8 and 9(b) of ref. 1 which relate photon density to primary energy and the absolute fluxes. The result is shown in Fig. 3 where it is compared with previous measurements of the cosmic ray energy spectrum. Our result is consistent with the extrapolation to lower energies of the Haverah Park data if there is a steepening of the spectrum at ~$3\times10^{16}$ eV. Comparison with balloon and satellite data at

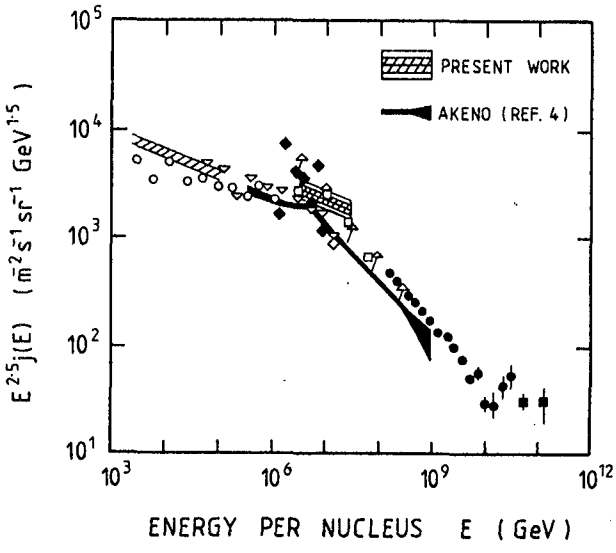


Fig. 3 Primary cosmic ray energy spectrum measurements (see ref. 3 for key to data). Our result at $3x10^{15}$-$3x10^{16}$ eV is indicated and is subject to statistical and systematic errors each of about 10%.

lower energies would indicate the presence of a "kneecap". The Akeno data also indicate the presence of a kneecap but at a factor of ~3 to 5 lower energy.

For the cosmic ray energy spectrum we derived from the 350 m data, we can predict the photon density spectrum for the 100 m system assuming different nuclear mass compositions with no other adjustments being made. This has been done for two extreme assumptions, 100% protons or 100% Fe-nuclei, using simulation results similar to those described in ref. 1 but appropriate to the 100 m system. The expected 100 m spectra are plotted in Fig. 2 for comparison with the data. (Note that for the 100 m system, $3x10^{15}$-$3x10^{16}$ eV corresponds to higher photon densities than for the 350 m system.) Unfortunately, with the detectors moved apart to 100 m some sensitivity to composition is lost (all sensitivity is lost for 350 m). Also, because of the relatively low power law index of the cosmic ray spectrum in this energy range the two curves are rather close together. Nevertheless, the data appear to favour a relatively light composition although a heavy composition is not ruled out. More data would be required to resolve this question. Whatever the composition, however, provided it remains unchanged down to $\sim10^{15}$ eV, the 100 m data would indicate that the cosmic ray spectrum we derived between $3x10^{15}$ and $3x10^{16}$eV continues unchanged down to $\sim10^{15}$ eV.

6. Acknowledgements. We are grateful to Professor J. Thomas of the Physics Department of the R.A.A.F. Academy for use of facilities at Alice Springs, and to the Area Administrator of D.S.C. Woomera for facilities at Woomera. This work has been supported in part by grants from the University of Adelaide and the A.R.G.S. and by provision of a Queen Elizabeth II Fellowship and Research Support Grant to R.J.P.

References.

1. R.J. Protheroe and J.R. Patterson, 1984: J. Phys. G: Nucl. Phy., 10, 841.
2. A.G. Gregory, J.R. Patterson and B.R. Dawson, 1983: Proc. 18th ICRC (Bangalore), 8, 145.
3. R.J. Protheroe, 1984: J. Phys. G: Nucl. Phys., 10, L99.
4. M. Nagano et al., 1984: J. Phys. G: Nucl. Phys., 10, 1295.

# STUDY OF THE COMPOSITION OF COSMIC RAYS WITH ENERGY .7<E<3. EeV

Baltrusaitis, R.M., Cassiday, G.L., Cooper, R., Elbert, J.W.,
Gerhardy, P.R., Loh, E.C., Mizumoto, Y., Sokolsky, P., & Steck, D.
Department of Physics, University of Utah, Salt Lake City, UT 84112

Gaisser, T.K., & Stanev, T.
Bartol Research Foundation of the Franklin Institute
University of Delaware, Newark, Delaware

ABSTRACT

The longitudinal shower development of EAS observed in the Fly's Eye is used to determine the distribution of $X_{max}$, the depth in the atmosphere of the EAS maximum. Work in progress to compare data and Monte Carlo simulations of proton and iron primaries is described. Preliminary evidence is in favor of a substantial contribution from light primaries.

1. Introduction. The overall longitudinal development of the EAS detected by the Fly's Eye(1) can be used to determine the depth in the atmosphere in gm/cm$^2$ of the EAS maximum $X_{max}$. The distribution in $X_{max}$ is in principle sensitive to the composition of the primary particles since iron nuclei and protons will give rise to $X_{max}$ distributions that peak at shallower and deeper depths and have narrower and wider widths, respectively. It also follows that a mixed composition will have a broader $X_{max}$ distribution than any single source.

In what follows, we discuss the reconstruction of longitudinal shower profiles and the systematics of determining $X_{max}$ distributions and then discuss work in progress on Monte Carlo simulations, which include the details of the Fly's Eye acceptance, for pure protons, iron, and a mixed composition.

2. Shower Size Measurement. A fit to the relative time of arrival of light to succeeding phototubes in the event-detector plane yields $R_p$, the impact parameter of the shower to the detector, and the zenith and azimuthal angles of the EAS. Measured values of optical gathering power, efficiencies and electronic gains and pedestals are used to convert photoelectron yields into apparent brightness, i.e., numbers of photons arriving at the detector from the source. This can be converted into intrinsic source fluorescent brightness after correcting for: (a) directly produced Cerenkov light beamed in the direction of the detector; (b) Cerenkov light scattered in the direction of the detector due to Rayleigh and Mie scattering; and (c) atmospheric attenuation of light. The details of these corrections are described in reference 1. The intrinsic fluorescence brightness can be translated directly into a shower size using the known nitrogen fluorescence efficiency.

The Cerenkov light production model, and in particular, the dependence of the Cerenkov light intensity on emission angle has been checked by using a sample of events seen by both Fly's Eye I and Fly's Eye II, a smaller station situated 3.3 km from Fly's Eye I. We find good consistency in size estimates of sections of EAS viewed

simultaneously at different emission angles by the two eyes.

The size versus depth distributions are fitted with a Gaussian form and the $X_{max}$ and energy of the event determined(1). The Gaussian form fits most showers well. Figure 1 shows a typical shower profile.

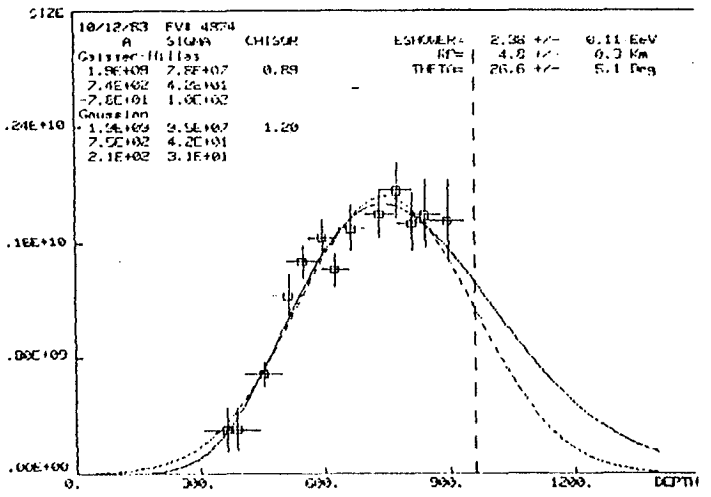


Figure 1. Typical Longitudinal Shower Profile

3. Systematics of Shower Maximum Distributions The absolute depth of $X_{max}$ is the parameter most sensitive to systematic errors of any that we measure. Symmetric random errors in the zenith angle, $\theta_z$, result in non-symmetric errors in $X_{max}$. Symmetric errors in $R_p$ also yield non-symmetric errors in $X_{max}$ because of the exponential atmospheric density distribution. There is also an intrinsic correlation between $X_{max}$ and the shower energy. Showers whose reconstruction err to smaller $R_p$ and larger $\theta_z$ will have systematically deeper $X_{max}$ and smaller estimated energy while errors that lead to larger $R_p$ and smaller $\theta_z$ yield smaller $X_{max}$ and larger energy estimates. This is a direct consequence of random errors and the exponential nature of the atmosphere. Any additional systematic bias in $\theta_z$ or $R_p$ will shift the $X_{max}$ distributions accordingly.

To reduce these effects to a minimum, we consider events that are very well reconstructed, with $R_p$>2.0 km, projected track length >50°, $SR_p/R_p$<.1, $S\theta_z$<10° and relative uncertainties in Gaussian width, $X_{max}$, and energy of <.4. These cuts also have the effect of reducing the Cerenkov subtractions to a level where 50% variation in the Cerenkov light model parameters do not significantly affect the $X_{max}$ distributions. Since any residual reconstruction bias will affect data near the tails of the energy distribution, we cut on .7<E<3 EeV, around the maximum of our energy acceptance. We believe residual systematic effects in this data sample will produce less than a ± 50 gm/cm$^2$ shift in the average $X_{max}$. We note that the width of the $X_{max}$ distribution is much less sensitive to systematic errors. We estimate the systematic error in the width to be ± 10 gm/cm$^2$. The resultant distribution in $X_{max}$ is shown in Figure 2. The average $X_{max}$ for this sample is 730±60 gm/cm$^2$ while the width (standard deviation) is 120±40 gm/cm$^2$.

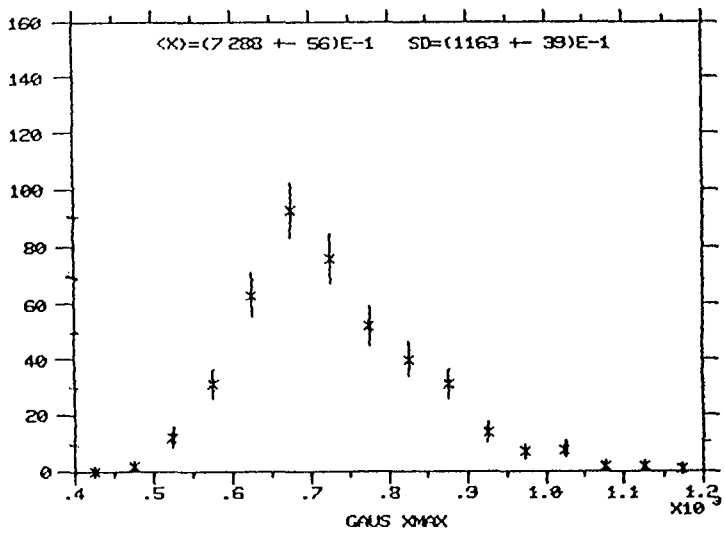


Figure 2. Distributions of $X_{max}$ in $gm/cm^2$.

4. Monte Carlo Generation

Proton and iron induced showers are generated in a Monte Carlo program with the following input. Protons are assumed to obey Hillas pure scaling with the only scale violating effects being rising cross-sections as parameterized by Gaisser and Yodh(2). The mean inelasticity is assumed to be .5. For the case of iron primaries a superposition model is assumed. The Monte Carlo follows hardons and electromagnetic particles down to 1/30th of the primary energy after which parameterizations of shower development are used. We use these showers to predict the number of photoelectrons and relative time delays observed in the detector and generate fake events which are then passed thru the same reconstruction and analysis programs as the real data. This work is in progress but preliminary indications are that the depth of maximum distribution for heavies is substrantially narrower than that for protons. It is important to note that comparing the observed $X_{max}$ distributions to theoretical predictions without taking into account the details of detector response can lead to misleading conclusions.

5. Conclusions. Although we are not yet ready to quote quantitative comparisions between the data and Monte Carlo simulations, preliminary evidence based on comparisons of the widths of the $X_{max}$ distribution to Monte Carlo is in favor of a substantial contribution from light primaries to the cosmic ray composition at these energies. Detailed comparisons will be forthcoming.

6. Acknowledgements. We gratefully acknowledge the United States National Science Foundation for its generous support of this work under grant PHY8201089.

References.

1. Baltrusaitis, R.M., et al., Nuclear Instruments Methods (to be published).
2. Gaisser, T.K., and Yodh, G.B., Ann., Rev. of Nucl. and Particle Science, 30 (1980), p.475.

# THE MUON CONTENT OF EAS AS A FUNCTION OF PRIMARY ENERGY

P. R. BLAKE, W. F. NASH, M. S. SAICH and A. J. SEPHTON
University of Nottingham, England.

1. Introduction At Haverah Park the muon content of EAS has been measured over the wide primary energy range $10^{16}$ to $10^{20}$ eV. At the Bangalore Conference it was reported (Blake et al, 1983) that the relative muon content of EAS decreases smoothly [$\sim \rho(600\ m)^{-0.94}$) over the energy range $10^{17}$ - $10^{19}$ eV and therefore concluded that the primary cosmic ray flux has a constant mass composition over this range. In the same paper (on the basis of a preliminary analysis) it was also reported that an apparent significant change in the power index occurs below $10^{17}$ eV [$\rho_c(250\ m)^{-0.78}$]. Such a change would indicate a significant change in primary mass composition in this range.

Further analysis confirms the earlier conclusions concerning EAS of energy $\geq 10^{17}$ eV. However post-Bangalore analysis of data in the $10^{16}$ - $10^{17}$ eV range revealed a previously overlooked selection bias in the Bangalore data set. This paper presents the full analysis of the complete data set in the energy range $10^{16}$ - $10^{17}$ eV with the selection bias eliminated.

2. Methods Three 10 $m^2$ muon detectors ($\sim$ 400 MeV threshold) were operated in conjunction with the deep water Cerenkov tank array (operated by the University of Leeds EAS group) at the Haverah Park site. Two of these muon detectors were immediately adjacent to large area water Cerenkov detectors, enabling a direct measurement of the ratio of the muon response to the water Cerenkov response ($\rho_\mu / \rho_c$) to be made. The water Cerenkov response ($\rho_c$) is dominated at low core distances by the electromagnetic response. The directly measured ratio ($\rho_\mu / \rho_c$) has the advantage of not being very sensitive to EAS parameters and therefore not sensitive to any inaccuracies in determining these parameters.

3. Results ($10^{16}$ - $10^{17}$ eV) The basic problem in establishing an accurate determination of the muon content over a large primary energy range arises from the measurement technique. Inevitably in most arrays (including the Haverah Park array) the core distance range covered is a strong function of primary energy (or shower size). The ratio ($\rho_\mu / \rho_c$) itself will be a function of core distance and thus direct determination of $\rho_\mu / \rho_c$ at a specific core distance is limited to a small range of primary energies. If a relationship of the form $\rho_\mu = k\ \rho_c^{\alpha}$ is adopted, k can normally be regarded as constant at a particular core distance (R); the power index (normally 0.94) may be a function of core distance and shower size. A core distance dependence would arise if the lateral density distributions of $\rho_\mu$ or $\rho_c$ significantly change with shower size. Measurements indicate that the lateral distribution of $\rho_\mu$ is unchanging at energies > $10^{16}$ eV. However the lateral distribution function of the electromagnetic component (and therefore $\rho_c$) does

show some change as the electromagnetic cascade maximum penetrates more deeply into the atmosphere as $E_p$ increases. Thus in determining the exponent '$\alpha$' it is sensible to limit the core distance range to as small a core distance interval as is statistically feasible.

The available experimental data were divided into three overlapping intervals of core distance:- 50 m $\leq$ R $\leq$ 150 m; 100 m $\leq$ R $\leq$ 200 m; and 150 m $\leq$ R $\leq$ 250 m. The data were further subdivided into four $\sec\theta$ intervals 1 → 1.1 → 1.2 → 1.3 → 1.4 and six shower 'log' size intervals. The data were then used to calculate the mean measured muon and water Cerenkov responses at R = 100 m, 150 m and 200 m. The results for $1.0 < \sec\theta < 1.1$ are displayed in Table 1 & Figure 1.

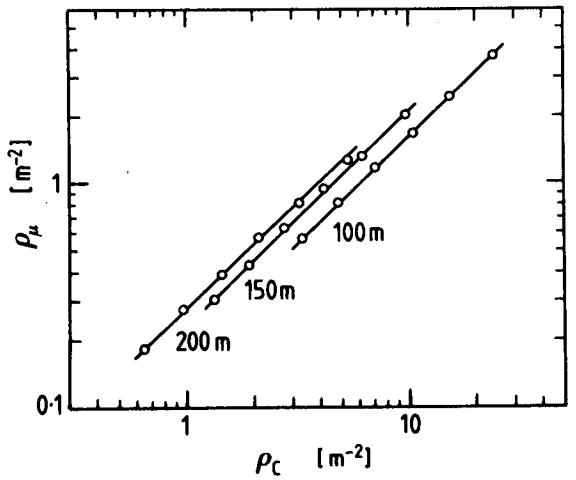


Clearly the $\rho_\mu/\rho_c$ ratios change smoothly over this decade of primary energy.

Table 2 shows the best fit values of $\alpha$ obtained from linear regression fits on the relationship $\rho_\mu = k\rho_c^{\alpha}$ for all the R and $\sec\theta$ intervals.

FIGURE 1 Measured $\rho_\mu$ versus measured $\rho_c$ at three specific core distances.

| R | $\rho_{150}$ /m$^2$ | N | $\overline{\rho_\mu}$ /m$^2$ | $\pm\,\Delta\rho_\mu$ | $\overline{\rho_c}$ /m$^2$ | $(\overline{\rho_\mu}/\overline{\rho_c})$ | $\pm\,\Delta\rho_\mu/\rho_c$ |
|---|---|---|---|---|---|---|---|
| 100 m | 1.23 | 2466 | 0.560 | 0.011 | 3.306 | 0.169 | 0.003 |
| | 1.81 | 2362 | 0.805 | 0.017 | 4.833 | 0.167 | 0.004 |
| | 2.66 | 1793 | 1.188 | 0.028 | 7.091 | 0.168 | 0.004 |
| | 3.90 | 1106 | 1.664 | 0.030 | 10.586 | 0.157 | 0.003 |
| | 5.73 | 529 | 2.430 | 0.11 | 15.841 | 0.154 | 0.007 |
| | 8.41 | 234 | 3.764 | 0.25 | 24.209 | 0.155 | 0.010 |
| 150 m | 1.23 | 2040 | 0.306 | 0.007 | 1.333 | 0.230 | 0.005 |
| | 1.81 | 2303 | 0.432 | 0.009 | 1.915 | 0.226 | 0.005 |
| | 2.66 | 2065 | 0.634 | 0.014 | 2.773 | 0.229 | 0.005 |
| | 3.90 | 1397 | 0.930 | 0.025 | 4.119 | 0.226 | 0.006 |
| | 5.73 | 820 | 1.301 | 0.045 | 6.239 | 0.209 | 0.007 |
| | 8.41 | 378 | 2.025 | 0.104 | 9.907 | 0.205 | 0.010 |
| 200 m | 1.23 | 904 | 0.179 | 0.006 | 0.648 | 0.276 | 0.009 |
| | 1.81 | 1335 | 0.272 | 0.007 | 0.979 | 0.278 | 0.007 |
| | 2.66 | 1540 | 0.368 | 0.010 | 1.438 | 0.268 | 0.007 |
| | 3.90 | 1287 | 0.584 | 0.016 | 2.098 | 0.278 | 0.008 |
| | 5.73 | 886 | 0.809 | 0.027 | 3.255 | 0.249 | 0.008 |
| | 8.41 | 470 | 1.255 | 0.058 | 5.141 | 0.244 | 0.011 |

Table 1 (previous page) Mean muon ($\bar{\rho_\mu}$) and water Cerenkov $\bar{\rho_c}$ densities as a function of core distance (R) and shower size ($\rho_{150}$) - $1.0 \leq \sec\theta \leq 1.1$.
[$\rho_{150}$ is the water Cerenkov response in vertical equivalent muons at 150 m from the EAS axis. N = no. of EAS used in the analysis]

| R | Secθ 1.0 - 1.1 | Secθ 1.1 - 1.2 | Secθ 1.2 - 1.3 | Secθ 1.3 - 1.4 |
|---|---|---|---|---|
| 100 m | 0.95(0.01) | 0.92(0.02) | 0.90(0.02) | 1.01(0.04) |
| 150 m | 0.94(0.02) | 0.95(0.02) | 0.99(0.02) | 0.99(0.06) |
| 200 m | 0.94(0.02) | 0.94(0.03) | 0.93(0.08) | 0.90(0.05) |

Table 2 Values of $\alpha$ in the relationship $\rho_\mu = k\rho_c^{\alpha}$ as a function of R and θ.

Clearly, at least for low zenith angles, an average value of $\alpha = 0.94$ fits the data well in the core distance range 50 m → 250 m and over the primary energy range $1.6 \times 10^{16}$ eV < $E_p$ < $1.6 \times 10^{17}$ eV.

4. Muon Content $10^{16} - 10^{19}$ eV Data acquired in the primary energy range $10^{17} - 10^{18}$ eV from the infilled 500 m detector array at Haverah Park enables $\rho_\mu$ (200 m) and $\rho_c$ (200 m) to be determined for the decade of energy above $10^{17}$ eV. The results are plotted in Figure 2 which shows the complete data from $10^{16} - 10^{18}$ eV.

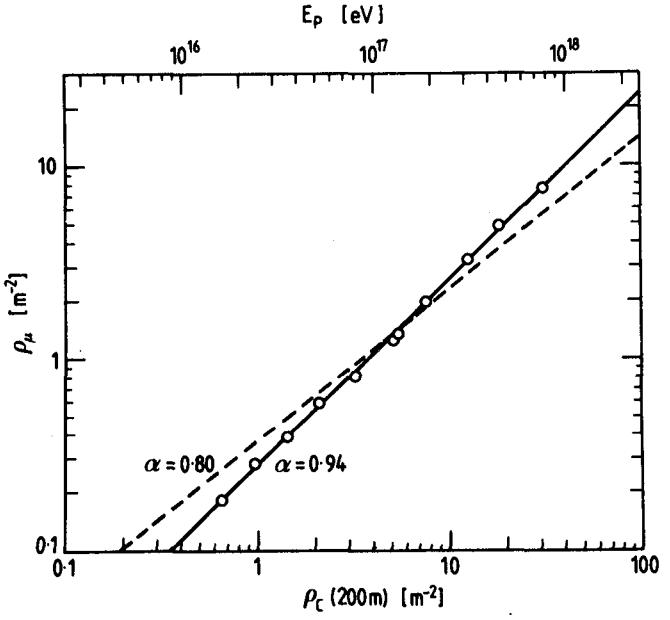


FIGURE 2 Measured $\rho_\mu$ versus $\rho_c$ at 200 m over energy range approximately $10^{16} - 10^{18}$ eV.

It is clear that a relationship of the form $\rho_\mu$ (200 m) $\propto \rho_c$ (200 m)$^{0.94}$ fits smoothly and well over these two decades of energy. This implies a smooth gradual change in the height of the electromagnetic cascade maximum throughout these two decades.

Thus the muon data yields strong evidence that there is no marked primary mass change occurring in the $10^{16}$ to $10^{17}$ eV region as has been suggested. If there is a significant change in primary mass, as suggested by Chantler et al (1983), then the muon density would be approximately 50% higher at $10^{16}$ eV than is measured leading to a value of $\alpha \sim 0.8$ [Blake et al, 1983]. Such a low value of $\alpha$ is clearly incompatible with the measured data (see Figure 2).

Comparison of the $10^{17}$ to $10^{18}$ eV decade with energies above $10^{18}$ eV has been carried out at a core distance of R = 600 m. In this region the data and conclusions remain unchanged since Blake et al (1983). Again the observations yield a smooth and normal change in muon content in the range $10^{17}$ eV to $10^{18}$ eV, implying no significant primary mass change over the energy range.

5. Discussion and Conclusions The results presented above lead to the conclusion that the muon content of EAS (relative to the water Cerenkov response) decreases smoothly in a constant manner at primary energies above $10^{16}$ eV and therefore suggest a constant primary mass composition in this energy region. A direct and constant relationship between the primary mass energy ($E_p$) and the water Cerenkov response $\rho_c$ (R) is assumed. The water Cerenkov response at 500 m core distance, $\rho$(500), [or at 600 m, $\rho$(600)] is used as the shower size parameter at Haverah Park for energies > $10^{17}$ eV and the relationship between $\rho$(500) and $E_p$ is of the form $E_p = 3.87 \times 10^{17} [\rho(500)]^{1.018}$ [HILLAS, Model A]. Thus $\rho_\mu \propto \rho_c^{0.94}$ implies $\rho_\mu \propto E_p^{0.92}$ at 500 m from the EAS axis.

Assuming therefore that this result does indicate a constant primary mass composition at energies greater than $10^{16}$ eV it does give strong support to the results from other studies of muons in EAS at these energies. The Akeno group (Nagano et al, 1984) find that the size spectra for both electrons and muons are unchanging above $10^{16}$ eV. Thus any change from heavy primary nuclei to a light mass composition flux must occur at energies below $10^{16}$ eV.

References

Blake, P. R., et al.; 18th Int. Cos. Ray. Conf., Bangalore, 11, 289 (1983).

Chantler, M. P., et al.; J. Phys. G 9, L27 (1983).

Nagano, M., et al.; J. Phys. G. 10, 1295 (1984).

# ON THE POSSIBILITY OF DETERMINING THE AVERAGE MASS COMPOSITION NEAR $10^{14}$ eV THROUGH THE SOLAR MAGNETIC FIELD

J. Lloyd-Evans*
NASA/Goddard Space Flight Center, Greenbelt, MD 20771

ABSTRACT

The discovery of primary U.H.E. gamma-rays has spawned plans for a new generation of air shower experiments with unprecedented directional resolution ($\lesssim 1^0$). Such accuracy permits observation of a cosmic ray "shadow" due to the solar (and lunar) disc. Particle trajectory simulations through models of the large scale solar magnetic field have been performed. The shadow is apparent above $10^{15}$ eV for all cosmic ray charges $|Z| < 26$; whereas, at lower energies, trajectories close to the Sun are bent sufficiently for this shadow to be lost. The onset of the shadow is rigidity dependent, and occurs at an energy per nucleus of $\sim Z \times 10^{13}$ eV. The possibility of determining the average mass composition near $10^{14}$ eV from 1 year's observation at a mountain altitude array is investigated.

1. Introduction. A challenge, proposed as a comment by Clark [1], to observe a narrow angle shadow in the cosmic ray flux due to solar and lunar absorption has not been taken up by air shower experiments. The reason is clear; for a statistically significant ($> 3\sigma$) deficit from the Sun or Moon, the whole-sky event number to be registered (assuming 1 sr exposure) is $\sim 3.10^6 \times d\theta^2/f$ ($d\theta$ = semi angle of directional resolution (degs); $f \simeq 0.1$, is the duty cycle for observing the Sun or Moon). Thus, with current resolution (typically $d\theta \sim 2°$) $\sim 10^8$ events are required. However, the discovery of primary U.H.E. $\gamma$-rays has spawned plans for a new generation of air shower arrays with unprecedented directional resolution [2,3]. It may be possible [3] to obtain $d\theta \sim 0.5°$, so that with a reasonable trigger rate of $\sim 0.2$ sec$^{-1}$, observation of cosmic ray shadows would be possible in 1 year's integration time.

The Moon acts as a 'passive absorber' at all air shower rigidities ($> 10^{13}$ eV/nucleus) since the effect of geomagnetic fields are insignificant above TeV energies. The directional resolution of air shower arrays is notoriously difficult to estimate; the lack of calibration point sources has resulted in reliance on calculations of the cumulative effects of numerous experimental limitations. Consequently, observation of the Moon's shadow will greatly aid the search for potential U.H.E. sources.

That the Sun is an 'active absorber' (i.e., the shadow is rigidity dependent) in the air shower regime can be seen simply. Above an energy where the particles' gyroradii are comparable to the solar radius, a narrow angle shadow cannot be observed. Putting $B \sim 1G$, $r_g \sim$

* Also University of Maryland, Department of Physics and Astronomy College Park, MD 20742

$7 \times 10^{10}$ cm and adopting the high energy limit (rigidity $\alpha$ total energy/z) the loss of a shadow is expected for energies of order z x $2.10^{13}$ eV. If the rigidity dependence can be modelled accurately, we have the possibility of using the large scale solar magnetic field as a crude magnetic spectrometer [4].

Here, we consider a simple model for the field within 1 A.U. and calculate trajectories of particles with arrival directions within 1° of the Sun. The discriminating power of the technique for charge resolution near $10^{14}$ eV is estimated, and limitations due to field approximations are discussed.

2. Method. Application of the potential source surface technique [5], and the 'garden-hose' field topology [6] have been very successful in interpreting the measured ecliptic field topology near 1 A.U. [7]. We consider a simple potential source surface at 2 $r_0$, and extend the field to 1 A.U. using Parker's equations [6] with $\Omega = 2.7 \times 10^{-6}$ and V = 400 Km $s^{-1}$. Fluctuations are imposed by adding a component of equal magnitude at an angle of $|d\theta|$r.m.s. = 20° over a scale length of 1 $r_0$. A 4 sector structure is also imposed, with the field direction reversing across the sector boundary.

Particle trajectories are computed by step-wise numerical integration of the equations of motion, with the particle's constant velocity as a constraint. The calculations have been checked by examining the circular orbits of particles fired perpendicular to uniform fields. The step-length is the smaller of (a) $10^{-2}$ x gyroradius or (b) $10^{-2}$ $r_0$. A step-length 10 x smaller results in negligible trajectory differences. Negatively charged particles are fired back from the Earth within a ~ 1° cone centered on the Sun. Trajectories are followed until they either intercept or miss the solar surface. Two thousand five hundred trajectories are computed over the acceptance cone for each field configuration and rigidity.

In Figure 1, the proportion of events within the cone which intercept the Sun is shown as a function of particle total energy for proton and Fe primaries (Model II). For comparison, the results for a simple dipole field, with no fluctuations, are also shown (Model I).

3. Discussion. It must be emphasized that: (1) the 'saturation obscuration' (in this case 18%) and zero obscuration are model independent, depending solely on the air shower array's field of view (in this case $d\theta = 0.6°$); (2) the separation of nuclear species is model independent, being $\alpha$ Z; (3) as indicated in Figure 1, the energy at which the shadow appears is very model dependent. In particular, the magnitude and scale length of the field within ~ $5r_0$ are of paramount importance. Model II may considerably underestimate the field magnitude within $2r_0$, but overestimates the scale length. We believe there is a factor of ~ 5 uncertainty in the energy at which the shadow appears, and that Model II is a reasonable lower limit to the transition energy.

In Figure 1 the rise-energy (over which the obscuration rises from 10 to 50%), $E_{50\%}$, is ~ Z x 5 TeV, and $E_{90\%}$ ~ Z x 18 TeV (or, as a fraction of $E_{50}$: $\Delta E_{50}$ ~ 0.49, $\Delta E_{90}$ ~ 1.9). These two parameters would be severly underestimated (and hence the power to discriminate between composition models curtailed) if (a) the field of view was

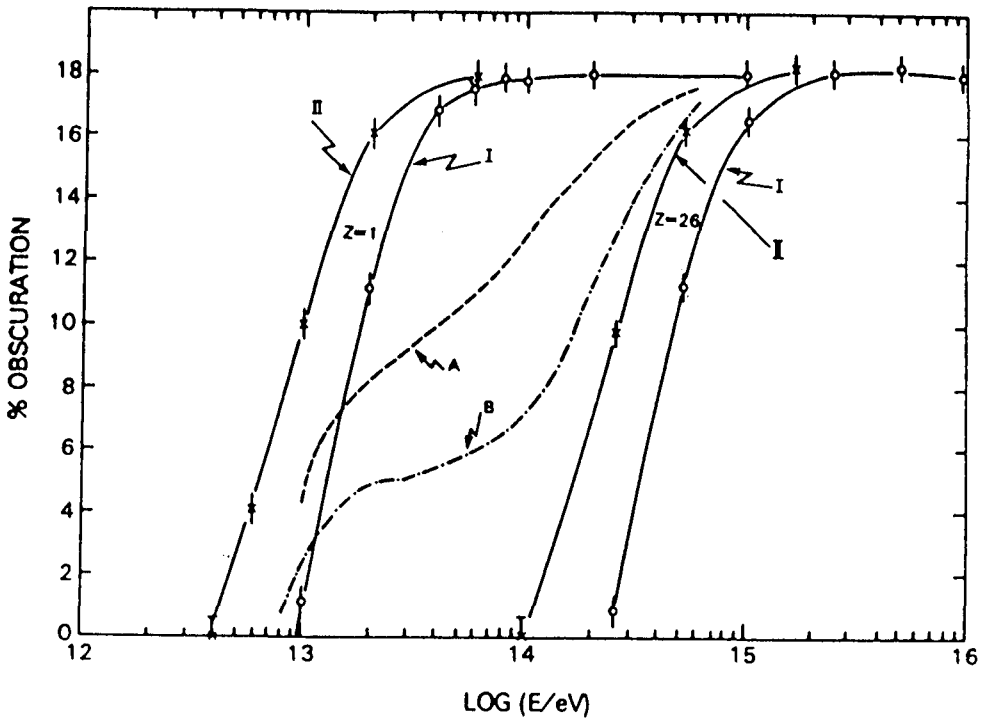


Fig. 1. The appearance of a solar shadow within a 1.2° acceptance cone for protons and Fe nuclei for field representations I, II (see text). The dotted curves show the resulting transition for two simple composition models (see text).

underestimated or (b) large, unknown, variations in the average magnetic field strength occurred over a 1 year timescale. Possibility (a) is removed by normalizing the saturation obscuration to that for the Moon (see Section 1). The global magnetic field varies by ~ x 3 near the photosphere through the solar cycle and by 20-40% at 1 A.U [8]. Thus, long term monitoring of the photospheric fields, currently undertaken, is required to minimize the effects of (b).

The values $\Delta E_{50}$, $\Delta E_{90}$ can be compared to those calculated by a simple impact parameter approach [9]. Averaging over all impact parameters within the field of view which penetrate the solar surface, we obtain $\Delta E_{50} \simeq 0.45$, $\Delta E_{90} \simeq 1.5$, in close agreement with those determined above.

To investigate the mass resolution of the technique, we show the predicted transition for two models of the mass composition in the $10^{13}$ eV to $10^{15}$ eV decades in Figure 1. Curve (B) has an energy dependent, fractional composition (p: $\alpha$: CNO: $10 < Z < 20$: Fe) of (40-15 log (E/TeV): 15: 15: 15: 15 + 15 log(E/TeV) %), and curve (A) of (45-2.5 log(E/TeV): 15: 15: 15: 10 + 2.5 log(E/TeV) %). These models, though simple, are chosen to represent extreme bounds on the controversial variation in compositon (see, for example refs. [10], [11]). The energy window for composition discrimination lies near $10^{14}$ eV, and a statistical precision of $\lesssim$3% is required to choose between models. We conclude that this technique only becomes attractive if the transition energy has been underestimated by $\gtrsim$x 5; then a high

statistics experiment (~ 1 $sr^{-1}$ $s^{-1}$ for 1 year) could explore the less well known $10^{14}$-$10^{15}$ decade.

Future work will incorporate more reasonable field topologies within $5r_0$ to obtain the transition energy with greater precision.

4. Conclusions. The planned U.H.E γ-ray arrays can calibrate their directional resolution from observation of a cosmic ray shadow centered on the Moon. A solar shadow will also exist above ~ $10^{15}$ eV/nucleus. Trajectory simulations within a first order approximation to the solar magnetic field indicate that this shadow is rapidly lost below ~ Z x $10^{13}$ eV. Unless the directional resolution of arrays can be improved still further, or a substantial underestimate has been made in the transition energy, the possibility of distinguishing between composition models in the $10^{14}$-$10^{15}$ eV decade is remote.

References

1. Clark, G. W., [1957], Phys. Rev. 108, 450.
2. Brooke, G., et al. OG 9.4-7, this Conference.
3. Lambert A., Lloyd-Evans, J., OG 9.5-2, this Conference.
4. Watson, A. A., priv. comm.
5. Schatten, K. H. et al., [1969], Solar Phys, 6, 442.
6. Parker, E. N., [1958], Ap. J., 128, 664.
7. Svalgaard, L., and Wilcox, J. M., [1978], Ann. Rev. Ast. Astrophys., 16, 429.
8. Hoeksema, J. T., Ph.D. Thesis, [1984], CSSA-Astro-84-07, Stanford Univ., and references therein.
9. Bell, M. C., et al., [1974], J. Phys. A., 7, 420.
10. Linsley, J., [1983], PICRC, Bangalore, 12, 135.
11. Yodh, G. B., [1984], Moriond Conference "Cosmic Rays and Astrophysics", La Plagne, France.

# A New method to determine the Chemical Composition of the Cosmic Rays beyond $10^{15}$eV

Y. Muraki

Inst. for Cosmic Ray Research, Univ. Of Tokyo, Tanashi, Tokyo

## abstract

The chemical composition of primary cosmic rays beyond $10^{15}$eV could not be measured by the direct method. Here I would like to propose more sensitive method to determine the chemical composition. The idea has been checked by the simulation and compared with the exsisting data concerning on $N_e$-$N_\mu$ and $N_e$-$N_\gamma$.

The simulation will be also cmpared with the experimental results coming from ANI experiment in a near future.

# Cosmic Ray Composition between $10^{15}$ to $10^{17}$ eV obtained by Air Shower Experiments

Y. Muraki

Inst. for Cosmic Rays, Univ. of Tokyo, Tanashi, Tokyo 188

## abstract

Based on the air shower data, the chemical composition of the primary cosmic rays in the energy range $10^{15}$-$10^{17}$eV has been obtained. The method is nased on a well known $N_e$-$N_\mu$ and $N_e$-$N_\gamma$. Our simulation is calibrated by the CERN SPS $p\bar{p}$ collider results and very reliable.

## 1. Introduction and Model

When the first $p\bar{p}$ collider results from CERN has reported in the end of 1981, we have started a Monte Carlo calculation with the use of the data on the nuclear nuclear interaction. The first result has been already published in a proceeding of the Bagalore conference and the simulation model is described in detail therin[1], however, here we describe briefly the simulation model : $\langle n_s \rangle \propto E_o^{1/6}$ , $\sigma_{tot} \propto (\ln\sqrt{s})^2$, $K/\pi \sim 0.15$, $\langle P_T \rangle \sim 0.4$ GeV/c and no energy dependency. The effect of geo-magnetic field and the scattering in the air have been taken account of.

## 2. Transition Curve

The transition curve of the electron number $N_e$ is shown in Fig. 1 as a function of the altitude. ● and X represent the proton and iron primaries respectively with the same incident energy $E_o = 2 \times 10^{16}$eV. The error bar implies the region of 90% air shower involved, while ● and X represent the mean value.

Fig. 1 Transition curve for proton(o) and iron(X)

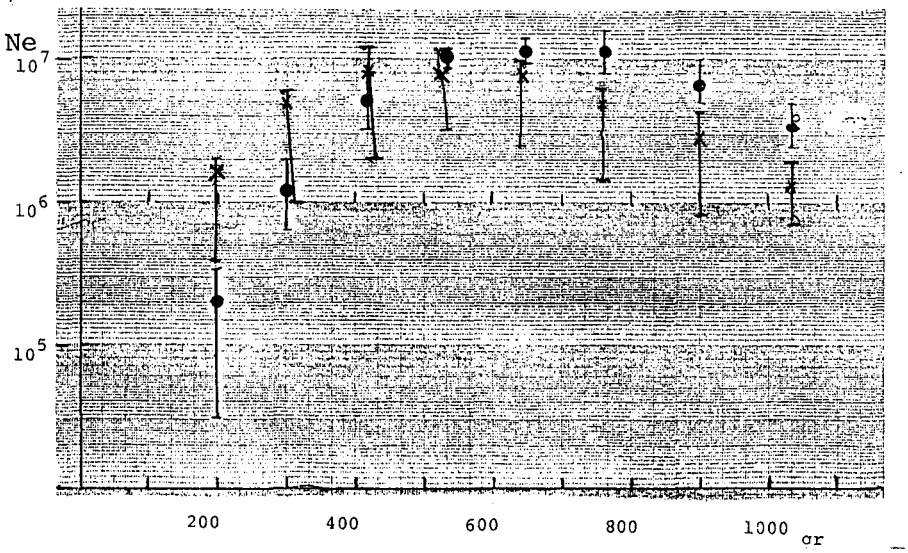


## 3. $N_e$-$N_\mu$ plot and Trigger Bias

It is interesting to compare present result with the previous calculation by Jōgo [2]. Our result of proton(----) primary fits well with the result based on CKP model for proton promaries rather than sacling model with iron primaries calculated by Jōgo. However we must take account of the trigger bias involved in the data taking. As shown in Fig. 3, even if the composition of primary cosmic rays could be 90% iron(x) nad 10% proton(●) beyond $10^{15}$eV, it is identified as proton dominant by the $N_e$ trigger. To avoid such a misunderstanding, $N_\mu$ trigger is preffered.

Fig. 2 $N_e$-$N_\mu$ plot

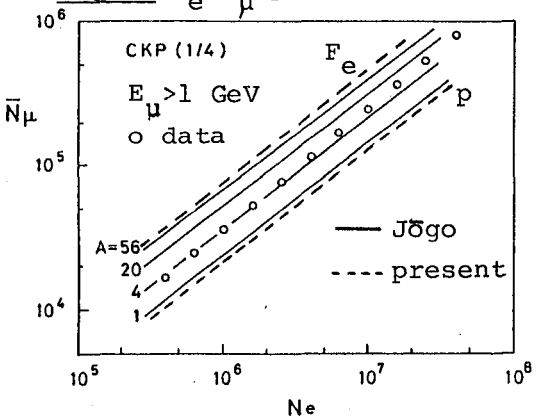


Fig. 3 Trigger bias (●)P,(x)$F_e$

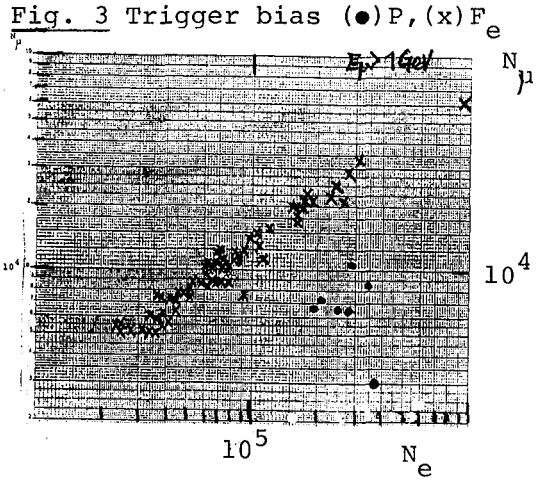

## 4. $N_\mu$-$N_e$ Trigger Data

Fig. 4 represents $N_e$-$N_\mu$ contour plot by $N_e$ trigger. In a range of $N_e \gtrsim 10^7$, no trigger bias is observed even if the data have been taken by $N_e$ trigger[3].

In the same $N_e$-$N_\mu$ plot of Fig.4, we draw the line with the same incident energy for various kind of primaries (Fig. 5). The highest peak of the contour corresponds to the size s=1.1. The corresponding size for each primary is s=1.0-1.2 for proton , s=1.2-1.3 for He, s=1.3-1.4 for CNO, and s=1.4-1.5 for iron in 900 grams(Akeno).

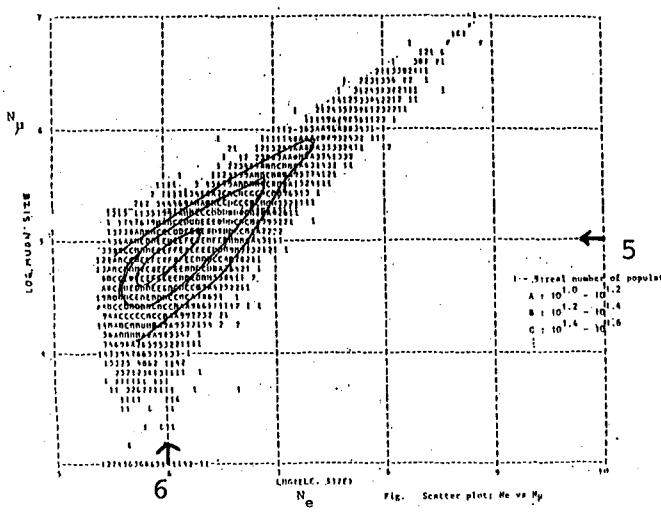


Fig. 4 $N_\mu$-$N_e$ plot

a,b,c corresponds the number of events :
a : $10^{1.0}$-$10^{1.2}$
b : $10^{1.2}$-$10^{1.4}$
c : $10^{1.4}$-$10^{1.6}$
(data from Ref. 2)
real number means real population

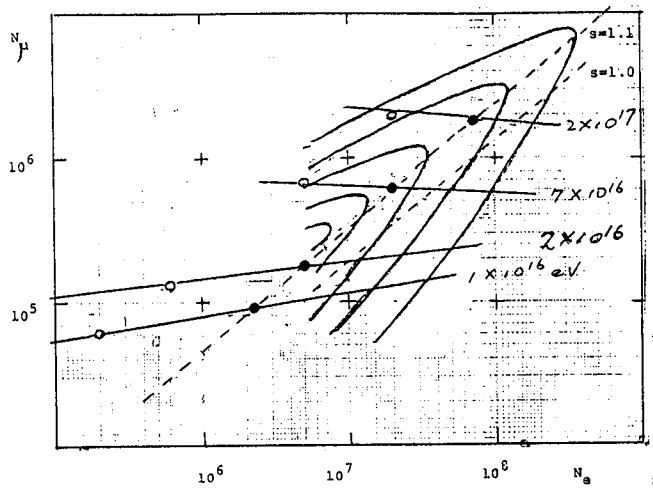


Fig. 5 Contour plot

the same incident energy line is drawn by line. the same age is represented by the dotted lines.
(data from Ref. 3)

Note added: above logic holds even if the primary composition is 90% $F_e$+ 10 % P. We assumed peak corresponds to proton.

Fig. 7

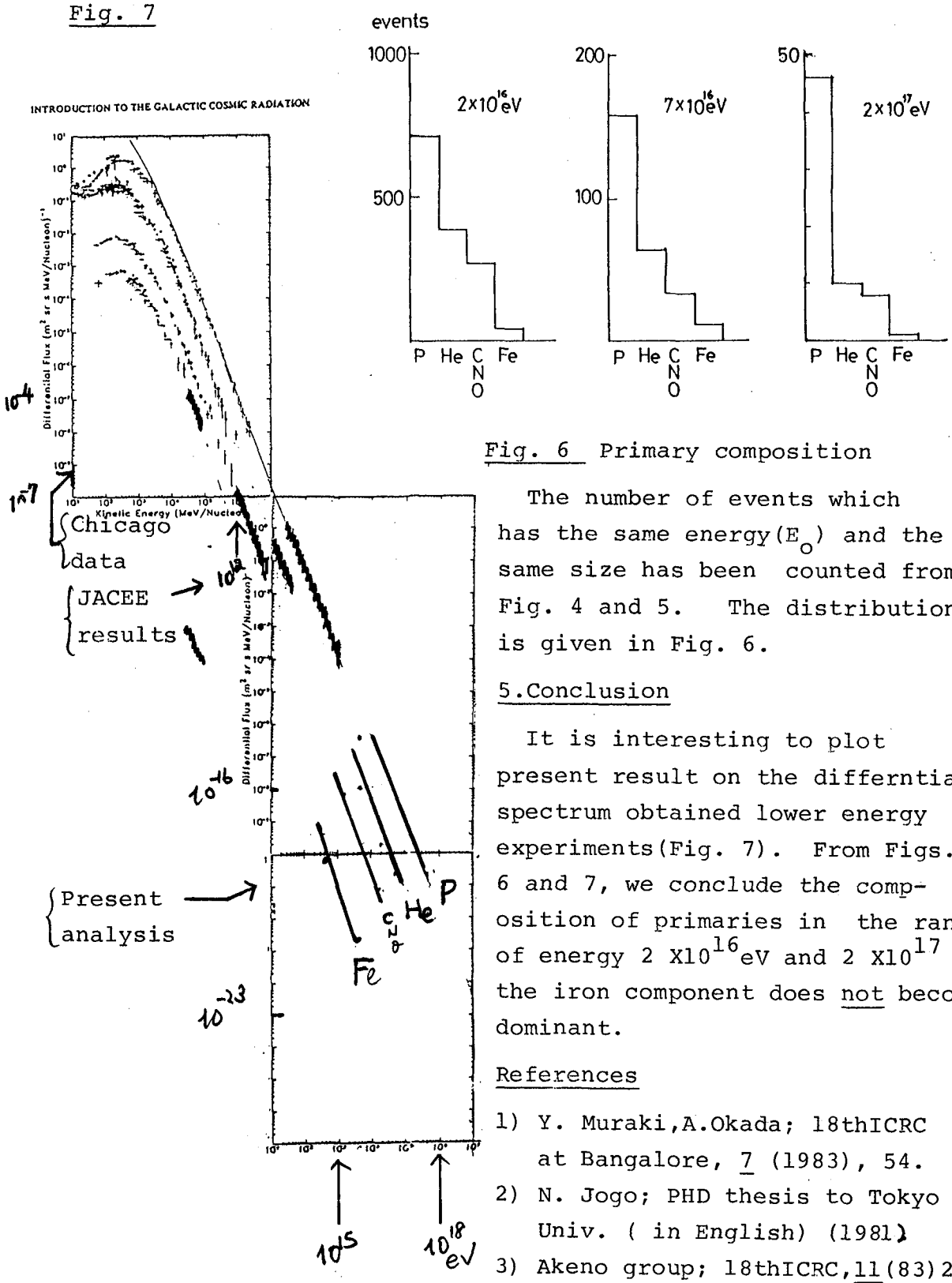


Fig. 6 Primary composition

The number of events which has the same energy($E_o$) and the same size has been counted from Fig. 4 and 5. The distribution is given in Fig. 6.

## 5.Conclusion

It is interesting to plot present result on the differntial spectrum obtained lower energy experiments(Fig. 7). From Figs. 6 and 7, we conclude the composition of primaries in the range of energy 2 X$10^{16}$eV and 2 X$10^{17}$ eV, the iron component does not become dominant.

## References

1) Y. Muraki,A.Okada; 18thICRC at Bangalore, 7 (1983), 54.
2) N. Jogo; PHD thesis to Tokyo Univ. ( in English) (1981)
3) Akeno group; 18thICRC,11(83)281.

# FLUCTUATIONS OF DEVELOPMENT MAXIMUM DEPTH AND NUCLEAR COMPOSITION OF PRIMARY COSMIC RADIATION

M.N.Dyakonov, A.A.Ivanov, S.P.Knurenko, D.D.Krasilnikov, V.A.Kolosov, I.Ye.Sleptsov, G.G.Struchkov, V.N.Pavlov

Institute of Cosmophysical Research & Aeronomy, Lenin Ave., 31 677891 Yakutsk, USSR

ABSTRACT

The EAS cascade curves from the Cerenkov light lateral distribution measurements are recovered and the maximum depth fluctuations of the shower development $\sigma X_m$ both on the Cerenkov and charged EAS components are defined. At $E_o \simeq 10^{18}$ eV the mean content of protons is greater than 85%, and p-air cross section $\sigma_{p\text{-}air} \leq 750$mb.

1. Method. The lateral distributions of the EAS Cerenkov light Q(R) in the interval of the core distances R = 20 ÷ 1500 m and in a wide range of primary energies $E_o = 8.10^{16} \div 1{,}5.10^{19}$eV on the EAS Cerenkov light observations at the Yakutsk array for 1970-1983 are analyzed. In Fig.1 the average cascade curves of the EAS electrons $N_e(X)$ recovered from Q(R) by the method [1] are presented. Errors of $N_e(X)$ due to the measurement errors of Q(R) , the uncertainty of the angular distribution function of the electrons in partial showers [2] and aerosol distribution in atmosphere [3] are shown by dashes.

2. Results. Dependence of the average depth of maximum $\bar{X}_{max}$ on $E_o$ is as follows:

$$\bar{X}_m = (720 \pm 16) + (73 \pm 14) \cdot \lg(E_o/10^{18}) \qquad (1)$$

It is the main not only for a choiceof the EAS development model (here and further we shall mean by it a choice of the multiplicity law and the energy spectrum of secondary particles) but also for the determination of the energy dependence of hadron-air cross section and of nuclear composition of primaries.

The cascade curves presented in Fig.1 and described by the gamma distribution allow to obtain the total energy $E_{EM}$ of the EAS electron-photon component on the energy dissipated by electrons over the observation level $X_o$.

$$E_{EM} = \frac{\beta}{t_o} \sqrt{1 + 3.5\,(X_m/X_o)^6} \cdot \int_o^{X_o} N_e(X)\,dX \,, \qquad (2)$$

where $\beta$ is critical energy and $t_o$ is a unit of radiation length in the air.

From analysis of relations $E_{EM}/E_o$ and $N_e(X_m)/N_e(X_m\text{-}300)$ we find out that the Landau hydrodynamic model with the multiplicity law of secondary particles $n_s \propto E_o^{1/3}$ and with

normal law of their rapidities corresponds the most to the experiment. This model also better agrees with experimental energy-dependent fluctuations in $X_m$:

$$\sigma_{X_m} = (66\pm4) - (12\pm2) \cdot \lg(E_o/10^{18}) \qquad (3)$$

The dependence (3) is obtained by data of 980 shower events on a slope of the lateral distribution function (LDF) of charged particles (black triangles in Fig.2)and by 150 events on the recovery methods $N_e(X)$ on Q(R)(open squares). This dependence slightly differs from our earlier results [4] owing to more correct account of measurement errors and increase of the EAS statistics. For the comparison in Fig.2 the expected dependences $\sigma_{X_m}$ on $E_o$ are presented for the models HDM and MPM. The latter one has $n_s \propto \ln E_o$ and almost constant energy spectrum of secondary particles in units of rapidities. Nuclear composition of primaries was taken in the calculation as consisting of protons and nuclei of the group VH(A = 51) in different ratios determined by the mean mass number $\langle A \rangle$. Such mass composition at fixed $\langle A \rangle$ gives the largest values of the depth of maximum and its fluctuations in comparison with any other composition of primaries. Therefore at fixed $E_o$ and the EAS development model the low boundaries of errors of $\bar{X}_m$ and $\sigma_{X_m}$ give the upper estimation $\langle A \rangle$ and $\sigma_{p\text{-}air}$. An alternative possibility is monochromatic nuclear composition of primaries which leads to the smallest meanings of $\bar{X}_m$ and $\sigma_{X_m}$ at fixed $\langle A \rangle$.

3. Discussion. In Fig.2 a different character of the dependence $\sigma_{X_m}$ on $E_o$ for HDM and MPM at the same meaning $d\bar{X}_m/d\lg E_o$ = ER is explained by the fact that both models preliminarily were reduced to the same $\bar{X}_m$ = 720 g.cm$^{-2}$ at $E_o$ = $10^{18}$eV by the variation $\langle A \rangle$. Therefore the composition on MPM with the increase of $E_o$ changes from the enriched heavy nuclei ($\langle A \rangle \simeq 40$) to more mixed one and the fluctuations increase. And on HDM the composition from more mixed ($\langle A \rangle \simeq 6$) becomes a purely proton one and $\sigma_{X_m}$ decreases. The opposite character of the dependence $\sigma_{X_m}$ on $E_o$ according to the MPM model at various meanings of ER is caused by the fact that at $(ER)_{calc.} < (ER)_{exp.}$ one should enrich the nuclear composition by heavy nuclei and otherwise - by protons. And only at absolute equality $(ER)_{calc.} = (ER)_{exp.}$ the composition must not change with energy. Obtained $\sigma_{X_m}$ on (3) is in favour of the increase of the interaction cross section with energy and high values of ER ($|d\sigma_{X_m}/d\lg E_o|$) evidence the enrichment of the nuclear composition by protons with the increase of $E_o$, i.e. $d\langle A \rangle/d\lg E_o < 0$.

In Fig.3 the dependences $\overline{X}_m$ and $\sigma_{X_m}$ on $\langle A \rangle$ for various meanings of p-air cross sections are presented. Here by selection of the scale the experimental data on $\overline{X}_m$ and $\sigma_{X_m}$ are combined into the dashed region which allows to localize those meanings $\sigma_{p\text{-air}}$ and $\langle A \rangle$ which satisfy the measurements (choice of meanings of these parameters is shown in the bottom in Fig.3)

Thus, if the Landau hydrodynamical model is realized then according to our measurements the mean content of protons in the primary cosmic rays is greater than 85 % and p-air cross section $\sigma_{p\text{-air}} \leq 750$ mb at $E_o = 10^{18}$ eV.

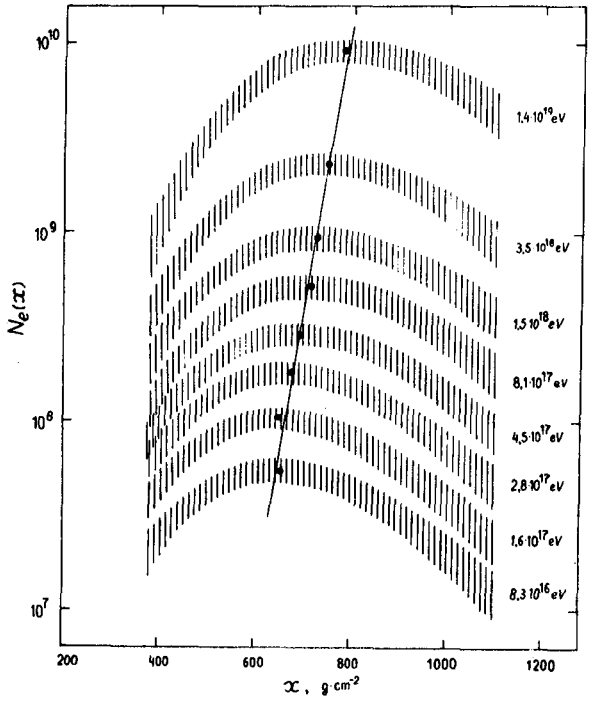


Fig.1. Cascade curves of development of the EAS electrons. Points indicate locations of the maximum depth of the EAS development.

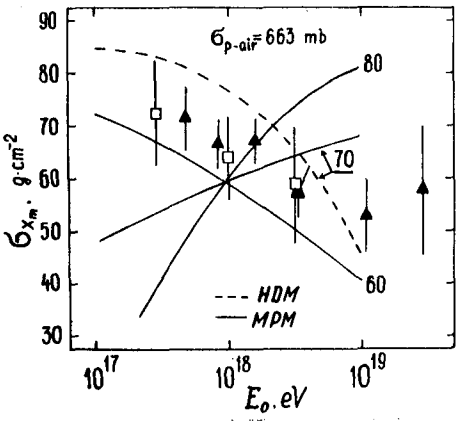


Fig.2. Dependence of fluctuation value $\sigma_{X_m}$ of the shower development maximum depth on the primary particle energy. Triangles and squares are experimental data, lines - calculated values. Figures near the curves are $d\bar{X}_m/d\lg E_o$.

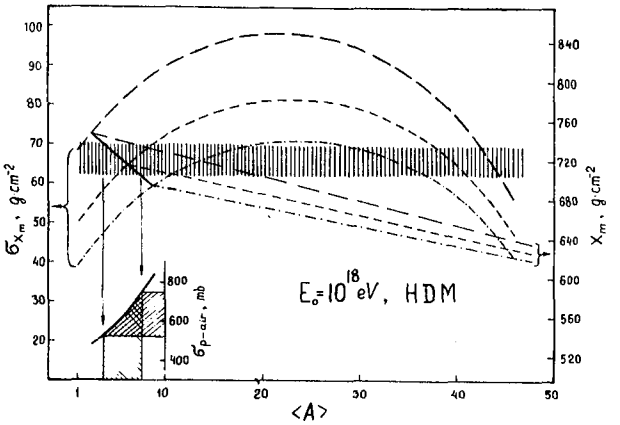


Fig.3. Dependence of the mean value $\bar{X}_m$ and $\sigma_{X_m}$ on the mean atomic weight of the primary ensemble. Dashed region is the region of measured values $\bar{X}_m$ and $\sigma_{X_m}$ with errors. Dashed, dotted and dash-dotted lines show the calculation for $\sigma_{p\text{-}air}$ = = 460, 660 and 840 mb, respectively. Values $\langle A \rangle$ and $\sigma_{p\text{-}air}$ which satisfy the experiment are determined by a solid line.

References.

1. Dyakonov, M.N., et al., (1981), Proc.17-th ICRC, Paris, 6, 106.
2. Dyakonov, M.N., i dr., (1975), Izv.AN SSSR, ser.fiz., t.39, № 6, 1249.
3. Dyakonov, M.N., (1983), Proc.18-th ICRC, Bangalore,6, 210.
4. Dyakonov, M.N., (1983), Proc.18-th ICRC, Bangalore,6, 111.

# ESTIMATION OF COMPOSITION OF COSMIC RAYS WITH $E_o \approx 10^{17} - 10^{18}$ eV

A.V.Glushkov, N.N.Efimov, N.N.Efremov, I.T.Makarov, M.I.Pravdin

Institute of Cosmophysical Research & Aeronomy
Lenin Ave., 31, 677891 Yakutsk, USSR

L.I.Dedenko

Institute of Nuclear Physics, MSU, 117234 Moscow, USSR

ABSTRACT

Fluctuations of the shower maximum depth obtained from analysis of electron and muon fluctuations and the EAS Cerenkov light on the Yakutsk array data and data of other arrays are considered. On the basis of these data the estimation of composition of primaries with $E_o = 5 \cdot 10^{17}$ eV is receive. Estimation of $\gamma$ -quanta flux with $E_o \geq 10^{17}$eV is given on the poor-muon showers.

1. Introduction. In [1] the elongation rate theorem for any parameters $P = P(X_m)$ registered at observation level X was obtained:

$$ER = (\partial P/\partial \lg E_o)_X/(\partial P/\partial X)_{E_o}, \quad (1)$$

$$ER = (X_m/X)(\partial P/\partial \lg E_o)_X/(\partial P/\partial X)_{E_o} \quad (2)$$

From here it follows:

$$\sigma(X_m) = (\sigma P)_X/(\partial P/\partial X)_{E_o}, \quad (3)$$

$$\sigma(X_m) = (X_m/X)(\sigma P)_X/(\partial P/\partial X)_{E_o} \quad (4)$$

Formulae (1) and (3) are used when $P = P(X - X_m)$, (2) and (4) - for parameters $P = P(X_m/X)$.

2. Experimantal $\sigma(X_m)$ and ER. When estimating ER and $\sigma(X_m)$ from the lateral distribution function (LDF) of the EAS Cerenkov light it is necessary to use (1) and (3) [2]. Let's introduce the LDF for R = 200-600 m as $Q \sim R^{-n_Q}$. According to our data we obtain $(\partial n_Q/\partial \sec\theta)_{E_o} = 1.9 \pm 0.3$; $(\partial n_Q/\partial \lg E_o)_X = 0.13 \pm 0.02$ and $\sigma(n_Q)_X = 0.123 \pm 0.018$. Corresponding to them the meanings ER and $\sigma(X_m)$ are given in the Table.

Formulae (2) and (4) are used in the case of LDF of charged particles. At the Yakutsk array the LDF approximation as $\rho(R) \sim (R/70)^{-1}(1+R/70)^{-b}$ is accepted: $(\partial b/\partial \lg E_o)_x = 0.16\pm0.05$; $(\partial b/\partial \sec\theta)_{E_o} = 1.8\pm0.4$; $\sigma(b)_x = 0.2\pm0.02$. On data [3] for $E_o = 5\cdot10^{17}$ eV the $X_m = 680$ g/cm$^2$. Obtained results are given in the Table.

Table

| Parameter | ER | $\sigma(X_m)$ | Work |
|---|---|---|---|
| $n_Q$ | 70±17 | 66±18 | our |
| b | 61±28 | 78±30 | -"- |
| $\lg(Q/\rho_e)$ | 64±17 | 60±20 | -"- |
| $\lg(\rho_e/\rho_\mu)$ | 70±22 | 71±30 | -"- |
| $\lg(\rho_\mu/\rho_e)$ | 79±18 | 60±16 | [4] |
| $T_{70}(\mu)$ | 73±23 | 78±22 | [4] |
| LDF($\rho_c$) | 79±14 | 71±6 | [5] |
| $\tau_{1/2}(\rho_c)$ | 70±5 | 60±4 | [5] |
| $\tau_{1/2}(Q)$ | 45±17 | 60±12 | [6] |
| LDF(Q) | - | 69±14 | [7] |
| Average | 68±6 | 68±6 | |

Analogous estimations of ER and $\sigma(X_m)$ follow from analysis of ratios of the EAS Cerenkov light density to electrons $\lg(Q/\rho_e)$ and electrons to muons with $E_\mu \geqslant 1$ GeV $\lg(\rho_e/\rho_\mu)$ measured at R = 300 m from a shower core (Table).

3. Estimations of Composition. To estimate the composition of primaries we use average $\langle ER\rangle$ and $\langle\sigma(X_m)\rangle$ from the Table. In [8] it is shown that based upon superposition principle for any mixed composition $\langle \ln A\rangle = \sum w_i \ln A_i$ and for dispersion $\sigma^2_{\ln A} = \sum w_i(\ln A_i - \langle \ln A\rangle)^2$ we have:

$$\sigma^2(X_m) = \sigma^2_{\langle \ln A\rangle} + (K^2\sigma_p^2 + C^2)\sigma^2_{\ln A}, \qquad (5)$$

where $\sigma_p$ and $\sigma_{\ln A}$ are fluctuations of $X_m$ at proton or any other pure composition with atomic number $\langle \ln A\rangle$:

$$\sigma_{\langle \ln A\rangle} = \sigma_p(1 - K\langle \ln A\rangle).$$

We accepted K = 0.15, C = 0.43 $\langle ER\rangle = 29\pm4$ g/cm$^2$, $\sigma_p$ = 56 and 71 g/cm$^2$. Calculation results are shown in Fig.1. The region limited by dashed lines corresponds to experimental values $\langle\sigma(X_m)\rangle = 68\pm8$ g/cm$^2$. It is seen that the experiment contradict the composition of the primaries at $E_o = 5\cdot10^{17}$ eV only from heavy nuclei or the mixed composition with large

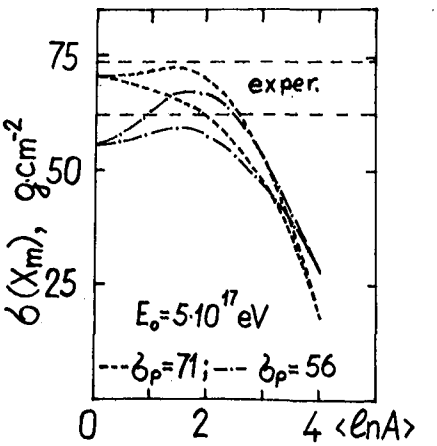


Fig.1

content of heavy nuclei.

In Fig.2 experimental fluctuations of muon number $N_\mu(\geqslant 1$ GeV) taken into account of instrumental errors are shown. The calculations on the models [3] for our experiment are shown by lines. The mixed composition of primaries included: 31% - A=1, 22% - A=4, 12% - A=14, 21% A=31 and 14% - A=51 ($\langle \ln A \rangle = 1.88$). The cross section of inelastic processes were used as in [9]. Fluctuations of $X_m$ in showers from primary nuclei were found according to the superposition principle. Experimental meanings of $X_m$ are taken from [3].

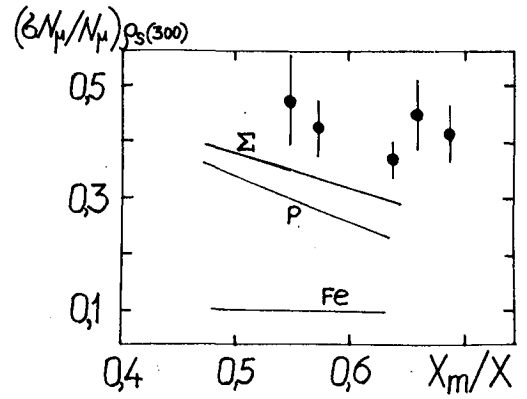


Fig.2.

As before the experiment contradicts the composition only from the heavy nuclei but the expected fluctuations at mixed composition are smaller than the measured ones. Agreement at mixed composition will be if to account cross section growth 1.5 times slower than it is in [9].

4. $\gamma$-quanta. In [10] experimental results of the muon component measured at the Yakutsk array by 3 underground scintillation detectors with total area 108 $m^2$ and with 1 GeV threshold are presented. Each detector consists from 6 sections with the area 6 $m^2$ each. 1000 showers with $\theta \leqslant 45°$ and effective registration area $3{,}7 \cdot 10^5$ $m^2$ for 14000 hours were selected.

The whole massif of the showers for anomalously small content of muons is analyzed. In Fig.3 one event which has the measured muon number 12 times lesser than the expected one (4,6$\sigma$ deviation) is shown. Such a deviation cannot be explained by any fluctuations of the shower maximum depth and by Poisson fluctuations of the detector recordings. Therefore this shower is considered to be formed by a primary $\gamma$-quantum. If to estimate a total flux of $\gamma$-quanta with $E_0 \geqslant 10^{17}$ eV on one event for all the above registration period then their intensity is $2{,}9 \cdot 10^{-14}$ $m^{-2} \cdot s^{-1} \cdot sr^{-1}$, i.e. $\sim 10^{-3}$ from total flux of the primaries with $E_0 \geqslant 10^{17}$ eV. Its arrival direction is in the plane of the Galaxy with coordinates: $b^{II} = -8°$ and ~~longitude~~ $l^{II} = 153°$.

5. Conclusions Experimantal data on fluctuations of the shower maximum depth and on muon number $N_\mu(E_\mu \geqslant 1$ GeV) at $E_0 \approx 10^{17} - 10^{18}$ eV contradict to the composition only of heavy nuclei. The most clise to the experiment in this energy

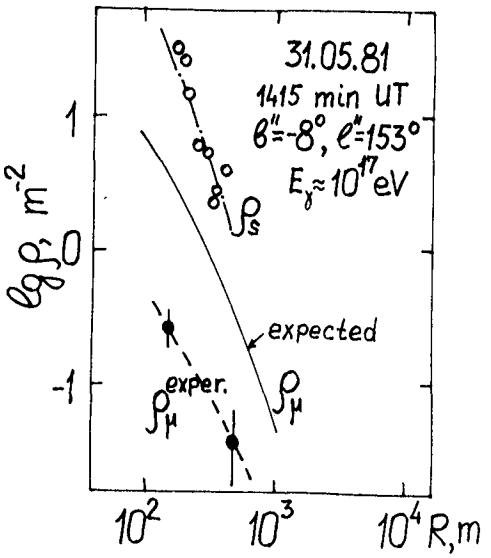


Fig.3.

range is the mixed composition which contains not less than 40% of protons ($\langle \ln A \rangle \approx$ 1,5+0,5). The only proton composition is though unlikely but it is still impossible to exclude it. The $\gamma$-quanta flux is $\sim 10^{-3}$ from the total flux of the primaries at $E_o \geqslant 10^{17}$ eV.

References.

1. Linsley, J.,(1977),Proc.15-th ICRC, Plovdiv, 12, 89.
2. Gaisser, T.K. et al.,(1979),Kyoto, Proc.16-th ICRC, 9, 275.
3. Glushkov, A.V. et al.,(1985),This Conf., EA.
4. Blake, P.R., et al.,(1983),Proc.18-th ICRC, Bangalore, 6, 107.
5. Walker, R. and Watson, A.A.,(1982),J.Phys.,G8, 1131.
6. Prosin, V.V.,(1982),Thesis, NIIYAF MGU.
7. Dyakonov, M.N. et al.,(1983),Proc.18-th ICRC, Bangalore, 6, 111.
8. Linsley, J.,(1983),Rapport Paper for 18-th ICRC, Bangalore.
9. Hillas, A.M.,(1979),Proc.16-th ICRC, Kyoto, 9, 13.
10. Diminstein, O.S. et al.,(1983),Proc.18-th ICRC, Bangalore, 6, 118.

# ALL PARTICLE ENERGY SPECTRUM OF COSMIC RAYS IN $10^{15}$ to $10^{20}$eV Region

D.D.Krasilnikov, M.N.Dyakonov, A.A.Ivanov, V.A.Kolosov, F.F.Lischenyuk, I.Ye.Sleptsov

Institute of Cosmophysical Research & Aeronomy, Lenin Ave., 31 677891 Yakutsk, USSR

ABSTRACT

Average estimations of the shower energy components are presented and their sum gives $\langle E_o(\rho_{600})\rangle$ - an average function of the relation of $E_o$ with the shower size parameter $\rho_{600}$ measured at the Yakutsk EAS array. Using this relation to the EAS spectrum obtained at the Akeno and Yakutsk arrays the energy spectrum of the cosmic ray total flux within $15 \lesssim \lg(E_o,[eV]) \lesssim 20$ by the EAS methods is recovered.

1. Introduction. Earlier beginning from 1971 we estimated the primary energy $E_o$ on the atmospheric Cerenkov light flux density on the core distance 400 m at the Yakutsk EAS array [1] . Last years the experimental data on a maximum depth, muon energy spectrum and other average characteristics of the EAS development are obtained which are important to estimate the shower energy components. By a balance of the latters one can determine the $E_o$.

2. Estimation of $E_o$ by Energy Balance Method. The shower primary energy consists of the next components: $E_o = E_{ei} + E_{\mu i} + E_{hi} + E_{e\gamma} + E_h + E_\mu + E_\nu = E_i + E$, where the first three terms show the energy loss into the atmosphere ionization ($E_i$) by electrons, muons and by splitting the nuclei and the last four ones - the energy dissipated in the earth in the form of electron-photon, nuclear-active, muon and neutrino components (E). Our estimation [2] differs from one [4] by accounting of the atmospheric Cerenkov light losses [5]on which $E_{ei}$ - a main component of the $E_o$ is estimated and by use of the new measurement results of the muon energy spectrum for $E_\mu$.

$E_{ei}$. For $10^{17} \lesssim E_o \lesssim 10^{19}$eV the relation of $E_{ei}$ with the atmospheric Cerenkov light total flux $\Phi_H$ (in number of photons) and from the depth of maximum of showers $X_{max}$ ($g.cm^{-2}$) is given by $E_{ei} = 2.07 \cdot 10^4 (1.04 + 5.8 \cdot 10^{-4} \cdot X_{max})^{-1} \cdot \mathcal{T}^{-1} \cdot \Phi_H$, eV where $\mathcal{T} = \mathcal{T}_m \cdot \mathcal{T}_a < 1$ is a light transmittance

coefficient by atmosphere due to molecular (Rayleigh $\mathcal{T}_m$) and aerosol ($\mathcal{T}_a$) scatterings. According to [6 et al] a main aerosol part is in a ground layer of ~1 km thickness. If to assume that the aerosol is concentrated at depth > 900 g.cm$^{-2}$ and $\mathcal{T}$ = 0.6 at $E_o = 10^{16}$eV then $\mathcal{T}$ = 0.62 at $E_o$ $10^{18}$eV. According to these estimations we took $\mathcal{T}$ = 0.60 ± 0.04. Then due to the experimental dependence $X_{max}$ from $\rho_{600}$ and the observed correlation of $\Phi_H$ with $\rho_{600}$ [7] we found the average value $\lg(E_{ei}[eV]) = (0.98\pm0.05)\cdot\lg\rho_{600}$ + + $17.620^{+0.079}_{-0.097}$.

$E_{\mu i}$. Its value is small and is observed to be equal to the average meaning expected from calculations by different EAS development models, $E_{\mu i} = (0.12 \pm 0.09)\cdot E_\mu$.

$E_{hi}$. If to suppose that the average part of hadrons on the atmosphere $P_h(X) = 0.02\pm0.01$ from $N_e(X)$, average energy of the nuclear splitting $\varepsilon_{nd}$ = 0.5 GeV [8] and adding the usual ionization losses of hadrons we found $E_{hi} = (5.6\pm2.2)\cdot10^{-2}\cdot E_{ei}$. If $P_h(X)$ and $\varepsilon_{nd}$ are somewhat overestimated then it is probably quite compensated in estimation of $E_{hi}$ by not accounted here the effect of photonuclear reactions [9].

$E_\mu$. When the muon component registration threshold $\varepsilon_{\mu,thr}$ = 1 GeV, as it is at the Yakutsk array, then $E_\mu = \bar{\varepsilon}_\mu\cdot N_\mu(>1\text{ GeV})$ where the muon component energy $\bar{\varepsilon}_\mu$ = $= [N_\mu(>1\text{ GeV})]^{-1}\cdot\int_0^{\varepsilon_{\mu,max}}\varepsilon_\mu\cdot dN_\mu(>\varepsilon_\mu) \simeq a\cdot(\nu-1)^{-1}\cdot$ $\cdot(1+a^{-1})^{\nu}$ for the energy spectrum of the shower muons in form $N_\mu(>\varepsilon_\mu, GeV)\propto(\varepsilon_\mu + a)^{-\nu}$ which refers to one muon with $\varepsilon_\mu$ > 1 GeV. Calculations show that when the muons generated only due to decay of pions and kaons then the muon energy spectrum does not almost depend on the EAS development model and the $\varepsilon_\mu$ very poorly depends on $E_o$. From unique measurement results of the muon energy spectrum in showers with $N_e = 2\cdot10^5$ at sea level [10] we find that a = = 10 GeV, $\nu$ = 1.64 and $\bar{\varepsilon}_\mu$ = 18.2 GeV. At $\varepsilon_{\mu,thr}$ = 1.1 GeV [11], 5 GeV [12] and in the case $N_e = 10^6$ [13] the results confirm the mentioned approximation (Fig.1). Using $\bar{\varepsilon}_\mu = (16 \pm 3)$GeV and the observed relation $\lg N_\mu(>1\text{ GeV}) =$ $= (0.84 \pm 0.08)\cdot\lg\rho_{600} + 6.491^{+0.042}_{-0.046}$ [3] we obtain

$$\lg(E_\mu,[eV]) = (0.84\pm0.08)\cdot\lg\rho_{600} + 16.699^{+0.086}_{-0.107}$$

$E_\gamma$. Assuming that the neutrino carries away 27, 90 and 67% of the muon energy due to decay of pions, kaons and muons, respectively, and the ratio of kaons to pions is $0.22\pm0.09$ [8] we obtain $E_\gamma = (0.64 \pm 0.18)\cdot E_\mu$.

Adding all the above components of $E_0$ based considerably on the experiment the average estimation is as follows:

$$\lg(E_0,[eV]) = (0.98 \pm 0.03)\cdot\lg\rho_{600} + 17.754^{+0.066}_{-0.077}.$$

3. Energy Spectrum of the Primaries. Using the above estimation of $E_0$ for the EAS spectrum obtained on the Akeno and Yakutsk array data in a corrected form [3] the energy spectrum of all the particles at energies $15 \lesssim \lg(E_0, [eV]) \lesssim 20$ is recovered. It is shown in Fig.2 where the dashed lines correspond to the results at $E_0 \pm \Delta E_0$. As it is seen this spectrum reveals significant irregularities and being approximated by a form $J(E_0)dE_0 \propto E_0^{-\gamma-1}dE_0$ it has the following exponents:

| $\Delta\lg E_0$ | 15.÷16. | 16.÷17.5 | 17.5÷18.2 | 18.2÷18.9 | 18.9÷19.4 | 19.4÷20. |
|---|---|---|---|---|---|---|
| $\gamma+1$ | 2.59±.18 | 2.91±.13 | 2.99±.04 | 3.63±.05 | 2.47±.09 | 3.48±.11 |

Integral intensities with account of accuracy of the determination of $E_0$ are as follows:

| $\lg(E_0,[eV])$ | 15 | 16 | 17 | 19 |
|---|---|---|---|---|
| $I(>E_0)$, m.s.sr | $(2.3\pm0.6)10^{-6}$ | $(5\pm1.6)10^{-8}$ | $(6\pm2)10^{-12}$ | $(3\pm1)10^{-14}$ |

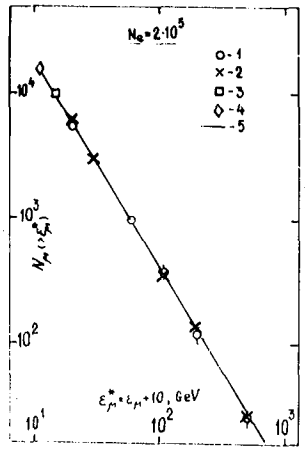


Fig.1. 1- [10], 2- [13], 3- [12], 4- [11], 5- $N_\mu(>\mathcal{E}_\mu) \propto (\mathcal{E}_\mu + 10)^{-1.64}$

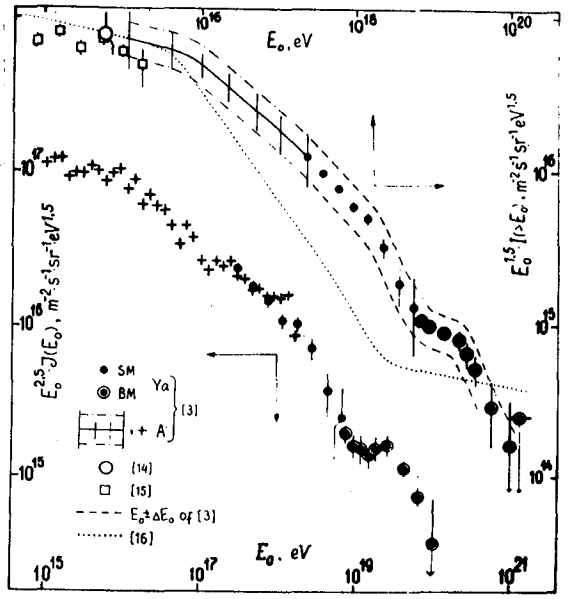


Fig.2. 1-Yakutsk and 2 - Akeno [3], 3- [14], 4 - [15], 5- at $E_0 + \Delta E_0$ (upper) and $E_0 - \Delta E_0$ (lower), 6 - [16].

4. Discussion. A good agreement with results of energy balance of small EAS [14] and of a direct calorimetry [15] testifies a correctness of $E_o - \rho_{600}$ obtained by us. The latter one is $\lg E_o = (0.94 \pm 0.03)(\lg N_e - 8.042) + 17.754^{+0.066}_{-0.077}$ for measurements at Akeno (920 g.cm$^{-2}$).

For $\lg(E_o, [eV]) \lesssim 19$ the spectrum reveals a consistent steepening with energy $E_o$ which considerably differs from its earlier accepted form [16 et al]. It more corresponds to a picture expected at the diffusion of the mixture of the galactic origin nuclei [17]. The irregularity (rather "bump"-type) at $19 \lesssim \lg(E_o, [eV]) \lesssim 20$ is difficult to interpret by evidence of an extragalactic component: the particles of these energies also arrive from low galactic latitudes mainly and their anisotropy phase changes with $E_o$ [18 et al].

References

1. Egorov, T.A., et al., (1971), Proc.12-th ICRC, Hobart, 6, 2164.
2. Krasilnikov, D.D., i dr., (1983), Kosmicheskiye Luchi s Energiei Vyshe $10^{17}$ eV, Yakutsk, 117-143.
3. Krasilnikov, D.D., et al., (1985), (This Conference).
4. Diminstein, O.S., et al., (1975), Proc.14-th ICRC, München, 12, 4318.
5. Dyakonov, M.N., et al., (1983), Proc.18-th ICRC, Bangalore, 6, 210.
6. Tennekes, H., (1974), The Atmosphere Boundary Layer, Phys.Today, 52.
7. Kolosov, V.A., (1982), Thesis, FIAN SSSR.
8. Murzin, V.S., Sarycheva, L.I., (1968), Kosmicheskiye Luchi I Ikh Vzaimodeistvie, M., Atomizdat, 391.
9. McComb, T.J.L., et al., (1979), Proc.16-th ICRC, Kyoto, 9, 126.
10. Grishina, N.V., et al., (1981), Proc.17-th ICRC, Paris, 6, 3.
11. Hara, T., et al., (1983), Proc.18-th ICRC, Bangalore, 11, 281.
12. Khrenov, A.B., (1961), ZhETF SSSR, t.41, 1402.
13. Atrashkevich, V.B., et al., (1983), Proc.18-th ICRC, Bangalore, 11, 229.
14. Nikolsky, S.I., (1962), 5-th Interamer.Seminar on C.R. La Paz, 2, 18-1.
15. Grigorov, N.L., et al., (1971), Proc.12-th ICRC, Hobart, 5, 1748.
16. Greisen, K., (1965), Proc.9-th ICRC, London, 2, 609.
17. Ginzburg, V.L., Syrovatsky, S.I., (1963), Proiskhozhdeniye Kosmicheskikh Luchei, izd.AN SSSR, M., 384.
18. Krasilnikov, D.D., et al., (1983), Proc.18-th ICRC, 9, 223.

# EAS SPECTRUM IN THE PRIMARY ENERGY REGION ABOVE $10^{15}$ eV BY THE AKENO AND THE YAKUTSK ARRAY DATA

D.D.Krasilnikov, S.P.Knurenko, A.D.Krasilnikov, V.N.Pavlov, I.Ye.Sleptsov, V.P.Yegorova

Institute of Cosmophysical Research & Aeronomy, Lenin Ave., 31, 677891 Yakutsk, USSR

ABSTRACT

The EAS spectrum on scintillation density $\rho_{600}$ in primary energy region $E_0 \simeq 10^{15}$-$10^{20}$ eV on the Yakutsk array data and recent results of the Akeno is given.

## 1. Introduction

At present the EAS observations at sea-level take the widest energy range of primaries. The observed EAS spectra on particle number N in a shower at $E \lesssim 10^{18}$eV and on particle density $\rho_{600}$ at a distance R=600 m from axis at $E_0 > 3.10^{17}$eV are obtained. Either for the recovery of the spectrum on $E_0$ or for the comparison it is reasonable to obtain these results in aform of "corrected"spectra where effects of the development fluctuations (different for N and $\rho_{600}$ ) and N and $\rho_{600}$ measurement dispersions (different for various arrays) are taken into account. To consider the EAS spectrum on the whole it is required also to use in the analysis a common basic unit of measurement of the shower particle number (density) and a common parameter of the shower size. Yet it is reasonable and possible only on the basis of $\rho_{600}$ : there is the experimental estimation of $\rho_{600}$ and $E_0$ relationship and only in the Akeno array data there is the possibility of transition from N to $\rho_{600}$ .

## 2. Results

a) Yakutsk. In the central part of the array [4] the registration of showers was triggered by a small master (SM) and on the whole array - by a big master (BM). For the analysis the shower events were selected with an axis within fixed receiving areas (different for various ranges of $\rho_{600}$ ) and for those periods of the array operation T, when ~100 % - efficiency of registration and levels of $\delta\rho_{600}$ summary relative deviations of fluctuations of the shower development and their measurement dispersions obtained from a total measurement simulation [5] and accepted for the analysis [1,2] were provided. Each shower was individually treated as follows: 1) from approximation of measured particle densities

by $\rho(R)_i \propto R^{-n_i}$ [5] $n_i$ and $\rho_{600,i}$ were determined; 2) $\rho_{600,i}$ was reduced to the zenith angle $\theta = 0^\circ$, atmospheric temperature 240 K and pressure 1006 mb ( $\rho_{600}$ and $E_0$ relationship at the atmospheric depth X=1025 g.cm$^{-2}$ at these parameters was found) using the absorption length measured in the experiment $\lambda(\rho_{600}) = (218 \pm 15) + (172 \pm 15) \cdot \sec\theta$, g.cm$^{-2}$, $\theta < 60^\circ$, a barometric coefficient $\alpha_p = -0{,}25 \pm 0.03$ % per mb and temperature coefficient $\alpha_T(\rho_{600}) = 0.30 \pm 0.11$ % per K. For $-0.35 < \lg\rho_{600} < 0.6$ as an intermediate parameter of shower size the $\rho_{300,i}$ having the absorption length $\lambda(\rho_{300}) = 251 \pm 21$ g.cm$^{-2}$, $\theta < 40^\circ$ and $\rho_{600} = (0.14 \pm 0.01) \cdot \rho_{300}^{0.89 \pm 0.02}$ were used.

Data used in spectrum construction on the whole have following common characteristics:

| | $\lg[\rho_{600}, m^{-2}]$ | $\delta\rho_{600}$ | $ST\Omega$, $m^2 s \cdot sr$ | Number of events |
|---|---|---|---|---|
| SM | -0.35 ÷ 1 | 0.40÷0.17 | $(0.16 \div 4.33) \cdot 10^{13}$ | 534 |
| BM | 1 ÷1.5 | 0.22÷0.21 | $(1.88 \div 4.40) \cdot 10^{15}$ | 109 |
| BM | > 1.5 | 0.21 | $5.69 \cdot 10^{15}$ | 79 |

Introducing into the observed intensities the corrections for the summary effect of the development fluctuations and measurement dispersions with the correction factor [2] K= $= 0.98 [1 + \delta\rho_{600}^2]^{-0.5\gamma(\gamma-1)}$ the differential $f_0(\rho_{600})$ and the integral $F_0(>\rho_{600})$ corrected EAS spectra (see Figure) were obtained.

The differential spectrum for $-0.3 < \lg\rho_{600} < 1.7$ displays significant irregularities and at the description by $f_0(\rho_{600}) = A(\rho_{600}/10)^{-\gamma-1}$ has the following parameters:

| $\lg\rho_{600}$ | -0.3÷0.5 | 0.5÷1.2 | 1.2÷1.7 | 1.7÷2.3 |
|---|---|---|---|---|
| lg A | -13.37÷0.04 | -13.63÷0.02 | -13.92÷0.05 | -13.20÷0.09 |
| $\gamma+1$ | 2.95÷0.04 | 3.58÷0.05 | 2.45÷0.10 | 3.43÷0.11 |

The spectrum on $\rho_{600}$ obtained by the relationship $\rho_{600} = (2.05 \pm 0.11) \cdot (Q_{400}/10^7)^{0.99 \pm 0.02}$ from the transformation of the density spectrum of the shower atmospheric Cerenkov light $Q_{400}$ [1] and having the form of the spectrum of loss in atmosphere confirms the change for $-0.3 < \lg\rho_{600} < 1$.

In the Figure a dashed line corresponds to the observed spectrum on Haverah Park data [6] reduced by us to the scintillation density $\rho_{600}$ due to [7]. In this case according

to [8] the effect of $\delta\rho_{600}$ at $\lg\rho_{600} \lesssim 1$ is small ($\lesssim 10\%$ on intensities) and at $\lg\rho_{600} \gtrsim 1$ somewhat increases. Taking into account this fact we find a satisfactory agreement of the results of both arrays. It is remarkable that the Haverah Park spectrum reveals also the steepening tendency for $1.8 \lesssim \lg\rho_{600} \lesssim 2.3$.

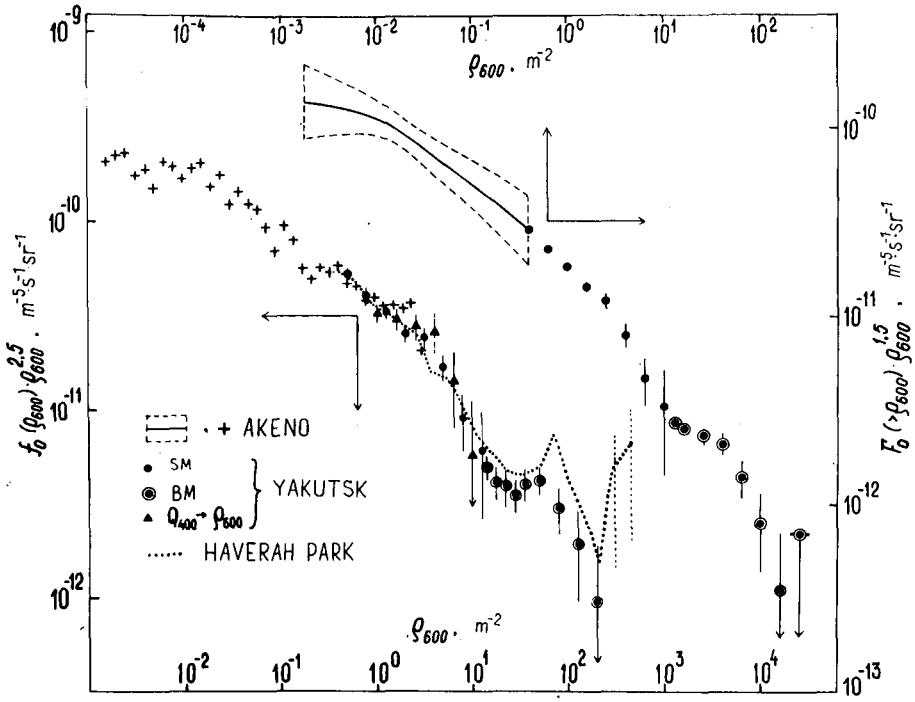


b) Akeno. The observed EAS spectrum at sec $\theta = 1.1$ (at the depth 1011 g.cm$^{-2}$) is given by $f(N_e)dN_e = A(N_e/10^6)^{-\gamma_N-1}$ with $A = (1.2 \pm 0.2)\cdot 10^{-13}$ m$^{-2}$s$^{-1}$sr$^{-1}$part.$^{-1}$, $\gamma_N = 1.49 \pm 0.17$ for $5 < \lg N_e < 6$ and $\gamma_N = 1.80 \pm 0.12$ for $6 < \lg N_e < 8$. Some corrections were made: the spectrum is reduced to the Yakutsk level 1025 g.cm$^{-2}$ with absorption length $\lambda(N_e) = 235$ g.cm$^{-2}$; the effect of the shower development fluctuations was taken into account on [9] with average correction factor $\bar{K}_\delta = 0.89\cdot[1 + \delta N_e^2]^{-0.5\gamma_N(\gamma_N-1)} = 0.77$ where the deviations were taken according to [10] to be 0.7 for $5 < \lg N_e < 6$ and 0.44 for $6 < \lg N_e < 8$.

From [11,12] we find $\lg\rho^*_{600} = \lg[\rho^*_{600,e} + \rho^*_{600,\mu}] = 0.961\ \lg N_e - 7.46$ at the depth 966 g.cm$^{-2}$ at T = 279 K.

Recounting $\rho_{600}$ to depth 1025 g.cm$^{-2}$ with $\lambda(\rho_{600}) = 390$ g.cm$^{-2}$ at T = 240 K with $\alpha_T = 0.3$ % per K and to the Yakutsk basic unit of muon equivalent having the relationship $u_\mu/u_e = 1.15$ with the electron equivalent unit [3] the relationship $\lg \rho_{600} = 0.96 \cdot \lg N_e - 7.534$ is obtained.

In the Figure the differential and integral corrected EAS spectra on $\rho_{600}$ from the Akeno data are given. For $\lg \rho_{600} < 0.12$ we obtain: $f_o(\rho_{600})d\rho_{600} = A_o(\rho_{600}/10^{-1.80})^{-\gamma-1}d\rho_{600}$ with $A_o = (1.2 \pm 0.2) \cdot 10^{-5.297}$ m$^{-2}$·s$^{-1}$·sr$^{-1}$(part./m$^2$)$^{-1}$, $\gamma = 1.55 \pm 0.18$ for $-2.76 < \lg \rho_{600} < -1.80$ and $\gamma = 1.88 \pm 0.13$ for $\lg \rho_{600} > -1.80$.

## 3. Conclusion

In the considered 5-decade energy range the EAS spectrum on $\rho_{600}$ reveals significant irregularities. For $\lg \rho_{600} < 1.2$ the steepening (rather consecutive) of inclination of $f_o(\rho_{600})$ with increase of $\rho_{600}$ occurs: $-\gamma-1 = -2.55 \pm 0.18$; $-2.88 \pm 0.12$; $-2.95 \pm 0.04$ and $-3.58 \pm 0.05$ for $\Delta \lg \rho_{600} = -2.76 \pm -1.8$; $-1.8 \pm -0.3$; $-0.3 \pm 0.5$ and $0.5 \pm 1.2$, respectively. At $\lg \rho_{600} > 1.2$ the irregularity is observed: $-\gamma-1 = -2.45 \pm 0.1$ at $1.2 < \lg \rho_{600} < 1.7$ and $-\gamma-1 \lesssim -3$ at $1.7 < \lg \rho_{600} < 2.3$. We assume that four shower events with $\lg \rho_{600} > 2.3$ from the spectrum of [6] if to eliminate the effects of methodical character could indicate the possible existence of the other irregularity in the range out of the control of the Yakutsk array.

## References


1. Krasilnikov, D.D. i dr., (1983), Kosmicheskie luchi s energiei vyshe $10^{17}$eV, Yakutsk, 117.
2. Krasilnikov, D.D. i dr., (1985), Izv.AN SSSR, ser.fiz. 49, No.1.
3. Nagano, M. et al., (1984), J.Phys.G, 10, 1295.
4. Kerschenholz, I.M. et al. (1973), Proc.13-th ICRC, Denver, 4, 2507.
5. Dyakonov, M.N. et al., (1981), Proc.17-th ICRC, Paris, 9, 166.
6. Bower, A.J. et al., (1981), Proc.17-th ICRC, Paris, 9, 166.
7. Bower, A.J. et al., (1983), J.Phys.G, 9, L.53.
8. Brooke, G. et al., (1979), Proc.16-th ICRC, Kyoto, 8, 13.
9. Kalmykov, N.N., (1969), Yadernaya fizika, 10, 121.
10. Kulikov, G.V., (1973), Thesis, MGU.
11. Hara, T. et al., (1983), Proc.18-th ICRC, Bangalore, 11, 272.
12. Nagano, M. et al., (1984), J.Phys.Soc.Japan, 53, 1667.

# COSMIC RAY SPECTRA MEASUREMENTS AT THE YAKUTSK EAS ARRAY

A.V.Glushkov, T.A.Egorov, N.N.Efimov, M.I.Pravdin

Institute of Cosmophysical Research & Aeronomy,
Lenin Ave., 31, 677891 Yakutsk, USSR

G.B.Khristiansen

Scientific-Research Institute of Nuclear Physics,
Moscow, USSR

1. Introduction. The EAS spectra on $\rho_{600}$ obtained at the Yakutsk array for 38000 operation hours in 1974-1982 are presented. The refined value of the conversion factor from $\rho_{600}$ to $E_0$ is given and based on it the primary energy spectrum is obtained.

2. Methods. At the Yakutsk EAS array the showers are classified on parameters which are well measured in real showers: in the central part - on $\rho_{300}$ and on the whole array - on $\rho_{600}$. The shower spectra are constructed first on these parameters, then - a single spectrum on $\rho_{600}$.

The $\rho_{300}$ and $\rho_{600}$ values are determined on the particle lateral distribution function (LDF) obtained in Yakutsk (for instance, [1]) and on approximation $\rho \sim R^{-n}$ using the experimental points closest to $R^*$ (300 and 600 m) [2]. In [1] and [2] somewhat different methods of selection of showers for a construction of spectra are also used.

3. Results. The differential spectra on $\rho_{600}$ from the Yakutsk EAS array data for 38000 operation hours from January 1974 to April 1982 are given in Fig.1. They are presented the physical and instrumental errors of $\rho_{600}$ uncorrected since the conversion factor will be further used for transformation of $\rho_{600}$ to $E_0$ uncorrected as well.

From Fig.1 it is seen that the spectra obtained by two somewhat different methods do not contradict each other on the whole. However, at $\rho_{600} \leq 10$ m$^{-2}$ the spectrum according to [2] is $\sim 1.5$ times higher than one in [1].

The spectrum $\rho_{600}$ (HP) (Haverah Park) is presented with the recount to $\rho_{600}$ (Y) (Yakutsk) using the dependence $\rho_{600}(Y) = (1{,}72 \pm 0{,}25) \cdot \rho_{600}(HP)^{1{,}06 \pm 0{,}03}$. Such a dependence is obtained from the comparison of the detector responses at these arrays [1].

From Fig.1 the irregular change of spectra, in particular, "bump" at $\rho_{600} > 20$ is evident. However, there is no a common opinion in estimation of such "bump" confidence. To our point of view it is necessary to find out the possible methodical details before concluding the existence of any irregularities of the spectrum, the more so that in this region the insufficient statistics is available and the EAS characteristics at $E_0 > 10^{19}$ eV are investigated not enough.

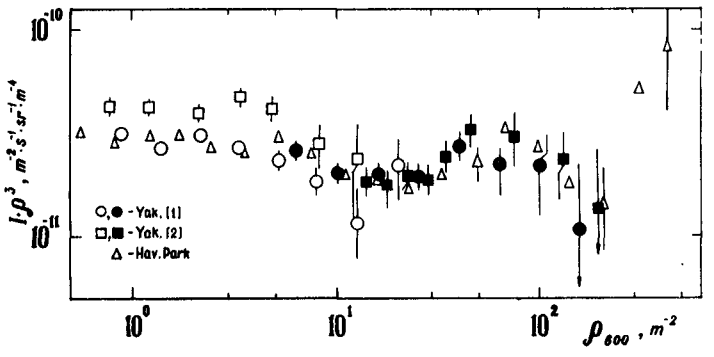


Fig.1

The parameter $\rho_{600}$ for the Yakutsk EAS array is reliably measured and besides it is proportional to $E_o$. The relationship between $\rho_{600}$ and $E_o$ in [1] is found by the calorimetric method and in [2] - either by the same method or only on the Cerenkov light method (on $Q_{400}$).

In the total balance of $E_o$ the portion $E_i$ (energy dissipated by electromagnetic component in the atmosphere) is $\sim$ 80%. It is found as $E_i = K \cdot \Phi$, where $\Phi$ is the total EAS Cerenkov light flux in the atmosphere. The value $K$ depends weekly on the shower development model and is $K \approx 3{,}8 \cdot 10^4$ eV/photon$\cdot$eV$^{-1}$ (photon number is expressed per unit of energy range; for photomultipliers used in Yakutsk the frequency range energy is 2,6 eV).

The conversion factors from $\rho_{600}$ to $E_o$ obtained in [1] and [2] by a calorimetric method differ by 1,4-1,5 times. It is associated mainly with the different estimation of the light absorption in the atmosphere and with the different values of the average energy of muons.

In [1] the light absorption is taken to be $(27 \sec\theta)\%$, in [2] it is 40% for all the zenith angles $\theta$. The average energy of muons with $E_\mu \geqslant 1$ GeV is taken to be 7 GeV [1] and it is 16 GeV in [2].

If to suppose that the light absorption occurs only in near the ground atmosphere layer as in [2] and it increases as $\sec\theta$ (i.e. the absorption is $33 \cdot \sec\theta\,\%$), and if the average energy of muons is taken to be 9 GeV (such a refined estimation seems to be proper), then we obtain:

$$E_o = (5{,}0 \pm 1{,}4) \cdot 10^{17} \cdot \rho_{600}(0^\circ)^{0{,}96 \pm 0{,}04} .$$

From here we obtain on the Yakutsk EAS array data at sea level the following dependences of charged particle number $N_s$ and of muon number $N_\mu$ ($\geqslant 1$ GeV) on $E_o$:

$$E_o = (7{,}8 \pm 2{,}1) \cdot 10^{17} (N_s/10^8)^{0{,}86 \pm 0{,}06} ,$$

$$E_o = (1{,}8 \pm 0{,}5) \cdot 10^{17} (N_\mu/10^6)^{1{,}15 \pm 0{,}04} .$$

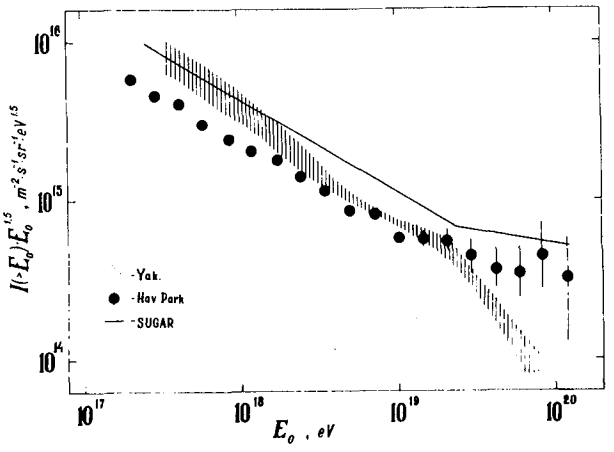


Fig.2

4. Discussion. The integral energy spectrum on the Yakutsk EAS array data by the above conversion factor is presented in Fig.2. The shaded region corresponds to data of [1] and [2]. Note that the achieved at present accuracy of the energy calibration allows to determine the absolute intensity in the range $10^{18}$ eV with the accuracy to 1,8. The spectrum of the SUGAR array data is presented on [3] using the obtained dependence between $N_\mu$ and $E_0$ and taking into account the difference in thresholds $E_\mu$.

The discrepancy from the Haverah Park spectrum at the extremely high energies is that at the Haverah Park EAS array were registered 4 showers with very high values of $\rho_{600}$ (two last points in Fig.1). At the Yakutsk EAS array such showers were not detected and the experimental data do not contradict the possibility of the existence of cutoff spectrum.

The reasons of the discrepancy of the Yakutsk and Haverah Park $\rho_{600}$ spectra are not completely revealed. It is without exception that there are differences in the geometry of arrays, types of detectors and analysis method.

5. Conclusion. We think that it is necessary to analyze all the details of registration, treatment and analysis of showers based on the common methods to find out the nature of the observed irregularities of spectra.

References

1. Vasiliyev, I.V. et al., (1983), Kosmicheskiye Luchi s Energiei Vyshe $10^{17}$ eV, Yakutsk, 19-29.
2. Krasilnikov, D.D. et al., ibidem, 117-143.
3. Horten, L. et al., (1983), Proc. 18-th ICRC, Bangalore, vol.6, p.124.

# COMPOSITION OF PRIMARY COSMIC RAYS NEAR THE BEND FROM A STUDY OF HADRONS IN AIR SHOWERS AT SEA LEVEL

Mincer, A.I., Freudenreich, H.T., Goodman, J.A.,
Tonwar, S.C., Yodh, G. B.
Department of Physics and Astronomy
University of Maryland, College Park, MD

Ellsworth, R.W.
George Mason University, Fairfax, VA

Berley, D.
National Science Foundation, Washington, DC

## ABSTRACT

Data on hadrons in air showers arriving at sea level in College Park, Maryland have been studied to find sensitivity to primary cosmic ray composition. The rate of showers which satisfy minimum shower density and hadron energy requirements as well as the rate of showers containing hadrons delayed with respect to the electron shower front are compared to Monte Carlo simulations. The data on the rate of total triggers and delayed hadrons are compared to predicted rates for two models of primary composition. The data are consistent with models which require an increasing heavy nuclei fraction near $10^{15}$ eV. The spectra which are consistent with the observed rate are also compared to the observed shower size spectrum at sea level and mountain level.

1. Introduction. In this paper we present analysis of a two year run of the Delayed Hadron Experiment at sea level in College Park, Maryland. Four segmented ionization calorimeters (Figure 1), each of area ~1.5m$^2$ were used to study the energy and arrival time distribution of hadrons near the core of

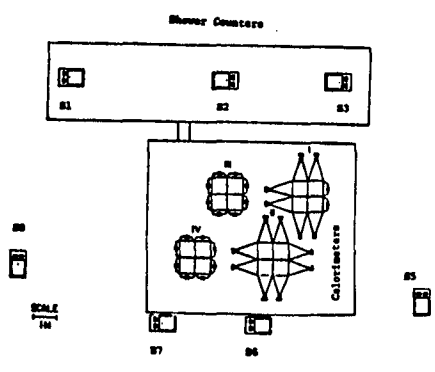


Figure 1: Experimental layout

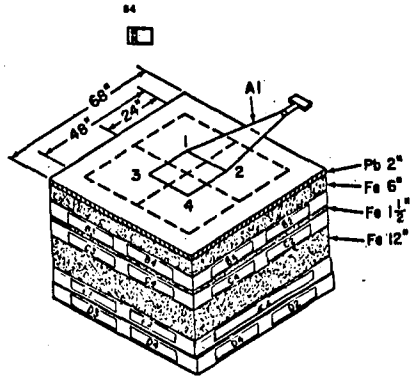


Calorimeter profile

extensive air showers. A small air shower array of 12 scintillation counters located near the calorimeters were used to record the density and arrival time of the electromagnetic component of the air shower. The details of the design of this experiment have been presented elsewhere.[1]

2. The Experiment. Events were required to pass the following offline cuts in order to be included in our data sample: 1) A signal greater than 75 equivalent particles must be recorded in the top layers of at least one hadron calorimeter. 2) The average shower density in the four counters "A" directly above the calorimeters must have an average density of greater than 13.5 ptls/$m^2$ and at least two of the four counters must equal or exceed this density. 3) All four A counters must have fired a timing discriminator set at 0.1 particle and shown a timing signal consistent with the other shower counters.

Signals were recorded at four depths in each of four quadrants in all calorimeters. The arrival time of a signal > 3 equivalent particles was recorded for three of these counters within each quadrant. Data from the B layers (located under 150 gm/$cm^2$) are displayed in Figure 2 as a scatter plot of B signal against arrival time relative to the A counter above it. Events in which the hadronic counter signal is large are consistent with a resolution of 2.5 ns. The data show several events with large signal and delay (these are described in detail in paper HE 6.2-7 of this conference) as well as a significant tail of low signal delayed events.

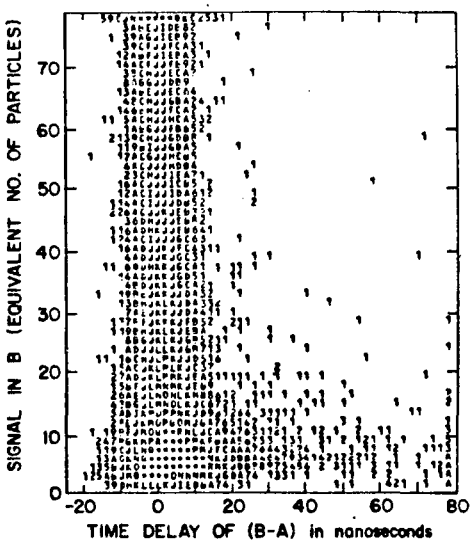


Figure 2

The rate of events passing all offline cuts is 3.15 ± .04 events per hour. The rate of events which contain at least one calorimeter counter delayed by greater than 20 ns and having a signal greater than 20 equivalent particles is 0.050 ± 0.004 events per hour. These two event rates are compared to simulations for various compositions in the next section.

3. Simulation of the Experiment. In order to interpret the data taken in this experiment it is necessary to compare it to a Monte Carlo calculation which simulates the interaction of cosmic rays in the atmosphere and the response of our detector to these particles. The details of the air shower simulation used have been given elsewhere.[2] In this paper we shall give a brief description of the simulation.

The program generates air showers in energy intervals from $E_0$ to $2E_0$ on a spectrum with a slope of $E^{-2.6}$. The data from each of these intervals may then be combined in different proportions to produce different spectra. Over the range of spectral indecies investigated in this work this method produces a smooth spectrum. Nuclei of atomic number A are simulated using a superposition model where A nucleons are generated at the same angle and energy. The simulation uses a cross section which increases with energy for nucleon air interactions.

Interactions are simulated using a modified scaling model in which the rise in central rapidity density seen at the SPS collider is included by steepening the X distribution of produced secondaries in an energy dependent manner. The Monte Carlo includes production of nucleon anti-nucleon pairs as well as pions and kaons. Leading particle effects are included for various projectiles and the effect of nuclear targets is simulated. All hadrons are followed from their production until they either reach detector level, interact, decay or

drop below 2 GeV. The electromagnetic shower is calculated by accumulating each gamma ray produced in a meson decay. The gamma rays are then projected to detector level using approximation B[3] and the lateral spread of their showers is computed using a modified NKG[4] lateral distribution function. The information on both the hadrons and electromagnetic shower are written out on to tape where they are fed into our detector simulation program.

For each hadron which reaches detector level in our simulation we store its energy, position, particle type, momentum, arrival time, and local shower density. The response of our detector to each incident hadron and its accompanying electromagnetic shower is simulated. The number and distribution of triggers and delayed events are computed by applying offline cuts to the simulated data. We then compute an efficiency for triggering for each primary species and energy interval. The simulation of detector response is accomplished by comparison with direct calibration and Monte Carlo calculation.[5]

4. Comparison of Data and Simulation. This experiment provides a set of experimentally measured quantities which may be compared with simulations to test various composition models. It does not measure primary composition directly. Those models which predict rates which are inconsistent with our measured rates can be ruled out within the context of the high energy physics model used. It is important to note that by the use of models which predict significant deviations from observed interaction properties above measured energies different results may be obtained. In this paper, we compare our data to a high energy model which requires a minimum extrapolation from observed data. We also attempt to use models for primary spectra which are consistent with extensive air shower data.

The two models which we consider here represent divergent theories of cosmic ray propagation. In the first (model Md), the spectrum of the light and medium nuclei are assumed to be that given by the JACEE Experiment[6] while the spectra of the heavy nuclei (Si and Fe) are chosen to be somewhat flatter up to a rigidity dependent steeping, resulting in an increasing fraction of heavy nuclei. In the second model (model L), we follow the proposal of Linsley[8] in choosing a proton dominant composition which contains a flattening of the proton spectrum at $10^{14}$ eV. In Table 1 we list the parameters of each of these models. In Table 2 we present the predicted rates for this experiment for each model.

5. Results. The results of the comparison between our experimental data and our Monte Carlo simulation show that model Md of primary composition which has a significant enrichment of heavy nuclei near the break fits both our trigger rate and delayed event rate. Model L would produce a trigger rate 60 percent above the observed value while producing only 50 percent of the fraction of delayed events observed.

Model Md has been shown to be in agreement with our predicted rates for trigger rate and for delayed event rate. It has also been shown elsewhere to be consistent with measured muon distributions. This model is used to compute the expected flux of air showers at sea level and mountain level. Figure 3 shows these results. The discrepency between the simulation and the reported data[8,9] is consistent with the spread between various measurements.

Table 1
Composition Models

| | Slope (below break) | Break rigidity | Slope (above break) | |
|---|---|---|---|---|
| **Model Md** | | | | |
| Protons | -2.75 | 200 TV | -3.3 | |
| Alphas | -2.78 | 200 TV | -3.3 | |
| C-N-O | -2.6 | 200 TV | -3.2 | |
| Silicon | -2.55 | 200 TV | -3.1 | |
| Iron | -2.55 | 200 TV | -3.1 | |
| **Model L** | | | | |
| Protons | -2.7 | 100 TV | -2.5 | up to 10,000 TV then -3.1 |
| Alphas | -2.7 | 500 TV | -3.1 | |
| C-N-O | -2.7 | 500 TV | -3.1 | |
| Silicon | -2.75 | 500 TV | -3.1 | |
| Iron | -2.75 | 500 TV | -3.1 | |

Table 2
Rate Predictions

| Model | Event Rate (per hour) | Delayed Event Rate (per hour) | Fraction Delayed |
|---|---|---|---|
| Data | 3.15 ± .04 | 0.050 ± 0.004 | 0.016 |
| Md | 3.2 | 0.05 | 0.015 * |
| L | 5.1 | 0.04 | 0.008 |

* The Md model was chosen to give the best fit to this data.

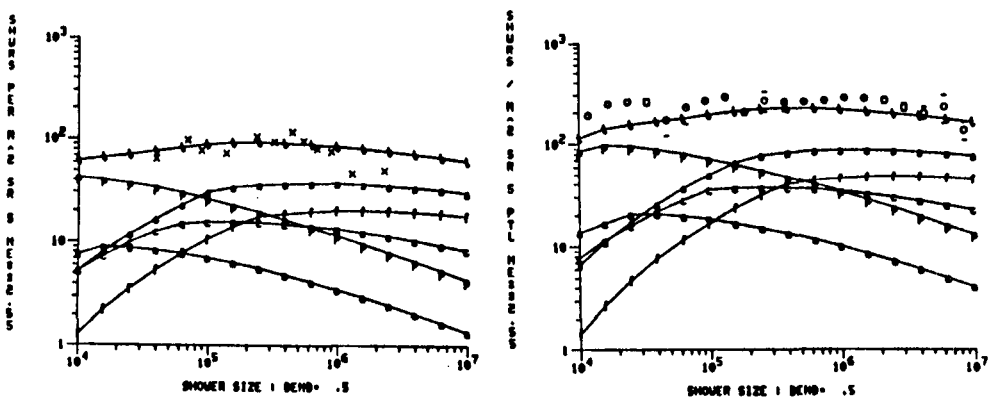

Sea level Mountain level

Figure 3: Vertical shower flux: x = sea level data, O = mountain level data, t = sum of simulated species

References


1. A. Mincer, Ph.D. thesis, University of MD, 1984 (unPublished)
2. J. A. Goodman et al., Phys. Rev. D26, 1043 (1982)
3. B. Rossi, High Energy Particles (Prentice-Hall, New York, 1952)
4. A. M. Hillas and J. Lapikens, Proc. 15th ICRC, Plovdiv, 1977, Vol. 8, p. 460
5. A. I. Mincer et al., N.I.M. (1984) to be published
6. T. M. Burnett et al., Phys. Rev. Letters 51, 1010 (1983)
7. J. Linsley, Proc. 18th ICRC, Bangalore, Vol. 12, p. 135
8. F. Ashton et al., Proc. 16th ICRC, Kyoto, Vol. 13, 243 (1979)
9. B. S. Acharya, Ph.D. Thesis, Tata Inst. of Fundamental Research, 94, (1983)

# THE COMPOSITION OF COSMIC RAYS NEAR THE 'BEND' ($10^{15}$eV) FROM A STUDY OF MUONS IN AIR SHOWERS AT SEA LEVEL

Goodman, J.A.,[1] Gupta, S.C.,[1] Freudenreich, H.,[1] Sivaprasad, K.,[1] Tonwar, S.C.,[2] Yodh, G.B.,[1] Ellsworth, R.W.,[3] Goodman, M.C.,[4] Bogert, D.,[5] Burnstein, R.,[6] Fisk, R.,[5] Fuess, S.,[5] Morfin, J.,[5] Ohska, T.,[5] Bofill, J.,[7] Busza, W.,[7] Eldridge, T.,[7] Friedman, J.I.,[7] Kendall, H.W.,[7] Kostoules, I.G.,[7] Lyons, T.,[7] Magahiz, R.,[7] Mattison, T.,[7] Mukherjee, A.,[7] Osborne, L.,[7] Pitt, R.,[7] Rosenson, L.,[7] Sandacz, A.,[7] Tartaglia, M.,[7] Taylor, F.E.,[7] Verdier, R.,[7] Whitaker, S.,[7] Yeh, G.P.,[7] Strongin, B.,[7] Abolins, M.,[8] Brock, R.,[8] Cohen, A.,[8] Ernwain, J.,[8] Perkins, G.,[8] Hatcher, R.[8] and Werthmann, A.[8]

[1]Univ. of Maryland, College Park, MD 20742
[2]Tata Inst. of Fundamental Research, Bombay, India
[3]George Mason University, Fairfax, Virginia
[4]Argonne National Laboratory, Argonne, Illinois
[5]Fermi National Lab., Batavia, Illinois
[6]Illinois Inst. of Technology, Chicago, Illinois
[7]Mass. Inst. of Technology, Cambridge, MA
[8]Michigan State University, East Lansing, Mich.

## ABSTRACT

A study of the distribution of muons near shower cores has been carried out at sea level at Fermilab using the E594 neutrino detector to sample the muons with E > 3 GeV. These data are compared with detailed Monte Carlo simulations to derive conclusions about the composition of cosmic rays near the bend in the all particle spectrum.

We report results from a set of Monte Carlo simulations generating EAS with primary energy in excess of 50 TeV. The set contains showers initiated by protons (A=1), alpha (A=4), CNO (A=14), medium (A=24) and heavy (A=56) primaries. For the primaries heavier than protons a successive breakup model for nucleii-air collisions is assumed. We have, in all, 2300 proton, 1400 alpha, 1000 CNO, 1000 medium and 1200 heavy initiated showers. Each shower record contains details of the electron lateral distribution and the muon and hadron lateral distributions as a function of energy, at the observation level of 1000g/cm.

To simulate experiment, each shower was thrown 500 times randomly over a square of 200 m x 200 m, centered on that of the detector system described elsewhere. For each throw, the electron in the 'trigger' detectors and the muons in the calorimeter were estimated from the lateral distributions. The number of 'detected' electrons and muons in each case was determined by a Poisson fluctuation of the number incident. This set of 'simulated data' was then subject to the same cuts as the data (with an additional upper limit of 100 on the number of muons to take into account the failure of the algorithm that estimates the muons). The resultant predicted distribution of muons, electrons, the rate of events etc. were then compared to those observed. Preliminary results on the rate favors a heavy primary dominated cosmic ray spectrum in energy range 50-1000 TeV.

# Composition of Primary Cosmic Rays at Energies $10^{15}\sim10^{16}$ eV Inferred from Mt.Fuji Emulsion Chamber Experiment

*Mt.Fuji Emulsion Chamber Collaboration*:

**Amenomori,M., Nanjo,H. and Konishi,E.** (*Hirosaki University, Hirosaki, Aomori*) **Hotta,N.** (*Utsunomiya University, Utsunomiya, Tochigi*) **Mizutani,K.** (*Saitama University, Urawa, Saitama*) **Kasahara,K., Kobayashi,T., Mikumo,E., Sato,K. and Yuda,T.** (*Institute for Cosmic-Ray Research, University of Tokyo, Tanashi, Tokyo*) Mito,I. (*Shibaura Institute of Technology, Shibaura, Tokyo*) **Shibata,M.** (*Yokohama National University, Yokohama, Kanagawa*) **Shirai,T., Taira,T., Tateyama,N. and Torii,S.** (*Kanagawa University, Yokohama, Kanagawa*) **Sugimoto,H. and Taira,K.** (*Sagami Institute of Technology, Fujisawa, Kanagawa*)

The $\Sigma E\gamma$ spectrum in $10^2\sim 5\times10^3$ TeV observed at Mt.Fuji ( $\sim$ 3725 m a.s.l.) strongly suggests that the flux of primary protons in $10^{15}\sim10^{16}$ eV is lower by a factor of $2\sim 3$ than a simple extrapolation from lower energies; the integral proton spectrum tends to be steeper than $E^{-1.7}$ around $10^{14}$ eV and the spectral index becomes $\sim 2.0$ around $10^{15}$ eV. If the total flux of primary particles has no steepening up to $\sim10^{15}$ eV, then the fraction of primary protons to the total flux should be $\sim$ 20 % in contrast to $\sim$ 45% at lower energies.

1. Introduction. As well known, the integral energy spectrum of all primary particles steepens to $E^{-2.0}$ over $\sim5\times10^{15}$ eV in contrast to $E^{-1.6}$ at lower energies. This "knee" of the spectrum may come from 1) a change of the acceleration mechanism resulting in a steeper source spectrum and/or 2) a breakdown of magnetic trapping in the galaxy. Study on the composition around the "knee" is an important key to resolving the problems of the origin and propagation of cosmic rays. However, the definite result has not yet been obtained because of the too low primary flux for the direct observation and too poor response of the air shower observation to the primary mass.

The emulsion chambers ( EC ) at Mt.Fuji have been extended to the scale of 1000 $m^2\times$ year, and a few hundred events produced by primaries with energy $10^{15}\sim10^{16}$ eV have been accumulated[1] . Meanwhile, accelerators has clarified the feature of nuclear interactions up to 150 TeV (in lab. energy). These circumstances enable us to investigate the primary composition around the "knee" by analysing the EC events through simulations based on a reliable model of nuclear interactions.

2. $\gamma$-ray Family. A group of high energy particles (mostly $\gamma$-rays with energy > a few TeV) produced by successive collisions of a primary particle with air nuclei is called a family. Particles which penetrate deep in the atmosphere can produce families effectively, otherwise

produced particles are usually absorbed in the atmosphere. Therefore protons are most efficient in producing families; the average energy of protons responsible for $\gamma$-ray families with $\Sigma E\gamma>100$ TeV is $\sim 2\times 10^{15}$ eV while that of irons is almost one order of magnitude higher.

It has been found that the fraction of proton-induced families in all families in $\Sigma E_\gamma>100$ TeV is $\sim$ 70% even if protons constitute only $\sim$ 10% of all particles around $10^{15}$ eV. Therefore, if we convert the family intensity into the primary flux assuming that all families are produced by protons, we obtain an upper bound of the proton flux within an accuracy of 30%.

3. Monte-Carlo Simulation. The Monte-Carlo method has been used to simulate the family phenomena and to deduce the primary intensity by comparing the obtained family flux with the experimental one. Important factors in the simulation are the cross-section of nuclear interactions, the leading particle spectrum and the secondary particles spectrum (especially, the degree of scale breaking in the fragmentation region). These are summarized in the following.

*Cross Section* Using the data of $pp$ and $\bar{p}p$ interactions up to 150 TeV, the mean free path of the N-Air collision is expressed as $\lambda=\lambda_0\times E^{-\delta}$, where $E$ is in TeV, $\delta$ is 0.04 $\sim$ 0.06 and $\lambda_0=82$ g/cm$^2$.

*Elasticity* Two cases of the elasticity distribution are assumed as shown in Fig.1. Case *A* disregards the difference between protons and neutrons and gives the average elasticity of 0.44. In case *B* is considered the absence of the diffraction peak in charge exchange processes, for which we refer to p-C and p-Be data[3] at 100 - 400 GeV. The average elasticity in a non-charge exchange process like p+Air$\rightarrow$p+X is 0.45 while that of p+Air$\rightarrow n$+X is 0.28. With a charge exchange probability of 28 %, the average elasticity in case *B* becomes 0.40.

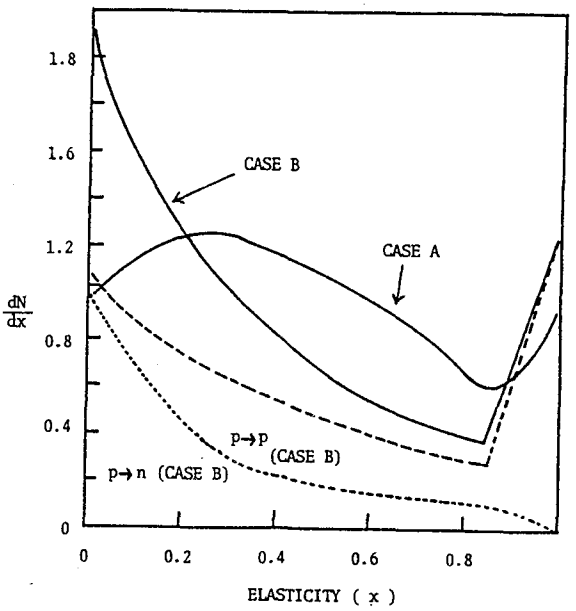


Fig.1 Elasticity distribution.

*Energy distribution of secondary particles* The QCD-jet[2] automatically introduces a mild scale braking in the fragmentation as shown in Fig.2a. The rapidity distribution shown in Fig.2b is compatible with the CERN-SPS data. To see the effect of a strong violation of scaling in the fragmentation region we employed a fireball model of which the multiplicity grows as $E^{1/4}$.

In Table 1, the models are characterized by the parameters discussed

above. The calculated flux of $\gamma$-ray families at $\Sigma E\gamma$=100 TeV for each model is listed by normalizing the flux to model QA6.

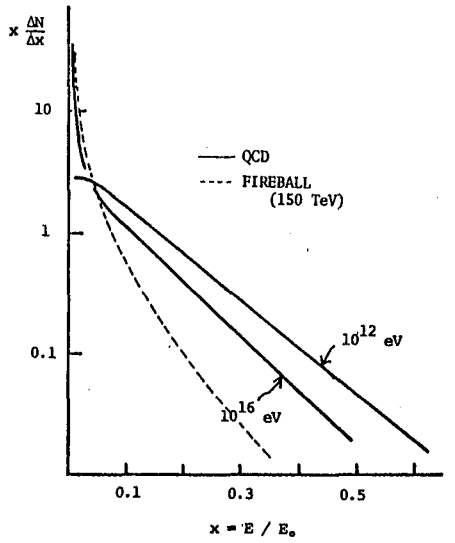


Fig.2a $x$-distribution of secondary pions in p-Air collisions at $10^{12}$ eV and $10^{16}$ eV. A mild-violation of scaling is seen in the model with QCD jet.

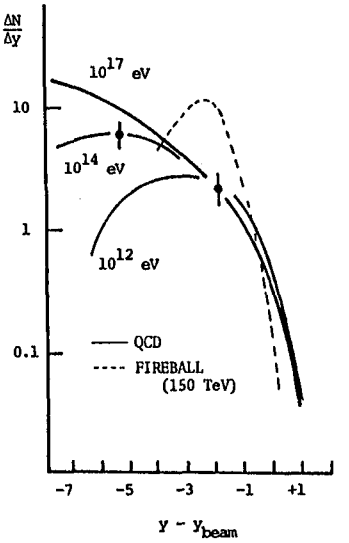


Fig.2b $y$-distribution corresponding to Fig.1. Black dots show data by the CERN-SPS. Correction due to Air-target effect is included.

Table 1. Interaction model and the relative flux of $\gamma$- ray family.

| model | $x$ distribution | elasticity | m.f.p.($\delta$) | flux ratio |
|---|---|---|---|---|
| QA4 | QCD | case A | 0.04 | 1.32 |
| QA6 | QCD | case A | 0.06 | 1 |
| QB6 | QCD | case B | 0.06 | 0.72 |
| FA4 | Fireball | case A | 0.04 | 0.41 |

4. Proton Spectrum in $10^{15}\sim10^{16}$ eV. Under the assumption that all $\gamma$-ray families are produced by protons, an expected spectrum of protons is deduced as shown in Fig.3. The upper bound is given by model QB6 and the lower one by model QA4. As mentioned already, a maximum of 30 % decrease might take place in the expected flux (due to the heavy primary contribution). Even if we take the experimental errors (both statistical and systematic) into account, we are forced to conclude that the proton spectrum should steepen around $10^{14}$ eV, and the ratio of protons to all particles in $10^{15}\sim10^{16}$ eV should be lower by a factor of $2\sim3$ than that at lower energies.

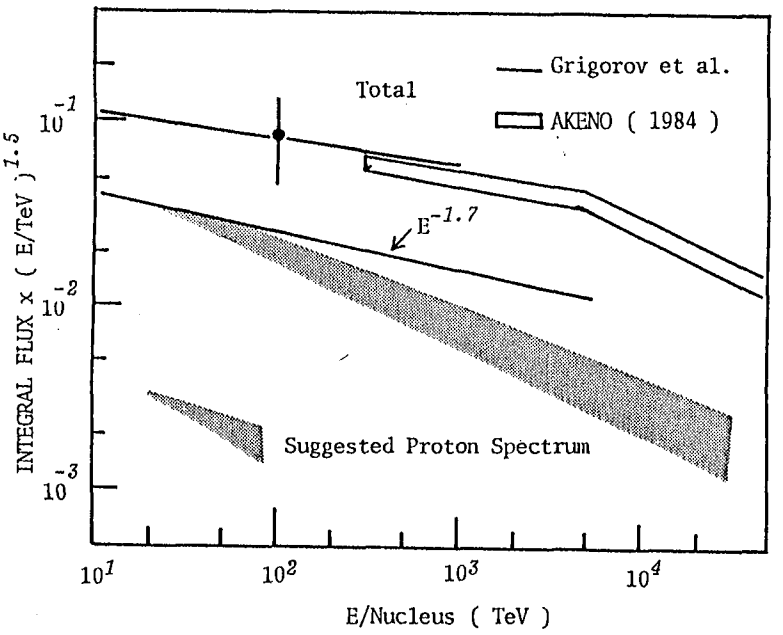


Fig.3 Expected primary proton spectrum.

5. Discussion. By an analysis of air shower data, some authors reported a proton-dominant composition[4]. In their estimation, a scaling violation in the central region are included to be consistent with the CERN-SPS data while the $x$-distribution in the fragmentation region is not properly considered, which is most effective to the cosmic-ray propagation in the atmosphere. Even if we assume a strong scaling violation (FA4) which is unrealistic already at the accelerator energies as shown in Fig.2b, the expected proton flux never exceeds the simple extrapolation from low energies.

The general (i.e., all observed particles independent of family correlation) hadron and $\gamma$ spectra observed at Mt.Fuji also supports the present picture[5]. In Ref.6, we estimated the composition around the "knee" by the use of the "rigidity cut-off model". The proton spectrum there is consistent with the present estimation.

**Acknowledgement.**

Data analysis and simulation calculation were done using the computer FACOM M380 of the Institute for Nuclear Study, the University of Tokyo and the FACOM M180II-AD of Kanagawa University.

**References**

1. Mt.Fuji group, M.Amenomori et al., Phys. Rev. D25 (1982) 2807.
2. L.Ding et al., Proc. of 18th ICRC (Bangalore), vol.5, p.483 (1983).
3. L.W.Jones, Proc. of 18th ICRC (Bangalore), vol.5, p.17 (1983).
4. See for example; J.Wdowczk and A.W.Wolfendale, Nature 306 (1983) 347.
5. Mt.Fuji group, M.Amenomori et al., in this conference, HE3.1-3.
6. Mt.Fuji group, M.Amenomori et al., Proc. of Int. Sympo. on Cosmic Rays and Particle Physics, p.494 (1984).

# EAS FLUCTUATION APPROACH TO PRIMARY MASS COMPOSITION INVESTIGATION

J.N.Stamenov, V.D.Janminchev *
INRNE, Sofia, Bulgaria
*High Pedagogical School, Shoumen, Bulgaria

ABSTRACT. The analysis of muon and electron fluctuation distribution shapes by means of the statistical method of invers problem solution gives the possibility to obtain the relative contribution values of the five main primary nuclei groups. The method is model-independent for a big class of interaction models and can give good results for observation levels not too far from the development maximum and for the selection of showers with fixed sizes and zenith angles not bigger then $30^{0}$.

1.INTRODUCTION. The extensive air showers(EAS)are today the main and possibly the only information source about the mass composition of the primary cosmic radiation in the ultrahigh energies, because the use of the direct methods are still limited now to energies $10^{13}$-$10^{14}$ eV.

The analysis of the dependences of the second momenta of the different component fluctuation distributions of the other EAS parameters/1-4/shous, that the primary cosmic radiation at energies greater than $10^{15}$eV can not consist of one nucley type only and the content of primary protons and iron nuclei in the mixed mass composition must be essential.

2.METHOD. The EAS fluctuation distribution shapes have an essential sensitivity/1/to the relative contributions of the five main nuclei groups:P,$\alpha$,M,H,VH in the primary composition of the cosmic radiation with ultrahigh energy, but the information content could be derived with help of a complicated "noise" system/2,5/.These fluctuation distributions can be treated as an invers problem/5,6/aiming to precise the information about the mass composition and to estimate the relative contributions $w_{aj}$ of the j nuclei groups.

After this point of view/5,6/it is necessery to solve the invers problem starting from the equation:

$$W_i = \sum_{j=1}^{5} M_{ij} \cdot w_{aj}$$

where $M_{ij}$ is the matrix of the model and apparatos "noises" for a definite model calculation of EAS development and for definite EAS experiment(including detector types and arrangment,algorithms of the data treatment and so on); $W_i$ are the the number of showers with a definite $K_\mu=(N_\mu/<N_\mu>)$ and $N_e$=const including the information in the $i^{th}$-been of the corresponding $W(K_\mu)=W(N_\mu/<N_\mu>)$ experimental distribution also; $w_{aj}$ are the relative contributions of the usual five ($j$ = 1-5) main primary nuclei groups with A= 1,4,14,26,52 in the primary energy interval E,E+dE.

3. RESULTS AND DISCUSSIONS. Applying the statistical method of the invers problem solution,developed by V.Pavljuchenko/7/by the analysis of pseudoexperimental fluctuation distributions $W(K_\mu)$ it is shown/6/,that the estimations $w_{aj}$ are model-independent in the ranges of the errors $\sigma_{w_{aj}}$ if the conditions $|\alpha_{ex}-\alpha_{cal}|<0.05$ and $(\sigma_\mu/N_\mu)_p<0.5$ are satisfied. This is fulfiled for a big number of interaction models which describe eventhough the main phenomenological EAS characteristics,particulary the muon-size dependence $N_\mu\sim N_e^{\alpha}$ ,where $\alpha_{cal}$ is in the calculated relation $N_\mu\sim N_e^{\alpha_{cal}}$ and $\alpha_{ex}$-the corresponing experimental value.

The value $(\sigma_\mu/N_\mu)_p$ depends on the interaction model and is conected with the shower maximum position over the observation level in the studed energy range and is a principal limit for the method of analisis.In this conection an optimal observation level exists for each energy interval,where the method of the fluctuation distribution shape analisis gives the best estimations $w_{aj}$ for the primary mass composition.

The zenith angle interval,where the showers are registrated,plays an important role in the shower fluctuation investigations.It is shown/8/,that the muon flux fluctuations in the interval $\theta<60^\circ$ are not so informative as in $\theta<30^\circ$,because the differences between P and Fe shower fluctuations decrease with $\theta$ (fig.1).But in the both cases,the relative change of $(\sigma_\mu/N_\mu)$ remains no more than 15%,which is insignificant for the analysis of the fluctuation distributionshapes.Further,the expected differences between muon-size dependences

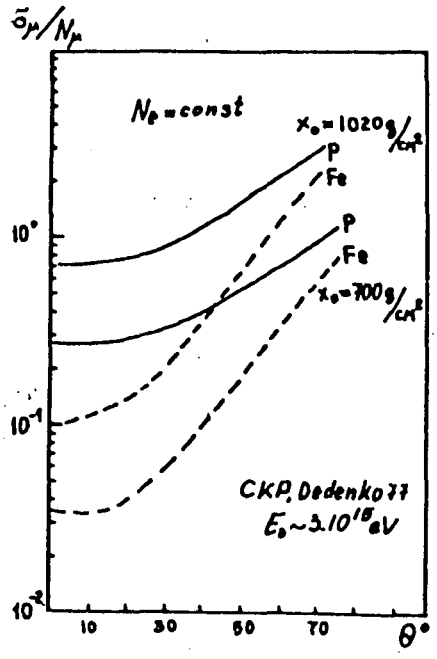


fig. 1

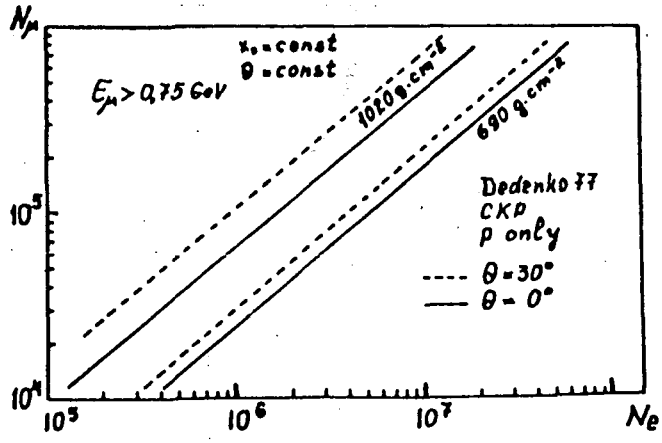


fig.2

for $\theta = 0^\circ$ and $\theta = 30^\circ$ at mountain altitudes are $\sim 10\%$ (fig.2) in distinction to the situation at sea level, where this difference becomes $\sim 50\%$. The corresponding Thien Shan experimental data/9/ confirm this expectation for mountain altitudes (fig.3). From here it follows, that the shower selection of axis in the zenith angel interval $\theta < 30^\circ$ is good enough for the further primary mass composition investigation.

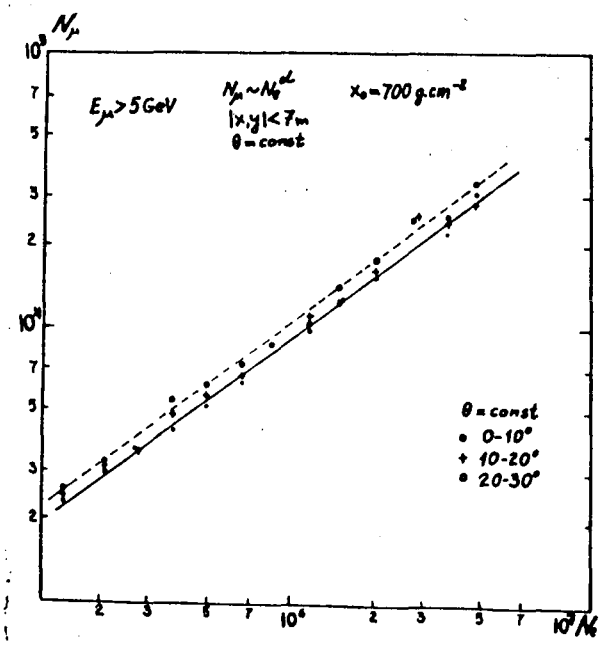


fig.3

The relative primary nuclei group contributions $w_{aj}$ obtained by the solution of the inverse problem are however distored by two factors:

1) the method of the inverse problem solution/6/;

2) the efficiency of the registration of EAS, initiated by primaries with different atomic number A· in the selection of showers with fixed size $N_e$=const or fixed muon number $N_\mu$= const at the observation level.

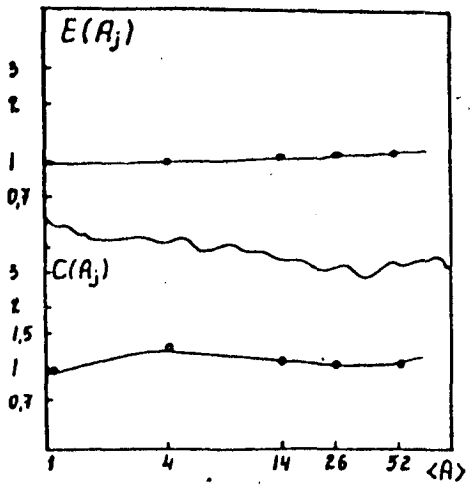


fig.4

These two distortions are discribed with the corresponding distortion functions: $C(A_j)$ and $E(A_j)$ (fig.4). It is shown, that the biggest systematical correction is necessery for the $w_{aj}$ value. The efficiency function $E(A_j)$ remains very weak for showers at observation levels not too far from the development maximum.

4. CONCLUSIONS. Taking into account all these considerations and remarks, we conclude that the primary mass composition in the energy interval $10^{15}$ - $10^{16}$ eV, obtained on the basis of the Tien-Shan data/10/, is mixed and it remains rich on protons as that at lower energies:

| A | 1 | 4 | 14 | 26 | 52 |
|---|---|---|---|---|---|
| $w_{aj}$(%) | 39 ± 4 | 13 ± 7 | 16 ± 6 | 17 ± 6 | 15 ± 5 |

REFERENCES

/ 1/ Kirov I.N. et al., 1980, Proc.ISCRC, Sofia, 61
/ 2/ Hara T. et al., 1981, Proc. 18th ICRC, Paris, 6, EAI-2
/ 3/ Khristiansen G.B. et al. 1977, Proc. 15th ICRC, Plovdiv, 8, 148
/ 4/ Katsarsky L.N. et al., 1977, Proc. 15th ICRC, Plovdiv, 12, 46
/ 5/ Nikolsky S.I. et al., 1981, Short reports, 8, 49
/ 6/ Nikolsky S.I. et al., 1983, Proc. 18th ICRC, Bangalore, OG4-14
/ 7/ Pavljuchenko V.P. et al., 1981, Short reports, 8, 53
/ 8/ Nikolsky S.I. et al., 1981, Preprint FIAN, N 65
/ 9/ Kirov I.N. et al., 1983, Proc. 18th ICRC, Bangalore, EAI.1-13
/10/ Stamenov J.N. et al., 1983, Proc. 18th ICRC, Bangalore, OG

# THE PRIMARY COMPOSITION BEYOND $10^5$ GeV AS DEDUCED FROM HIGH ENERGY HADRONS AND MUONS IN AIR SHOWERS

Peter K.F. Grieder
Physikalisches Institut
University of Bern
Switzerland

ABSTRACT

We present data obtained from a large set of air shower simulation calculations using our highly refined hadronic interaction and shower simulation model, in an attempt to solve the problem of primary chemical composition beyond $10^5$ GeV total energy. We discuss briefly that high energy hadrons in air showers offer a rather unique primary mass signature and show that the interpretation of high energy muon data is much more ambiguous. Our predictions are compared with experimental data where such data are available.

1. Introduction. The present work represents a search for observables and methods that would allow to identify unambiguously the mass group of a primary initiating a shower from either ground based or deep underground observations. We have shown in our early work (Grieder, 1977) that the significant information which requires the least number of simultaneous observables is to be found among the most energetic constituents of air showers. More recently we have shown that high energy hadrons in air showers observed at ground level offer a unique mass signature. We have also shown that these data in conjunction with experimental results indicate that the chemical composition beyond $10^5$ GeV does not seem to change significantly from that at lower energies (Grieder, 1984).

In the following we summarize the results of our work on the relationship between high energy muons and primary mass for the energy range from $10^5$ GeV to $10^8$ GeV and compare these data with our previous results based on hadrons.

2. Model and Calculation. The present calculations are based on our two-component model for hadronic interactions which violates Feynman scaling in the central region and reproduces CERN pbar-p data very well. The calculations consider all significant particles and processes and include the electromagnetic component as well. The essential differences between proton and heavy primary initiated showers are due to the significant difference in the respective inelastic cross sections and in the high energy nuclear physics that governs the interactions. Both are considered in our calculations. For the nuclear physics aspects it is chiefly the fragmentation modi of the primary nuclei and, above all, the number of collision partners that are involved in nucleus - nucleus collisions that are problematic. There our current knowledge is still very marginal.

We have shown previously (Grieder, 1983) that it is chiefly this latter problem that troubles the interpretation of high energy muon data with respect to primary composition. In comparison to proton showers, it is the widely varying number of collision partners in the first few collisions of heavy primaries and their subsequent fragments with air nuclei that cause large fluctuations in the secondary particle multiplicity and in a number of other observables, such as the number of high energy muons per shower. In comparison to proton showers, the relative enhancement of muon production in heavy primary initiated showers resulting from the greater height of the first interaction and a lesser energy per nucleon diminishes with increasing primary energy because of the more rapid increase of the cross section for proton primaries in showers of comparable total energy, which rises the point of the first interaction of proton showers, thus stimulating muon production via pion decay. Furthermore, since the energy per nucleon of a proton primary is almost two orders of magnitude higher than that of an iron primary of comparable total energy, the central pion multiplicity is of comparable order of magnitude or larger than the combined multiplicity of fragmentation region pions from all first generation collisions of nucleons from iron nuclei and their fragments.

3. Results and Conclusions. In the following we are presenting a set of muon data from our recent all-component calculations. The data are shown in figures 1a) to 1f) and cover a range from $10^5$ to $10^8$ GeV total primary energy, for proton and iron initiated showers. It was assumed that 10 nucleons of the primary nucleus interact in each of the first iron initiated interactions. Total fragmentation of the nucleus was assumed to occur in the first interaction. Other break-up modi have also been investigated, with the result that distinction between iron and proton showers was even less, as expected.

For low energy muons the well known picture envolves which shows an increase of the muon number with primary energy that goes as energy to power 0.8, with the usual enhancement factor of about 2 or more for iron showers (c. f. figure 1a). However, for muon energies in excess of 100 GeV, relativistic effects in conjunction with the energy and mass dependence of cross sections change the trivial relationship at high primary energy. This becomes evident upon inspection of figures 1b) through 1f). The cross-over of the two curves depends on muon energy, of course, as shown in figures 1d), 1e) and 1f).

Because of the multiplicity law on one hand and the competition between interaction and decay of pions as a function of energy on the other, it is evident that pions from different rapidity regions are responsible for muons of a given energy group resulting from either proton or iron initiated showers of the same total primary energy. These facts in conjunction with the above mentioned high energy nuclear physics aspects govern the muon number in a particular energy group in proton or iron initiated showers.

From the above considerations it is evident that a given muon detector, located at a particular depth underground, corresponding to a

certain energy cut off is only suitable for investigating a distinct primary energy range with respect to chemical composition. Moreover, because of the remaining ambiguities, data from at least two or more underground detectors located at different depths will be required to get a unique answer. Upon folding of the known primary energy spectrum with the multi muon rates, a coarse mass determination can be achieved, provided that the detectors cover an adequate area. Present underground installations are still marginal in size for reliable multi muon detection. This point is discussed elsewhere (Grieder, HE 5.4-4, this conference).

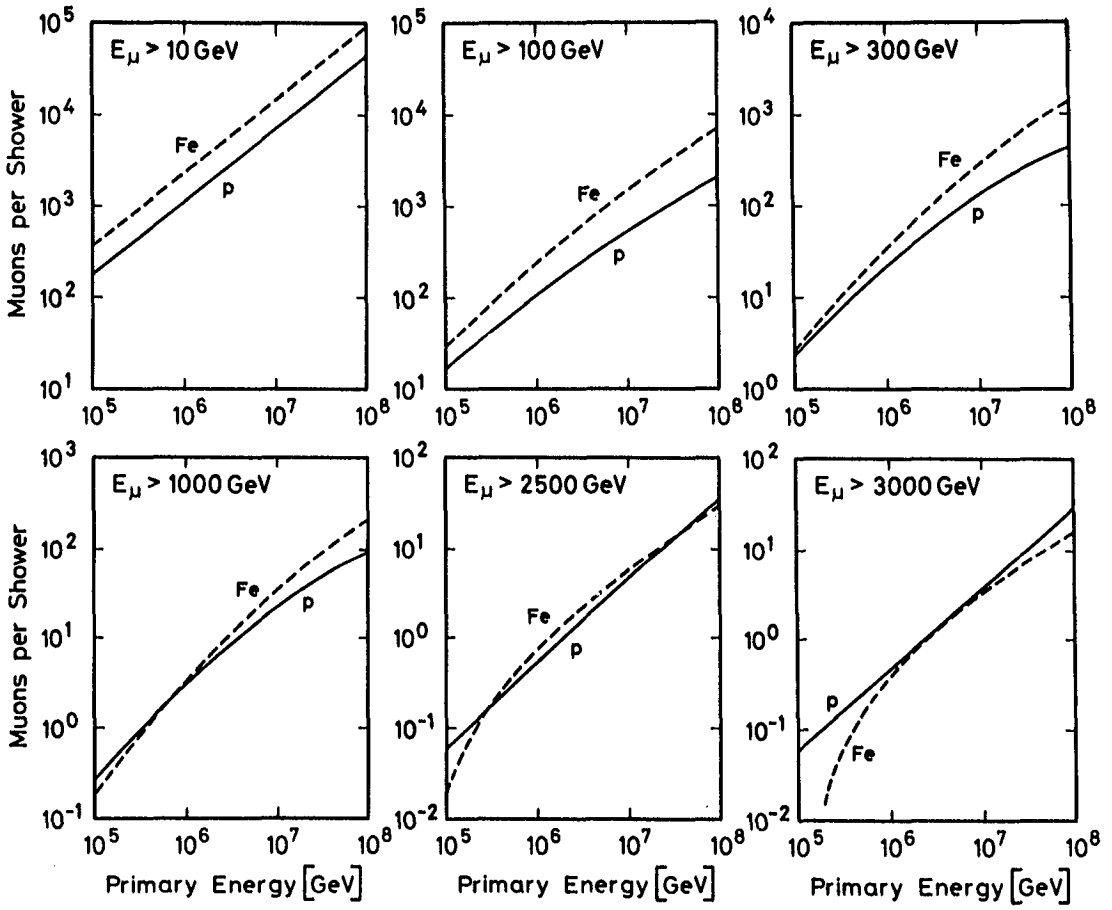


Fig. 1 Muon number versus primary energy in proton and iron initiated showers for different muon cut off energies, as specified.

At lower muon energies experimentally observed correlations between muon number and primary energy (or shower size) have so far failed to manifest an unambiguous transition from a so-called normal to an iron rich composition at the expected location in the primary spectrum, as is shown in figure 2. Thus we also conclude from these data that the composition is more likely to change little if at all, and that the bend in the spectrum is due to another cause.

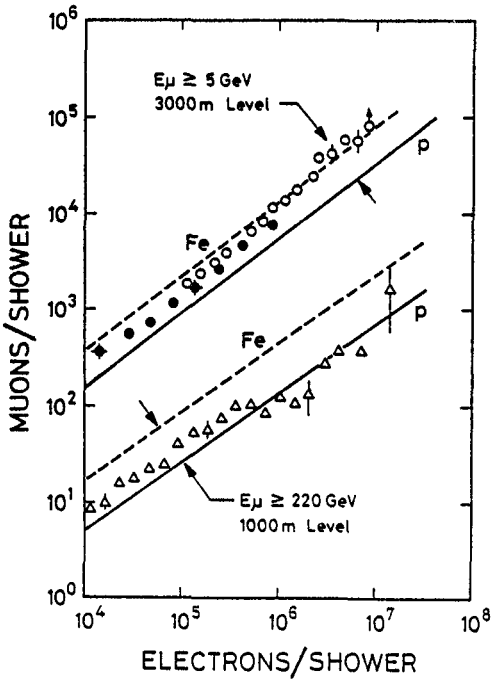


Fig. 2 Muon - electron correlations for proton and iron initiated showers. The dashed and solid lines are from our calculations. The full and open circels are experimental data from Tien Shan (Kabanova et al., 1973 and Machavariani et al., 1979), the triangular symbols from the Kolar Gold Fields (Acharya et al., 1983).

Lack of space does not allow us to summarize the hadron data here. For details on this topic the reader is referred to the earlier mentioned reference (Grieder, 1984). In spite of the fact that hadrons offer theoretically a more clearcut primary mass signature than muons, we fully realize that high energy muons have their experimental merits.

4. Acknowledgements. We are grateful to the Swiss National Science Foundation for supporting this project.

References

1. Acharya, B.S., et al. (1983), Proc. 18th I.C.R.C., Bangalore, India, 9, p. 191.
2. Grieder, P.K.F. (1977), Rivista del Nuovo Cimento, 7, p. 1.
3. Grieder, P.K.F. (1983), Proc. 18th I.C.R.C., Bangalore, India, 11, p. 459.
4. Grieder, P.K.F. (1984), Nuovo Cimento 84 A, p. 285.
5. Kabanova, N.V., et al. (1973), Proc. 13th I.C.R.C., Denver, Col., 4, p. 2534.
6. Machavariani, S.K., et al. (1979), Proc. 16th I.C.R.C., Kyoto, Japan, 8, p. 240.

# IMPLICATION OF EAS DATA FOR THE STUDY OF PRIMARY COSMIC RAYS ABOVE $10^5$ GEV

L.Papova
Institute of Nuclear Research and Nuclear Energy, Sofia, Bulgaria

J.Wdowczyk
Institute of Nuclear Problems, Lodz, Poland.

1. Introduction Due to the strong decrease of the energetic cosmic ray flux its direct detection at the top of atmosphere with air crafts is limited at the present time to about $10^5$Gev. The intensity of all primary particles can be approximated in the range $10^2$-$10^5$Gev by power function with power index 2.65. There are predominantly protons (about 40 %) and the rest is represented by several groups of nuclei (He, C-N-O, mean and heavy nuclei). In the range of $10^5$-$10^8$Gev considerable disagreement is observed between the estimations of the primary spectrum that is most probably connected with the uncertainity of the indirect derivation of the energy and the type of primary particles on the basis of ground parameters of extensive air showers.

In this paper we will discuss our results for the primary spectrum in the range $10^5$-$10^8$ Gev, obtained by implication of EAS data from mountain altitudes[1] registered with Tian Shan and Chacaltaya apparatuses.

2. Energy spectrum of primary cosmic rays at $10^5$-$10^8$ Gev The mean energy of primary cosmic flux is obtained on the basis of electron and muon size spectra of EAS. For that purpose we have simulated the development of electron and muon components in EAS initiated by primary particles with fixed energy and atomic number. It was assumed the so called high multiplicity model for hadron interactions, normal mass composition of primary particles that is the same as below $10^5$Gev. From the simulated showers we have constructed the fluctuation histograms of the total electron number and that of muons in EAS for several values of primary energy and groups of nuclei. The histograms are approximated by Gamma distributions the parameters of which are represented as functions of primary energy. It allows to obtain the conversion factor , W, with which we can convert shower size in primary energy, needed in order to obtain theoretically fluctuation distributions of primary energies. They were used to derive energy spectrum of all primary particles from the measured intensities of extensive air showers with different electron and muon size. It is compared in fig.1 with the curve that is an approximation of the direct registration at lower energies. Our spectrum derived from the measured electron size distribution of EAS at mountain altitide smootly links the satelite data showing some tendency of a bump around $10^6$Gev. The spectral index is changing from 2.4 to 2.76. In the same figure we have compared the corresponding estimation for primary energy spectrum of Nagano et al[2] obtained on the basis of Akeno data. They give too low intensities of the primaries most probably due to the relatively small

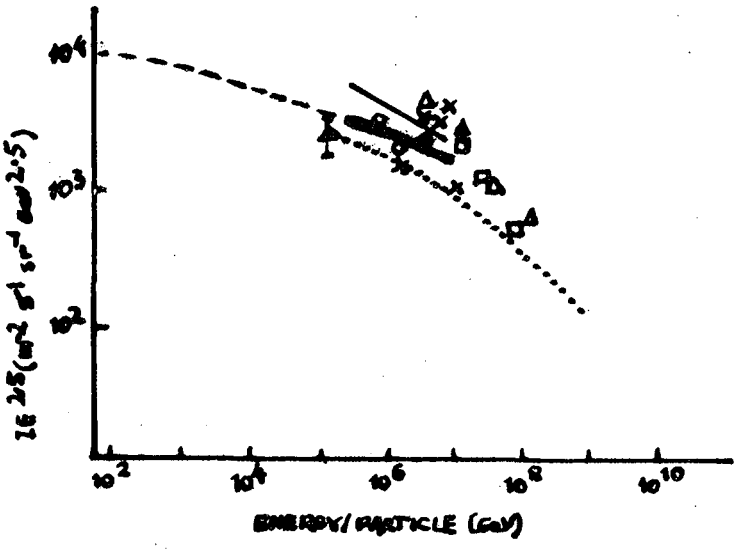


Fig.1 The all-particle energy spectrum ; dash line - approximation of satelite and baloon data (Grigorov et al[3] o ) ; JACEE collaboration[4] ⋈ ; thick line - present calculation on the basis of electron size spectrum; full line - present calculations for muon size spectrum; dotted line - Nagano et al[2] estimations on the basis of Akeno data; Khristiansen et al[5] × ; Efimov et al [6] □ ; La Pointe et al[7] △ .

size of showers detected with fixed intensity. (As a ground parameter they used the number of electrons in the maximum of showers. So far as shower cascade curves are not determined around the maximum in Akeno (920 $g.cm^{-2}$) these authors have multiplied Akeno data by the ratio, $R=N^{Ch}_{max}/N^{Ch}_{920}$ , taken from the Chacaltaya experiments at different zenith angles).

Our primary spectrum derived from the muon size distribution disagrees with the measured spectrum at lower energies. The high-multiplicity model predicts higher intensities of all primary particles from the converting of muon data. They do not link to the intensities of cosmic particles with lower energies. Better consistency could be obtained if we assume the new phenomenological model[1] with breaked Feynman scaling, because the latter gives smaller values for the mean energy of primary particles initiating showers with a fixed size than in the case of high-multiplicity model. Apart of that, our complex analysis of all muon data[1] gave also ground in favour of the new phenomenological model if we assume normal primary composition in the range $10^5$-$10^8$ Gev. However, when we applied the new phenomenological model for calcula-

tion of electron component characteristics and for convertion of electron shower size in primary cosmic ray spectrum we obtain considerable disagreement. It forced us to inspect both our model assumptions for interactions and mass compositio of cosmic rays.

3. Discussion In order to clear up why the new phenomenological model predicts slower development of the electron component of EAS whereas its predictions are fitting the muon data from different experiments we have to mention first of all that in the simulation of electron-photon cascades we assumed the upper value (37.7 g/cm$^{-2}$) of the radiation length. The latter is varying from 35 in different authors calculations. It is necessary to stress also that unlike with the case of the muon component, the electron component is governed predominantly by the very first pion interactions [1] occuring at very high energies ($\gtrsim 10^5$ Gev). The highest accessible energies of the modern accelerators do not exceed $2.10^5$ Gev as is the case of the SPS experiment in CERN with proton-antiproton colliding beams. So far as pion interactions are not measured at high energies we have adjusted their properties from the measurements with accelelerators at lower energies. Analysing EAS data we made conclusion that some increase of the total inelastic cross section and the total coefficient of inelasticity in pion-air nucleus collisions should provoke increase of the effective multiplicity and consequently faster development of the electron component in EAS. Similar conclusion we derive from the examination of the hadron component of EAS [2]. In fact there are some experimental evidences [9-13] from low energy accelerator experiments allowing to assume considerably pion interaction cross section and inelasticity at energies above $10^5$Gev. However , it must be poined out that several authors [14-17] have already shown that such corrections only partly improve the consistency of the calculated properties of electron and hadron components of EAS with experimental data.

It is worth-while to note that there is without doubt un increase in the yeld of baryon (and anti-baryon) production at very high energies observed already in the SPS Collider experiment [18]. Tonwar [19] finds in cosmic ray experiments strong evidence for such increase in the fraction of baryons with energy, the value reaching at least 15 % by $10^5$Gev. (The percentage of baryons in our calculations with high-multiplicity model had been neglected whereas it was assumed to be about 10 % in the new phenomenological model). It is certainly possible that the observed fast development of EAS above $10^5$Gev is partly due to the considerable baryon production that leads to shorter mean path of cosmic ray interactions in the air.

At last we can not dismiss high energy gamma rays in the primary spectrum above $10^5$Gev. All gamma ray saurces detected at present time have energy spectra wkth power index about 1 in comparing with 2.6 of other particles. Thus, the $\gamma$/proton ratio may approaching $10^{-3}$ at $10^6$Gev [20]. In this connection is the hypothesis of Wdowczyk and Wolfendale [20] that about 30 objects as Cyg X-3 is needed in the Galaxy to produce the bulk of the cosmic ray particles if as much energy went into particles as into gamma rays. However in order to obtain as much muon as they are observed in showers initiated by gamma rays emitted from the specific sources (Cyg X-3

and Crab) we have to assume some convergence of the electromagnetic cross section of photon production to that of the strong interaction pion production at too low energies (say, about $10^5$-$10^8$Gev).

This, we can conclude that the problem of determination of the energy and mass spectrum of primary cosmic flux insists further complex investigation of both particle interactions at high energies and the astrophysical mechanisms of different particles acceleration.

References

1. L.Popova "Verification of the New Phenomenological Model for Hadron Interactions at High Energies", Acta Universitatis Lodziensis, Lodz, Poland, 1984
2. Nagano M. et all. J. Phys. G : Nuclear Phys. ,1984 (in press)
3. Grigorov N.L. et al. Proc. 12 ICRC, 5, 1746, 1971
4. JACEE Collaboration Proc. A.I.P. 49, 85, 978,1982; Proc. 17 and 18 ICRC, 1981, 1983
5. Khristiansen G. B. et al. Proc. 18 ICRC OG4 - 13, 1983
6. Efimov N. I. et al. Proc. 18 ICRC OG 4.15, 1983
7. La Pointe et al Canad. J. Phys. 46, 568, 1968
8. Popova L. This Conf. Proceedings HE 4.2 - 11, 1985
9. Jones L. Cosmic Ray Workshop on HEI, La Paz, 19, 1982
10. Voyvodic L. Cosmic Ray Workshop on HEI, La Paz, 19, 1982
11. Tasaka S. et al. Phys. Rev. D25, 1165, 1982
12. Gaisser T. et al Proc. 18 ICRC 1983
13. Lund D. et al. Phys. Rev. D15, 11, 1163, 1977
14. Capdevielle J. N. et al. Nuovo Cim. 56, 6, 672, 1982
15. Hillas M. A. Proc. Paris Workshop on Cascade Simulation,1981
16. Gawin J. et al. Proc. 18 ICRC EA 1.2-22, 1983
17. Danilova T.V. et al. Preprint 14 Lebedev Phys. Inst. Ac.Sc. USSR, 1984, Moscow
18. Carlson Per, XI Int.Winter Meeting on Fundamental Physics, Toledo, Spain, 1983
19. Tonwar S.C. Proc. Madison Conf. on Forward Collider Physics, 562, 1981; Proc. 17 ICRC Rapp.Talk,1981
20. Wdowczyk J. and Wolfendale A.W. Nature 305, 609, 1983

# HIGH-ENERGY MULTIPLE MUONS AND HEAVY PRIMARY COSMIC-RAYS

Mizutani, K.
Department of Physics, Saitama University, Urawa, Japan

Sato, T., Takahashi, T. and Higashi, S.
Department of Physics, Osaka City University, Osaka, Japan

**Abstract**

The three-dimensional simulations have been carried out on high-energy multiple muons. On their lateral spread, the comparison with the deep-underground observations so far indicates that the primary cosmic rays seems to include heavy nuclei of high content. The calculated results also suggest us a method to determine the average mass number of primary particles in the energy around $10^{15}$ eV.

## 1. Introduction

The cosmic-ray composition in the energy around $10^{15}$ eV provides us with a useful clue to clarify acceleration and propagation mechanism of cosmic rays. However, the restriction of observation limits the direct measurements to a lower energy region. On the other hand, on the informations given indirectly from the observations of very high-energy phenomena in the atmosphere, the reliability has increased, because that the characteristic feature of high-energy interactions has been clarified by the scale-up of accelerators.

According to a systematic study of gamma-ray family phenomena observed with emulsion chambers at Mt. Fuji(1),(2), which gives us one of those indirect informations, the heavy-nuclei content seems to increase in those energy region. This feature is consistent with some observations of extensive air showers(3). In order to investigate further this feature, as described in the previous report(4), we carried out the Monte Carlo simulations on high-energy multiple muons, and compared with the experimental results of deep-underground observations (5),(6). On the lateral spread of multiple muons, which is not much affected by experimental bias, the observations coincide with those calculated under the assumption of the primary cosmic rays with heavy nuclei of high content. For the purpose of the further examination, our simulation study has been continued with the same method. The results suggest us one of a method to determine the average value of mass number of cosmic rays at very high energy.

## 2. Simulations

The three-dimensional Monte Carlo simulations have been carried out on the high-energy multiple muons which are produced in the upper layer of the atmosphere and reach to the sea level and also to the point of great depth underground(4).

On the nature of hadron interactions in the atmosphere, it is assumed in the simulations that the Feynman scaling is held in the fragmentation region of particle production and the collision cross section increases as increasing of energy corresponding to the $\ln^2 s$ dependence. In the nucleus-nucleus collision, some of nucleons in the incident nucleus interact with the target nucleons and induce multiple productions of pions and kaons. The remaining part of the incident nucleus breaks up into lighter nuclei and nucleons according to an assumed fragmentation probability. In the above assumptions, we adopt almost the same model parameters as those used in the simulations(5),(6) by which the observed feature of gamma-ray families at Mt. Fuji was investigated. The decay probability of charged pions and kaons into muons depends on the atmospheric density. The structure of the atmosphere is determined on the basis of the US standard atmosphere. Also, the effects are taken into account of energy losses and of geomagnetic field.

## 3. Results and discussions

The lateral distribution of muons in the simulated phenomena was compared with the experimental results of multiple muons obtained at the great depth underground(7),(8) in the previous report(4). The comparison is shown again in Fig. 1. The parameter of lateral spread $r_0$ has been determined by assuming muon density $\rho(r)$ expressed as the linear exponential form $\exp(-r/r_0)$. As increasing of mass number of primary particles, the average height of muon production increases, and then the lateral spread of multiple muons broadens. The experimental results on the lateral spread prefer the hypothesis of the primary cosmic rays including heavy nuclei of high content to the proton-dominant case. This feature agrees with the information obtained from the emulsion-chamber experiment(1),(2). By using the above comparison, one may determine the average mass number of primary particles. The lateral spread, however, depends on cross section and transverse momentum of interactions. The obtained value of mass number only by the above comparison is, therefore, influenced by

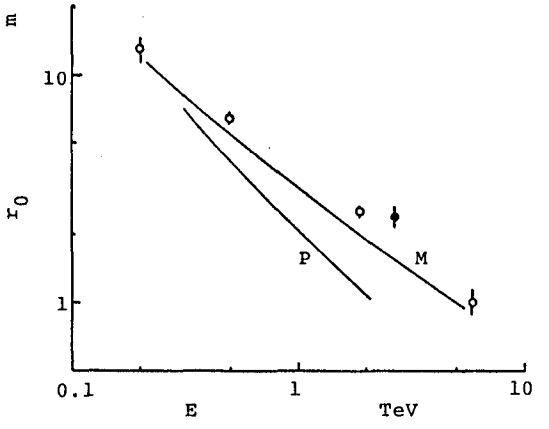


Fig. 1. Energy dependence of the parameter of lateral spread for constituent muons in the multiple-muon phenomena(4). The solid curves represent the simulation results for various values of the threshold energy of muons at sea level E. Two cases are shown of primary cosmic rays: the proton-dominant (P) and the heavy-nucleus-dominant (M) cases. The circles indicate the experimental results at the Kolar Gold Fields(7) (the open circles) and at the Homestake Gold Mine(8) (the solid circles).

their dependence on energy, and includes ambiguity in the assumptions of the calculations.

The figure of energy spectrum of constituent muons in a phenomenon also depends on the mass number of primary particles. The characteristic feature differs with distance from the center of the phenomenon. The spectrum in the case initiated by a heavy nucleus relatively steepens compared to that of a light-nucleus case. In the restricted region within a certain radius near the center, this tendency is much evident. To the contrary, in the region far from the center, the opposite tendency appears. In the intermediate region, the spectral figure does not depend of

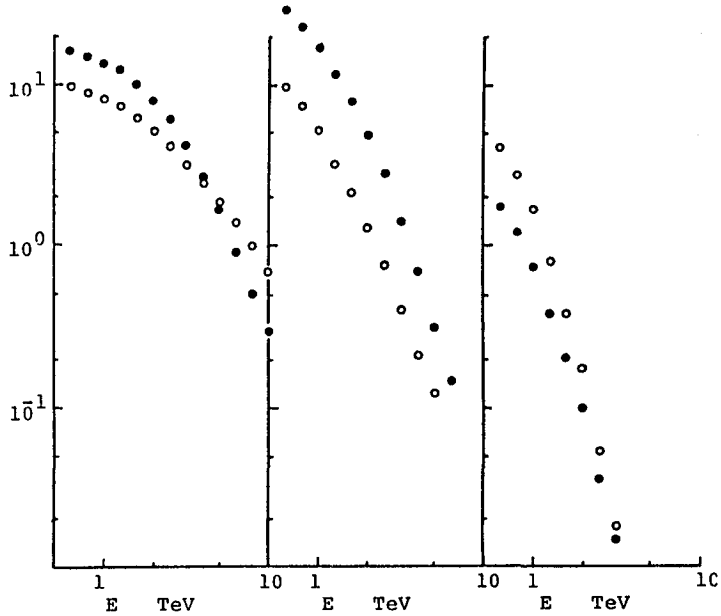


Fig. 2. Integral energy spectra of constituent muons in the multiple-muon phenomena. The circles indicate the simulation results observed at sea level in various ranges. r < 2 m (a), 2 m < r < 6 m (b) and 6 m < r < 10 m (c), for the cases initiated by protons (the open circles) and iron nuclei (the solid circles) with the energy from $10^{15}$ eV to $10^{16}$ eV.

the mass number of the primary particle. This feature is shown in Fig. 2. These characteristics allows us to devise a method for determining the average mass number of primary particles. Foe example, if one detects high-energy multiple muons associated with extensive air showers, and measures the energy of their constituent muons in the high-energy region, then he may take the spectra of those muons in various ranges as shown in Fig. 2. The reliability of the calculation and the applied assumptions would be confirmed by examining an agreement between observed and calculated values in the intermediate region where the spectral form does not depend of the mass number of primary particles. The distance of that region shifts according to the assumptions for cross-section value and average transverse momentum, and also the spectral form in that region varies according to the

production spectrum in the fragmentation region of hadron interaction. If the assumptions were not appropriate, the observed results would not coincide with the calculated ones. After the above examination in the intermediate region, a comparison is made of the observed spectral form with the ones calculated for various nuclei of primary particles in the central region. Evaluating the possibility, for example, in the observation of about 3 years using a TeV-region spectrometer of about 20 $m^2$ in scale observing muons with an air-shower array, the average mass number of primary particles can be determined with an accuracy of about 50 % in the energy around $10^{15}$ eV. Considering the current situation that the direct observation is not much easy, this is one of the methods to be investigated for the measurements of composition of primary particles. We also anticipate the results on high-energy multiple muons obtained from the huge detecters of proton-decay experiments at deep underground, to be compared with our calculated results.

**Acknowledgements**

The authors are grateful to Prof. S.Ozaki for his fruitful discussions. This work was supported by the computer FACOM M380R of Institute for Nuclear Study, University of Tokyo.

**References**

1. Akashi,M. et al., Phys. Rev. D, 24, 2353 (1981).
2. Amenomori,M. et al., Phys. Rev. D, 25, 2807 (1981).
3. Nagano,M. et al., J. Phys. G, Nucl. Phys., 10, L235 (1984).
4. Mizutani,K. and Sato,T., 18th ICRC (Bangalore), 11, 458 (1983).
5. Kasahara,K., Torii,S. and Yuda,T., 16th ICRC (kyoto), 13, 70 and 76 (1979).
6. Shibata,M., Phys. Rev. D, 24, 1847 (1981).
7. Krishnaswamy,M.R. et al., 15th ICRC (Plovdiv), 6, 161 (1979).
8. Cherry,M.L. et al., 17th ICRC (Paris), 10, 342 (1981).

OG 5.2-10

# COMPOSITION OF PRIMARY COSMIC RAYS NEAR THE KNEE

B. S. Acharya, M.V.S. Rao, K.Sivaprasad and B. V. Sreekantan
Tata Institute of Fundamental Research, Bombay 400005, India

## Abstract

The size dependence of high energy muons and the size spectrum obtained in the KGF air shower experiment suggest that the mean mass of cosmic rays remains nearly constant at $\sim 15$ upto $5 \times 10^6$ GeV and becomes one beyond. The composition model in which nuclei are removed at $7.5 \times 10^4$ GeV/nucleon due to photodisintegration and the proton spectrum steepens at $6.7 \times 10^6$ GeV due to leakage from the galaxy, which explains the KGF data, is shown to be consistent with data from other experiments also.

## Introduction

Data on various components on EAS from different experiments seem to suggest models of primary cosmic ray composition which are completely at variance with each other. The dependence of number of high energy muons on shower size together with the size spectrum from the KGF experiment[1] suggests that the mean mass number remains nearly constant upto about $4 \times 10^6$ GeV and becomes 1 beyond. The size dependence of 5 GeV muons and their fluctuations from the Tien Shan experiment[2] indicate that the composition remains unaltered over a wide range of primary energies which covers the knee in the primary spectrum. The elongation rate derived from early Cerenkov measurements [3,4] and observations on the fraction of delayed hadrons[5] have been interpreted in terms of an iron-rich composition near the knee, resulting from rigidity cut-off with a critical rigidity $\sim 10^5$ GV. Here we show that a composition model in which nuclei are removed due to photodisintegration near the source itself and the proton spectrum steepens due to leakage from the galaxy at a much higher energy, which explains the KGF data, can also account for most of the other data, if proper account is taken of the systematic effects in various experiments.

## Composition from the KGF data

The $N_\mu - N_e$ dependence of muons of energy $\geqslant 220$ GeV and the size spectrum from the KGF experiment[1] are shown in Fig.1. Acharya et al[1] have shown that the muon data does not agree with the rigidity cut-off model[6] with a critical rigidity of $10^5$ GV and extragalactic protons becoming dominant at $10^9$ GeV, which predicts an increasing mean mass number with shower size in the size region $10^4$-$4.10^5$ and a high mean mass number at higher sizes. An important feature to be noted from Fig.1 is that the discontinuity in the $N_\mu - N_e$ dependence occurs at a size ($4.10^5$) which is a factor of 5 smaller than that at which the size spectrum steepens ($2.10^6$). In the lower size region, the mean mass number seems to be independent of size since the experimental slope of $N_\mu - N_e$ dependence agrees with the prediction for a constant composition. The data suggests a pure proton composition above a shower size of $10^6$.

These features can be understood in a model suggested by Chatterjee[7] in 1964, which is a modification of Peters' rigidity cut off model. In Chatterjee's model, the galactic component undergoes rigidity cut off at a critical rigidity of $3.10^5$ GV and a pure proton extragalactic component becomes dominant at $2.10^6$ GeV, well before the cut off energy for iron nuclei.

An essential feature of the model is that the mean mass number is not allowed to increase with energy in the region where the composition is changing, by bringing in the extragalactic protons well below the iron cut-off energy . The difficulty with this model is that, apart from the need to exactly match the two proton components to yield a smooth spectrum, the energy dependence of the anisotropy[8] is difficult to understand. Also,the JACEE proton spectrum does not show any steepening upto $6.10^5$ GeV. The photo-disintegration model suggested by Hillas[9] in which nuclei are removed in the source itself at $\sim 10^5$ GeV/nucleon due to photodisintegration and protons suffer severe energy losses at a few times $10^6$ GeV due to photo pion production can also explain the data since protons continue almost upto the iron cut-off energy. Again the anisotropy is difficult to understand in this model, if the knee in the primary spectrum is due to energy losses in the photo pion production process.

Incroporating the good features of the two models, we propose the following model. Nuclei are removed due to photodisintegration at an energy/nucleon of $7.5 \times 10^4$ GeV, as in Hillas' model. Upto this energy, the spectra of various components are, as given by JACEE measurements[10],expressed as $K\ E^{-2.68}\ dE$, with K = 1.29,0.76,0.90,0.35 and 0.57 for mass numbers 1,4,14, 26 and 56. The iron spectrum is taken as the difference between the all particle flux from the Tien Shan experiment[11] (which agrees with the Grigorov all particle spectrum) and the sum of all components from JACEE. The spectral index of protons increases by 0.5 at $6.7 \times 10^6$ GeV due to leakage from the galaxy. The values of the critical energies are estimated by identifying the discontinuity of $N_\mu - N_e$ dependence at $4 \times 10^5$ as due to removal of iron nuclei and the steepening of the size spectrum at $2.10^6$ as due to leakage of protons and using the scaling model with rising cross sections[12]. Cosmic rays upto $\sim 10^{10}$ GeV are of galactic origin. The anisotropy can be understood as due to leakage of protons. There is no need for a second component. The spectra of various components and the all particle spectrum according to this model are shown in Fig.2. The Tien-Shan spectrum is higher than the model since they use the same composition to derive the primary energy spectrum over the energy region where it is continuously changing according to this model. The mean mass number and percentage of iron as a function of primary energy (a) and size at 920 g/cm$^2$ (b) in this model are shown in Fig.3. It can be seen that the mean mass remains nearly constant even though the composition is continuously changing upto $4 \times 10^6$GeV ($N_e = 5 \times 10^5$) and becomes 1 beyond. The percentage of iron reaches a maximum of 32% at $4 \times 10^6$ GeV and then falls off to zero. The proton fraction also increases with energy. Obviously, this model explains the $N_\mu - N_e$ dependence. The size spectrum at 920 g/cm$^2$ expected from this model is compared with the KGF data in Fig.4(Curve b). The first three experimental points are corrected for detection efficiency of flat showers and shown as filled circle. The agreement is obvious. Curve (a) is for the same model, but the spectral index for all the components is 2.72 with intensities normalised at 100GeV/nucleon. Thus, the present model, with the spectra mentioned earlier, explains the KGF data.

Comparison with other experimental data

Estimates of the position of shower maximum, $t_m$, from measurements of pulse profile[3] and lateral structure of Cerenkov photons[4] in small showers have indicated iron-rich composition in the energy region $10^6$-$10^7$GeV.The measurements of pulse profiles have been shown to be subject to the systematic errors[13,14] and thus may not be reliable. The values of $t_m$obtained from

lateral structure are systematically smaller than those from pulse profile measurements suggesting that they also may be subject to systematics. Recent measurements[15,16] using large areas of photomultipliers and triggering with Cerenkov light itself, thus being relatively bias-free, are shown in Fig.5 along with earlier measurements at higher primary energies, which do not seem to have such systematic effects. It can be seen that these new measurements do not show the abnormal elongation rate and do not require an iron-rich composition. In order to see the change of composition in this model, accurate measurements over a wide energy range from a single experiment are required.

The composition derived from delayed hadrons[5] relies heavily on Monte Carlo simulations. Even though the authors paid careful attention to the details of the simulation, some of the factors, such as the neglect of nuclear target effects, a cut off energy of 3 GeV for hadrons in the simulations together with the finding of Mincer et al[17] that low energy hadrons do produce large signals at a surprisingly large rate, would result in a larger fraction of delayed hadrons in both proton and nucleus initiated showers, thus reducing the requirement of iron from 40% at $10^6$GeV. Thus the present model, which predicts the iron abundance to increase with energy, with a value of 25% at $10^6$GeV, would be in agreement with their data. The Tien Shan data on low energy muons[11], which requires unchanging composition, is however difficult to understand in this model.

## Conclusions

The composition model in which nuclei are removed at $7.5 \times 10^4$GeV/nucleon in the source and proton spectrum steepens at $6.7 \times 10^6$GeV due to leakage from the galaxy explains most of the EAS data. Study of anisotropy of suitably selected mu-rich showers can distinguish between the photo disintegration and rigidity cut off models, since the former does not predict any anisotropy for nuclei near the cut off energies.

## References


1. B. S. Acharya et al, Conf. Papers 18th ICRC, Bangalore, 9, 191 (1983).
2. I. N. Kirov et al, Proc. Int. Seminar on Cosmic Ray Cascades, Sofia, 61 (1980).
3. G. Thornton and R. Clay, Phys. Rev. Lett. 43, 1622 (1979).
4. A. A. Andam et al, Phys. Rev. D 26, 23 (1982).
5. J. A. Goodman et al, Phys. Rev. D26, 1043 (1982).
6. R. Cowsik et al, Conf. Papers, 17th ICRC, Paris, 2, 120 (1981).
7. B. K. Chatterjee, Ph.D. Thesis, University of Bombay, 1964 (Unpublished).
8. J. Linsley, Conf. Papers, 18th ICRC, Bangalore, 12, 135 (1983).
9. A. M. Hillas, Conf. Papers, 16th ICRC, Kyoto, 8, 7 (1979).
10. T. H. Barnett et al, Phys. Rev. Lett., 51, 1010 (1983); Proc. Int. Symp. on Cosmic Rays and Particle Physics, Tokyo, 468, (1984).
11. I. N. Kirov et al, Conf. Papers, 17th ICRC, Paris, 2, 109 (1981).
12. B. S. Acharya et al, Conf. Papers, 16th ICRC, Kyoto, 9, 109 (1979).
13. K. J. Oxford and K. E. Turver, Phys. Rev. Lett. 44, 959 (1980).
14. M. V. S. Rao, Proc. Int. Workshop on Very High Energy Gamma Ray Astronomy, Ootacamund, 197 (1982).
15. T. A. Alimov et al, Conf. Papers, 18th ICRC, Bangalore, 11, 387 (1983).
16. N. Inone et al, ibid, p.402.
17. A. I. Mincer et al, Conf. Papers, 18th ICRC, Bangalore, 9, 383 (1983).

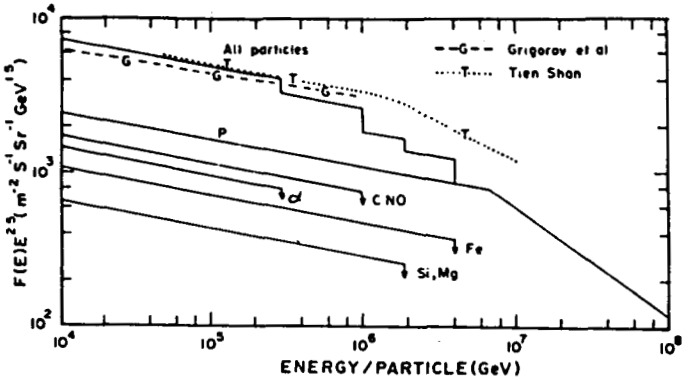


Fig. 2

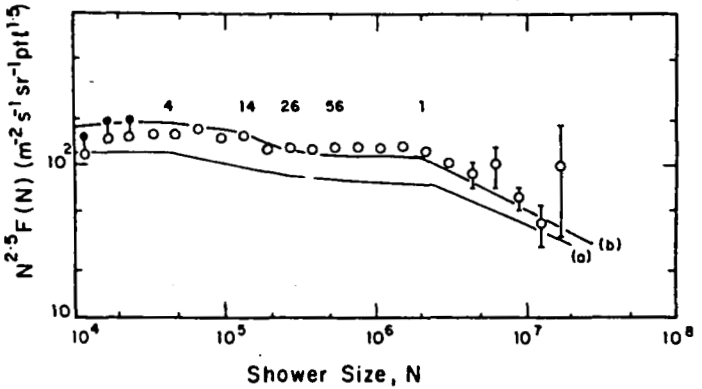


Fig. 4

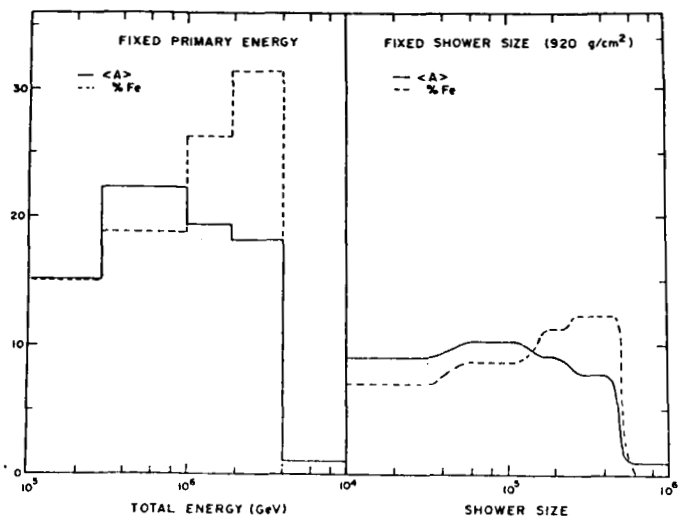


Fig.3

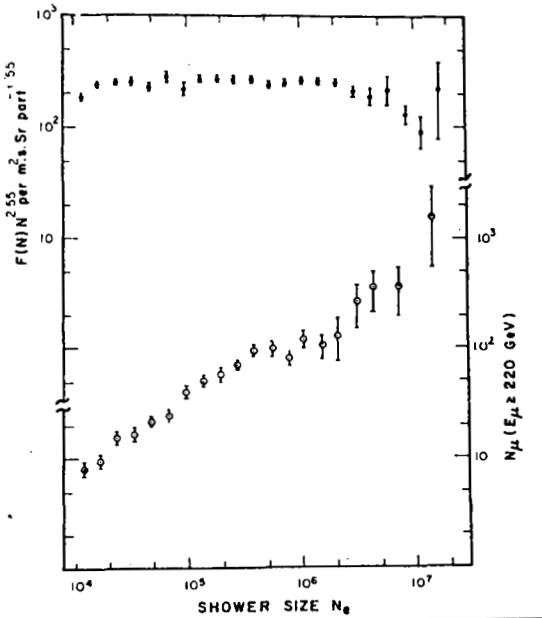


Fig.1

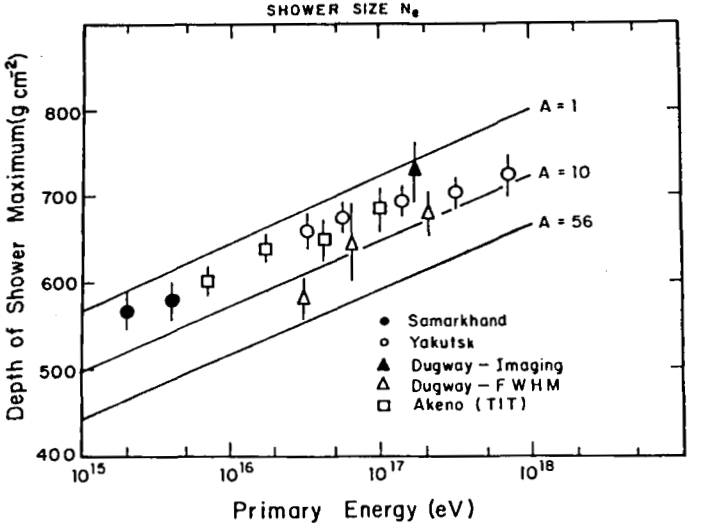


Fig.5

# EAS CERENKOV MEASUREMENTS OF THE COMPOSITION OF THE COSMIC RAY FLUX AROUND $10^{16}$eV

B.R. Dawson, J.R. Prescott and R.W. Clay.
Physics Department, University of Adelaide, South Australia 5001

1. Introduction Information can be obtained about the nature of a primary cosmic ray by looking at the way in which an EAS develops in the atmosphere. Thus, heavy nuclei will give rise to showers that develop high in the atmosphere and the depth of maximum development will be subject to much smaller fluctuations than will be the case, say, for showers originating from protons. This development can be followed directly by optical methods based on the observations of Cerenkov light or fluorescence light. In the case of Cerenkov observations, there are two complementary techniques: measurement of the time profile of the Cerenkov pulse with resolution of a few nanoseconds and measurement of the lateral distribution of the Cerenkov light. In each case the measured quantities must be related to some characteristic development parameter, such as the depth of maximum, by means of theoretical. Both techniques are complementary and ideally, simultaneous measurements on both would be desirable but, so far little has been done along these lines.

At the time of the Bangalore Conference it seemed clear that for energies above about $10^{17}$eV the depth of maximum changes slowly with energy at an elongation rate of about 50 gcm$^{-2}$ per decade but that in the energy interval $10^{16}$eV to $10^{17}$eV the elongation rate becomes much larger and, in the decade below $10^{16}$eV , the depth of maximum is much deeper in the atmosphere than would have been expected on the basis of the shower behaviour at higher energies. Comparisons with calculations based on a scaling model with rising cross sections suggest that this behaviour can be accounted for if the primaries are of a mixed composition but that in the energy region $10^{15}$ to $10^{16}$eV the primaries are predominently iron, although the data from Samarkand (Alimov et al 1983) would be compatible with a mixed composition. The situation at somewhat lower energies, $10^{13}$-$10^{15}$eV , is less clear, largely because of the difficulty in observing in this energy region, but there is a suggestion that the composition may be approaching the mixed composition that is well-known from direct measurements in the energy region accessible to balloons and satellites.

2. The experiment The present paper describes measurements on the lateral distribution of Cerenkov light from EAS in the energy region $10^{15}$ to $5\times10^{16}$eV which were carried out at the Buckland Park field station of the University of Adelaide in association with the particle array. There were nine Cerenkov light detectors consisting of open-faced EMI 9623B photomultipliers with broad collimation. Their location is shown in figure 1. The overall arrangements for the experiment were therefore similar to those described by Kuhlmann and Clay (1981) but differed in having a better signal-to-noise ratio, better stability and calibration and in being more automatic in operation.

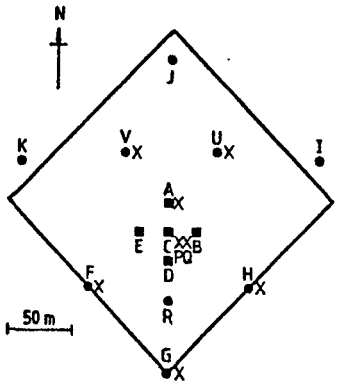


Figure 1: The Cerenkov lateral distribution array with the elements of the Buckland Park particle array used in the experiment.

The data were collected on clear moonless nights from October 1983 to March 1984. The Cerenkov recording system was triggered by the particle array which was also used to assign shower size, core location and arrival direction to each event. The triggering requirements were coincident signals corresponding to >2 particles $m^{-2}$ in three of the central five (ABCDE) detectors. During 103 hr recording time, 9575 of these particle events were recorded. A total of 1279 of these events was selected for the purpose of measuring the Cerenkov lateral distribution. These showers arrived within 35 degrees of the zenith, were well-analysed in terms of the particle data and possessed at least 5 Cerenkov densities. This selection put a lower limit on the acceptable shower size at about $10^5$ particles.

3. Analysis The use of the particle array for triggering is not ideal because there is necessarily an a priori selection bias towards late-developing showers. However, in the present case the selection biases associated with the particle array and its analysis procedures have been investigated by an extensive series of simulations. The data below are compared with model calculations in which the actual selection properties of the array and the analysis procedures are included.

In our interpretation of the measured lateral distributions we have used the calculations of Patterson and Hillas (1983b) which show that the shape of the lateral distribution within 150m of the shower axis is sensitive to shower development. Outside this radius the shape is not so sensitive, and the flux at a large radius is a measure of the energy of the primary particle. Ideally, this radius should be $\gtrsim$200m , although for small showers it is often only possible to measure the lateral distribution out to ~150m . The flux at 150m is still expected to be a measure of the primary energy, but it will be subject to larger fluctuations than the flux at a larger radius. Patterson and Hillas suggest that the flux ratio Q(50m)/Q(150m) (as suggested by Andam et al 1982) is the best measure of the shape of the lateral distribution inside 150m. They have related this parameter to $H_m$ , the distance along the shower axis to shower maximum. We have fitted exponentials of the form $Q(r) = A \exp(-br/10^4)$ to our data for $25m<r<150m$ and have found them to be good fits. Indeed, in the majority of cases the exponential is also a good fit at larger radii. Using these fits, the ratio Q(50)/Q(150) was found for each event and hence $H_m$ . Knowing the zenith angles of the shower axes, depths of maximum were derived assuming an exponential atmosphere with a scale height of 8.0km.

The 1279 showers analysed in this manner have been binned in a variety of ways. Figure 2 shows the data plotted as depth of maximum (DOM) vs

the equivalent shower size at a depth of 1000 $gcm^{-2}$ , $N_e(1000)$ , the latter being calculated from the observed size and a shower attenuation length of 185 $gcm^{-2}$ (Clay and Gerhardy 1982). Alternatively, the data may be binned in terms of a primary energy estimator. Here we use the Cerenkov flux at a distance of 150m from the shower axis, Q(150), as shown in figure 3. In both cases, the error bars represent standard deviations within the bins. Figure 3 shows that in terms of energy there is a bias towards the selection of late developing (large DOM) showers. This bias is not so obvious in figure 2 which is based on shower size. In this case there appears to be sufficient mixing of low energy showers to mask this effect.

The experimental distributions were interpreted using Monte Carlo simulations of proton and iron-produced showers in which the selection effects of the particle array were taken explicitly into account. (We believe that there is no significant bias specifically associated with the Cerenkov array). In these simulations, shower energies were selected from a broken-power-law energy spectrum between $10^{13}$ and $10^{18}$eV. A depth of maximum for each shower was selected using the distributions given by Protheroe and Patterson (1984). Given a DOM, the sea level size of the shower was calculated by assuming the $E_p - N_e(max)$ conversion given by Hillas (1983) and by using a shower development profile given by Patterson and Hillas (1983a). The simulated showers were then allowed to fall on the particle array using appropriate zenith and azimuth angle distributions and those showers which triggered the array were reanalysed for core position and shower size using the same shower analysis program as was used for the experimental data. Thus, provided that selection biases exist only for the particle array, the simulated data are now directly comparable with the experimental distributions. Figures 4 and 5 show selected simulation results. Here again the error bars represent standard deviations, which reflect the fluctuations in the DOM. The bias imposed by the array is especially evident in figure 5. The only showers observed below $10^{15}$eV are late developing proton events.

In our attempts to match the experimental DOM vs $N_e(1000)$ distribution, a number of mixtures of proton and iron-produced showers was tried. It was found that a mixture of 95% Fe and 5% P produced a distribution consistent with the data (fig.2).This mixture also produced an agreement in the energy representation when a particular $Q(150) - E_p$ assignment was made (fig. 3). It is noted that it is not necessary to invoke a changing composition across the energy range in question in order to match the data. Unfortunately there are not sufficient data in the high energy region to see the expected effect of a change in composition back to predominantly light nuclei above about $3x10^{16}$eV. (e.g. Nagano 1983).

Thus we conclude that, having used simulations which include a realistic model of longitudinal development and the effects of particle array selection bias, we find that our data are consistent with a cosmic ray primary composition rich in iron over the energy range $3x10^{15}$ to $5x10^{16}$eV.

Acknowledgements We thank R.J. Protheroe for his valuable advice concerning the simulations and J.R. Patterson and A.G. Gregory for many

useful discussions and practical help. The work was supported by the Australian Research Grants Scheme and a research grant of the University of Adelaide.

References

Alimov T.A. et al (1983), Proc. 18th ICRC, (Bangalore), 11, 387.
Andam, A.A, Chantler, M.C., Craig M.A.B., Orford K.J., Shearer J.A.L., Turver K.E., and Walley G.M., (1982), Phys. Rev. D. 26, 23.
Clay R.W., and Gerhardy P.R., (1982), Aust. J. Phys. 35, 441.
Hillas A.M., (1983), Proc. Cosmic Ray Workshop, Univ. of Utah, ed. T.K. Gaisser, p16.
Kuhlmann J.D. and Clay R.W. (1981), J. Phys. G. 7, L183.
Nagano M., Proc. 18th ICRC, (Bangalore), 12, 475.
Patterson J.R. and Hillas A.M. (1983a), J. Phys. G. 9, 323.
(1983b), J. Phys. G. 9, 1433.
Protheroe R.J. and Patterson J.R. (1984), J. Phys. G. 10, 841.

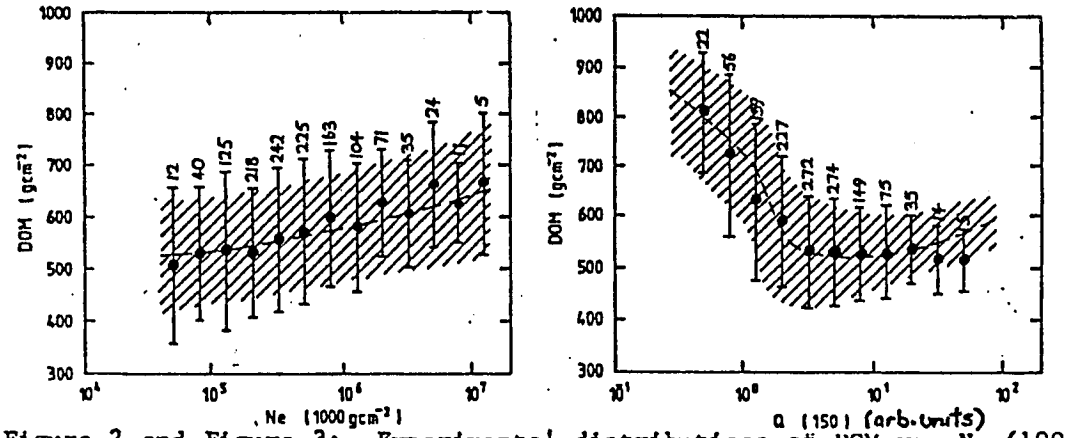


Figure 2 and Figure 3: Experimental distributions of DOM vs. $N_e$ (1000) and primary energy estimator Q(150). Error bars in each figure represent standard deviations and the numbers indicate the number of events in each bin. The dashed lines and hatched regions represent the means and standard deviations of simulated data (95%Fe,5%P)(see text).

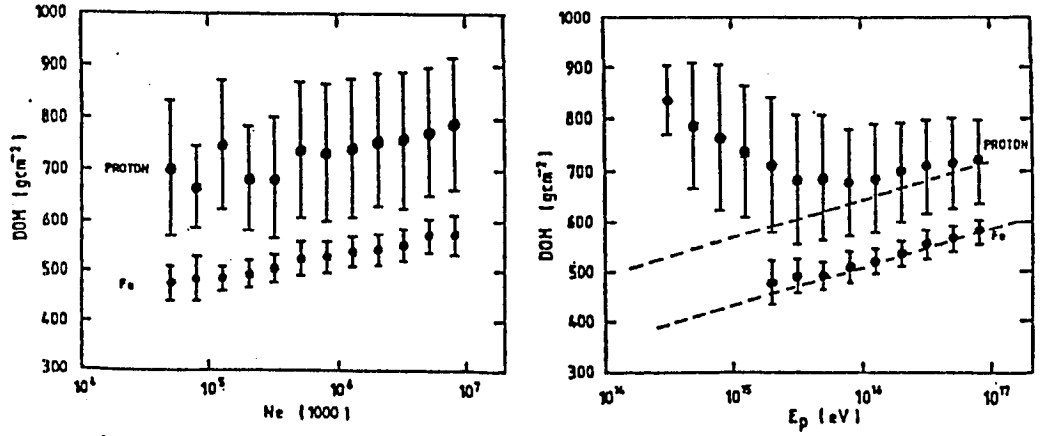


Figure 4 and Figure 5: Simulated distributions of DOM vs. $N_e$(1000) and primary energy $E_p$ which take into account array selection biases. Error bars indicate standard deviations. The dashed lines in figure 5 represent the input distributions of mean DOM from Protheroe and Patterson (1984).

# ELECTRON AND MUON PARAMETERS OF EAS AND THE COMPOSITION OF PRIMARY COSMIC RAYS IN $10^{15} \sim 10^{17}$eV

T. Cheung and P.K. MacKeown
Department of Physics
University of Hong Kong
HONG KONG

ABSTRACT

With a view to estimating the relative intensities of protons and heavy nuclei in primary cosmic rays in the energy region $10^{15} \sim 10^{17}$eV, a systematic comparison has been made between all available observed data on various parameters of EAS with the results of simulation. The interaction model used is an extrapolation of scaling violation indicated by recent $p\bar{p}$ collider results. A composition consisting of various percentages of Fe in an otherwise pure proton beam was assumed. Greatest overall consistency between the data and the simulation is found when the Fe fraction is in the region of 25%.

1. Introduction Direct measurements of the composition of the primary cosmic ray beam have by now been extended to particle energies of the order of $10^{14}$eV. It seems clear however that above this energy only indirect estimates will be available for a long time to come. These high energies are however of the greatest astrophysical interest; the knee in the primary spectrum at $3\ 10^{15}$eV is already known for over a quarter of a century yet its significance is still far from clear, whether it represents a source feature, a propagation effect, a reflection of changes in hadronic interactions or some combination of these. In particular data from different types of experiments conflict so that, even in the propagation effect scenario, it is problematical whether the knee at $3\ 10^{15}$ V represents the rigidity at which leakage effects start setting in, or have already terminated [1]. The present report is confined to the region above the knee, and attempts on the basis of an assumed model for high energy interactions and reported measurements on various E.A.S. parameters (excluding time profiles) to find a composition most consistent with all the data. The basic approach is simple minded i.e. to add varying amounts of Fe to an otherwise pure proton beam and compare the characteristics of simulated showers with experiment.

2. Calculations The model for hadronic interactions used incorporates scaling violation [2] for the leading particle at energies greater than $210^{13}$eV, and radial scaling for other distributions. The inelastic cross-section for hadron collisions is assumed to increase with energy, and the influence of the target air nuclei on inelasticity and multiplicity, as evidenced by recent accelerator data, have been taken into account; more details of the model can be found in paper HE4.3-12 at this conference. We note that although this scaling violation model has been adopted as a plausible, and consistent, framework for the calculations it is not above criticism [3].

Three dimensional Monte Carlo simulations for proton and Fe

nucleus initiated events with primary energies in $10^{15}$ - $10^{17}$eV were carried out. Log-normal distributions in different quantities, with variances as determined by the simulations, and a primary differential spectrum of slope -3.0 were used to relate parameters at fixed shower size (as measured) with the simulations at fixed primary energy. In establishing longitudinal development profiles of electrons and muons when more than one primary species is present, for comparison with equi-intensity cuts, the approximate method described in paper HE4.3-12 was used.

The quantities investigated so far are the fluctuations in muon size $\sigma_{N\mu}/\langle N_\mu \rangle$, $N_\mu$ vs. Ne correlations, electron longitudinal development, muon longitudinal development and lateral distribution. This roughly is the order of their sensitivity to primary composition; the ratio $\sigma_{N\mu}/\langle N_\mu \rangle$ although it varies most is also however ambiguous in some regions, while the muon lateral distribution is almost independent of primary mass and will not be considered further here. The muon longitudinal development, as reflected in equi-intensity cuts is considered in greater detail in paper HE4.3-12 at this conference.

3. Results The data on electron size equi-intensity cuts used were: Chacaltaya (550 $gcm^{-2}$) intensities $10^{-6}$, $10^{-7}$, $10^{-8}$, $10^{-9}$and $10^{-10}m^{-2}$, $s^{-1}$ $sr^{-1}$. Tien Shan (690 $gcm^{-2}$) $10^{-6}$, $10^{-7}$, $10^{-8}$ and Akeno (930 $gcm^{-2}$) $10^{-6}$, $10^{-7}$, $10^{-8}$, $10^{-9}$, $10^{-10}$. A comparison of these data with some results of the simulations (taking the coefficient in the integral primary

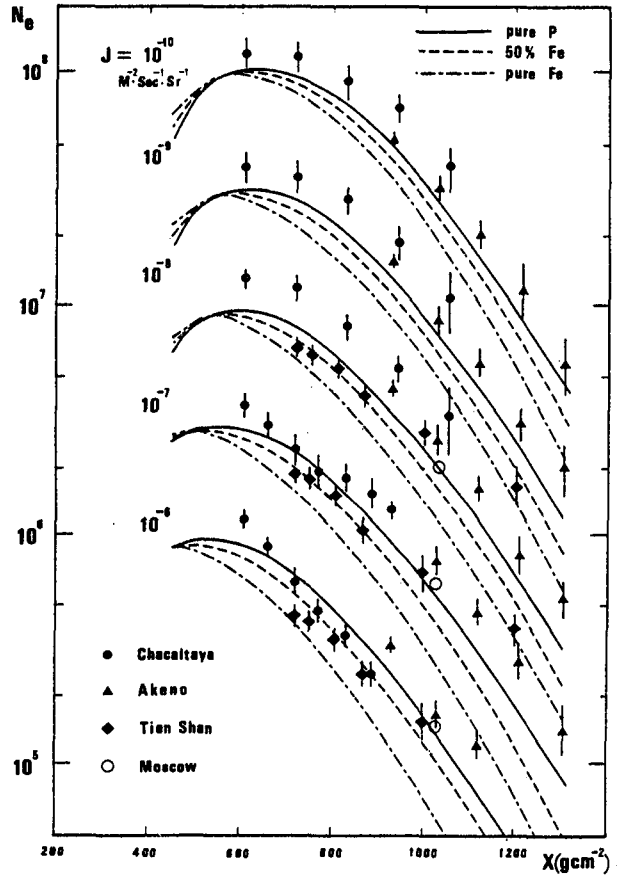


Fig.1 The longitudinal development of electrons from equi-intensity cuts for various compositions compared with observed points (A = $2.510^6$)

spectrum A = 2.5 $10^6$ [4]) are shown in fig.1. In the belief that the shape of the experimental curves may be more reliable than the determination of absolute sizes, a normalisation of the simulated curve i.e. a revision of A, to each experiment has been carried out by requiring the value of $\chi^2$ (normalised), calculated using the data of the experiment and the simulated curve, to be a minimum (the variance in both the data and simulation results being allowed for). For each of the 3 experiments such minimum values of $\chi^2$ have been obtained for each of 4 compositions i.e. pure protons, 25% Fe, 50% Fe and pure Fe.

Exactly the same procedure was carried out for the data on muon equi-intensity cuts: Chacaltaya at $10^{-8}$ and $10^{-9}m^{-2}s^{-1}sr^{-1}$, Tien Shan at $10^{-7}$ and $10^{-8}$ and Akeno $10^{-8}$ and $10^{-9}$, each composition yielding 6 values of minimum $\chi^2$ - some data are shown in fig.3 of paper HE4.3-12. Direct comparison was also made with $N_\mu$ vs Ne curves derived at Chacaltaya, Tien Shan, Akeno and Moscow - an example is shown in fig.2, and with the dependence of $\sigma_{N\mu}/\langle N_\mu \rangle$ on shower size as determined at Tien Shan, Akeno and Moscow - the comparison with Akeno data is shown in fig.3. In this way 7 further $\chi^2$ values are obtained for each composition.

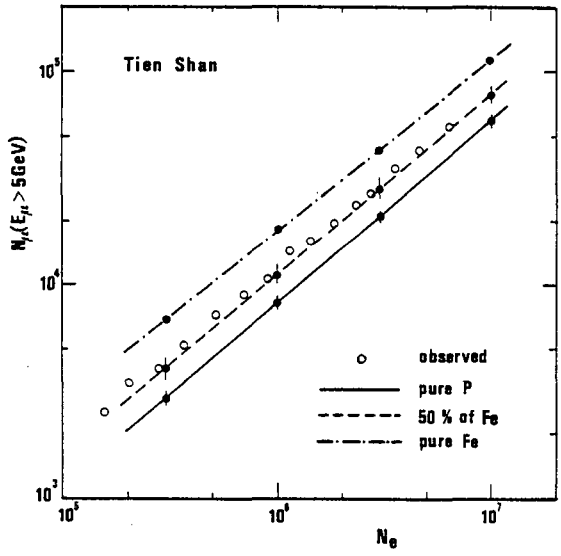


Fig.2 Comparison of $N_\mu$ vs $N_e$ data at Tien Shan [5] with simulations.

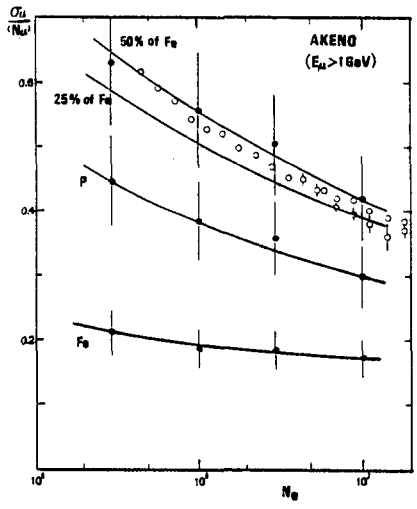


Fig.3 Muon size fluctuations at Akeno [6] compared with simulations.

The distributions in $\chi^2$ for the four assumed compositions are shown in fig.4. The median values of $\chi^2$ are given in the table. Generally the longitudinal developments favour very small admixtures of Fe, the major exception being the lowest energy Chacaltaya data - long known to be somewhat different; it is best fitted by a composition of pure Fe. The various $N_\mu$ vs $N_e$ dependences as well as the muon

| Composition | pure p | 25%Fe | 50%Fe | 100%Fe |
|---|---|---|---|---|
| $\chi^2$ median | 0.96 | 0.62 | 0.82 | 7.51 |

fluctuations would generally favour somewhat more Fe. However, as the table indicates, when viewed overall a proportion of 25% is most favoured, if not very convincingly.

In the above considerations only the shapes of the equi-intensity curves were considered. If we turn to absolute values and take a coefficient A = 3.75 $10^6$ (cf. A = 2.5 $10^6$ in [4]) in the primary spectrum (this will lead to agreement between the electron size at shower maximum at J = $10^{-10}m^{-2}s^{-1}sr^{-1}$ at Chacaltaya, where least sensitivity to the nature of the primaries exists, see fig.1), consistency with muon longitudinal developments, for any composition, can only be obtained by assuming systematic errors in muon size determinations. These are not serious for Tien Shan or Akeno (in magnitude $\lesssim$ 20%) but for Chacaltaya suggests overestimates of muon size up to a factor of 2. Adjusting observed muon sizes to be consistent with the intensity, values of $\chi^2$ were again obtained for $N_\mu$ vs $N_e$ relations, and $\sigma_{N_\mu}/\langle N_\mu \rangle$. The general effect is to favour somewhat more Fe than 25% but the difference is not very great.

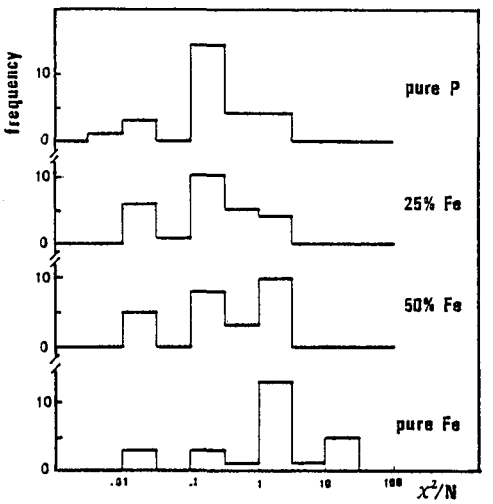


Fig.4 $\chi^2/N$ distributions

References

[1] Hillas A.M., in Shapiro M.M. (Ed.) (1983) Composition and Origin of Cosmic Rays, Dordrecht, D. Reidel

[2] Wdowczyk J. and Wolfendale A.W., (1984) J. Phys. G: Nucl. Phys. 10, 257-272.

[3] Hillas A.M., (1984). Nature 312, 347-348.

[4] Gaisser T.K. and Hillas A.M., (1977) 15th Int. Conf. Cosmic Rays Plovdiv, Conference Papers, 8, 353-357.

[5] Danilova T.V. et al., (1981) 17th Int. Conf. Cosmic Rays, Paris, Conference Papers, 6, 146-149.

[6] Hara T. et al., (1983) 18th Int. Conf. Cosmic Rays, Bangalore, Conference Papers, 11, 285-288.

# Arrival Directions of Large Air Showers, Low-Mu Air Showers and Old-Age Low-Mu Air Showers Observed at Mt. Chacaltaya

Kaneko, T.
Department of Physics, Okayama University, Okayama 700, Japan
Hagiwara, K.
The Institute of Physical and Chemical Research, Wako, Saitama 351, Japan
Yoshii, H.
Faculty of General Education, Ehime University, Matsuyama 790, Japan
Martinic, N., Siles, L. and Miranda, P.
Instituto de Investigaciones Fisicas, Universidad Mayor de San Andres, LaPaz, Bolivia
Kakimoto, F., Obara, T., Inoue, N.* and Suga,K.**
Department of Physics, Tokyo Institute of Technology, Meguro, Tokyo 152, Japan

ABSTRACT

Arrival directions of air showers with primary energies in the range $10^{16.5}$eV to $10^{18.0}$eV show the first harmonic in right ascension(RA) with amplitude of 2.7±1.0% and phase of 13-16h. However, the second harmonic in RA slightly seen for showers in the range $10^{18.0}$eV to $10^{19.0}$eV disappeared by accumulation of observed showers. The distribution of arrival directions of low-mu air showers with primary energies around $10^{15}$eV observed at Chacaltaya from 1962 to 1967 is referred to, relating to the above-mentioned first harmonic.

Also presented in this paper are arrival directions of old-age low-mu air showers observed at Chacaltaya from 1962 to 1967, for recent interest in gamma-ray air showers.

## 1. Arrival directions of large air showers

Arrival directions of large air showers observed at Mt. Chacaltaya (16°20'52"S in latitude and 68°7'57"W in longitude, 5200m a.s.l. or 550 $gcm^{-2}$ atmospheric depth) until 1979 were reported at the Paris Conference (1). In the present paper we report on arrival directions of large air showers observed at Chacaltaya until 1984. The air-shower array and the detectors after 1979 were same as those described in the previous paper (1). Procedures to determine the arrival directions($\theta$,$\phi$) and the electron sizes($N_e$) as well as the uncertainties for showers observed after 1979 are also same as those described in the previous report(1). The primary energies($E_o$) of showers observed after 1979 were determined from a relation between $E_o$ and $N_e$ at the maximum development($N_{e\,max}$) given as $E_o(eV)=2.0\times 10^9(eV)\cdot N_{e\,max}$ described also in the previous report(1). $N_{e\,max}$ was estimated from $N_e$ and the effective atmospheric depth where the shower was observed($550gcm^{-2}\times\sec\theta$), following the longitudinal development of electrons determined at Chacaltaya(2).

*Present addres: Graduate School of Science and Technology,Kobe University, Nada, Kobe 657, Japan
**Present addres: Department of Physics, Meisei University,Hodokubo 337, Hino-shi, Tokyo 191, Japan

Table 1 and 2 show the results of harmonic analyses in right ascension of the arrival directions of showers with zenith angles smaller than 60°. In the tables, figures in upper row correspond to the first harmonic and those in the lower row correspond to the second harmonic. As is seen in tables 1 and 2, the first harmonic is predominant at primary energies in the range $10^{16.5}$eV to $10^{18.0}$eV as was seen for showers observed until 1979(1). However, the second harmonic slightly seen for showers observed until 1979 with primary energies in the range $10^{18.0}$eV to $10^{19.0}$eV disappeared by including the showers observed until 1984.

Table 1.

| Energy ($E_o$ in eV) | Number of showers | Amplitude (r in %) | Phase (in hour) | $k_o$ | p(>r) | period |
|---|---|---|---|---|---|---|
| $10^{16.5}$-$10^{17.0}$ | 17477 | 2.7± 1.1 | 13.1±1.5 | 3.11 | 0.05 | 1981 |
| | | 1.2± 1.1 | 11.2±2.8 | 0.61 | 0.55 | -1984 |
| $10^{17.0}$-$10^{17.5}$ | 12914 | 2.6± 1.1 | 15.5±1.7 | 2.21 | 0.11 | 1977 |
| | | 0.9± 1.2 | 0.2±3.6 | 0.28 | 0.76 | -1984 |
| $10^{17.5}$-$10^{18.0}$ | 3372 | 4.9± 2.4 | 16.3±1.8 | 1.99 | 0.14 | 1977 |
| | | 1.9± 2.4 | 10.0±3.5 | 0.30 | 0.74 | -1984 |
| $10^{18.0}$-$10^{18.5}$ | 593 | 6.6± 5.8 | 7.0±2.7 | 0.65 | 0.52 | 1977 |
| | | 4.4± 5.8 | 10.0±3.5 | 0.29 | 0.75 | -1984 |
| $10^{18.5}$-$10^{19.0}$ | 117 | 6.0±13.1 | 12.2±4.4 | 0.10 | 0.90 | 1977 |
| | | 17.8±13.1 | 2.0±2.4 | 0.93 | 0.39 | -1984 |

Table 2.

| Energy ($E_o$ in eV) | Number of showers | Amplitude (r in %) | Phase (in hour) | $k_o$ | p(>r) | period |
|---|---|---|---|---|---|---|
| $10^{17.0}$-$10^{18.0}$ | 21534 | 2.7± 1.0 | 15.0±1.3 | 3.94 | 0.02 | 1964 |
| | | 0.6± 1.0 | 8.8±3.9 | 0.19 | 0.83 | -1984 |
| $10^{18.0}$-$10^{19.0}$ | 1118 | 3.5± 4.2 | 2.7±3.3 | 0.35 | 0.71 | 1972 |
| | | 6.2± 4.2 | 8.7±2.3 | 1.01 | 0.34 | -1984 |

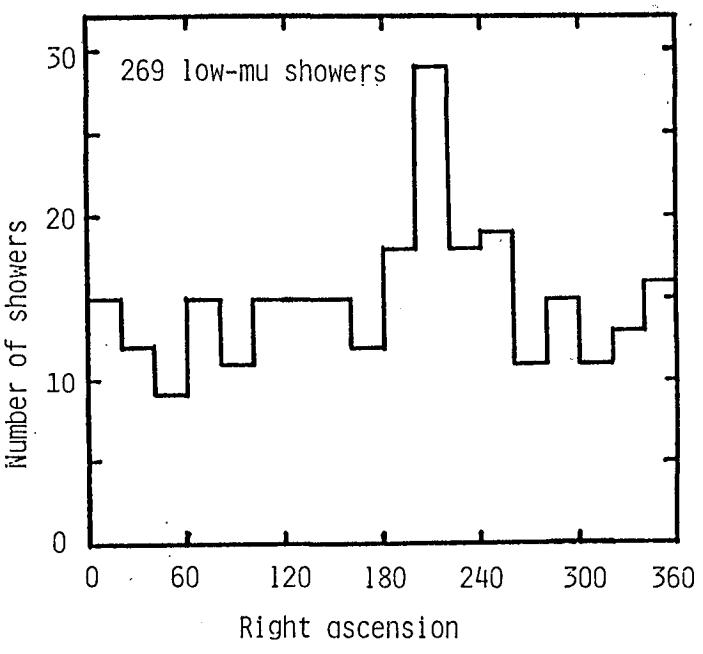


Fig. 1

## 2. Arrival directions of low-mu showers

Relating to first harmonic at primary energies in the range $10^{16.5}$eV-$10^{18.0}$eV, arrival directions of low-mu showers observed at Chacaltaya should be mentioned. Figure 1 shows the distribution of low-mu showers with zenith angles smaller than 60° along right ascension. The average size of the showers is about $3\times10^5$ and the proportion of the low-mu showers is about one thousandth of all showers. This figure was drawn in 1978 after the Calgary Conference in 1967 (3) by including all showers observed from 1962 to 1967. An excess of the

showers is observed between 180°(12.0h) and 260°(17.3h) in right ascension. At that time,we assumed that these low-mu showers were candidates of gamma-ray showers. However, these low-mu showers may be showers produced by primary protons which encountered the first interactions in the deep atmosphere or produced mainly neutral pions at the first interactions, referring to the argument described in section 3. Then, it is very interesting that the right ascension where the excess of low-mu showers are observed coincides with the phase of the first harmonic described in section 1 at primary energies in the range $10^{16.5}$eV to $10^{18.0}$eV, since that fact may be related with the composition of primary cosmic rays.

## 3. Arrival directions of old-age low-mu showers

Relating to the low-mu showers, it is worth while mentioning the arrival directions of old-age low-mu showers observed at Chacaltaya from 1962 to 1967. Arrival directions of these showers were plotted on the celestial sphere in 1967 as shown in figure 2 but was not published(4).

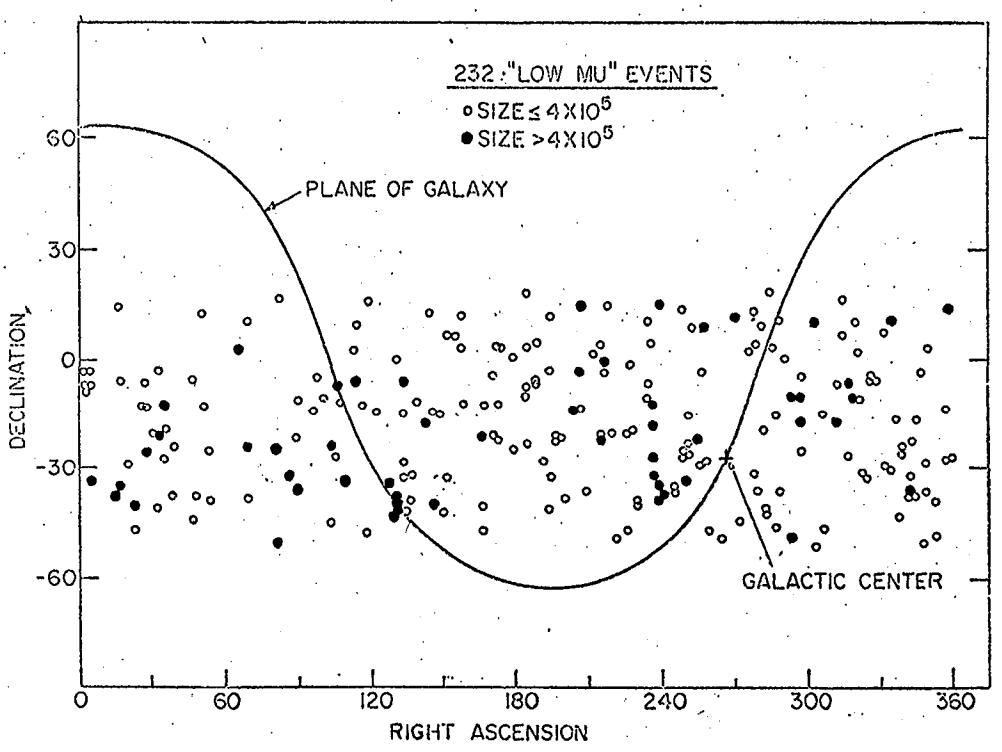


Fig. 2

The following criteria were imposed to select these showers:

(1) The zenith angle of shower is smaller than 37°($\sec\theta<1.25$).

(2) The number of muons observed in the 60m$^2$ shielded detector is smaller than four.

(3) The expected number of electrons at the muon detector is larger than 2000/60m$^2$.

(4) The shower initiation point is in the first 80gcm$^{-2}$ of the atmosphere. The point is estimated from the zenith angle (550gcm$^{-2}\times\sec\theta$: depth of observation), the electron size and the lateral distribution(s) by comparing the value of s with those of s for gamma-ray initiated purely electromagnetic showers. This is a criterion effective to select old-age showers produced probably primary gamma rays.

Areas in which the densities of arrival directions were several times higher than average are found near ($\alpha$:135°,$\delta$:-40°),(240°$\sim$255°,-20°$\sim$-40°) and at some locations adjoining the blank area seen around(10°,-20°). The first location corresponds exactly to that of Vera X-1(09h00m13.18s,-40°21'25.3"). The Adelaide group reported recently gamma-ray air showers from this X-ray source synchronized with period of the eclipsing binary [5]. There are some X-ray sources in the second location and a strong X-ray eclipsing binary X1700-377(3.4d period;17h00m32.70s,-37°46'28.8") is neaby. Regarding to the third location, a high peak is seen at galactic latitude of -60° to -70° when the distribution of the arrival directions is examined in galactic latitude. The expected number of showers for this region is 13.5: the number observed is 27. For showers with $N_e$ smaller than $4\times10^5$, the corresponding number are 10.4 and 25.

Stimulated by the interesting old BASJE results looked back upon the past and mentioned in sections 2 and 3, the BASJE group has begun the preparation for a new project to observe low-mu and gamma-ray showers with 32 $1m^2$ unshielded scintillation detectors located around the $60m^2$ muon detectors, among which 12 detectors are moved from the locations in the present large array, and to determine the arrival directions within an uncertainty of 1°. The observation will be begun in the middle of 1986.

References

(1) Anda, R. et al: Proc. 17th Inter. Cosmic Ray Conf., Paris,2(1981)164
(2) Kakimoto, F. et al: J. Phys. G:Nucl. Phys.,5(1983)339
(3) Kamata, K. et al: Canadian J. Phys.,46(1968)s72
(4) Drawn for internal discussion among members of the Bolivian Air Shower Joint Experiment(BASJE). The members of BASJE at that time were I. Escobar, V. Domingo, J. Gaebler, K. Kamata, M. LaPointe, K. Murakami, O. Saavedra, S. Shibata, K. Suga and Y. Toyoda
(5) Protheroe, R. J. et al: Astrophys. J.(Letters) 280(1984)L47

# Anisotropy of Cosmic Rays of Energy $10^{15}$eV to $10^{17}$eV Observed at Akeno

T.Kifune, K.Nishijima*, T.Hara, Y.Hatano, N.Hayashida, M.Honda, K.Kamata, Y.Matsubara**, M.Nagano, G.Tanahashi and M.Teshima**

Institute for Cosmic Ray Research, University of Tokyo, Tanashi, Tokyo, 188 Japan
* The Graduate School of Science and Technology, Kobe University, Kobe, 657 Japan
** Department of Physics, Kyoto University, Kyoto, 606 Japan

## ABSTRACT

Anisotropy of cosmic rays is studied with EAS data by muon trigger. The present results support those obtained by electron trigger which suggest the significant anisotropy of second harmonics with phase around $100^{\circ}$ in right ascension for showers of $10^{16}$-$10^{17}$eV, and predominant arrival direction of $230^{\circ}$ in right ascension for muon-rich showers. It seems that the phase of the first harmonics in the energy range below $10^{17}$eV is about $300^{\circ}$ in right ascension and the second harmonics near $6X10^{14}$eV is statistically significant with an amplitude of $0.39\pm0.13\%$ in direction of $83\pm10^{\circ}$ in right ascension.

## 1. Introduction

Anisotropy of arrival direction of cosmic rays in the energy range larger than $10^{15}$eV has been studied by various selection conditions on air showers at the EAS Array of Akeno. The results by the trigger of electron density were reported in the previous conference(Hara et al. 1981 and 1983a). In comparison, selection of air showers by discriminating muon density(muon trigger) has the following advantage. (1) Muon size $N_{\mu}$ is less fluctuating than electron size Ne as an estimater of primary energy Eo. (2) The muon detectors are the proportional counters in shielded room, of which response is less affected by the temperature variation.

The EAS recorded by muon trigger(case I) is available since the autumn of 1982 for Eo larger than $10^{15}$eV. About 90,000 EAS's are accumulated during two years of 1983 and 1984 and are analyzed for anisotropy. Also presented in this paper is the result by another muon trigger(case II), though whose result is preliminary. In this trigger, the event rate per hour is recorded without detailed informations in each detector of the array. The number of accumulated showers is $1.1X10^{6}$ during half a year since June 1984.

## 2. Experimental condition and method of analysis

The EAS Array at Akeno(Hara et al. 1979) has nine muon stations, with a threshold energy of 1 GeV. Effective area of each station which consists of 50 proportional counters is 25 $m^2$. The following two experiments have been performed with muon trigger.

In case I, when more than 4 muons hit each of 4 muon stations located near the central area of the array, the EAS data are recorded. The location of EAS core, zenith angle and electron size are determind from electron data. Primary energy of each observed shower is estimated from $N_{\mu}$(Hara et al. 1983b).

In case II, the rate of air showers when more than 5 muons which are

spatially separated from each other hit one of 9 muon stations is recorded. The median energy of these showers is found to be $6X10^{14}$eV by the analysis of AS data obtained by the calibration run with the same trigger condition. The harmonic analysis is applied to get the anisotropy after the correction of non-observation period by the method described in Hara et al.(1983a). The anisotropy of muon-rich showers is studied in case I as well as the anisotropy of total showers. The showers whose $N_\mu$ to Ne ratio is 2 times larger than the mean value over all the showers are defined as muon-rich showers.

3. Results and Discussions

Results of case I are presented in Table 1 for the total showers and in Table 2 for muon-rich showers. The obtained amplitude and phase of maximum intensity in right ascension are listed in the tables as well as the number of showers N in each energy bin and the parameter of reliability k where the probability of obtaining amplitude greater than r from the uniform distribution is given by $w(>r)=\exp(-k)$ $(k=r^2N/4)$. Also in Fig.1a and b, the phases of first and second harmonics are shown as a function of primary energy respectively. In the figures, open circles designate the results for total showers and closed circles for muon-rich showers.

Table 1 (Case I. Total showers)

| | | first harmonics | | | second harmonics | | |
|---|---|---|---|---|---|---|---|
| Eo | N | amplitude (%) | phase (degree) | k | amplitude (%) | phase (degree) | k |
| $1.3X10^{15}$eV | 1480 | 3.1±3.7 | 46± 68 | 0.36 | 0.9±3.7 | 104±117 | 0.03 |
| 2.8 | 15461 | 0.6±1.1 | 284±104 | 0.15 | 0.9±1.1 | 93± 73 | 0.31 |
| 6.0 | 24558 | 1.6±0.9 | 313± 33 | 1.53 | 0.2±0.9 | 49±116 | 0.03 |
| $1.3X10^{16}$eV | 20289 | 1.7±1.0 | 290± 34 | 1.40 | 0.1±1.0 | 37±180 | 0.00 |
| 2.8 | 16129 | 2.2±1.1 | 299± 29 | 1.95 | 1.5±1.1 | 129± 21 | 0.94 |
| 6.0 | 9388 | 2.2±1.5 | 293± 39 | 1.09 | 3.2±1.5 | 72± 13 | 2.37 |
| $1.3X10^{17}$eV | 3203 | 1.9±2.5 | 288± 77 | 0.28 | 1.5±2.5 | 73± 47 | 0.18 |
| 2.8 | 758 | 5.9±5.1 | 340± 50 | 0.66 | 5.9±5.1 | 155± 25 | 0.65 |
| 6.0 | 127 | 7.2±12.6 | 103±100 | 0.16 | 15.3±12.6 | 144± 24 | 0.74 |

Table 2 (Case I. Muon-rich showers)

| | | first harmonics | | | second harmonics | | |
|---|---|---|---|---|---|---|---|
| Eo | N | amplitude (%) | phase (degree) | k | amplitude (%) | phase (degree) | k |
| $1.3X10^{15}$eV | 280 | 5.2±8.5 | 106± 93 | 0.19 | 16.5±8.5 | 149± 15 | 1.90 |
| 2.8 | 4842 | 4.4±2.0 | 215± 27 | 2.31 | 1.9±2.0 | 49± 30 | 0.45 |
| 6.0 | 8583 | 1.1±1.5 | 134± 81 | 0.25 | 1.4±1.5 | 62± 32 | 0.40 |
| $1.3X10^{16}$eV | 6421 | 2.5±1.8 | 260± 40 | 1.00 | 1.9±1.8 | 133± 26 | 0.60 |
| 2.8 | 4310 | 1.6±2.2 | 317± 77 | 0.28 | 0.7±2.2 | 80± 93 | 0.05 |
| 6.0 | 2462 | 2.8±2.9 | 14± 59 | 0.48 | 1.4±2.9 | 31± 60 | 0.11 |
| $1.3X10^{17}$eV | 737 | 10.6±5.2 | 317± 28 | 2.08 | 4.1±5.2 | 60± 36 | 0.32 |
| 2.8 | 112 | 5.5±13.4 | 342±139 | 0.08 | 6.2±13.4 | 90± 62 | 0.11 |

Although the present results are quite preliminary, the following features can be noted.

(1) The first harmonics shows a roughly constant phase around $300^o$ below

$10^{17}$eV. This is slso seen in Fig.2a, where thin circles indicate the harmonic diagrams for energy bin from $2.8X10^{15}$ to $1.3X10^{17}$eV each and bold circle indicates that of sum(amplitude, 1.59±0.47% and phase, $298^{o}\pm17^{o}$ R.A. with k=5.63) for this energy region.

(2) The second harmonics of total showers appear to show a tendency of maximum intensity at phase $91^{o}\pm28^{o}$ in right ascension with amplitude of 0.50±0.48% below $10^{17}$eV, as seen in Fig.2b, where the designations of circles are the same in Fig.2a.

(3) Muon-rich showers have the maximum phase of the first harmonics near $220^{o}$ below $10^{16}$eV. Fig.3 shows the data for energy from $2.8X10^{15}$eV to $1.3X10^{16}$eV and those sum indicated by thin and bold circles respectively.

The features (2) and (3) are consistent with the results obtained by electron trigger(Kifune et al. 1985), though present results are not statistically significant. For the feature (1), anti-sidereal amplitude is 0.80±0.48% for the same energy region which is relatively small compared with that of sidereal time variation. The phase of about $300^{o}$ is different from the results

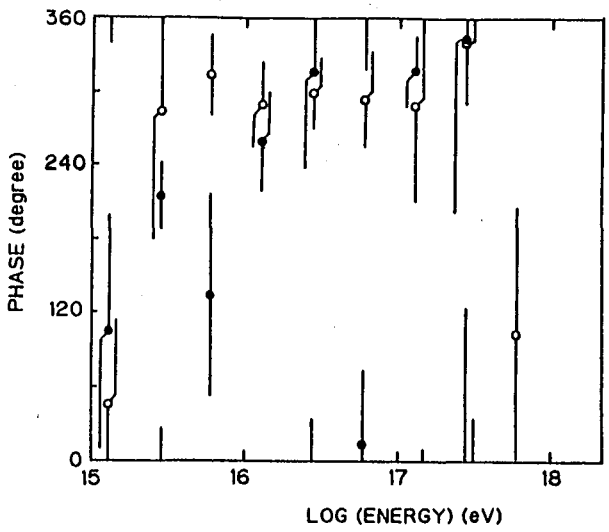


Fig.1a Phase of first harmonics

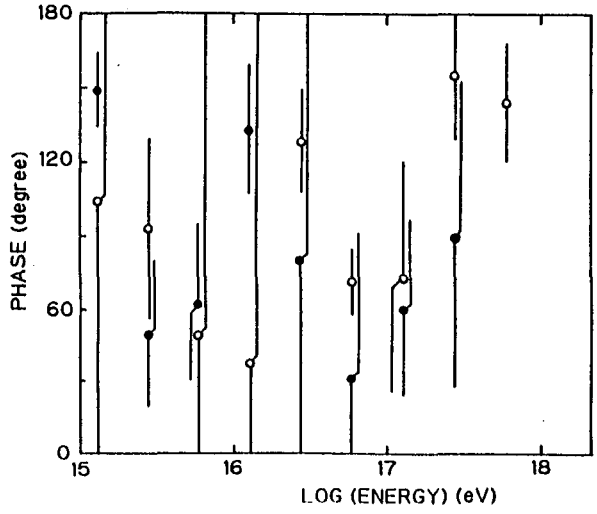


Fig.1b Phase of second harmonics

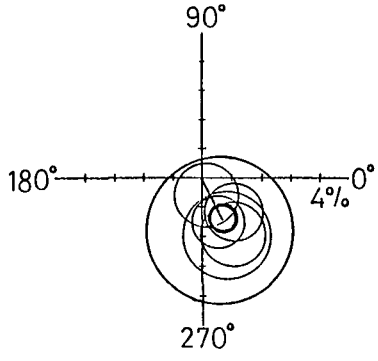


Fig.2a Harmonic diagram of first harmonics for total showers below $10^{17}$eV.

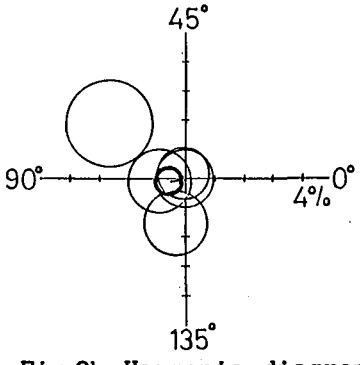


Fig.2b Harmonic diagram of second harmonics for total showers below $10^{17}$eV.

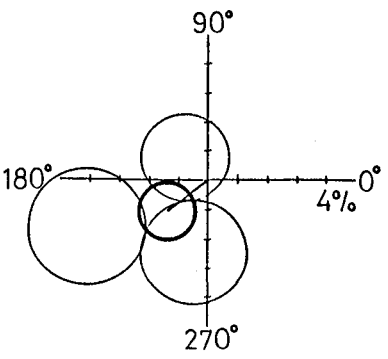


Fig.3 Harmonic diagram of first harmonics for muon-rich showers below $10^{16}$eV.

obtained by electron trigger below $3X10^{16}$eV, even if the magnitude of error is taken account of. One of the posibilities to explain this difference is to attribute it to the difference of triggering bias. If we presume muon size to be better estimater of primary energy than electron size, the data triggered by electrons include contaminations of events which have different primary energies in the same electron size bin, so the reliability of energy dependence of the anisotropy for the case of electron trigger is possibly less than that for muon trigger, especially for lower energy. However in present stage we need to examine this feature more carefully.

Table 3 (Case II)

| | first harmonics | | | second harmonics | | |
|---|---|---|---|---|---|---|
| Time variation | amplitude (%) | phase (degree) | k | amplitude (%) | phase (degree) | k |
| Sidereal | 0.02±0.13 | 33±180 | 0.01 | 0.39±0.13 | 83± 10 | 4.14 |
| Solar | 0.10±0.13 | 142± 78 | 0.27 | 0.07±0.13 | 52± 57 | 0.13 |
| Anti-sidereal | 0.07±0.13 | 187±104 | 0.15 | 0.29±0.13 | 27± 13 | 2.39 |

The preliminary results in case II are presented in Table 3, and harmonic diagrams of first and second harmonics for sidereal time are shown in Fig.4a and b respectively. It appeares that second harmonics of sidereal time variation has statistically significant amplitude of 0.39±0.13% with k=4.14. The phase of maximum intensity is $83^{\circ}\pm10^{\circ}$. The similar results in the second harmonics are obtained by muon triggered data at $2X10^{15}$eV conducted by Murakami et al.(1985) at Akeno.

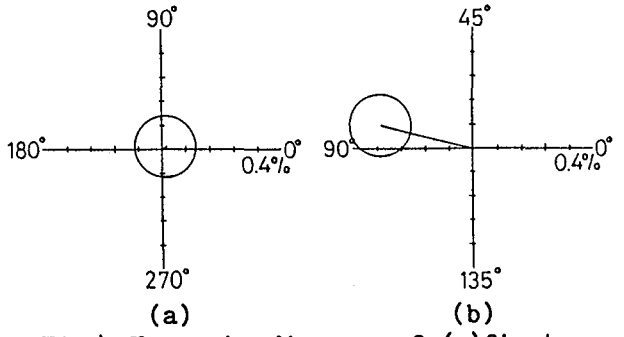


Fig.4 Harmonic diagram of (a)first harmonics and (b)second harmonics, for $6X10^{14}$eV in case II.

It should be noted that statistics are not sufficient at present, and observations are being continued to confirm the anisotropy of cosmic rays.

Acknowledgements

The authors are indebted to the technical staffs in Akeno Crew for obtaining and analyzing the data. We also thank Prof. Murakami in Nagoya University for useful discussions. The data reductions are done by FACOM M380 at Computer Room, Institute for Nuclear Study, University of Tokyo.

References

Hara, T. et al. 1979, Proc. 16th ICRC(Kyoto), 8, 135.
Hara, T. et al. 1981, Proc. 17th ICRC(Paris), 9, 179.
Hara, T. et al. 1983a, Proc. 18th ICRC(Bangalore), 9, 211.
Hara, T. et al. 1983b, Proc. 18th ICRC(Bangalore), 9, 198.
Kifune, T. et al. 1985, submitted to J. Phys.
Murakami, K. et al. 1985, private communication.

# ARRIVAL DIRECTIONS OF COSMIC RAYS OF E > .4 EeV

Baltrusaitis, R.M., Cady, R., Cassiday, G.L., Cooper, R., Elbert, J.W., Gerhardy, P.R., Ko, S., Loh, E.C., Mizumoto, Y., Salamon, M., Sokolsky, P., Steck, D.

Department of Physics, University of Utah, Salt Lake City, UT 84112

ABSTRACT

The anisotropy of cosmic rays observed by the Utah Fly's Eye detector has been studied. Emphasis has been placed on examining distributions of events in galactic coordinates. No statistically significant departure from isotropy has been observed for energies greater than 0.4 EeV (1 EeV = $10^{18}$ eV). Results of the standard harmonic analysis in right ascension are also presented.

1. Introduction. At the highest energies, the arrival directions of cosmic rays are expected to begin to reveal their origins. In this analysis the observed number of events is compared to the number predicted for an isotropic distribution as a function of both galactic longitude and sin (galactic latitude) for each energy interval, so searches can be made for clustering in two dimensions. The event distributions have also been fit to two different models for galactic latitude dependence: 1. An excess of events from the general direction of the galactic plane of the form $I_{(b)} = I_0[(1 - f) + f \exp(-b^2)]$ where b is the galactic latitude in radians (1), and 2. A gradient with respect to galactic latitude of the form $I_{(b)} = I_0(1 + s \cdot b)$, where b is the galactic latitude in degrees. A similar analysis of the data is performed in the two-dimensional celestial coordinates, and fits have been made to the amplitude A and phase $\alpha_0$ of the first harmonic of the form $I_{(\alpha)} = I_0(1 + A \cos(\alpha - \alpha_0))$, where $\alpha$ is the right ascension.

2. Description of Analysis. We report here the arrival directions of extensive air showers observed by the Utah Fly's Eye detector, situated at 41°N latitude, between the dates of Nov. 1981 and April 1985. A detailed description of the detector is reported in ref. 2. Only data recorded on clear nights with no clouds higher than 10° above the horizon were accepted. The total live time corresponding to these "weather cuts" is 58.2 days. Further cuts on the data were made to ensure well-measured tracks with good control over the error in direction: the average error in zenith angle after cuts is $\sigma = 3.8°$. Events passing all cuts were then binned in both galactic and celestial coordinates for four energy intervals: 0.4 - 1.0 EeV, 1.0 - 3.0 EeV, 3.0 - 10.0 EeV, and > 10 EeV. All distributions were made in equal-area bins of 5° in galactic longitude (or right ascension) versus 0.4 in sin latitude (or sin declination).

Since the Fly's Eye can only operate on clear moonless nights, the irregular pattern of observation times precludes the assumption of uniform acceptance in right ascension made by experiments running continously. The procedure used to calculate the number of

events expected as a function of galactic longitude and sin(latitude) from an isotropic distribution is outlined in this section. The distribution in celestial coordinates follows exactly the same prescription.

The absolute start and stop times for each data run have been recorded. For each 15 minute interval of detector on-time, the zenith angle for each bin of galactic coordinates is computed. Since the distribution in azimuth is uniform, the detector acceptance in zenith angle is the only quantity necessary to compute the acceptance times live-time product at each time interval and each pair of coordinates. Two different techniques have been used to find the acceptance as a function of zenith angle. The first is to use the Monte Carlo simulation of the detector. In principle, this allows an absolute rate determination in galactic coordinates, although only the relative rate was used for this analysis. The second technique uses the measured zenith angle distribution of the data itself to get the relative acceptance. An acceptance of 1 gives a flat distribution in $\cos(\theta_z)$, so measuring the deviation from a fixed number gives the $\theta_z$ dependence. The relative acceptance in zenith angle calculated directly from the data agrees very well with that predicted by the Monte Carlo simulation: the results reported here were shown to be insensitive to the distribution used.

The acceptance-weighted live times thus generated give the relative rates expected in each bin of galactic coordinates. The absolute normalization is then fixed by demanding that the total number of events predicted be equal to the total number of events observed in each energy interval. Deviations in the data from isotropy should then appear as local excesses (or deficits) of events compared with the number predicted.

Given the number of events observed and predicted in each bin, fits to various models for a possible anisotropy can be made. The number of events expected is weighted by the appropriate model-dependent factor (for example, $(1 + s \cdot b)$ to fit for a galactic latitude gradient s), the "expected" array is renormalized to preserve the same total number of events, and the joint probability for the observed to predicted distribution is calculated. Maximizing the probability with respect to variation in the parameters of the model (for example, s) gives the best fit to the data as well as the associated errors on the best-fit values of the parameters.

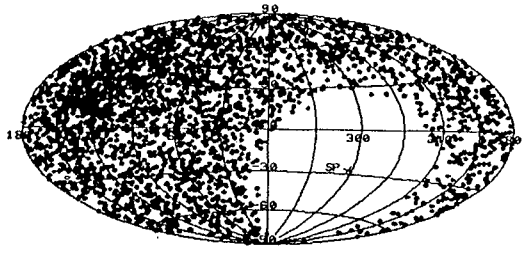


Fig. 1. The Fly's Eye Acceptance.

3. Results and Discussion. Figure 1 shows our acceptance in galactic coordinates from Monte Carlo events between 3-10 EeV. Note that the region between galactic longitude 240° to 0° and galactic latitude +30 to -90° are not visible to the Fly's Eye. Observed rates projected onto a single axis must, of course, be evaluated with this fact in mind.

The ratio of events observed to events expected as a function of galactic latitude are shown in Fig. 2. Table 1 gives the results for the two galactic models considered. Column a) shows fits to a latitude gradient s of the form $(1 + s \cdot b)$; column b) shows the fits to a galactic plane excess $(1 - f + fe^{-b^2})$ with b in radians. No statistically significant deviations from isotropy are observed, although the trend in the latitude gradient agrees with that observed by other experiments (3). The data disagrees mildly with the analysis presented in ref. (1) for the galactic plane excess model, at about 1 $\sigma$ level. However, our inability to see a rather large region of the galactic disk, in particular the galactic center, should be kept in mind when interpreting these results.

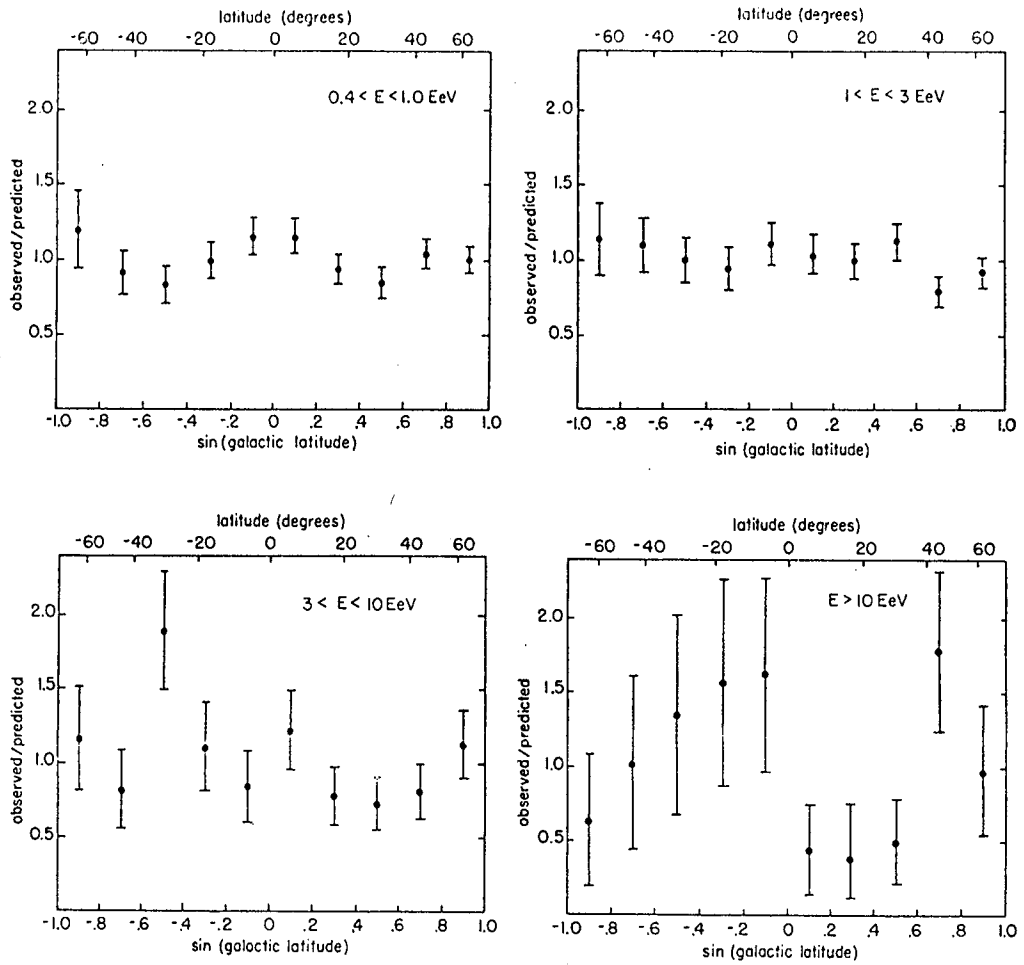


Fig. 2. Observed rates as a function of galactic latitude.

Table 1. Galactic latitude fits

| Energy (EeV) | <E> (Eev) | Number of Events | a) Slope $s(10^{-3}/deg)$ | b) Galactic Plane Excess f |
|---|---|---|---|---|
| 0.4-1.0 | .64 | 760 | -0.1 ± 1.6 | 0.06 ± 0.20 |
| 1.0-3.0 | 1.7 | 575 | -1.5 ± 1.7 | 0.15 ± 0.21 |
| 3.0-10.0 | 5.0 | 170 | -1.5 ± 3.0 | 0.0 ± 0.3 |
| >10.0 | 18.8 | 45 | 0.6 ± 6.0 | $0^{+.5}_{-1.0}$ |

In celestial coordinates, the fits were made to the amplitude and phase of the first harmonic in right ascension, and are shown in Table 2. Here, there is some evidence for non-zero anisotropy, again in agreement with other experiments.

Table 2. First harmonic in right ascension

| Energy (EeV) | Amplitude A | Phase $\alpha_0$ (degrees) |
|---|---|---|
| 0.4-1.0 | .15 ± .08 | 300 ± 30 |
| 1.0-3.0 | .07 ± .08 | 25 ± 80 |
| 3.0-10.0 | .25 ± .16 | 350 ± 40 |
| >10.0 | .34 ± .34 | 290 ± 60 |

4. Conclusions. If we believe that the cosmic rays above 1 EeV are predominantly protons from our own galaxy, then it is perhaps surprising that there is no evidence in our data for an enhancement from the general direction of the galactic disk. Certainly, more evidence on the composition of cosmic rays at this energy will be crucial to a real understanding of production sources and mechanisms. If a significant fraction of the observed cosmic rays are in fact galactic iron, or are "universal" extra-galactic protons, then the observed smoothness of the data would be reasonable.

Acknowledgment

This work was supported by the U.S. National Science Foundation under grant PHY-8201089.

References

1. Wdowczyk, J. and Wolfendale, A.W., J. Phys. G: Nucl. Phys. 10 (1984) 1453.
2. Baltrusaitis, R.M. et al., The Utah Fly's Eye Detector, submitted to Nucl. Inst. Meth.
3. Astley, S.M. et al., Proc. Int. Conf. on Cosmic Rays (Paris) 2, 156, 1981.

# The sidereal anisotropy of cosmic rays around $3 \cdot 10^{15}$ eV observed at a middle north latitude.

K. Murakami
Cosmic Ray Research Laboratory, Nagoya University
Chikusa, Nagoya 464, JAPAN

T. Kifune and N. Hayashida
Institute for Cosmic Ray Research, University of Tokyo
Tanashi, Tokyo 188, JAPAN

ABSTRACT

The sidereal time variation of cosmic rays (median primary energy : $3 \cdot 10^{15}$ eV) is investigated with air shower observations at Akeno, Japan (900 m a.s.l.) which started in September 1981. Air showers are detected by a coincidence requirement on several muon detectors. The result obtained for three years is suggestive of a big semi-diurnal variation (0.37 % in amplitude). On the other hand, the diurnal variation is rather small than the semi-diurnal one. The feature of the sidereal anisotropy supposed from the present result looks quite different from that below $10^{14}$ eV.

1. Introduction. In Bangalore Conference (1983), a review on sidereal anisotropies in air shower observations was given by Linsley (1). The anisotropy beyond $10^{14}$ eV is still ambiguous, because of poor statistics and also because most of results except that by Daudin et al. (2) are not from air shower observations proper to the study of the sidereal anisotropy. Recently we have carried out air shower observations at Akeno, Japan ($35^{0}47'$N, $138^{0}30'$E, 900 m a.s.l.) with the aim of studying the sidereal anisotropy around $3 \cdot 10^{15}$ eV.

2. Observations. The observations are made by using four muon detectors (25 $m^2$, 50 proportional counters, 2 m thick concrete) being located 100 ~ 200 m apart from each other. The detection of air showers is done by the following triggering requirements. Fifty proportional counters in each muon detector are divided into four groups of ten counters with spacing of three counters. For detection of shower, at first, a coincidence of incident particles is selected in the mode of "any two groups out of four counter groups" in each muon detector, and next, another coincidence is done in the mode of "any three- or four-fold coincidence" among the coincidence signals fed from those four muon detectors.

The response function was obtained from the analysis of air showers (1844 events) detected by the above-mentioned conditions. The result (normalized integral response function) is shown in Fig. 1, where solid points and open circles are values derived via the determinations of muon size and electron size, respectively. In this analysis the following points are noted. (1) The median primary energy is about $3 \cdot 10^{15}$ eV. (2) The zenith angle distribution of detected air showers per solid angle is proportional to $\cos^{5.2}\theta$ ($\theta$ : zenith angle). (3) Although the present triggering was doubted if it was favoured for detecting muon-rich showers, no significant distinction from cases of electron triggering was found.

The continuous observations have been carried out since September

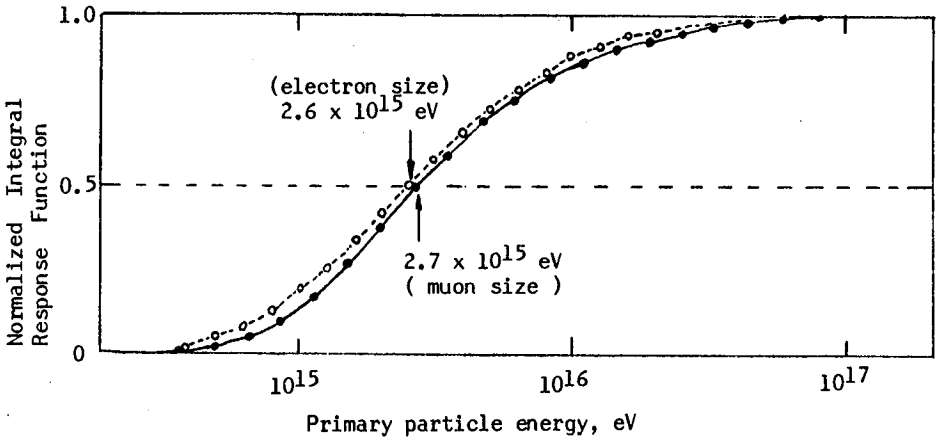


Fig. 1 Response function.

1981. In the following, a result obtained for three years until August 1984 is reported. The number of events is, in total, 2,237,059 showers observed in 962 days, after the rejection of days in which complete observations (with stable operation under constant condition throughout the day) were not fulfilled.

3. Results. Fig. 2 shows harmonic vectors in solar, sidereal and anti-sidereal time, averaged over three-year data without correction for barometric pressure effect or so on. The barometric pressure effect is of - 0.19 ± 0.03 % per mb. Open circles, P, shown in the figure are vectors expected from the barometric pressure effect. The other vectors, S, are variations of rate of single-particle incidences into four muon detectors including background radia-

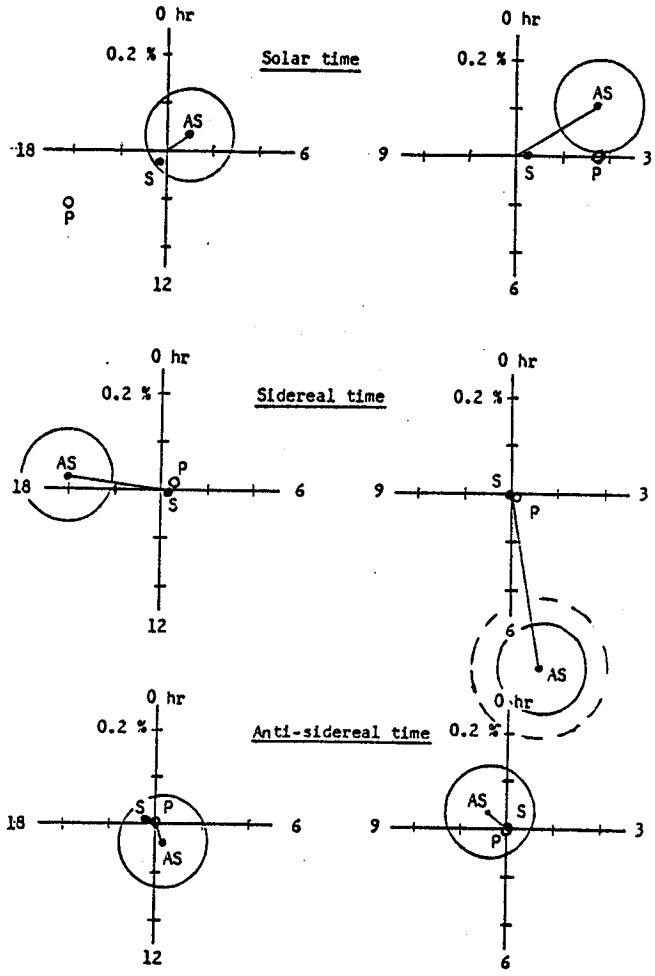


Fig. 2 Harmonic vectors.

tion from surrounding concrete. The regression coefficient to air shower rate is at most of a factor 2, and so the variation related with single-particle rate is negligible. The error circle around air shower rate AS means the standard deviation of mean amplitude derived from the scatter of hourly values. This deviation is of 0.1 % and almost equal to that estimated from total number of recorded air showers. The dotted circle will be explained in the last paragraph.

The results are summarized as follows :

(1) The solar diurnal variation is very small. There is, however, a discrepancy from the vector P expected from barometric pressure effect. Main part of this discrepancy may be interpreted as atmospheric temperature effect.

(2) The solar semi-diurnal vector is not inconsistent with the barometric pressure effect.

(3) The amplitude of sidereal diurnal variation is as much as twice of the standard deviation and so the existence of the diurnal anisotropy is still hazy.

(4) The semi-diurnal vector in sidereal time is of 0.37 ± 0.10 % and 5.7 ± 0.8 hour. The existence of this vector will be discussed again in the last paragraph.

(5) The diurnal as well as semi-diurnal variations in anti-sidereal time are small.

4. Sidereal semi-diurnal variation. As mentioned above, it seems that a big sidereal semi-diurnal vector is existent. Further analyses on this anisotropy were made. One is the monthly shift of semi-diurnal vector on solar time coordinate, as shown in Fig. 3. Except the shift from (Feb., Aug.) to (Sep., Mar.), the anti-clockwise turning of the vector with month is very suggestive of the existence of the sidereal anisotropy. However, another analysis shows that the sidereal vector obtained for each half-year is rather widely distributed than the scatter expected from statistical fluctuation of hourly values, as shown in Fig. 4. The dotted circle in Fig. 2 is corresponding to this wide distribution of the vector. Therefore, in order to confirm the existence, it may be necessary to wait for more accumulation of the data. At present we have no idea to interpret why the vector scatters so widely, although we are trying to seeking for the reason.

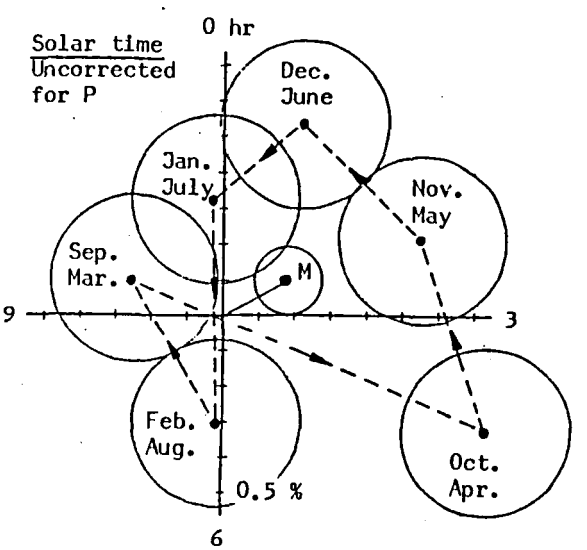


Fig. 3 Monthly vector of semi-diurnal variation in solar time.

5. Summary. The sidereal time variation around $3 \cdot 10^{15}$ eV was investigated with air shower observations at Akeno which started in September

1981. The result obtained for three years gives a big semi-diurnal vector in sidereal time, 0.37 ± 0.10 % and 5.7 ± 0.8 hour. Although we need to accumulate more data in order to confirm the existence, it is very interesting that the semi-diurnal vector seems bigger than the diurnal vector, because the diurnal vector has been confirmed to be bigger than the semi-diurnal vector at north latitudes in the region below $10^{14}$ eV.

Although the above semi-diurnal vector was given with the standard deviation estimated from the fluctuation of hourly value, if we consider the wide distribution of the vector obtained for each half-year, the statistic for confirming its existence is still unsufficient (now the significance level = 1 %).

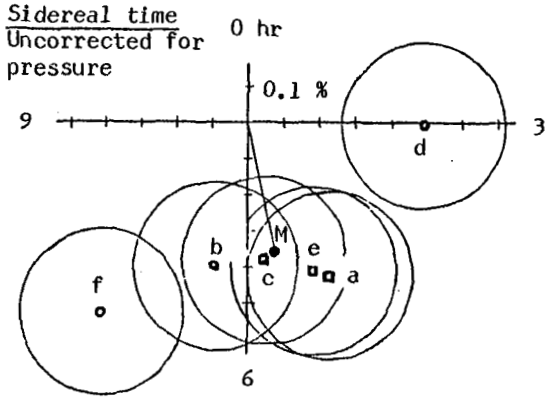


a : Sep. 1981 - Feb. 1982
b : Mar. 1982 - Aug. 1982
c : Sep. 1982 - Feb. 1983
d : Mar. 1983 - Aug. 1983
e : Sep. 1983 - Feb. 1984
f : Mar. 1984 - Aug. 1984
M : Sep. 1981 - Aug. 1984

Fig. 4 Distribution of sidereal semi-diurnal vector for each half-year.

The barometric pressure effect is explainable mainly with longitudinal development of muon size.

6. Acknowledgement. The authors express thanks to Mr. K. Hoji in Institute for Cosmic Ray Research, University of Tokyo and Mrs. M. Hayase and Mr. S. Shibata in Cosmic Ray Research Laboratory for their valuable assistances. The authors thank Mr. S. Shimonaga in Sharp Co. for his precious suggestion and assistance.

References.

1. Linsley J. : Conf. Papers 18th ICRC, Bangalore, 12, 135, (1983).
2. Daudin J. et al. : Nuovo Cimento, 3, 1017, (1956).

# ARRIVAL DIRECTION DISTRIBUTION OF COSMIC RAYS OF ENERGY > $10^{18}$ eV

P.V.J. Eames, J. Lloyd-Evans†, C. Morello††, R.J.O. Reid and A.A. Watson
Department of Physics, University of Leeds, LEEDS 2, UK.

† Now at NASA/Goddard Space Flight Centre, USA.
†† Permanent address: CNR, Istituto di Cosmo-Geofisica, Torino, Italy.

## ABSTRACT

The Haverah Park air-shower experiment recorded over 8500 events with primary energy > $10^{18}$ eV between 1963 and 1983. An analysis of these events for anisotropies in celestial and galactic co-ordinates is reported. No very striking anisotropies are observed.

1. Introduction. Seven years ago the Haverah Park group (Edge et al 1978) published a detailed analysis of the arrival direction distribution of cosmic rays above $6 \times 10^{16}$ eV. Since that publication there have been numerous 'up-dates' reported in conference proceedings and reviews. In this report we concentrate on the cosmic rays above $10^{18}$ eV where additional running has enabled us to increase our data from 4202 events (Edge et al 1978) to 8565. The additional data have been recorded with the same angular resolution as in the earlier work (rms variation in solid angle < $10^{-2}$ sr); the energy resolution has been slightly improved by the addition of $3 \times 2.25$ m$^2$ detectors at 1 km from the array centre. We describe here the results of an analysis in celestial and galactic co-ordinates; fuller details will be reported elsewhere.

2. Harmonic Analysis in Right Ascension. The results of an harmonic analysis in right ascension over the declination range $90 < \delta < -6^{\circ}$ are given as a function of energy in Table 1. Following our previous practice the data are divided in energy $1 - 2 \times 10^{18}$ eV (E5), $2 - 4 \times 10^{18}$ eV (E6), $4 - 32 \times 10^{18}$ eV (E7,8,9) and $> 3.2 \times 10^{19}$ eV (E10). For brevity the notation E5 etc. will be used here. The first and second harmonics are given. Only amplitude uncertainties are quoted; probabilities of those amplitudes arising by chance from a random distribution equal $\exp(-k_o)$ and the phase uncertainty is $57.3/(2k_o)^{\frac{1}{2}}$ degrees, where $k_o = r^2n/4$ (Linsley 1975).

Table 1

| | from Edge et al (1978) | | | | Present Work | | | |
|---|---|---|---|---|---|---|---|---|
| | n | $r_1$% | $\theta_1{}^{\circ}$ | $k_o$ | n | $r_1$% | $\theta_1{}^{\circ}$ | $k_o$ |
| E5 | 2832 | 6.3 ± 2.7 | 50 | 2.83 | 5764 | 4.4 ± 1.9 | 67 | 2.76 |
| E6 | 978 | 7.9 ± 4.5 | 37 | 1.52 | 1939 | 3.7 ± 3.2 | 17 | 0.65 |
| E7,8,9 | 364 | 7.9 ± 7.4 | 280 | 0.55 | 812 | 5.7 ± 5.0 | 272 | 0.66 |
| E10 | 28 | 57 ± 27 | 163 | 2.27 | 50 | 42 ± 20 | 179 | 2.16 |
| | | $r_2$% | $\theta_2{}^{\circ}$ | | | $r_2$% | $\theta_2{}^{\circ}$ | |
| E5 | 2832 | 3.0 ± 2.7 | 169 | 0.64 | 5764 | 2.7 ± 1.9 | 175 | 1.01 |
| E6 | 978 | 11 ± 5 | 71 | 2.74 | 1939 | 4.3 ± 3.2 | 80 | 0.89 |
| E7,8,9 | 364 | 18 ± 7 | 75 | 2.95 | 812 | 13 ± 5.0 | 83 | 3.59 |
| E10 | 28 | 25 ± 27 | 59 | 0.45 | 50 | 12 ± 20 | 166 | 0.18 |

It is disappointing to report that the doubling of the Haverah Park data has led to a decrease in all of the amplitudes above $10^{18}$ eV. Of the 8 amplitudes listed the significance, as measured by $k_o$, of only 3 have increased. However the most significant amplitude of the new set was also the most significant of the original set: the 2nd harmonic in the energy bin E7,8,9 now has a probability of arising by chance of 2.8%. For 371 events in a similar energy range ($5 \times 10^{18} - 4 \times 10^{19}$ eV) the Yakutsk group find $r_2 = 7.6 \pm 7.3\%$ at $\theta = 114^o$ (Efimov et al 1983). The joint amplitude (n = 1183) is $r_2 = 11 \pm 4\%$, $\theta = 89^o$ with a chance probability of 2.8%.

The probability that the observed sets of 8 $k_o$'s arise by chance from a random distribution has risen from 3% to 10%.

3. Analysis in Galactic Co-ordinates. In 1981 we introduced an analysis in galactic latitude from which a series of gradients of observed number/expected number as a function of galactic latitude was obtained (Astley et al 1981). The initial analysis was with a data base intermediate in size between that discussed in Edge et al (1978) and that now available; a S-N assymetry was claimed. The gradients given by Lloyd-Evans and Watson (1982) are listed together with the new gradients in Table 2. A correction to the binning algorithm used in calculating the gradients has been made and about 25% more data has been added above $10^{18}$ eV. The gradients are compared with results from other experiments in Figure 1. The Haverah Park gradients show deviations from expectation significant at the 4% level ($\chi^2_8 = 1.97$) and in addition (ignoring the most energetic (extragalactic?) events in E10) there is a clear tendency for the gradients to fall and then change sign as the energy increases. However there are strong systematic differences between the various experiments, none of which are consistent with the above gradients, for which no satisfactory explanation has yet been found.

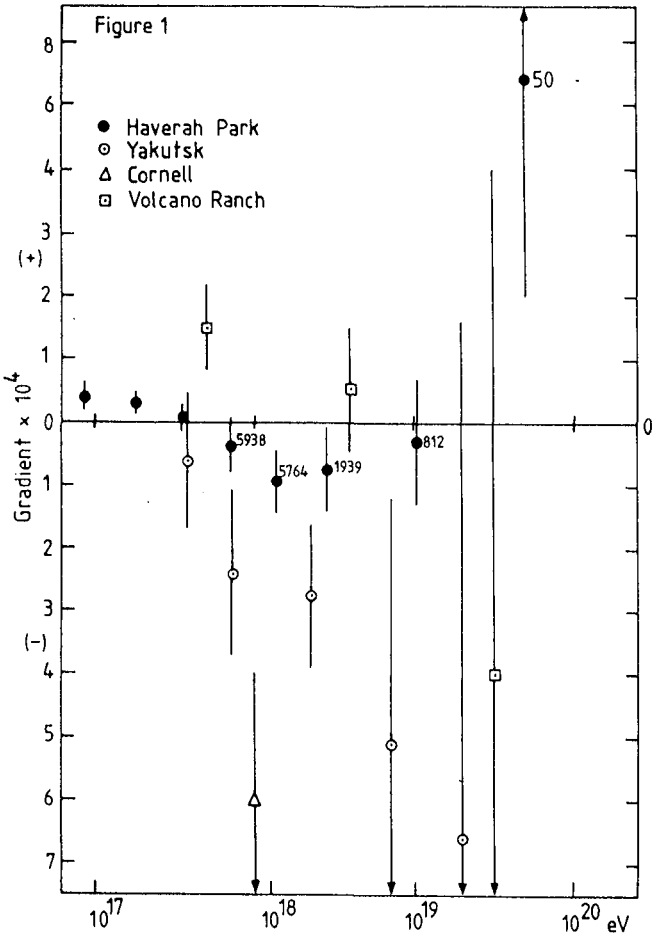


4. Discussion. Wdowczyk and Wolfendale (1984) in an interesting discussion of cosmic ray anisotropy have suggested that the observation of an S-N gradient above $10^{18}$ eV is an artefact arising from the limited galactic latitude coverage of the Northern Hemisphere experiments.

Table 2

| Energy interval | Lloyd-Evans & Watson (1982) | | Present Work | |
|---|---|---|---|---|
| | n | gradient ($\times 10^4$ deg$^{-1}$) | n | gradient ($\times 10^4$ deg$^{-1}$) |
| E1 | 18829 | $-1 \pm 3$ | 18829 | $3.9 \pm 2.4$ |
| E2 | 39982 | $-2 \pm 2$ | 39982 | $3.2 \pm 1.6$ |
| E3 | 20635 | $-4 \pm 3$ | 20635 | $0.7 \pm 2.2$ |
| E4 | 5938 | $-8.5 \pm 4.3$ | 5938 | $-3.6 \pm 4.1$ |
| E5 | 4349 | $-13 \pm 5$ | 5764 | $-9.2 \pm 4.1$ |
| E6 | 1499 | $-16 \pm 9$ | 1939 | $-7.5 \pm 7.0$ |
| E7,8,9 | 610 | $-22 \pm 13$ | 812 | $-3.3 \pm 10$ |
| E10 | 38 | $92 \pm 85$ | 50 | $66 \pm 47$ |

They propose instead that the data should be tested against a model which invokes a galactic plane excess and which predicts that the angular width of the galactic plane as seen in cosmic rays should shrink slowly with increasing energy.

The prediction of this model in which it is suggested that

$$I(b) = I(0)\left[(1 - f_E) + f_E \exp(-b^2)\right]$$

is compared with the data in Figure 2 for $f_E$, the galactic latitude enhancement factor, = 0.3 (Wdowczyk and Wolfendale 1985, Figure 1(d)). There is some evidence for a galactic plane enhancement.

We have investigated the galactic plane enhancement directly by comparing the number of events within $\alpha \pm 5^o$ of the galactic plane for the declination range $61.6 < \delta < -6^o$. For bins E5, E6, E7,8,9 the observed number of events was 268, 93 and 36 while 250, 83 and 36 were expected. There is clearly no significant evidence of enhancement.

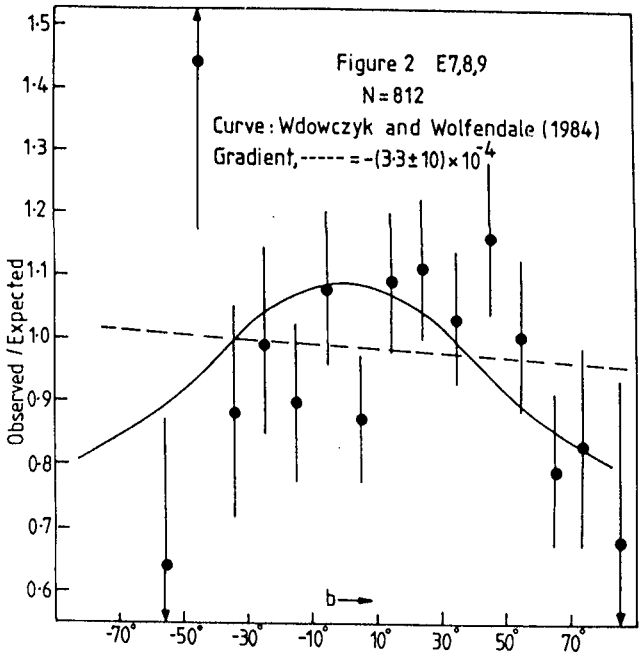


In Figure 3 we compare the first harmonics of Table 1 with the predictions of Hill and Schramm (1985). The best estimate of the amplitude, s, (Linsley 1975) is shown together with 95% and 5% confidence levels. The predictions are derived from a model in which cosmological and bright

local extragalactic source fluxes are combined. The injection spectrum slope $\gamma = 2.0$ favoured through their fit of spectrum data predicts rather higher anisotropies above $5 \times 10^{18}$ eV than are observed.

5. Conclusion. High energy cosmic rays ($E > 10^{18}$ eV) are remarkably isotropic. In particular we remind the reader that above $3.2 \times 10^{19}$ eV (50 events) there is no evidence for a galactic plane anisotropy but there is some evidence for an anisotropy of $(40 \pm 20)\%$ in a direction nearly normal ($\alpha = 180^{o}$) to the galactic plane. Of the 8 events above $10^{20}$ eV which we have observed, 4 are more than $40^{o}$ above the galactic plane.

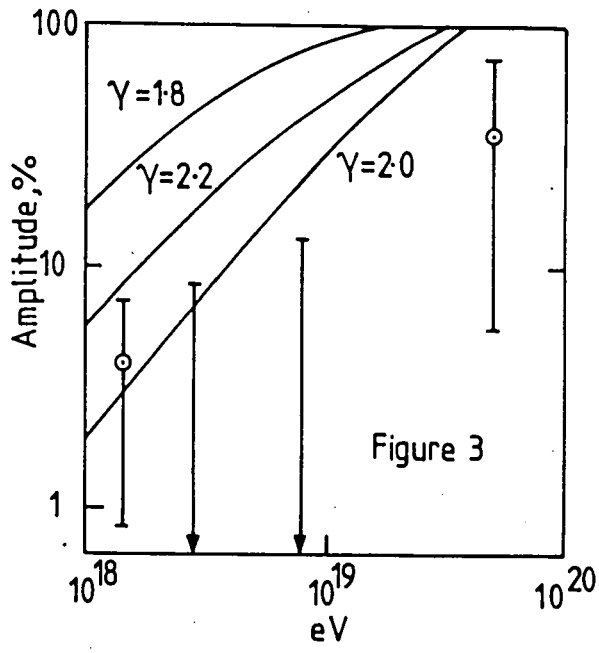

Figure 3

Acknowledgement. We thank John Linsley for allowing us to present his data in the form shown in Figure 1. CM thanks NATO for a research fellowship while the support of SERC to work at Haverah Park is gratefully acknowledged.

References

S M Astley et al 1981 Proc. 17th ICRC (Paris) 2, 156.
D M Edge et al 1978 J Phys G 4, 133.
N N Efimov et al 1983 Proc. 18th ICRC (Bangalore) 2, 149.
C T Hill and D M Schramm 1985 Phys Rev D 31, 564.
J Linsley 1975 Phys Rev Lett 34, 1530.
J Lloyd-Evans and A A Watson 1982 in 8th European Cosmic Ray Symposium, Editors Iucci et al, Techno print, Bologna p81.
J Wdowczyk and A W Wolfendale 1984 J Phys G 10, 1453.

# OBSERVATION OF ARRIVAL TIMES OF EAS WITH ENERGIES $\geqslant 6 \times 10^{14}$ eV

SUN Luorui

Department of Physics, Zhengzhou University, China.

## 1. Introduction

The earth's atmosphere is continually being bombarded by primary cosmic ray particles which are generally believed to be high-energy nuclei. The fact that the majority of cosmic ray primaries are charged particles and that space is permeated with random magnetic fields, means that the particles do not travel in straight lines. This makes the identification of distant sources very difficult. Nevertheless, studies of the arrival time and direction distribution of cosmic rays are still used to seek significant information on problems of their origin. From the beginning of the 1950's to the middle of the 1960's about 50 experiments were carried out to study the arrival directions of EAS with energy range from about $10^{14}$ to $10^{17}$ eV. Linsley and Watson [1] summarised the results of these experiments and gave a review at 15th Cosmic Ray Conferece.

On the other hand, the arrival time distribution of EAS may also transfer some information about the primary particles. Actually, if the particles come to our earth in a completely random process, the arrival time distribution of pairs of successive particles should fit an exponential law. This is derivable from Poisson's distribution. Several groups [2,3] have reported a non-random component in the arrival times of EAS with $E \geq 10^{14}$ eV, but others[4] did not find it.

The work reported here was carried out at Sydney University from May 1982 to January 1983. The results are discussed and compared with that of some other experiments.

## 2. Experiment System

This experiment work was carried out by using the Sydney Small Air Shower Array. This sea level array has been described in detail elsewhere[5]. The array is composed of four fast timing scintillators arranged as a 25m×25m horizontal square with four triggering scintillators in a 4m×4m square in the same plane as the fast timing scintillators. The triggering scintillator square is close

but not at the centre of the fast timing square. Pulses from the scintillators are sent via fast rise time coaxial cables to the recording electronics which is in an air conditioned hut with the triggering scintillators. The recording electronics uses NIM/CAMAC System. A master trigger pulse is produced if three out of four of the triggering scintillators receive shower particles. Showers are analysed in a desk-top compuer which is employed to control the recording system. The shower direction is found by a weighted least-squares fit of a plane shower front to relative arrival time of each detector. Then, using the maximum likelihood method to estimate the shower size and core position. Finally, the celestial coordinates of the incident direction of the event is found out. The rate of analysed showers is 127 per day or one every 11.3 minutes on average. The time needed for the full analysis is about 30 seconds.

## 3. Analysis and results

The data discussed here were obtained in the period from May 27 in 1982 to January 12 in 1983 at the campus of Sydney University (latitude 33° s). During this period more than 23000 showers were recorded. The data are analysed in two different ways as follows.

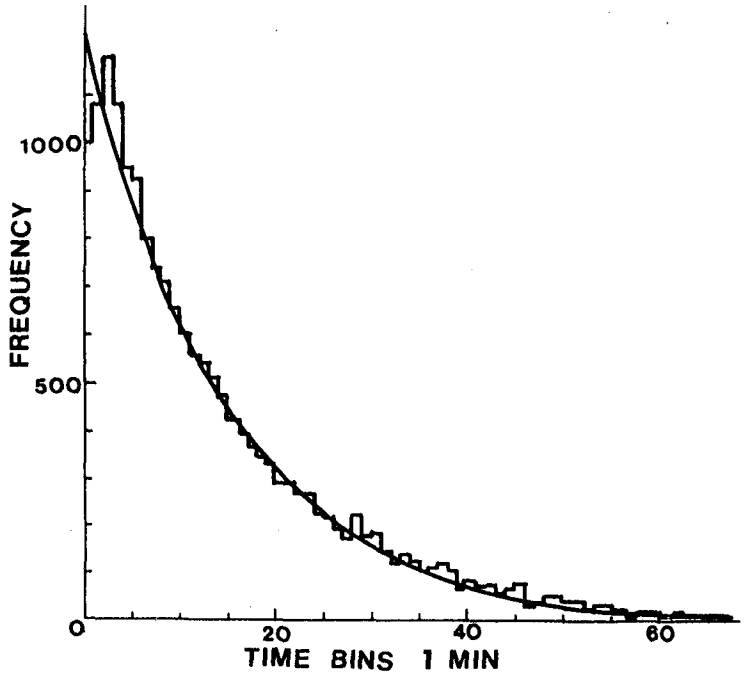


Fig. 1 Cosmic ray arrival time distribution

Firstly, all the data are used to plot the arrival-time distribution of the events, that is, the distribution of time-separation t between consecutive events on a 1 minute bin size (Fig. 1). The smooth curve shows the expected exponential distribution of the arrival times assuming that the time of occurrence of the events is completely random:

$$n = N \cdot (e^{-\lambda t_1} - e^{-\lambda t_2})$$

where $\lambda$ is the average number of events per unit time. As can be seen

from Fig. 1, the observation data are compatible with random expectation. After adding the estimated losses for the observation data, no deviations are greater than $3\sigma$. So that no experimental evidence for abnormal behaviour in the inter shower arrival time distribution has been found.

Then, the data are analysed with respect to the sidereal time variation. Since the experiment was interrupted occasionally for maintenance and by power failures, some allowances for this interruption must be made before the analysing. After rejecting certain numbers of events from those "over-exposure" time intervals, the run time for every sidereal hour interval is unified. The data are analysed by using the "random walk" harmonic method and the results are:

the fractional amplitude $r = (1.9 \pm 1.1)\ \%$,
the probability of observing an amplitude $\geq r$ $p = 0.21$,
the phase of maximum $\psi = 74^\circ \pm 33^\circ$.

To compare these results with that of the experiments summarised in Ref. (1), they are plotted together in Fig. 2 (after Kiraly et al (6)). the value of p of the present experiment sits at the middle of Fig. 2 (1), and the value of $\psi$ just falls in the gap of the old data in Fig. 2 (2). If anything this confirms the isotropy of arrival directions.

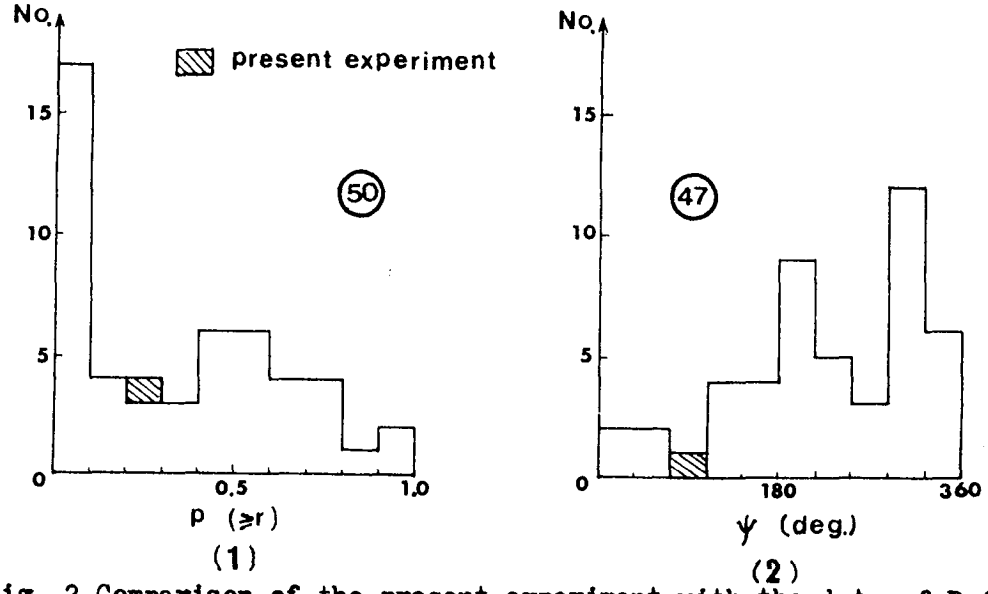


Fig. 2 Comparison of the present experiment with the data of Ref. (1). The ordinates are the frequencies and the circles contain the numbers of experimental sets contributing to the data (excluding the present experiment).

The data are also tabulated on Mercator Projections and a series of chi-squared tests is applied. The results are shown in Fig. 3. The largest value of $\chi^2$ for the tabulation is 57. The probability that $\chi^2$ should have exceeded this value for one or more of eight independent

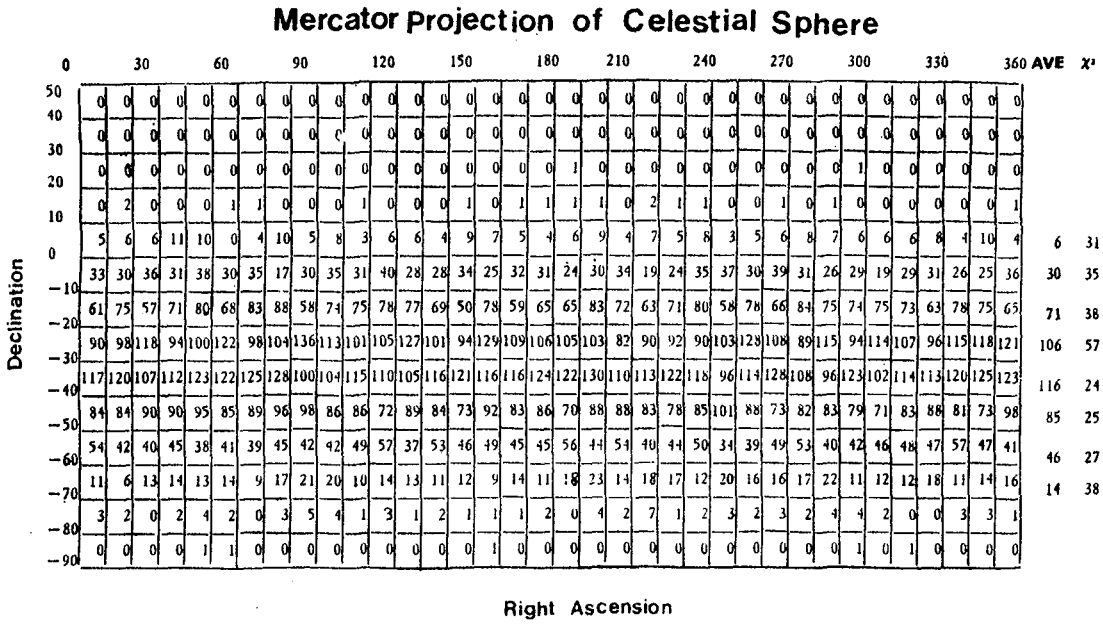


Fig. 3 Cellular division of Mercator Projection of celestial sphere for 17164 showers.

bands is 12%. Thus the chi-squared tests show no significant evidence of anisotropy in the tabulated distributions.

4. Acknowlegement

The auther wishes to thank Prof. H. Messel, Prof. C. B. A. McCusker, Prof. M. M. Winn and Dr. J. Ulrichs in Sydney University for their constructive suggestions and support.

References

1. Linsley, J. et al, Proc. 15th ICRC, Plovdiv, Vol. 12 (1977), 203.
2. Bhat, C. L. et al, Nature, V288 (1980), 146.
3. Badino, G. et al ,Lett. Al Nuovo Cimento, V28 (1980), 93.
4. Fegan, D. J. et al, Proc. 17th ICRC, Paris, Vol. 6 (1981), 296.
5. Sun, L. et al, Nucl. Instr. & Meth. , 223 (1984), 173.
6. Kiraly, P. et al, Rivista del Nuovo Cimento, 2 (1979), 1.

# COSMIC RAY INTENSITY VARIATIONS AT PRIMARY RIGIDITIES NEAR 1900 GV

Y.W. Lee, P.K. MacKeown and L.K. Ng
Physics Department
Univeristy of Hong Kong

ABSTRACT

Preliminary analysis of an experiment monitoring cosmic ray muons yields a first sidereal harmonic amplitude for rigidities around 1900 GV of $(7.95\pm3.97)10^{-4}$ at 5.1±1.9h right ascension. A significant anti-sidereal first harmonic is, however, also seen.

1. Introduction Over the past ten years or so steady progress has been made in determining the anisotropy of arrival directions of cosmic rays over a very wide energy region of the primary particles. We report here on preliminary results from an experiment designed to monitor the temporal variation of cosmic ray muons with energies greater than about $1.6\ 10^{11}$ eV carried out in a road side tunnel in Hong Kong at $\lambda = 22.23^{o}$N, $\phi_E = 114.6^{o}$E. Details of the experiment are reported in [1] and in an accompanying paper at this conference (Lee and Ng , HE 4.5-15).

2. Basic Data of the Experiment The telescope, composed of individually monitored cylindrical proportional counters, is situated under a rock burden of varying thickness with an intensity weighted average depth of 573 hg $cm^{-2}$. This corresponds to a mean muon threshold energy of 157 GeV. Using a factor of 12.2 to relate the muon threshold to primary rigidity [2], [3] we have a value for the median rigidity, $R_{med}$ = 1915 GV.

The present report is based on observations made in the period November 1983 - March 1985, during which time the duty cycle was 80%. No selection, or cuts, have been imposed at this stage on the data, which totals $1.27\ 10^{7}$ counts - an average count rate of 1280 $hour^{-1}$. A small systematic decrease in the count rate is observed, with an average fractional rate of change equal to $(-1.6\pm0.6)10^{-5}$. This would contribute to a first harmonic, (at 6 h), a fractional amplitude of $0.32\ 10^{-4}$, much smaller than the formal standard deviation, $\sqrt{2/N} = 4\ 10^{-4}$, dictated by the statistics of observation.

3. Harmonic Analysis An analysis of the data to extract first and second harmonics at solar, sidereal and antisidereal frequencies has been performed. Only data from uninterrupted solar days of operation were included. This was analysed, month by month, by binning it into 12 cell phase histograms. For sidereal and antisidereal frequencies the phase corresponding to the centre of the bi-hourly solar cell was used in determining a, weighted, mean phase for each cell of the composite histogram, with suitable correction to equalise exposure time for each such cell also being applied. Using fractional deviations of a cell from the overall cell mean for the month as variable the first and second harmonics for the three cases were calculated, (in the case of the sidereal and antisidereal histograms using a trapezoidal rule integration because the mean phases of the cells in these cases, in

general, are not equidistant). The mean square deviation (variance) of the cell rate, averaged over the 16 months was 14% larger than the Poissonian expectation.

The harmonic amplitudes r, and phase of maximum $\phi$, are shown in the table. The formal standard deviation on the amplitudes is

| | amp. x $10^4$ | phase/h | $k_o$ | amp. x $10^4$ | phase/h | $k_o$ |
|---|---|---|---|---|---|---|
| Solar | 1.19 | 19.0 | 0.05 | 7.60 | 0.1±2.0 | 1.77 |
| Sidereal | 7.95 | 5.1±1.9 | 2.62 | 6.14 | 4.4±2.5 | 1.20 |
| Anti-Sidereal | 9.57 | 11.7±1.6 | 2.91 | 1.63 | 0.0 | 0.08 |

$\sigma_r = \sqrt{\frac{2}{N}} = 3.97\ 10^{-4}$, while for the phases $\sigma_\phi = \sigma_r/r$ is shown for those amplitudes which are significant. Also shown in the table is the parameter $k_o \equiv r^2N/4$, which determines the significance of these dispersions [4]. From the presentation of the data on harmonic dials, fig.1, it is clear that both the sidereal and antisidereal first harmonic amplitudes are formally significant. The unwelcome appearance

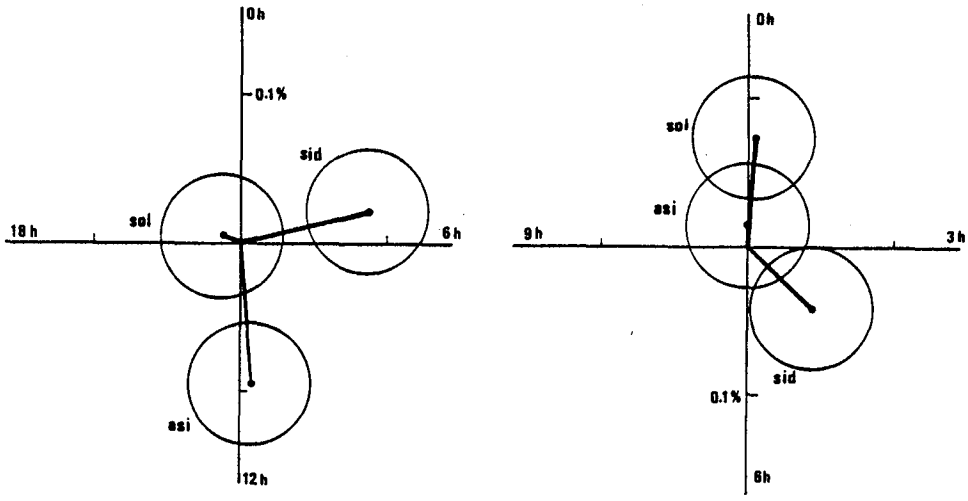


Fig.1 The first and second harmonics at solar, sidereal and anti-sidereal frequencies and their standard deviations

of the latter we have not so far succeeded in explaining. It does not seem that meteorological factors, not yet incorporated in the analysis, can account for such a large effect. Straightforward regression of the observed counting rates on the sea-level pressure, and the atmospheric temperature at the 200 mbar level yield coefficients $-0.04\pm0.02\%$ mbar$^{-1}$ and $+0.12\pm0.07\%$ K$^{-1}$ respectively. Further investigation is in progress to understand this aspect.

4. Results on Sidereal Harmonics Allowing for the non-Gaussian distribution and bias in the mean [4], the expectation values for two sidereal amplitudes, their 95% and 5% confidence levels, their phase of maximum and its 68.3% confidence level are:

$$\xi_1 = 7.95(1.50,\ 14.71)10^{-4} \qquad \phi_1 = 5.1\pm2.1 \text{ h},$$

$$\xi_2 = 5.28(0.0,\ 11.7)10^{-4} \qquad \phi_2 = 4.4\pm3.6 \text{ h}.$$

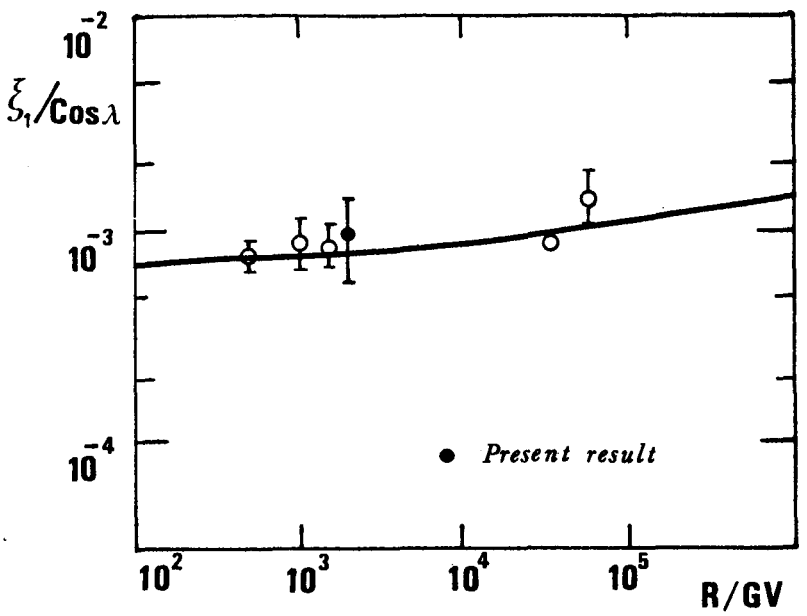


Fig.2 The projected first sidereal harmonic, corrected for solar motion, as a function of rigidity; the curve is due to Tan, paper OG 5.4-13 at this conference.

Although barely significant, especially in view of the unexplained anti-sidereal amplitude noted earlier, both these values are of similar magnitude to those found by other workers in similar regions of rigidity. A correction for solar motion relative to the local interstellar medium, following the parameters used in [2], when applied to the first harmonic amplitude leads to a value $\xi_1/\cos\lambda = 9.86\ 10^{-4}$ at $\phi = 4.80\pm2.1$ h. This projected amplitude along with its formal standard deviation is shown in fig.2. Also shown there are the values of other workers as corrected in [2], along with a prediction by Tan, based on his non-uniform galactic disc model for cosmic ray propagation (paper OG 5.4-13 at this conference), corresponding to his

parameter $\ell_s$ = 5 kpc.

5. Acknowledgements We are grateful to the Commissioner of Transport, Hong Kong Government for facilities provided in the Aberdeen Tunnel, the Director of the Hong Kong Royal Observatory for the supply of meteorological data, and to the Director of Computer Services, H.K. University Centre of Computer Studies and Applications for the provision of Computer facilities.

References

[1] Ng, L.K. and MacKeown, P.K., (1979), 16th Int. Conf. Cosmic Rays, Kyoto, Conference Papers, 4, 232-234.

[2] Cutler, D.J., Bergeson, H.E., Davis, J.F. and Groom, D.E. (1981), Ap. J., 248, 1166-1178.

[3] Fujimoto, K., Murakami, K., Kondo, I. and Nagashima, K., (1976), Proc. Int. Cosmic Ray Symp. High Energy Cosmic Ray Modulation, University of Tokyo, 50-53.

[4] Linsley, J., (1975), Phys. Rev. Lett., 34, 1530-1533; 14th Int. Conf. Cosmic Rays, Munich, Conference Papers, 2, 592-597.

# Search for Bursts in Air Shower Data

Bruce, T.E.G., Clay, R.W., Dawson, B.R., Protheroe, R.J.,
* Blair, D.G. and * Cinquini, P.

Physics Department, University of Adelaide, South Australia, 5001.

* Physics Department, University of Western Australia
Western Australia, 6009.

1. Introduction There have been reports in recent years of the possible observation of bursts in air shower data (e.g. Smith et al 1983, Fegan et al 1983). If such events are truly of an astrophysical nature then they represent an important new class of phenomenon since no other bursts have been observed above the MeV level. The spectra of convential gamma ray bursts are unknown at higher energies but their observed spectra at MeV energies appear generally to exhibit a steepening in the higher MeV range and are thus unlikely to extrapolate to measurable fluxes at air shower energies (see e.g. Clay et al, 1982). On the other hand, we now know that astrophysical objects are indeed capable of producing ultra high energy gamma rays and we should treat seriously the possibility of a burst acceleration mechanism.

We have looked for deviations from randomness in the arrival times of air showers above ~ $10^{14}$ eV with a number of systems and results so far are presented here. This work will be continued for a substantial period of time with a system capable of recording bursts with multiple events down to a spacing of 4 μs . Following the suggestion of Fegan et al (1983) that their event may be related to a glitch of the Crab pulsar, we have also searched our earlier data for the possible association of air shower events with a glitch of the Vela pulsar.

2. Detecting Systems Four detecting systems were used in this work. Data from the earlier Buckland Park array was used to search for bursts from the direction of the Vela pulsar. This system has been described in detail elsewhere (Crouch et al [1981]). Data from the new Buckland Park array with a substantially lower energy threshold has been searched for evidence of any non-random component. This array is described in this conference (Clay et al 1985a). We have also used two simple air shower triggers employing, in each case, two scintillators in coincidence. One detector pair was operated at Adelaide with a 5.6m spacing (detector area 0.16 $m^2$) and a median detected shower size of $Ne = 4 \times 10^4$ particles. The second system, operated at Perth, consisted of two scintillators (area .07 $m^2$) with a spacing of 6m giving a median shower size of $3 \times 10^4$ particles.

3. Searches for any Non-Random Effect We have previously searched for non-random effects in our air shower time spacing distribution by testing our spacing distributions to see whether or not the exponential form extended to small time spacings. A non-random effect associated with bursts would be likely to result in an excess of small spacings. Since we have no 'a priori' reason for expecting a particular burst time scale, we have fitted exponentials (see Fig 1) for each data set above a

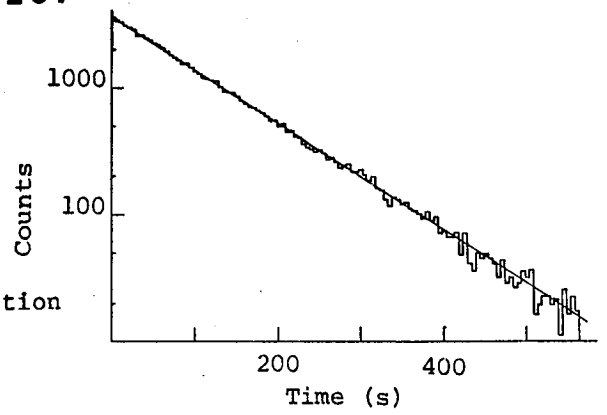


Fig 1. Pulse spacing distribution measured at Adelaide.

lower time spacing limit chosen subjectively by taking into account the recording pulse rate and then compared the number of events expected below this limit with the number actually observed. The results are shown in table 1.

Table 1

| Experiment (Recording-Time) | Spacing range for fitted exponential | Mean event spacing | Number exp. below range | Number obs. below range |
|---|---|---|---|---|
| Buckland Park (964 hrs) | 150-1000s | 312.6s | 4193±63 | 4192 |
| Adelaide (2139 hrs) | 50-1000s | 103s | 28732±106 | 28576 |
| Perth (2488 hrs) | 400-4000s | 977s | 3139±43 | 3183 |

One might also ask whether or nor there is any evidence for bursts in the data sets in terms of any series of small time intervals rather than an excess in the total number of small time intervals. We have examined our data and calculated for each system the number of times expected for observing a series of 3, 4 or 5 successive intervals, each below a certain minimum spacing. The results are shown in table 2.

Table 2

| Experiment | Number of times consecutive time intervals are <t. | | | | | |
|---|---|---|---|---|---|---|
| (time-interval t) | 3 intervals | | 4 intervals | | 5 intervals | |
| | expected | observed | exp. | obs. | exp. | obs. |
| Adelaide (20s) | 230 | 221 | 35.9 | 44 | 6.1 | 8 |
| Buckland Park (2s) | 1301 | 1270 | 196 | 245 | 30 | 41 |
| Perth (200s) | 62.7 | 71 | 11.8 | 10 | 2.2 | 2 |

It is apparent that our data showed no evidence of any non-random effects with a total exposure of 5591 array-hours.

4. Discussion Previous experiments which have reported the observation of UHE bursts have operated for periods of the order of a year. That is, long monitoring periods are required. In order to design an experiment to search for such bursts with the greatest efficiency in terms of data processing effort and use of the available data, it is instructive to examine tables 1 and 2. Bursts of the type detected by Fegan et al. and Smith et al. would have been detected readily by the technique employed in Table 2 but probably not at all by the method used in Table 1. A useful way of searching for bursts would then be to minotor any short time intervals between air shower events and to search for any periods which exhibit a series of such short time intervals. We are now using a time interval measurement device which responds to pairs of events with time spacings below 0.5s (compared to a mean rate of one per 9s with the new Buckland Park array) and records the occurrence of such an event together with the spacing (in units of 4μs). Bursts can then be identified by the observation of a succession of such short intervals. This is statistically powerful since the probability of having many successive small intervals by chance falls rapidly with the number of intervals.

5. The Association of Bursts with a Pulsar Glitch Fegan et al 1983 suggested that their observed burst may have been associated with a pulsar glitch. The Vela pulsar is at a declination which is easily observed from Adelaide and we have searched our 1979-1981 data set ($1.3 \times 10^5$ events) for all events within our angular uncertainty arriving from the direction of the Vela pulsar (see Protheroe et al., 1984). The result of this search is shown in Fig. 2. These data show no evidence for any clumping. There is one day which contained three events but such an occurence has a probability of ~66% in a data set of this kind. The Vela pulsar exhibited a glitch in this time period as indicated but no closely correlated events stand out.

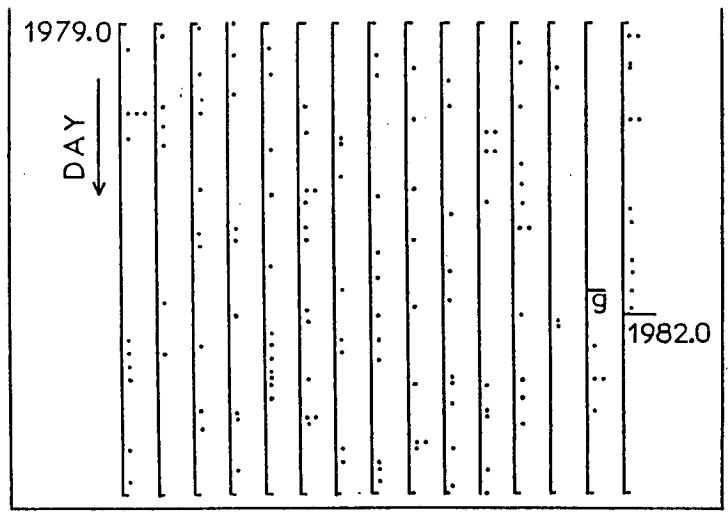


Fig. 2 The day of arrival of events from the direction of the Vela pulsar. Each column represents 75 days of data. The time of a glitch is shown as g.

6. Acknowledgements Dr. G.W. Royle is thanked for providing information on glitches of the Vela pulsar. This work is suported by the Australian Research Grants Scheme.

References

1. Clay, R.W., Gerhardy, P.R., and Gregory, A.G. (1982) Ap and Sp. Sci. 83, 279
2. Clay et al (1985a) This conference. OG 9.4-4
3. Crouch, P.C., Gerhardy, P.R., Patterson, J.R., Clay, R.W. and Gregory, A.G. (1981) Nucl. Inst and Meth., 179, 467
4. Fegan, D.J., McBreen, B., and O'Sullivan, C. (1983) Phys Rev Lett, 51, 2341-2344
5. Smith, G.R. Omgen, M., Buller, E., and Standil, S. (1983) Phys Rev D 28 1601-1603
6. Protheroe, R.J., Clay, R.W. and Gerhardy, P.R. (1984) Ap. J. (Lett) 280, L47

# AIR SHOWER ARRIVAL DIRECTIONS MEASURED AT BUCKLAND PARK

P.R. Gerhardy*, R.W. Clay, J.R. Patterson, J.R. Prescott,
A.G. Gregory, R.J. Protheroe

Physics Department, University of Adelaide, South Australia, 5001.

*Present address: Physics Department, University of Utah,
Salt Lake City, Utah, U.S.A.

The Buckland Park air shower array (Crouch et al 1977, Crouch et al 1981) was operated for 3 years from 1979 to 1981 particularly for the study of anisotropies in the region of the knee of the size spectrum. The array which has been described in detail elsewhere was situated at a latitude of 35°S and had an effective size threshold of $\sim 3 \times 10^5$ particles ($\sim 3 \times 10^{15}$ eV for vertical showers). A number of results from this experiment have already been published including anisotropy analyses (Gerhardy and Clay, 1983) and searches for very high energy gamma ray sources (Clay et al. 1984, Protheroe et al. 1984, Protheroe and Clay 1984, Protheroe and Clay 1985). Here we wish to present our final distribution of measured shower arrival directions (Table 1).

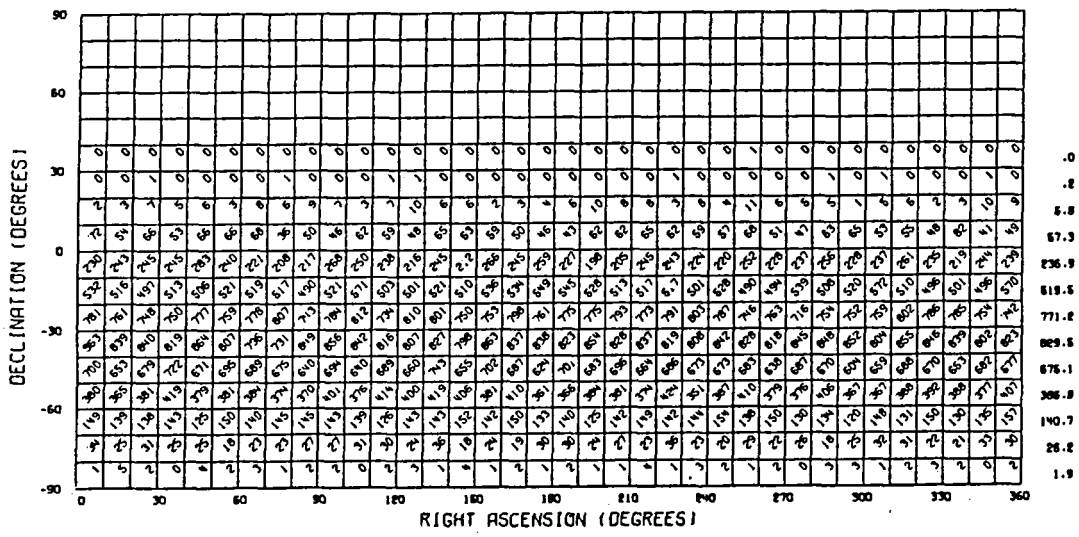


These $1.3 \times 10^5$ events were selected as indicated in detail in Gerhardy and Clay (1983) and were essentially those events with well measured arrival directions. They are the same data set used in the above references but no complete sky map has previously been presented.

This work was supported by the Australian Research Grants Committee.

References

Clay, R.W., Gerhardy, P.R., and Liebing, D.F. (1984) Aust. J. Phys, 37, 91.

Crouch, P.C., Kuhlmann, J.D., Clay, R.W., Gregory, A.G., Patterson, J.R., Thornton G.J. (1978) Proc 15th Int. Cosmic Ray Conf. (Plovdiv), 13, 166, 1977.

Crouch, P.C., Gerhardy, P.R., Patterson, J.R., Clay, R.W., Gregory, A.G. (1981) Nucl. Inst. Meth., 179, 467.

Gerhardy, P.R. and Clay, R.W. (1983) J. Phys. G., 9, 1279.

Protheroe, R.J. and Clay, R.W. (1984) Proc. Astron. Soc. Aust. 5, 586.

Protheroe, R.J. and Clay, R.W. (1985) Nature (In the press).

Protheroe, R.J., Clay, R.W., and Gerhardy P.R. (1984) Ap. J. Lett, 280, L47.

OG5.4-1

# A Simulation of High Energy Cosmic Ray Propagation I

M. Honda, T.Kifune, Y. Matsubara*, M. Mori*, K. Nishijima** and M. Teshima*

Institute for Cosmic Ray Research, University of Tokyo, Tokyo, 188 Japan
*Department of Physics, Kyoto University, Kyoto, 606 Japan
**The Graduate School of Science and Technology, Kobe University, Kobe, 657 Japan

## Abstract

We simulate high energy cosmic ray propagation of the energy region $10^{14.5}$-$10^{18}$ eV in the inter steller circumstances. In conclusion, the diffusion process by turbulent magnetic fields is classified into several region by ratio of the gyro-radius and the scale of turbulence. When the ratio becomes larger then $10^{-0.5}$, the analysis with the assumption of point scattering can be applied with the mean free path $E^2$. However, when the ratio is smaller than $10^{-0.5}$, we need a more complicated analysis or simulation. Assuming the turbulence scale of magnetic fields of the Galaxy is 10-30pc and the mean magnetic fields strength is 3 micro gauss, the energy of cosmic ray with that gyro-radius is about $10^{16.5}$ eV.

## 1 Introduction

Many authors have studied cosmic ray propagation in magnetic fields[1]. Especially, Gleeson and Axford had solved a diffusion equation with the assumption that cosmic ray are scattered by scattering centers. The recent observation of Galactic magnetic field[2] shows the average field strength is about 3 micro gauss and the turbulent fields are about 1.5 micro gauss. The gyro-radius of cosmic ray in the energy region, in which we are interested, becomes 0.1-300pc. The random magnetic fields cannot deflect the cosmic rays so hardly, but an amount of small deflection may cause a large scattering angle as a result. We know that, in some cases, we can sum up the effects in terms of point scattering and mean-free-path(mfp). However, we are not sure this is the case in the cosmic ray propagation in the turbulent magnetic fields, especially when the gyro-radius of the cosmic ray becomes near to the scale of irregularities. The assumption of point scattering can be an over simplification in the study of cosmic ray propagation in that energy region. It should be checked by the numerical calculation or simulation.

In this paper, we present a Monte Carlo simulation of cosmic ray propagation in the Galactic space and show a result in terms of diffusion tensor. Gleeson and Axford showed the diffusion tensor have three independent element ($K_{//}$, $K_{\perp}$, $K_T$). The analytic form of these element as a function of mean free path are given by

$$K_{//} = \frac{1}{3}\lambda c \quad , \tag{1}$$

$$K_{\perp} = \frac{K_{//}}{1 + (\omega \frac{\lambda}{c})^2} \quad \text{and} \tag{2}$$

$$K_T = \frac{(\omega \frac{\lambda}{c})\, K_{//}}{1 + (\omega \frac{\lambda}{c})^2} \quad , \tag{3}$$

where $\lambda$ is the mfp and $\omega$ is the gyro frequency of cosmic rays in that magnetic field. When we leave from the idea of point scattering of cosmic

ray, we should not use mfp at the beginning of the study. Rather it should be given as the result of diffusion process. In our simulation, we calculate the two diagonal elements $K_{//}$ and $K_{\perp}$. We check the consistency comparing these formula. When the consistency is maintained, we try to calculate the mfp from the formula.

2 Generation of random magnetic fields

It seems to be a difficulty in the simulation with irregular magnetic fields to make the flux line conserved. This difficulty is avoided in our case by generating the vector potentials by random numbers. The steps to generate the random magnetic fields are following. First we embed a lattice in the simulation space, whose lattice constant is chosen as the scale of the irregularity of the magnetic field. We generate the vector potential $A=(A_x,A_Y,A_Z)$ for each lattice point with the probability given by

$$\exp(-A_i/t)\ dA_i \quad (i=x,y,z), \tag{4}$$

where t is a parameter to adjust the irregular magnetic fields strength. The vector potential in the point other than the lattice points are given by linear interpolation. The irregular magnetic fields are given by

$$\vec{DH} = \mathrm{rot}(\vec{A}), \tag{5}$$

with the random vector potential A. The total fields are given as the sum of irregular magnetic field and average field. When we wish to simulate the turbulent magnetic fields with some spectrum like the Kolmogorov's one, we prepare a series of lattices with different lattice constants. And sum up the irregular magnetic fields with the weight given by the spectrum.

The motion of the cosmic ray particles is determined by equation of motion;

$$m\frac{d\vec{v}}{dt} = q(\vec{E} + \vec{v} \times \vec{H}). \tag{6}$$

However, in our simulation we neglect the effects from $\vec{E}$. In other words, we assumed the magnetic fields is statical. This assumption can be justified because the velocity of cosmic ray is essentially light velocity, but the velocity of the magneto-hydrodynamical waves are around $10^{-3}$ times of light velocity in the interstellar circumstances. This also means that in our simulation, we neglect the effect of Fermi type acceleration or the diffusion process in energy axis.

3 Simulation

Our simulation is carried out as follows. We assumed that the average magnetic field($H_0$) is aline with z-axis, and the average strength of the magnetic field is 3 micro gauss and that of the turbulent magnetic fields are 1.5 micro gauss in average. (We note that what is really meaningful is the ratio $\langle DH\rangle/H_0$, which is 1/2 in our case. The absolute strength is needed when we translate the gyro-radius to the energy in the relation to the scale of the turbulence in relation to the (maximum) turbulent scale ($=L_0$)). We first put a number of cosmic ray particles at the origin and follow the motion numerically determined by the equation. The step time for solving (6) numerically is chosen as 1/10 of the gyro frequency and is changed with gyro frequency. This step time is chosen so that the error caused by it is small in our numerical calculation and that the simulation is executed within the reasonable cpu-time. Taking the statistics of the position of cosmic ray in terms of $\sigma_{\perp}=\sqrt{\langle x^2+y^2\rangle}$ and $\sigma_{//}=\sqrt{\langle z^2\rangle}$, we can calculate

$K_\perp$ from the time dependence of $\sigma_\perp$ and $K_{//}$ from the time dependence of $\sigma_{//}$. The random magnetic field is regenerated every 250 step to accelerate the conversion of diffusion constants to average value.

## 4 Results

In fig.1, we show a result of our simulation in the form of dimension-less quantity; $K_i/(c \times L_0)$, where i stands for // and $\perp$, c right velocity and $L_0$ for maximum turbulent scale. The simulation of fig.1 is carried out by assuming that the magnetic fields' turbulence follows the Kolmogorov spectrum. The crosses and close ones show $K_{//}$ and $K_\perp$ respectively. We also made a simulation by assuming of the only one turbulent scale. We found a little difference between them. In both cases, however, we can say that the qualitative tendencies are the same. Therefore the farther simulation is executed assuming the only one scale in turbulence of magnetic field.

Fig. 1

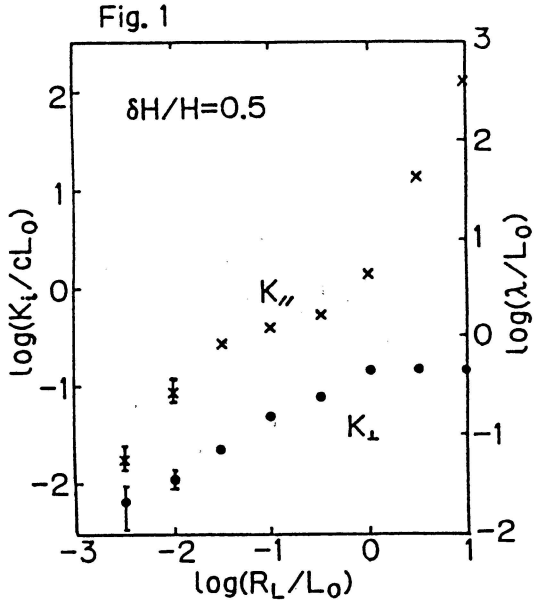


The whole region can be divided into several regions by the diffusion tensor dependences on the $R_L$. When $R_L$ is in the region between $10^{-1.5} xL_0$ and $10^{-0.5} xL_0$, the ratio $K_{//}/K_\perp$ is almost constant and both are proportional to $R_L^{0.3-0.4}$. When $R_L$ becomes lager than $10^{-0.5} xL_0$, $K_{//}$ is proportional to $R_L^2$ and $K_\perp$ is almost constant. We also gave a scale in fig.1 to read the mfp directly from $K_{//}$ using (1). We find in the region where the $R_L$ is larger than $10^{-0.5} xL_0$, (2) gives consistent relation between $K_\perp$ and $K_{//}$ assuming the mfp. However, the relation (2) is not fold for $R_L$ smaller than $10^{-0.5} xL_0$. We may see that there is an another region, where the radius is smaller than $10^{-1.5} xL_0$, the slope of $K_{//}$ dependences on the $R_L$ changes to steeper($\sim R_L^1$). However, the ambiguity of the calculation becomes large in this region and the reliability of simulation may be small.

We also executed simulations with the condition $\langle DH \rangle / H_0 = 1$ and 1/4 assuming of the only one (maximum) turbulent scale. These results are shown in fig.2 and in fig.3. The simbols are same with fig.1. The whole region is divided into three regions at the $R_L$; $10^{-1.5} xL_0$ and $10^{-0.5} xL_0$. The dependences of $K_{//}$ and $K_\perp$ on $R_L$ are the same with the case of $\langle DH \rangle / H_0 = 1/2$. However, there is a quantitative difference in the value of $K_{//}$, $K_\perp$ and in the ratio $K_{//}/K_\perp$. They are rather rapidly varying functions of the $\langle DH \rangle$.

## 5 Summary and Discussions

If we assume that the turbulent scale($L_0$) is 30pc and the average magnetic field strength is 3 micro gauss, the energy of the cosmic ray with the gyro-radius $10^{-0.5} xL_0$ is $10^{16.5}$ eV for the protons. For the higher energy cosmic rays, the assumption of point scattering in the study of its propagation in Galactic space is a fairly good approximation with the mfp$\sim E^2$. However the facter in front of the power of E is a rapidly varying

Fig. 2

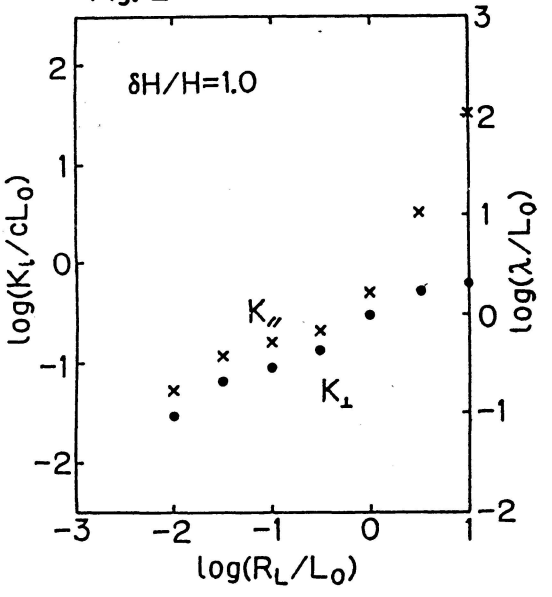


Fig. 3

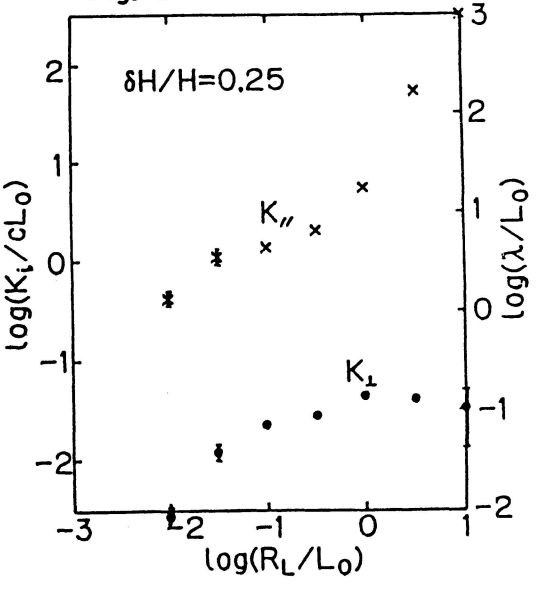


function of $\langle DH \rangle$. We note, however, that this is a result of the accumulation of small deflection by the magnetic fields and the facter should be obtained by different method; for example simulation. For the lower energy cosmic rays than $10^{16.5}$ eV, the diffusion constants do not follow the formula (1)-(3). To study the cosmic ray propagation in this region, we need a simulation or more sophisticated analytic methods. It is noted that in this region the ratio of $K_{//}$ and $K_{\perp}$ is almost constant. If we assume the average strength of turbulent magnetic field is 1.5 micro gauss, the ratio is about 10. For the smaller energy cosmic ray than $10^{15.5}$ eV, the result of the simulation show a relatively large difference between different random number series. This fact might indicate that the other mechanism than the diffusion process like convectionshold be considred in the study of the propagation of cosmic ray with this energy in the Galaxy.

Acknowledgements

The authors thank the other member of Akeno group for their discussions especially from the experimental view point. They also are gratefull to Prof. K.Murakami for the advice in the start of this work. The simulation were made by the use of FACOM M380 of the computer room in the Institute for Nuclear Study.

References

1, Gleeson,L.J. and Axford,W.I., Ap. J. 149, L115 (1967),
Jokipii,J.R., Rev. Geophys. and Space Phys. 9, p27 (1971),
Barge,P., Millet,J., and Pellat, R., Ap. J. 284, p817 (1984),
2, Lee, L.C. and Jokipii, J.R., Ap. J. 206, p735 (1976),
Verschuur,G.L. Fundamentals of Cosmic Physics, 5 p113 (1979).
Simard-Normandim, M. and Kronberg, P.P., Astrophys.J. 242, p74(1980).

OG5.4-2

# A Simulation of High Energy Cosmic Ray Propagation II

M.Honda, K.Kamata, T.Kifune, Y.Matsubara*, M.Mori*, K.Nishijima**, G.Tanahashi, and M.Teshima

Institute for Cosmic Ray Research, University of Tokyo, Tokyo, 188 Japan
*Department of Physics, Kyoto University, Kyoto, 606 Japan
**The Graduate School of Science and Technology, Kobe University, Kobe, 657 Japan

Abstract

The cosmic ray propagation in the Galactic arm is simulated. The Galactic magnetic fields are known to go along with so called Galactic arms as a main structure with turbulences of the scale about 30pc. We study the distribution of cosmic ray in Galactic arm and discuss the escape time and the possible anisotropies caused by the arm structure.

## 1 Introduction

In the previous paper[1], we have reported a method to simulate the propagation of the cosmic ray in the turbulent magnetic fields. (We refer that paper as I here after). In this paper, we make a little extension of the work in I. The magnetic field in Galaxy is now considered to be alined along the Galactic arm. We simulate the propagation of the cosmic ray in the Galactic arm. It is expected that the cosmic ray is trapped in magnetic field of arm just like in TOKAMAK. We are interested in the distributions of cosmic rays in the Galactic arm by following reasons. As the origin of anisotropy of the arrival direction of cosmic ray, one may consider two reasons; the source distribution and the propagation in the Galaxy (including the leakage from it). If the distribution of the cosmic ray is not uniform, we can expect the anisotropy from the latter reason. As many authors suggested, the main reason of the acceleration of cosmic ray is by the shock waves from the supernova[2], the both reasons for anisotropy can be considered as the same thing. The study of the distribution of cosmic ray becomes important. We will study the possible anisotropy caused by the arm structure (or by the distribution of cosmic ray in the arm) and the escape of cosmic ray from the Galactic arm.

## 2 Magnetic field in Galactic Arm and Model

The method of Rotation Measure as well as others[3-4] gave us the informations of the Galactic magnetic fields. It can be summarized as follows; the main structure of magnetic fields is aline along the Galactic arms and its average strength is 3.0 micro gauss. About the turbulence of magnetic fields, the strength is about 1.5 micro gauss and the scale of the turbulences is 10-30pc in average.

As a model of the Galactic arm, we consider a right cylinder with the radius of 300pc, which is comparable to the thickness of Galactic disc determined by the rotation measure. We identify the axis of the cylinder with the z-axis. The 'average' magnetic field is assumed to be alined along the cylinder axis. The magnetic field is assumed as the sum of 'average' one and the turbulent ones. The 'average' magnetic fields varies with radius by

$$H(r) = H_0 \times \exp(-r^2/r_0^2) \quad , \qquad (1)$$

where $r_0$ is taken to be the radius of galactic arm; 300pc. $H_0$ is determined so that the average of the magnetic field inside the arm is 3 micro gauss. (The average of turbulent magnetic fields is 0.) The generation of turbulent magnetic fields is essentially same with I. However, the strength of the turbulent magnetic fields with same r is generated proportional to 'average' magnetic field in average. The scale of magnetic fields' turbulence are taken 30pc.

## 3 Simulation

The simulation is executed almost same way with I. However, in this case the initial distribution of cosmic ray is taken as the uniform distribution in the Galactic arm. The directions of velocity are assume uniform. When a cosmic ray goes beyond $r_1$ from the arm axis, it is considered to escape from the arm. In this simulation $r_1$ is taken 600pc, with which distance, the gyro radius in the magnetic field given by (1) is comparable to or larger than $r_1$ for protons with energy greater than $10^{16.5}$ eV. (In this paper, we assume implicitly that the cosmic rays are protons.) We observe the distribution of cosmic rays and calculate the escape probability of cosmic ray from the arm. To save the cpu time, we made a trick that the escaped particles are resumed into the arm with the position determined by the probability proportional to the distribution of other cosmic rays. This resumption is executed for the every time step corresponding to 250 years. With this trick the number of cosmic rays in simulation is kept constant. The escape probability is calculated from the resumed particle number after the distribution of cosmic ray is considered stational for a few $10^4$ years. The step time for the calculation of cosmic ray particle motion is taken 1 year for $10^{16}$ eV and $10^{16.5}$ eV and 10 years for greater energy than $10^{17}$ eV. The step time is same or smaller than that of I.

## 4 Result

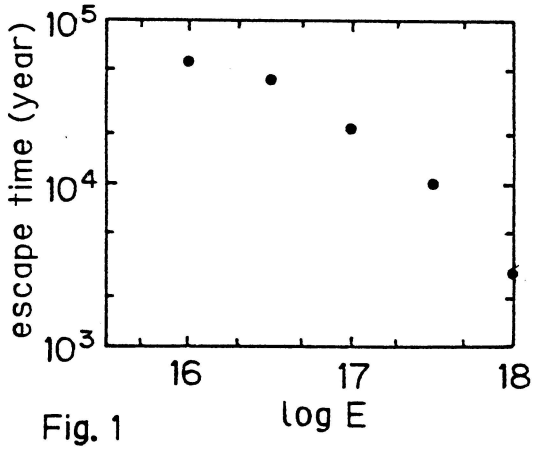


Fig. 1

In fig.1, we show the escape time calculated by the escape probability. It is interesting that the escape time for the cosmic ray with energy $10^{16\text{-}16.5}$ eV is consistent with the extrapolation of the life time of lower energy by $E^{-(0.3\text{-}0.4)}$. The slope of the escape time larger than $10^{17.5}$ becomes steeper, which can be considered as the reflection of the structure of the Galactic arm. We note the escape time of the energy $10^{16}$ eV may show a smaller value, because the $r_1$ used in this simulation is too small to consider that the cosmic ray at $r_1$ surely escape from the arm. They can be return into the arm with the gyro motion by the magnetic field. In the region $10^{16.5\text{-}17.5}$ eV, the escape time is proportional to $E^{-(0.5\text{-}0.6)}$.

In fig.2, we show the r-distributions of the cosmic ray for various energy after $10^5$ years when the distribution of cosmic ray is considered already stational. The r-distribution of cosmic ray with the energy lower than $10^{17.5}$ eV show a similar feature. In this energy region the cosmic ray density decrease exponentially. We can consider that the cosmic rays are trapped in the Galactic arm. The r-distribution with the energy $10^{18}$ eV show

a large difference from the lower one, which shows a slower decrease with r. This distribution suggests that the cosmic ray is not trapped in the arm so long time and easily escape from the arm. This is also shown in the escape time of this energy. It also noted that the distribution of cosmic ray with the energy $10^{16}$eV is different from the $10^{16.5-17.5}$eV in the shape of the slope. This may indicate the distribution of cosmic ray with that energy is still in the course of the formation of stational form within the simulation corresponding to $10^{5}$ years. After the formation of the stational form, the escape probability can be smaller.

In fig.3, we show the $V_\theta$ in average over all cosmic rays for various energies. $V_\theta$ is defined by;

$$V_\theta = \frac{X \cdot V_y - Y \cdot V_x}{\sqrt{X^2 + Y^2}} \qquad (2)$$

We can see the $V_\theta$ become considerably large for larger energy than $10^{16.5}$eV. It takes its maximum at $10^{17.5}$ and in the energy $10^{18}$eV it becomes smaller value. This value have direct relation to the anisotropy of the arrival direction of cosmic rays. In the energy $10^{16.5}$eV, we can expect a few % of excess of the number of cosmic rays coming from the rotational direction around the arm axis and in the energy $10^{17.5}$eV a few 10%. In the energy of $10^{16}$eV, this value also show a non-zero $V_\theta$ value. However, this value fluctuates with time and also varies with r. We are not sure the we can expect the anisotropy in this energy.

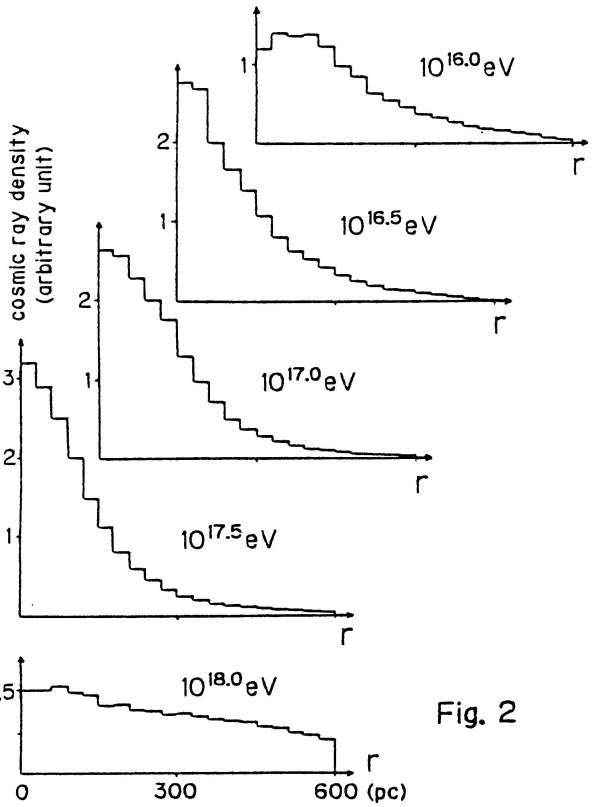


Fig. 2

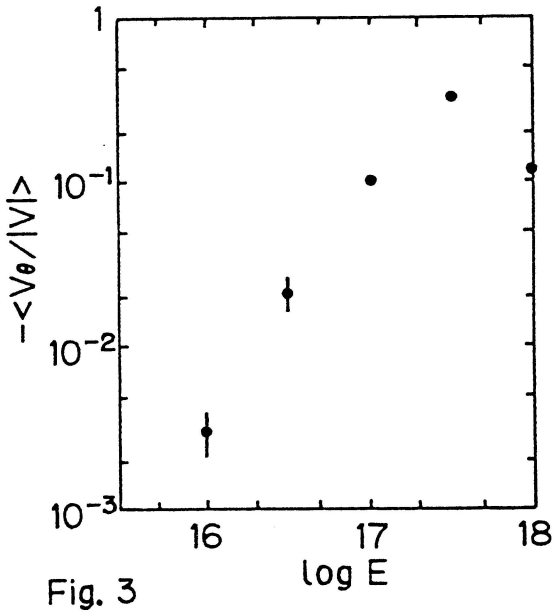


Fig. 3

In fig.4 we show the average of $|V_z/V|$ in various energies. If the direction of cosmic ray velocity is isotropic, this value is 0.5. In the energy $10^{18}$eV, it shows a large deviation from 0.5 to a larger value: 0.6. The direction of velocity of cosmic rays, which stay in the arm for long time, are not uniform in this energy. In the lower energy, the value

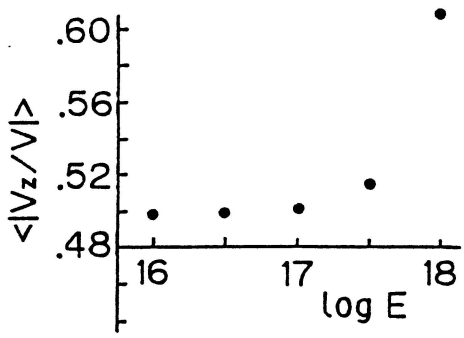


Fig. 4

is very near to 0.5. In the context of anisotropy, $|V_z/V| > 0.5$ means there is an excess in the numbers of cosmic rays coming from the direction parallel to the arm axis. In this case the anisotropy is observed as the second harmonics.

## 5 Summary and Discussions

We have shown that the cosmic rays with the energy lower than $10^{18}$ eV are trapped in the Galactic arm. As the physical consequences, we can expect a few % (first harmonics) anisotropy of the arrival direction of cosmic rays in the energy region $10^{16.5-17.5}$ eV to the rotational direction around the arm axis. We note this is the direct consequence of the distribution of cosmic ray and the gyro-rotation of them in the magnetic field. In the energy $10^{18}$ eV, the cosmic ray become easy to escape from the Galactic arm. The cosmic ray, which stay long time in the arm have smaller pitch angles. Therefore we can expect the anisotropy of second harmonics to the direction of arm axis. (Of course, if there is typical source near to the Earth, the anisotropy in this energy region is affected by it.) For the lower energy than $10^{16}$ eV, the effect of arm structure in anisotropy of the arrival direction is uncertain. The anisotropy observed in this energy may be the reflection of the local structure of the Galactic magnetic field. It should be noted the magnitude of the anisotropy predicted here is consistent with the observations[5]. However, the direction determined by the observation is different from our result. The observation of the anisotropy in the energy region above $10^{16.0}$ eV have some ambiguity yet caused by poor statistics. The more elaborate experiments are expected.

## Acknowledgements

The authors thank the other members of Akeno group for their discussions and for showing their experimental results. They also are grateful to Prof. K.Murakami for the discussion from the experimental point of view and his encouragements. The simulation were made by the use of FACOM M380 of the computer room in the Institute for Nuclear Study.

## References

1, Honda, M.et al. Proc. 19th ICRC, La Jolla OG5.4-1.
2, Blanford, R.D. and Ostriker, J.P. Ap. J. 221 L29 (1978).
Bell, A.R. Mon. Not. R. Astr. Soc. 182 p147 (1978)
Axford, W.I. in Origin of Cosmic Rays, IAU Sym. 94 (1981)
3, Lee, L.C. and Jokipii, J.R. Ap. J. 206, p735 (1976),
Simard-Normandim, M. and Kronberg, P.P., Ap. J. 242, p74(1980)
4, Verschuur, G.L. Fundamentals of Cosmic Physics, 5 p113 (1979)
5, Kifune, T. et al. submitted to J. Phys.
Kifune, T. et al. Proc. 19th ICRC, La Jolla OG5.3-3
Linsley, J. and Watson, A.A. 15th ICRC, Plovdiv 12 p203 (1977)

# COSMIC RAYS IN THE $10^{16}$ TO $10^{19}$ eV RANGE FROM PULSARS

Amri Wandel and Donald C. Ellison

Astronomy Program, University of Maryland, College Park, Maryland 20742

Abstract. We calculate the flux of cosmic rays (CRs) produced by a distribution of pulsars that are (1) born with rapid rotation rates, (2) slowdown as they evolve, and (3) produce energetic nuclei with a characteristic energy proportional to their rotation rates. We find that, for energy independent escape from the disk of the galaxy, the predicted spectrum will be essentially what is observed between ~ $10^{16}$ to $10^{19}$ eV if the slowdown law as inferred for radio pulsars can be extrapolated to young pulsars with shorter periods.

1. Introduction. The recent discovery of ultra-high energy $\gamma$-rays from compact sources such as Cygnus X-3 (Samorski and Stamm 1983) has renewed speculation that compact objects may produce a significant fraction of the observed galactic CRs (Hillas 1984b; Chanmugam and Brecher 1985). Almost immediately upon the discovery of pulsars, they were suggested as possible sources of CRs (e.g. Ostriker and Gunn 1969). However, two major problems led most researchers to discount pulsars as important contributors to the CR flux. The first is the highly unlikely possibility that pulsars can produce nuclei in the GeV range with the observed CR composition. The observed composition at these energies is essentially the same as universal abundances (e.g. Meyer 1985) and strongly argues against sources as exotic as pulsars.

The second problem concerns the ability of pulsars to produce ultra-high energy nuclei. Pulsars store vast amounts of energy in their rotational motion, and their large surface magnetic fields combined with rapid rotation imply vacuum potentials in the CR energy range. However, it was considered doubtful that pulsars could produce nuclei with energies even remotely approaching the limit of their vacuum potentials (e.g. Arons 1981).

Recent developments have prompted us to reexamine pulsars as possible CR sources. First, a relatively self-consistent explanation for CRs below ~ $10^{15}$ eV has been developed (e.g. Axford 1981). In this model, expanding supernova blast waves accelerate CRs out of the ambient interstellar medium. While many important details remain to be clarified, supernovae, combined with first-order Fermi shock acceleration, can be expected to account for the observed CR energy spectrum, energy budget, and composition up to ~ $10^{15}$ eV. Above this energy, however, it becomes highly unlikely that supernova shocks can accelerate particles (Lagage and Cesarsky 1983; Wandel 1985; for an alternative view, see Jokipii and Morfill 1985). A feature in the CR spectrum is seen near $10^{15}$ eV and the spectrum steepens above ~ $10^{16}$ eV, suggesting that these CRs may have a distinct origin. From ~ $10^{16}$ to $10^{19}$ eV the observed CR spectrum is well described by a power law with index -3 (e.g. Hillas 1984a). Measurments of the composition become very difficult at these energies and few constraints on CR composition exist above ~ $10^{16}$ eV.

Second, Michel and Dessler (1981) have proposed that active radio pulsars may be surrounded by fossil disks left over from the collapse that produced the neutron star. In this model, the neutron star and disk act essentially as two coupled unipolar generators and are capable of

maintaining potential differences of the order of the vacuum potential, i.e., $\sim a^2 B\Omega$, where a is the radius, $\Omega$ is the angular velocity, and B is the surface magnetic field of the pulsar. These authors suggest that nuclei can be accelerated from the disk (having near solar abundance) to energies on the order of this potential.

We also note that $\gamma$-rays with energies in excess of $10^{16}$ eV have been observed from Cgynus X-3 (Samorski and Stamm 1983). This is reasonably clear proof that compact objects can accelerate nuclei to CR energies regardless of our inability to understand how they do it.

In light of this, we examine a simple model for the production of CRs by a galactic distribution of pulsars. These pulsars would be born with high magnetic fields and millisecond (ms) periods, and would evolve according to the slowdown relation, $d\Omega/dt \propto \Omega^n$, where n is the braking parameter. The range in radio pulsar periods implies that this source would cutoff below $\sim 10^{16}$ eV and produce CRs rays up to $\sim 10^{19}$ eV, where another feature in the spectrum is observed. Cosmic rays above $\sim 10^{19}$ eV would be produced by yet another source that is most likely extra-galactic (Hilles 1984a).

2. Model. We assume that pulsars are born at the rate, $Q(\Omega)$. Their evolution may be described by a diffusion equation in $\Omega$ space:

$$\frac{d}{d\Omega}(N\dot{\Omega}) = Q(\Omega), \tag{1}$$

where $\dot{\Omega} = d\Omega/dt$ and $N(\Omega)d\Omega$ is the number of pulsars per unit volume in $d\Omega$. For simplicity we assume that all pulsars are born with the same $\Omega_{max}$, i.e., $Q(\Omega) = Q_o\delta(\Omega-\Omega_{max})$. Equation (1) can then be solved to give

$$N = -Q_o/\dot{\Omega}. \tag{2}$$

Now, on very general terms, the magnetic torque should slow the pulsar so that

$$\dot{\Omega} \propto \Omega^n, \quad \text{with } n = 3. \tag{3}$$

This result, which is essentially a dimensional consideration and is quite model independent, is also backed by observations of radio pulsars (for a detailed discussion see Michel 1982).

Next we assume that pulsars produce nuclei with energies comparable to the vacuum potential, i.e.,

$$E_{vp} \sim \frac{e}{c} a^2 B\Omega \sim 6 \times 10^{19} \left(\frac{a}{10\ km}\right)^2 \left(\frac{10^{-3}s}{P}\right) \left(\frac{B}{10^{12}\ G}\right) eV, \tag{4}$$

where P is the pulsar period in seconds.

The particle spectrum produced by a distribution of pulsars, each having a differential flux, $f_\Omega(E)$, is given by

$$F(E) = \int N(\Omega) f_\Omega(E) d\Omega. \tag{5}$$

If the particle spectrum of a specific pulsar is peaked at its vacuum potential, i.e., $f_\Omega(E) \propto \delta[E-E_{vp}(\Omega)]$, eqs. (2)-(5) can be solved to yield

$$F(E) \propto E^{-n}, \quad 10^{16} \lesssim E \lesssim 6 \times 10^{19}\ eV, \tag{6}$$

where we have assumed that the flux of particles emitted by a pulsar is independent of $\Omega$. The energy range is determined by a spread in pulsar periods from ~ 1 ms to 4 s. If n = 3, this is just the observed slope of the CR spectrum in the above energy range.

The above solution can be shown to be independent of the spectrum emitted by an individual pulsar. For an emitted spectrum of the form

$$f_{\Omega}(E) \propto \Omega^{q} E^{\alpha}, \qquad (7)$$

we find that $F(E) \propto E^{-n+q}$ and is essentially independent of $\alpha$ if $\alpha > -1$ (Wandel and Ellison 1985).

3. Discussion It is remarkable that a straightforward application of zeroth-order pulsar theory yields a spectrum consistent with the observed CR spectrum above ~ $10^{16}$ eV. There are, however, many complicating factors that may alter this result. (a) Pulsars may be born with a distribution of periods, or with periods considerably longer than 1 ms. We note that the ms pulsars that have been observed to date may have been spun-up, have low magnetic fields, and would not produce the energetic particles we envision. A recent survey at 1.4 GHz (Manchester et al. 1985) suggests, however, that many short-period pulsars would be discovered by searches with improved sensitivity. (b) Pulsars may not produce nuclei at energies near the vacuum potential. Cygnus X-3 produces highly energetic nuclei, but is not of the class of objects considered here. (c) Instead of a delta function at $E_{vp}$ as we have assumed, an individual pulsar may produce particles with a distribution of energies. However, due to the rapid pulsar evolution, the distribution of CRs produced by a population of pulsars is insensitive to the shape of the spectrum from a single pulsar, as discussed above. (d) We assume that the particle flux produced by an individual pulsar is independent of $\Omega$ [i.e. $|q| \ll 1$ in eq. (7)]. The flux is determined by the details of the pulsar model and may depend on the geometry and magnetic field, which are assumed to vary slowly. Note, however, that if the emitted particle flux is related to the rotational energy loss, $dE/dt = I\Omega\dot{\Omega}$ (I = moment of inertia), the flux would be expected to be a strong function of $\Omega$. (e) The braking parameter may not be constant and equal to 3. For instance, if the neutron star has a finite quadrupole moment (e.g. due to an internal field or a secular rotational instability), gravitational radiation would be emitted. If the neutron star looses angular momentum mainly due to gravitational radiation, then n ~ 5. For parameters typical of the Crab pulsar (Ostriker and Gunn 1969; Alper and Pines 1985), gravitational quadrupole radiation dominates magnetic dipole radiation only for P < 1-2 ms, so that the relevant $\Omega$ range is not affected significantly. (f) We must consider the effect of propagation on the source spectrum, eq. (6). This is treated below.

At energies below ~ $10^{15}$ eV, the interpretation of the secondary to primary nuclei ratios implies that the CR source spectrum is significantly steepened by propagation and energy dependent escape from the galaxy (e.g. Protheroe et al. 1981). At the energies considered here, however, there is no direct evidence that the source spectrum is modified by propagation. On the contrary, if we extrapolate the inferred scattering mean free path, $\lambda_s$, from lower energies (Ormes 1983) to $10^{16}$ eV, we find it is (for protons) of the order of the scale height of the galactic disk, and increases for higher energies. This suggests that

the diffusion approximation is not justified at energies above $10^{16}$ eV. If these high energy particles are not confined, the observed CR spectrum is not modified by an energy-dependent leakage term, as it is at lower energies, hence the slope of the observed spectrum will be the same as the source spectrum.

The observed CR flux above $\sim 10^{16}$ eV requires $\sim 4 \times 10^{50}/t_r$ erg/s, where $t_r$ is the CR residence time in the disk and we have assumed a typical disk volume (e.g. Hillas 1984b). For scatter free propagation, $t_r \sim 10^{3.5}$ yr. However, the mean free path at $\sim 10^{16}$ eV may be smaller than the scale height of the disk (e.g. if heavy nuclei contribute), in which case $t_r$ would be significantly larger (e.g. if $\lambda_s \sim 50$ pc, $t_r \sim 10^5$ yr). The energy required to power the observed CR spectrum above $\sim 10^{16}$ eV would, in that case, be $\sim 10^{38}$ erg/s (cf. Hillas 1984b). This is only a fraction of the rotational energy loss of the Crab pulsar ($I\Omega\dot{\Omega} \sim 5 \times 10^{38}$ erg/s). At higher energies, the residence time in the disk decreases to the scatter free value, but on the other hand, the energy required to power CRs decreases as 1/E while the energy input available from pulsars is $\propto NI\Omega\dot{\Omega} \propto E$. The rotational energy in pulsars is, therefore, more than sufficient to power CRs above $10^{16}$ eV.

In addition, the increase in anisotropy of CRs which is observed above $\sim 10^{15}$ eV, may also be due to the mean free path becoming comparable to the thickness of the disk. If $\lambda_s$ is ~100 times the gyroradius, the transition energy should be in the range of $10^{15}$ to $10^{16}$ eV as observed.

4. Conclusions. We have found that the observed cosmic ray spectrum in the energy range, $\sim 10^{16}$ to $10^{19}$ eV can be produced by a distribution of pulsars if they are born with ms periods, evolve according to $\dot{\Omega} \propto \Omega^3$, and emit nuclei with energies characteristic of their vacuum potentials. As indicated, this simple model makes several assumptions, some of which are ad hoc. However, we find it remarkable that the proper CR spectrum and energy range are reproduced with minimal assumptions and with virtually with no free parameters. This result is essentially independent of the spectral details of individual pulsars.

References

Alper, M.A. and Pines, D. 1985, Nature, **314**, 334.
Arons, J. 1981, in Origin of Cosmic Rays, IAU No. 94, eds G. Setti et al., p.175.
Axford, W.I. 1981, 17th ICRC (Paris), **12**, 155.
Chanmugam, G. and Brecher, K. 1985, Nature, **313**, 767.
Hillas, A.M. 1984a, A. Rev. Ast. Astro., **22**, 425.
Hillas, A.M. 1984b, Nature, **312**, 50.
Jokipii, J.R. and Morfill, G.E. 1985, Ap. J. Lett., **290**, L1.
Lagage, P.O. and Cesarsky, C.J. 1983, Astr. Ap., **118**, 223.
Manchester, R.N. et al. 1985, M.N.R.A.S., **212**, 975.
Meyer, J.P. 1985, Ap. J. Supp., **57**, 173.
Michel, F.C. 1982, Rev. Mod. Phys, **54**, 1.
Michel, F.C. and Dessler, A.J., 1981, 17th ICRC (Paris), **2**, 340.
Ormes, J.F. 1983, 18th ICRC (Bangalore), **2**, 187.
Ostriker, J.P. and Gunn, J.E. 1969, Ap. J., **157**, 1395.
Protheroe, R.J. et al. 1981, Ap. J., **247**, 362.
Samorski, M. and Stamm, W. 1983, Ap. J. Lett., **268**, L17.
Wandel, A. 1985, in preparation.
Wandel, A. and Ellison, D.C. 1985, in preparation.

# ENERGY DEPENDENCE OF COSMIC RAY COMPOSITION ABOVE $10^5$ GEV/NUCLEUS

John Linsley
Department of Physics and Astronomy
University of New Mexico, Albuquerque, NM 87131

Carl E. Fichtel
NASA Goddard Space Flight Center
Greenbelt, MD 20771

ABSTRACT

It is argued that above $10^5$ GeV/nucleus, in the range where charge-resolved spectra have not yet been determined, the appropriate measures of equal-energy composition are $\langle \ln A \rangle$ and $\{\ln A\}$, the mean value and dispersion relative to the mean of lnA, where A is the mass number. Experimental data which are sensitive to changes in $\langle \ln A \rangle$ with increasing energy are examined. It is found that, taken as a whole, they show no change (±0.5) between $10^5$ and $10^6$ GeV, and a *decrease* of 1.5±0.5 between $10^6$ and $10^8$ GeV, with no further change (±0.5) above $10^8$ GeV. Taken as a whole, the various indirect estimates of the absolute value of $\langle \ln A \rangle$ above $10^5$ GeV/nucleus are also consistent with this pattern. For a wide range of astrophysically plausible composition models the value of the other measure, $\{\ln A\}$, is insensitive to changes in $\langle \ln A \rangle$. Because of this the existing data on $\{\ln A\}$ can likewise easily be reconciled with this pattern.

1. Introduction. The energy spectra of all the elements, insofar as they have been measured to date at the top of the atmosphere or above it, are well explained by a simple leaky box model with fragmentation in the interstellar medium and a rigidity dependent escape length. However, measurements of charge-resolved spectra are increasingly difficult at higher energies. Particles are usually selected on the basis of energy per nucleus, the practical upper limit being at present about $10^5$ GeV/nucleus. The composition of cosmic rays with equal energy is strongly biased in favor of heavy elements compared to cosmic rays with equal magnetic rigidity. Below $10^5$ GeV/nucleus the equal-energy mass spectrum is in fact nearly rectangular from protons to iron.

Above $10^5$ GeV/nucleus the evidence on cosmic ray composition is indirect. There is overwhelming evidence that nearly all of these cosmic rays are bare atomic nuclei, as at lower energies, rather than electrons, $\gamma$-rays, neutrinos, dust grains, or exotic objects such as quark globs, magnetic monopoles, or mini-black holes. The indirect experiments are sensitive to primary mass rather than charge, but in view of the low resolution, conversions from one to the other are carried out assuming that $Z = A/2$ for nuclei other than protons. With a few exceptions the indirect methods select primaries of a given energy per nucleus, rather than energy per nucleon. They are unable at present to resolve the mass spectrum into individual nuclei or even groups of neighboring mass. With a few exceptions they can be classified into two groups: those

which measure the average primary mass and those which measure the width of the primary mass distribution. In most cases the theoretical line separation is proportional to lnA rather than A. For this reason, and to avoid giving undue importance to elements in the Fe group, it is preferable to use lnA as the underlying variable, and to group the experiments into some which measure the mean value <lnA> and others which measure {lnA}, the dispersion of lnA relative to the mean. The remainder of this work summarizes the available experimental evidence on the energy dependence of these two quantities, with emphasis, of course, on energies above $10^5$ GeV/nucleus.

2. Low Energy Region. The behavior of <lnA> and {lnA} as a function of energy/nucleus is shown in Fig. 1. For energies $\leq 10^5$ GeV the points are calculated from directly observed charge spectra (see Linsley 1983). In this region the value of <lnA> increases from 1.0 at $10^2$ GeV to 1.7 at $10^4$ GeV and then levels off. Although one cannot rule out a certain degree of heavy enrichment at the sources in the upper part of this range (Juliusson 1975, Goodman *et al.* 1979), it is not necessary to assume any such enrichment; the increase of <lnA> can be explained entirely by a diminished path length at higher energies, resulting in less fragmentation of nuclei such as Fe during propagation from the sources to the earth. There is direct evidence from the JACEE experiment that the value of <lnA> is not significantly greater at $10^5$ GeV than at $10^4$ GeV (Burnett *et al.* 1983), and there is direct evidence from an experiment by Sood (1983) that the intensity of Fe nuclei at the top of the atmosphere is no greater at $10^5$ GeV than predicted by the standard model.

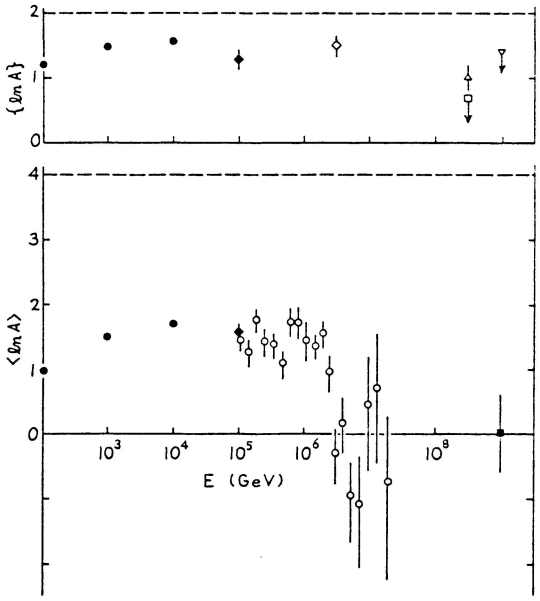


*Fig. 1. Energy dependence of <lnA> and {lnA}. CLOSED CIRCLES, calculated from charge-resolved spectra obtained in many balloon experiments; CLOSED DIAMONDS, Burnett et al. 1983; CLOSED SQUARE, Linsley & Watson 1981 from $\langle x_m \rangle$ obtained in several air shower experiments; OPEN CIRCLES, Acharya et al. 1983; OPEN DIAMOND, Nikolskii et al. 1979; TRIANGLE, Hara et al. 1983; INVERTED TRIANGLE, upper limit from $\{x_m\}$ obtained in several air shower experiments; OPEN SQUARE, upper limit from $\{\ln N_\mu\}$ (Volcano Ranch experiment).*

3. High Energy Region. A number of ground level experiments measure <lnA>. Calibration is a problem, so some results are sensitive mainly to *changes in* <lnA> vs E, while others yield estimates of the absolute value of <lnA>. One approach uses data on $x_m$, the atmospheric depth at which air showers reach maximum development; another uses data on $N_\mu$, the number of muons for a fixed number of electrons at ground level. For a given primary A, barring any sudden unexpected changes in the character of high energy interactions, $\langle x_m \rangle$ and $\langle \ln N_\mu \rangle$ are expected

to be almost linear functions of lnE. Then for a mixed primary composition, according to the superposition principle of Peters (1960), they are linear functions of <lnA>. Consequently one expects to detect significant changes in <lnA> by observing changes in the experimentally measured rates of increase, $d(\langle x_m \rangle)/d(\ln E)$ and $d(\langle \ln N_\mu \rangle)/d(\ln E)$.

The former is called the 'elongation rate'. The first systematic investigation capable of applying the elongation rate test indicated that <lnA> undergoes a large decrease in going from $\sim 10^6$ to $10^8$ GeV (Thornton and Clay 1979). Since then the energy dependence of the elongation rate has been investigated by many groups using a wide variety of methods (Kalmykov *et al.* 1979, Antonov *et al.* 1979, Walker and Watson 1981, Chantler *et al.* 1982, Kvashnin *et al.* 1983, Alimov *et al.* 1983, Inoue *et al.* 1983, Cady *et al.* 1983). Although the later results are not all perfectly consistent, taken as a whole the $\langle x_m \rangle$ results require a decrease in <lnA> of 1.5 or more, which corresponds to changing from a mixed (low energy) composition to one highly proton enriched, between $10^6$ and $10^8$ GeV. In the region above this change, where the elongation rate test indicates little or no further change in <lnA>, the absolute value of <lnA> was found from a detailed analysis of $\langle x_m \rangle$ data to be $0\ ^{+0.6}_{-0}$ Linsley and Watson 1981).

The other indicator, $d(\langle \ln N_\mu \rangle)/d(\ln E)$, is less sensitive and more difficult to calibrate. The independent variable in actual experiments is $N_e$ rather than E, but one expects $N_e$ to be nearly proportional to E for given primary A, so the same principles apply. A change in composition will cause the value of $d(\langle \ln N_\mu \rangle)/d(\ln N_e)$ to be less in a region where <lnA> is decreasing than it is where <lnA> is constant, but for low energy muons ($E_\mu$<10 GeV) the expected change (corresponding to the variation in <lnA> described above) is only 8-10% (Grieder 1983). This is not much more than the uncertainty in the reference value (the value for <lnA> $\sim$ constant), and the actual sensitivity could be even less. In fact, $d(\langle \ln N_\mu \rangle)/d(\ln N_e)$ for $E_\mu$<10 GeV does not show any significant variations in the region where it has been studied, from $\sim 10^5$ to $10^8$ GeV/nucleus. For higher energy muons the expected difference is greater, however, amounting to $\sim$ 15% for $E_\mu$ = 220 GeV. The only experiment on high energy muons capable of showing this kind of change has given results in good agreement with those from the $\langle x_m \rangle$ measurements (Acharya *et al.* 1983). A notable feature of this experiment is that the primary energy range extended down to $10^5$ GeV; that is, to the region where <lnA> has been measured directly using balloons (Burnett *et al.* 1983, Sood 1983). This result and the one by Linsley and Watson are shown in Fig. 1.

Constancy of <lnA> in the interval $10^5$-$10^6$ GeV is also indicated by data requiring other types of analysis: data on very high energy (TeV) muons (Elbert 1982, Battistoni *et al.* 1983, Matsuno *et al.* 1984, Allkofer *et al.* 1984), and on the energy spectrum of air shower hadrons, as analyzed by Grieder (1983, see also Dybovy and Nesterova 1983). Some other results on the hadron component have been seen as favoring a strong Fe enhancement in the interval $10^5$-$10^7$ GeV (Goodman *et al.* 1979, Amenomori *et al.* 1983). However, like earlier claims for an iron anomaly at lower energies, these claims are not well enough supported to withstand the overwhelming weight of contrary evidence.

It should be noted that many of the indirect experiments are sensitive primarily to {lnA} rather than <lnA>. These experiments measure air shower fluctuations. The quantities that have been studied mainly are, again, $x_m$ and $N_\mu$. Unfortunately {lnA} is not very sensitive to the various assumptions that can be made about cosmic ray composition. If one assumes that the possibilities range from pure protons (<lnA> = 0) to pure Fe (<lnA> = 4), then the maximum value that {lnA} can have is 2, not much greater than the observed value in the low energy domain. Even a small admixture of protons with otherwise pure Fe, or of Fe with otherwise pure protons, will appreciably enhance the shower fluctuations so as to give {lnA} $\sim$ 1, which is about as low a value as any of the experiments have given. Experiments which measure the fluctuations of $x_m$ escape this criticism somewhat because $\{x_m\}$ is sensitive to <lnA> as well as {lnA} (Linsley 1983). The observed fluctuations above $10^8$ GeV are consistent with pure proton primaries or with mixtures containing up to 50% of nuclei heavier than helium. They are not consistent with pure Fe primaries or with mixtures containing only a small percentage of light elements (Walker and Watson 1982, Dyakonov *et al.* 1983, Hara *et al.* 1983).

4. Conclusions. Below $10^5$ GeV/nucleus the equal-energy composition varies with energy in the manner expected due to fragmentation in the interstellar medium with a rigidity dependent path length. The increase of <lnA> in this region is not a property of the sources, but is rather a propagation effect. Between $10^5$ and $10^6$ GeV there is little change in <lnA>. Between $10^6$ and $10^8$ GeV the average primary mass decreases to about 1 (<lnA> $\sim$ 0). It then remains constant, from $10^8$ GeV to the highest observed energies (E $\sim$ $10^{11}$ GeV/nucleus).

References. ACHARYA *et al.* 1983, Proc. 18th ICRC 9, 191 (also ACHARYA, B. Thesis, Univ. of Bombay, 1983); ALIMOV *et al.* 1983, Proc. 18th ICRC 11, 387; ALLKOFER *et al.* 1984, Lett. Nuovo Cimento 41, 373; AMENOMORI *et al.* 1983, Proc. 18th ICRC 11, 114; ANTONOV *et al.* 1979, Proc. 16th ICRC 9, 263; BATTISTONI *et al.* 1983, Proc. 18th ICRC 11, 466; BURNETT *et al.* 1983, Proc. 18th ICRC 2, 105; CADY *et al.* 1983, Proc. 18th ICRC 11, 412; CHANTLER *et al.* 1982, J. Phys. G 8, L51; DYAKONOV *et al.* 1983, Proc. 18th ICRC 6, 111; DYBOVY and NESTEROVA 1983, Proc. 18th ICRC 6, 82; ELBERT 1982, Proc. Workshop on Very High Energy Cosmic Ray Interactions (Univ. of Pennsylvania) p. 312; GOODMAN *et al.* 1979, Phys. Rev. Lett. 42, 854; GRIEDER 1983, Proc. 18th ICRC 11, 323 (also 1984 preprint); HARA *et al.* Proc. 18th ICRC 11, 272; INOUE *et al.* 1983, Proc. 18th ICRC 11, 402; JULIUSSON 1975, Proc. 14th ICRC 8, 2689; KALMYKOV *et al.* 1979, Proc. 16th ICRC 9, 73; KVASHNIN *et al.* 1983, Proc. 18th ICRC 11, 394; LINSLEY 1983, Proc. 18th ICRC 12, 135; LINSLEY and WATSON 1981, Phys. Rev. Lett. 46, 459; MATSUNO *et al.* 1984, Phys. Rev. D 29, 1; NIKOLSKII *et al.* 1979, Proc. 16th ICRC 8, 335; PETERS 1960, Proc. 6th ICRC III, 157; SOOD 1983, Nature 301, 44 (also Proc. 18th ICRC 2, 109; THORNTON and CLAY 1979, Phys. Rev. Lett. 43, 1622 and Erratum, 45, 1463; WALKER and WATSON 1981, J. Phys. G 7, 1297; WALKER and WATSON 1982, J. Phys. G 8, 1131.

# IMPLICATIONS OF THE EXPERIMENTAL RESULTS ON HIGH ENERGY COSMIC RAYS WITH REGARD TO THEIR ORIGIN

Carl E. Fichtel
NASA Goddard Space Flight Center
Greenbelt, MD 20771

John Linsley
Department of Physics and Astronomy, University of New Mexico
Albuquerque, NM 87131

1. Introduction. In an earlier paper at this conference (OG5.4-4) by Linsley and Fichtel (1985), it was shown that current cosmic ray evidence supports a change in the cosmic ray composition in the region between $10^6$ and $10^8$ GeV total energy in the direction of a smaller average value of A. Compared to normal celestial abundances, the heavy nuclei are much less abundant, and, in fact, the composition measurements above $10^8$ GeV are consistent with there being only protons. Here, these results combined with those of the energy spectrum and anisotropy of the cosmic rays and other astrophysical information will be examined to try to determine their implications for the origin of the cosmic rays. In the next two sections, there will be a consideration of the implications of one or more than one type of source in the galaxy to see which are consistent with the interpretation of current measurements. In the last section, the nature of the source types that would be required are discussed.

2. Consideration of a One Source Type. These sources would presumably be distributed throughout the galactic plane. The possibility of a single source at the galactic center or elsewhere is a special case. The most likely possible sources of cosmic rays, at least for the lower energies ($10^6$ GeV), appear to be supernovae and pulsars. Since the models generally envision the acceleration of the outermost layer (in the case of a supernova) or surrounding material (for a pulsar), there is not a major problem in reproducing the observed composition at lower energies at least in broad terms when subsequent fragmentation in the interstellar medium is considered.

Figure 1 summarizes current information on the observed total energy spectra. It is clearly not possible to obtain agreement with the all particle energy spectrum by assuming that all types of particles have an energy spectrum that continues as a power law with the same slope to arbitrarily high energies. It is also not reasonable to expect this to occur if these particles are galactic, because, even if they have such a spectrum at the source, there is a rigidity above which they cannot be held easily in the galactic arms in the plane (Peters, 1959; Fichtel, 1963). Using an estimated magnetic field value based on current information that is slightly smaller than used in the latter paper, that rigidity is estimated to be between $10^6$ and $10^7$ GeV. Clearly the steepening in the all particle spectrum at or somewhat below $10^7$ GeV is consistent with this concept, and the change in slope at $10^{10}$ GeV (actually suggested by Fichtel, 1963, before it was reported by Linsley, 1963) may suggest an extragalactic component, although other

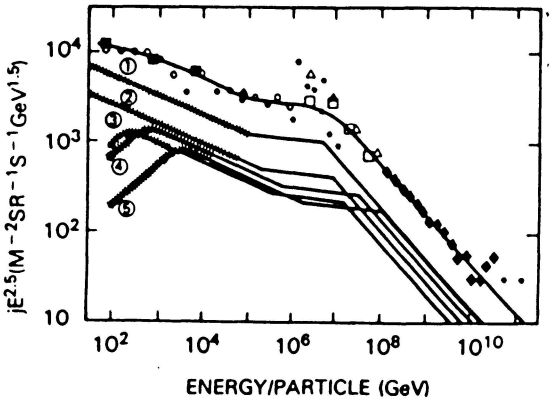


Fig 1: Cosmic Ray Particle intensity as a function of kinetic energy per particle. The references corresponding to the symbols in the figure for nuclei of all types are as follows: closed square, Ryan et al. (1972), Simon et al. (1980); and Burnett et al. (1983a): closed triangle, Burnett et al. (1983b); open circle, Grigorov et al. (1971); asterisk, Khristiansen et al. (1983); open square, Efimov and Sokurov (1983); open triangle, La Pointe et al. (1968); closed diamond, Cunningham et al. (1980); closed circle, Bower et al. (1983). The circled numbers refer to the following 1 H (protons); 2 He; 3, (C,N,O); 4, (10 < Z < 20); 5, (21 < Z < 30). The hatched portion (++++) of the curves are based on a large number of balloon flight results, including: Ormes and Webber, (1965); Freier and Waddington, (1968); Lezniak and Webber, (1971); Webber et al. (1972); Ryan et al. (1972); Ormes and Balasubrahmanyan, (1973); Juliusson, (1974); Fisher et al. (1974); Arons and Ormes, (1975); Juliot et al. (1975); Lund et al. (1975); Fisher et al. (1976); Hagen et al. (1977); Caldwell and Meyer, (1977); Maehl et al. (1977); Weber et al. (1977); Wefel et al. (1977); Lezniak and Webber (1978); Garcia-Munoz et al. (1979); Simon et al. (1980). The remainder of the curves are the cosmic ray particle intensity spectrum predicted for a single source model with a rigidity dependent escape, as explained in the text.

explanations are possible. Spectra which continue as a constant power law until a rigidity where particles begin to escape clearly, however, will not explain the moderate flattening of the spectrum from $10^5$ to almost $10^7$ GeV. As one approaches the rigidity where particles escape relatively easily, it is not unreasonable in a trapping and diffusion region to expect a lessening of the escape rate just below the rigidity where escape becomes relatively easy, as a result of the rigidity being large enough so that the smaller irregularities in the field are in effect not being seen by the particles. There must, of course, also not be a high intensity of large scale irregularities. One does not know if this is the situation, but it is at least plausible.

For Figure 1, a one source model was chosen with a power law of the form

$$j_Z = A_Z E^{-a} \qquad (1)$$

for energies above the rounded portion of the maxima, and with the relative abundances shown as deduced from the balloon instrument results. The slope in Figure 1 may be interpreted as consisting of two parts, a and b, where a is given by equation (1) and b is a rigidity dependent escape term, as suggested by Ormes and Protheroe, (1983). Below $10^5$ GeV, but above the rounded portion at low energies, the value of (a+b) used in Figure 1 is 2.7. Following this thinking and that of the last paragraph, b then decreases somewhat as escape becomes slightly less likely at $10^5$ GeV and then increases markedly at $5\times10^6$ GeV. The values of (a+b) used in Figure 1 are 2.55 and 3.05 for $10^5$GeV<$5\times10^6$GeV and R>$5\times10^6$GeV respectively. It is now known (see, for example, Linsley, 1983) that there is an energy dependent anisotropy, which is consistent with a galactic population up to about $10^{10}$ GeV.

The measurements of the composition, or more exactly, the average value of the logarithm of the number of nucleons per nucleus, were discussed by Linsley and Fichtel (1985). The determined values of $\langle \ln A \rangle$ as a function of energy are shown in Figure 2 together with the variation of $\langle \ln A \rangle$ with energy predicted by the energy spectra shown in Figure 1. Clearly the curve, (a) in the figure and the data do not agree. It should be noted that the general shape of this curve, that is the rise to a higher value and then a leveling to a constant, is a result of the same source energy spectra for all nuclear species and a rigidity dependent escape. It does not depend significantly on the

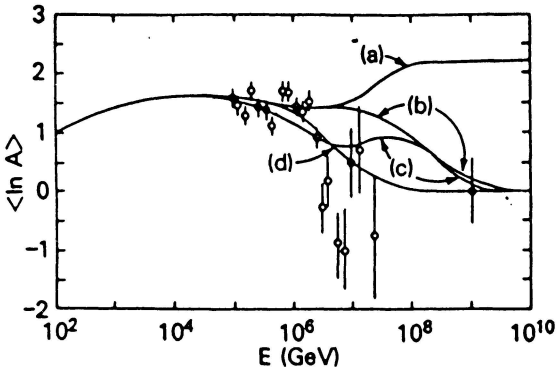


Fig 2: The average value of lnA as a function of particle kinetic energy. Closed square, Burnett et al. (1983b); open circles, Acharya et al. (1983) with <Nμ> converted to <lnA> using simulation results given by Acharya (1983); closed circle, Linsley and Watson (1981). Due to the experimental errors some of the open circles fall below <lnA> = 0, in formal violation of the astrophysical constraint, for primary nuclei, that <lnA> should be zero (pure protons) or greater. The results below $10^4$ GeV are normalized to the balloon results listed in the caption of Figure 1. Curve (a) refers to the single source model discussed in the test, whose spectra are shown in Figure 1. Curve (b) refers to a single source model in which the highest energy particles pass through much more matter. Curve (c) refers to the two source type model discussed in the text, wherein the spectra of both sources change at $3x10^6$ GeV/C due to escape from the arms. Curve (d) refers to the two source type model discussed in the text, wherein one source has truncated spectra, which are shown in Figure 3.

source spectral shape. A possibility for a change in the composition of the type observed in a single source model is that it is a propagation effect. If, as seems almost certain, the magnetic fields in the Galaxy beyond the galactic arms are significantly weaker than in the arms and the matter density beyond 1 kpc from the plane is small, $<10^{-2}$ cm$^{-3}$, then the cosmic ray saturation density for the galaxy is well below that in the arms, and the lifetime is such that the matter traversed is very much less than that required to give the fragmentation of the heavy nuclei needed to cause predominantly heavy-nuclei-free cosmic ray composition above about $10^7$ GeV.

3. Two Source Type Models. The introduction of two-source models is naturally aimed at avoiding the difficulties that have just been described. The discussion in this paper will be restricted to galactic sources being in the plane. Even subsequent acceleration models, which would not address the composition change at $10^6$ to $10^7$ GeV, are generally discussed in terms of the galactic plane. The basic concept which seems plausible is that one type of source dominates below about $10^6$ GeV and the other above about $10^7$ GeV with there being an overlap or transition region. As the apparently simplest assumption, the source type supplying the lower energy region will be taken to have the characteristics of the one-source-type model, but with no change in spectral slope until the escape from the galaxy. It will be assumed that the source at high energies, consisting of protons or mostly protons, whatever its origin, has a smaller slope, but also being a diffuse galactic source must have its steepening at the same rigidity as the lower energy type of source and by the same amount. An example of the results of this approach is shown in Figure 2 as curve (c), wherein the increase in slope due to escape from the arms occurs at $3x16^6$ GeV/C and the slope increases by 1.0 for all spectra. The energy spectrum matches well and the predicted <lnA> as a function of energy comes closer to the experimental values.

From an examination of the experimental data, however, it would appear that the composition may change at a somewhat lower energy; hence, either the escape rigidity must be overestimated or the lower energy source must not accelerate particles efficiently to quite this rigidity. If the escape rigidity is lowered significantly, it is not possible to obtain agreement with the total energy spectrum unless a more complex energy spectrum is assumed for the high energy source. The result for the total particle energy spectrum obtained by assuming that the lower energy cosmic ray spectra changes slope at $5x10^5$ GeV, while

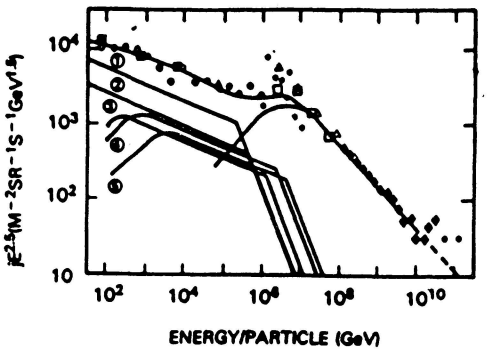


Fig 3: Cosmic ray particle intensity spectrum predicted by a two source type model in which the dominant low energy source has a source spectral change at $5x10^5$ GeV and the high energy source reflects a spectral slope change at $5x10^6$ GeV due to the effect of escape. The data are those referenced in Figure 1.

the higher energy source spectral change due to escape from the arms is around $5x10^6$ GeV, is shown in Figure 3. The predicted behavior of the composition (lnA> vs E) is shown as curve (d) in Figure 2. There is good agreement here with this broadened set of assumptions. Also, the increasing anisotropy is consistent with this model as it would be with any diffuse galactic source model as noted earlier. Should <lnA> not decrease as rapidly with energy as the data in Figure 2 show, as suggested by Nikolski and Stamenov (1983) and Dyakonov et al. (1983), the conclusions with regard to the nature of the two source types would be unchanged except that the higher energy source type would have more heavy nuclei. The significant point is that an acceptable two-source-type model seems possible.

4. What are the Two Source Types. As noted earlier, there seem to be several plausible theories to explain the cosmic rays comprising the component below about $10^6$ GeV. The source of higher energy galactic cosmic rays must be able to accelerate particles to $10^{10}$ GeV. Further, this component is probably dominated by protons or may at most be a mixture of protons and relatively small amounts of helium and heavy nuclei compared to the celestial normal abundances. With regard to the composition, there seem to be at least two ways in which it might be achieved; the source could be a basically proton source (or produce neutrons which decay to protons), or the source could have a normal composition, but the particles could subsequently traverse enough material or photons in the source region to cause sufficient fragmentation of the heavier elements to leave a mixture of largely protons and some helium nuclei at least for part of the energy range. Possible source models include one associated with pulsars, although the highest energies are a difficulty, and a rapidly rotating massive black hole at the galactic center.

References

Berezinsky, V.S., et al. 1979, Proc. 16th ICRC (Kyoto), 4, 188.
Dyakonov, M.N., et al. 1983, Proc. 18th ICRC (Bangalore) 6, 111.
Fichtel, C.E., 1963, Phys. Rev. Letters, 11, 172.
Linsley, J., and Fichtel, C.E., 1985, Proceedings XIX Internat. Cosmic Ray Conf., Paper OG5.4-4.
Linsley, J., 1983, Proc. 18th ICRC (Bangalore) 12, 135-191.
Nikolski, S.I., and Stamenov, J.N., 1983, Proc. 18th ICRC (Bangalore) 2, 111, 115.
Ormes, J.F., and Protheroe, R.J., 1983, Ap. J., 272, 756.
Peters, B., 1959, Nuovo Cimento Suppl., 14, 436.

OG-5.4-6

# THE PRIMARY COSMIC RAY MASS COMPOSITION AT ENERGIES ABOVE $10^{14}$ eV

J.Gawin, J.Wdowczyk
Institute of Nuclear Science and Technology
90-950 Lodz, ul Uniwersytecka 5, Box 447, Poland

J.Kempa
Department of Physics, University of Lodz,
90-236 Lodz, ul Nowotki 149-153, Poland

1. INTRODUCTION. It has been demonstrated by us (Gawin et al 1984) that the experimental data on EAS at the energy interval $10^{15}$ - $10^{17}$ eV seems to be described best if it is assumed that the Galactic cosmic rays are described by some sort of a two component picture. The first component is of a mixed composition similar to that at lower energies and the second is dominated by protons. Overall spectrum starts to be enriched in protons already at energies about $10^{15}$ eV but the effective mass of the primaries remains constant up to energies around $10^{16}$ eV. That results from the fact that composition gradually changes from multi-component to mixture of protons and heavies.

That picture receives also some sort of support from recent observations of relatively high number of energetic protons in JACEE and Concorde experiments (Burnett et al 1984 and Capdevielle 1984).

2. THE MASS COMPOSITION FOLLOWING FROM TWO COMPONENT PICTURE OF THE GALACTIC COSMIC RAYS.

The integral ebergy spectra of the primary particles of different masses are described by following expression:

$$j_A(>E)=(C_A/1.7)\ E^{-1.7}\ \exp(-(E/D_A)^2)(1+E/3.33\ 10^4)^{0.3}\ ,$$

insentity in $m^{-2}\ s^{-1}\ sr^{-1}$ and energy in GeV/ nucleus.

| A | $C_A$ | $D_A$ |
|---|---|---|
| p | $1.72\ 10^4$ | $3.33\ 10^5$ |
| $\alpha$ | $9.2\ 10^3$ | $6.67\ 10^5$ |
| CNO | $6.2\ 10^3$ | $2.17\ 10^6$ |
| H+VH | $9.2\ 10^3$ | $4.33\ 10^6$ |
| Fe | $6.2\ 10^3$ | $8.66\ 10^6$ |

The integral spectrum of the additional proton component

$$j_p(>E)=2.78(E^{-1} - 2.5\ 10^{-7})\ ,\text{for } E\leq 2\ 10^6 \text{ GeV}$$
$$=2.78\ 10^6\ E^{-2}\ ,\text{for } E\geq 2\ 10^6 \text{ GeV}\ .$$

3. THE FLUXES OF HADRONS AT SEA LEVEL. We have already demonstrated (Kempa and Wdowczyk 1983) that the fluxes of hadrons at mountain altitudes can be well described using the discussed here mass composition and the picture of high energy interactions described elsewhere in this proceedings (HE- 1.2-4). In figure 1 we have compared the fluxes of hadrons observed at sea level with predictions based on the above stated assumptions. We can see that the agreement is moderately good.

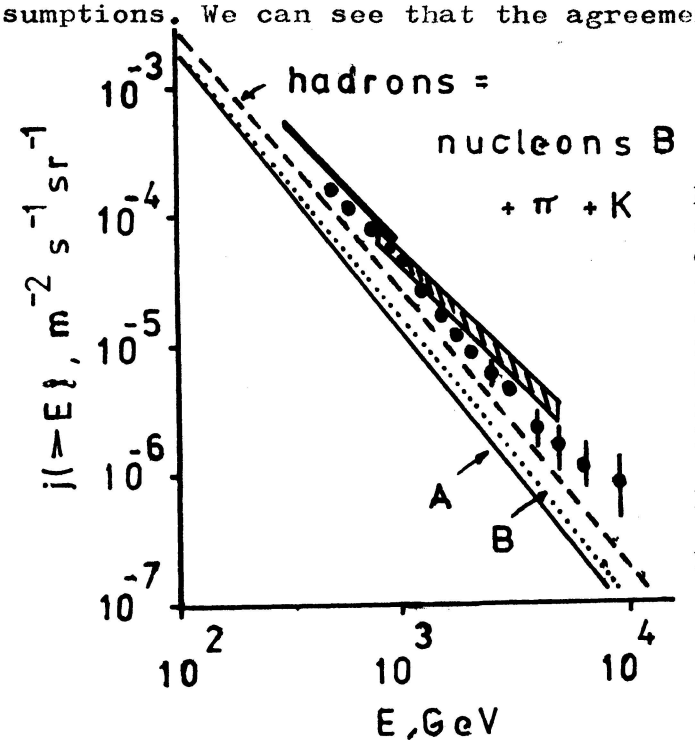


Fig.1. Hadron energy spectra at sea level. The dotted line is the prediction for the two component spectrum B-flux of nucleons for the two component model and A- the flux of nucleons for the heavy enriched spectrum (Tan et al 1982).(•-Siohan 1976, — Arvela et al 1981, ▯ Ashton et al and Baruch et al 1977)

4. FLUXES OF HIGH ENERGY MUONS. Under the same assumptions about high energy interactions and primary particle mass composition we have calculated the fluxes of high energy muons in the atmosphere. The fluxes were calculated taking formulae for p-nucleus interaction,making detailed allowance for the muon energy losses in the atmosphere and the losses due to the muon decays. Probabilities of the decay were calculated taking into account varying energy of muons with depth. Curvature of the atmosphere was taken into account in the calculations for the inclined direction. The results of calculations are compared with experimental data in figures 2-4. In figure 2 the comparison is made for muons recorded at ground level,in figure 3 underground at shallower depth and in figure 4 at large depths. It should be pointed out that the good agreement seen in figures is obtained without any normalisation.The predicted intensities are plotted as they are obtained from the assumed primary spectra mass compositions and assumptions about the picture of high energy interactions. In figure 2 are also plotted predictions obtained for the heavy enriched spectrum ( Tan et al 1982 ).

In calculations of the depth intensity curve the fluctuations in muon range were taken into account.

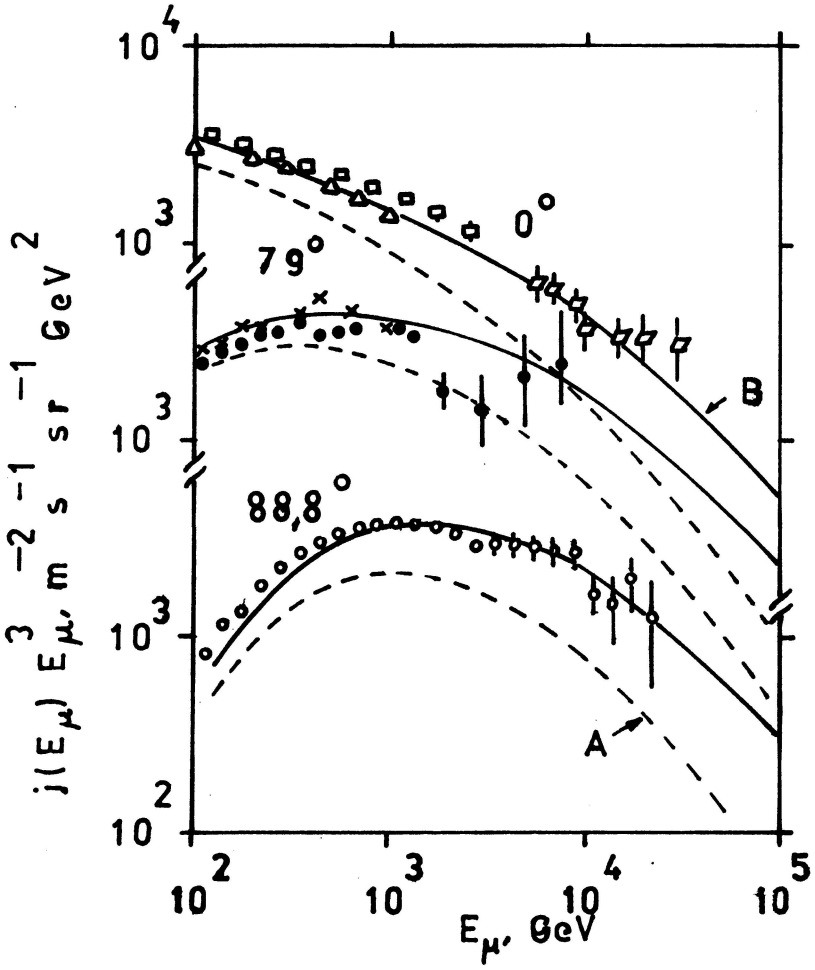


Fig.2. The muon energy spectra at various angles. The continous lines are the predictions based on the two component model, the dotted lines are the predictions for the heavy enriched spectrum (Tan et al 1982) ( ♦ Allkofer et al 1981, △ ---- 1971, × Jokish et al 1979, ϕ Khrenov 1977, ϕ Matsuno et al 1984, ○ Thompson et al 1977)

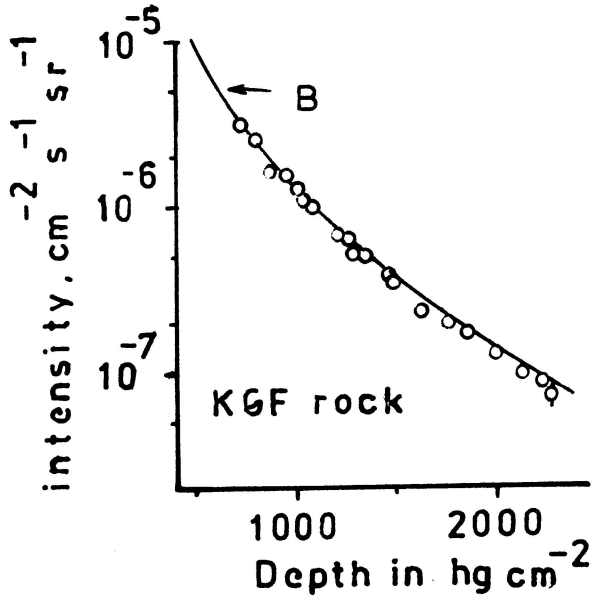


Fig.3. Depth intensity curve (after Krishnaswamy 1981) for shallow depths compared with that calculated from the muon spectrum obtained by us (B).

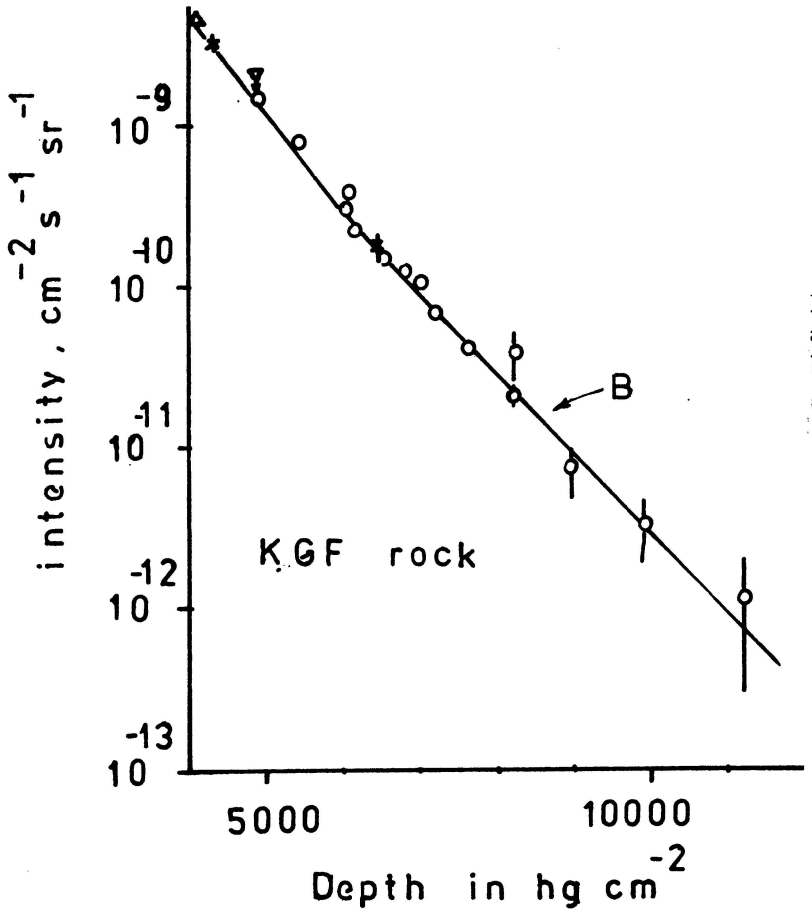


Fig.4. The same as in figure 3 but for the greater depths.

5. CONCLUSIONS. We have demonstrated that the fluxes of high energy secondary particles observed in atmosphere can be well predicted on the basis of the two component picture of the Galactic cosmic ray and the picture of high energy hadron - nucleus interaction deduced from the accelerator data.

REFERENCES

Allkofer O C et al 1971 Proc.12th ICRC,Hobart,7,p.1314
---------- 1981 Proc.17th ICRC,Paris,10,p.321
Arvela H et al 1981 Proc.17th ICRC,Paris,5,p.270
Ashton F et al 1977 Proc.15th ICRC,Plovdiv,7,p.458
Baruch J E F et al 1977 Proc.15th ICRC,Plovdiv,7,p.403
Burnett T H et al 1984 Proc.Int.Symp.on C.R. and Particles Phys.,Tokyo,p.468
Capdevielle J N 1984 ibid p.394
Gawin J et al 1984 Acta Universitatis Lodziensis,7,p.59
Jokish H et al 1979 Phys.Rev.D,19,p.1368
Kempa J and Wdowczyk J 1983 J.Phys.G:Nucl.Phys.,9,p.1271
Khrenov B A 1977 Proc.15th ICRC,Plovdiv,10,p.252
Krishnaswamy M R 1981 Ph.D.Thesis,University of Bombay
Matsuno S et al 1984 Phys.Rev.D,29,p.1
Tan Y H et al 1982 Report of the University of Tokyo 99822
Thompson G et al 1977 Proc.15th ICRC,Plovdiv,8,p.21

OG 5.4-7

# U.H.E. PARTICLE PRODUCTION IN CLOSE BINARY SYSTEMS

A. M. Hillas
Physics Department, University of Leeds
Leeds LS2 9JT, UK

ABSTRACT

Cygnus X-3 appears to generate so much power in the form of charged particles of up to $\sim 10^{17}$ eV that the galaxy may need $\lesssim 1$ such source on average to maintain its flux of u.h.e. cosmic rays. Accreting gas must supply the energy, and in a surprisingly ordered form, if it is correct to use a Vestrand-Eichler model for radiation of gammas, modified by the introduction of an accretion wake. Certain relationships between $10^{12}$ eV and $10^{15}$ eV gamma rays are expected.

## 1. Evidence for emission of gamma rays at distinct orbital phases

Ultra high energy gamma-rays have been observed from Cygnus X-3 and a few other X-ray binary sources.

First, to establish that underlying the variability there is a well-established pattern, Figure 1 compares the time profiles of the radiation observed from the direction of Cygnus X-3 by several independent workers. The flux (usually presented as a departure from the normal all-sky background) is plotted (on an arbitrary amplitude scale) against phase of the 4.8-hour binary orbit, with phase zero, as usual, corresponding to the minimum intensity of the X-ray signal, presumed to be when the X-ray source near a supposed neutron star is partly hidden behind the larger companion star. Apart from the early but very lengthy data set 1, the phase in all plots has been calculated from the X-ray data of van der Klis and Bonnet-Bidaud — the orbital period slowly changing with time. The observers do agree on brief periods of emission during the orbit: the $10^{15}$ eV observations indicated a burst of gamma-ray emission near phase 0.25 in the orbit, whilst at $10^{12}$ eV the main emission occurs near phase 0.63. However, during the lengthy Crimean observations, the phase of the main emission would switch between roughly these two regions (though the exact alignment of the phase plot from this early date is difficult). And the latest $10^{15}$ eV observations at Haverah Park (this conference) show the emission much stronger around the 0.63 peak. The Whipple Observatory (Mt. Hopkins) observers have demonstrated considerable month-to-month variability in flux (and two of their time profiles

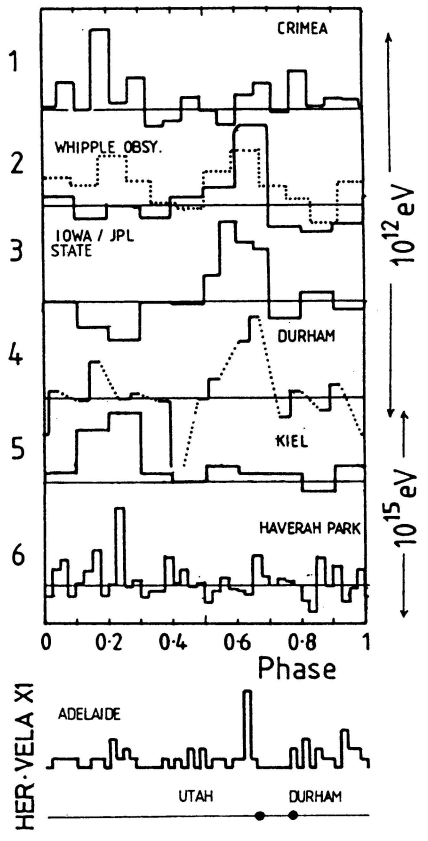


Figure 1. (Refs 1-6) Occurence of gamma rays from Cygnus X-3 vs orbital phase. Below: Vela X-1 phase plot (7), and observations of Her X-1.

are shown): year-to year variability is also found at Haverah Park.

The particles causing the observed air showers are taken to be photons because (a) they are uncharged, being deflected $<2^{\circ}$ in the 12 kpc or so from Cygnus X-3, (b) they do not decay in the 40,000 year journey, eliminating neutrons and neutral atoms (which would become ionized), and (c) the time dispersion <0.15 orbital period implies a Lorentz factor $>1.5\times10^{4}$: if the threshold energy is 0.5 TeV, $m_{primary} < 33$ MeV. (For Her X-1, the 1.2-second modulation implies a time spread $\lesssim$ 1.5 sec after 5 kpc (1 TeV): $m < 3$ MeV. For the Soudan mine radiation, not discussed here, if $E_{prim} \sim 5$ TeV, $m_{prim} < 400$ MeV.)

2. Mode of production of the gamma-rays

The basic process put forward by Vestrand & Eichler (8) is still basically the most promising, but it requires modification. In its original form, this model had a neutron star in orbit around the companion, and accelerating protons to high energies, emitting them (roughly) in all directions, and those few that grazed the top of the atmosphere of the large star would suffer nuclear collisions and generate neutral pions and hence gamma-rays. Just at certain points in the orbit, a distant observer would see gamma rays briefly as the source passed behind the star, and later as it re-emerged. At phase 0.25 we might be seeing the re-emergence pulse if the atmosphere were swollen by gas emission. However, a pulse near phase 0.8 is dubious, whilst the prominent pulse at $\sim$0.63 occurs when the neutron star is well to the front of the companion!

This latter phase may not be an accidental feature, as the (sole) report of gamma rays from Vela X-1 (Figure 1) shows sharp emission at the same phase. Is there a gas target in this direction? This is in fact the direction in which an accretion wake is expected if accretion occurs from a stellar wind (see Figure 2). Such a wake is seen as an X-ray absorption in Cen X-3, for instance (9). If the radial wind has a speed $v_w$ and the n-star orbital speed is $v_o$, the wake will lag behind the outward radius by an angle $\tan^{-1}(v_o/v_w)$: i.e. $45^{\circ}$ if $v_w = v_o$ — appearing at phase 0.625, or $35^{\circ}$ (phase 0.60) if $v_w = v_{escape} = \sqrt{2}v_o$.

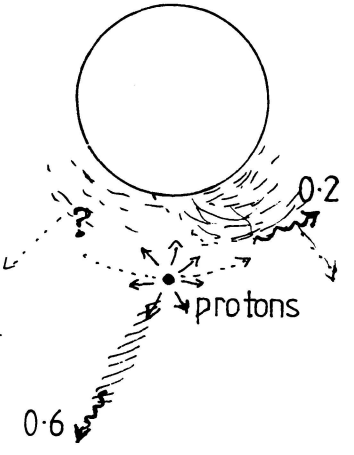


Figure 2. Supposed geometry for Cygnus X-3.

To support the V & E model, one may note that the gamma ray spectrum extends to $10^{16}$ eV, but that gamma rays cannot pass through a region where $B_{\perp} > 4\times10^{18}\ eV/E_{\gamma}$ gauss — about 400 gauss in this case. As statistical particle acceleration to such energies is unlikely (especially in weak fields) on the available time scale (10), it is highly probable that the particle acceleration occurs in a region of stronger (e.g. pulsar) field than this, so the gamma rays are produced in a place outside the acceleration region — i.e. on a "target". Electrons are unlikely to survive the strong fields involved in acceleration to $10^{17}$ eV: hence the assumption of protons (10).

The observation of brief gamma-ray emission from Her X-1 at the time (11) interpreted as the moment of reappearance of the n-star from obscuration by a dense accretion disc also supports a gas-target picture in the case of this source.

3. Significance, for cosmic rays, of magnitude of power output

(a) The cosmic ray power output of Cygnus X-3 may be estimated roughly as follows. Above $10^{15}$ eV, the Haverah Park flux is $\sim 3\times10^{-14}$ photons $cm^{-2}$ $s^{-1}$: these bring an energy flux $1.1\times10^{-10}$ erg $cm^{-2}$ $s^{-1}$ per decade (e.g. in the decade to $10^{16}$ eV). The published time profile indicated a pulse duty ratio $\sim 0.02$, so if there had been a suitable gas target in place all round the orbit the photon energy received would have been 50 times this. Allowing for absorption of a factor 3 (by pair production on primeval radiation) en route, an efficiency $\sim 1/6$, say, for converting proton energy to gammas, a source distance $r = 12$ kpc, and supposing the particles appear in a solid angle $\Omega$, the total power emitted in the proton beam is

$$W = (\Omega/4\pi)\times6\times3\times50\times1.1\times10^{-10}\times4\pi r^2 = (\Omega/4\pi)\times1.7\times10^{39} \text{ erg s}^{-1} \text{ per decade.}$$

The proton spectrum must extend to $\sim 10^{17}$ eV to produce photons up to $10^{16}$ eV, and most of these protons should escape into the galaxy. To maintain the present flux of galactic cosmic rays above $10^{16}$ eV the galaxy probably needs an energy input $\sim 5\times10^{37}$ erg $s^{-1}$ above $10^{16}$ eV (12) — based on a roughly estimated trapping lifetime $\sim 2.5\times10^{5}$ years at this energy (12). Hence one such object active for only part of the $10^5$ year storage time could supply the galaxy's flux of $10^{16}$-$10^{17}$ eV protons.

(b) *Accelerated spectrum?* Perhaps the neutron star can generate a power-law spectrum of protons (like the observed gamma spectrum), but alternatively, for direct (non-statistical) acceleration it may emit most of its power near the upper energy limit — say $10^{17}$ eV, the roughly $E^{-2}dE$ spectrum of gamma rays resulting from cascading in the target area. (It has been shown elsewhere (12) that if a magnetic field exceeding a few tens of gauss is present in the target area one can generate a cascade rapidly by synchrotron radiation following pair production, without needing very much matter — and the result has a spectrum very much like the overall gamma spectrum from Cygnus X-3.) The power in the $10^{17}$ eV protons then has to be sufficient to supply the energy in several decades of gamma rays.

If such a powerful source is indeed not often present, we are evidently lucky to see it! Is the existence of other sources then an embarrassment? The other $10^{15}$ eV sources in this galaxy (Vela X-1 and Her X-1) are in fact much weaker — but there may turn out to be many more. If the accelerated beam is quasi-monoenergetic, one must indeed expect a greater number of sources that emit particles of lower energy, to yield the known cosmic ray spectrum: there must be more TeV sources. Is the source 4U 0115+63 — found to be intense at $10^{12}$ eV (preprint from Turver's group) but not seen at $10^{15}$ eV — a member of such a population? The evolutionary history needed to explain the overall spectrum of particles in the galaxy is as yet unknown, and it is not apparent that a power law would emerge in any simple manner.

(c) *Mode of acceleration?* Acceleration by a large-scale emf generated by moving conductors in a strong magnetic field seems most likely, but the pulsar action of the neutron star itself is probably inadequate, (i) because Cygnus X-3 is probably an old n-star, whose rotational energy store would have run out long ago, and (ii) Vela X-1 has a spin period of 5 minutes, from X-ray evidence — much too feeble. Hence the accreting matter is presumably supplying the energy and also the high speed necessary. (See also (13)). However, the particles we detect are not emitted near the normal to the orbit (or to the Her X-1 disc), but closer to the

plane of the disc (or at least the orbit) – probably closer to Michel's (14) picture than Lovelace's. It is remarkable that the particle power is not small compared with the X-ray power – as though accretion energy is efficiently converted to electrodynamic energy rather than heat.

4. Possible observations

If the gamma-ray spectrum is generated by cascading from $10^{17}$ eV protons, the TeV gammas are seen where the gas target is thicker, and the $10^{15}$ eV gamma pulse should appear somewhat displaced – at the tenuous edge of the gas (but with much overlap). (To check this, contemporaneous measurements are needed, as the exact pulse position wanders somewhat.)

The phase of the prominent pulse, on this picture, is determined by the angle of the accretion wake; hence wandering of the wake probably signals changes in wind speed and may be related to variations in source power, and possibly to impending outbursts.

If the upper limit of the gamma spectrum is limited by transmission through a magnetic field (15) rather than by the primary proton beam, it is likely to be different for the pulse at phase 0.25 (generated close to the large star) and that near 0.63 – generated well away from the star.

If, as widely believed, there is a stellar wind in Cygnus X-3 that has a significant optical depth to X-rays – say 5 g $cm^{-2}$ – $\sim$10% of the protons will interact even outside the special "gas target" positions, giving a widely spread weaker flux of gamma rays. If this is not present, it will constrain the angle into which the protons are emitted, and we may then need to explain the pulses in terms of real directional acceleration of the charged particles. (This has seemed less likely at present, unless the particle acceleration occurs so far away from the neutron star that the position of the companion plays a part in determining the field orientation.)

*Puzzle:* Where are the X-rays generated? The source must be very large if it is not occulted by the gas target that is being supposed to intervene at phase 0.63: the X-ray intensity is a maximum here (unlike Cen X-3).

References


1. Neshpor et al (1979) Astrophys. Space Sci. 61, 349-355
2. Weekes, T C et al. (1981) Astron. Astrophys. 104, L4-6
3. Lamb, R C et al. (1982) Nature 296, 543-4
4. Dowthwaite, J C et al. (1983) Astron. Astrophys. 126, 1-6
5. Samorski W & Stamm W (1983) Ap. J. Lett. 268, L17-22
6. Lloyd-Evans, J et al. (1983) Nature 305, 784-7
7. Protheroe, R J, Clay, R W & Gerhardy P R (1984) Astrophys.J. 280,L47-50
8. Vestrand W T & Eichler D (1982) Astrophys. J. 261, 251-8
9. Jackson J C (1975) M.N.R.A.S. 172, 483-92
10. Eichler D & Vestrand W T (1984) Nature 307, 613-4
    Protheroe R J (1984) Nature 310, 296-8
11. Dowthwaite J C et al. (1984) Nature 309, 691-3
12. Hillas A M (1984) Nature 312, 50-1
13. Chanmugam G & Brecher K (1985) Nature, 313, 767-8
14. Michel F C (1985) Astrophys. J. 288, 138-41
15. Stephens S A & Verma R P (1984) Nature 308, 828-30

# VIRGO CLUSTER AS A HIGH ENERGY COSMIC RAYS SOURCE

S. Karakuła and W. Tkaczyk
Institute of Physics, University of Łódź, Poland

ABSTRACT

The extragalactic charged particles are reflecting from the Galaxy by its magnetic field. Assuming magnetic field in the Galaxy as quasilongitudinal we have evaluated mean transparency of Galaxy for extragalactic protons defined as a fraction of particles at a given energy from a given direction passing by the galactic plane. The anisotropy caused by the Galactic magnetic field reflection of protons can explain observed arrival directions of EAS at large angle to the galactic plane. Our analysis shows that the increase with energy observed in $\langle \sin b^{II} \rangle$ is self-consistent with changing in the cosmic ray energy spectrum at high energy ($E > 10^{19}$ eV) in the case when extragalactic cosmic ray source with spectral index -2.2 is at the position of the Virgo Cluster.

## I. INTRODUCTION

The measurements of energy spectrum and anisotropy of cosmic rays are the basic source of information about its origin. The main difficulty to identify the cosmic rays sources is the Galactic magnetic field. In the past we analized propagations of cosmic rays protons emmited by Galactic sources distributed as Galactic matter (Karakuła et al., 1972). The comparison of the calculated and observed extensive air showers (EAS) anisotropy shows that if protons are the primary cosmic rays of energy greater than $10^{18}$ eV they should be predominantly extragalactic. The study of EAS (i.e. Watson, 1980: Linsley and Watson, 1981) shown that cosmic rays at energies above $10^{19}$ eV are likly to be of extragalactic origin. The anisotropy of arrival directions of the highest energy cosmic rays is observed from the directions of the large angle to the galactic plane ($b^{II} \cong 74^{o}$) (Cunningham et al., 1980 and 1983). The experimental data confirmed the flattening of the cosmic ray energy spectrum at energy greater than $10^{19}$ eV and the exponent of the integral energy spectrum is $-1.4 \pm 0.1$ (Cunningham et al., 1980 and 1983: Bower et al., 1983).

In this paper we have considered the cluster or supercluster origin of high energy cosmic rays model, but for lower energy $E \lesssim 10^{18}$ eV we assumed Galactic location of cosmic ray sources. For the quasilongitudinal magnetic field in the Galaxy we have evaluated the mean transparency of the Galaxy for extragalactic protons. Our analysis shows that the increase with energy observed in $\langle \sin b^{II} \rangle$ (Cunningham et al., 1980) is self-consistent with changing in the cosmic ray energy spectrum at high energy ($\gtrsim 10^{19}$ eV) in the case when extragalactic cosmic ray source with spectral index -2.2 is at the position of the Virgo Cluster ($b^{II} = 74^{o}$).

## 2. THE TRANSPARENCY OF THE GALAXY FOR EXTRAGALACTIC PROTONS

The trajectory of arriving protons from the particular extragalactic directions were calculated assuming the mathematical model of the magnetic field in the Galaxy. In our calculations the magnetic field in the Galaxy was assumed as the quasilongitudinal model of Thielheim and Langhoff (1968). In this model the field lines are parallel to the spiral arms but with opposite orientation above and below the galactic plane. The strength of the component of the field parallel to the arms in details was described in our paper Karakuła et al., (1972). The galactic disc, where the trajectories of protons were calculated, was defined by $|z| \leq 0.4$ kpc (distance perpendicular to the galactic plane) and $R \leq 15$ kpc (radius from the Galactic Center). The equation of motion of the protons in the Galactic magnetic field was solved numerically. Our calculations indicated that some of the extragalactic particles are reflecting from the Galaxy by its magnetic field. Only extragalactic particles entering the Galaxy on the observing level can be registrated as an EAS. We have evaluated the mean transparency of the Galaxy which was defined as a fraction of the number of particles at a given energy from a given position of source passing through the plane located at a Solar System and perpendicular to the direction of the extragalactic source (observer plane). In practice for large $b^{II}$ this plane is the galactic disc plane ($z=0$). We have followed large number of the protons trajectories for selected energies. The positions of the starting point of the protons trajectories was at random selected on the plane outside the Galactic disc. The real magnetic field in the Galaxy has a regular and irregular components (magnetic clouds). Our model of the magnetic field in large scale describes the regular component. The nature and feature of irregular component are not known up to now. For our considerations we also assume that the general properties of this component should be weaker than the regular component and should follow the last one in whole Galaxy. So from the point of view of our considerations there is no difference between random occuring irregularities of magnetic field in the time of protons propagation and at random selected positions of the starting point of the proton trajectory for the model of regular Galactic magnetic field. Moreover in that case we evoid the problem of focusing of particles in quasilongitudinal magnetic field. The mean transparency parameter defined above is characteristic for the whole Galaxy. Figure 1 shows the mean transparency of Galaxy for extragalactic protons for the selected directions of the group of galaxies. The transparency of Galaxy increases with energy. We can also notice that the energy of protons, when galactic mag-

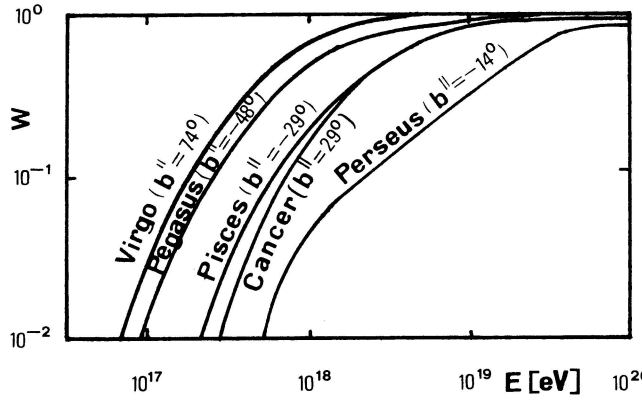


Fig. 1. The mean transparency of Galaxy as a function of proton energy.

netic field has a small influence on particles, strongly depends on the arriving positions relative to the Galactic plane.

## 3. THE EXPECTED FLUX OF THE COSMIC RAYS FROM THE VIRGO CLUSTER

The base of our analysis was the Haverah Park EAS data (Cunningham et al., 1980) indicating that the mean value of $\langle \sin b^{II} \rangle$ increases with energy.

In this paper we want to examine if the observed changes in energy spectrum of cosmic rays and $\langle \sin b^{II} \rangle$ are self- consistent, as far as our simple assumptions allow:

i) the galactic cosmic ray differential energy spectrum ($I_G$) for energy greater than $10^{19}$ eV has a power index -3.1,

ii) some extragalactic sources with an unknow spectrum ($I_{Ex}$) located at a position $b_o^{II}$ can give contribution to the observed flux,

iii) the probability of the registration of the extragalactic charged particles depends on its energy, because of the influence of the Galactic magnetic field.

In such case the mean value of $\sin b^{II}$ can be expressed by:

$$\sin b^{II} = \frac{\int I_G \cdot P(b^{II}) \cdot \sin b^{II} \cdot db^{II} + w(b_o^{II}) \cdot I_{Ex} \cdot P(b_o^{II}) \cdot \sin b_o^{II}}{\int I_G \cdot P(b^{II}) \cdot db^{II} + w(b_o^{II}) \cdot I_{Ex} \cdot P(b_o^{II})},$$

where:

$P(b^{II})$ - the probability of registration by Haverah Park array as the function of $b^{II}$,

$w(b^{II})$ - the transparency of the Galaxy versus energy for extragalactic protons.

The integral in the numerator of above expression gives the contribution from the galactic cosmic ray flux. The second component of this sum represents the contribution from the extragalactic point source located at the position $b_o^{II}$, after integration over the galactic latitude with the delta Dirac function. The denominator expresses the normalization coefficient in the definition of the mean value $\sin b^{II}$. The dependence of $\langle \sin b^{II} \rangle$ on the energy observed by Haverah Park was used to calculate the ratio of $I_{Ex}/I_G$ for extragalactic source which is located at the position of the Virgo Cluster. The ratio $I_{tot}/I_G$ is a constant for energy $E < 10^{19}$ eV and increases for the greater energy. Fig. 2 shows the differential total ($I_{tot} = I_G + I_{Ex}$) cosmic

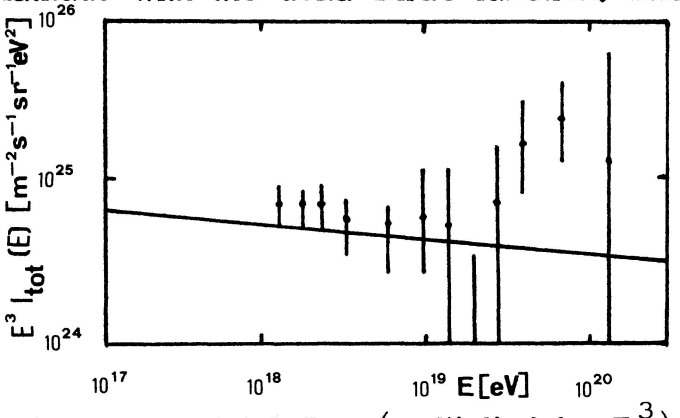


Fig. 2. The total flux (multiplied by $E^3$) calculated from $\langle \sin b^{II} \rangle$ as a function of energy.

ray flux multiplied by $E^3$ calculated from Haverah Park measurements of $\langle \sin b^{II} \rangle$ .

## 4. DISCUSSION AND CONCLUSIONS

From the comparisons of our results (Fig. 2) with experimental data of cosmic ray energy spectrum (Cunningham et al., 1980: Hillas, 1984) we can conclude good agreement. We have made the same calculations for different positions ($b_o^{II}$) of the extragalactic point sources but the best agreement we have got only for the position of the Virgo Cluster. It can be strong indication that high energy cosmic rays ($E > 10^{19}$ eV) are originated from this cluster. We can also notice that the differential cosmic rays energy spectrum of the Virgo Cluster has the spectral index $\simeq -2.2$, and in the energy range $\simeq 10^{18}$ eV the intensity of the Galactic and extragalactic fluxes are equal. In the lower energy region the Galactic cosmic ray flux is dominand.

## REFERENCES

Bower, A.J. et al., 1983, J.Phys. G: Nucl. Phys. 9, L53.

Cunningham, G., Lloyd-Evans, J., Pollock, A.M.T., Reid, R.J.O., and Watson, A.A., 1980, Astrophys. J. (Letters), 236, L71.

Cunningham, G., Lloyd-Evans, J., Reid, R.J.O., and Watson, A.A., 1983, Proc. 18th Int. Cosmic Ray Conf., (Bangalore), 2, 157.

Hillas, A.M., 1984, Ann. Rev. Astron. Astrophys., 22, 425.

Karakuła, S., Osborne, J.L., Roberts, E., and Tkaczyk, W., 1972, J. Phys. A: Gen. Phys. 5, 904.

Linsley. J., and Watson, A.A., 1981, Phys. Rev. Lett., 46,459.

Thielheim, K.O., and Langhoff, W., 1968, J. Phys. A: Gen. Phys. 1, 694.

Watson, A.A., 1980, Bull. Am. Phys. Soc., 25, 576.

# MODELING COSMIC RAY ANISOTROPIES NEAR $10^{18}$ eV

P. Sommers and J. W. Elbert

University of Utah, Department of Physics
201 JFB, Salt Lake City, UT 84112 USA

ABSTRACT

A galactic magnetic field reversal near the Sagittarius spiral arm may be responsible for the southern excess (or northern shortage) of cosmic rays near $10^{18}$ eV. The north-south asymmetry produced by such a reversal would increase with energy in the same manner as the observed asymmetry [1,2]. The existence of a reversal has been inferred from analyses of Faraday rotation measures [3,4].

I. The puzzle. Cosmic ray fluxes in the EeV range (1 EeV=$10^{18}$ eV) display a prominent anisotropy. The flux is suppressed at northern galactic latitudes, and the effect increases with energy through the decade .5-5 EeV [1,2]. This measured anisotropy should be instrumental in any attempt to piece together a picture of the Galaxy's magnetic field and the sources of high energy cosmic rays. Other pieces of this puzzle are the following:

1. The cosmic rays at this energy are probably mostly protons. This is based mainly on studies of the depth of maximum of air showers and the variance in the depths of maximum [5].

2. The mean galactic magnetic field near the sun has a magnitude of about 2.2 μG, and at least near the sun it is directed clockwise about the galactic center as viewed from north of the Galaxy [6]. Protons moving perpendicular to the field lines have orbit diameters D = E, where E is the energy in EeV and D is in kpc. The energy decade .5-5 EeV therefore provides probes up to distances of 5 kpc.

3. The sources of these cosmic rays are probably galactic. By virtue of Liouville's theorem, the anisotropic observed flux cannot come from an isotropic extragalactic flux. If the extragalactic flux is not isotropic but is coming primarily from the Virgo cluster, then it is very difficult to explain how the anisotropy could be turned into a southern excess over a whole decade of energies. It is conceivable, though, that some of the cosmic rays in this energy decade are coming from the southern side of the Galaxy (rather than from the Virgo cluster). For example, acceleration by galactic wind termination shock [7] might occur between the Galaxy and the Magellanic clouds and could preferentially fill the southern half of an extended halo. If the ordered magnetic field were confined to a thin enough disk, then a southern excess would be expected as these particles diffuse northward. Any such model would be rather contrived, however, since it would require a southern source to be prominent only in a limited energy band where no remarkable spectral bump is observed. In the following we will assume that EeV cosmic rays are of galactic origin.

4. The magnitude of the disordered part of the galactic magnetic field is not much greater than the mean (ordered) field strength, even in dense clouds [8,9]. An abrupt large-angle change in a particle's direction is therefore rare. The scale of magnetic irregularities probably does not exceed 150 pc [10]. For EeV protons whose orbit circumferences are several kiloparsecs, the orbits therefore sense primarily the mean field but suffer frequent small deflections from magnetic irregularities.

5. The ordered galactic magnetic field is probably not confined to a thin disk, but may extend 3 kpc or more to either side of the plane. If the ordered field were confined to a thin disk of 1 kpc full thickness, for example, then at energies above 1 EeV no proton orbiting perpendicular to the field direction could be confined. At several EeV a pronounced excess would be detected from directions nearly parallel or anti-parallel to the field direction. Moreover, just below 1 EeV, protons orbiting perpendicular to the field lines would be confined only if their orbits met the galactic plane nearly perpendicularly. In particular, arrivals from the galactic center and anti-center directions would be strongly suppressed. In evaluating the thickness of the ordered magnetic field, it would be helpful to have not only the observed dependence of flux (at various energies) on the north-south variable (galactic latitude) but also the mean flux values projected onto the galactic center-anti-center axis as well as flux values projected onto the axis parallel to the mean field direction.

6. Analyses of Faraday rotation measures [3,4] suggest that a reversal of the ordered field occurs between the sun and the galactic center. Various estimates exist for the distance to the reversal, but a distance of 2 kpc may be realistic. Field reversals of this type are seen in other spiral galaxies (M51, M33, M81, NGC 6946, NGC 4258) [11,12]. Among the spiral galaxies whose fields have been mapped, M31 is exceptional in not showing a field reversal [13,14].

II. Assembling a picture. Putting together pieces 4 and 5 one finds that EeV cosmic rays are governed by a large-scale ordered magnetic field. In this context Hillas [15] has made the following cogent argument that a southern excess at Earth implies the existence of a radial gradient in the cosmic ray density: Liouville's theorem requires that the intensity (per unit area and solid angle) from the south at point P in figure 1 must equal the intensity from the north at earth. The observed southern excess at earth then implies that the intensity from the south at earth exceeds the intensity from the south at P. Similarly, the intensity from the north at Q exceeds the intensity from the north at earth. Therefore the northern and southern intensities increase with galactic radius. It can also be shown that if the density of cosmic ray orbit centers increases linearly with galactic radius near the sun, then the observed north-south asymmetry should increase linearly with energy (i.e. orbit size).

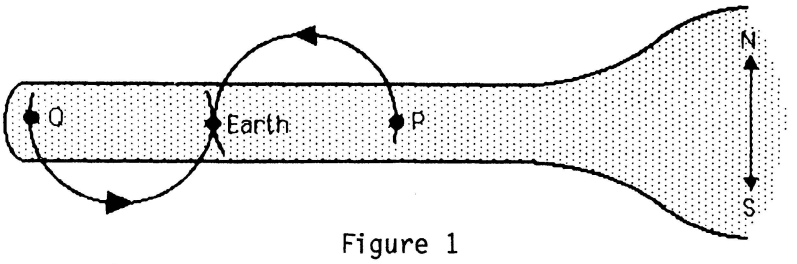


Figure 1

If the orbits shown in Hillas' figure are proton orbits at 4 EeV (where the southern excess is very prominent), then points P and Q are separated by 8 kpc. Even if one considers trajectories of median pitch angle, the inferred radial gradient persists over 4 kpc. A source density variation over such large distances would not be due simply to variation within or between spiral arms. We know of no reason why high energy cosmic ray sources should be more abundant at larger galactic radii.

If the cosmic ray density gradient is not due to a source gradient, then it must be due to some propagation effect. Instead of excess sources outside the sun's galactic orbit, one can look for a sink region closer to the galactic center. A field reversal region is an effective evacuation site for cosmic rays. Figure 2 shows some of the fast-escaping trajectories near a reversal. (The shaded regions are regions where grad$|B| \neq 0$.)

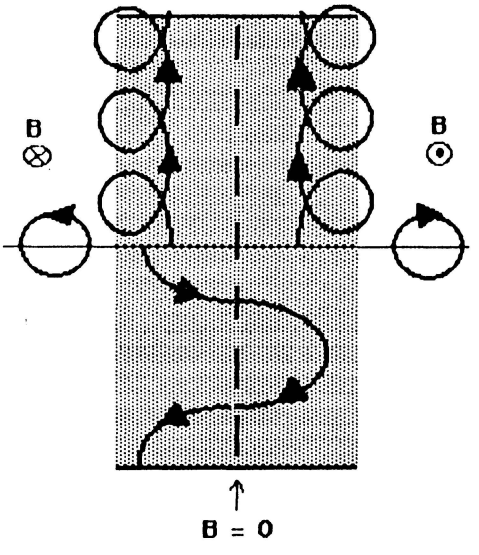


Figure 2

The field reversal zone is then a region of low cosmic ray density, so a density gradient points away from that region (radially outward at the sun's position). Orbits of very high energy cosmic rays could be affected directly by the field reversal, causing a pronounced shortage at high northern latitudes.

Our numerical simulations confirm that the energy dependence of the northern shortage (southern excess) can arise from a uniform source density if there is a field reversal at about 2 kpc with a gradient region of .5 kpc on either side of it and if there is some admixture of isotropic flux from the halo or intergalactic space.

III. Remarks. A definitve explanation for the northern shortage of EeV cosmic rays may not be possible without more detailed knowledge of the galactic magnetic field and cosmic ray sources. If careful analysis determines that the ordered magnetic field is, after all, confined to a thin disk, then a planar excess model [16] (i.e., shortage at north and

south poles) might be a complete explanation for the anisotropy. Or perhaps it will be found that a significant fraction of EeV cosmic rays are heavy nuclei, in which case a spiral arm source density gradient could be the correct explanation. In fact, each puzzle piece is rather fuzzy. In support of the field reversal explanation, we only claim that it is a picture which is composed of the pieces described above and which requires no special ad hoc pieces.

Acknowledgement.
This research was supported by the United States National Science Foundation under grant number PHY8415294.

References

1. Astley, S.M. et al. Proc. ICRC 17 (Paris) 2, 156 (1981).
2. Efimov, N.N. et al. Proc. ICRC 18 (Bangalore) 2, 149 (1983).
3. Simard-Normandin, M. & Kronberg, P.P. Ap. J. 242, 74 (1980).
4. Thomson, R.C. & Nelson, A.H. Mon. Not. R. astr. Soc. 191, 863 (1980).
5. Chantler, M.P. et al. J. Phys. G 9, L27 (1983).
6. Manchester, R.N. Ap.J. 188, 637 (1974).
7. Jokipii, J.R. & Morfill, G.E. Ap.J. 290, L1 (1985).
8. Troland, T.H. & Heiles, C. Ap.J. 252, 179 (1982).
9. Fleck, R.C. Ap.J. 264, 139 (1983).
10. Jokipii, J.R. et al. Ap.J. 157, L119 (1969)
11. Sawa, T. & Fujimoto, M. Publ. Astron. Soc. Japan 32, 551 (1980) (and references therein).
12. Klein, U. et al. Astron. Astrophys. 108, 176 (1982).
13. Beck, R. Astron. Astrophys. 106, 121 (1982).
14. Sofue, Y. & Takano, T. Publ. Astron. Soc. Japan 33, 47 (1981).
15. Hillas, A.M. High Energy Astrophysics (Moriond Meeting 1984, pp. 11-26) Kim Hup Lee Co. (Singapore).
16. Wdowczyk, J. & Wolfendale, A.W. J.Phys. G 10, 1453 (1984).

# Anisotropy and the Knee of the Energy Spectrum

R.W. Clay

Physics Department, University of Adelaide,
South Australia 5000

1. Introduction The measured cosmic ray energy spectrum exhibits clear structure (the knee) at ~ 3 x $10^{15}$ eV (sea level shower size ~ 3 x $10^5$ particles). Additionally, at energies in this general region, there occur apparent changes in shower development such that the observed characteristics of showers at this energy appear different to those characteristics observed at somewhat higher energies (see eg. Linsley 1983). At energies just below this region, the cosmic ray anisotropy amplitude apparently begins a progressive increase with energy. The latter effect does not clearly fit with the first two since there appears to be no significant change exactly at the knee. However, the phase of the first harmonic of the anisotropy appears to show a substantial change just where the energy spectrum shows structure and in the middle of the shower development changes. The first harmonic phase appears to change from ~ 18 hours R.A. to ~ 5 hours R.A. (see eg. Clay (1984)) as the energy of observation moves through the knee. In this paper I wish to examine the latter change in some detail by taking into account information contained in the second harmonic of the anisotropy.

2. Anisotropy measurements near the Knee Anisotropy measurements at one location are not sufficient to define the true celestial anisotropy since only a limited range of declinations is observable at a given latitude. This limitation is particularly severe for air shower arrays which use scintillators to sample the electron-photon component since atmospheric attenuation with increasing zenith angle is severe. This effect was useful for collimation in early experiments. Available anisotropy results are therefore, unfortunately, rather incomplete with measurements being biased towards temperate latitudes with convenient land sites. The overall sky coverage of most experiments is ~ 20° to 60° N and ~ 15° to 40° S. At ~ $10^{15}$ eV, just below the knee, there is a good deal of agreement between the various experiments on the observed phase of the first harmonic. This is remarkable because the southern observations really view an independent part of the celestial sphere to the northern observations.

There is an ambiguity in anisotropy results presented in terms of first harmonics. A sine wave is fitted to the data in right ascension but there is no information on what properties of this fourier component are of physical significance. It is not obvious, although it is conventionally stated, that the phase of the maximum of the fitted wave is physically appropriate, unless, for instance, one is interested in searching for the superposition of a number of high energy gamma ray sources. In the latter case, the anisotropy maximum will indicate a direction with an excess of sources. However, for the diffusion of

charged particles, the position of maximum on the celestrial sphere will give the direction of the "upstream" diffusion direction and there will be a minimum in the "downstream" direction. In general, a particular declination will not include both the upstream and downstream directions leading to an ambiguity for latitudes which include observation of only the downstream direction.

I have pointed this out before (Clay 1984) and shown that, on the basis of the observed directions of first harmonic maxima at $\sim 10^{15}$ eV , one might interpret the global data as representing a diffusive flow of cosmic rays along the galactic spiral arm. In order that this be so, it is necessary that, at energies below the knee, the southern hemisphere phase of the first harmonic minimum is the physically interesting parameter since this represents the direction towards which diffusion is occurring. Other explanations of the overall anistropies at these energies are possible and one suggestion has been that they may be due to unresolved ultra high energy gamma ray sources (Wdowczyk and Wolfendale 1983). A test between these possibilities would be to see whether or not there is any additional reason in the data for the first harmonic minimum to appear to be more physically significant rather than the maximum.

In the diffusive model, since the spiral arm is of limited extent in the sky, one would expect a relatively sharp peak of the anisotropy in the source direction and a similar trough in the downstream direction. In the gamma ray source model, only positive effects due to an admixture would be expected and no particular sharp dips or peaks would be necessary. In the latter case, one might in general expect only a diffuse excess for general galactic directions unless only specific galactic region contained the most powerful sources. An examination of the second harmonic can help resolve these possibities.

3 Inclusion of the Second Harmonic Figure 1 shows data obtained by Farley and Storey (1954). The phase of the first harmonic maximum is indicated and it would appear that there is no particular significance in this phase. The total data set can be described quite well with the inclusion of the second harmonic as illustrated. Also, an examination of figure 1 suggests that the region at about 8 hours is likely to be physically interesting rather than the 20 hour phase. This is in the vicinity of the minimum of the first harmonic.

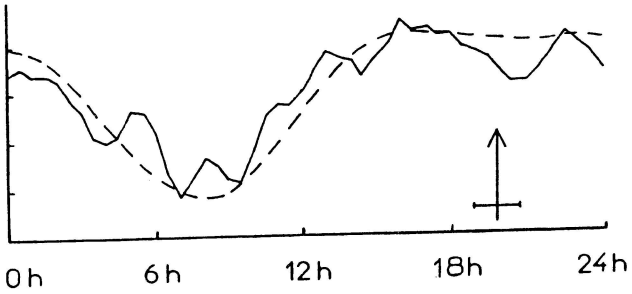


Fig. 1 Data presented by Farley and Storey 1954. The combination of their first and second harmonics are included (unnormalised) together with an indication (arrow) of the phase of the first harmonic maximum.

I have examined the data included in the compilation of anisotropies by Linsley and Watson (1977) and have also included more recent Adelaide data (Gerhardy and Clay 1983). Where appropriate I have combined data from similar latitudes and energies and have added first and second harmonics to derive representations of the original data in terms of R.A. or sidereal time. I then examined these distributions to see whether or not they subjectively contained a peak or a trough and, at what celestial direction this occurred. Some results of this procedure are shown in figure 2 with peaks indicated by + and troughs by −.

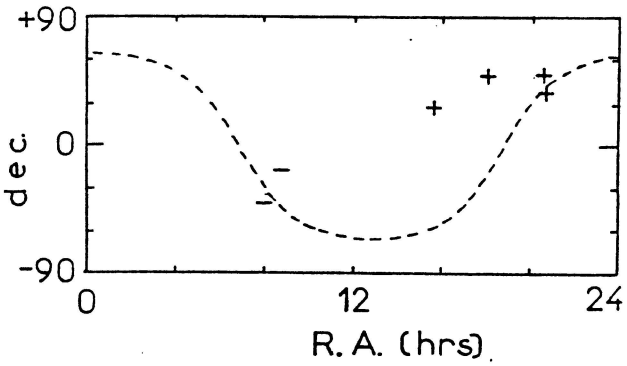


Fig. 2 The positions of peaks (+) or troughs (−) in anisotropy data available for energies ~ $10^{15}$ eV.

Figure 2 indicates that this procedure lends weight to the hypothesis that the cosmic ray flow below the knee is diffusive with its source in the inward spiral arm direction. There are peaks from a number of experiments clustering generally in that direction and there are also apparently troughs in the opposite direction from independent experiments in the other hemisphere.

At higher energies, the situation is much less clear. It seems to me likely that the statistical uncertainty in detail of the anisotropy is such that the technique cannot be used for such small data sets where the overall flux is low.

4. Conclusions When anisotropy results are presented in terms of the phase of first harmonic maximum, that particular direction may not be the physically significant direction for the data set. Additional use of the second harmonic can clarify this when data with sufficient statistics are available. It appears that, at least at $10^{15}$ eV, cosmic ray anisotropy data are most compatible with diffusion along the galatic spiral arm from the inner to outer galactic regions.

References

Clay, R.W. (1984) Aust. J. Phys, 37, 97.
Farley, F.S.M. and Storey. J.R. (1954) Proc. Phys. Soc. A67, 996.
Gerhardy, P.R. and Clay, R.W. (1983) J. Phys. G, 9, 1279
Linsley, J. and Watson, A.A. (1977) Proc. 15th Int. C.R.C. (Plovdiv), 12. 203.
Linsley, J. (1983) Rapporteur 18th Int. C.R.C. (Bangalore) 12, 135.
Wdowczyk, J., and Wolfendale, A.W. (1983) Nature, 305, 609.

# ANISOTROPY OF COSMIC RAYS ABOVE $10^{14}$eV

Wdowczyk, J.
Institute of Nuclear Studies, Lodz, Poland.
Wolfendale, A.W.
Physics Department, University of Durham, Durham, U.K.

ABSTRACT

A survey is made of the anisotropy of cosmic rays at energies above $10^{14}$eV. It is concluded that cosmic γ-rays may have an effect in the range $10^{14}$-$10^{16}$eV, above which protons dominate. Evidence is presented for an excess in the general direction of the Galactic plane which grows with increasing energy until about $10^{19}$eV, indicating a Galactic origin for these particles. At higher energies an Extragalactic origin is indicated.

1. Introduction. Many surveys of cosmic ray anisotropy measurements have been made in recent years and a consistent picture is emerging as to the manner in which the amplitude of the first harmonic and its phase varies with energy. In our own work (Wdowczyk and Wolfendale, 1984a,b) we have extended the analysis to a study of both first and second harmonics and separately for the northern and southern hemispheres. Figure 1 gives the results for the amplitudes and Figure 2 concerns the phases.

It is our objective to explain the observed trends; this can be done most conveniently by energy range.

2. The range $10^{14}$-$10^{16}$eV. Inspection of Figure 2 leads us to suggest that for E : $10^{14}$-$10^{16}$eV we are dealing with a region where γ-rays contribute significantly to the anisotropy, this suggestion following on earlier work (WW 1983) which in turn was prompted by the Cygnus X-3 observations. Gamma ray sources are expected preferentially at small Galactic longitudes and this feature appears in Figure 2 (viz. the shaded area near $\ell \simeq 0°$ for $10^{14}$-$10^{16}$eV). At higher energies γ-rays are apparently unimportant insofar as the anisotropy is concerned.

3. $10^{16}$-$10^{19}$eV. A different feature appears at higher energies. Between about $5.10^{17}$eV and $10^{19}$eV there appears to be an enhancement centred on the Galactic plane but as the energy falls the pattern appears to be rotated. Figure 3 shows the situation. The obvious explanation is that we are dealing here with charged particles; the change of $\phi$ with falling energy is in the sense of that expected due to the curvature of the local magnetic field lines (the field analysis having come from earlier work by Karakula et al., 1972, Osborne et al., 1973, and Ellis and Axon, 1978).

4. Energies above $10^{19}$eV. In our earlier work (WW 1984a,b) we defined a Galactic plane excess parameter, $f_E$, defined by $I(b) = I(O)\ \{(1-f_E + f_E \exp -b^2\}$ where b is the Galactic latitude. The analysis shows that $f_E$ rises with energy, being $\sim 0.1$ at $10^{18}$eV, 0.3 at $5.10^{18}$eV and 0.6 at $2.10^{19}$eV. However, at the very highest energies, $f_E$ appears to drop

(to $\tilde{\sim}$ 0.25) indicative of the bulk of the particles being extragalactic, a result that is in accord with other work.

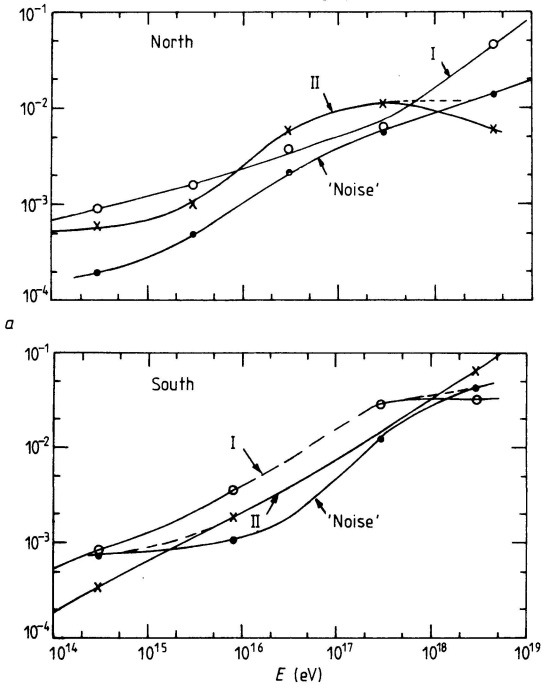


Fig. 1. Amplitudes of the first (I) and second (II) harmonics of anisotropy measurements averaged over successive decades of energy. The measurements in the Northern hemisphere (upper part) were from extensive air shower arrays located at latitudes from 43°N to 62°N. Those in the Southern hemisphere (lower part) cover the range 16°S to 37°S. The curve denoted 'noise' relates to expectation from a true distribution with zero anisotropy, measured isotropies arising simply by chance. The significance level is one standard deviation.

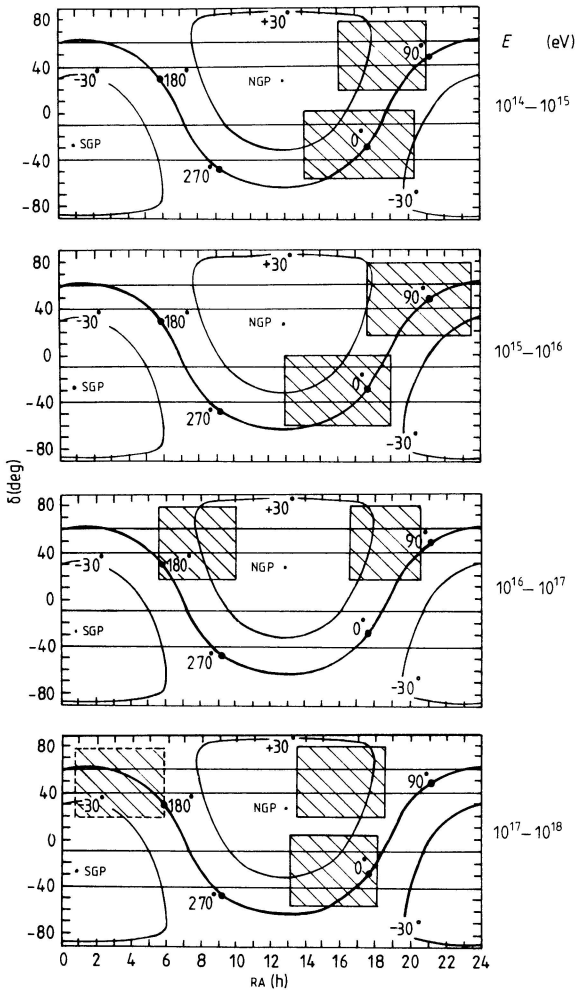


Fig. 2. Celestial plots showing the directions from which much of the excess flux arises. The data suggest the presence of an excess associated with the Galactic plane in the Inner Galaxy for the energy region $10^{14}$-$10^{16}$eV. At higher energies the excess from the Inner Galaxy moves to Northern Galactic latitudes, reaching $b \simeq 30°$ for the range $10^{17}$-$10^{18}$eV.

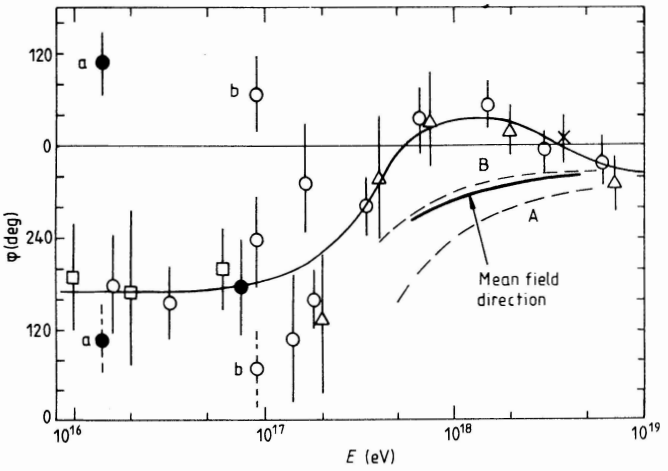


Fig. 3. Angle $\phi$ through which the prediction of the Galactic plane excess should be rotated in order to fit best the observed pattern of intensity against RA (after WW, 1984a). The points marked 'a' and 'b' are plotted twice. The full curve is intended to guide the eye. The broken curves give the directions from which detectors in the Northern hemisphere should record maximum intensities using the Galactic magnetic field models of Karakula et al. (1972). The data available on the very local field direction, which allows for irregularities, give the line indicated 'mean field direction' - for comparison with the trend of $\phi$ it should be displaced to lower energies by $\sim 3$.

5. Conclusions. The present analysis suggests that $\gamma$-rays play a key role in explaining the trend of anisotropy phase with energy in the range $10^{14}$-$10^{16}$eV. Very recently support has come from the Backsan experiment (Alexeenko and Navarra, 1985) but the hypothesis cannot be regarded yet as completely proven: a 'Galactic ridge' of muon poor showers with high precision is a pre requisite. Above $10^{16}$eV the behaviour of the anisotropy with energy is indicative of charged particles providing the bulk of the anisotropy, those below $10^{19}$eV being Galactic and the very highest energies extragalactic in origin.

References

Alexeenko, V.V., and Navarra, G. (1985), Nuovo Cim. (in press).
Ellis, R.S., and Axon, D.J. (1978), Astrophys. Space Sci. 54, 425.
Karakula, S. et al. (1972), J. Phys. A.: Gen. Phys. 5, 904.
Osborne, J.L., Roberts, E., and Wolfendale, A.W., (1973), J. Phys. A: Math., Nucl. Gen. 6, 421.
Wdowczyk, J., and Wolfendale, A.W. (1983), Nature, 305, 609: (1984a), J. Phys. G, 10, 1453, (1984b), J. Phys. G., 10, 1599.

OG 5.4-12

# A MODEL FOR THE PROTON SPECTRUM AND COSMIC RAY ANISOTROPY

Xu Chun-xian
Institute of High Energy Physics, Academia Sinica
P.O.Box 918 Beijing, China

## 1. Introduction.

The problem of the origin of the cosmic rays is still uncertain. Since the observed cosmic ray composition, spectrum and anisotropy involve a lot of factor, for example, the spectrum of the primordial cosmic rays, the mechanism of acceleration and propagation as well as the distribution of the interstellar medium and magnetic field. Unfortunately, all of these are remained open, though people gets more and more information and ideas. As a theory, it should explain the support of particles and energy, the mechanism of acceleration and propagation as well as some important features obtained directly from cosmic ray experiments, such as the power spectrum and the knee at about $10^{15}$eV[1], the near constant amplitude of the first harmonic of anisotropy among $10^{11}$-$10^{14}$eV and the amplitude varying as $E^{0.5}$ above $5\times10^{15}$eV[2,3]. And it should also account for the relative abundance and the flux of cosmic rays. But so far there is no model which can interpret all of these phenomena.

In a general opinion the cosmic rays of $10^{10}$-$10^{18}$ eV are the galactic origin,but above they are the extragalactic origin. People also acceptes that the cosmic rays propagate in a diffusion way, variaty of diffusion mechanism derive different diffusion coefficient as a function of energy. But anyhow diffusion always makes the energy spectrum steeper.

There are two kinds of models for interpreting the knee of the cosmic ray spectrum. One is the leaky box model[1] in which every nuclei has different escape starting rigidity,the heavier the higher, but the flux of heavy nuclei is much less. Another model[4] suggests that the cut-off rigidity of the main sources causes the knee. The present paper studies the spectrum and the anisotropy of cosmic rays in an isotropic diffuse model with explosive discrete sources in an infinite galaxy.

## 2. The transport equation and its solution.

In an isotropic diffusion model cosmic ray density,N(r,t,E), obeys the following equation[5]

$$\frac{\partial N}{\partial t} - D\nabla^2 N + \frac{\partial}{\partial E}(NW) + BN = Q. \qquad (1)$$

where D is the diffusion coefficient, the third term is due to energy loss, W=dE/dt, the fourth term is negitive source and Q is the source. Firstly, starte our argument from one discrete source and assume as follows:

(1) Because the ages of the main point sources within 1kpc (table.1) are about $10^4$y[6], even for the highest energy proton its half lifetime(caused by Compton scattering, synchrotron radiation and bremstruhlung altogether) is several

decades to few hundred times long as its age. So we neglect the energy loss.

(2) Assume the P-P interaction contributs to the negtive source term only, $B=cn\sigma_{ine}$, where c is the speed of light, n the density of hydrogen, $\sigma_{ine}$ the inelastic cross-section of P-P interaction. From accelerator experiments[7] the total cross-section of P-P is obtained among energy range 10-1.5x10$^6$ GeV, and $\sigma_{ine}=0.8\,\sigma_{tot}$. Fitting these data, get the formula

$$B(E)=3\times10^{-17}[35.3-2.2(\ln E)+0.3(\ln E)^2]\ (1/s). \quad (2)$$

here n =1 has been taken.

(3) The charged cosmic rays propagate through resonant scattering with the turbulent hydromagnetic wave. Zhang et al[8] derived

$$D=\frac{1}{12\pi}\frac{\beta}{\sqrt{1-\beta^2}}\frac{\bar{B}}{e}\frac{mc^2}{\Lambda\varepsilon_B}.$$

rewrite it as

$$D=\frac{Pc}{12\pi e}\frac{\bar{B}c}{\Lambda\varepsilon_B}. \quad (3)$$

where $\bar{B}$ and $\varepsilon_B$ is the mean intensity and energy density of the fundamental magnetic field, respectively. $\Lambda$ is the fraction of turbulent in the mean field. Take $B=3\mu G$, $\Lambda=0.01$, $\varepsilon_B=0.3eV/cm^3$, then for the proton of greater than 10GeV,

$$D=1.67\times10^{15}E(cm^2/s).$$

Table 1. List of SNR near the solar system

| NAME | t(10 y) | r(kpc) | E (eV) |
|---|---|---|---|
| CTB 72 | 3.2 | 0.7 | 2x10 |
| Cyg. Loop | 3.5 | 0.6 | 10 |
| HB 21 | 2.3 | 0.8 | 3x10 |
| CTB 1CT | 4.7 | 0.9 | 2x10 |
| CTB 13 | 3.2 | 0.6 | 10 |
| HB 9 | 2.7 | 0.8 | 2x10 |
| S 149 | 4.3 | 0.7 | 10 |
| Monoceros | 4.6 | 0.6 | 7x10 |
| Vela | 1.1 | 0.4 | 10 |
| Lupus | 3.8 | 0.4 | 4x10 |
| Loop | 3.0 | 0.05 | 10 |

In general the coefficient has a form $D\propto E^{\frac{1+\nu}{2}}$, say $E^{0.5}$, but the recent data from HEAO-3 show that the index trends to rising and $D\propto E^{0.7}$ can account for the experimental data quite well. A compare shows that the diffusion coefficient adopted by our paper is close to that with the index 0.7 at high energies.

(4) The i-th point source ejects particles transiently with a spectrum $N_0E^{-\Gamma}$ at t=0. So that $Q=N_0E^{-\Gamma}\delta(\vec{r}-\vec{r}_i)\delta(t_i)$

Combining of all these and transforming $N=\mathcal{N}e^{-\beta t}$, we get solution of Eq.(1)

$$N_i=\frac{N_0E^{-\Gamma}}{(4\pi Dt_i)^{1.5}}\exp[-\frac{r_i^2}{4Dt_i}-B(E)t_i] \quad (4)$$

where $t_i$ is the age of the point source, $r_i$ the radial distance with its origin at the source position. Mathematically, the formula(4) makes sense for any value of $r_i$ and $t_i$, but considering the causality only such sources with $(r_i/t_i)<c$ contribute to the observed flux. So we take account such sources only.

3. The predict spectrum of proton.

From Eq.(4) see that for very old/and distant pointsource its density $N_i$ has a very large Gaussian width, i.e. $\nabla N_i=0$, so we can treat them altogether as a background $N_B$. Therefor

we have

$$N=N_B+\sum_i N_i \qquad (5)$$

supposing v is isotropy and neglecting higher than second harmonic anisotropy of I, then $N=4\pi I/v$, we have

$$I=I_B+\sum_i I_i \qquad (6)$$

Taking the parameters =1.5, $N=4\times10^{47}$, $I_B=2.5\times10^{4}E_{4eV}^{-2.8}$ (m.s.sr.GeV)$^{-1}$ and inserting these values of $r_i$, $t_i$, of the eleven supernovea in Eq.(6), we have the result(Fig.1). You can see that the predict results fits the data of the proton quite well. In fact, because of the cut-off energy of the eleven supernovea, the value of $I_B$ is almost uniquely determed by the data of the proton of $10^{11}$ -$10^{12}$eV. It is clear that the time scale of change of the proton intensity $\tau>1/cn\sigma_{inel}=10^{7}$ y, it agrees with long time data of cosmic rays.

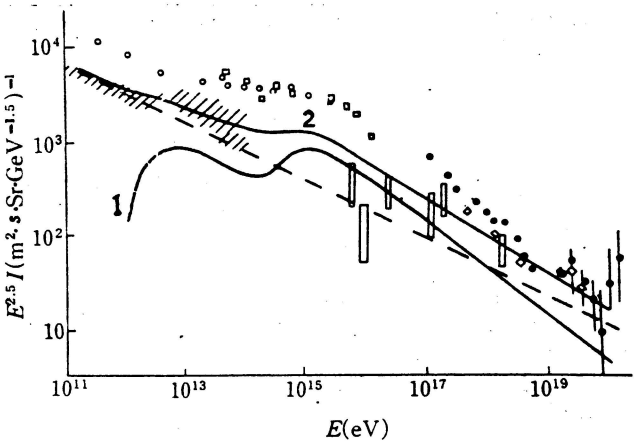


Fig. 1 The differential spectrum of primary cosmic rays Curve 1 is the sum of intensities contributed by eleven supernovae. The dashed line represents the background $I_B$. Curve 2 is the predicted differential spectrum of primary protons. Shaded area and sign □ are the data of protons, the rest are somewate contaminated by other nuclei.

4. The anisotropy of cosmic ray.

Under above mentioned case, the amplitude of first harmonic anisotropy has been obtained

$$\vec{\delta}_i=\left(\frac{3r_iN_i}{2Ct_iN}\right)\vec{r}_{oi} \qquad (7)$$

where $r_i$ is the unit vector from the Earth to the i-th point source. Considering the motion of the Earth with respect to the cosmic ray background there will be Compton-Getting anisotropy, independent of energy but relevant to the spectrum index

$$\delta_c=(\gamma+2)v/c \qquad (8)$$

so the final resultant anisotropy, can be expressed as

$$\vec{\delta}_F=\vec{\delta}_c+\sum_i\left(\frac{3r_i}{2Ct_i}\right)\left(\frac{N_i}{N}\right)\vec{r}_{oi} \qquad (9)$$

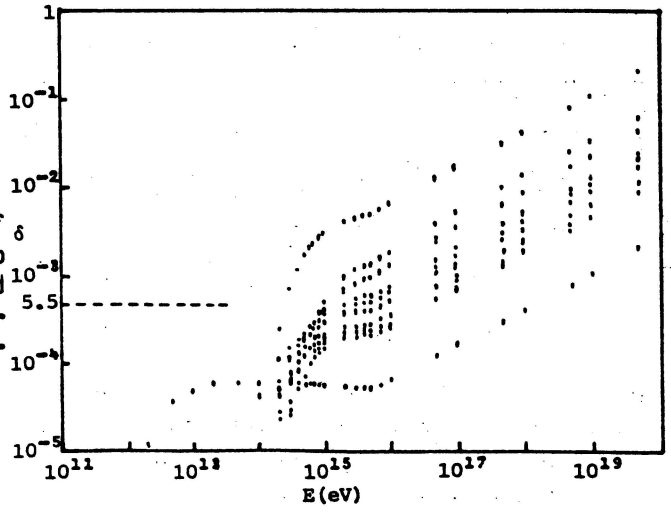


Fig.2. The expected amplitudes of the anisotropy caused by eleven SNR individually.

The experimental data show that

$N=4\pi I/c=1.2\times10^{-3}E^{-2.66}(1/m^3)$ for $E\leq5\times10^6$ GeV
$N=1.1\ E^{-3.1}(1/m^3)$ for $E>5\times10^6$ GeV

Inserting these values of $r_i$, $t_i$, $N_i$ of the eleven supernovea individually and the value of N into Eq.(7), using the trial values $N_0=1.32\times10^{45}$, $\Gamma=1.2$(corresponding to the source emission $10^{50}$ ergs in the particle form),the anisotropies as a function of energy were calculated.The results are given in Fig.2.

We find that each of these anisotropies is smaller than $6\times10^{-5}$ below $10^{14}$eV, but varies as $E^{0.4}$ above $5\times10^{15}$eV.So whatever the direction of each anisotropy is, the resultant anisotropy always has a $E^{0.4}$ variation. On hte other hand, the measured anisotropies are about $5.5\times10^{-4}$ in the energy range $10^{11}$-$10^{14}$eV. Combination of these information together leads us to draw the conclusion that the Compton-Getting anisotropy is dominant, $\delta=\delta_c=5.5\times10^{-4}$below $10^{14}$eV.By substituting $\gamma=2.66$ in Eq.(8), we get the velocity of 35km/s with respect to the cosmic ray background.

## 5. Discussion and conclusion.

The anisotropy mentioned above is in principle for proton. However, the anisotropy is dependent on the species of cosmic rays.Unfortunately,so far the identification of the species of cosmic ray in EAS is uncertain yet.Recently,a few of discrete $\gamma$-ray sources in the energy range $10^{15}$-$10^{16}$eV has been detected.People have noted the possible effect of $\gamma$-rays on the anisotropy and the intensity of cosmic rays[9].

The conclusion to be drawn from this study may be summarized as follows: Taking some reasonable parameters,the model can account for the features of the proton spectrum and the approximate constancy of the cosmic ray intensity in a long period.It also can interprete the power law of the anisotropy above energy $5\times10^{15}$eV,and the Compton-Getting effect is responsible for the anisotropies in the energy range $10^{11}$-$10^{14}$ eV. Furthermore, we got the streaming velocity of 35km/s with respect to the cosmic ray background.

Finally, I am grateful to Prof.A.W.Wolfendale for his helpful discussion and useful information.

REFERENCES

1.Hillas,A.M.,Proc. of the Cosmic Ray Workshop(Ed.by T.K. Gaisser),University of Utah, 1983 p.1
2.J.Linsley and A.A.Watson, 15th ICRC 12(1977)203
3.Ormes,J.F., 18th ICRC 2(1983)187
4.Peters,B.and N.Westergaard, Astrophys. Space Sci.,48(1977)21
5. Osborne,J.L., Origin of Cosmic Rays(Ed.by J.L.Osborne and A.W.Wolfendale),D.Reidel Pub.Co.,Dordrecht,Holland(1974)203
6.J.Nishimura et al., 16th ICRC 1(1979)488
7.Battiston,R. et al., CERN/EP, No. 111 1982
8.Zhang He-qi et al., Chinese Journal of Space Science, 1(1981)15
9.J.Wdowczyk and A.W.Wolfendale, Nature 305(1983)609

# INTERPRETATION OF COSMIC-RAY ANISOTROPY BELOW $10^{14}$ eV

L.C.Tan
Department of Physics and Astronomy
University of Maryland
College Park, MD 20742
USA

We have found that the measured data on the degree of anisotropy of cosmic rays are consistent with our proposed nonuniform galactic disk model. Moreover, we point out that the abrupt increase of the anisotropy of cosmic rays beyond $10^{14}$ eV should imply a change of their mass composition.

It appears that a nearly constant degree of anisotropy of cosmic rays ($\delta$) below $10^{14}$ eV is in conflict with the usual leaky box model(1). Thus it is interesting to examine the cosmic-ray anisotropy calculation in our proposed nonuniform galactic disk (NUGD) model(2).

In the NUGD model the observed $\delta$ value should be characteristic of the magnetic tube (Box 1 in Fig. 1 of OG 7.2-10), because the solar system is assumed to be located inside it. Along the magnetic tube cosmic-ray protons should present a streaming motion. It is adequate to describe this motion by using a one-dimensional slab model

$$\frac{dN_{pI}}{dx_I} = -\frac{N_{pI}}{\lambda_p^i} + \int_{E_p}^{\infty} \frac{1}{\lambda_p^i} \frac{dN_p(E_p,E'_p)}{dE_p} N_{pI}(E'_p)dE'_p \quad , \tag{1}$$

where $N_{pI}$ is the proton intensity in Box 1, $x_I$ is the pathlength travelled by cosmic rays along the magnetic tube, $E_p$ is the total energy of a proton, $\lambda_p^i$ is the mean inelastic interaction length of interstellar protons and $dN_p/dE_p = 1/E'_p$ is the energy distribution of protons after their inelastic interactions with the interstellar medium(ISM). At high energies the diffusive motion approximation of cosmic rays means

$$x_I = x_{0I} E_p^{-\delta_e} \quad , \tag{2}$$

where $x_{0I}$ is a constant and $\delta_e = 0.7$(3). Eq. (1) then can be reduced to

$$\frac{dN_{pI}}{dx_I} = -\frac{N_{pI}}{\lambda_p^{att}} \quad , \tag{3}$$

where $\lambda_p^{att} = \lambda_p^i/(1-1/\gamma_p)$ and $\gamma_p$ is the differential spectral exponent of the high-energy proton spectrum. Hence in the solar neighbourhood the proton intensity $N_{pIs}$ should be

$$N_{pIs} = N_{p0I} \exp(-x_{0Is} E_p^{-\delta_e}/\lambda_p^{att}), \tag{4}$$

where $N_{p0I}$ is the initial value of $N_{pI}$ and $x_{0Is} = 0.4\lambda_p^i$ (4). For $E_p \geq 10^{11}$ eV the mean gradient of cosmic rays along the magnetic tube is

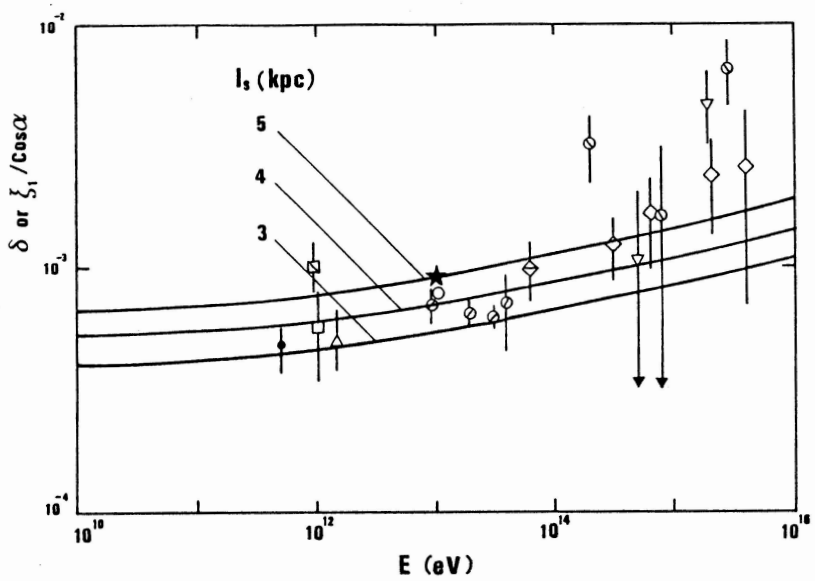


Fig. 1

$$\frac{1}{N_{pI}} \frac{dN_{pI}}{dl_I} = \frac{x_{Is}}{l_s \lambda_p^{att}} \quad , \tag{5}$$

where $l_s$ is the distance along the magnetic tube between the $H_2$ cloud region and the solar system. Under the diffusive motion approximation of cosmic rays we also have

$$\tau_{Is} = l_s^2 / 2\kappa_I \quad , \tag{6}$$

where $\kappa_I$ is the diffusion coefficient of cosmic rays in Box I and $\tau_{Is}$ is the transit time to reach the solar neighbourhood. Since

$$\tau_{Is} = x_{IS} / (m_p \bar{n}_I c), \tag{6}$$

where $m_p$ is the proton mass, $\bar{n}_I$ is the mean hydrogen atom density of the ISM in Box I and c is the velocity of light, we can get

$$\kappa_I = m_p \bar{n}_I c l_s^2 / (2x_{Is}) \quad , \tag{8}$$

and the degree of anisotropy of cosmic rays(5)

$$\delta = \frac{3\kappa_I}{c} \frac{1}{N_{pI}} \frac{dN_{pI}}{dl_I} = \frac{3 m_p \bar{n}_I l_s}{2 \lambda_p^{att}} \quad . \tag{9}$$

It is interesting to note that in Eq. (9) the increase of the cosmic-ray diffusion coefficient with energy is just compensated for by the opposite variation of the cosmic-ray intensity gradient, so that a nearly constant $\delta$ value should be obtained. In Fig. 1 the predicted $\delta$ curves are based on $\bar{n}_I$ =1.2 H atoms$cm^{-3}$ (6) and the value of $\lambda_p^1$ suggested in Ref. (7). An additonal increase of $\lambda_p^{att}$ is included to take the contribution of heavy nuclei in the ISM into account. From Fig. 1 the scattering of $l_s$ values estimated from various data is found to be within =± 1 kpc.

However, it should be emphasized that except the datum denoted by a star(8) the measured data collected in Ref. (9) and shown in Fig. 1 do not refer to $\delta$ itself. Thus by normalizing our predicted curve to the star we finally obtain $l_s = 5\pm1$ kpc. Further, the measured data shown in Fig.1 indeed show a slightly increasing trend, which should be the first astronomical evidence of the rising of the p-p inelastic interaction cross section with increasing energy in the context of the NUGD model.

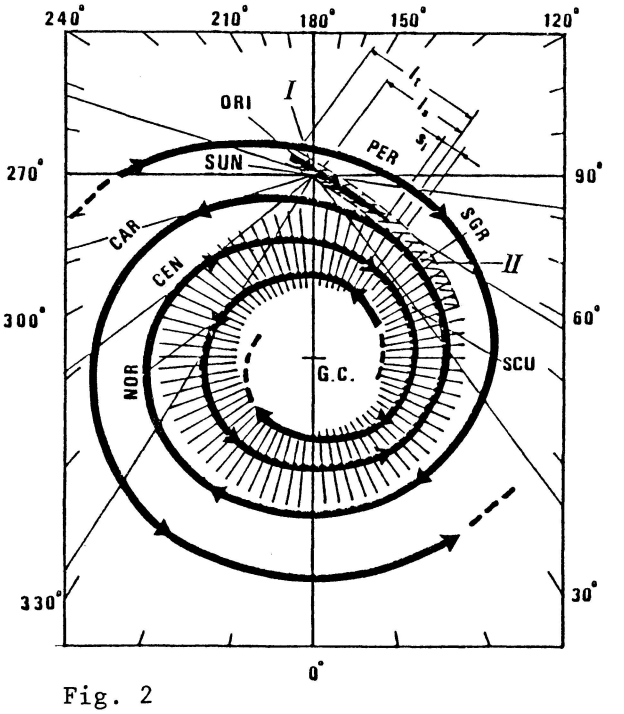


Fig. 2

From our deduced $l_s$ value we can estimate the astronomical counterpart of our model elements. In Fig. 2 the geometrical relationship between the $H_2$ cloud ring (the radially hatched region) and the large-scale interstellar magnetic field (the spirally solid lines) is shown. As the reversal of field direction occurs between the Orion arm and the Sagittarius arm, a neutral line should exist between both arms. The existence of a neutral line should obstruct the exchange of cosmic-ray particles between two adjacent arms. As a result, in the $H_2$ cloud ring only from a narrow region exterior to the Sagittarius arm (the region II in Fig.2) cosmic-ray particles can stream along the Orion arm to reach the solar neighbourhood.

Actually, in our model picture each small region including a dense $H_2$ cloud and its magnetically connected surrounding gas may be viewed as a coherent entity which is called as a cell(10). All the magnetically connected cells form a subtube and all subtubes form the magnetic tube. In view of the fluctuation of interstellar magnetic field the direction of the subtube, in which the solar system is located, may be different from the general direction of the Orion arm. Thus the measured value of the maximum phase for the 1st harmonics of cosmic-ray intensity variation may be understood.

It is noticeable that in order to avoid affecting the spectral shape of heavy nuclei, the NUGD model requires an assumption that in the distant component of cosmic rays there should exist a serious deficit of heavy nuclei. Actually, similar assumptions also appear in many other double-component models of cosmic-ray propagation. However, in our model the deficit should occur in the preacceleration stage of cosmic rays ( e.g., by an unfavourable preacceleration condition for heavy nuclei in their acceleration sites above the $H_2$ cloud region). Thus the observed heavy nuclei of cosmic rays should be of local origin. Moreover, from an analysis of the high-energy electron spectrum(4) it is found that only about 5 % of observed protons come from the local region.

Consequently, in the sample of locally produced cosmic rays the abudances of heavy nuclei relative to protons must be higher the directly observed values by a factor of 20. The assumed relative abudances of cosmic-ray nuclei in the sample of locally produced cosmic rays are shown in Fig. 3 as the horizontal lines. In Fig. 1 we have noted that an abrupt increase of the degree of anisotropy of cosmic rays occurs beyond $10^{14}$ eV. Here we try to attribute this increase to the failure of our NUGD model due to the insufficient confinement of cosmic rays at very high-energies. Therefore, at very high energies the locally produced cosmic rays would fill the intensity vacancy left by the distant component of cosmic rays. As a result, the observed abudances of cosmic-ray nuclei should approach to the local abudances shown in Fig. 3. In view of the situation that above $2\times10^{15}$ eV the dominant contribution to the observed cosmic rays may come from one single source, these abudaces may never be reached. Nevertheless, a variation of cosmic-ray mass composition with increased contribution of heavy nuclei should be expected to happen around $10^{15}$ eV.

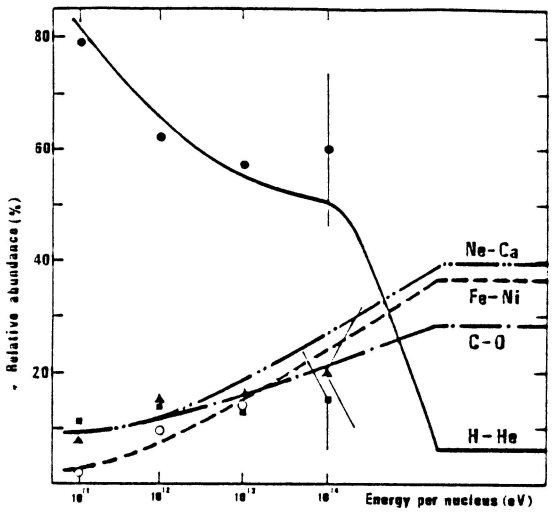


Fig. 3

References:

1. Silberberg,R. et al., 1983, Proc. 18th Internat. Cosmic.Ray Conf. (Bangalore), 2, 179.
2. Tan,L.C. and Ng,L.K. 1983, Ap. J., 269, 751.
3. Ormes,J. and Protheroe,R.J. 1983, Ap. J., 272, 756.
4. Tan,L.C. 1985, Ap. J., in press.
5. Ginzburg,V.L. and Syrovatskii,S.I. 1964, Origin of Cosmic Rays (Oxford: Pergamon).
6. Gordon,M.A. and Burton,W.B. 1976, Ap. J., 208, 346.
7. Hillas,A.M. 1979, Proc. 17th Internat. Cosmic Ray Conf. (Kyoto), 6, 13.
8. Nagashima,K. et al., 1977, Proc. 15th Internat. Cosmic Ray Conf. (Plovdiv), 2, 154.
9. Linsley,J. 1983, Proc. 18th Internat. Cosmic Ray Conf. (Bangalore), 12, 135.
10. Elmegreen,B.G. 1981, Ap. J., 243, 512.

# ON GALACTIC ORIGIN OF COSMIC RAYS WITH ENERGY UP TO $10^{19}$ eV

N.N.Efimov, A.A.Mikhailov

Institute of Cosmophysical Research & Aeronomy
Lenin Ave., 31, 677891 Yakutsk, USSR

Abstract

The experimental data on ultrahigh energy cosmic ray anisotropy are considered. In supposed models of galactic magnetic field the main characteristics of expected anisotropy are estimated and are compared with the experimental data. In is shown that particles with energy up to $10^{19}$ eV are of galactic origin.

Spectrum. The observed spectrum and cosmic ray intensity at $10^{17} - 10^{19}$ eV can be explained by galactic sources [1,2]. At present the most difficulties occur in the explanation of EAS experimental data on anisotropy.

Is there really anisotropy? One of the arguments in favour of anisotropy is the agreement of phases of the 1-st harmonic on data of Yakutsk and Haverah Park EAS arrays [3] (Fig.1). The common (Yakutsk and Haverah Park) chance probability of constancy of the 1-st harmonic phase at energy range $5\cdot10^{17} < E_0 < 2\cdot10^{19}$ eV is $10^{-4}\div10^{-5}$. The next argument in favour of anisotropy can be taken the presence of a gradient in particle distribution on galactic latitude [4,5]. The chance probability of such a gradient on data of Yakutsk and Haverah Park arrays in total is $10^{-5} \div 10^{-7}$ (Fig.2).

From the above it follows that cosmic ray anisotropy in energy range $10^{18} - 10^{19}$ eV is real.

Experimental anisotropy. Because of small statistics the experimentators on EAS data determine the anisotropy based on event number on large solid angle $\Delta\Omega$ ($\Delta\delta_1 \sim 90°$, $\Delta\alpha \sim 30\div60°$, $\delta_1$ - declination, $\alpha$ - the right ascension). In [6] we showed that anisotropy determined in such a way differs from one $\delta$ determined by usual way on expected intensity: $\delta = (I_{max} - I_{min})/(I_{max} + I_{min})$ where I - cosmic ray intensity. Below we shall show it.

The particle number from the definite part of celestial sphere is

$$n(\alpha,\delta_1) = \int K(\theta(t))\,J(\alpha,\delta_1)\,\Omega(\theta(t),\varphi(t))\,S(\theta(t))\,dt,$$

where $K$ - the probability of detection; $\Omega$, $S$ - the solid

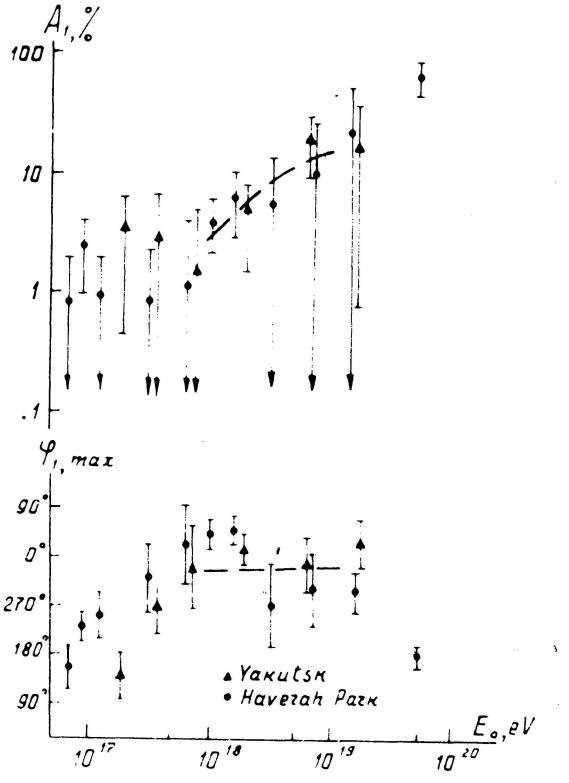


Fig.1. Amplitudes and phases of the 1-st harmonic; dashed line - the expected values in the case of protons from sources in the disc

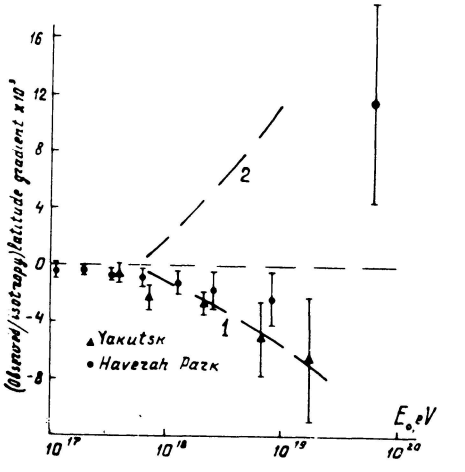


Fig.2. The gradient $n_{obs.}/n_{isotr.}$ on galactic latitude $b$. Dashed line - the expected values in the case of protons: 1 - Yakutsk, 2 - Sydney

angle and the effective area of the array; $\theta$, $\varphi$ - the zenith and azimuthal angles, $t$ - observation time. The number of events on intervals of the right ascension is

$$n(\Delta\alpha_i) = \int_{\Delta\alpha_i}\int_{\Delta\delta} n(\alpha, \delta_1)\, d\alpha\, d\delta_1 .$$

Then the anisotropy is

$$\delta^* = \left[n_{max}(\Delta\alpha) - n_{min}(\Delta\alpha)\right] / \left[n_{max}(\Delta\alpha) + n_{min}(\Delta\alpha)\right] .$$

It is seen that anisotropy $\delta^*$ determined on event number on a large solid angle is not identical with anisotropy $\delta$ determined on intensity. Note that the some correction of the 1-st harmonic amplitude in energy range $10^{18} - 2.10^{19}$ eV (Fig.1) can be made deviding it into $\cos b$ where $b$ - the average galactic latitude of the observed showers. The anisotropy vector (Fig.1) is observed at the angle $b$. Similar idea was supposed in [7].

Galactic model. Discussed here anisotropy characteristics at $E_0 > 10^{18}$ eV (the 1-st harmonic phases, a gradient

of particle distribution at positive latitudes) at quasi-rectilinear motion of particles can be explained qualitatively by sources distributed in the galactic disc (evidently the maximum of particle arrival being from galactic plane where the number of sources is large). At allowed on radiodata magnetic fields of disc (2-3 $\mu G$ ) and halo ( $\lesssim 1$ $\mu G$ ) the quasirectilinear motion is expected in the considered energy range in a case of protons [1,2] . The observed on experimental data ratio of showers equator-pole $n(|b|<30°)/n(|b|>30°) \approx 2$ about $10^{19}$ eV [5] can be also explained in the case of protons by sources in galactic disc (in the first approximation the particle number proportional to the radius of ball sectors of the region of sources).

Consider how these experimental data agree on amplitude with the expected one from galactic sources. Calculating the individual trajectories of antiprotons from the Earth in sign-constant longitudinal magnetic field of the disc and halo (the sign-constant field of the disc is considered to be more probable, see, for instance, [8] ) we estimated the expected anisotropy from sources distributed uniform in galactic disc (the central sources can be excluded from the number of possible ones [2] ). The expected anisotropy was estimated (Figs.1,3) by the expected particle number on a large solid angle as in the case of experimental data (in detail see [6]). The given anisotropy appears to be 2-3 times less than the expected one determined on intensity, though they coincide in phase. Note that the account of the inhomogeneous distribution of sources in the disc changes weekly the estimated anisotropy [6] . The observed ratio of showers equator-pole on Yakutsk array data [5] (Fig.3) is decreased due to the exposition time of regions of sky [5] .

We estimated the expected gradient of particles on galactic latitude (Fig.2, see also [9] ) from calculated lengths of trajectories in galactic disc using formally the obtained dependence of particle number upon trajectory lengths [6] (in the case of small solid angle, $\Delta b = 10°$, $\Delta l \sim 120°$, we can not strictly use the this dependence).

On $\chi^2$-criterium we compared the observed event number on right ascension [5] with the expected one in the case of protons from sources in the disc. We supposed that the observed number of events is a sum of anisotropic galactic (G-portion) and isotropic extragalactic cosmic ray components. In the Table are shown G at which $\chi^2$ is minimum, in brackets - upper limits of G.

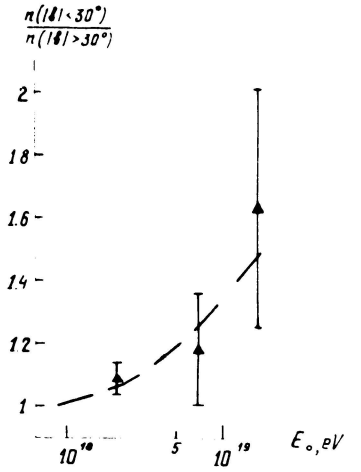


Fig.3. The ratio of showers equator-pole. Dashed line - expected in the case of protons from sources in the disc

Table

| $E_o$, eV | Number of showers | G,% |
|---|---|---|
| $2,1 \cdot 10^{18}$ | 3147 | 80(100) |
| $6,7 \cdot 10^{18}$ | 256 | 100(100) |
| $1,7 \cdot 10^{19}$ | 115 | 100(100) |

On results of comparison of the observed and expect anisotropies on amplitude and phase of the 1-st harmonic, on ratio of the number of showers equator-pole, on $\chi^2$-criterium the particles with energies up to $10^{19}$ eV can be considered of galactic origin.

Our detailed calculations on galactic model show [2,6] that at energies above $10^{18}$ eV the maximum of particle arrival from the high galactic latitudes is not expected. The observed excess of particles from the high latitudes [4,5,7,10]at energies $E_o > 2 \cdot 10^{19}$ eV, to be more accurate, from direction of centre of the Local supercluster to be probably caused by extragalactic sources.

Conclusion. The particles with energies up to $10^{19}$ eV are of galactic origin and above $2 \cdot 10^{19}$ eV are rather of extragalactic origin.

References.

1. Syrovatskii, S.I., (1969) Preprint, P.N.Lebedev Inst., No. 151.
2. Beresinsky, V.S., Mikhailov, A.A., (1983) Proc.18-th ICRC, Bangalore, 2, 174.
3. Hillas, A.M., (1984) Ann.Rev.of Astron. and Astrophys., 22, 1.
4. Watson, A.A., (1984) Proc.COSPAR/IAU Symp., Austria, 1.
5. Efimov, N.N., et al., (1983) Proc.18-th ICRC, Bangalore, 2, 149.
6. Mikhailov A.A., (1983) Kosmicheskiye luchi s $E_o > 10^{17}$eV, Yakutsk, 3.
7. Linsley, J., (1983) Proc.18-th ICRC, Bangalore, Rapp.paper.
8. Rusmaikin, A.A., Sokoloff, D.D., (1977) Astroph.and Sp.Sci., 52, 375.
9. Mikhailov, A.A., (1984) Bull.NTI. Problemy kosmofiziki i aeronomii, Yakutsk, oktyabr, 3.
10. Nikolsky, S.I., (1982) UFN, 136, 349.

# ABUNDANCE OF LOW ENERGY (50-150 MeV) ANTIPROTONS IN COSMIC RAYS

Apparao, K.M.V., Biswas, S., Durgaprasad, N.
and Stephens, S.A.
Tata Institute of Fundamental Research
Homi Bhabha Road, Bombay 400005, India

ABSTRACT

We present the progress of our nuclear emulsion experiment to determine on abundance of low energy antiprotons in cosmic rays. We have not detected any so far and obtain an upper limit of $\bar{p}/p \lesssim 4 \times 10^{-4}$ in the energy range 50-150 MeV.

During the last International Conference on Cosmic Rays at Bangalore, we[1] reported preliminary results of an experiment to determine the abundance of low energy antiprotons in cosmic rays. We are using a nuclear emulsion stack of 200 Ilford G5 emulsion pellicles exposed on July 3, 1972 at Fort Churchill, Canada for 13h 45m at a depth of 1.7 g.cm$^{-2}$ of residual atmosphere. We scanned at a depth of mostly 2 cms from the top edge, for nuclear interactions containing one high energy track and then followed all tracks in the upper hemisphere towards the edge of the entry. This will pick out interactions produced by a particle coming from outside the stack. The signature of a low energy anti-proton is a track corresponding to a slow particle (<200 MeV) of protonic mass and producing an interaction with a visible energy release more than the kinetic energy of the incoming proton[2].

In the previous ICRC we had reported five candidates. These were obtained by making grain density measurements along the track, which indicated the direction of motion of the particle producing the track, i.e. whether the particle

is coming into the interaction or produced in the interaction and going away from the interaction. None of the candidates stopped in the emulsion at the point of interaction. We have now scanned a total volume of 7.8 $cm^{-3}$ of emulsion. A total of about 19,590 interactions were looked at and 10,169 tracks were followed towards the top of the stack. Out of these 288 tracks left the stack at the top and grain density measurements were carried out on them. Those that showed that they are proceeding towards the interaction are called candidates for $\bar{p}$ and were subjected to blob-gap measurements in all pellicles through which they pass. We have made extensive grain density and blob-gap measurements on relativistic alpha tracks in various regions of the stack to determine variations of the sensitivity of the emulsion in a single pellicle as well as from pellicle to pellicle. We used stopping protons and electron pairs to obtain the calibration curves for ionization versus range.

With the above effort, we found that the previous candidates are not anti-protons. We also found another 15 candidates, which also did not turn out to be antiprotons. We have calculated the gathering power of our volume to be $2.38 \times 10^{3}$ $m^{2}.sr.s.MeV$ yielding as an upper limit to $\bar{p}$ flux of $\sim 4 \times 10^{-4}$ $m^{-2}.s^{-1}.sr^{-1}.MeV^{-1}$ in the energy range 50-150 MeV. This flux limit is to be compared to the flux of $(1.7 \pm 0.5) \times 10^{-4}$ $m^{-2}.\ sr^{-1}.\ s^{-1}.\ MeV^{-1}$ obtained by Buffington et al.[3]; however the flux obtained by Buffington et al. is in the energy range 130-320 MeV. The upper limit to the $\bar{p}/p$ ratio in the energy range 50-150 MeV is obtained using the proton flux in this energy range of $0.96 \pm 0.07$ $m^{-2}.\ s^{-1}.\ sr^{-1}$ $MeV^{-1}$ obtained* from IMP-6 satellite on this date, and is $4.3 \times 10^{-4}$ $(1\sigma)$.

---

* We are thankful to Dr. T. von Rosenvinge for this information.

In the last ICRC we reported an event which we interpreted as an anti-triton event on the basis of grain density measurements. Since then we have made blob gap measurements and multiple scattering measurements on the track in all the pellicles through which it passes. After taking into account the plate to plate variations, we found that the ionization measurements made the identification of the incoming track between t and $He^3$ ambiguous; perhaps more consistent with $He^3$ nucleus (Fig. 1). In Fig. 2 we show the plot of normalised ionization parameter obtained from blob-gap measurements, versus the multiple scattering parameter for 100μ cell length. (The parameter for 100μ is obtained from values obtained from higher cell lengths and the usual third difference method to remove distortion effects). The curves for $H^3$ and $He^3$ are shown. Here again we do not find convincing evidence that the incoming track is a triton, eventhough the measurements do not fit well with a $He^3$ curve. Therefore, we do not believe the track to be due to an anti-triton.

Acknowledgements: Our thanks are due to Dr. R. Silberberg and the authorities of the Naval Research Laboratory, USA for loaning the emulsion stack. We appreciate the patient scanning and measuring work of Ms. S. Savitri, Mrs. S.P. Prabhudesai, Mrs. R. Chandrasekhar, Mr. D.M. Pawar and Mr. D. Mane.

References

1. Apparao, K.M.V., Durgaprasad, N., Stephens, S.A. and Biswas, S., 1983, Proc. 18th ICRC, Vol.2, pps.75 and 79.
2. Apparao, K.M.V., 1967, Nature Phys. Sci., 24, 98.
3. Buffington, A., et al. 1981, Ap.J. Lett., 247, L105.

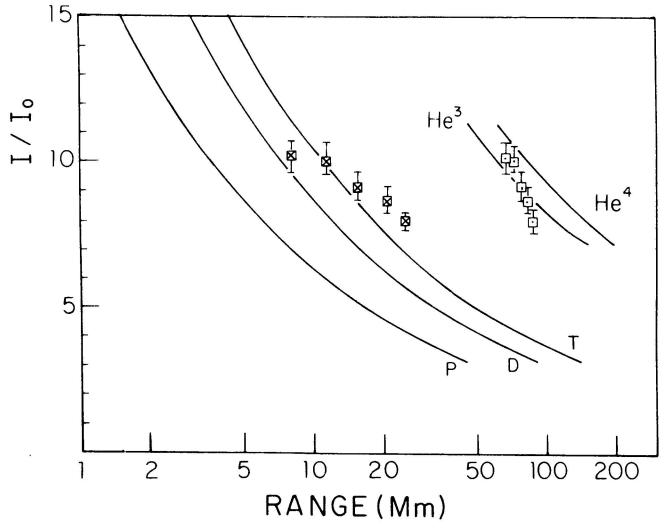


Fig. 1. Normalised ionisation parameter $I/I_o$ obtained from blob-gap measurements versus residual range. The curves for protons (P) and $He^4$ are obtained from calibration tracks. The measurements of the candidate track are plotted once on the triton curve and once on $He^3$ curve to examine the fits.

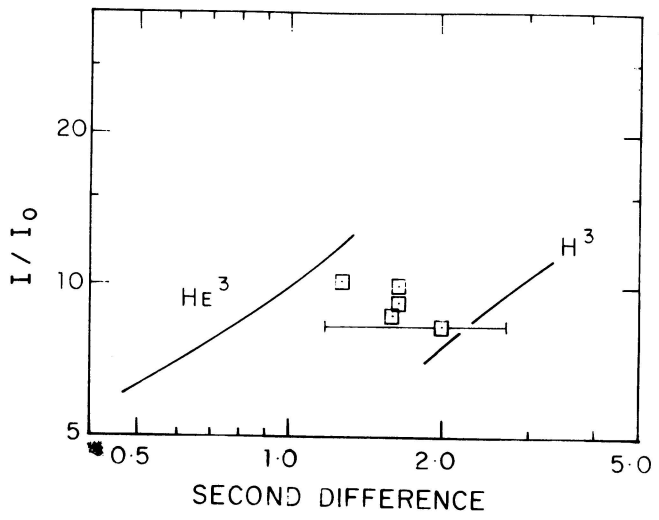


Fig. 2. Normalised ionisation parameter $I/I_o$ obtained from blob-gap measurements versus scattering parameter. The measured values for the candidate track are plotted; typical error is shown.

330

# SEARCH FOR HEAVY ANTINUCLEI IN THE COSMIC RADIATION

**Niels Lund and Miriam Rotenberg**
**The Copenhagen-Saclay HEAO Collaboration**
**Danish Space Research Institute, Lundtoftevej 7, DK-2800 Lyngby**

## Introduction

The cosmic radiation is one of the few channels through which the existence of significant amounts of antimatter in the Universe may be demonstrated. Such a finding would be of fundamental importance for cosmology as well as for particle physics.

The data from the Danish-French Cosmic Ray Spectrometer on the HEAO-3 satellite offers an opportunity to search for heavy antinuclei, since all the relevant parameters (charge, velocity, arrival direction, and satellite position at the time of arrival) are measured for each recorded nucleus.

## Instrumentation and initial data selection

The HEAO-3 instrument is described in detail in (3). The charge and velocity of each particle is determined from the signals produced in a stack of five Cerenkov counters.

The consistency of the signals are used to check for particles undergoing nuclear interactions while traversing the instrument. For this investigation, however, the consistency requirements have been relaxed somewhat from the values used generally, in order not to reject antinuclei, which are expected to yield signals differing slightly from those of their positive counterparts.

The particle velocity is determined from a fit to the Cerenkov signals. We use a routine which determines not only the best fit velocity, but also the lower and upper bounds for a velocity interval outside which the true values should only lie in one case out of $10^5$.

Particles with inconsistent values of the velocity signals have been rejected.

The present analysis is limited to elements heavier than fluorine since the reliability of the time-of-flight system has been found to degrade somewhat for lighter elements.

Pilot runs showed that the number of particles with zenith angles less than 90° which could be assigned a unique charge is quite small. Consequently we restrict the data base to particles with zenith angles greater than 90°.

## Trajectory tracings

Before beginning the trajectory tracings the acceptable velocity range mentioned above is converted to a rigidity interval by using a very wide range of possible isotopic masses for each element. This procedure

takes into account the possibility that a short lived fragment produced in the atmosphere may follow a different trajectory than the ones available to the stable isotopes.

The helix-method (4) is used for the trajectory tracings. The magnetic field model used is a 14. order model based on MAGSAT data (5). For each rigidity value it is checked if any of the two possible charge signs corresponds to an acceptable arrival situation. Dependent on the outcome of the tracings the particles are divided into four classes:

1) Both charge signs are possible. This class contains all events for which at least one positive rigidity and at least one negative rigidity are acceptable.

2) Only a positive sign is possible, i.e., particles for which at least one positive rigidity is acceptable and none of the negative rigidities are acceptable.

3) Only a negative sign is possible, i.e., all positive rigidities forbidden, but at least one negative is allowed.

4) Neither sign is allowed, all positive as well as negative rigidities are forbidden.

A very conservative criterion for classifying a rigidity as "forbidden" has been used. It is demanded that the corresponding trajectory intersects the solid Earth within a trajectory length of one Earth radius from the satellite position.

In order to allow for some error in the determination of the particle arrival directions, any particle which is initially in class 2, 3 or 4 is recalculated using a zenith angle diminished by 2 degrees relative to the measured value.

Results

Of the initial data set about 25% or 34070 events are classified as positive only, 15 events are negative only (antiparticle candidates) and 10 events are impossible regardless of the sign assumed. The rest, 103266 events, are consistent with either charge sign.

Details on the 25 particles of classes 3 and 4 can be found in tables 1 and 2.

Inspection of these 25 events reveals that 7 antiparticle candidates and 2 impossibles were all recorded on one single day (Nov. 11, 1979). The total set comprises data from over 400 days. We have found no satisfactory explanation for this burst of unusual trajectories. There were no signs of instrument or satellite malfunctions. A Forbush decrease occurred on this day, but we see no particular reson to connect the two events. The geomagnetic activity index was between 1 and 2+. We have noted that 8 of the 9 unusual events were recorded in the vincinity of the Sourth Atlantic Anomaly. The instrument was switched off during the passages through the Anomaly and the 8 events occurred in the first few minutes after switch on. The connection

between the switching of the experiment and the peculiar events is not obvious, however, because in the total data set there are several thousand such passages without irregularities. We have therefore decided to reject all events (of all classes) recorded on this day from this work.

The remaining 8 impossible events indicate the level of background for the antiparticle search. This background may be due to inadequacies of the measured data (charge, velocity, and arrival direction for the particles) or it may arise due to inadequacies of the magnetic field model. The MAGSAT model does not describe local crust related magnetic anomalies and does not take into account magnetic disturbances which might exist at the specific time of our particle recordings.

When analyzing the geographic distribution of the remaining "impossibles", it appears that the problem lies with the magnetic field data because these particles have preferentially been detected at low geomagnetic cut-off values where magnetospheric disturbances have the largest effect. We have therefore investigated the effect of excluding data obtained at locations with geomagnetic L-values greater than 1.5. It turns out that most of the "particle" candidates remain in this selection whereas all the "antiparticle" candidates and all but one of the "impossibles" are gone. This last "impossible" event may be reasonably attributed to the uncertainty of the time-of-flight imformation. In fact, an independent analysis leads us to suspect a residual contamination at the $10^{-4}$ level for the time-of-flight system. We also note that all but one of the Nov. 11 events have L-values greater than 1.5.

## Conclusion

Using the 22676 "positive only" events in the data selection corresponding to $L \leq 1.5$ as a measure of our "exposure factor" to heavy antinuclei and noting that no corresponding antinuclei were found we can give an upper limit (95% confidence) to the ratio of antinuclei to nuclei as $1.4 \times 10^{-4}$ for particles with $|Z| > 9$. In table 3 we compare the upper limit resulting from this work with previous results of searches for heavy antimatter in the cosmic radiation. It is seen that, if one regards only antiparticles heavier than fluorine, then the present result represents a reduced upper limit over previous data. When taken together, all the available experiment data now push the upper limit for the ratio of antiparticles to particles well below $10^{-4}$.

As a final remark we may stress that we have found no satisfactory explanation for the 9 unusual particle tracks seen on November 11, 1979. We would appreciate being informed of other geophysical "curiosities" which might have been observed on this date.

## Acknowledgements

The authors would like to thank all their collaborators in the Copenhagen-Saclay Collaboration for their efforts in providing the data base for this work. In particular we want to thank Prof. B. Peters for his continuing interest and useful comments throughout the project.

TABLE 1 Antiparticle candidates

| Date | GMT | Lat. | Long. | L-value | Zen. | Az. | Z | p GeV/c | 4.3 σ range |
|---|---|---|---|---|---|---|---|---|---|
| 791111 | 07 59 | -43.3° | 32.1° | 2.51 | 128° | 20° | 10 | 4.13 | 3.74 - 4.89 |
| 791111 | 07 59 | -43.3 | 32.3 | 2.51 | 123 | 44 | 14 | 1.58 | 1.52 - 1.65 |
| 791111 | 08 00 | -43.5 | 37.0 | 2.52 | 135 | 18 | 13 | 4.66 | 4.19 - 5.54 |
| 791111 | 08 01 | -43.6 | 39.7 | 2.52 | 107 | 29 | 19 | 8.02 | 7.40 - 9.31 |
| 791111 | 09 37 | -43.0 | 27.3 | 2.49 | 119 | 36 | 14 | 2.16 | 1.98 - 2.45 |
| 791111 | 09 37 | -42.8 | 28.9 | 2.49 | 129 | 15 | 14 | 5.38 | 4.66 - 6.41 |
| 791111 | 09 38 | -42.4 | 31.6 | 2.49 | 122 | 36 | 14 | 2.11 | 1.94 - 2.35 |
| 791215 | 14 46 | -43.6 | 74.8 | 3.0 | 105 | 138 | 10 | 1.17 | 1.14 - 1.19 |
| 800129 | 17 18 | -38.0 | 133.4 | 2.5 | 109 | 79 | 13 | 7.22 | 6.70 - 8.22 |
| 800205 | 09 08 | -43.4 | -175.8 | 2.4 | 130 | -63 | 12 | 2.14 | 1.94 - 2.48 |
| 800206 | 00 04 | 41.8 | 148.9 | 1.6 | 95 | 55 | 12 | 6.28 | 5.27 - 6.70 |
| 800415 | 02 20 | -43.6 | -36.4 | 1.63 | 109 | 46 | 10 | 3.09 | 2.97 - 3.28 |
| 800715 | 20 13 | -36.8 | 61.2 | 2.2 | 114 | 52 | 18 | 7.15 | 6.73 - 7.90 |
| 801025 | 09 35 | -36.5 | -171.7 | 1.75 | 99 | 123 | 10 | 8.73 | 7.44 - 12.94 |
| 801031 | 13 38 | -41.2 | 102.0 | 3.0 | 107 | 116 | 12 | 8.81 | 7.66 - 11.94 |

TABLE 2 "Impossible particles"

| | | | | | | | | | |
|---|---|---|---|---|---|---|---|---|---|
| 790930 | 20 57 | -42.8° | 104.8° | 3.3 | 135° | -75° | 12 | 4.30 | 3.89 - 5.02 |
| 791005 | 18 06 | 41.8 | -71.3 | 3.1 | 119 | -48 | 13 | 1.21 | 1.20 - 1.22 |
| 791017 | 17 08 | -43.3 | 72.2 | 3.0 | 134 | 86 | 13 | 1.97 | 1.82 - 2.21 |
| 791111 | 10 05 | 16.2 | 116.3 | 1.0 | 146 | 114 | 16 | 56.36 | 15.4 - ∞ |
| 791111 | 11 22 | -25.9 | 48.2 | 1.6 | 109 | 171 | 12 | 6.73 | 6.34 - 7.44 |
| 791208 | 21 04 | -43.5 | 18.2 | 2.3 | 168 | 70 | 10 | 1.28 | 1.26 - 1.32 |
| 800628 | 17 08 | -43.6 | -176.0 | 2.4 | 147 | -107 | 20 | 5.43 | 4.87 - 6.31 |
| 800823 | 00 50 | -43.5 | 57.6 | 2.4 | 152 | -54 | 14 | 2.68 | 2.34 - 2.97 |
| 800912 | 05 19 | 35.6 | 2.6 | 1.5 | 144 | -79 | 10 | 16.36 | 10.13 - ∞ |
| 801105 | 06 32 | 38.7 | -12.3 | 1.8 | 129 | 14 | 20 | 20.07 | 11.42 - ∞ |

TABLE 3 Searches for antinuclei

| | | 95% confidence upper limit |
|---|---|---|
| Badhwar et al (1978) | Z = 2 | $1.7 \times 10^{-4}$ |
| Smoot et al (1975) | Z > 2 | $0.8 \times 10^{-4}$ |
| Present work | Z > 9 | $1.4 \times 10^{-4}$ |

References


1) G.F. Smoot, et al, Phys. Rev. Lett., 35, (1975), 258.
2) G.D. Badhwar, et al, Nature, 274, (1978), 137.
3) M. Bouffard, et al, Astr. Sp. Sc. 84, 3, (1982).
4) B. Byrnak, et al, Nucl. Instr. Meth., 16, 303, (1979).
5) R.A. Langel, et al, Geoph. Res. Lett., 7, (1980), 793

# PROPAGATION AND SECONDARY PRODUCTION OF LOW ENERGY ANTIPROTONS IN THE ATMOSPHERE*

T. Bowen and A. Moats
Department of Physics
University of Arizona, Tucson, AZ 85721, USA

1. Introduction. Current theories, in which the observed antiproton component is attributed strictly to secondary production in high energy inelastic collisions of protons with the interstellar medium or the atmosphere, apparently fail to explain the relatively high $\bar{p}$ vertical intensities measured at mountain and balloon altitudes. Therefore, a more careful calculation of the theoretical secondary intensity spectra is required before more exotic sources for these excess $\bar{p}$'s can be explored.

In this paper, we have used a one-dimensional diffusion equation (valid if $\theta_{lab} \lesssim 20^{o}$ down to sea level) to calculate the expected vertical intensity of $\bar{p}$'s due only to secondary production in the atmosphere; any assumed primary p spectrum can also be included. Two adjustable parameters, the inelasticity and charge exchange in nucleon-nucleus collisions, were included in our algorithm. In order to obtain an independent estimate of their values, we first calculated the proton vertical intensities in the atmosphere, adjusting the parameters until our curves fit the experimental proton data, and then assumed that these values were identical in antinucleon-nucleus collisions.

2. Results. Our calculations followed a method suggested to us by T. K. Gaisser in which the atmosphere was divided into "slabs" of equal thickness $\Delta x$; slabs of 1 g/cm$^2$ were used. In calculating the differential proton intensities, a primary proton spectrum of the form[1] $j_p = 2(E + 2.15)^{-2.75}$ cm$^{-2}$-s$^{-1}$-sr$^{-1}$-GeV$^{-1}$, where E is the proton kinetic energy in GeV, was assumed. Protons and neutrons from higher Z nuclei were assumed to have the same spectral shape, and all protons and nuclei whose momenta were less than the vertical cutoff rigidity were excluded. Then, working from the top of the atmosphere down to sea level, the proton intensity of the i + 1 slab was calculated using the equations $n(i+1) = n(i) + (dn(E)/dx)\Delta x$ and

$$\frac{dn_p(E)}{dx} = -\frac{n_p(E)}{\lambda_{inel}^{air}} + \left(\frac{dE}{dx}\right)\frac{\Delta n_p}{\Delta E} + \int_{E_0=E}^{\infty} \frac{1}{\lambda_{inel}^{air}} \frac{dN(E,E_0)}{dE} [(1-\alpha)n_p(E_0) + \alpha n_n(E_0)]dE_0 \ , \quad (1)$$

with a similar equation [without the ionization loss[2] term $(dE/dx)(\Delta n_p/\Delta E)$] for the neutron intensity, $n_n$. All of the values of n on the right-hand side are the values from the slab i above. $\lambda_{inel}^{air}$ is the inelastic mean-free path of proton-air nuclei collisions, scaled from p-$^{12}$C data.[3,4] The last term in the equation above adds in the protons gained from inelastic collisions of higher energy protons with air nuclei, with $dN(E,E_0)/dE$ defined as the probability of a proton with initial energy $E_0$ possessing energy E after collision. A uniform probability distribution ranging from 0 to $\varepsilon E_0$ for $dN(E,E_0)/dE$, with average elasticity $\varepsilon/2$, was assumed. $\varepsilon$ and the probability $\alpha$ of charge exchange were our adjustable parameters. With the values $\alpha = 0.333$ and $\varepsilon = 0.9$, our computed proton intensities matched the experimental data quite well (see Fig. 1). We then used these values for $\varepsilon$ and $\alpha$ in our antiproton intensity calculations.

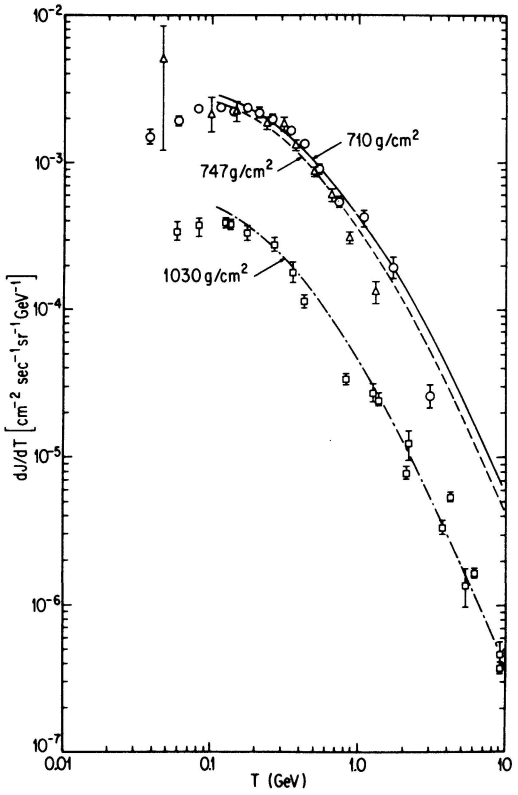


Fig. 1. The curves show the calculated results for vertical proton intensities at 710, 747, and 1030 g/cm$^2$ depth. The data is a compilation by Barber et al., Ref. 14.

Using the same method, the antiproton intensity due only to secondary production was calculated with equations analogous to Eq. (1), but with the term,

$$\int_{E_0=E}^{\infty} \frac{1}{\lambda_{inel}^{air}} \frac{1}{\sigma_{inel}^{air}} \frac{d\sigma_{\bar{p}}^{air}(E,E_0)}{dE} n_{nucleon}(E_0)dE_0 \quad ,$$

added on the right side for the production spectrum of $\bar{p}$'s in proton-air collisions, which is taken from a parameterization of Tan and Ng,[5] attenuated with an attenuation length of 122 g/cm$^2$ as depth increases. The form of dE/dx and $dN(E,E_0)/dE$ were the same as used in the proton calculations. $\lambda_R^{air}$, the $\bar{p}$ mean-free path in air for annihilation and inelastic scattering, was estimated by scaling a power-law fit to $\bar{p}$-$^{12}$C reaction cross sections from data compiled by G. Bruge[6] and provided to us by J. C. Peng, LAMPF; the result is shown in Fig. 2, curve d, along with another estimate,[7] curve e. Three different forms of $\lambda_{inel}^{air}$, the antiproton mean-free path in air for inelastic, non-annihilation collisions, were tried, as shown in Fig. 2. In version c, $\lambda_{inel}^{air}$ was assumed to be equal to $\lambda_{inel}^{air}$ for protons. A curve from Szabelski and Wolfendale[7] was used in version b. Finally, in version a, we attempted a realistic estimate for $\lambda_{inel}^{air}$ by assuming that $\lambda_{inel}^{air} / \lambda_{annih}^{air} = \sigma_{annih}(\bar{p}p)/\sigma_{inel}(\bar{p}p)$. Since there is little data available on $\sigma_{inel}(\bar{p}p)$ [non-annihilation], we assumed that it is the same as the pp inelastic cross section.[8] Below 0.5 GeV, $\lambda_{inel}^{air}$ depends entirely on quasi-elastic $\bar{p}$-nucleon scattering; for our realistic estimate shown in curve a, the quasi-elastic scattering was taken to be 1/10 as probable as for the p-nucleon case, based upon special Monte Carlo runs using ISABEL INC for $\bar{p}$-$^{12}$C inelastic scattering at 180 and 400 MeV[9] arranged for us by P. L. McGanghey at Los Alamos.

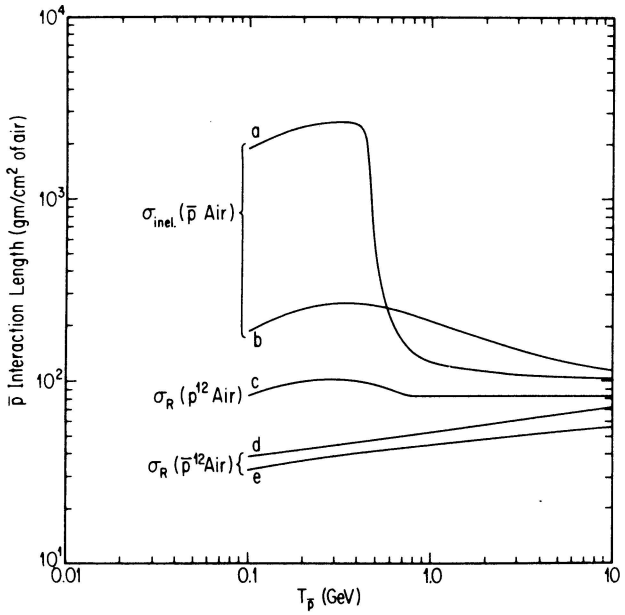


Fig. 2. Antiproton-air interaction lengths (mean-free paths) employed in the calculations: (a) $\bar{\lambda}^{air}_{inel}$ derived from our most realistic estimate of $\sigma_{inel}(\bar{p}\text{-air})$; (b) $\bar{\lambda}^{air}_{inel}$ from Ref. 7; (c) $\bar{\lambda}^{air}_{inel}$ derived if $\sigma_{inel}(\bar{p}\text{-air}) = \sigma_R(p\text{-air})$; (d) $\bar{\lambda}^{air}_R$ derived from our fit to $\sigma_R(\bar{p}\text{-}^{12}C)$ data; (e) $\bar{\lambda}^{air}_R$ from Ref. 7.

The results of our antiproton calculations, along with experimental data for the $\bar{p}$ vertical intensities at mountain altitudes, are shown in Fig. 3. At mountain altitude, both curves a and c are consistent with observations by the Arizona group,[10] although we feel that the comparison with curve a, our most realistic estimate, is the more significant one. At balloon altitudes, our secondary $\bar{p}$ intensity estimates are an order of magnitude below the intensities reported by Buffington et al.[11] and Golden et al.[12]

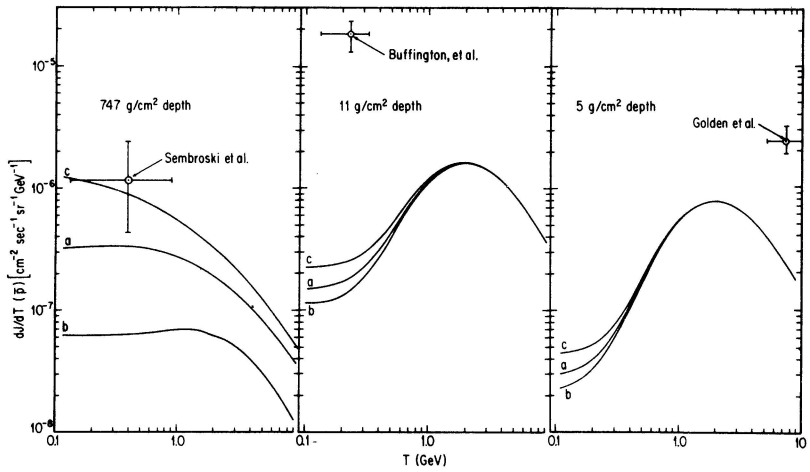


Fig. 3. The curves show calculated antiproton intensities produced by atmospheric interactions at 747 g/cm$^2$ 11 g/cm$^2$, and 5 g/cm$^2$ depth. The data points are taken from Refs. 10, 11, and 12. The designations (a), (b), and (c) correspond to utilizing curves (a,d), (b,e), and (c,d), respectively, from Fig. 2.

These results assume that there is no primary $\bar{p}$ spectrum. We then added to version "a" a primary $\bar{p}$ spectrum normalized by passing through the point of Golden et al.[12] at 8.5 GeV of the form $j_{\bar{p}}=(2.4\times10^{-6})[(E+0.94)/9.44]^{-\gamma}$. If $\gamma=2.75$ as for the proton spectrum, then the resultant low energy spectrum at mountain altitude (747 g/cm$^2$) was 2.0% greater than the purely secondary $\bar{p}$ spectrum; with $\gamma=2.1$ as suggested by Stecker and Wolfendale,[13] the primary $\bar{p}$ contribution at mountain altitude increases to 4.8%. Then $\gamma$ was adjusted until the calculated low energy $\bar{p}$ intensity at 747 g/cm$^2$, due to the primaries, equaled the difference between the data from Bowen et al.[10] and the calculated result for purely secondary $\bar{p}$ spectrum [Fig. 3(747 g/cm$^2$), curve a]. A rather flat spectrum, $\gamma=0.95$, is required. We also determined the most probable energy of the primary antiprotons contributing to the low energy $\bar{p}$'s at 747 g/cm$^2$: for $\gamma=2.1$, it was 30 GeV; for $\gamma=1.5$, 240 GeV; for $\gamma=0.9$, 3800 GeV. Obviously, more data on the antiproton intensities at high altitudes, as well as additional data on $\bar{p}$ cross sections, are needed before making an analysis with fewer approximations.

*This work was supported by NSF Grant PHY-82-07697.

1. Compilation presented by D. Müller, Proceedings of Workshop on Very High Energy Cosmic Ray Interactions, Philadelphia, April 22-24, 1982, p. 448.

2. "Review of Particle Properties," Revs. Mod. Phys. 56, No. 2, Part II, p. S49 (April 1984).

3. Compilation by N. J. DiGiacomo et al., Phys. Rev. Lett. 45, 527 (1980).

4. G. Bellettini et al., Nucl. Phys. 79, 609 (1966).

5. L. C. Tan and L. K. Ng, J. Phys. G: Nucl. Phys. 9, 227 (1983). We used the parameterization for the "Stephens spectrum" multiplied by 1.43 to account for nuclei with $Z > 1$ and by 0.71 for shadowing of air nucleons when comparing equal g/cm$^2$ of air and hydrogen targets.

6. Compilation presented by G. Bruge, Symp. on Nuclear Spectroscopy and Nuclear Interactions, Osaka, March 21-24, 1984 (Report D Ph-N-Saclay No. 2136) of PS184 collaboration results along with earlier results compiled in K. Nakamura et al., Phys. Rev. Lett. 52, 731 (1984).

7. J. Szabelski and A. W. Wolfendale (private communication).

8. V. Flaminio et al., "Compilation of Cross Sections III: p and $\bar{p}$ Induced Reactions, CERN-HERA 84-01 (17 Apr. 1984).

9. M. R. Clover et al., Phys. Rev. C 26, 2138 (1982); M. R. Clover, P. L. McGaughey, and Y. Yariv (private communication).

10. T. Bowen, E. W. Jenkins, J. J. Jones, A. E. Pifer, and G. H. Sembroski, Papers of 18th Int. Cosmic Ray Conf., Bangalore, Aug. 22-Sept. 3, 1983, vol. 2, p. 96.

11. A. Buffington et al., Astrophys. J. 248, 1179 (1981).

12. R. L. Golden et al., Phys. Rev. Lett. 43, 1196 (1979).

13. F. W. Stecker and A. W. Wolfendale, Nature 309, 37 (1984).

14. H. B. Barber et al., Phys. Rev. D 22, 2667 (1980).

# SECONDARY ANTIPROTON PRODUCTION IN RELATIVISTIC PLASMAS

C. D. Dermer* and R. Ramaty
NASA/Goddard Space Flight Center
Greenbelt, MD 20771

I. Introduction. We investigate the possibility that the reported excess low energy antiproton component of the cosmic radiation results from proton-proton (p-p) interactions in relativistic plasmas. Because of both target and projectile motion in such plasmas, the antiproton production threshold in the frame of the plasma is much lower than the threshold of antiproton production in cosmic ray interactions with ambient matter. The spectrum of the resultant antiprotons therefore extends to much lower energy than in the cosmic ray case.

We calculate the antiproton spectrum for relativistic thermal plasmas and estimate the spectrum for relativistic nonthermal plasmas. As possible production sites, we consider matter accreting onto compact objects located in the galaxy. Possible overproduction of $\gamma$-rays from associated $\pi^\circ$ production can be avoided if the site is optically thick to the photons but not to the antiprotons. A possible scenario involves a sufficiently large photon density that the $\pi^\circ$ $\gamma$-rays are absorbed by $\gamma$-$\gamma$ pair production. Escape of the antiprotons to the interstellar medium can be mediated by antineutron production.

II. Observations and Constraints on Secondary Production Models. Golden et al. (1979) have reported an antiproton to proton ($\bar{p}/p$) ratio of $5.2(\pm 1.5)\times10^{-4}$ in the cosmic radiation in the energy range 4.7-11.6 GeV. Bogomolov et al. (1979), on the basis of only two events, report a $\bar{p}/p$ ratio of $6(\pm 4)\times10^{-4}$ at energies between 2 and 5 GeV. Buffington et al. (1981) report a $\bar{p}/p$ ratio of $2.2(\pm 0.6)\times10^{-4}$ between 130 and 320 MeV, and also determine that the antihelium to helium ratio $\bar{\alpha}/\alpha < 2.2\times 10^{-5}$ in the energy range 130-370 MeV/nucleon. Upper limits on prior antinucleus searches can also be found in this paper.

As is well known, the simple "leaky box" model of cosmic ray propagation predicts a $\bar{p}/p$ ratio smaller by a factor of 3-5 than the values measured in the Golden and Bogomolov experiments. Because of the kinematic cutoff associated with the high $\bar{p}$ production threshold in p-p collisions when one of the protons is at rest, the $\bar{p}/p$ ratio predicted by this model is some two orders of magnitude lower than the value reported by Buffington et al., even after the effects of solar modulation are taken into account (Tan and Ng 1983a). The low $\bar{\alpha}/\alpha$ ratio, in comparison with the $\bar{p}/p$ ratios, suggests a secondary origin of the $\bar{p}$, although primary cosmic ray antiproton theories, with subsequent breakdown of the $A > 1$ antinuclei, have been proposed (e.g., Stecker et al. 1983).

Theories of secondary $\bar{p}$ production in p-p collisions in the galaxy are constrained by the observed galactic gamma-ray luminosity. The observed antiproton flux $\Phi_{\bar{p}}(E)$ implies a total galactic $\bar{p}$ production rate

*NAS/NRC Resident Research Associate

$$Q(\bar{p}) \sim \frac{4\pi V}{c} \int_0^\infty dE \, \frac{\Phi_{\bar{p}}(E)}{\beta \cdot \tau(E)} \sim (3.5 \times 10^{-14} V/\tau) \ \bar{p}/\text{sec},$$

where V is the galactic confinement volume and $\tau$ is the average galactic $\bar{p}$ residence time. Taking $V \sim \pi(15 \text{ kpc})^2 (1 \text{ kpc}) \sim 1.2 \times 10^{67}$ cm$^3$ and $\tau \sim 10^7$ yrs gives $Q(\bar{p}) \sim 2.1 \times 10^{39}$ $\bar{p}$/sec. If the production of a secondary $\bar{p}$ is accompanied by the production of $\langle n \rangle$ $\pi^\circ$-decay gamma rays, the resultant $\gamma$-ray luminosity of the galaxy $Q(\gamma) \sim \langle n \rangle Q(\bar{p})$. In the case of the production of >100 MeV photons in cosmic ray interactions, $\langle n \rangle_{cr} \sim 2.7 \times 10^3$, from the calculations of Stephens and Badhwar (1981) and Tan and Ng (1983a). If the $\bar{p}$ in the cosmic radiation are entirely cosmic ray secondaries, the > 100 MeV luminosity of the galaxy should therefore be at least $5.7 \times 10^{42}$ $\gamma$/sec, in contrast to the measured value of $\sim 2.5 \times 10^{42}$ $\gamma$/sec from the work of Bloemen et al. (1984). This latter number is an upper limit, since it includes a significant contribution from bremsstrahlung and inverse Compton $\gamma$-rays.

Various models have been designed to either increase the $\bar{p}$ lifetime $\tau$, incorporate additional $\bar{p}$ sources, or conceal the $\pi^\circ$ $\gamma$-rays. Although the integral production rate of $\bar{p}$ can then be made to agree with observations, most models still fail to predict a substantial low energy $\bar{p}$ flux because of the low energy cutoff that results from secondary interactions with stationary targets, in disagreement with the experiment of Buffington et al. (1981). Models that provide deceleration of the $\bar{p}$ after production or require that the Solar System occupies a special position in the galaxy have also been proposed (Stephens and Mauger 1984; Tan and Ng 1983b).

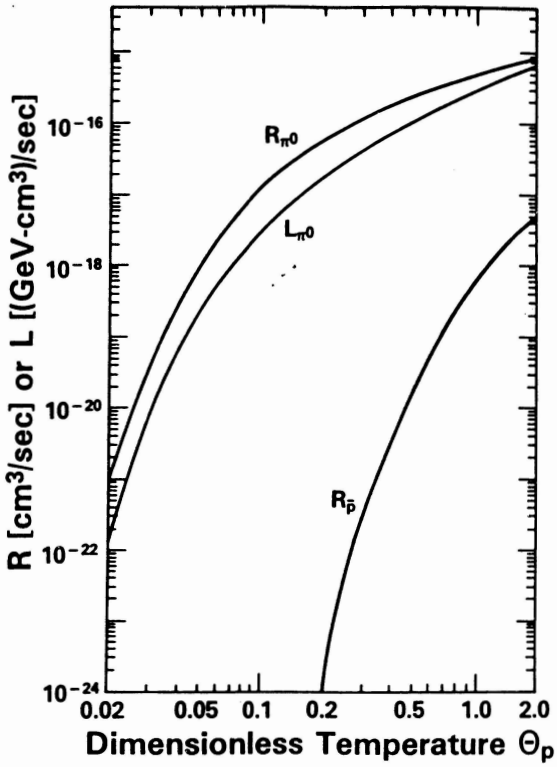


III. Secondary Discrete Source Model. We examine the possibilities that the low energy antiprotons observed in the cosmic radiation are produced through secondary p-p interactions in relativistic plasmas in the vicinity of a neutron star or black hole. At proton temperatures $\Theta_p = kT/m_p c^2 \gtrsim 0.2$ ($\Theta_p = 1$ corresponds to $\sim 10^{13}$ K), a significant number of secondary $\bar{p}$ can be produced. We have calculated the rate coefficients and production spectra (Weaver 1976; Dermer 1984) for secondary $\bar{p}$ using the

Fig. 1. The rate coefficients for secondary $\pi^\circ$ and $\bar{p}$ production from p-p collisions in a relativistic plasma at temperature $\Theta_p = kT/m_p c^2$. Also shown is the $\pi^\circ$ luminosity coefficient giving the total energy in secondary $\pi^\circ$ $\gamma$-rays produced at temperature $\Theta_p$.

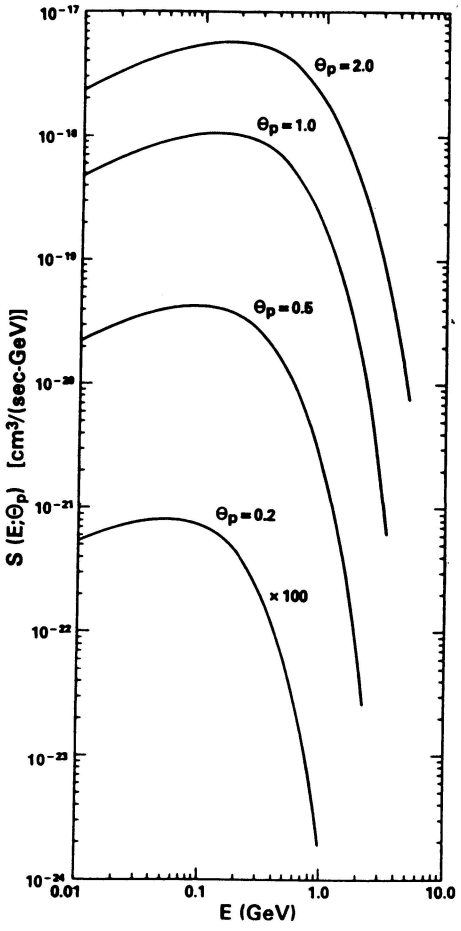


invariant cross section of Tan and Ng (1982) and the results are shown in Figs. 1 and 2. We have also calculated the rate and luminosity coefficients from secondary $\pi^\circ$ production data. From Fig. 1 we find that the efficiency for $\bar{p}$ production compared to $\pi^\circ$ production is greater than in the cosmic ray case for $\Theta_p \gtrsim 0.5$, so the total $\pi^\circ$-decay $\gamma$-ray luminosity will not exceed limits implied by $\gamma$-ray observations of the galaxy. In addition, a number of absorption processes likely to occur near compact objects, such as photon-photon or magnetic pair production, can further reduce the $\pi^\circ$ $\gamma$-ray luminosity.

The $\bar{p}$ spectra shown in Fig.2 for a variety of temperatures extend to low energies without the appearance of the kinematic cutoff found in the cosmic ray problem. The spectra peak at higher energies with increasing temperature, and exhibit an exponential decline above the peak temperature. But in all cases a very low energy secondary $\bar{p}$ component is calculated, which could possibly explain the low energy $\bar{p}$ observation of Buffington et al. (1981).

Fig. 2. Secondary $\bar{p}$ production spectra at various temperatures $\Theta_p = kT/m_pc^2$ are given as a function of kinetic energy E.

IV. Discussion. Possible production sites of the $\bar{p}$'s include the galactic bulge binary X-ray sources or the objects associated with the $\gamma$-ray point sources (e.g. Cyg X-3). Models for disk accretion (Eilek 1980) and spherical accretion incorporating shocks (Meszaros and Ostriker 1983) could yield proton temperatures as high as $\Theta_p \sim 1$. Although the establishment of a thermal distribution of protons may not be possible at these temperatures, this assumption affords the simplest calculations. Preliminary estimates employing nonthermal proton spectra in relativistic plasmas suggest low energy $\bar{p}$ spectra similar in form to the results of Fig. 2.

Transport of the secondary $\bar{p}$ from the production site can occur because antineutrons $\bar{n}$, produced in equal numbers as the $\bar{p}$ (Gaisser and Maurer 1973), are not confined by the ambient plasma magnetic field. The $\bar{n}$ will escape to the interstellar medium and subsequently decay into $\bar{p}$ (the calculations of Figs. 1 and 2 refer only to these particles). Because of the finite lifetime of the $\bar{n}$, an upper limit can be placed on the mass of black holes that serve as production sites for the $\bar{p}$. Requiring that the marginally relativistic $\bar{n}$ escape to ~ 10 Schwarzschild

radii implies a maximum black hole mass of $<10^7 M_\odot$. Past activity around such a massive black hole at the Galactic Center could have produced the antiprotons without a large contemporaneous gamma emission. A detailed treatment of $\bar{p}$ production in a relativistic plasma must also include distortions of the emergent $\bar{n}$ and $\gamma$-ray spectrum due to the intense gravitational field of the compact object, and possible reacceleration of the source spectrum in the galactic environment.

V. Conclusions. We have presented a model that can produce low energy antiprotons through secondary p-p interactions in relativistic plasmas. Such a model is in agreement with the observation of low energy antiprotons in the cosmic radiation and the observed $\gamma$-ray luminosity of the galaxy. Moreover, it agrees with the present lack of observations of antinuclei in the cosmic radiation, whose formation by secondary production processes is entirely negligible.

VI. References

J. B. G. M. Bloemen et al. 1984, Ap. J., 279, 136.
E. A. Bogomolov et al. 1979, Proc. 16th ICRC (Kyoto), 1, 330.
A. Buffington et al. 1981, Ap. J., 248, 1179.
C. D. Dermer 1984, Ap. J., 280, 328.
J. A. Eilek 1980, Ap. J., 236, 664.
T. K. Gaisser and R.H. Maurer 1973, Phys. Rev. Letters, 30, 1264.
R. L. Golden et al. 1979, Phys. Rev. Letters, 43, 1196.
P. Meszaros and J.P. Ostriker 1983, Ap. J., 273, L59.
F. W. Stecker et al., 1983, Astrophy. Space Sci., 96, 171.
S. A. Stephens and G.D. Badhwar, Astrophy. Space Sci., 76, 213.
S. A. Stephens and B. G. Mauger, in "High Energy Astrophysics", proceedings of the Nineteenth Recontre de Moriond Astrophysics Meeting, p. 217.
L. C. Tan and L. K. Ng 1982, Phys. Rev. D., 26, 1179.
L. C. Tan and L. K. Ng 1983a, J. Phys. G, 9, 227.
L. C. Tan and L. K. Ng 1983b, Ap. J., 269, 751.
T. A. Weaver 1976, Phys. Rev. A., 13, 1563.

# THE FLUX OF SECONDARY ANTI-DEUTERONS AND ANTIHELIUM PRODUCED IN THE INTERSTELLAR MEDIUM

O.C. Allkofer and D. Brockhausen
Institut für Reine und Angewandte Kernphysik
Universität Kiel, D- 2300 Kiel, F.R.G.

Abstract

Several measurements have been performed to find antiprotons in the primary cosmic radiation. Because it is difficult to get completely separated secondary produced antiprotons from primary ones, calculations based on accelerator results have been performed for the flux of secondary produced antideuterons and antihelium.

1. Introduction. Antiprotons in the primary cosmic radiation have been detected in the kinetic energy range between 130 MeV and 11.6 GeV by different groups and different methods (Golden et al., 1979; Bogomolov et al., 1979; Buffington et al., 1981).
It was not conclusively possible to demonstrate if there was a contribution of primary antiprotons. Since cross-sections for secondary produced $\bar{d}$, $^{3}\overline{He}$ and $^{4}\overline{He}$ are some orders of magnitude lower than for $\bar{p}$ the secondary background would be negligible.

2. Methods. Using the data for the production of $\bar{d}$ in pp-collisions at $\sqrt{s}$ = 45 GeV and $\sqrt{s}$ = 53 GeV and for the production of $^{3}\overline{He}$ at $\sqrt{s}$ = 19.4 GeV (Albrow et al., 1975; Gibson et al., 1978; Armitage et al., 1979; Bussière et al., 1980) the following fits for the invariant cross-sections for the production of $\bar{d}$ and $^{3}\overline{He}$ were obtained:

$$\left(E\frac{d^3\sigma}{dp^3}\right)_{\bar{d}} = 4\ (1 - x_R)^{16}\ \exp\ (-2.62p_T)\ \times\ 10^{-3}\left[mbc^3/(GeV)^2\right],$$

$$\left(E\frac{d^3\sigma}{dp^3}\right)_{3\overline{He}} = (1 - x_R)^{24}\exp(-2p_T) \times 10^{-7} \left[mbc^3/\ (GeV)^2\right],$$

$x_R = \frac{E^*}{E^*_{max}}$ : radial scaling variable;

$E^*$: energy of the antiparticle in the center-of-mass system;

$E^*_{max}$ : maximum energy of the antiparticle in the center-of-mass system;

$p_T$ : transverse momentum.

The measured invariant cross-sections, which were used for the fits, have a statistical error of about 30 %.

With a mass dependence for the invariant cross-section (Bussière et al., 1980) the fit for the invariant cross-section of $^4\overline{He}$ was obtained:

$$\left(E\frac{d^3\sigma}{dp^3}\right)_{4\overline{He}} = (1 - x_R)^{32}\exp\ (-2p_T) \times 10^{-12} \left[mbc^3/\ (GeV)^2\right].$$

These 3 formulas have been used for the whole energy range because no data exist for other energies.
Integrating the invariant cross-sections over the whole solid-angle we obtained the differential cross-sections for the production of $\overline{d}$, $^3\overline{He}$ and $^4\overline{He}$. Figure 1 shows the results for primary protons with an energy of 1000 GeV.
Using these differential cross-sections and an interstellar energy spectrum of protons given by Tan and Ng (1983) of the form:

$$j_p(T_p) = 2.0 \times 10^4\ T_p^{-2.75}\ (m^{-2}sr^{-1}s^{-1}\ GeV^{-1}),$$

where $T_p$ is the kinetic energy of the protons in GeV, the flux of antiparticles $\overline{d}$, $^3\overline{He}$ and $^4\overline{He}$ has been derived on the basis of the leaky box model with the mean escape length $\lambda = 5\ g\ cm^{-2}$ independent of energy (Gaisser and Levy, 1974) and under neglect of the inelastic interactions of the produced antiparticles.

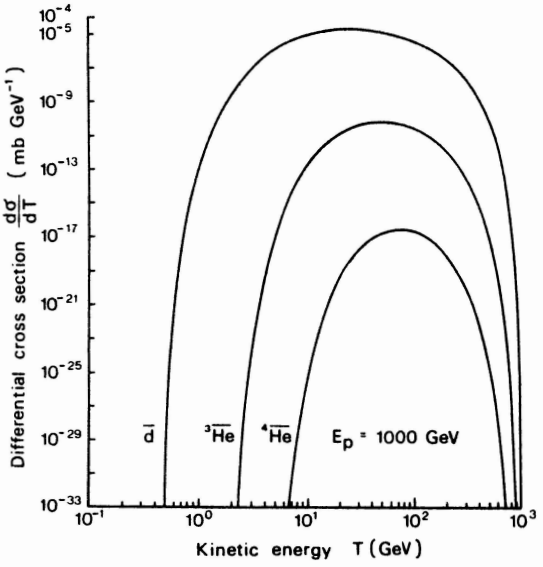


Fig. 1. The differential cross-section for the production of $\bar{d}$, $^3\overline{He}$ and $^4\overline{He}$ for a primary proton of 1000 GeV.

3. Results. Figure 2 shows the curves of the secondary fluxes in dependence from the kinetic energy of the produced antiparticles.

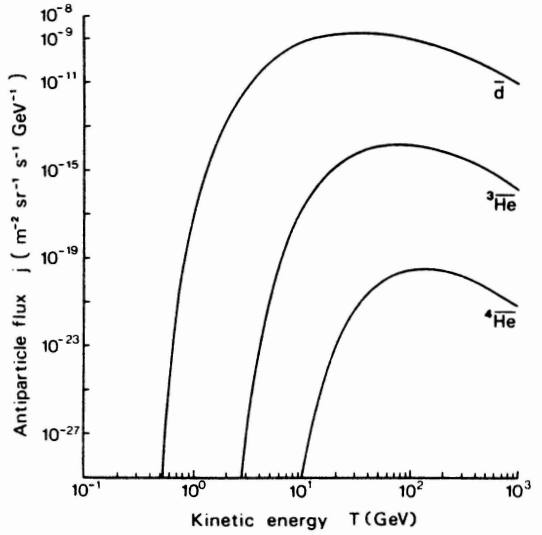


Fig. 2. The secondary flux of $\bar{d}$, $^3\overline{He}$ and $^4\overline{He}$ in dependence from their kinetic energy.

With these results the event rates for the secondary antiparticles could be calculated. Table I shows the values for the maximal flux using a geometry factor of 1 $m^2$sr.

TABLE I

Event rates for the detection of secondary antiparticles for a geometry factor of 1 $m^2$sr

| Particle | Event rate ($yr^{-1}$) |
|---|---|
| $\bar{p}$* | $5.4 \times 10^{3}$ |
| $\bar{d}$ | $4.7 \times 10^{-2}$ |
| $^{3}\bar{He}$ | $4.4 \times 10^{-7}$ |
| $^{4}\bar{He}$ | $9.4 \times 10^{-13}$ |

* The $\bar{p}$ event rate is calculated from the measured differential $\bar{p}$-flux of Buffington et al. (1981).

References

Albrow, M.G., et al., 1975, Nucl. Phys. B 97, 189.

Armitage, J.C.M., et al., 1979, Nucl. Phys. B 150, 87.

Bogomolov, E.A., et al., 1979, Proc. 16th Int. Conf. Cosmic Rays Kyoto 1, 330.

Buffington, A., et al., 1981, Astrophys. J. 248, 1179.

Bussière, A., et al., 1980, Nucl. Phys. B 174, 1.

Gaisser, T.K., and Levy, E.H., 1974, Phys. Rev. D 10, 1731.

Gibson, W.M., et al., 1978, Nuovo Cimento Letters 21, 189.

Golden, R.L., et al., 1979, Phys. Rev. Letters 43, 1196.

Tan, L.C., and Ng, L.K., 1983, J. Phys. G: Nucl. Phys. 9, 227.

# ANALYSIS OF EXPERIMENTAL DATA ON INTERSTELLAR ANTIPROTONS IN THE LIGHT OF MEASUREMENTS OF HIGH-ENERGY ELECTRONS AND $^3$He NUCLEI

L.C.Tan
Department of Physics and Astronomy
University of Maryland
College Park, MD 20742
USA

We have reexamined the interstellar antiproton calculation in view of the recent progress in measurements of interstellar electrons and $^3$He nuclei. It is found that the divergence between our predicted antiproton flux and the existing datum at very low energies is increased.

It appears that our proposed nonuniform galactic disk (NUGD) model (1) can qualitatively explain the unexpectedly large flux of interstellar antiprotons ($\bar{p}$'s). Nevertheless, it should be noted that some ambiguities existed in the prototype of the model. For instance, it was unclear what fraction of observed $\bar{p}$'s is of local origin. Moreover, previously the value of cosmic-ray escape pathlength ($\lambda_e$) was suggested with quite a large arbitrariness.

In order to improve the model itself we have compared the high-energy electron spectrum predicted for it with measured data(2). This comparison is significant in the estimation of astrophysical parameters inherent in the model. Therefore, we find that in the observed proton flux the fraction $\varepsilon$ of the protons being of local origin is only 5±1 %, indicating that the dominant part of cosmic-ray protons is contained in the distant component of cosmic-rays. Further, the deduced $\lambda_e$ value in the $H_2$ cloud region is about 3 times that suggested by the leaky box model, which is consistent with our conclusion that the main part of observed $\bar{p}$'s is produced in the $H_2$ cloud region(1).

Thus an improved calculation is performed to deduce the interstellar $\bar{p}$ flix based on our newly obtained parameter values in the NUGD model. In our calculation(see the model elements shown in Fig. 1 of OG 7.2-10) the $\lambda_e$ value in Box 1 or Box 2 is taken from the empirical relationship given in Ref. (3) (hereafter we use the subscripts 1, 2, I and II to express the quantities referred to Boxes 1, 2, I and II respectively),

$$\lambda_{e12}(R(GV/c)) = 35 \left( 1 + \left( 1.88 / R \right)^2 \right)^{-n/2} R^{-0.7} , \qquad (1)$$

where the HEAO 3 data(3) for both the B/C and N/O ratio prefer a value of n=3, only the subiron to iron ratio requires a lesser value of n. However, we note that the preliminary data on iron nuclei obtained by the same group(4) also exhibit a flux increase with decreasing energy which is faster than that predicted for the leaky box model. The reason for it at present is unknown. Since one of the basic assumptions in our NUGD model is that the 'leaky box' concept should be applicable to its individual elements, for the time being the inconsistency shown above

makes it reasonable to neglect the data on iron-group of nuclei and keep n=3 in Eq. (1). Thus the deduced $j_{\bar{p}12}$ (i.e., the $\bar{p}$ flux predicted for the leaky box model) is shown in Fig. 1 as the curve OPLB, which is comparable with our previous prediction( the curve TLBF in Fig. 1).

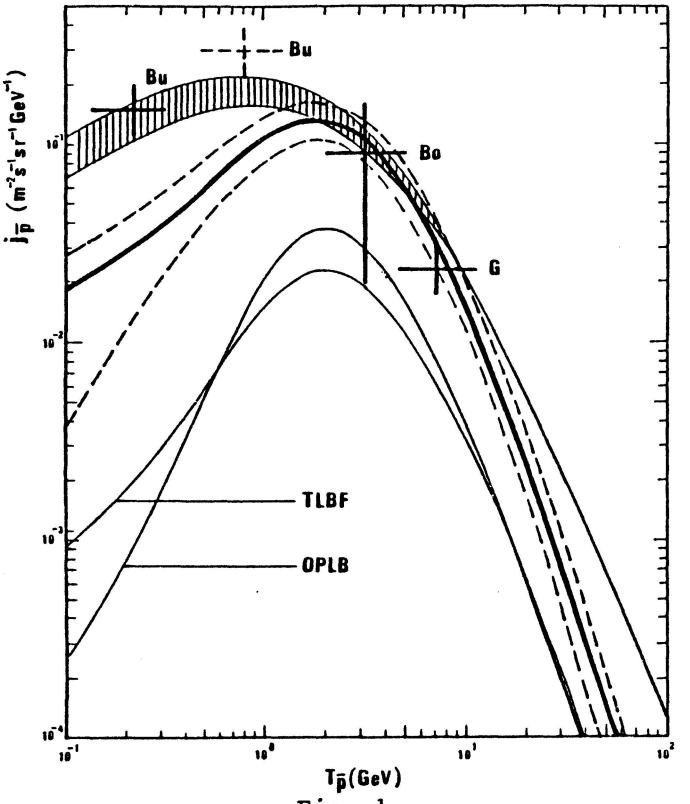

Fig. 1

In the deduction of the source term of $\bar{p}$'s in the $H_2$ cloud region the contribution of 'primary' $\bar{p}$'s, which originate from Box 2 and flow into Box II, should be taken into account (2). Thus the contributions coming from the 'primary' and the 'secondary' (i.e., locally produced) components of $\bar{p}$'s in $q_{\bar{p}II}$ are shown in Fig. 2 for the case of $\delta = 0.7$, where $\delta$ is the power index of the rigidity (R) dependence of $\lambda_e$. It appears that the dominant part of $\bar{p}$'s is indeed locally produced.

Obviously, the estimation of the $\bar{p}$ flux in the dence $H_2$ cloud region, $j_{\bar{p}II}$, should be dependent upon the assumed value of cosmic-ray convection velocity, V. Nevertheless, the convection motion of cosmic rays should play a less serious role in view of the fact that 10 GeV cosmic rays have a diffusion coefficient of about $10^{30}$ cm$^2$/s (2). Therefore, the allowable range of the $\bar{p}$ flux may be estimated by assuming some extreme values of V. Here we will consider the cases of V = 0 (no convection motion) and V = 300 km/s (the estimated velocity of galactic wind for the normal galaxy(5)). Thus $j_{\bar{p}II}$ and the $\bar{p}$ flux after the adiabatic deceleration in the assumed boundary layer ($j_{\bar{p}de}$), and the $\bar{p}$ flux reaching the solar neighbourhood from Box II ($j_{\bar{p}s}$), are shown in Fig. 3 for the case of $\delta = 0.7$. Since the observed $\bar{p}$ flux in the solar neighbourhood should contain both the distant and the local components, so that we have

$$j_{\bar{p}NUGD} = ( 1 - \varepsilon ) j_{\bar{p}s} + \varepsilon j_{\bar{p}12} . \qquad (2)$$

In Fig. 1 we compare our newly predicted $j_{\bar{p}}$ (the thick solid line) and its allowable range due to uncertainties of $\lambda_{e0II}$ and $\delta$ (the region between both dashed lines) with our previous prediction (the shaded region) and the existing $\bar{p}$ data(6)-(8). It is found that the consistency of our new prediction with the measured data at $T_{\bar{p}}$, the $\bar{p}$ kinetic

energy, above about 1 GeV is significantly improved. However, the divergence between our new prediction and the very low-energy datum(8) is increased, though it is still less than 2 standard deviations.

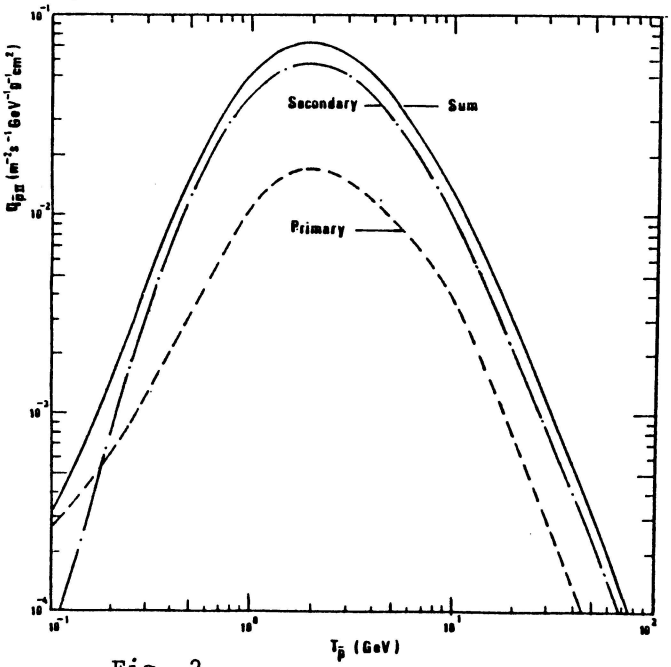


Fig. 2

It follows that the reliability of the datum Bu (8) shown in Fig. 1 may be questionalbe, because the recently measured $^3$He data in the corresponding energy range do not show a similarly abnormal increase(9). Actually, Jordan and Meyer(9) require a nearly constant value of $\lambda_e$ ($\doteq$ 15 gcm$^{-2}$) to explain the measured ratio of $^3$He to $^4$He in the energy range of 0.1 - 10 GeV/n. Note their deduced $\lambda_e$ value, being about 3 times that suggested by the leaky box model, is in agreement with our reported value of $\lambda_{eII}$(2). Thus the analysis of the isotope composition of cosmic-ray He nuclei excludes any abnormal increase of $\lambda_{eII}$ at low energies, and hence any underestimation of $j_{\bar{p}II}$ in our calculation.

Furhtermore, if the left divergence between our new prediction and the datum Bu is due to the existence of an exotic $\bar{p}$ source, the source should be significant only below 1 GeV. It is because we have already explained the existing $\bar{p}$ data at $T_{\bar{p}}$ higher than 1 GeV based on the existing model. It appears that our calculation is in conflict with the extragalactic origin of observed $\bar{p}$'s(10), because at least at $T_p \geq 1$ GeV the contribution of the exotic $\bar{p}$ source should be negligible.

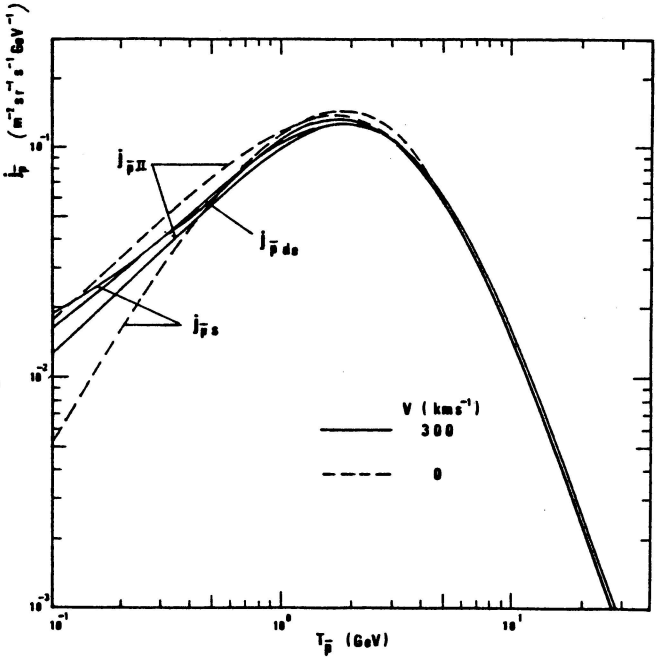


Fig. 3

References:
1. Tan,L.C. and Ng,L.K. 1983, Ap. J., 269, 751.
2. Tan,L.C. 1985, Ap.J., in press.
3. Ormes,J. and Protheroe,R.J. 1983, Ap. J., 272, 756.
4. Juliusson,E. et al., 1983, Proc. 18th Internat. Cosmic Ray Conf. (Bangalore), 2, 21.
5. Ipavich,F.M. 1975, Ap.J., 196, 107.
6. Golden,R.L. et al., 1979, Phys. Rev. Letters, 43, 1196.
7. Bogomolov,E.A. et al., 1979, Proc. 16th Internat. Cosmic Ray Conf. (Kyoto), 1, 330.
8. Buffington,A. et al., 1981, Ap. J., 248, 1179.
9. Jordan,S.P. and Meyer,P. 1984, Phys. Rev. Letters, 53, 505.
10. Stecker,F.W. et al., 1983, Astrophys. & Space Sci., 96, 171.

# OBSERVED ANTIPROTONS AND ENERGY DEPENDENT CONFINEMENT OF COSMIC RAYS: A CONFLICT?

S.A. Stephens
Tata Institute of Fundamental Research
Homi Bhabha Road, Bombay 400005, India

ABSTRACT

In the frame work of energy dependent confinement for cosmic rays, the energy spectrum inside the source is flatter than that observed. Antiproton ($\bar{p}$) observation suggests large amount of matter is being traversed by cosmic rays in some sources. As a result, secondary particles are produced in abundance. We have calculated their spectra and it is shown that the energy dependent confinement model is in conflict with some observations.

1. Introduction. The observed secondary to primary nuclei in cosmic rays decrease with energy suggesting that matter traversed by cosmic rays depends upon energy. Therefore, it was postulated (Eg. Juliusson et al. [1]) that the confinement of cosmic rays in the Galaxy is energy dependent. Recent observations show that the behaviour of this dependence is $\alpha R^{-\delta}$ above ~ 2 GV/c with $\delta$ = 0.6 to 0.7 [2,3]. This would mean that the accelerated spectrum of cosmic rays has a spectral index $\beta$ = 2.15 to 2.05. $\bar{p}$ observations show that cosmic rays traverse a large amount of matter inside some sources. Because of the flatness of source spectrum, secondary particles are copiously produced [4], and the effect of energy loss processes is less felt by the particles. Recently, it is shown that supernova (SN) explosion in dense cloudlets can explain $\bar{p}$ observations [5]. This work was based on the Nested Leaky Box Model [6], in which cosmic ray source spectrum has $\beta$ = 2.75. In this paper, we calculate the secondary particle production in SN, which explode in dense cloudlets, in the framework of energy dependent confinement model. We then compare the spectra of $\gamma$-rays, electrons and positrons with observation.

2. $\gamma$-ray Emission from Sources. We have established a set of coupled differential equations to describe the propagation of protons, $\bar{p}$, $e^{\pm}$ inside SN envelope, by taking into account all energy loss processes including adiabatic cooling during expansion [7]. The initially accelerated spectra is obtained by normalizing the interstellar spectra at 2 GV/c and thus we obtained $1.65 \times 10^4$ $R^{-2.15}/(m^2.sr.s.GV/c)$ for nucleons and 90 $R^{-2.15}/(m^2.$ sr. s. GV/c) for electrons. We consider that the SN expansion continues in the cloudlet till about 50 $g.cm^{-2}$ matter is being traversed by cosmic rays. Because of the flat spectrum of nucleons, it is found that only 10% of the observed nucleons in cosmic rays have to come from such sources in order to account for the observed $\bar{p}$; the corresponding value for $\beta$ =2.75 is 30% [8]. The effect of synchrotron radiation on electron spectrum is also small and the spectrum

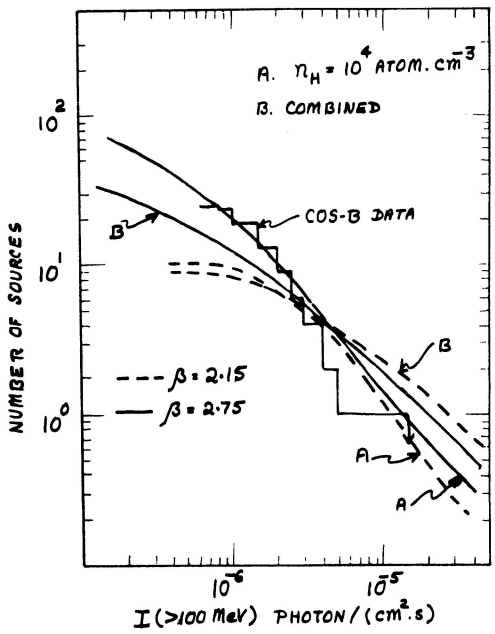


*Fig.1 Integral distribution of γ-ray sources is shown as a function of intensity above 100 MeV. The dashed curves are for energy dependent model and the solid curves are for Nested Leaky Box model.*

at high energies is not much depleted.

We have calculated the spectrum of γ-rays resulting from $\pi^\circ$ decay and bremsstrahlung processes. If 90% of the observed cosmic rays come from SN exploding in normal interstellar medium, the scaling required to estimate the total brightness of the source from the normalized interstellar spectrum is $\approx 10^{62}$. In order to calculate this number, we consider a galactic volume of R = 15 kpc and h = 0.5 kpc, in which cosmic rays are stored for $3 \times 10^7$ yrs. In this volume, the rate of SN explosion in interstellar medium is one in 30 yrs. We assume that acceleration is complete in ~200 yrs and the adiabatic cooling effective during the adiabatic phase. The number of SN required in cloudlets to account for the observed $\bar{p}$ is calculated and the relative number to that explode in interstellar space is found to be 0.129, 0.093, 0.075 and 0.061 for $n_H = 10^4$, $4 \times 10^4$, $10^5$ and $2.5 \times 10^5$ atom.$cm^{-3}$ respectively. Making use of these parameters, we have calculated the luminosity distribution of γ-ray sources in the Galaxy as described elsewhere [9].

We have shown in Fig. 1, the luminosity distribution of γ-ray sources for energies 100 MeV, assuming that the distribution of SN in the Galaxy is similar to the molecular hydrogen [10]. The dashed Curve A is calculated for $n_H = 10^4$ $cm^{-3}$ and Curve B after folding in the observed density distribution of clouds [11]. These are compared with the Cos-B distribution [12], which is shown by the histogram. It is clear from this figure that there is no serious conflict with the data. For comparison, we have shown by solid curves the predictions with $\beta = 2.75$ [9]. We have also estimated the spectral hardness of γ-ray sources, which is defined as I (> 300 MeV)/ I(> 100 MeV). It is found that over the life of the SN, this varies only by small amount from

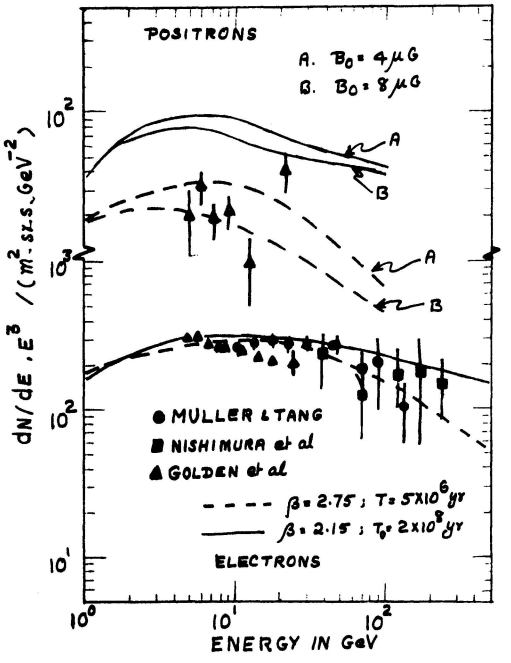


*Fig. 2 Electron spectrum is shown in the lower part and positron spectrum in the upper part. The solid curves are for energy dependent model and the dashed curves for Nested Leaky Box model.*

0.475 to 0.46, due to the flat input spectrum. This value is indeed in conflict with the observed values [12], most of which are much smaller.

3. Electron Spectrum. We have calculated the equilibrium spectrum of electrons and positrons in interstellar space by considering two kinds of source spectra $Q_{e^\pm}$. One of them is from SN exploding in dense cloudlets, which contribute ≈ 10% of the observed nucleons, and the other from SN explosion in normal interstellar medium. The equilibrium spectrum is obtained by solving the equation.

$$\frac{dJ_{e^\pm}}{dt} = \frac{\partial}{\partial E}\left(J_{e^\pm}\frac{dE_{e^\pm}}{dt}\right) + Q_{e^\pm} - J_{e^\pm}/T(E) \quad \ldots \quad (1)$$

in which T(E) is taken to be $T_0E^{-\delta}$, and $T_0$ is varied to obtain a good fit to the data. We have plotted in the lower part of Fig. 2, the observed flux values from recent experiments [13-15]. The solid curve is the calculated spectrum using a value of $T_0 = 2\times10^8$ yrs. This value of $T_0$ is inconsistent with $1.4\times10^7$ yrs obtained from $^{10}$Be data at low energies [16]. We have also shown the calculated equilibrium spectrum for $\beta = 2.75$ [17] with $T = 5\times10^6$ yrs, which is consistent with the observed value within errors.

Making use of the same value of $T_0$ obtained from the study of electrons, we have calculated the equilibrium spectrum of positrons. This spectrum is shown in the upper part of Fig. 2 by solid curves. The two curves A and B correspond to magnetic fields in the dense cloudlets assuming that the field strength scales as $(B_0\sqrt{n_H})$ with $B_0 = 4$ and 8 μG respectively. It is clear that the observed spectrum [18] is not

in agreement with the calculations. If one reduces the value of $B_o$ or $T_o$, the deviation from the data would increase further. We have also shown the calculated positron spectrum for $\beta = 2.75$ [18] and one notices a good agreement with the observation.

4. Discussion. Many difficulties associated with the energy dependent confinement model have been pointed out earlier [19]. They include power requirement, streaming velocity at high energies and the smooth spectral shape extending to very high energies. We have shown here that, though the expected luminosity distribution of sources is not in conflict with the Cos-B data, the observed spectral hardening of $\gamma$-ray sources is not in agreement with the expectation. Secondly, the observed electron spectrum is clearly in conflict with the expectation [13]. Thirdly, the model predicts too large a flux of positrons. The above conclusions are further strengthened if the value of $\delta$ is indeed 0.7 [2].

The analysis made here is based on the hypothesis that antiprotons are produced in sources as secondary particles. However, if $\bar{p}$ comes from external galaxies [20], one may perhaps circumvent the present inconsistencies. However, it has been shown by Stephens [21] from a study of muon charge ratio at sea level that the extragalactic hypothesis and energy dependent confinement model cannot co-exist.

References

[1] E. Juliusson et al., Phys. Rev. Letters, 29, 445 (1972)
[2] J.F. Ormes and R.J. Protheroe, Ap.J., 272, 756 (1983)
[3] L. Koch-Miramond, Proc. 18th ICRC (Bangalore), 9, 275 (1983)
[4] P.O. Lagage and C.J. Cesarsky, "High Energy Astrophysics" Ed. J. Audouze and J.T. Thanhvan, p.203 (1984)
[5] B.G. Mauger and S.A. Stephens, Proc. 18th ICRC (Bangalore) 9, 171 (1983)
[6] R. Cowsik and L.W. Wilson, Proc. 13th ICRC (Denver), 1, 500 (1973)
[7] S.A. Stephens, This Conference OG 2.5-2
[8] S.A. Stephens and B.G. Mauger "High Energy Astrophysics", Ed. J. Audouze and J.T. Thanhvan, p.217 (1984); To appear in Ap.Sp.Sci.(1985)
[9] S.A. Stephens, This Conference OG 2.5-3
[10] W.B. Burton and M.A. Gorden, Ap.J., 207, L189 (1976)
[11] R.A. Linke and P.F. Goldsmith, Ap.J., 235, 437 (1980)
[12] W. Hermson, Ph.D. Thesis, University of Leiden (1980)
[13] D. Muller and J. Tang, Proc. 18th ICRC (Bangalore), 2, 60 (1983)
[14] J. Nishimura et al., Ap. J., 238, 94 (1980)
[15] R.L. Golden et al., Ap.J., 287, 622 (1984)
[16] M. Garcia Munoz et al., Proc. 17th ICRC (Paris), 2, 72 (1981)
[17] S.A. Stephens, This Conference, OG 6.2-9
[18] R.L. Golden et al., This Conference
[19] T.N. Rengarajan et al., Proc. 13th ICRC (Denver), 1, 384 (1983)
[20] F.W. Stecker et al., Ap. Sp. Sci., 96, 171 (1983)
[21] S.A. Stephens, Proc. 18th ICRC (Bangalore), 12, 71 (1983): To appear in Astron. Ap. (1985).

# ANTIPARTICLES IN THE EXTRAGALACTIC COSMIC RADIATION

F.W. Stecker
Laboratory for High Energy Astrophysics
NASA Goddard Space Flight Center
Greenbelt, Maryland, U.S.A.

and

A.W. Wolfendale
Physics Department
University of Durham
Durham, U.K.

ABSTRACT

It may be possible to account for a previously puzzling feature - a "bump" in the energy range $10^{14}$-$10^{15}$ eV - of the cosmic ray spectrum by hypothesizing a primary extragalactic origin for the bulk of the observed cosmic ray antiprotons, although such an explanation is not unique. In this model, most of the cosmic rays above $10^{15}$ eV are extragalactic. We describe a method of testing this hypothesis experimentally.

1. Introduction. One of the most fundamental questions in cosmology is the question of the existence of antimatter in significant quantities in the universe. Does antimatter play an equal role with matter in the makeup of the galaxies? This question has now become a question of fundamental importance to physics as well. In the contemporary paradigm of grand unified gauge theories it is related to the question of the nature of CP violation at high energies (1,2). Recent theoretical work based on the concepts of grand unified theories has resulted in the development of a plausible baryon-antibaryon domain theory in which matter and antimatter are created in separate regions of survivable size to begin with (3-5). Various observational aspects of this theory have been previously discussed (6,7) and the subject of baryon symmetric cosmology has been recently reviewed elsewhere (8,9).

2. Primary Antimatter. The present status of cosmic ray antiproton measurements and the attempts to understand them have been recently reviewed (10) and an exegesis of the primary extragalactic origin hypothesis has also been recently given (11). We will discuss further implications of potential basic import to cosmic ray research here and we will also propose an experimental search program based on these considerations. We start with the hypothesis that the baryon symmetric domain cosmology leads to a flux of extragalactic cosmic rays consisting of roughly equal amounts of protons and antiprotons with the sources of these cosmic rays being primarily active galaxies (12) and with helium and antihelium nuclei being supressed by destruction processes in these sources (11). We assume that the galactic wind is too weak to keep out the extragalactic cosmic radiation. Observations favor the interpretation that the galactic wind is in reality a "breeze" (13).

The measured spectrum of cosmic radiation can be represented by a power

law in energy of the form $KE^{-\Gamma}$ with the spectral index $\Gamma \simeq 2.75$ for several decades above the 10 GeV energy level. It appears likely that this radiation is produced primarily in galactic sources (14,15). Furthermore, the source spectrum of this radiation is expected to have a lower spectral index $\Gamma_s$ than that observed at the earth which has been steepened by energy dependent propagation effects. A value for $\Gamma_s$ of approximately 2.0 to 2.2 appears to be likely for two reasons. (A) Measurements of the ratio of secondary to primary nuclei in the cosmic radiation suggest that the mean lifetime in the Galaxy owing to trapping by the tangled galactic magnetic fields falls with energy as $E^{-\delta}$ where the most recently derived value (16) of $\delta \simeq 0.7$. (B) The theoretical shock acceleration models for cosmic ray production currently favored (17) generally yield production spectra with $\Gamma_s$ close to 2.

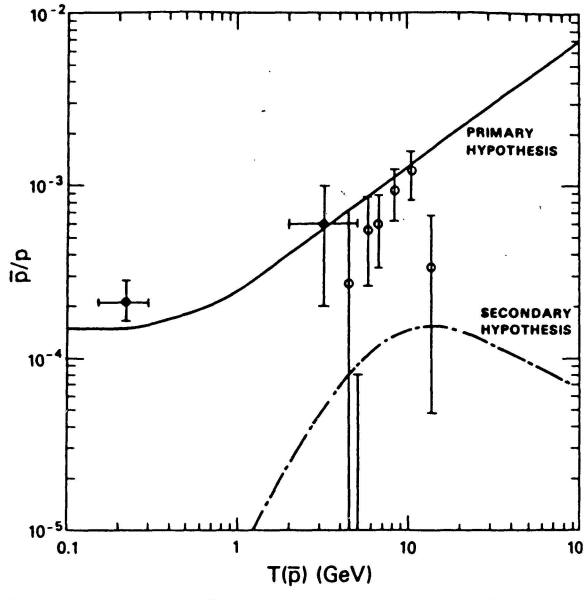


If we assume that there exists a general acceleration mechanism for generating cosmic rays which acts in both galactic and extragalactic sources to give a universal source spectrum with $\Gamma_s \simeq 2$, as is now thought to be the case with shock acceleration, then the extragalactic cosmic ray component should reflect this source spectrum. Thus, with the antiprotons assumed to be both primary and extragalactic and the bulk of the protons to be galactic, the expected ratio of antiprotons to protons should increase with energy as $E^{\delta}$.

Figure 1. Observations and theoretical $\bar{p}/p$ ratios as a function of kinetic energy. The data points are from Refs.(18-20). The theoretical curves take account of solar modulation effects.

Taking $\delta \simeq 0.7$, antiprotons could make up approximately one per cent of the cosmic ray flux at an energy of $\simeq$ 500 GeV and even $\sim$ 50 per cent at higher energies. This has important observational implications (see section 3). The situation is indicated in Figure 1 which shows the present data on $\bar{p}/p$ ratios as a function of kinetic energy and the theoretical curve corresponding to a primary extragalactic antiproton flux. Solar modulation flattens the theoretical curve at low energies. Additional secondary production of antiprotons (as shown) is relatively unimportant. It can be seen that the theoretical curve for the extragalactic primary origin hypothesis provides an encouragingly good fit to the present $\bar{p}$ data. Thus, our hypothesis has possible observational support.

Figure 2 shows the effect of extrapolating the extragalactic intensity of both protons and antiprotons (this introduces a factor of two) with a spectral index of 2 to higher energies and superposing it on the galactic cosmic ray spectrum with index $\Gamma \simeq 2.75$. Note that such an

extrapolation implies that the extragalactic and galactic cosmic ray fluxes become comparable at an energy of about $10^5$ GeV and that extragalactic particles predominate above this energy. It is interesting that the resultant flattening in the spectrum occurs at this particular energy where there have been claims (22) of a flattening in the cosmic ray spectrum as inferred from measurements of extensive air showers. A steepening in the spectra of both the galactic and extragalactic components would be required by the observations for energies above $10^6$ GeV.

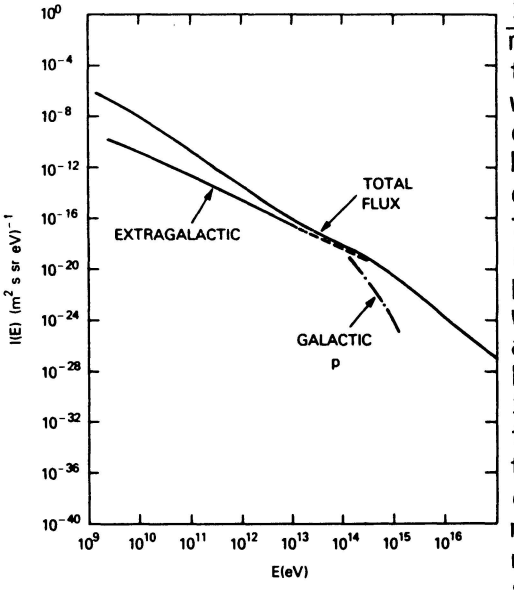


3. Experimental Tests. Since our model indicates that the antiproton-to-proton ratio which should increase with energy, measurements of the sign of the charges of cosmic rays at the highest practical energy and the determination of the spectra of the various charged components of the cosmic radiation up to that energy will provide a test of our hypothesis as well as the black hole hypothesis (21) and the photino hypothesis (Cf. Fig. 1 here with Fig. 2 of paper OG 6.1-9). Such a test requires the placement of the experiment above the atmosphere so that the incoming cosmic ray nuclei can be measured directly. Furthermore, the sign of their charges (and magnitude) may be measured by use of a superconducting magnet. A detector of

Figure 2. The effect of extragalactic primary protons and antiprotons on the total cosmic-ray spectrum according to the model discussed in the text. It can be seen that this model may account for the putative flattening in the observed cosmic ray spectrum near $10^{14}$ eV.

this type, with an attainable energy of about 500 to 1000 GeV, could be flown aboard a space shuttle (23,24). In addition, an emulsion stack experiment could be flown on a high altitude balloon or on the space shuttle to look for antihelium nuclei, even at the reduced level implied by our hypothesis. A polar orbit would be desirable to avoid the geomagnetic cutoff. In view of the almost impossible odds of creating a secondary $^4$He antinucleus, the unambiguous detection of even one such particle would provide irrefutable evidence of primary cosmic ray antimatter. (The observed low-energy antiprotons in the cosmic radiation are also quite difficult to explain as secondaries from cosmic-ray interactions.)

If the $\bar{p}/p$ ratio is observed to continue to increase as $E^{0.7}$ or thereabouts at higher energies, then our hypothesis of extragalactic antiprotons from antimatter galaxies will have very strong support. This would rule out the photino and black hole hypotheses. The observation of antihelium nuclei would, as already mentioned, provide certainty. The extent to which non-observation of antihelium disproves our hypothesis is unclear, but if $\bar{\alpha}/\alpha \ll 10^{-5}$ (the value expected very

approximately on the basis of $\bar{\alpha}$'s leaking from "normal" antimatter galaxies) then the difficulty would be severe.

The authors would like to thank Dr. Jonathan Ormes for helpful discussions.

REFERENCES

1. Brown, R. W. and Stecker, F. W., Phys. Rev. Lett. 43, 315 (1979).
2. Senjanovic, G. and Stecker, F. W., Phys. Lett. 96B, 285 (1980).
3. Sato, K., Phys. Lett. 99B, 66 (1981).
4. Kuzmin, V.A., Tkachev, I.I. and Shaposhnikov, M.E., Phys. Lett. 105B, 167 (1981).
5. Mohanty, A. K. and Stecker, F. W., Phys. Lett. 143B, 351 (1984).
6. Chechetkin, V.M., Khlopov, M. Yu. and Sapozhnikov, M. G., Rev. del Nuovo Cimento 5, 1 (1982).
7. Stecker, F.W., in Early Evolution of the Universe and its Present Structure, ed. G.O. Abell and G. Chincarini, Reidel Pub. Co., 6. Dordrecht, Holland, 437 (1983).
8. Stecker, F.W., Ann. N.Y. Acad. Sci. (Proc. 10th Texas Symp. on Relativistic Astrophys.) 375, 69 (1981).
9. Stecker, F.W., in Progress in Cosmology, ed. A.W. Wolfendale, Reidel Pub. Co., Dordrecht, Holland, 1 (1982).
10. See review by R.J. Protheroe in Composition and Origin of Cosmic Rays ed. M.M. Shapiro, D. Reidel Pub. Co., Dordrecht, Holland, 119 (1983).
11. Stecker, F.W., Protheroe, R.J. and Kazanas, D., Ap. and Space Sci. 96, 171 (1983).
12. Ginzburg, V. L. and Syrovatskii, The Origin of Cosmic Rays, Pergamon Press, London (1964).
13. Jones, F.C., Astrophys. J. 229, 747 (1979).
14. Dodds, D. Strong, A.W. and Wolfendale, A.W., Mon. Not. Royal Astron. Soc. 171, 569 (1975).
15. Stecker, F.W., Phys. Rev. Lett. 35, 188 (1975).
16. Ormes, J.F. and Protheroe, R.J., Astrophys. J. 272, 756 (1983).
17. Drury, I., Axford, W.I. and Summers, D., Mon. Not. Royal Astron. Soc. 198, 833 (1982).
18. Golden, R.L., et al., Astrophys. Lett. 24, 75 (1984).
19. Bogolmolov,E.A.et al.,Proc. 16th Int. Cosmic Ray Conf. 1, 330 (1979).
20. Buffington, A. et al., Astrophys. J. 248, 1179 (1981).
21. Kiraly, et al. Nature, 293, 120 (1981).
22. Kempa, J., et al., J. Phys. A7, 1213 (1974).
23. Stecker, F.W. and Wolfendale, A.W. Nature, 309, 37 (1984).
24. Ormes, J.F., et al. in Proc. Workshop on Cosmic Ray Exp. for the Space Station (1985).

# GALACTIC COSMIC RAY ANTIPROTONS AND SUPERSYMMETRY

F. W. Stecker
NASA Goddard Space Flight Center, 665
Greenbelt, MD 20771, U.S.A.

T. Walsh and S. Rudaz
Physics Dept.
University of Minnesota
Minneapolis, MN 55455, U.S.A.

ABSTRACT

We consider the physics of the annihilation of photinos ($\tilde{\gamma}$) as a function of mass in detail, in order to obtain the energy spectra of the cosmic-ray $\bar{p}$'s produced under the assumption that $\tilde{\gamma}$'s make up the missing mass in the galactic halo. We then compare the modulated spectrum at 1 a.u. with the cosmic-ray $\bar{p}$ data. A very intriguing fit is obtained to all of the present $\bar{p}$ up to 13.4 GeV data for $m_{\tilde{\gamma}} \sim 15$ GeV. We predict a cutoff in the $\bar{p}$ spectrum at $E = m_{\tilde{\gamma}}$ above which only a small flux from secondary production should remain.

1. Introduction. It has recently been suggested (1) that annihilation from a dark matter halo made up of 3 GeV $\tilde{\gamma}$'s may account for the surprisingly large low-energy $\bar{p}$ flux reported in Ref. 2. Other interesting possibilities exist for producing such fluxes which are also of potential cosmological and astrophysical importance (e.g. Ref. 3 and OG 6.1-8). The photino hypothesis also affords a test for whether we live in a universe where supersymmetry (boson-fermion symmetry) is relevant. Indeed, measurements of cosmic-ray $\bar{p}$'s from $\tilde{\gamma}$ annihilation can enable the cosmic-ray physicist to determine the mass of the $\tilde{\gamma}$. This, however, requires a calculation of the energy spectrum of cosmic-ray $\bar{p}$'s produced in $\tilde{\gamma}$ annihilation and $\bar{p}$'s and modulation of this spectrum in order to directly compare with observed fluxes. We present here the results of such a calculation.

2. Photino (and Higgsino) Physics. Supersymmetry is a relatively new principle in particle physics which has been invoked to account for the "smallness" of the W-boson mass (compared with the grand unification scale) and possibly to incorporate gravity into a unified field theory. According to this principle, each ordinary boson and fermion has a supersymmetric partner and the lightest supersymmetric particle (LSP) should be stable. A prime candidate for the LSP is the $\tilde{\gamma}$ (or, more generally, a possible mass state admixture of the $\tilde{\gamma}$ (having gauge interactions) and neutral higgsino (having Yukawa interactions)). If such a stable particle is made in the early big-bang, it becomes a candidate for the dark matter in the universe (along with other possibilities such as massive neutrinos, axions, black holes, etc.). The mass density of such particles in the universe scales inversely with the annihilation cross section times velocity $\langle\sigma v\rangle$. A value near the critical density can be obtained by choosing a reasonable value for the prime unknown parameter involved in the calculation (4,5), viz., the mass of the scalar fermion which mediates the annihilation, $m_{\tilde{\gamma}}$. For two particular values for the $\tilde{\gamma}$ mass, $m_{\tilde{\gamma}} = 3$ GeV, chosen in Ref. 1, and

$m_{\tilde{\gamma}}$ = 20 GeV, we obtain the following formulas for the mass density of photinos as a fraction of the closure density:

$$\Omega_{\tilde{\gamma}} \simeq \begin{pmatrix} 1.0 \\ 0.4 \end{pmatrix} h^{-2} (m_{\tilde{f}}/50\ \text{GeV})^4 \quad \begin{matrix} , m_{\tilde{\gamma}} = 3\ \text{GeV} \\ , m_{\tilde{\gamma}} = 20\ \text{GeV} \end{matrix} \qquad (1)$$

where h is the Hubble constant in units of 100 km $s^{-1}$ $Mpc^{-1}$. In both cases, the mass of the scalar fermion $\tilde{f}$ required to obtain $\Omega_{\tilde{\gamma}} = 1$ is ~50 GeV, a value which may find some support in interpretations of the monojet events observed at the CERN $p\bar{p}$ collider (6). Photinos of mass much above 20 GeV will not give cosmologically significant mass densities.

The energy spectrum of the $\bar{p}$'s produced in $\tilde{\gamma}$ annihilations may be obtained from studies of quark-jet fragmentation in $e^+e^-$ collider experiments. In these experiments, the fractional energy distribution functions obtained for the various secondary particles produced are observed to scale with energy (7). We may write

$$\frac{1}{\sigma}\frac{d\sigma}{dx} = 2.89\,\beta\,\left(\frac{s}{\beta}\frac{d\sigma}{dx}\right) \qquad (2)$$

with the numerical factor in units of $\mu b\ GeV^2$. Here s is the square of the cms energy, $\beta$ is the relative velocity and x is the energy of the $\bar{p}$ expressed as a fraction of the mass of the annihilating $\tilde{\gamma}$. From an analysis of the various experiments found in the literature, we find that the $\bar{p}$ distribution function can be represented as falling between upper and lower limits given by

$$\frac{s}{\beta}\left(\frac{d\sigma}{dx}\right) \simeq \begin{cases} < 8.5 \exp(-11x) + 0.25 \exp(-2x) \\ > 7.7 \exp(-14.5x) + 0.17 \exp(-2.5x) \end{cases} \qquad (3)$$

The total annihilation cross section is given by (4)

$$\langle \sigma\beta \rangle \simeq \frac{8\pi\alpha^2}{m_{\tilde{f}}^4}\left[\Sigma_f\, q_f^2 \beta_f m_f^2\right] \qquad (4)$$

where the f's are the quarks and leptons (fermions) produced in the annihilation and $\beta_f = (1-m_f^2/m_{\tilde{\gamma}}^2)^{1/2}$.

3. Fluxes from $\tilde{\gamma}$ Annihilation in the Galactic Halo. If we assume that the galactic halo mass is made up almost entirely of $\tilde{\gamma}$'s, from rotation curve determinations (see,e.g.(8)) we find that a uniform halo has a mass density on average of ~ 1 GeV/$cm^3$ within 10 kpc of the galactic center. A halo with an isothermal mass distribution would have a mean mass density at 10 kpc galactocentric distance of ~ 0.4 GeV/$cm^3$. Dividing by the photino mass $m_{\tilde{\gamma}}$ then gives the photino number density $n_{\tilde{\gamma}}$. The production rate of antiprotons produced by annihilation is

$$Q(E_{\bar{p}}) = n_{\tilde{\gamma}}^2 \sigma\beta c \zeta_{\bar{p}} f(E_{\tilde{\gamma}}) \quad cm^{-3}s^{-1}GeV^{-1}, \qquad (5)$$

where $\zeta_{\bar{p}}$ is the number of $\bar{p}$'s produced in the annihilation (determined by $m_{\tilde{\gamma}}$) and the spectral production function $f(E_{\tilde{\gamma}})$ is normalized so that its integral is unity. The diffusion coefficient for cosmic rays at 10 kpc (the solar galactocentric distance) in the energy range involved (rigidity P in GV) is (9)

$$D \simeq 10^{26} \beta P^{0.7} \text{ cm}^2\text{s}^{-1} \quad (6)$$

which implies that the relevant antiprotons diffuse ~ 100-200 pc in the mean lifetime $\tau \sim 5 \times 10^{14}$ s determined for the galactic disk in the solar neighborhood. The $\bar{p}$ flux in interstellar space is then

$$I_{\bar{p}} = Q\tau\beta c/4\pi = 1.2\times10^{24} Q \text{ cm}^{-2}\text{s}^{-1}\text{sr}^{-1}\text{GeV}^{-1} \quad (7)$$

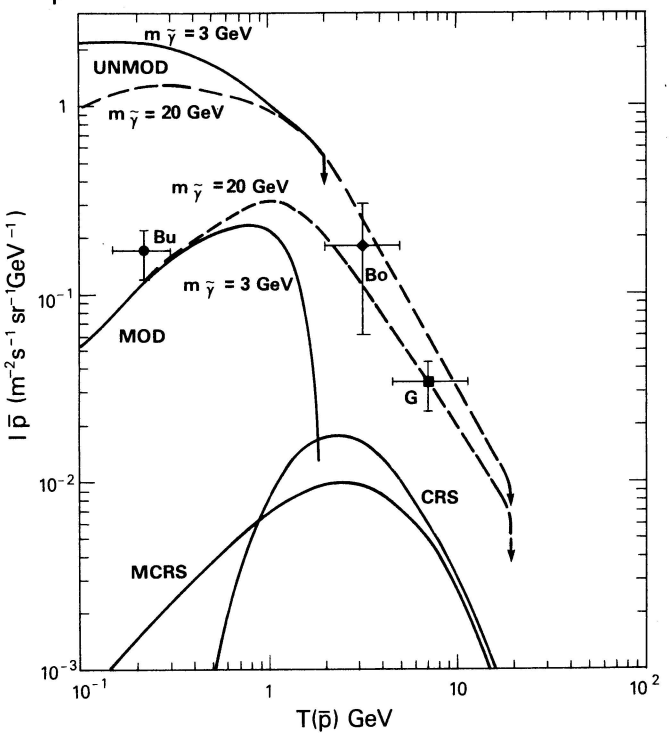


Fig. 1 Unmodulated and modulated spectra for 3 GeV and 20 GeV photino annihilation compared with data and cosmic-ray secondary production spectra (CRS) and modulated CRS (MCRS).

4. Solar modulation. The effect of solar modulation is most important in the low energy range of Ref.2. We have estimated the amount of proton modulation occurring during the relevant time period of the solar cycle, viz., June 1980, based on the Pioneer Helios-1 and ISEE-3 data (10). This yields expressions for the effective diffusion coefficient for modulation by the solar wind. The interstellar $\bar{p}$ spectrum may then be numerically modulated to compare with the observations (11).

5. Results. Fig. 1 shows the interstellar and modulated spectra obtained for 3 GeV and 20 GeV $\tilde{\gamma}$ masses, compared to the observations (2,12,13) and the standard secondary $\bar{p}$ calculations (14). The spectra are normalized to fall near the data points, however, such a fit is well within the uncertainty of the flux calculation. Both functions in eq. (3) yield similar results. Fig. 2 shows the $\bar{p}/p$ ratio as a function of energy for 3 GeV (A), 15 GeV (B) and 20 GeV (C) photino masses and the standard secondary production predictions (D). The data are from Refs. 2, 12, and 13.

There may be some evidence for a ~15 GeV photino mass cutoff in the highest data point. In any case, it is clear that (1) photino masses of

this order yield an annihilation spectrum with a shape and possible flux that fits all of the present data on cosmic-ray $\bar{p}$'s, and 2) owing to the kinematic cutoff in the annihilation spectrum, future high energy observations (15,16) to look for a cutoff in the $\bar{p}$ spectrum can, in principle, determine both the existence of a galactic photino halo and the mass of the photino itself.

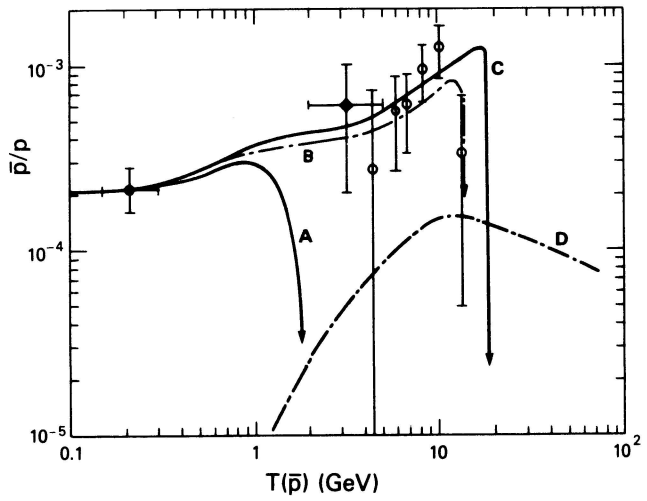


6. Acknowledgements. We thank John Perko for the numerical modulation. Two of us (FWS, SR) would like to thank the Lewes Center for Physics for hospitality during the initial phase of this work.

Fig. 2. $\bar{p}/p$ as a function of kinetic energy and data.

References

1. J. Silk and M. Srednicki, Phys. Rev. Lett. 53, 624 (1984).
2. A. Buffington, et al. Ap.J. 248, 1179 (1981).
3. F.W. Stecker, Nucl. Phys. B252, 25 (1985).
4. H. Goldberg, Phys. Rev. Lett. 50, 1419 (1983).
5. J. Ellis, et al., Nucl. Phys. B248, 453 (1984).
6. K. Enqvist, et al. CERN preprint TH-4095 (1985).
7. R. Brandelik, et al. Phys. Lett. 94B, 444 (1980); W. Bartel, et al. Phys. Lett. 104B, 325 (1981); S.L. Wu, Phys. Rpts. 107, 59 (1984).
8. S.M. Faber and J.S. Gallagher, Ann. Rev. Astr. Ap. 17, 135 (1979).
9. J. Ormes, et al., Proc. 18th Intl CRC (Bangalore) 2, 187 (1983).
10. F.B. McDonald, et al., these proceedings paper SH 4.7-3.
11. J. Perko, Ph.D. thesis, U. New Hampshire (1984).
12. E.A. Bogomolov, et al., Proc. 17th Intl CRC (Paris) 9, 146 (1981).
13. R. L. Golden, et al. Ap. Lett. 24, 75 (1984).
14. R. J. Protheroe, Ap.J. 251, 387 (1981).
15. Stecker, F.W. and Wolfendale, A.W. Nature 309, 37 (1984).
16. Ormes, J.F., et al. in Proc. Workshop on Cosmic Ray Exp. for the Space Station (1985).

OG6.1-11

# GALACTIC ANTIPROTONS OF 0.2-2 GEV ENERGY

E.A.Bogomolov, G.I.Vasilyev, M.G.Iodko, S.Yu.Krut'kov,
N.D.Lubyanaya, V.A.Romanov, S.V.Stepanov, M.S.Shulakova

Ioffe Physical-Technical Institute,
Academy of Sciences of the USSR, Leningrad, USSR.

ABSTRACT

Balloon measurements of the galactic antiproton flux in the energy range 0.2-2 GeV are presented. The experiments were carried out in the summer of 1984 with magnet spectrometers flown at a residual pressure of $\sim 10$ g·cm$^{-2}$ and cut-off rigidity of $\sim 0.6$ GV. An upper limit for the antiproton to proton flux ratio has been obtained of

$$\bar{p}/p \ (0.2\text{-}2 \text{ GeV}) < 5\times10^{-4}.$$

1. Introduction. Detection of antiprotons in the primary cosmic radiation in the energy range $\sim$ 0.1-10 GeV [1,2,3] and subsequent analysis of the observational data showed that the experimental data cannot be accounted for in the context of ideas involving antiproton production in the interaction of high energy cosmic rays with the interstellar medium. As a result, hypotheses have appeared involving production of antiprotons in compact dense objects [4], in molecular hydrogen clouds [5], in the evaporation of primary black holes [6], and due to possible existence of antimatter in the Universe [7]. Since the largest discrepancy between experiment and theory is found to exist in the low energy region, it appeared reasonable to carry out measurements at a few hundred MeV energy by an independent method and to obtain data on the antiproton spectrum in the intermediate energy range up to $\sim$ 2 GeV. Our first experiments in this area have been carried out in the energy range 0.2-2 GeV with two magnet spectrometers in the summer of 1984 in two balloon flights made in the North at a cut-off rigidity of $\sim$ 0.6 GV.

2. Method and Instrumentation. Each magnet spectrometer ( see Figure 1 ) consisted of a deflecting permanent magnet (M), a spark chamber assembly (SC1-SC4) with optical readout, and a telescope made up of scintillation counters ($SC_1, \overline{SC}_2, \overline{SC}_3, \overline{SC}_4, SC_5$) and a gas Čerenkov detector ($\bar{C}$) to determine the direction of particle arrival and for the velocity and charge discrimination of particles. The background due to the electrons ( both atmospheric and galactic ) and atmospheric muons and pions ( produced primarily in the top part of the instrument ) which could simulate traversal of the instrument by antiprotons was supressed by the gas Čerenkov counter ( with a threshold Lorentz factor $\gamma = 3.1$ ) with an efficiency $> 99.9$ %. The possible simulation of antiprotons by albedo protons was eliminated by a time-of-flight analysis of the incident particles. The expected background in the experiment could simulate antiprotons at a level of $\bar{p}/p < 3 \times 10^{-5}$. The geometry factor of the instrument for particle momenta $> 0.4$ GeV/c is 1.1 $cm^2 sr$, the average line integral-0.68 kGm.

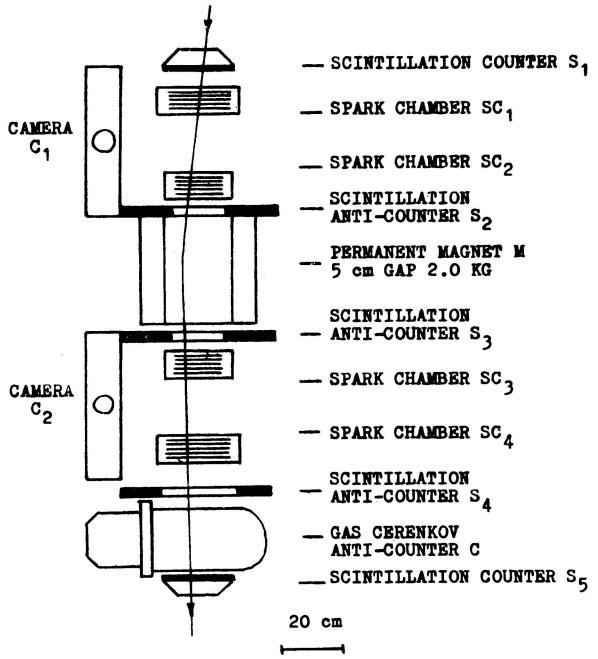


Fig.1. A schematic diagram of the IPTI Magnet Spectrometer.

3. Results. Two balloon flights of the two magnet spectrometers have been carried out in the summer of 1984. The flight on 28-30 June at a residual pressure of $\sim 9$ $g \cdot cm^{-2}$ lasted for 26 hrs, and that on 30-31 June at a residual pressure of $\sim 14$ $g \cdot cm^{-2}$, for 5 hrs. About 16.500 events we-

re recorded altogether. About 30 % of the information has been processed up to now by the selection criteria chosen [8]. Figure 2 shows the magnetic deflection distribution of singly-charged particles recorded in the flights.

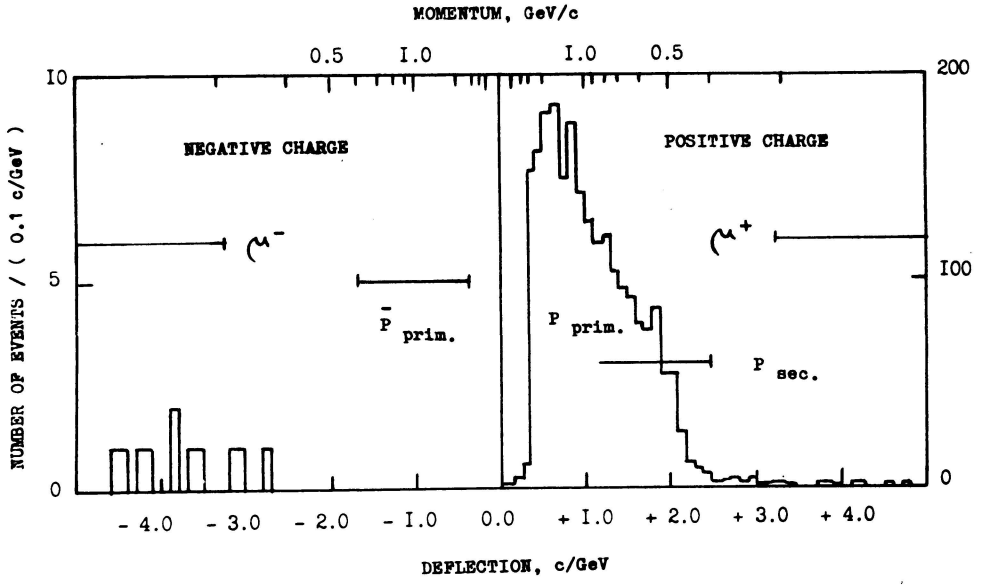


Fig.2. The deflection distribution of singly-charged particles recorded at $\sim$ 10 g·cm$^{-2}$ of residual atmosphere and cut-off rigidity of $\sim$ 0.6 GV in 1984.

The positive deflection region extending from + 0.3 to + 2.5 (GeV/c)$^{-1}$ corresponds to galactic protons of 2 to 0.2 GeV and secondary protons produced in the residual atmosphere. The upper energy limit for the primary protons is determined by the effective threshold of the Čerenkov counter, and the lower limit, by the actual cut-off rigidity. The expected region of detection of galactic and atmospherically-produced antiprotons corresponds to deflections ranging from - 0.3 to - 2.5 (GeV/c)$^{-1}$. The deflections in excess of $\pm$ 3.0 (GeV/c)$^{-1}$ are due to atmospherically-produced muons.

A total of $\sim$ 2000 protons were recorded in the energy range 0.2-2 GeV. Not a single event was observed in the antiproton deflection range. Thus only an upper limit for

the $\bar{p}/p$ ratio has been found up to now, namely,

$$\bar{p}/p\ (0.2\text{-}2\ \text{GeV}) < 5\times10^{-4}.$$

While the measured upper limit for the $\bar{p}/p$ ratio is close to the expected value $\bar{p}/p \simeq (2\text{-}4)\times10^{-4}$ for the energy range 0.2-2 GeV [3,8], no definite conclusions can yet be drawn. Further analysis of the available data and new experiments planned for the summer of 1985 will hopefully improve the statistical significance of the results obtained.

References.

1. Bogomolov E.A.,Lubyanaya N.D.,Romanov V.A.,Stepanov S.V., Shulakova M.S., Proc.16th Intern. Cosmic Ray Conf., Kyoto, 1979, v.1, p.330.
2. Golden R.L.,Horan S.,Mauger B.G.,Badhwar G.D.,Lacy J.L., Stephens S.A.,Daniel R.R.,Zipse J.E., Phys. Rev. Lett., 1979, v.43, p.1196.
3. Buffington A.,Schindler S.M.,Pennypacker C.R., Astrophys. J., 1981, v.248, p.1179.
4. Ginzburg V.L.,Ptuskin V.S., Lebedev Physical Institute Preprint No 35, 1984.
5. Tan L.C.,Ng L.K., Astrophys. J., 1983, v.269, p.751.
6. Kiraly P.,Szabelski J.,Wdowczyk J.,Wolfendale A.W., Nature, 1981, v.293, p.120.
7. Stecker F.W.,Protheroe R.J.,Kasanas D., Astrophys. and Space Sci., 1983, v.96, p.171.
8. Bogomolov E.A.,Lubyanaya N.D.,Romanov V.A.,Stepanov S.V., Shulakova M.S., Proc.17th Intern. Cosmic Ray Conf., Paris, 1981, v.9, p.146.

# EVIDENCE FOR A DYNAMICAL HALO AROUND THE EDGE-ON GALAXY NGC 4631

I. Lerche[1], R. Schlickeiser[2]

1) Department of Geology, University of South Carolina
Columbia, SC 29208, USA

2) Max-Planck-Institut für Radioastronomie
Auf dem Hügel 69, 5300 Bonn 1, FRG

ABSTRACT

Radio continuum observations at five frequencies between 327 MHz and 10.7 GHz of the edge-on galaxy NGC 4631 confirm the prediction concerning the frequency dependence of the halo extent and the spatial variation of the radio spectral indices in the dynamical halo model made by Lerche and Schlickeiser. The measurements are presented, and a detailed comparison with theoretical predictions is made.

1. Introduction. Four years ago we studied the dynamics of cosmic ray particles in galaxies in the presence of a large-scale galactic wind (Lerche and Schlickeiser 1981a,b; 1982a,b,c — hereinafter referred to as LS1, LS2, LS3, LS4, LS5, respectively). Such a wind gives rise to convection and adiabatic deceleration of particles during their transport, adding to the well established diffusion in partially random magnetic fields and energy loss interactions with ambient matter, magnetic and radiation fields. We pointed out that due to these additional transport terms in particular the spectral behaviour of radio haloes in galaxies caused by synchrotron radiation of relativistic electrons would change at lower frequencies $\nu \ll \nu_D$ with

$$\nu_D = 1\ \mathrm{GHz} \left[ \frac{\mathrm{div}\ \underset{\sim}{u}}{10^{-15}\ \mathrm{s}^{-1}} \right]^{-2} (H_\perp / 4\,\mu\mathrm{G})^{-3} \qquad (1)$$

where $\underset{\sim}{u}$ is the galactic wind speed. Here we compare our predictions with recent observations of the edge-on galaxy NGC 4631 by Werner (1984, 1985) and Sukumar and Velusamy (1985).

2. Predicted and Measured Radio Emission in the Dynamical Halo Model. In LS4 we solved the steady-state transport equation describing the propagation of relativistic electrons, injected with a power law energy distribution $\propto E^{-P}$ in the galactic disk ($z = 0$), perpendicular to the galactic plane with ("dynamical halo") and without ("static halo") a galactic wind starting with zero velocity in the plane and streaming away from the disk. For both alternatives we predicted remarkable and measurable differences in the behaviour of the total integrated radio flux density $I(\nu)$, the size $E(\nu)$ of the halo perpendicular to the galactic plane at different frequencies, and the spatial variation of the synchrotron spectral index $\delta(z)$ in different ranges of frequency ($S(\nu) \propto \nu^{-\delta}$).

These differences occur at frequencies smaller than $\nu_D$, which corresponds to that electron energy where the energy loss against adiabatic deceleration ($dE/dt = -1/3\ \mathrm{div}\ \underset{\sim}{u} \cdot E$) equals that for radiation losses

$(dE/dt = -b_r (H^2/8\pi) E^2)$. At frequencies larger than $\nu_D$ both models predict the same. Consider each quantity in turn:

(a) Inclusion of a galactic wind in the transport equation implies a break of $I(\nu)$ around $\nu_D$ from a $\nu^{-(p-1)/2}$-behaviour at low frequencies ($\nu \ll \nu_D$) to a $\nu^{-p/2}$-behaviour at high frequencies ($\nu \gg \nu_D$), i.e. a change in spectral index by $\Delta\Gamma = 0.5$. We noted before (LS3) that NGC 4631 indeed shows this property. In the case of the static model no break is found and the $\nu^{-p/2}$-behaviour holds for all frequencies.

(b) In the static model the size of the halo increases with decreasing frequency, i.e. $E_s(\nu) \propto \nu^{-(1-a)/4}$ where parameter a describes the power law dependence of the particle's diffusion coefficient ($D(E) = D_o E^a$). In the dynamical model we find that at frequencies smaller than $\nu_D$, $E_d(\nu) \propto \nu^{a/4}$, whereas at high frequencies $\nu > \nu_D$, $E_d(\nu) = E_s(\nu)$. Figure 1 shows the measured frequency dependence of the halo extent at four different intensity levels for NGC 4631 by Werner (1985). In agreement with our predictions of the dynamical model the extent of the halo does not increase at frequencies less than 1.4 GHz. On the 5% intensity level Werner (1985) finds a dependence $E(\nu) \propto \nu^{0.15\pm0.10}$ at frequencies below 4750 MHz, and a variation of $E(\nu) \propto \nu^{-0.8\pm0.5}$ between 4750 and 10700 MHz. The inferred value for $a = 0.6 \pm 0.4$ is in good agreement with the value $a = 0.6 \pm 0.2$ (Schlickeiser 1983) from studies of the cosmic ray nucleon propagation in our Galaxy.

(c) Figure 2 shows the behaviour of the spectral index gradients in the two models as predicted four years ago (LS2). At high frequencies $\nu > \nu_D$, $\delta(z)$ agrees in both models, whereas there are striking differences at lower frequencies, $\nu < \nu_D$. In the galactic plane ($z = 0$), $\delta_d(z = 0)$ is by 0.25 smaller than $\delta_s(z = 0)$. This difference may be doubled (0.50) if instead of the infinitely thin line source of electrons at $z = 0$ an extended source distribution is taken (LS5, Lerche and Schlickeiser 1985). With increasing height $\delta_d(z)$ first slightly decreases before a sharp increase occurs. On the other hand, $\delta_s(z)$ increases gradually with increasing height.

These predictions can be compared with the variation of the radio spectral indices as a function of height above the plane measured in NGC 4631 by Sukumar and Velusamy (1985), and shown in Figure 3. The excellent agreement with the predictions of the dynamical model in Figure 2 is apparent. The high-frequency (610 - 1412 MHz) index shows a gradual steepening with z, as expected for the electron spectrum evolution due to synchrotron losses. The low-frequency (327 - 610 MHz) index flattens with increasing z (up to about 3 kpc) and then steepens with height, as predicted. The difference $\Delta\delta$ between the high- and low-frequency spectral indices near the plane (at $z = 0$) is $\sim 0.35$, well within the theoretical range from 0.25 - 0.5. Similar results have been obtained by Werner (1984) who compared spectral indices derived from measurements at 608.5, 1412, 4750 and 10700 MHz. He also proved that the radio halo emission is synchrotron radiation by measuring the linear polarization.

3. Conclusions. The radio measurements of Werner (1984, 1985) and Sukumar and Velusamy (1985) of the external edge-on galaxy NGC 4631 con-

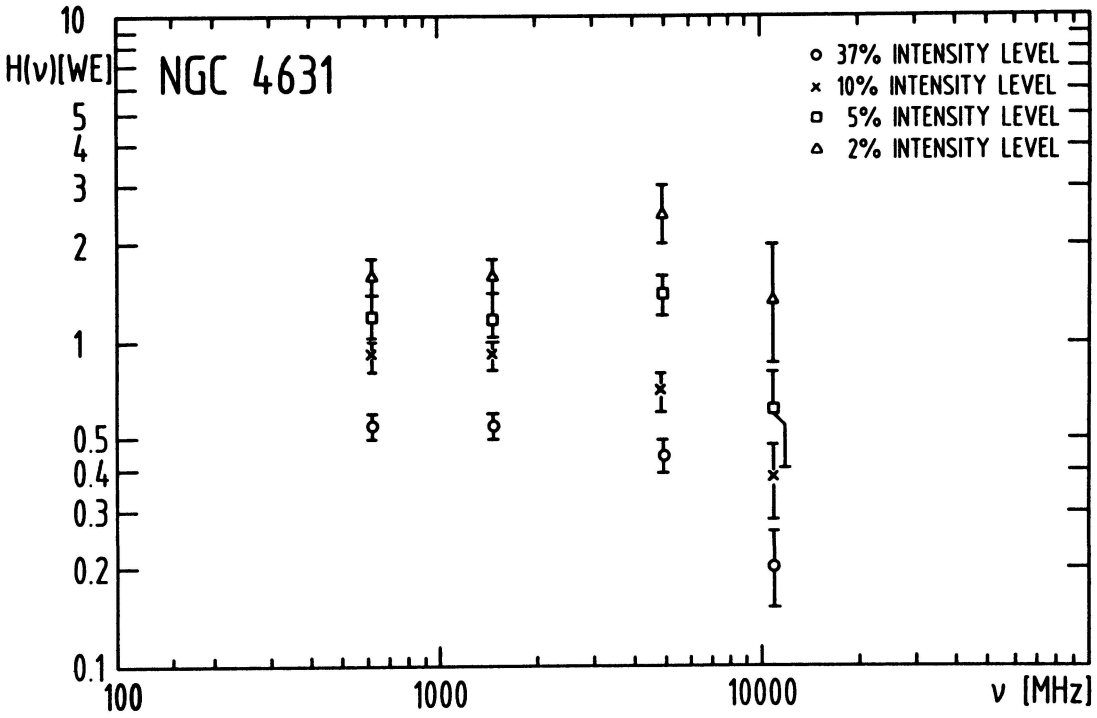


Fig. 1: Frequency dependence of the halo size of NGC 4631 at different intensity levels (from Werner 1985)

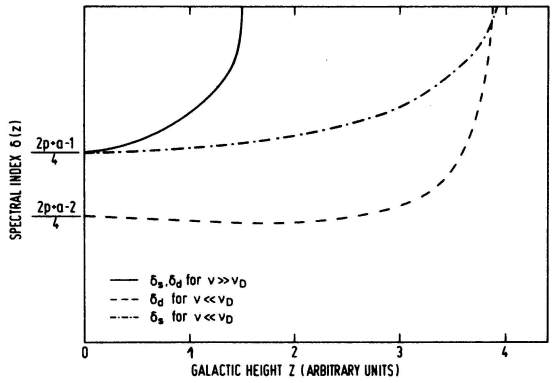


Fig. 2: Predicted variation of the synchrotron spectral index for small ($\nu \ll \nu_D$) and large ($\nu \gg \nu_D$) frequencies in the static (s) and dynamical (d) model. p is the spectral index of injected electrons ($\propto E^{-p}$) in the plane z = 0; a the assumed power law dependence of the diffusion coefficient ($D \propto E^a$) on the energy of relativistic electrons (from Lerche and Schlickeiser 1981b).

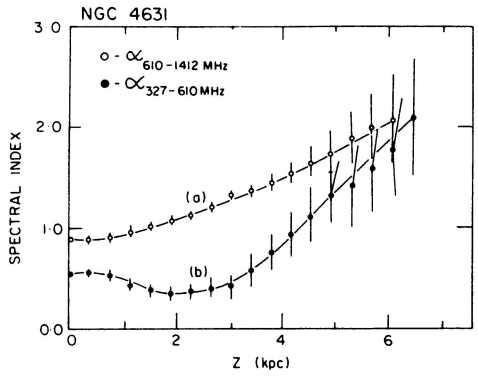


Fig. 3: Measured variation of the radio spectral index as a function of height above the plane in NGC 4631: (a) α(610 - 1412 MHz), (b) α(327 - 610 MHz) (from Sukumar and Velusamy 1985)

firmed the predictions of LS (1981, 1982) on the spectral behaviour of its radio halo in the presence of a large-scale galactic wind. This is unambiguous evidence for the existence of large-scale convective motion of matter from the disk into the halo region in NGC 4631. Since NGC 4631 is morphologically similar to our Galaxy, conclusions drawn for NGC 4631 also apply to our Galaxy.

References

Lerche, I., Schlickeiser, R., (1981a), Astrophys. J. Suppl. 47, 33 (LS1)
———————————, (1981b), Astrophys. Letters 22, 161 (LS2)
———————————, (1981c), Proc. 17th Intern. Cosmic Ray Conf. (Paris) Vol. 2, 244 (LS3)
———————————, (1982a), Astron. Astrophys. 107, 148 (LS4)
———————————, (1982b), Monthly Notices Roy. Astron. Soc. 202, 1041 (LS5)
———————————, (1985), in preparation
Sukumar, S., Velusamy, T., (1985), Monthly Notices Roy. Astron. Soc. 212, 367
Werner, W., (1984), PhD Thesis, Rheinische Friedrich-Wilhelms-University, Bonn
Werner, W., (1985), Astron. Astrophys. 144, 502

# HALO OF NGC 4631 AND MODELS OF COSMIC-RAY TRANSPORT

R. Cowsik and S. Sukumar
Tata Institute of Fundamental Research, Bombay 400005
India.

## ABSTRACT

The halo of edge-on spiral galaxy of NGC 4631 is studied from 327 MHz to 10700 MHz to delineate the models of cosmic-ray transport. Preliminary studies show that the spectral steepening as a function of height above the plane can be understood in terms of the simplest cosmic-ray transport models, viz. simple isotropic diffusion in an infinite medium. More detailed study will be presented at the time of the conference.

1. Motivation. Twenty-seven years ago, Ginzburg in his classic paper emphasized the importance of the study of galactic halos in understanding the modes of cosmic ray transport and acceleration [1]. Despite his continued insistence [see for example ref.2] the observational status is progressing rather slowly. As emphasized by Ginzburg spiral galaxies seen edge-on are ideal for the study of the distribution of matter, cosmic rays and magnetic fields in the halo. Only recently, radio maps of spiral galaxies with adequate resolution and sensitivity at different frequencies have become available [3-6]. We would like to focus our attention on NGC 4631 which is a nearly edge-on Sc-spiral subtending more than 15 arc min along the major axis. Special efforts were made to map this source at 327 MHz by using the Ooty Synthesis Radio Telescope [7-8]. The importance of having a good map at such low frequencies are two fold : first, since the lower energy electrons are expected to suffer smaller synchrotron and Compton losses they can be transported to great distances efficiently so that the outer extent of the halo can be better delineated; second, the low frequency observations when combined with the earlier observations at 610 MHz and 1412 MHz can be used to study the variations in the spectral index of the halo as a function of scale height above the galactic plane. The map obtained with OSRT [8] is reproduced in figure 1. Since the distance of the galaxy is 5.2 Mpc [9] each arc minute corresponds to a length of 1.5 kpc. Notice that the halo extends up to 7.5 kpc radius and the aspect ratio at $\sim$ 50 mJy is $\lesssim$ 2.

In contrast with the rather limited observational data on halos, the theoretical studies on cosmic-ray propagation have become very complex and sophisticated. Recently Lerche

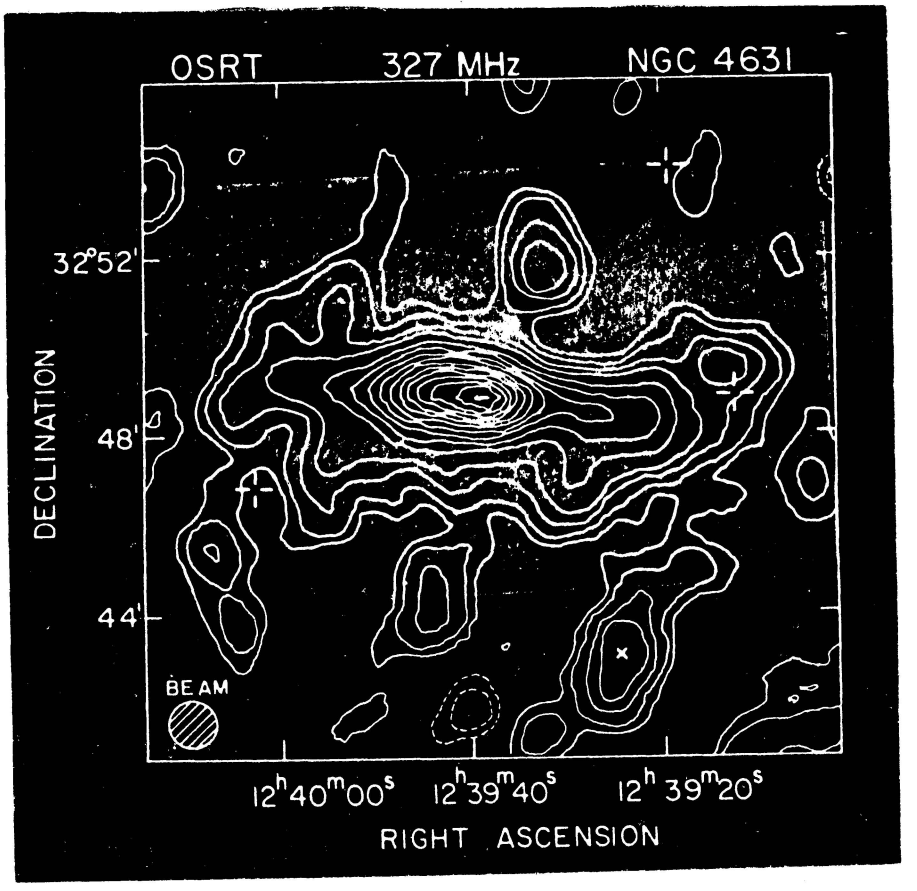


Fig.1 Overlay of ORST map of NGC 4631 at 327 MHz with a resolution of 60 x 60 arcsec$^2$, on a Palomar Sky Survey print. The first four contours are at 7.5, 15, 30, 45 and then increasing with contour interval of 30 mlv per beam. Negative contours are dashed. Courtesy-'60 National Geographic Soc.-Palomar Sky Survey.

and Schlickeiser [10] have published solutions to the propagation equations including a variety of processes like energy-dependent diffusion, convection, adiabatic deceleration, radiative losses and so forth. In principle one would be able to compare the predictions of such theories with observations to assess the importance of the various physical processes that are operative in the source. The number of parameters that are needed to specify the theoretical models are quite large, especially when we include those needed to specify the distribution of the sources of cosmic-ray electrons and protons which in interactions with the gas will generate secondary positrons and electrons. Because of this a very many different set of parameters can give an adequate fit to the data and we would not have gained much understanding. Keeping in mind these points we start with the simplest possible transport theories and see to what extent the

observations can be explained. If there be any unexplained feature we would progressively make the models more sophisticated. At the time of writing this only a very preliminary study has been completed; we present the results of this study here and further developments would be presented at the time of the conference.

2. The Simplest Model for Galactic Halos. Consider a distribution of sources of cosmic-ray protons and electrons (assumed to be identical) embedded in an infinite diffusion medium which is homogeneous and isotropic. The radiative losses suffered by the electrons during transport is taken to be independent of position. The transport of protons is independent of energy. Thus the most general transport kernel $\mu$ ($\underline{r}$, $\underline{r}'$, E, E', $t_1$, $t_2$) simplifies for protons to

$$\mu(r,t) = [2\pi^{1/2}(Kt)^{3/2}]^{-1} \exp(-r^2 / 4Kt) \qquad (1)$$

Here $r = |\underline{r} - \underline{r}'|$, $t = [t-t']$, K is the diffusion constant and $\mu$ is defined for an unit source strenght per unit volume per unit energy interval and per steradian. Under conditions of steady state the kernel integrates to

$$\mu(r) = [Kr]^{-1} \qquad (2)$$

The spatial part of the source distribution is taken to be the same for both the proton and the electron components.

$$N(r') \sim \exp - (\omega'/\omega_o + |z'|/z_o) \qquad (3)$$

where axial symmetry is assumed and $\omega$, z, (and $\Theta$) are the cylindrical co-ordinates. Now the spectral density of cosmic-ray protons is written as

$$S_p \sim \int N_p (r',E) (K |\underline{r} - \underline{r}'|)^{-1} d^3r' \qquad (4)$$

The source function for the secondary electrons and positrons is proportional to the product of the gas density G(r) and the spectral density of protons

$$N_{sec} (E,r) = \int \sigma(E',E) S_p(E',r) G(r) dE' \qquad (5)$$

where $\sigma(E',E)$ is the cross-section per particle of energy E' colliding with a gas atom to generate an electron or positron per unit energy interval at E through the decay of the secondary mesons and muons etc. The gas density G(r) is taken to be

$$G(r) \sim G_o \exp - (\omega/\omega_g + |z|/z_g) \qquad (6)$$

The spectral density of primary and secondary electrons at r are now given by

$$S_e \sim \int_0^\infty N_e(E',r')\ \mu(E,E',|r-r'|,t)\ dE'\ dt \qquad (7)$$

$$S_{sec} \sim \int N_{sec}\ (E',r')\ \mu(E,E',|r-r'|,t)\ dE'\ dt \qquad (8)$$

with obvious notation. In the simplified model of cosmic ray transport considered here the kernal $\mu$ in equations (7), (8) is given simply by

$$\mu(E',E,r,t) = \delta\left(E' - \frac{E}{1-bEt}\right)[2\pi^{1/2}(Kt)^{3/2}]^{-1} \exp-(r^2/4Kt) \qquad (9)$$

with b representing the rate of energy loss of an electron of unit energy. The function allows easy integration of equations(7) and (8). We compare in Fig.2 the expected variation of the spectral index at 1000 MHz with the observed variation with z. One sees that even this simple model gives a reasonable representation of the observations.

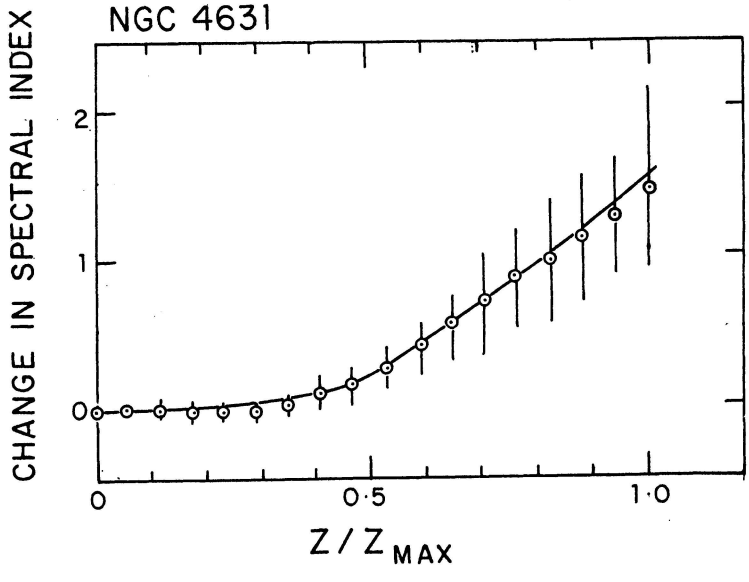


Fig.2. Spectral index variation along Z direction. Observed points circled; solid line indicates model fit.

References.
1. Ginzburg, V.L. (1958), Progress in elementary particle and cosmic ray physics, 4, 438.
2. Ginzburg, V.L. (1985), in Cosmic Pathways (Tata McGraw Hill, ed. R. Cowsik).
3. Ekers, R.D. and Sancisi, R., (1977), Astron. Astrophys. 54, 973
4. Beck, R. et al (1979), ibid, 77, 25.
5. Klein, U. and Emerson, D.T. (1981), ibid, 94, 29.
6. Hummel, E. (1980), ibid Suppl., 41, 151.
7. Swarup, G. (1984), J. Astron. Astrophys. 5, 139.
8. Sukumar, S. and Veluswamy, T. (1985), MNRAS, 212, 367.
9. Sandage, A. and Tammann, G.A. (1975), Astrophys. J., 196, 313.
10. Lerche, I. and Schlickeiser, R. (1982), Astr. Astrophys. 107, 148.

374

# Observation of Cosmic Ray Positrons From 5 to 25 GeV

R. L. Golden, B.G.Mauger, and S. Horan
Department of Electrical and Computer Engineering
New Mexico State University
Las Cruces, NM 88003
USA

G. D. Badhwar, J. L. Lacy, J. E. Zipse
NASA, Johnson Space Center
Houston, TX 77058
USA

R. R. Daniel, S. A. Stephens
Tata Institute For Fundamental Research
Homi Bhabha Road
Bombay, India

1. Introduction. We report here the positron data gathered in conjunction with electron data published elsewhere (1). The basic recognition scheme was to look for low-mass positive particles that cause a cascade in a 7 radiation length shower counter. The mass criteria is imposed by selecting particles that were accompanied by Cherenkov light but whose rigidity was below the proton Cherenkov threshold. Thus the proton Cherenkov threshold represents an upper limit to the range of the experiment.

2. The Apparatus. The principal detector elements are (from top to bottom): a gas Cherenkov detector (G); plastic scintillators S1 and S2; 8 multiwire proportional counters (M1-M8); and a lead-scintillator shower counter comprised of 7 layers. Each layer of the shower counter consisted of 1 scintillator and 1 radiation length of lead (P1-P7). The multiwire proportional counters (MWPC) were arranged in three pairs located at the top, middle and bottom of the spectrometer with the remaining two chambers located at the 1/4 and 3/4 points in the spectrometer stack. All phototubes were pulse-height analyzed, 8 measurements were made of the particle position on the x axis (axis of deflection), and 5 measurements were made on the y axis. Data readout was initiated for every occurence of an S1*P1*P7 coincidence. The geometric factor of the instrument was 324±5 cm^2-str and the live time fraction was 0.80. The data were gathered on a balloon flight from Palestine Texas on May 20,1976. The data gathering period was 6.4 x 10^4 seconds at an average altitude corresponding to 5.8 gm*cm^-2.

3. Data Analysis. Selection of the positrons started with using the same criteria used for the e-:

1) MWPC data. There must be at least 5 valid MWPC readouts for the X coordinate, and 3 valid readouts for the Y axis. The

reconstructed trajectory must fit to a valid, continuous track with a chi-squared of less than 50 in the x axis and 30 in the Y axis. And finally, one MWPC from each of the pairs have valid readouts.

2) Charge. The average of the pulse-heights for scintillators S1 and S2 correspond to less than 1.8 $I_o$ where $I_o$ is the pulse-height for a Z=1, $\beta$=1 vertically incident particle.

3) Cherenkov Detector. The Cherenkov detector be above a discriminator level corresponding to 0.25 photo-electrons.

4) Shower Counter. The sum of the shower-counter pulse-heights correspond to at least 50 $I_o$

Criteria 1 differs slightly from that used in (1). The old MWPC criteria required that the bottom MWPC pair both have valid readouts. This was replaced with the criterion that each pair must have a valid readout. It was found that the revised criterion has a 13% higher efficiency without any degredation of resolution.

The criteria 1-4 yield a sample which is roughly 80% protons and 20% positrons. The main source of background is the high noise level in the Cherenkov detector. In order to reduce the background we require a minimum Cherenkov pulse-height corresponding to about 1 photoelectron. The Cherenkov mirror was divided into 4-quadrants, each viewed by a separate phototube. Phototubes from opposite quadrants were summed before digitization. Trajectory analysis was used to determine which quadrant pair should have registered the light. It was demanded that the correct pair have at least the minimum pulse-height, and the other pair have less than the minimum pulse height. This selection is called criterion 5. Application of these criteria to the e- sample revealed that 93% passed the test, and an estimated 75% of the remaining protons were rejected.

The next criterion was to examine the shower counter output. Each set of P1-P7 outputs was fitted to the hypothesis that there was an electromagnetic cascade. The starting point and energy of the shower were used as unconstrained variables in the fit. Criterion 6 was that the shower fit have a chi-square of less than 10. Once again it was observed that 93% of the e- pass this test, and in this case about 30% of the remaining protons were rejected.

Figure 1a shows the deflection (1/rigidity) spectrum of the events selected by criteria 1-4. We have include both positive and negative deflections (corresponding to positive and negative charged particles). The peak near zero deflection is due to protons above Cherenkov threshold. The gradual rise with increasing positive deflection is due to the combination of positrons and protons accompanied by an accidental G pulse. The decline above 0.2 c/GV is due to the geomagnetic cutoff. The events to the left of zero deflection are the e-. Note that the corresponding geomagnetic cutoff is smeared due to bremsstrahlung losses. Figures 1b and 1c show the progressive effects of criteria 5 and 6. The peak due to protons above Cherenkov threshold is broadened by the finite resolution of the rigidity resolution. We have

chosen the upper limit for the experiment to be 0.04 c/GV which is 1.5 standard deviations below the proton Cherenkov threshold. With this restriction it is possible to generate a sample of protons by applying the e+ selection criteria except demanding that no G pulse occur. Given this sample of protons, and the e- it is possible to perform quantitative evaluations of the remaining background in the e+ sample.

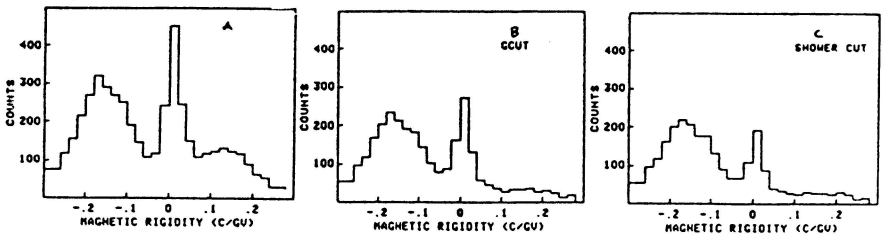


Figure 1 Effects of Positron Selection Criteria

The starting point distributions for protons, e- and our candidate sample of e+ will be shown at the conference. The e- distributions are peaked sharply at about +1 radiation length. This is as expected for electrons (and positrons) except that the peak is slightly offset due to an arbitrary factor in the shower fitting program. The proton distributions reflect a basically flat interaction probability biased by the criteria that there be at least a 50 $I_o$ shower sum. The e+ candidates show that the sample is comprised of mostly electron-like events with a small admixture of protons except at high energies, where the proton component dominates.

A background subtraction was made on the assumption that all e+ would have starting points between $+3.5X_o$ and $-2.5X_o$ . If one counts events outside this region in the proton distributions, one can form a background multiplication factor M = (total protons)/(protons outside the electron starting point limits). Each rigidity interval is then analyzed and the number of e+ is determined by the formula #e+ = (#candidates inside limits)-M*(#candidates outside limits). Table 1 gives some of the details of the background subtraction process for e+. Table 1 also gives the number of e- determined by applying criteria 1-6 and performing a similar background subtraction.

Table 1. Background subtractions

| deflection c/GV | e+ crit 1-6 | Proton bkgrnd | Atmos bkgrnd | e+ w/o bkgrnd | e- w/o bkgrnd |
|---|---|---|---|---|---|
| 0.04-0.08 | 74 ± 15 | 69.6 ± 19.5 | 2.8 | 1.6 ± 16.5 | 132 ± 15 |
| 0.08-0.12 | 51 10 | 41.5 13.8 | 4.7 | 4.8 12.0 | 304 18 |
| 0.12-0.16 | 60 6 | 22.3 9.4 | 7.1 | 30.6 10.2 | 377 18 |
| 0.16-0.20 | 55 5 | 19.2 8.8 | 8.1 | 27.7 9.9 | 412 21 |
| 0.20-0.24 | 54 1 | 3.8 3.8 | 10.8 | 39.4 8.5 | 268 17 |
| 0.24-0.28 | 28 0 | 0.0 4.3 | 13.3 | 14.7 7.3 | 137 13 |

4. Results. Reference 1 contains the details of the exposure factors (solid angle x area x time x efficiency) for e- during the flight. The exposure factors for the e+

observation are obtained by using the e- data in the rightmost column in Table 1. The ratio of e- in Table 1 to the number in (1) gives a correction to the exposure factor reported in (1). Table 2 gives the computed exposure factors and fluxes. Reference 1 gives a detailed discussion of the corrections for geomagnetic cutoff, solar modulation and bremsstrahlung energy losses. In (1) a mean ISM energy ( $\bar{E}$ ), an equivalent bin width ( $\Delta E$ ) and a propagation efficiency (p) are computed for each deflection interval in Table 1. These factors are also given in table 2.

Table 2 Positron Flux Calculations

| $\bar{E}$ (GeV) | e+ counts | $e+/(e^+ + e^-)$ | exposure cm^2 -str-sec | p | $\Delta E$ (GeV) | flux e+/(m^2-str-sec-GeV) |
|---|---|---|---|---|---|---|
| 21.7 | 1.6 ± 16.5 | 0.01 ± 0.12 | 408 ± 23 | 1.05 | 14.5 | (0.3±2.7)E-3 |
| 13.1 | 4.8 ± 12.0 | 0.02 ± 0.04 | 463 ± 12 | 1.02 | 5.13 | (0.2±0.5)E-2 |
| 9.39 | 30.6 ± 10.2 | 0.08 ± 0.02 | 480 ± 13 | 0.99 | 2.61 | 0.025 ± 0.008 |
| 7.37 | 27.7 ± 9.9 | 0.06 ± 0.02 | 501 ± 13 | 0.71 | 1.57 | 0.050 ± 0.018 |
| 6.08 | 39.4 ± 8.5 | 0.13 ± 0.03 | 557 ± 13 | 0.43 | 1.02 | 0.161 ± 0.035 |
| 5.19 | 14.7 ± 7.3 | 0.10 ± 0.05 | 588 ± 13 | 0.18 | 0.75 | 0.190 ± 0.094 |

Figure 2 shows the fluxes as determined in Table 2, along with the results of other observers, and the fluxes predicted for a simple leaky box (with energy dependendt leakage) and 7 gm/cm^2 of matter traversed. A least squares fit to the fluxes in table 2 gives a spectral index of -4.2±0.6 and an integral flux (above 5.2 Gev) of (0.51±0.09) e+/m^2-str-sec-GeV. The chi-square for the fit was 2.1.

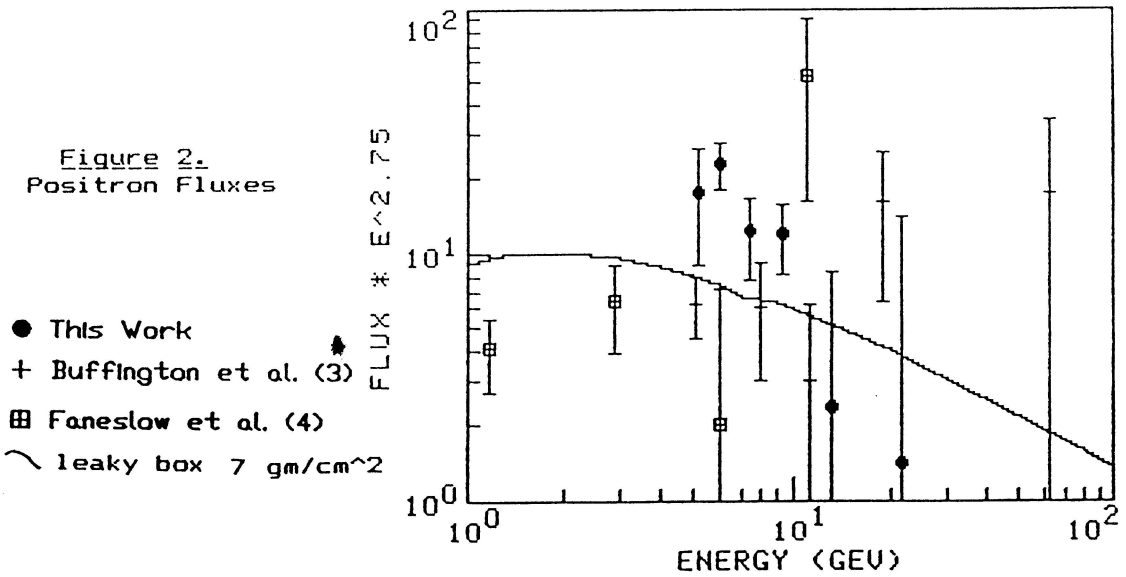


Figure 2.
Positron Fluxes

References
(1) Golden, R. L. et al. (1984), Ap. J. 287, 622.
(2) Stephens, S. A. (1981), Proc 17th ICRC (Paris) 4, 282.
(3) Buffington, A. et al. (1975), Ap. J. 199, 669.
(4) Faneslow, J. L. (1969), Ap. J. 158, 771.

# AN OBSERVATION OF COSMIC RAY POSITRONS FROM 10–20 GEV*

Dietrich Müller+ and Jonathan Tang
Enrico Fermi Institute, University of Chicago
Illinois 60637 USA.

ABSTRACT A balloon flight of the University of Chicago electron telescope has been performed in Hawaii in April 1984. Making use of the east-west asymmetry in the geomagnetic cut-off rigidity, we have successfully separated the cosmic-ray positrons and negatrons over the range 10–20 GeV. The positron to electron ratio, $e^+/(e^+ + e^-)$, was measured to be 17%±5%, significantly higher than the ratio measured in the 1-10 GeV range by other experiments. This increase appears to suggest that either a primary component of positrons become significant above 10 GeV, or that the spectrum of primary negatrons decreases above 10 GeV more sharply than that of secondary positrons.

INTRODUCTION Cosmic ray electrons consist of both positrons and negatrons. Present measurements of the combined positron and negatron flux cover energies up to almost 1000 GeV, while data on the charge composition beyond 10 GeV are very scarce. The combined energy spectrum exhibits a characteristic steepening around 30 GeV, which is commonly attributed to radiative energy losses in interstellar space. If interpreted in the context of the leaky box model, the steepening is consistent with a galactic containment time of $10^7$ years, in close agreement with results based on measurements of the $^{10}$Be abundance. However, these interpretations of the electron spectrum are usually made under the assumption that the source spectrum of electrons follows that of nuclear cosmic rays and that the electron flux is dominated by primary negatrons. This assumption must be verified by separate measurements of positrons and negatrons: Both positrons and negatrons are produced in about equal proportions as secondary products of interactions of cosmic ray nuclei with interstellar gas. The source spectrum of these secondary particles is directly related to the spectrum of parent particles (mostly protons) and can be calculated with good accuracy for various propagation models (Orth & Buffington, 1976). Any significant excess of negatrons, however, must be attributed to primary acceleration in cosmic ray sources. Below 10 GeV, such primary negatrons have been found to be the dominant component.

Most of the existing data on cosmic ray positrons come from balloon borne magnet spectrometers (Fanselow et al 1969, Buffington el al 1975, Daugherty et al 1975), but both momentum resolution and counting statistics have limited the accessible energy range. An alternate opportunity to separate positive and negative particles is provided by the earth's magnetic field. The cut-off rigidity varies with the geographic location, the direction of incidence of the particle and with the particle charge. The cut-off rigidities for negatrons at Hawaii are shown in figure 1.

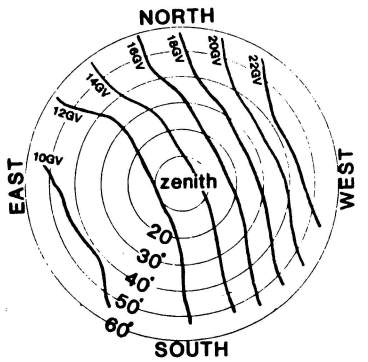

Fig.1 View of Sky, Hawaii contors of negatron cutoff rigidities

*Supported, in part, by NASA grant NSG-7464.
+Also Department of Physics.

For positrons, east and west exchange roles. Therefore, there exists a range of energies and directions for which, for a given geographic location, the earth's field transmits only particles of one polarity. The utilization of this effect was pioneered by Daniel and Stephens (1965,1967). However, the first measurements (Anand et al, 1969; Agrinier el al, 1969) were severely limited due to insufficient statistics and systematic uncertainties.

In April 1984, we have performed a balloon flight from Hawaii using our electron telescope to separate negatrons and positrons in the range 10-20 GeV. The flight had a duration of 11 hours at a float altitude corresponding to 4 $gm/cm^2$ residual atmosphere in the vertical. The following describes our measurement.

INSTRUMENTATION This instrument has been described previously in detail (Tang, 1984). Here we just summarize the main features: The instrument is an electronic counter telescope with a geometric factor of about 0.1 $m^2$ sterad. For each particle traversing the detector, the following quantities are measured: (1) the charge number $|z|$ with a plastic scintillator, (2) the trajectory through the instrument with a multiwire proportional chamber hodoscope, (3) the direction of traversal with a time-of-flight measurement, (4) the transition radiation emitted by electrons (but not protons) in a 6-layer transition radiation detector, and (5) the electromagnetic cascades produced in a 9 layer lead-scintillator shower detector of 18.5 radiation length depth. These cascades are characteristic for electrons and measure the electron energy with $\Delta E/E \approx 8\%$.

During the balloon flight, the instrument has been suspended with its axis inclined by 30 degrees against the vertical. The orientation of the gondola was measured with magnetometers, and, through the use of a commandable torque motor, the instrument could be oriented towards the west (to observe positrons) or towards the east (for a control measurement of negatrons). To determine the cut-off rigidities(shown in fig.1), we use the predictions of Shea and Smart (1974), and we note that cosmic ray measurements of Jordan and Meyer (1983) have been in agreement with these predictions.

ANALYSIS & RESULTS Electrons are selected from the data set according to procedures described in detail in our earlier work (Tang,1984). Due to the combination of a deep shower detector with a transition radiation detector, our instrument is capable of rejecting protons with the required rejection power of $10^4$. The residual proton contamination to our results is indicated in table 1. After applying the appropriate corrections for inefficiencies of individual detector elements, for the area-exposure time, and for energy losses in the residual atmosphere above the detector, we obtain the electron fluxes, grouped according to directions of incidence from EAST, and from WEST.

The measured EAST and WEST electron spectra are shown in Figure 2. They exhibit a clear east/west asymmetry between 10 to 20 GeV while showing the same flux at other energies. Cutoffs at 11 GeV (east) and 22 GeV (west) agree well with negatron cut-off calculations, which use codes by

Shea and Smart (1974). Each spectrum can be analyzed as a composite of (i) atmospheric secondary electrons, (ii) secondary electrons that appear as reentrant albedo particles, (iii) galactic negatrons, and (iv) galactic positrons.

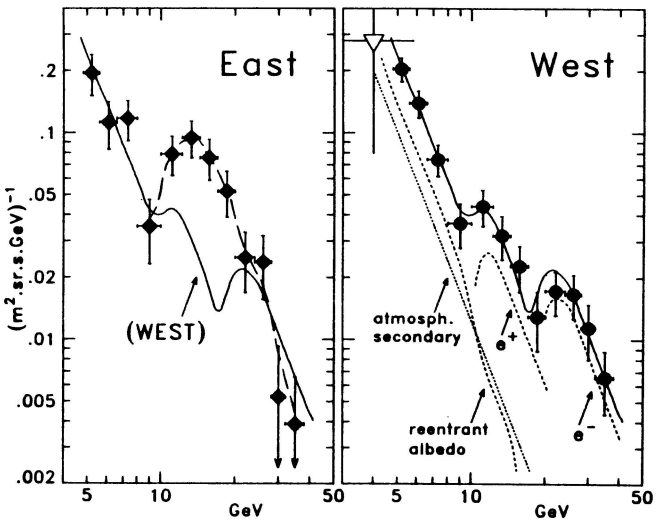


Fig.2 Differential Energy Spectra of Electrons, Hawaii '84
The solid curve (WEST) is the sum of the dotted curves.
The dashed curve is a hand fit to the EAST spectrum.
Reentrant albedo data point: ▽ Daniel & Stephens '67

Such an analysis for the WEST data is shown in Figure 2. The curve for atmospheric secondaries is derived from interpolating calculations by Beuermann (1971) for 7 gm/cm$^2$ of atmosphere. The reentrant albedo particles are expected to disappear above cut-off rigidities. In Figure 2, we estimated their fluxes such that the direct atmospheric and the reentrant secondaries add up to our data below 10 GeV. This procedure is consistent with the flux of reentrant albedo electrons at 4 GeV measured by Daniel and Stephens (1967).
The curve of galactic negatrons is obtained by folding our previously measured electron spectrum with calculations of geomagnetic cutoffs. Clearly, a significant amount of positrons is required to account for the fluxes from 10 to 20 GeV.

To derive the positive fraction of cosmic ray electrons, the WEST data are divided into 2 energy intervals shown in Table 1. N(total) is the number of selected events and N(proton) is the estimated number of residual proton background. N(atmos) is the number of atmospheric and reentrant albedo events estimated by extrapolating data below 10 GeV to higher energies. The net number of positrons, N(+) , is obtained by subtracting N(proton) and N(atmos) from N(total). We obtain N(sum), the sum of cosmic positrons and negatrons, using the EAST data and our previous measurement (Tang 1984). Finally, a factor f corrects for small effects due to the finite energy resolution of the detector and the variation of cut-off rigidities over extended regions of the sky. The positive fraction, $e^+/(e^+{+}e^-)$, is then the ratio of N(+) and N(sum), multiplied by f.

Table 1

| E(GeV) | N(total) | N(proton) | N(atmos) | N(+) | N(sum) | f | $e^+/(e^+{+}e^-)$ |
|---|---|---|---|---|---|---|---|
| 10–14.4 | 67±8.2 | 9.3±2.3 | 22.±5.8 | 35.8±10 | 248±30 | 1.05±.05 | .151±.048 |
| 14.4–20 | 34±5.8 | 3.3±0.8 | 8.6±3.4 | 22.1±7. | 97±13 | 0.90±.10 | .204±.072 |

DISCUSSION Our measurements of $e^+/(e^+{+}e^-)$ in cosmic-ray are shown in Figure 3. The error limits include statistical and systematic uncertainties. We compare our data with measurements at lower energies and with some calculations of propagation models using pathlengths which agree with B/C ratios (Protheroe, 1982). The calculations have shown that

the positron flux below 10 GeV is consistent with an entirely (>97%) secondary origin, due to interactions of nuclei (mostly protons) in the interstellar gas. Our results show an increase of the positive fraction above 10 GeV and are significantly higher than the model calculations.

There are two possibilities to understand this increase of $e^+/(e^++e^-)$: (1 ) a primary component of positrons becomes significant above 10 GeV; or (2) the flux of primary electrons (assumed to be almost entirely negatrons) decreases above 10 GeV more rapidly than that of secondary positrons. The first possibility may not be very likely, while the latter is corroborated by the fact that the total electron spectrum begins to bend over at the same energy region where $e^+/(e^++e^-)$ increases. Such a decrease of primary negatrons above 10 GeV could, for instance, have its origin in the acceleration region if synchrotron losses in that region limit the electron energies attainable during the acceleration time. Or it may be that sources of primary electrons are significantly further away than those of secondary positrons, leading to comparatively larger energy losses en route.

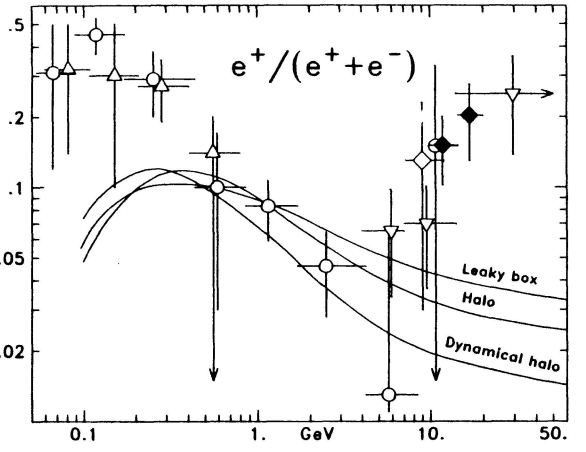


Fig.3 Positive Fraction of Cosmic Ray Electrons
data: ◆This Work, ▽ Buffington '75, △ Daugherty '75, ○ Fanselow '69, ◇ Agrinier '69. curves: Protheroe '82.

ACKNOWLEDGEMENT We acknowledge the assistance of E. Drag and the substantial contributions of R. Kroeger towards the success of this experiment, and we are indebted to the crew of the National Scientific Balloon Facility and the U.S. Navy for excellent balloon flight and support operations. We are also grateful for the help of Dr. Peter Meyer in sharing transportation and accommodation of our equipment.

References

Agrinier, et al. Lettere al Nuovo Cimento, serie I, 1 53 (1968).
Anand, K.C., Daniel R.R., and Stephens S.A., 11th ICRC Budapest (1969).
Beuerman, K.P., J.G.R., vol 76, no 19, 4291 (1971).
Buffington A., Orth C.D. and Smoot G.F., Ap. J. 199 699 (1975).
Daniel R.R., and Stephens S.A., Phys. Rev. Lett., 15 769 (1965).
Daniel R.R., and Stephens S.A., Proc. Indian Acad. Sci., 65A 319 (1967).
Daugherty, J.K., Hartman, R.C. and Schmidt P.J., Ap. J, 198 493 (1975).
Fanselow, J.L., Hartman, R.C. Hildebrand, R.H. and Meyer, P., Ap.J. 158 771 (1969).
Jordan, S. and Meyer, P., 18th ICRC, OG 45 (1983).
Orth, C. D. and Buffington, A. , Ap. J. 206 312 (1976).
Protheroe, R. J., Ap. J. 254 391 (1982).
Shea, M.A. and Smart, D. F., Tech. Rep. AFCRL-TR-74-0159, Air Force Cambridge Research Lab., Bedford, Ma. (1974).
Tang, K., Ap. J. 278 881 (1984).

# SPECTRAL SHAPE VARIATION OF INTERSTELLAR ELECTRONS AT HIGH ENERGIES

L.C.Tan
Department of Physics and Astronomy
University of Maryland
College Park, MD 20742
USA

Our analysis of the high-energy electron spectrum has shown that the electron intensity inside the $H_2$ cloud region, or in a spiral arm, should be much lower than that outside it and the observed electron energy spectrum should flatten again at about 1 TeV.

In the framework of the leaky box model the recently established rigidity $(R)_0$ dependence of the escape pathlength ($\lambda_e$) of cosmic rays (i.e., $\lambda_e \propto R^{-0.7}$)(1) would predict a high-energy electron spectrum which is flatter than the observed one. We explain this divergence by assuming that the leaky box model can only apply to cosmic-ray heavy nuclei, and light nuclei and electrons in cosmic rays may have different behaviours in the interstellar propagation. Therefore, the measured data on high-energy electrons should be analysized based on our proposed nonuniform galactic disk (NUGD) model(2).

In the NUGD model (see Fig. 1 of OG 7.2-10) Box 1 and Box 2 are the confinement volumes of primary nuclei and electrons in the solar vicinity and above the $H_2$ cloud region respectively, Box II is the dense $H_2$ cloud region and Box I represents the magnetic tube located in the central layer of the Orion arm. The $H_2$ cloud region is assumed to be inert, hence primary nuclei and electrons should originate from Box 1(the local component) or Box 2 (the distant component). Hereafter we use the subscripts 1, 2, I and II to express the quantities referred to Boxes 1, 2, I and II respectively.

By using Gauss's theorem,we have

$$\frac{1}{V_2}\int_{s_2} \vec{J}_{i2}\cdot\vec{n}_2 ds_2 = \frac{1}{V_2}\int_{V_2} \nabla\cdot\vec{J}_{i2}\, dr_2^3 , \qquad (1)$$

where $\vec{J}_{i2}$ is the net flow of the ith kind of particles in the coordinate space ($\vec{r}_2$) of Box 2, V, s and $\vec{n}$ are the volume, the surface area and the unit vector normal to s respectively. According to the 'leaky box' concept the right hand side of Eq. (1) may be replaced by $N_{i2}/\tau_{e2}$, where $\tau_{e2}$ is the mean escape lifetime of cosmic rays. Since

$$s_2 = s_{2\to II} + s_{2\to halo} , \qquad (2)$$

where $s_{2\to II}$ and $s_{2\to halo}$ are the area of the boundaries between Box 2 and Box II and Box 2 and the halo respectively, we can write

$$\int_{s_{2\to II}} \vec{J}_{i2}\cdot\vec{n}_2\, ds_2 + \int_{s_{2\to halo}} \vec{J}_{i2}\cdot\vec{n}_2\, ds_2 = \frac{V_2 N_{i2}}{\tau_{e2}} , \qquad (3)$$

We define the first and second terms on the left hand side of Eq. (3) as $V_2 N_{i2}/\tau_{e2\to II}$ and $V_2 N_{i2}/\tau_{e2\to halo}$ respectively.

Here the quantity $\frac{1}{V_{II}}\int_{s_{2\to II}} \vec{J}_{i2}\cdot\vec{n}_2\, ds_2$ is just the source term of the ith kind of particles in Box II due to the flow from Box 2, $q_{iII}$,

$$q_{iII} = \frac{1}{V_{II}}\int_{s_{2\to II}} \vec{J}_{i2}\cdot\vec{n}_2\, ds_2 = \frac{m_p \bar{n}_2 \beta_i c V_2}{V_{II}} \frac{N_{i2}}{\lambda_{e2\to II}} . \qquad (4)$$

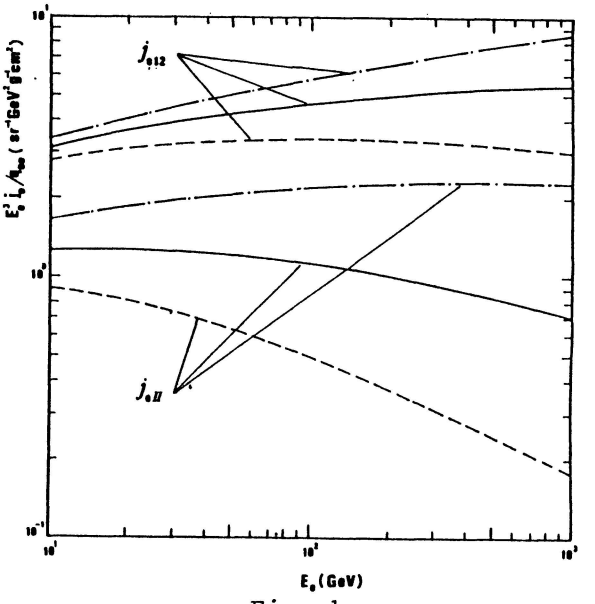

Fig. 1

Here we have used

$$\lambda_e = m_p \bar{n} \beta c \tau_e , \qquad (5)$$

where $m_p$ is the proton mass, $\beta c$ is the particle velocity and $\bar{n}$ is the mean matter density of the ISM. As $\lambda_{e2}$ is independent of the nature of the particles, from Eq. (3) $\lambda_{e2\to II}$ should also be independent of the nature of the particles. Therefore, in order to estimate $q_{iII}$ we only need to consider the main proton component of cosmic rays, which has the continuity equation in Box II at high energies,

$$N_{pII}\left(\frac{1}{\lambda_{eII}} + \frac{1}{\lambda_p^i}\right) = \frac{m_p \bar{n}_2 c V_2}{V_{II}} \frac{N_{p2}}{\lambda_{e2\to II}} + \int_{E_p}^{\infty} \frac{1}{\lambda_p^i} \frac{dN_p(E_p, E')}{dE_p} N_{pII}(E'_p) dE'_p , \qquad (6)$$

where $\lambda^i$ is the mean inelastic interaction length of interstellar protons and $dN_p/dE_p = 1/E'_p$ is the energy distribution of protons after their inelastic interractions. Under the power-law approximation ($N_p \propto E_p^{-\gamma_p}$) we can get

$$\lambda_{e2\to II} = \frac{m_p \bar{n}_2 c V_2 \lambda_{pII}^{eff}}{V_{II}} \frac{N_{p2}}{N_{pII}} , \qquad (7)$$

where $\lambda_{pII}^{eff} = 1/\left(\frac{1}{\lambda_{eII}} + \frac{1}{\lambda_p^{att}}\right)$ and $\lambda_p^{att} = \lambda_p^i / (1 - 1/\gamma_p)$. Owing to the fact that no cosmic-ray gradient exists in the inner Galaxy, the condition $N_{p2} = N_{pII}$ should be held. Then by combining Eqs. (4) and (8) we have

$$q_{iII} = N_{i2} / \lambda_{pII}^{eff} . \qquad (8)$$

Assuming that cosmic-ray electrons originate from a shock acceleration process, at high energies we should take their source term $q_{e2}$ $(=q_{e1}) \propto E_e^{-2}$ and their intensity $N_{e2}$ $(= N_{e1}) \propto E_e^{-3}$ due to electromagnetic losses. From Eqs. (7)-(8) we get

$$\lambda_{pII}^{eff} \propto \lambda_{eII} \propto E_e^{-0.7},$$

$$q_{eII} \propto E_e^{-2.3} \text{ and } N_{eII} \propto E_e^{-3.3},$$

which is fully consistent with recent observations. Thus our deduced $j_{e12}$ and $j_{eII}$ are shown in Fig. 1, in which the dot-dashed lines, the solid lines and the dashed lines represent the cases of $\delta = 0.8$, 0.7 and 0.6 respectively. From Fig. 1 it is immediately noted that the electron flux in the $H_2$ cloud region (and hence in the solar neighbourhood) should be much less than that in the distant regions (Boxes 1 and 2). Actually, this prediction is consistent with the observation(3).

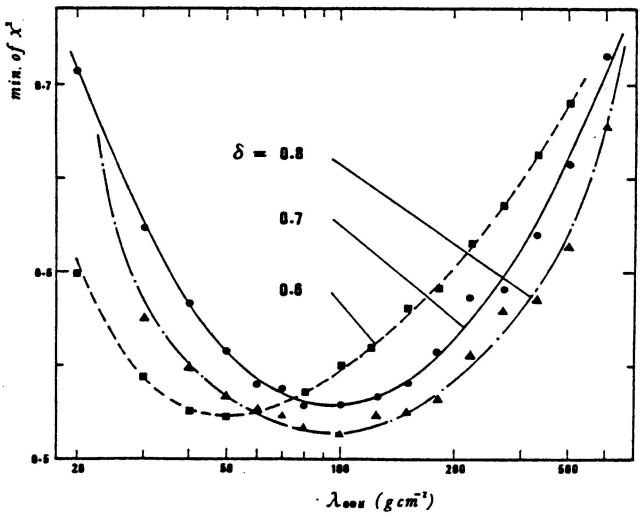


Fig. 2

Further, the attenuation factor of high-energy electrons along the magnetic tube (Box I) before reaching the solar neighbourhood is

$$\eta = \exp\left((\gamma_{eII} - 2)\ \ln(1 - a)\right), \tag{10}$$

where $\gamma_e$ is the spectral index of the electron spectrum, $a = bE_e x_{Is}$, $x_{Is}$ being the pathlength of electrons in Box I to reach the solar neighbourhood, and $b = 7\times10^{-3}$ $(GeV^{-1} g^{-1} cm^2)$(4). Thus the predicted electron intensity in the solar neighbourhood should be

$$N_{ep} = (1 - \varepsilon)\eta N_{eII} + \varepsilon N_{e12}, \tag{11}$$

where $\varepsilon$ is the fraction of protons coming from Box 1 in the observed proton flux.

Recent data on high-energy electrons (5)-(7) have been used to estimate astrophysical parameters inherent in the NUGD model. In Fig. 2 we show a plot of the minimum $\chi^2$ value, which is obtained by varying $q_{e0}$ (the source term $q_{e12} = q_{e0} E_e^{-\gamma_s}$ and $\gamma_s + \delta = 2.75$) and $\varepsilon$ simultaneously, against $\lambda_{e0II}$ $(\lambda_{eII} = \lambda_{e0II} E_e^{-\delta})$. From this plot the allowable range of $\lambda_{e0II}$ can be established.

In Table 1 we list the values of some model parameters estimated from our $\chi^2$ fitting procedure. It is noticeable that $\varepsilon = 5\pm1$ %, indicating that the dominant part of observed cosmic-ray protons should come from the $H_2$ cloud region. Moreover, the deduced $\lambda_{e0II}/\lambda_{e012} \doteq 3$ at $\delta = 0.7$, which is also consistent with our previous conclusion that most of secondary antiprotons should be produced in the $H_2$ cloud region(2).

In the magnetic tube (Box I) the diffusion coefficient of 10 GeV cosmic rays is estimated to be about $10^{30}$ $cm^2 s^{-1}$, which corresponds their mean free path of about 50 pc. This is consistent with the assumption that the scattering of cosmic rays by hydromagnetic waves should happen in the zone outside an arm, while along an arm there should be a free zone where cosmic rays are free to stream along the field lines with speeds of the order of the velocity of light(8).

| $\delta$ | $x_{0I}/\lambda_p^i$ [a] | $\epsilon$ (%) | $q_{e0}$ ($10^2 m^{-2} s^{-1} GeV^{-1} g^{-1} cm^2$) | $\lambda_{e0I2}$ ($10 gcm^{-2}$) | $\lambda_{e0II}$ ($10^2 gcm^{-2}$) |
|---|---|---|---|---|---|
| 0.8 | 0.9 | 4 | $3.1^{+1.9}_{-1.1}$ | $3.5^{+3.0}_{-1.3}$ | $1.0^{+1.2}_{-0.6}$ |
| 0.7 | 0.4 | 5 | $3.1^{+1.8}_{-0.9}$ | $4.0^{+4.0}_{-1.7}$ | $1.0^{+1.0}_{-0.5}$ |
| 0.6 | 0.1 | 6 | $2.4^{+1.4}_{-0.5}$ | $5.6^{+6.0}_{-2.5}$ | $0.5^{+0.7}_{-0.2}$ |

Table 1.

Finally, in Fig.3 we show the electron fluxes predicted for the NUGD model (see the explanation of the curves shown in Fig.2). It is noticeable that the predicted electron spectra for all the $\delta$ values considered exhibit a flattening at about 1 TeV. This flattening is understandable because at very high-energies observed electrons should only originate from their confinement volume in the solar vicinity (Box 1), and hence have a spectral index near to 3 (see Fig. 1). Our prediction is not in contradiction with the existing data(5). However, it is suggested to make improved measurements to examine the prediction presented above.

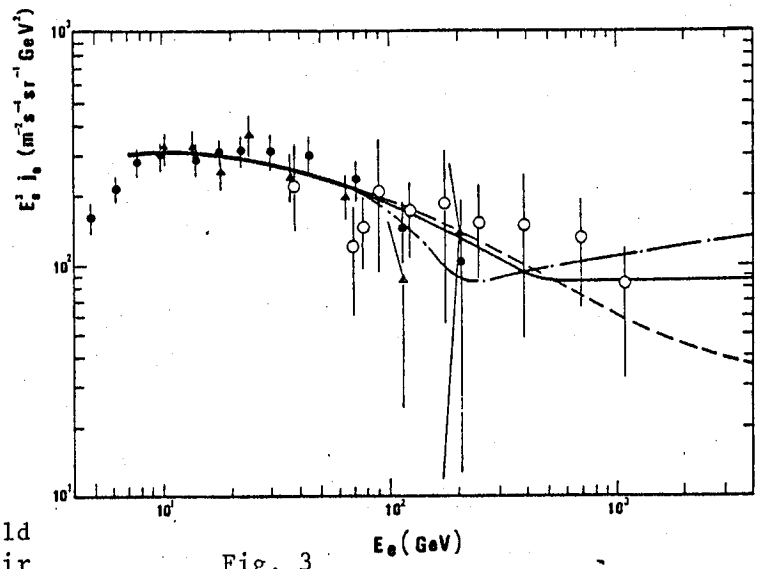


Fig. 3

References:
1. Ormes,J. and Protheroe,R.J. 1983, Ap. J.,272, 756.
2. Tan,L.C. and Ng,L.K. 1983, Ap. J., 269, 751.
3. Strong,A.W. et al., 1978, M.N.R.A.S., 182, 751.
4. Tan,L.C. 1985, Ap.J., 1985, in press.
5. Nishimura,J. et al., 1980, Ap. J., 238, 394.
6. Prince,T.A. 1979, Ap. J., 227, 676.
7. Muller,D. and Tang,J. 1983, Proc. 18th Internat. Cosmic Ray Conf. (Bangalore), 2, 60.
8. Holmes,J.A. 1974, M.N.R.A.S., 166, 155.

# Re-estimation of the Production Spectra of Cosmic Ray Secondary Positrons and Electrons in the ISM

C.M. Wong and L.K. Ng
Physics Department, University of Hong Kong
Hong Kong

## Abstract

The present work includes a detailed calculation of the production spectra of charged hadrons ($\pi^{\pm}$,$K^{\pm}$) produced by interactions of cosmic rays in the interstellar medium, and a thorough treatment of pion and muon decays. Newly parametrised inclusive cross sections of hadrons were used and exact kinematic limitations were taken into account. Single parametrised expressions for the production spectra of both secondary positrons and electrons in the energy range $10^{-1}$ - $10^{+3}$ GeV are presented. The results are compared with other authors' predictions. Equilibrium spectra using various models are also presented.

1. Introduction. It is well known that cosmic ray secondary positrons and electrons in the ISM arise from the $\pi\mu e$ decay chain of secondary $\pi$ produced in the interactions of cosmic rays with the ISM. Given the production spectra of $e^{\pm}$, their equilibrium spectra can be calculated by model predictions. And by combining with the available high-energy cosmic ray $e^{\pm}$ data, we can obtain a better understanding of cosmic ray propagation in the galaxy. However, there is no general agreement among the previous calculations of the production spectra of $e^{\pm}$. In this work, we have re-estimated these spectra based on newly parametrised inclusive cross sections of hadrons which are applicable at energies from the ISR down to those near the production threshold. Moreover, exact kinematic limitations are taken into account.

2. Production spectra of hadrons. Re-estimation of the production spectra of hadrons is motivated by the existence of large divergence among various inclusive cross section formulae[1], and the availability of newly parametrised formulae based on more recent accelerator data[2].

The production spectra of hadrons in p-p collisions is given by

$$P(E_h) = \frac{2\pi}{m_p} \int_{E_t}^{\infty} j(E_p)\,dE_p \int_0^{\theta_{max}} \left(E \frac{d^3\sigma}{dp^3}\right) p_t\, d\theta$$

where $E_t$ is the threshold energy of p-p collisions for a given hadron energy $E_h$, $\theta_{max}$ is the maximum angle of hadron emission in the laboratory system and $j(E_p)$ is the differential flux of interstellar protons taken from Ref.3. Calculation was done without applying any approximation to the integrations, and exact kinematic limitations were taken into

account. Results for $\pi^{\pm}$ and $K^{\pm}$ are shown in figure 1. The uncertainties in the input spectrum gives rise to the shaded areas at low energies.

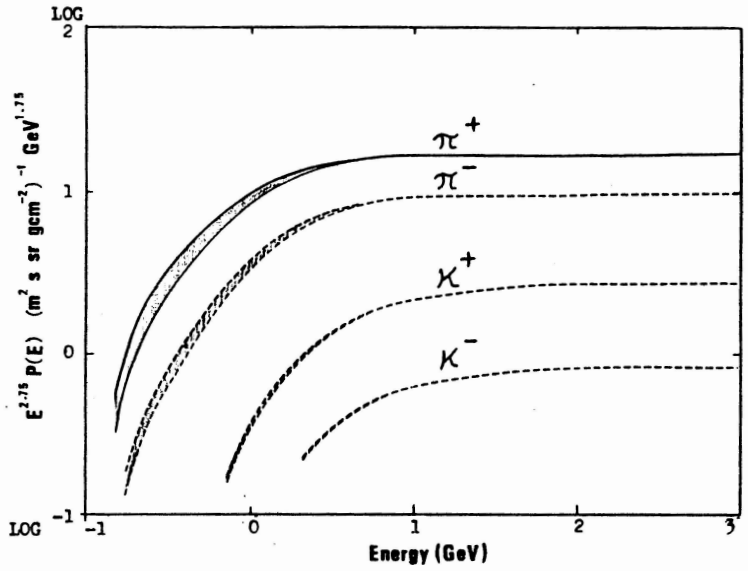


Fig. 1
Production spectra of charged hadrons in p-p collisions.

3. Production spectra of $e^{\pm}$. Production spectra of $e^{\pm}$ in interstellar space is obtained by rigorous treatment of pion and muon decays taking into account of precise decay kinematics and muon decay asymmetry. Correction for the cosmic ray and the ISM compositions[4] and the contribution from kaons[5] are then added. The results are given in figures 2 and 3.

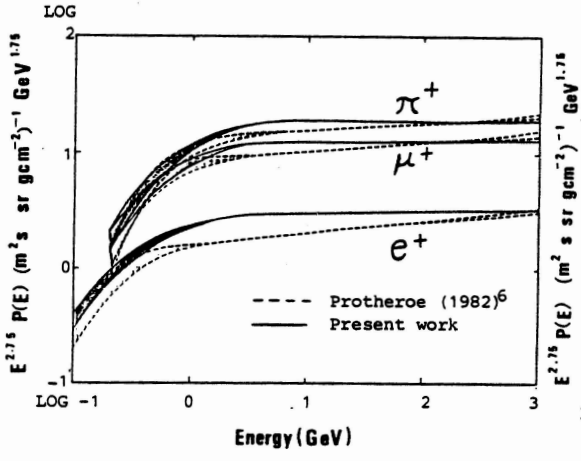


Fig.2 Production spectra of $\pi^+$, $\mu^+$ and $e^+$.

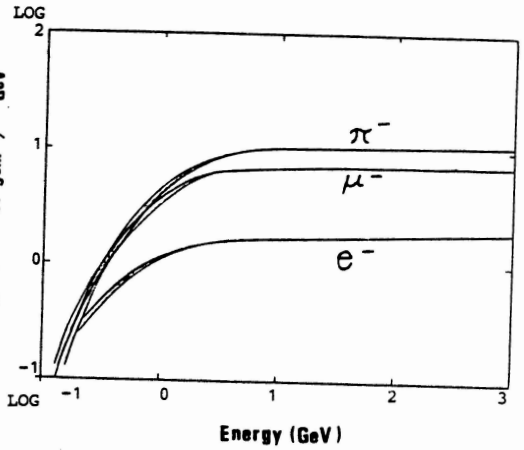


Fig.3 Production spectra of $\pi^-$, $\mu^-$ and $e^-$.

The spectra can be parametrised as follows with the coefficients listed in Table I.

$$Q(E_e) = \left[C_1 E_e^{-C_2}\right]/\left[1 + C_A E_e^{-C_B}\right] \text{ for } 0.1 \text{ GeV} \leqslant E_e \leqslant 1000.0 \text{ GeV}$$

where $C_A = C_3 + C_4 \ln E_e + C_5 \ln^2 E_e$ ,

$C_B = C_6 + C_7 \ln E_e + C_8 \ln^2 E_e$.

| Limit | $C_1$ | $C_2$ | $C_3$ | $C_4$ | $C_5$ | $C_6$ | $C_7$ | $C_8$ |
|---|---|---|---|---|---|---|---|---|
| Upper | 2.84 | 2.72 | 0.173 | -0.146 | -0.00992 | 0.892 | 0.00499 | 0.0389 |
| Lower | 2.84 | 2.73 | 0.252 | -0.148 | -0.0454 | 1.09 | -0.0127 | 0.0474 |

Above for positrons.

| Limit | $C_1$ | $C_2$ | $C_3$ | $C_4$ | $C_5$ | $C_6$ | $C_7$ | $C_8$ |
|---|---|---|---|---|---|---|---|---|
| Upper | 1.58 | 2.72 | 0.371 | -0.305 | 0.0698 | 0.768 | 0.0444 | 0.0536 |
| Lower | 1.58 | 2.72 | 0.433 | -0.312 | 0.0570 | 0.901 | 0.0688 | 0.0575 |

Above for electrons.

TABLE I

4. Results and discussion. Figure 4 compares the present calculated positron spectrum with the previous calculations. Our results are significantly higher than the others especially near the energy range 1 - 10 GeV. The differences are mainly due to different adoption of the inclusive cross section parametrisations and different assumed interstellar proton spectra. However, since in our calculation, more recent accelerator data have been used and rigorous kinematic treatment has been done, we believe the production spectrum has been improved.

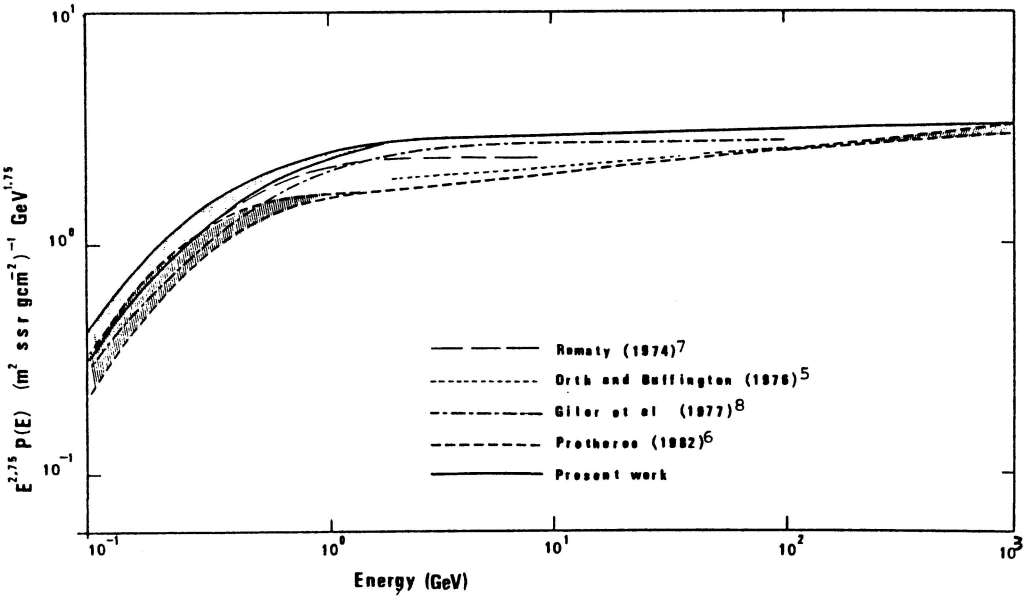


Fig.4 Production spectra of $e^+$ predicted by various authors.

For the purpose of illustration, equilibrium spectra have been calculated using this positron production spectrum and various propagation models as shown in figure 5. It is seen that the predicted curves are all close to the recent datum due to Golden et al[13].

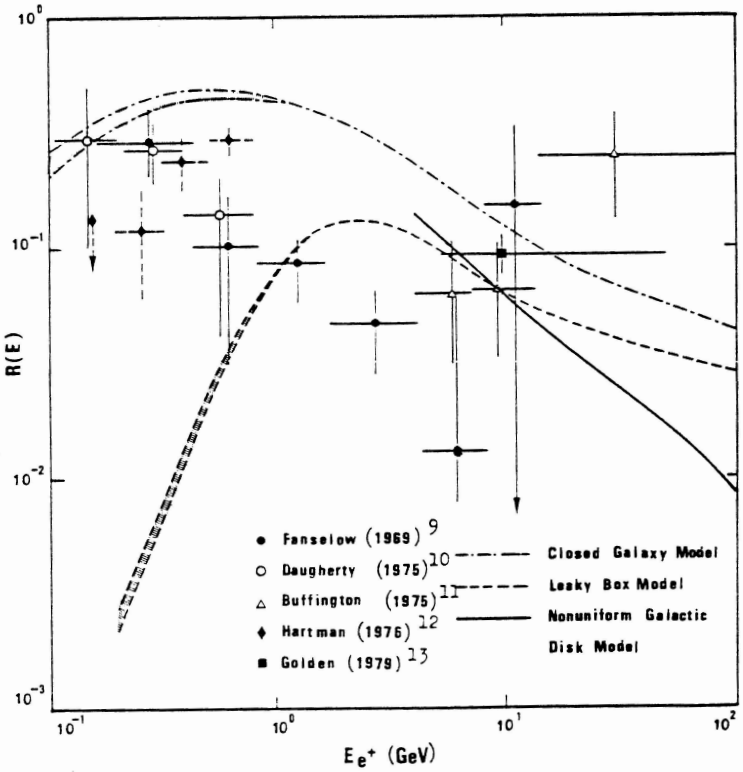


Fig.5 Equilibrium spectra of $e^+$ based on the present calculated production spectrum.

5. Acknowledgement. Authors are grateful to Dr. L.C. Tan and Dr. P.K. MacKeown for their helpful comments and to Professor D.J. Newman for his support and encouragement.

References.

1. Ghoshdastidar M R et al, Proc.17th ICRC 5 (1981) 1.
2. Tan L C et al, J. Phys. G: Nucl.Phys. 9 (1983) 1289.
3. Ormes J F et al, Ap. J. 272 (1983) 756.
4. Tan L C et al, J. Phys. G: Nucl. Phys. 7 (1981) 1135.
5. Orth C D et al, Ap. J. 206 (1976) 312.
6. Protheroe R J, Ap. J. 254 (1982) 391.
7. Ramaty R., High Energy Particles and Quanta in Astrophysics, MIT Press, Cambridge, (1974)122.
8. Giler M et al, J. Phys. A Math.Gen., 10 (1977) 843.
9. Fanselow J L et al, Ap. J. 158 (1969) 771.
10. Daugherty J K et al, Ap. J. 198 (1975) 493.
11. Buffington A et al, Ap. J. 199 (1975) 669.
12. Hartman R C et al,Ap. J. 204 (1976)927.
13. Golden R L et al, Proc. 16th ICRC (Kyoto) 1 (1979) 470.

# ELECTRONS AND POSITRONS FROM EXPANDING SUPERNOVA ENVELOPES IN DENSE CLOUDS

S.A. Stephens
Tata Institute of Fundamental Research
Homi Bhabha Road, Bombay 400005, India

ABSTRACT

If antiprotons ($\bar{p}$) in cosmic rays are produced as secondary particles in sources, it is expected that positrons are also created by the same process. In this paper we calculate the interstellar spectra of positrons and electrons by taking into account such sources, and compare them with observations.

1. Introduction. Large flux of $\bar{p}$, in excess of that expected on the basis of a few g.cm$^{-2}$ of matter traversed by cosmic rays, has been observed [1-3]. This excess has been explained as being produced in the expanding envelopes of supernova (SN), which explodes in dense cloudlets in the Galaxy [4]. It is shown that if 30% of the observed cosmic ray nucleons come from such sources, $\bar{p}$ observations can be explained satisfactorily [5]. As $\bar{p}$ being produced in interactions of cosmic ray nucleons with gas, it is expected that pions and kaons are also produced in these interactions, which decay to electrons and positrons. In these sources initially accelerated electrons are depleted at high energies due to synchrotron process. As a result, high energy spectrum of the electron component from these sources are expected to be rich in positrons. In this paper, we evaluate the equilibrium spectra of positrons and electrons in the Galaxy by including the electron component from these sources.

2. Electron Spectrum in the Same Source. The evolution of electron component inside SN envelope is coupled to that of nucleonic component and therefore, one needs to solve the following coupled equations.

$$\frac{dJ_p}{dt} = \frac{\partial}{\partial E}\left(J_p \frac{dE_p}{dt}\right) - \frac{\rho v}{\lambda} J_p + \int_{E'} \frac{\rho v}{\lambda} J_p \frac{dE'}{E'} \quad \ldots \quad (1)$$

$$\frac{dJ_{e^\pm}}{dt} = \frac{\partial}{\partial E}\left(J_{e^\pm} \frac{dE_{e^\pm}}{dt}\right) + Q_{e^\pm} \quad \ldots \quad (2)$$

In the above equations, 1st term on the RHS describes continuous energy loss of particles. In the case of protons, this energy loss corresponds to ionization and adiabatic cooling. For electrons, in addition to the above, one needs to include bremsstrahlung and synchrotron processes; the loss due to inverse Compton process is small compared to synchrotron process except at a very early phase of SN. 2nd term in Eqn. 1 is the loss of nucleons due to interaction and 3rd term takes care

of the finite inelasticity during collision. In these terms, v is the velocity of interacting particle, $\rho$ the density and $\lambda$ the interaction mean free path. The production term $Q_{e^\pm}$ is given as

$$Q_{e^\pm} = \iiint \frac{dE_\mu}{\psi_e} \cdot \frac{dE_\pi}{\psi_\mu} \cdot \{J_p \rho v\} dE_p \cdot \{2\pi (E \frac{d^3\sigma}{dp^3})\} p_\perp \, d\theta \ldots \quad (3)$$

In this equation, integral over $\theta$ describes the production of pions, in which $p_\perp$ and $\theta$ are the transverse momentum and angle of emission of pions; the invariant cross-section $E(d^3\sigma/dp^3)$ depends upon $E_p$ and hence the integral over $E_p$. The integrals over $E_\pi$ and $E_\mu$ take care of the energy distribution of decay products as pion decays to muon and muon to electron. The parameters relating to the production of pions and the evolution of SN are described elsewhere [5,6].

While evaluating Eqns. 1 and 2, we have set the initial condition that the energy spectra of nucleons and negatrons are simple power law in rigidity of the type $AR^{-2.75}$, where $A = 2.5 \times 10^4$ and 150 particles/cm$^2$.sr.s.GV/c) for nucleons and electrons respectively. It is assumed that the initial acceleration is complete at the onset of the adiabatic phase and the remnant leaves the cloudlet when cosmic rays traverse $\sim 50$ g.cm$^{-2}$ of matter. The magnetic field inside the cloud is expected to scale as $B^2 \alpha \rho n_H$, with $B_o = 4\mu G$ for $n_H = 1$ atom.cm$^{-3}$. The photon density corresponds to an outburst of optical photons of $10^{43}$ erg/s soon after the explosion, which decay with an e-folding time of 0.2 yrs.

3. Equilibrium Spectrum in Interstellar Space. The equilibrium spectrum of $e^\pm$ in interstellar space is evaluated by solving the continuity equation

$$\frac{dJ_{e^\pm}}{dt} = \frac{\partial}{\partial E} (J_{e^\pm} \frac{dE_{e^\pm}}{dt}) + Q_{e^\pm} - \frac{J_{e^\pm}}{T} \quad \ldots \quad (4)$$

In this equation, the source term $Q_{e^\pm}$ consists of 3 terms. (1) The electrons from SN, which explode in dense clouds. This is obtained from Eqn. 2 and normalized to the observed $\bar{p}$ flux value at 9 GeV [1]. The production term is then given by $J_{e^\pm}/T$. (2) The second term comes from sources in which cosmic rays traverse matter in an energy dependent manner [7]. It is assumed that at energies $\lesssim$2 GV/c, the matter traversed is $\approx$4 g.cm$^{-2}$ and above this energy it is proportional to $R^{-0.6}$. The secondary production of electrons is calculated using the equilibrium nucleon spectrum in the source and $Q_{e^\pm}$ is obtained after allowing for the energy dependent leakage. (3) The third term comes from the production of secondary electrons in interstellar space. In the case of negatrons, we have also included a term which is 70% of 150 $E^{-2.75}/T$. The resident time T in Eqn. 4 is considered to be free parameter and is adjusted to fit the observed electron spectrum.

4. Results. We have plotted in the lower part of Fig. 1, the observed flux values of electrons from recent experiments above 1 GeV [8-10]. For convenience, the flux scale is multiplied by $E^3$. The curve shown here is the calculated spectrum using a value of $5 \times 10^6$ yrs for T. One finds

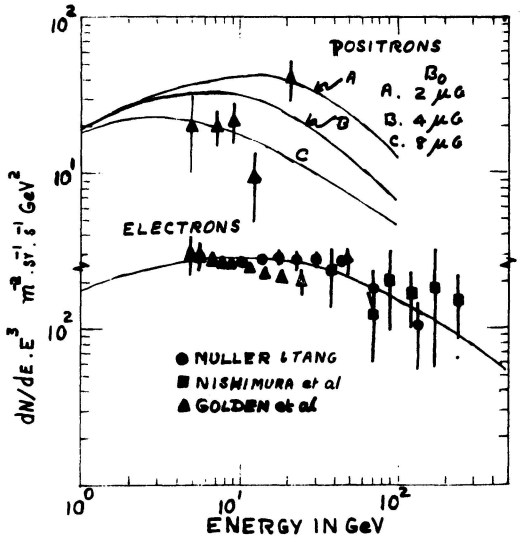


*Fig. 1 The spectrum of electrons is shown on the lower part of this figure and that of $e^+$ is shown on the upper part*

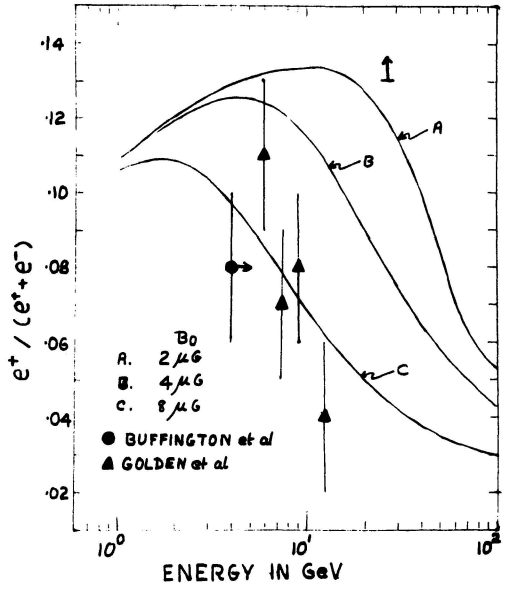


*Fig. 2 Positron fraction is plotted as a function of energy*

a good fit to the observed data points. We make use of the same interstellar parameters to calculate the positron spectrum from Eqn. 4.

The calculated positron spectrum in interstellar space is plotted in the upper part of Fig. 1. We have pointed out earlier that high energy electrons in SN envelopes are depleted by synchrotron energy loss process, and the positron spectrum is quite sensitive to the $B_o$ value used in Eqn. 2. Three curves shown in Fig. 1 is based on different values of $B_o$. The spectral steepening noticed in this figure is due to the combined effect of energy loss processes and the energy dependent matter traversal in sources. The data points plotted here are from Golden et al. [11]. One notices from Fig. 1 that the positron spectrum is quite consistent with the model that major contribution comes from sources which produce antiprotons in cosmic rays. The spread in the data points is such that one cannot obtain a precise value of $B_o$, though a value between 4 and 8 μG could fit the data points well.

We have shown in Fig. 2, the fraction of positrons as a function of energy for 3 different values of $B_o$ as in Fig. 1. The increase in this ratio with energy arises from the fact that initially accelerated electrons in SN, which explode in dense clouds are depleted due to synchrotron process and that the electron component at higher energies is dominated by secondary particles. The initial decrease in the ratio is primarily due to the depletion of secondary electrons through synchro-

tron process and later by the energy dependent source term in Eqn. 4. One also notices that the ratio attains an asymptotic value close to about 2% at very high energies. The absolute value of this ratio can be easily adjusted by about 20% by increasing the primary electron flux values by the same factor. In that case a small adjustment in the value of T could reproduce the good fit obtained for electrons in Fig. 1. We have also plotted the observed values of the fraction of $e^+$ [11,12]. One notices that the general trend of the data points are similar to the calculated values except for a normalization of about 20%, which is consistent with the errors in the results.

Thus we conclude that SN exploding in dense clouds seems to explain not only the $\bar{p}$ results but also the $e^+$ data. We have also shown elsewhere that the observed Cos-B $\gamma$-ray sources could also be explained [13].

References

[1] R.L. Golden et al., Phys. Rev. Letters, 43, 1196 (1979)
[2] E.A. Bogomolov et al., Proc. 17th ICRC, 9, 146 (1981)
[3] A. Buffington et al., Ap.J., 248, 1179 (1981)
[4] B.G. Mauger and S.A. Stephens, Proc. 18th ICRC (Bangalore), 9, 171 (1983)
[5] S.A. Stephens and B.G. Mauger, Proc. 19th Rencentre de Moriond Astrophysics Meeting, p.217 (1984); Ap.Sp.Sci. (1985) in press.
[6] G.D. Badhwar and S.A. Stephens, Proc. 15th ICRC, 11, 149 (1977)
[7] S.A. Stephens, Proc. 17th ICRC (Paris), 2, 214 (1981)
[8] D. Muller and J. Tang, Proc. 18th ICRC (Bangalore), 2, 60 (1983)
[9] J. Nishimura et al., Ap. J., 238, 94 (1980)
[10] R.L. Golden et al., Ap. J., 287, 622 (1984)
[11] R.L. Golden et al., this Conference
[12] A. Buffington et al., Ap. J., 199, 669 (1975)
[13] S.A. Stephens, This Conference, OG 2.5-3

# THE ELECTRON SPECTRA IN THE SYNCHROTRON NEBULA OF THE SUPERNOVA REMNANT G 29.7 - 0.3

L. Koch-Miramond and R.Rocchia, Service d'Astrophysique, Saclay, France
F.A. Jansen and R.Braun, Huyghens Laboratory, Leiden,
R.H. Becker, University of California, Davis

1. Introduction. The current observational situation concerning the presence or absence of synchrotron nebulae, presumably fed by an active pulsar (PSR) in the central region of supernova remnants (SNRs) is evolving rapidly, thanks to the high resolution maps obtained with the Very Large Array (VLA) in the radio range and with the Einstein and Exosat observatories in the X-ray range. The larger spectral coverage (0,04 - 20 keV) of Exosat and its spectro-photometric capabilities are decisive in this respect. Observations in the whole range of frequencies between radio and X-rays would help determining the range of synchrotron frequencies and hence of injected particle energies, establish the physical size of the nebula and advance our understanding of particle acceleration by PSRs.

The remnant G 29.7 - 0.3 has been studied intensively. The radio properties has been discussed by (1), (2), (3). High resolution maps obtained with the VLA show two spectrally distinct components, a flat spectrum core surrounded by a shell. The central component is 25% linearly polarized and has a centrally peaked radio brightness distribution characteristic of Crab-like remnants. While not visible at optical wavelengths due to the high visual absorption on the line of sight, G 29.7 - 0.3 is a very bright object in X-rays (2) (3), X-ray diffuse emission coïncident with the radio core was observed with the Einstein Observatory. For a distance of 19 kpc the estimated luminosity of the nebula was $\sim 4\ 10^{36}$ erg $s^{-1}$ in the 0.2 - 4.0 keV range and its linear diameter $\sim 2$ pc. The present paper shows Exosat results obtained with the imaging instrument (CMA) and the medium energy proportional counters (ME). Assuming that the featureless power-law spectrum obtained in the 2 to 10 keV range is synchrotron radiation from relativistic electrons, one derives constraints on magnetic field strength and age of the nebula. The energy spectra of the electrons responsible for the emission in the radio and X-ray ranges are discussed.

2. Results of the Exosat Observation. G 29.7 - 0.3 was observed on 29 August 1984, for $4\ 10^4$ s with the Exosat imaging instrument (CMA) and the medium energy proportional counters (ME) (4). The source was not seen in the CMA, the $3\sigma$ upper limit on the counting rate being $4\ 10^{-4}\ s^{-1}$. The counting rate due to the source in the ME Argon counters half-array was $2.7\ s^{-1}$. After background subtraction the observed spectral distribution is shown on figure 1. The best fit was obtained assuming a featureless power-law spectrum $dN/dE = 1.3\ 10^{-2}\ E^{-1.77}$ photon $cm^{-2}s^{-1}\ keV^{-1}$ and an absorbing hydrogen column density of $\sim 2.3\ 10^{22}\ cm^{-2}$. A $3\sigma$ lower limit on the $N_H$ value of $\sim 3\ 10^{22}\ cm^{-2}$ has been deduced from the upper limit of the CMA counting rate. Then the consistency between the CMA and ME data imposes: $\alpha = -1.0 \pm .15$ and $N_H = (3.3 \pm .3)\ 10^{22}\ cm^{-2}$. The figure 2 shows the incident X-ray spectrum.

Search for pulsations. Regular pulsations were searched for in the ME data by performing a fast Fourier transform. No statistically significant period has been found between 32ms and $10^4$ s. The resulting upper limit of pulsed fraction in this period range is $\sim 1.5\%$.

3. Discussion. The value of $N_H$ we have deduced can be compared with the lower limit of $N_{HI} = 2\ .\ 10^{22}\ cm^{-2}$ inferred from neutral hydrogen radio absorption

measurements by (3). The incident X-ray flux from the source is $(3.8 \pm .1)\ 10^{-11}$ erg.cm$^{-2}$ s$^{-1}$ in the 2 to 10 KeV range, corresponding to an intrinsic luminosity of $2\ 10^{36}$ erg.s$^{-1}$ for a distance of 19 kpc. This large distance was estimated by (5) from the surface brightness/diameter relationship for SNRs and confirmed by the VLA results of (3). The total X-ray luminosity in the 0.1 to 10 keV range is about $5\ 10^{36}$ erg.s$^{-1}$ assuming that the same power-law holds. We assume a synchrotron nebula on the basis of our X-ray data and of the radio polarization. The emission at all wavelengths is synchrotron emission from relativistic electrons accelerated by the central stellar remnant.

Assuming that the nebula contains a uniform magnetic field H, that all particles have energy such that maximum synchrotron emission is at 1 keV and that the energy of the nebula is equally divided between relativistic electrons and magnetic field (7), one finds $H \sim 7\ 10^{-5}$ Gauss and $E_p = E_H \sim 6\ 10^{46}$ ergs, with an angular radius of the nebula of 10 arc sec. from (2). The synchrotron lifetime of the X-ray emitting electrons is then $\tau \sim 150$ years. Doing that we have ignored electrons non radiating in X-rays; if now we consider the entire electromagnetic spectrum we get $H = 2\ 10^{-4}$ G, $E_p = 1.6\ 10^{47}$ erg and $\tau$ for electrons emitting at 1 keV of 35 years. The age of the SNR has been estimated by (8) from the surface brightness $\Sigma$ at 408 MHz assuming that the dynamical evolution of the shell is described by the Sedov equation i.e. unaffected by the presence of a central pulsar, then $\Sigma = 1.25\ 10^{-15} t^{-6}$ giving t = 660 years. Hence continuous injection of energy near the center is inferred from the short synchrotron lifetime of the electrons as compared to the SNR's age.

4. Energy and spectra of the electrons. If $\nu$ is the frequency corresponding to the maximum of the synchrotron spectrum $\nu = 4.6\ 10^{-6} H\ E^2$ (9). Assuming H = H equipartition $= 2\ 10^{-4}$ G, one finds that the radio emitting electrons have energy $E \sim 10^9$ eV and the X-ray emitting electrons $E \sim 3\ 10^{13}$ eV. Since the energy spectrum of the X-ray emitting electrons is dominated by synchrotron losses the observed X-ray spectral index of $-1.0 \pm 0.15$ implies a power-law distribution of the radiating electrons with $N(E) \propto E^{-3 \pm .45}$. Because synchrotron losses steepen a continuously injected spectrum of electrons by one power the inferred injection spectrum is proportional to $E^{-2 \pm .3}$. Also there should be a break at low energies to a radiation spectrum $S_\nu \propto \nu^{-0.13 \pm .12}$ (figure 3). For the equipartition field H = $2\ 10^{-4}$ G and an age of 660 years that should occur at a frequency of about $10^{14}$ Hz. Considering the spectrum of G 29.7 - 0.3 over 9 decades in frequencies (figure 3) and taking into account the uncertainties on measured spectral indices, a break (if unique) should be expected in the frequency range $10^{12}$ to $10^{15}$ Hz encompassing the infrared range.

The radio flux of the synchrotron nebula integrated over the range $10^7$ to $10^{11}$ Hz with the same spectral index $\alpha = -0.25$, as observed around 1 GHz by (2), is $4\ 10^{33}$ erg s$^{-1}$. Then the $L_X / L_R$ ratio is $\sim 10^3$, well above the theoritical minimum of $\sim 17$ deduced from (6), who were modeling the evolution of a single power-law particle spectrum in the Crab-like SNRs. Hence a different origin for the X-ray and radio producing electrons is not required. This conclusion still marginally holds if one considers a flat radio spectrum ($\alpha = 0$, $L_X / L_R \sim 500$ and $(L_X / L_R)_{min} \sim 600$ in (6). These considerations require that the difference of spectral indices between the radio and X-ray domains is 0.5. But this difference could be as large as 1, as suggested by our X-ray observations and by (3). In that case the electron spectral distribution could be more complex and its understanding would require the knowledge of the photon spectrum in the interval between radio and X-rays. Infrared informations are much valuable from this point of view.

5. Infra-red emission. The IRAS catalogue of point and small extended sources (extension $\leq$ 1 arc min) gives at $\alpha$(1950) = 18h43m46.5s; $\delta$(1950)=-03°02'33" a source flux of 4.84 Jy at 12$\mu$ and 8.63 Jy at 24$\mu$ (10). The corresponding points shown on figure 3 lie 2 decades above the extrapolated radio emission but the infra-red source does not coïncide with the central synchrotron nebula and lies closer to the brightest shell emission region A. So these data cannot be confidently used to constrain the electron spectrum. More work on the infra-red diffuse emission of this region is required.

6. Conclusions. The great similarity of the physical properties of G 29.7 -0.3 and of the three synchrotron nebulae containing a compact object observed to pulse in X-rays (11), (12) and Table 1, makes G 29.7 - 0.3 a very promising candidate for further search for pulsed emission. Further observations at infra-red wavelengths might reveal the break(s) in the emitted spectrum expected from the radio and X-ray power-law indices and give us more information on the production of the electron populations responsible for the emission of the nebula (13, (14), (15).

7. Acknowledgements. We thank the Exosat Observatory team at ESOC for their support during the observation and real-time reduction of the data, A.Peacock and collaborators at ESTEC for their help on ME data analysis and J.Jorrand at Saclay.

References

1. Becker,R.H., Kundu, M.R., 1976, Ap.J. 204, 427.
2. Becker, R.H., Helfand, D.J., Szymkowiak, A.E., 1983, Ap.J.Lett. 268,L93.
3. Becker, R.H., Helfand, D.J., 1984, Ap.J. 283, 154.
4. Koch-Miramond, L.,Rocchia, R., et al., 1984, 18th ESLAB Symposium on X-ray astronomy, in press.
5. Milne, D.K., 1979, Australian J. Phys. 32, 83.
6. Reynolds, S.P., Chanan, G.A., 1984, Ap.J. 281, 673.
7. Pacholczyck, A.G., 1970, Radio Astrophysics, Freeman
8. Clark, D.H., Caswell, J.L., 1976. M.N.R.A.S. 174, 267.
9. Ginzburg, V.L., Syrovatskii, S.I., 1964, The Origin of Cosmic Rays, Pergamon.
10. Perault, M., 1985, Private communication
11. Seward, F.D., 1983, in Supernova Remnants and their X-ray emission, Symposium IAU 101, ed. J.Danziger and P. Gorenstein, p.405.
12. Seward, F.D., Harnden Jr, F.R., Helfand, D.J., 1984, Ap.J.Letters, 287,L19.
13. Pacini, F., Salvati, M., 1973, Ap.J. 186, 249.
14. Reynolds, S.P., Chevalier, R.A., 1984, Ap.J. 278, 630.
15. Reynolds, S.P., 1985, Ap.J. 291, 155.

**TABLE 1. PROPERTIES OF DIFFUSE SYNCHROTRON NEBULAE**

| Names | Distance kpc | Size pc | Lx erg $s^{-1}$ | H * Gauss | Ep * ergs | $\tau$ * Years |
|---|---|---|---|---|---|---|
| G 184.6-5.8 (Crab) | 2.0 | 0.6 | $2\ 10^{37}$ | $2\ 10^{-4}$ | $2\ 10^{46}$ | 30 |
| G 29.7-0.3 (KES 75) | 19 | 1.8 | $5\ 10^{36}$ | $7\ 10^{-5}$ | $6\ 10^{46}$ | 150 |
| LMC 0540-693 | 55 | 1 | $1\ 10^{37}$ | $2\ 10^{-4}$ | $1\ 10^{47}$ | 33 |
| G 320.4-1.2 (MSH15-52) | 4.2 | 6.4 | $1.6\ 10^{35}$ | $9\ 10^{-6}$ | $2\ 10^{46}$ | $410^3$ |

* Based on the consideration of X-ray emitting electrons only (11).

OG 6.2-10

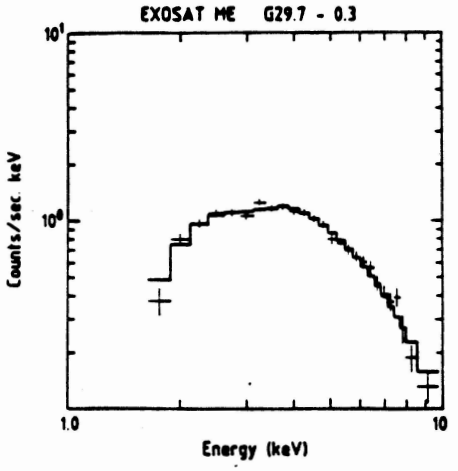


Figure 1: The observed ME spectrum of G 29.7-0.3 (full array). The thin bars represent the observed data points with $\pm$ 1 $\sigma$ errors. The thick histogram is the predicted distribution for a power-law spectrum with energy index $\alpha = -.77$ and an absorbing column density of $N_H = 2.3.10^{22} cm^{-2}$.

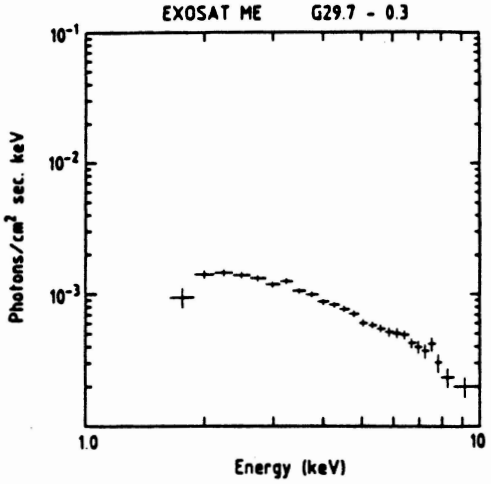


Figure 2: The incident photon spectrum of G 29.7-0.3 as deduced from the EXOSAT ME data.

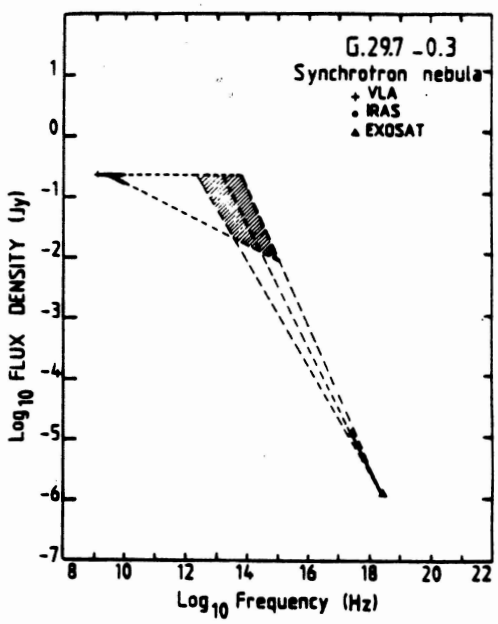


Figure 3: Emission spectrum of the synchrotron nebula in G 29.7-0.3 over 9 decades in frequency. Radio spectrum from (1,2,3), IRAS flux might be due to shell emission, X-ray spectrum from the present work. A spectral break is expected in the shaded area.

# RELATIVISTIC ELECTRON IN CURVED MAGNETIC FIELDS

Shuyuan An

Physics Department, Beijing Teachers College

China

## ABSTRACT

Making use of the perturbation method based on the nonlinear differential equation theory, the present work investigates the classical motion of a relativistic electron in a class of curved magnetic fields which may be written as $\vec{B}=\vec{B}(0,B_\varphi,0)$ in cylindrical coordinates $(R,\varphi,Z)$. Under general astrophysical conditions the author derives the analytical expressions of the motion orbit, pitch angle etc. of the electron in their dependence upon parameters characterizing the magnetic field and electron. The effects of non-zero curvature of magnetic field lines on the motion of electrons and applicabilities of these results to astrophysics are also discussed.

## INTRODUCTION

In astrophysics, some curved magnetic fields with sufficiently small field gradients may approximately be written in a local coordinate system as

$$\vec{B}=\vec{B}(0,B_\varphi,0), \qquad B_\varphi = B_0 > 0, \tag{1}$$

where $B_0$ is a constant, and $(R,\varphi,Z)$ denote the cylindrical coordinates. The classical motion of a relativistic electron of charge $-e$ in the field (1) can be exactly solved by the topological method, which was investigated by the author in some detail.[1] The purpose of the present paper is to find further the analytical solution for the motion, and then to extend the results to more general magnetic fields. In the following treatment, the influence of the radiation damping will be neglected.

## RESULTS

By virtue of the assumed ( without loss of generality ) initial position and velocity

$$\vec{r}\Big|_{t=0} = \vec{r}_0(R_0,0,0), \qquad \vec{v}\Big|_{t=0} = \vec{v}_0(v_{R0},v_{\varphi 0},v_{z0}), \tag{2}$$

the first integral of the equation of motion for a relativistic electron in the field (1) may be put into the form

$$d^2R/dt^2+\omega_b^2R = R_0^2v_{\varphi 0}^2/R^3 +\omega_b^2(R_0+v_{z0}/\omega_b), \tag{3}$$

$$R^2d\varphi/dt = R_0v_{\varphi 0}, \tag{4}$$

$$dz/dt = -\omega_b(R-R_0-v_{z0}/\omega_b), \tag{5}$$

in which $\omega_b = eB_0/\gamma mc$ is the relativistic cyclotron frequency, $\gamma$ the Lorentz factor, and $R_0$ the curvature radius of the field line passing through the initial point. Using the perturbation method based on Poincare' theory[2] to solve the nonlinear autonomous equations (3)-(5), with the initial conditions (2) and

$$\mu \equiv \beta c/\omega_b R_0 \ll 1, \qquad \beta_{\perp 0} \lesssim |\beta_{/\!/0}|, \tag{6}$$

where

$$\beta = v/c, \qquad \beta_{\perp 0} = (\beta_{R0}^2+\beta_{z0}^2)^{1/2}, \qquad \beta_{/\!/0} = \beta_{\varphi 0},$$

a condition that is adequately met in astrophysics, we get the equations of electron trajectory which, up to and including of the second order in $\mu$, are

$$(R/R_0)-1 \doteq \mu\left[(\beta_{z0}/\beta)+\mu(\beta_{/\!/0}/\beta)^2\right](1-\cos\omega t)+\mu(\beta_{R0}/\beta)\sin\omega t, \tag{7}$$

$$(z-u_c t)/R_0 \doteq \mu\left[(\beta_{z0}/\beta)+\mu(\beta_{/\!/0}/\beta)^2\right]\sin\omega t-\mu(\beta_{R0}/\beta)(1-\cos\omega t), \tag{8}$$

$$\varphi-(1-2\mu\beta_{z0}/\beta)\omega_{/\!/0}t \doteq 2\mu^2(\beta_{/\!/0}/\beta)\left[(\beta_{z0}/\beta)\sin\omega t-(\beta_{R0}/\beta)(1-\cos\omega t)\right], \tag{9}$$

where

$$\omega \doteq (1+3\mu^2\beta_{/\!/0}^2/2\beta^2)\,\omega_b, \qquad u_c \doteq -\mu^2\omega_b R_0\beta_{/\!/0}^2/\beta^2, \qquad \omega_{/\!/0}=v_{\varphi 0}/R_0.$$

On differentiating (3), (4) and (5) with respect to the time, one can obtain further the analytical expression of the electron velocity. It is apparent from (7)-(9) that the motion of the electron in the field (1) may be represented as the superposition of both the helical motion with gyration radius

$$\rho \doteq \mu\left[\frac{\beta_{\perp 0}^2}{\beta^2} + 2\mu\frac{\beta_{z0}}{\beta}\cdot\frac{\beta_{/\!/0}^2-\beta_{\perp 0}^2}{\beta^2} + \mu^2\left(\frac{\beta_{/\!/0}^4}{\beta^4} + \frac{\beta_{z0}^2}{\beta^2}\cdot\frac{\beta_{\perp 0}^2-2\beta_{/\!/0}^2}{\beta^2}\right)\right]^{1/2},$$

and the curvature drift motion with drift velocity $u_c$.

The pitch angle of an electron moving in a curved magnetic field, $\psi$, and its mean value $\bar{\psi}$, defined as

$$\bar{\psi} = \sin^{-1}\left[\frac{1}{2\pi}\int_0^{2\pi}\sin^2\psi\, d(\omega t)\right]^{1/2},$$

are customarily calculated in the reference frame where the drift velocity of the electron vanishes. Following this convention, the pitch angle for the electron in the field (1) is found to be

$$\psi \doteq \sin^{-1}\frac{\beta_{\perp 0}}{\beta}\left[1+\mu\frac{\beta_{z0}\beta_{//0}^2}{\beta\beta_{\perp 0}^2}\left(1+\frac{\beta_{z0}^2}{2\beta^2}\right)-\mu\frac{\beta_{//0}^2}{\beta^2}\left(\frac{\beta_{z0}}{\beta}\cos\omega t-\frac{\beta_{R0}}{\beta}\sin\omega t\right)\right], \tag{10}$$

$$\bar{\psi} \doteq \sin^{-1}(\beta_{\perp 0}/\beta)\left[1+\mu\left(\beta_{z0}\beta_{//0}^2/\beta\beta_{\perp 0}^2\right)\left(1+\beta_{z0}^2/2\beta^2\right)\right]. \tag{11}$$

In particular, for an electron in typical curvature motion, corresponding to $\beta_{\perp 0} \ll |\beta_{//0}|$, the eqs. (10) and (11) reduce to

$$\psi \doteq \bar{\psi} \doteq \left(\mu^2+2\mu\beta_{z0}/\beta+\beta_{\perp 0}^2/\beta^2\right)^{1/2}. \tag{12}$$

## DISCUSSION

In topics concerned with the properties of the motion and radiation of a relativistic electron in a magnetic field what is taken into account is usually the influence of radiation damping on the motion and pitch angle (the so-called "radiation compression")[3], and sometimes other effects like the magnetic lens. However, our results show that for a relativistic electron in typical curvature motion the influence of the curvature of magnetic field lines is also important.

The latter influence will become quite clear in the special case $v_{\perp 0}=0$ associated with primary particles flying out along magnetic field lines from the surface of pulsars. In this case, from (12), $\psi \doteq \bar{\psi} \doteq \mu$. This indicates that owing to the effect of the non-zero curvature of field lines, the initial motion of the electron, even if the initial transverse velocity vanishes, can not generally be maintained, but have to develop into the helical motion with the pitch angle $\psi \doteq \mu$ and the gyration radius $\rho \doteq \mu^2$, plus the curvature drift. Another special case occurs in $v_{\perp 0}=v_{z0}=-\mu v\beta_{//0}^2/\beta^2 \doteq -\mu v$ for which the pitch angle of the electron is strictly equal to zero.

It can be expected that these results should be conducive to calculating or predicting synchro-curvature radiations from some nonthermal sources, and could exert an influence on the process of the electron momentum distribution "one-dimensionalization" along curved magnetic field lines due to radiation damping. Furthermore, when the effect of radiation damping is taken into account, it may be easily deduced [3] that, as the result of the "radiation compression", a relativistic electron in the field (1) should move approximately along Cornu spiral in the guiding center frame, and tend finally towards the limiting motion corresponding to the latter special case mentioned above.

So far we have found the analytical solutions for a relativistic electron moving in the field (1). Let us consider now the class of curved magnetic fields

$$\vec{B} = \vec{B}(0,\ B_\varphi,\ 0), \qquad B_\varphi/B_0 = (R/R_0)^N \tag{13}$$

(where N is a real constant), which is more general than the field (1) and reduces to (1) at N=0. Most of commen curved magnetic fields with axial symmetry in astrophysics such as the dipole magnetic field may be expressed by (13) in a local frame of refrence if only the magnitude of the field gradient along magnetic field lines is negligibly small. To maintain the fields (13), there must be electric currents flowing in the direction parallel to $\hat{z}$, the density $\vec{j}$ of which is given by

$$\vec{J}/j_0 = (R/R_0)^{N-1}\,\hat{e}_z, \qquad j_0 = (N+1)cB_0/4\pi R_0, \tag{14}$$

where $j_0$ denotes the current density at the initial point. In application, one can select a confiquration of magnetic field from (13), (14) so that it is appropriate for the considered astronomical object. It may be verified that under the condition

$$\begin{aligned} &|N| \ll \mu^{-1}, && \text{for } \beta_{\perp 0} \sim |\beta_{\parallel 0}|, \\ &|N| \ll (\mu|\beta_{z0}|/\beta + \mu^2)^{-1}, && \text{for } \beta_{\perp 0} \ll |\beta_{\parallel 0}| \end{aligned} \tag{15}$$

preceding results based on the field (1), provided $\omega \doteq \omega_b$, will continue to be valid for the fields (13).

ACKNOWLEDGEMENT

The author is grateful to Prof. Liaofu Luo for useful discussions.

REFERENCES

1. An Shuyuan, (1984), Proc. National Cosmic Ray and High-Energy Astrophysics Conference, Chongqing, China, unpublished.

2. Hayashi, C., (1964) , Nonlinear Oscillations in Physical Systems, McGraw-Hill, New York.

3. Suvorov, E. V. et. al., (1973), Astrophys. Space Sci. 23, P189.

# AUTHOR INDEX

## BIBLIOGRAPHIC DATA SHEET

| 1. Report No. | 2. Government Accession No. | 3. Recipient's Catalog No. |
|---|---|---|
| NASA CP-2376 Volume 2 | | |

| 4. Title and Subtitle | 5. Report Date |
|---|---|
| 19th International Cosmic Ray Conference<br>Conference Papers | August 1985 |
| | 6. Performing Organization Code<br>665 |
| 7. Author(s)<br>Frank C. Jones, compiler | 8. Performing Organization Report No. |
| 9. Performing Organization Name and Address<br>Laboratory for High Energy Astrophysics<br>Goddard Space Flight Center<br>Greenbelt, MD 20771 | 10. Work Unit No. |
| | 11. Contract or Grant No. |
| | 13. Type of Report and Period Covered<br>Conference Publication |
| 12. Sponsoring Agency Name and Address<br>National Aeronautics and Space Administration<br>Washington, D. C. 20546 | 14. Sponsoring Agency Code |

15. Supplementary Notes

16. Abstract

These volumes contain papers submitted for presentation at the 19th International Cosmic Ray Conference, held on the campus of the University of California, San Diego in La Jolla, CA., August 11-23, 1985. The conference is held every other year. The present volume contains papers with Paper Codes OG 4.1 through OG 6.2 and dealt with the elemental and isotopic composition of cosmic rays, ultra heavy cosmic rays, cosmic rays with energies above 1 TeV, cosmic-ray anisotropy, and antiproton.

| 17. Key Words (Selected by Author(s)) | 18. Distribution Statement |
|---|---|
| chemical composition, isotopic composition, isotopic composition, anisotropy, cosmic rays, anti-protons, electrons, positrons, ultra-heavy cosmic rays | Unclassified - Unlimited<br>Subject Category - 93 |

| 19. Security Classif. (of this report) | 20. Security Classif. (of this page) | 21. No. of Pages | 22. Price* |
|---|---|---|---|
| Unclassified | Unclassified | | |

*For sale by the National Technical Information Service, Springfield, Virginia

National Aeronautics and
Space Administration

**Goddard Space Flight Center**
Greenbelt, Maryland 20771